SCHOLARLY PUBLICATIONS

A CURRENT AWARENESS BULLETIN
OF RESEARCH OUTPUT

@DTU

(18th Edition)

JUNE 2014

BY: CENTRAL LIBRARY

DELHI TECHNOLOGICAL UNIVERSITY
(FORMERLY *DELHI COLLEGE OF ENGINEERING)*
GOVT. OF N.C.T. OF DELHI
SHAHBAD DAULATPUR, MAIN BAWANA ROAD
DELHI 110042

PREFACE

This is the Eighteenth Issue of Current Awareness Bulletin started by Delhi Technological University, Central Library. The aim of the bulletin is to compile, preserve and disseminate information published by the faculty, students and alumni for mutual benefits. The bulletin also aims to propagate the intellectual contribution of Delhi Technological University (DTU) as a whole to the academia.

The bulletin contains information resources available in the internet in the form of articles, reports, presentations published in international journals, websites, etc. by the faculty and students of DTU. The publications of faculty and student which are not covered in this bulletin may be because of the reason that the full text either was not accessible or could not be searched by the search engine used by the library for this purpose.

The learned faculty and students are requested to provide their uncovered publications to the library either through email or in CD, etc to make the bulletin more comprehensive.

This issue contains the information published during June 2014. The arrangement of the contents is alphabetical. The full text of the article which is either subscribed by the university or available in the web is provided in this bulletin.

Central Library

CONTENTS

1. A Study on the Effect of Cosolvent Addition Pathway on the Optical and Morphological Properties of P3HT: PCBM Composite Films, ***SARITA S. NAIR, *D. KUMAR,** Department of Applied Chemistry & Polymer Technology, Delhi Technological University, and AMITAVA MAJUMDAR

2. Advanced Security Metric Model : ASM, ***@Manju Khari***, Divya Nigam

3. An efficient triple-tail cell based PFSCLD latch ***Neeta Pandey, *Kirti Gupta,** Department of ECE, Delhi Technological University and ManeeshaGupta

4. Analysis of the skilled work force effect on the logistics performance index—case study from India, *Amrita Jhawar, ***S. K. Garg*** and ***Shikha N. Khera***, Delhi School of Management, Delhi Technological University

5. Anisotropically Functionalized Carbon Nanotube Array Based Hygroscopic Scaffolds, Sehmus Ozden, Liehui Ge, Tharangattu N. Narayanan, Amelia H. C. Hart, Hyunseung Yang, ***Srividya Sridhar***, Department of Physics, Delhi Technological University, Bawana Road, Delhi, 110042, India, Robert Vajtai and Pulickel M. Ajayan

6. CONVERSION OF WASTE COOKING OIL INTO BIODIESEL, S. S. Kachhwaha and ***Amit Pal***, Department of Mechanical Engineering

7. Comparative Study on Load Balancing Techniques in Cloud Computing, ***N. S. Raghava*** and ***Deepti Singh***, Department of Information Technology, Delhi Technological University, Delhi, India

8. Decision Table based Model & implementation for Automatic prevention of Unauthorized Database Transactions by Trusted Database Users, ***$Rohit Jain,*** Computer Science and Engineering, DTU

9. Dynamic Growth of Hidden-Layer Neurons Using the Non-extensive Entropy, ***Seba Susan*** and ***Mayank Dwivedi***, Department of Information Technology, DTU

10. Effect of Dust Grain Parameters on Ion Beam Driven Ion Cyclotron Waves in a Magnetized Plasma, Ved Prakash, Suresh C. Sharma, Vijayshri, and ***Ruby Gupta***, Department of Applied Physics, Delhi Technological University

11. Electroactive Prussian Blue Encapsulated Iron Oxide Nanostructures for Mediator-Free Cholesterol Estimation, ***Rachna Sharma, ***R. K. Sinha***, Department of Applied Physics, Delhi Technological University and Ved Varun Agrawal

12. Flow Visualization around Perforated Circular Finned Tubes by CFD., ***£Yogesh Pal, ***Naushad Ahmad Ansari,*** and ***M. Zunaid***, Department of Mechanical Engineering, Delhi Technological University, Delhi, India

13. Friction Stir Processing of Aluminum alloys for Defense Applications, ***V. Jeganathan Arulmoni*** and ***R. S. Mishra***, Department of Mechanical & Production Engineering

14. Friedmann model with viscous cosmology in modified f(R, T) gravity theory, ***C. P. Singh***, and ***Pankaj Kumar***, Department of Applied Mathematics, DTU

15. High Gain Patch Antenna for WBAN Applications, ***N.S. Raghava***, Department of Electronics and Communication Engineering, Delhi Technological University, Asok De, Rishik Bazaz, Pushkar Arora, ***Aman Samaiyar*** Department of EEE, Delhi Technological University and Deepender Dabas

16. IMPROVED SYNTHESIS OF INDOLYLCHALCONES AND 2-AMINO-3-CYANO-4-INDOLYL-6-ARYLPYRIDINES USING ULTRASONIC IRRADIATION, ***Anshu Jaina, ***Yogita Madanb,*** and ***Davendra Kumara***, Department of Applied Chemistry and Polymer Technology

17. Indian Energy Crises and Biodiesel as Renewable Alternative Fuel, Manish Jain, ***Shashank Mohan*** and ***Amit Pal***, Department of Mechanical Engineering, DTU

18. INSURANCE SECTOR IN INDIA: A CASE ANALYSIS, ***Priyanka Chaudhary***, Delhi School of Management, Delhi Technological University

19. Manufacturingbloodexvivo:afuturisticapproachtodealwiththesupplyandsafetyconcerns, KohichiroTsuji, Ramesh Chandra, ***VimalK.Singh, ***AbhishekSaini***, and ***P.B.Sharma*** Stem Cell Research Laboratory, Department of Biotechnology, Delhi Technological University

20. Modeling carbon nanotube growth on the catalyst-substrate surface subjected to reactive plasma, ***Aarti Tewari*** and ***Suresh C. Sharma***, Department of Applied Physics

21. Multi-Response Optimization of Manual Material Handling Tasks through Utility Concept, Jaswinder Singh, P. Kalra and ***R.S. Walia***, Department of Mechanical and Production Engineering, Delhi Technological University

22. Optimal Switch Placement in Radial Distribution System Using GA and PSO, ***$Ashish Ranjan*** and ***J N Rai***

23. Optimization of CCGT power plant and performance analysis using MATLAB/Simulink with actual operational data, Naimul Hasan, ***Jitendra Nath Rai***, Department of Electrical Engineering and ***Bharat Bhushan Arora***, Department of Mechanical Engineering, Delhi Technological University

24. PERFORMANCE AND EMISSIONS ANALYSIS OF ETHANOL-DIESEL LENDS, ***Amit Pal, ***Prem Kumar, ***S Maji*** and ***S S Kachhawaha***, Delhi Technological University

25. Performance of Low-Cost Adsorbents for the Removal of fluoride ions – An overview ***$Suman Mann*** and ***Dr.Anubha Mandal***

26. Protein functionalized Pt nanoparticles-conducting polymer nanocomposite film: Characterization and immunosensor application, Avanish K. Srivastava, Ashok Mulchandani, Rajesh, ***Sujeet K. Mishra*** and ***Devendra Kumar,*** Department of Applied Chemistry

27. QoS Provisioning in Channel Allocation Strategy in Cognitive Radio Using Fuzzy Logic, Harsh K Verma, Maninder Jeet Kaur, and ***Moin Uddin***

28. Spectral Characterization of Sm3+ ions doped Oxy-fluoroborate Glasses for Visible Orange Luminescent Applications, Sk. Mahamuda, K. Swapna, M. Venkateswarlu, Suman Latha Shakya, G. Vijaya Prakash and ***A. Srinivasa Rao***, Applied Physics

29. Supercooling transition in phase separated manganite thin films: An electrical transport study, Pawan Kumar, P. K. Siwach, H. K. Singh, ***Pawan Kumar Tyagi** and **Sandeep Singh*, Department of Applied Physics

30. The Effect of Recession on the Buying Behavior of Consumers in New Delhi during the Economic Slowdown of 2013, Devika Singh and ***Saurabh Kumar***, Department of Mechanical Engineering

31. Thermodynamic Performance Evaluation of Multi-Evaporators single Compressor and single Expansion Valve and Liquid Vapour Heat Exchanger in Vapour Compression Refrigeration systems using Thirteen Ecofriendly Refrigerants for Reducing Global Warming and Ozone Depletion, ***R. S. Mishra***, Mechanical & Production Engineering

***Faculty @Research Scholar $PG Scholar #Alumni**
£Undergraduate Student ~ Ex Faculty <Ex Research Scholar
! Teaching-cum-Research Fellow

A Study on the Effect of Cosolvent Addition Pathway on the Optical and Morphological Properties of P3HT: PCBM Composite Films

SARITA S. NAIR, D. KUMAR

Department of Applied Chemistry & Polymer Technology, Delhi Technological University, Delhi 110042, India

AMITAVA MAJUMDAR

Moserbaer India Ltd., Udyog Vihar, Greater Noida 201 306, India

Correspondence to: D. Kumar; e-mail: dkumar@dce.ac.in; drdkumar@yahoo.co.uk.

Received: March 14, 2014
Accepted: May 26, 2014

ABSTRACT: In this work, we present an exhaustive study on the effect of a cosolvent addition pathway on the optical, structural, and morphological characteristics of poly(3-hexyl thiophene) (P3HT): [6, 6]-phenyl C_{61}-butyric acid methyl ester (PCBM) composite films. Our recommended pathway of cosolvent addition has shown to benefit the composite film by forming more crystallized and ordered P3HT polymer domains on the film surface as revealed by the UV–vis absorption, grazing incidence X-ray diffraction (GI-XRD), and atomic force microscopy measurements. GI-XRD measurements that were carried out at three grazing incidence angles (0.11°, 0.13°, and 0.3°) also substantiate a more prominent upright concentration gradient of the film processed through the modified method. The contact angle measurement reveals accumulation of more P3HT crystallites at the surface of co-solvent modified films. A highly quenched photoluminescence signal precise phase separation between the blended components of the modified film, promoting exciton dissociation at the donor–acceptor interfaces during photoinduced excitations. © 2014 Wiley Periodicals, Inc. Adv Polym Technol 2014, 00, 21445; View this article online at wileyonlinelibrary.com. DOI 10.1002/adv.21445

KEY WORDS: Aggregation, Concentration gradient, P3HT: PCBM, Self-assembly, Solvent effects

Introduction

While envisioning the framework for various potential technological applications such as polymer solar cells, field effect transistors, or organic light emitting diodes, a conjugated polymer as electron donor and soluble fullerene as electron acceptor system is most sought after.[1,2] Extraordinary interest shown in this polymer donor–acceptor mixture is due to the technical viability that this mixture presents large-scale fabrication by simple solution processing using a number of techniques such as spin coating, inkjet printing, and roller casting. A soluble fullerene such as [6, 6]-phenyl C_{61}-butyric acid methyl ester (PCBM) is the foremost choice for the electron-accepting component owing to its higher electron affinity. Although among the conjugated donor polymer with electronic and structural properties similar to semiconductors, a poly(3-hexyl thiophene) (P3HT) polymer is most sought after material.[3,4] Considering that individually these components are best available materials to date for assorted relevance, integration of these two potential components results in all the more interesting structural, electrical, and optical properties that can be exploited for the advancement of existing technologies.[5]

Numerous researchers have suggested many theories to redefine the fundamental electronic interactions among the components of the P3HT: PCBM system and studied the effects of component ratio, thermal annealing, solvent, and processing conditions on the performance of the devices made thereof using the P3HT-PCBM composites.[6,7] The composite (P3HT-PCBM) film's morphology and structure are shown to affect the performance of the device incorporating this film. Furthermore, spin-casted P3HT: PCBM films, in particular, present the advantage of modifying the components structure and film morphology by varying the preparing solvent, spin speed, and many other processing parameters.[8] We intend to comprehend properties of the P3HT: PCBM composite films with relevance to energy conversion application through solar cell technology. In solar cell technology, the P3HT: PCBM composite film has a very complex part to play. Even though the real morphology of the P3HT: PCBM film will be rather different in the model solar device, as it consists of a structure with a succession of various layers, depending on the surface energy, work function, and morphology of the underlying and overlying layers. However, a comprehensive study of the internal structure of the P3HT: PCBM film is fundamental prior to its use in any technological application. The most favorable morphology for this composite mixture depends on two provisions: First is the ordered structure within the individual P3HT

© 2014 Wiley Periodicals, Inc.

(donor or P-type) and PCBM (acceptor or N-type) component at the outset, which is critical for photon absorption and carrier mobility; and second is the well-controlled interface between the two components, which is required for efficient photoinduced exciton dissociation.[9] The P3HT: PCBM film modification has been carried out many times utilizing thermal annealing, solvent additives, and so on by a number of researchers.[10] However, the solvent–cosolvent mixture method has been more frequently used to modify the morphology of P3HT: PCBM thin films.[11] Many permutations and combinations of solvent mixtures have been practiced with the aim of the best possible composite morphology. This solvent mixture method works by solubilizing one component of the mixture by giving space to the other component to crystallize without any interference.[12] Though these efforts have proved somewhat successful, however these organic thin films are still far from the practical use of silicon technology in energy harvesting.

In line with the ongoing studies, we considered a well-organized growth of the P3HT: PCBM film by a way of the cosolvent addition to a P3HT: PCBM spin-coating solution for preferential crystallization of P3HT, even before the spin-coating operation for composite film preparation. Since the presence of amorphous PCBM aggregates is known to affect crystallization of P3HT donor polymer, in our reworked method we focused on how to diminish the influence of PCBM during P3HT crystallization by first adding the cosolvent to a P3HT only solution in a good solvent.[13] And after best possible crystallization of P3HT in the solvent–nonsolvent mixture, subsequent mixing of the PCBM solution prepared in a good solvent to the above solution was completed. To evaluate the effect of the cosolvent addition pathway on composite films morphology, we prepared films without any cosolvent and also the P3HT: PCBM films prepared with a cosolvent directly added to a solution of P3HT and PCBM composite in a good solvent.

Experimental

MATERIALS

P3HT polymer and PCBM were procured from Sigma Aldrich (St. Louis, MO, USA). Solvents 1,2 *ortho*-dichlorobenzene (*o*-DCB) and cyclohexanone (CHN) of analytical reagent grade were also procured from Sigma Aldrich. Glass substrates of sizes 5 × 5 cm were obtained from Moserbaer India.

METHODS

Preparation of P3HT-PCBM Films

Glass substrates chosen for fabrication were cleaned prior to the film production via ultrasonication for 20 min each in a boiling soap solution, deionized water, acetone, and isopropanol followed by drying with nitrogen and 26 min of UV–ozone exposure. For P3HT: PCBM composite film fabrication, 18.7 mg P3HT and 11.3 mg PCBM (1:0.6 weight ratio) were dissolved in 1 mL of *o*-DCB by stirring overnight at 50°C, yielding a solution with a total concentration of 30 mg/mL. After that, a P3HT-PCBM composite layer was spin coated at 500 rpm over the glass substrate with the prepared solution. Substrates were subsequently annealed at 85°C for 30 min in nitrogen atmosphere to evaporate the remaining solvent.

To study in detail the effect of the cosolvent addition pathway on the preparation of P3HT: PCBM composite film, two distinct methods were used to prepare spin-coating solutions and a comparison has been made between the two methods. The CHN solvent with a boiling point of 155.6°C was employed as a cosolvent for the pertinent study. The solution was stirred for 2 h in nitrogen atmosphere after cosolvent addition. The preference was given to the CHN cosolvent on account of its solubility index (P3HT solubility $S_{P3HT} = 0.2$ mg/mL and PCBM solubility $S_{PCBM} = 23.6$ mg/mL) that signifies more solubility to PCBM than P3HT chains. So, the addition of CHN (a marginal solvent for P3HT) promotes preferential crystallization of P3HT in the precursor solution. For each of these modifications, 5% volume of the cosolvent was added. A higher concentration of marginal cosolvent (>5%) promotes gel formation in a precursor solution over a period of time (after 2 h) at room temperature. This increase in the viscosity and darkening of color of solution with marginal cosolvent addition correlates with the increasing nondissolved P3HT crystallite portions in the precursor solution. Again, when the cosolvent concentration was less than 5%, changes in the film properties were insignificant. For convenience, we named films prepared via two methods as blended (BLND) (for films prepared from a solution with CHN added to the P3HT: PCBM mixture in the *o*-DCB solvent and mixed for 2 h prior to coating) and individual (i.e., individually mixed, for films prepared from solutions with first CHN added into a P3HT only solution in *o*-DCB, mixed for 2 h, and successive mixing of PCBM solution in *o*-DCB to the above-mentioned solution and again mixing the same for 10 min before coating). For comparison, we also prepared films from solutions without any cosolvent addition and named it as a conventional film.

MEASUREMENTS

The UV–vis absorption measurements ranging from 400 to 800 nm were performed using a Perkin Elmer Lambda 35 UV–vis spectrophotometer. Surface morphology of the films was represented using an atomic force microscope (AFM), VEECO DI-3100, with nanoscope (III) in the tapping mode. Grazing incidence X-ray diffraction (GI-XRD) measurements were made at three grazing incidence angles 0.11°, 0.13°, and 0.3° with a Rigaku ultima IV X-ray diffractometer (employing Cu Kα radiation). Contact angle measurements were carried out on the Drop Shape Analysis System (model DSA10MK2 from Kruss, Hamburg, Germany). Contact angle measurements using the sessile drop method were employed to evaluate the hydrophobic/hydrophilic nature of the surface. A photograph of the drop placed on the P3HT-PCBM–coated glass substrate surface was taken using a video camera, and the image-analysis system analyzed the contact-angle (θ), based on the shape profile of the drop.

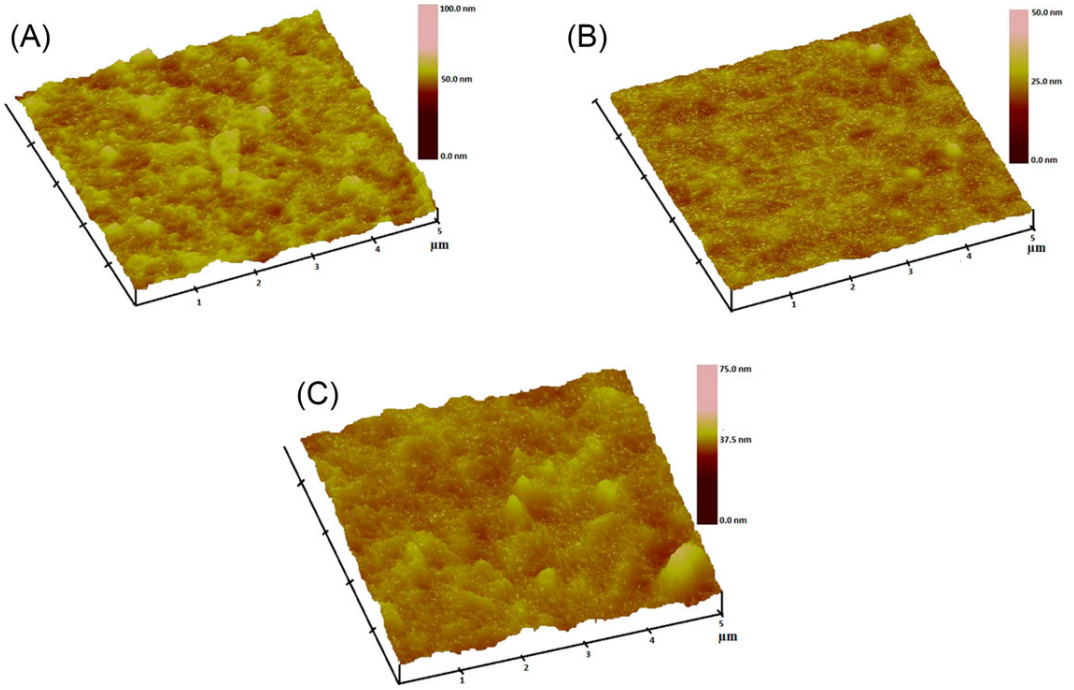

FIGURE 1. 3D AFM images of (5 ×5 μm) P3HT: PCBM blend films spin casted of (A) conventional solution, (B) individually mixed CHN added solution, and (C) BLND CHN addition approaches.

Results and Discussion

MORPHOLOGICAL CHARACTERISTICS

The morphological characteristics of P3HT: PCBM composite films were analyzed using the tapping mode AFM. Figure 1 shows the three-dimensional (3D) AFM images of the conventional, BLND cosolvent modified and individually mixed cosolvent modified films. Undoubtedly, all of the films have dissimilar surface characteristic morphology, which depends on the processing condition. P3HT-PCBM composite films, in general, consist of intermixed domains of P3HT and PCBM. Roughness characteristics of the casted films were assessed, and the root mean square (rms) roughness of the films is as follows: 2.077 nm for the conventional film without any modification, 1.575 nm for the individually mixed film, and 2.173 nm for the BLND cosolvent modified film. In the individually mixed method, sufficient precipitation of P3HT must have taken place in the *o*-DCB–CHN solvent mixture, even before addition of the PCBM solution in the last step. Therefore, well-systematized, unobstructed P3HT crystallization, and negligible disturbance from PCBM during P3HT crystallization resulted in a smoother surface with least rms roughness of 1.575 nm. In contrast, the BLND cosolvent modified film has full-size aggregates that are distributed in a random order within the polymer matrix and hence resulting in a higher rms roughness of 2.173 nm. In a blended CHN added sample though the CHN addition could also bring about the preferential precipitation of P3HT; however, the presence of PCBMs in *o*-DCB–CHN solution during the P3HT crystallization could hinder the well-ordered P3HT crystallization. So, unsystematic P3HT crystallite growth considering interference from a larger fraction of disordered PCBM phases in between resulted in an increase in roughness of the blend film.[14] The conventional or unmodified film without any cosolvent modification has PCBM domains well merged within the P3HT domains with both the components of the mixture coprecipitating at the same time during the spin casting.

STRUCTURAL CHARACTERISTICS

GI-XRD Measurements

To support the structural order in terms of crystallinity and orientation of polymer chains in the course of the cosolvent modification, GI-XRD measurements were carried out on spin-coated composite films. To facilitate structural evaluation of P3HT chains at the surface as well as in the bulk film of the composite, GI-XRD measurements were made at three grazing incidence angles (0.11°, 0.13°, and 0.3°). When measurements are carried out at an incidence angle smaller than the critical angle for P3HT, i.e., at 0.11°, total reflection takes place and only a momentary beam pass through the sample film just few nanometers below the surface, thus giving diffraction mainly from few tenths of nanometers beneath the surface. At the grazing incidence angle somewhat higher than the critical angle for external reflection (i.e., at 0.13° in the case of P3HT), X-ray enters deeper in the film giving diffraction from the depth of the film. For an organic material considered, the depth increases quickly with a small increase in the incidence angle near the region of the critical angle. Again, keeping the incidence angle well above the critical angle (i.e., at 0.3°) of the P3HT polymer and below the

critical angle of the substrate presents diffraction from the whole volume (bulk) of the film.[15] The low-intensity (lower crystallinity) peaks obtained for the conventional spin-coated film at 0.11° incidence without cosolvent modification point to hindered and disordered P3HT crystallization at the surface of films prepared in a solution with a single good solvent. Again, higher intensity diffraction peaks of both of the cosolvent-modified films support more crystallized and ordered P3HT growth on the cosolvent-modified films surface, in support to the other test results. In the case of individually mixed cosolvent modified film at 0.11° X-ray incidence, three distinct diffraction peaks of the type (h00) were evident, where $h = 1$–3 associated with α axis orientation of the lamellar intrachain P3HT. In addition, a diffraction peak of the type (010) was also indexed that matchup with the b axis orientation of interchain π–π stacked P3HT main chains, emphasizing the superior π–π stacking interaction among the polythiophene chains at the surface of individually mixed modified film. However, the BLND cosolvent modified and conventional unmodified films mainly showed (100) diffraction pattern and all other higher order diffractions were missing or were less pronounced (Fig. 2A).[16] Best observed crystallization of P3HT occurred at the surface of individually mixed CHN modified film evident of the highest (100) reflection peak intensities (at $2\Theta = 5.4°$) from the films. The reason for finest crystallization using the individually mixed cosolvent addition method is due to negligible disturbance by amorphous PCBM domains next to P3HT crystallization. Again, though the diffraction intensities of the BLND cosolvent modified film was higher than the conventional unmodified film, however, the surface of BLND cosolvent modified film was not as effectively crystallized as individually mixed cosolvent modified film, evident in its less intense diffraction peaks.

Table I presents interlayer distances, crystallite sizes, and full width half maximum values solved for (100) reflection from all the P3HT-PCBM films at 0.11, 0.13, and 0.3° grazing X-ray incidences. The P3HT crystallite size at the surface of the films was obtained by using the Scherrer formula and was found to be in the following order: individual cosolvent modified film > BLND cosolvent modified film >> conventional modified film. An inset of Fig. 2A shows the enlarged view of diffraction intensity profile with 2Θ ranging from 12 to 25°. To realize the structural characteristics at the greater depth of the composite films, GI-XRD measurements at 0.13° incidences were figured out in detail (Fig. 2B). At an incidence angle of 0.13°, diffraction intensities of individually mixed cosolvent casted film are still higher than BLND cosolvent casted and conventional unmodified films. However, a decrease in the intensity of diffraction peaks of individually mixed cosolvent casted film and a concurrent increase in intensities of BLND and conventional film were observed. This may be because as we move to greater depth of the individually mixed cosolvent modified sample, fraction of PCBM increases and the well-crystallized P3HT content decreases. Again, to confirm this observation, GI-XRD was also carried out at 0.3° incidence angle. Although P3HT domains in the individually mixed cosolvent casted film are still well crystallized as revealed by high intensity of its diffraction peaks; however, the differences in diffraction intensities (related to the crystallinity and the number of P3HT crystallites) that existed at the surface of sample films were reversed when the bulk of these three films were probed (Fig. 2C). This effect may be due to the

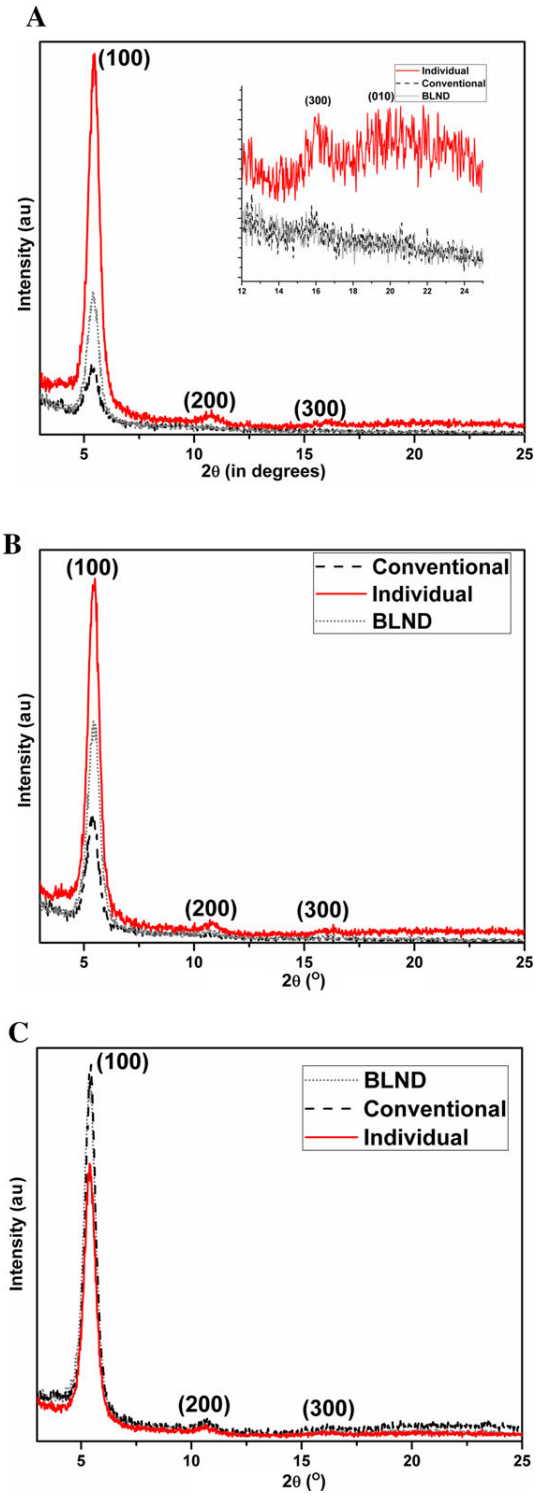

FIGURE 2. (A) GI-XRD profiles of films casted from P3HT: PCBM solutions modified with the CHN solvent by two different approaches at grazing incidence of 0.11° and inset shows the enlarged view of diffraction intensity profile with 2Θ ranging from 12 to 25°. (B) GI-XRD profiles of films at grazing incidence of 0.13°. (C) GI-XRD profiles of films at grazing incidence angle of 0.3°.

TABLE I

Summary of Interlayer Distances (d) and the Size of the Coherent P3HT Domains Resolved at the (100) Peak at Three Grazing Incidence Angles 0.11°, 0.13°, and 0.3° in the GI-XRD Pattern

Serial Number	Device	Grazing Incidence Angle (°)	2Θ Value (°)	Interlayer Distance d100 (Å)	FWHM	Grain Size (nm)
1	BLND	0.11	5.426	16.27	0.608	13.00
2	BLND	0.13	5.448	16.21	0.632	12.45
3	BLND	0.3	5.356	16.48	0.654	12.02
4	Individually mixed	0.11	5.440	16.23	0.580	13.70
5	Individually mixed	0.13	5.422	16.18	0.616	12.77
6	Individually mixed	0.3	5.375	16.33	0.638	12.33
7	Conventional	0.11	5.455	16.29	0.654	12.03
8	Conventional	0.13	5.399	16.35	0.635	12.40
9	Conventional	0.3	5.396	16.37	0.585	13.44

Individually mixed, conventional, and BLND devices refer to the different processing conditions.
BLND = film casted of P3HT: PCBM solution with CHN solvent added to the blend solution; individually mixed = P3HT: PCBM film casted of solution with CHN solvent added individually to the P3HT solution; conventional = P3HT: PCBM film casted of solution without any cosolvent modification; FWHM = full width half maximum.

presence of a greater fraction of PCBM in the bulk of individually mixed cosolvent casted film as compared to the BLND cosolvent modified and conventional unmodified films. Bulk reflections revealed better ordering and crystallization of P3HT domains in conventional and BLND cosolvent modified samples, which may be attributed to decreasing PCBM content in the bulk of these films. To reveal the upright concentration gradient in the composite films, a set of diffraction peaks at 0.11, 0.13, and 0.3° incidence angles from the three films were compared. There was an obvious upright concentration gradient in individually mixed cosolvent modified films with a better and more number of well-crystallized P3HT domains and lesser PCBM at the surface and more PCBM domains and lesser P3HT in the bulk of the films.[17] This dissimilarity between the surface and bulk characteristics of the film may be due to the differences in surface energies of P3HT and PCBM and again at the air interface P3HT will have more possibility to accumulate larger and well-developed crystallites with a negligible interference from PCBM.[18] In the conventional unmodified film, a reverse concentration gradient was indicated, i.e., well-crystallized P3HT domains were more in the bulk of the film and the surface was not effectively crystallized.

Contact Angle Measurements

To consider the surface properties of P3HT: PCBM thin films, water contact angles were measured (Fig. 3). The conventional P3HT: PCBM film without any cosolvent addition has a contact angle of 60.94°, whereas the individually mixed and BLND cosolvent modified films showed a contact angle of 83.29° and 62.01°, respectively. These surface properties are well in agreement to the composition of the films surface predicted by GI-XRD measurements. The static water contact angle of conventional P3HT: PCBM film is the lowest, indicating the lowest accumulation of hydrophobic P3HT at the top in such a film, whereas after cosolvent addition a change in the surface morphology was observed and hence a change in the surface properties of such films.[19] The individually mixed cosolvent addition method promoted the preferential highest possible crystallization of P3HT crystals, which mostly cover the surface of the P3HT: PCBM film owing to the lower surface energy of the P3HT polymer.[20] This is in accordance with the highest water contact angle observed for the individually mixed cosolvent modified film. While, in the blend cosolvent modified film, there was preferential crystallization of P3HT; however, crystallization was suppressed by the presence of PCBM, which is also evident in the lesser water contact angle of 62.01° than the individually mixed cosolvent modified film.

OPTICAL CHARACTERISTICS

UV–Vis Absorption Measurements

The addition of a secondary solvent into the regular solvent has been recognized to sustain an ordered growth of P3HT crystals from the solution mixtures. The strategy was to take advantage of a secondary solvent that alters the favored crystallization sequence to P3HT first, keeping PCBM dissolved in the solution, as the chosen cosolvent mixture offers more solubility to PCBM than P3HT.[21] This transformation in the crystal structure of P3HT in the solution mixture sustains in the blend film as well and affects the absorption of UV–vis radiation by the casted film. Figure 4 shows the comparative UV–vis absorption spectra of the polymer blend films casted of the solutions with the addition of CHN cosolvent, following two dissimilar schemes prior to spin coating. UV–vis absorption spectra of all of the casted P3HT: PCBM blend films exhibited one main absorption peak, to be precise at 512 nm, allied to intrachain π–π^* transition in P3HT chain, along with two shoulders in the higher wavelength region. An extensive conjugated chain of P3HT results in a shoulder peak at 550 nm, whereas the other one at 610 nm corresponds to the interchain transition among the P3HT chains.[22] For comparison, films were also prepared from a solution without any cosolvent modification. An assessment of the spectra of films with and without cosolvent modification depicts an increase in the intensity of the absorption peaks at 512, 550, and 610 nm with cosolvent addition, which is consistent with more ordered growth of P3HT crystals in the composite films with cosolvent addition. However, an assessment of spectra of films prepared following two distinct methods of cosolvent addition in a solution mixture, namely, individually mixed and BLND cosolvent

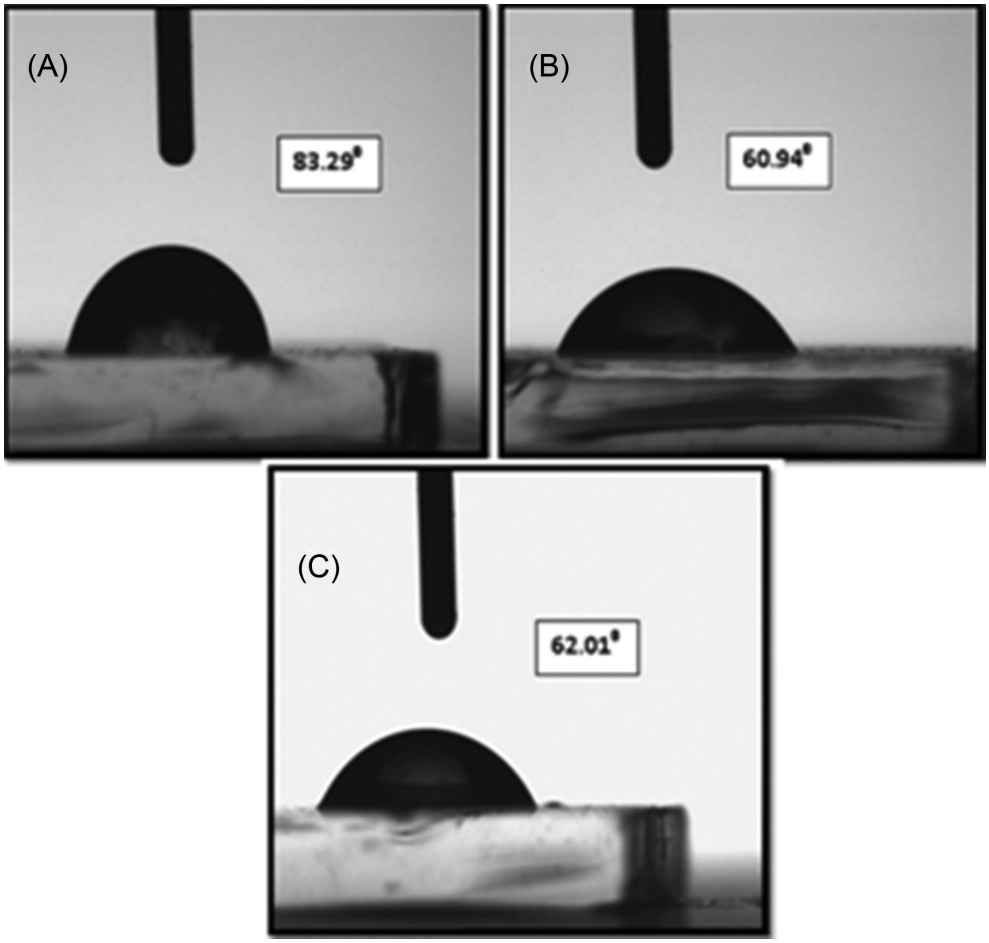

FIGURE 3. Images of water contact angles on P3HT: PCBM films casted of (A) individually mixed CHN added solution, (B) conventional solution, and (C) BLND CHN added solution.

addition methods, suggested that P3HT domains in films casted of most frequently employed method of cosolvent addition, that is to say BLND addition, were still not crystallized to preeminent degree. Details of the two processing pathways for cosolvent addition are specified in the Experimental section. A comparison of the individually mixed cosolvent modified (individual) film with the BLND cosolvent modified film shows an increase in the intensity of absorption peaks at 512 and 550 nm, suggestive of a more efficient growth of P3HT crystals in the former, likely due to the diminishing disorder by PCBM besides P3HT crystallization. Ordered P3HT growth in the individual mixed cosolvent modified film appears from the coil to rod transformation of P3HT chains, with cosolvent inclusion along with a subsequent increase in conjugated chain length and crystallization, proven by the increase in absorption peak at 512 and 550 nm.[23]

Photoluminescence Emission

Photoluminescence (PL) emission, a bulk phenomena owing its origin to the radiative (light emissive) relaxation of the photoinduced excitons, is considered in detail to recognize the donor–acceptor association in the composite film past the modification. Figure 5 shows the comparative PL emission spectra of the P3HT: PCBM films excited at a wavelength of 450 nm with BLND CHN modification, individually mixed CHN modification, and also without any modification. Higher PL emission in the conventional film without any cosolvent addition ascertains incomplete quenching and hence lesser exciton dissociation at the donor–acceptor interfaces. Higher PL intensity assigns larger phase separation between the less effectively crystallized components in the conventional film, as all the excitons created in one polymer do not reach the interface with the other polymer within the same film for excitons to dissociate to free charge carriers. This inconvenient occurrence can be attributed to a larger domain size of P3HT (13.44 nm) in the bulk of conventional film, which being greater than the excitons diffusion length inhibits the efficient charge transfer between the P3HT and PCBM. Also, there is no possibility of long-range quenching in such films as P3HT is not overall well crystallized. For this reason, the photoexcited excitons before reaching the interface return to a ground state by radiative emission giving intense PL signals. On the other hand, quenching in PL signals by effective charge transfer between the domains of P3HT and PCBM may be because of bit smaller sized P3HT domains, i.e., 12.02 and 12.33 nm in the

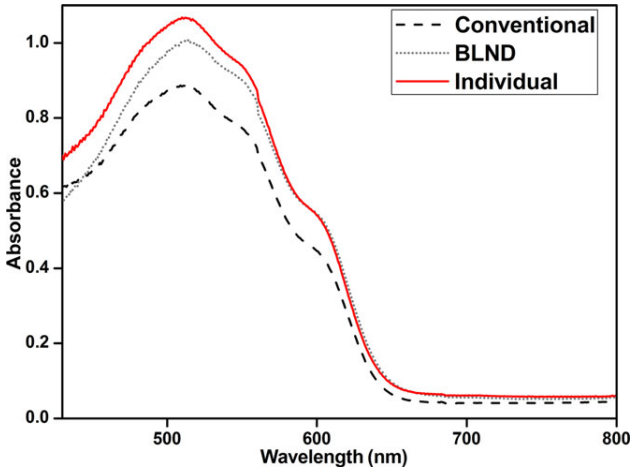

FIGURE 4. Comparative UV–vis absorption spectra of P3HT:PCBM films casted out of solutions modified with BLND CHN addition and individually mixed CHN addition.

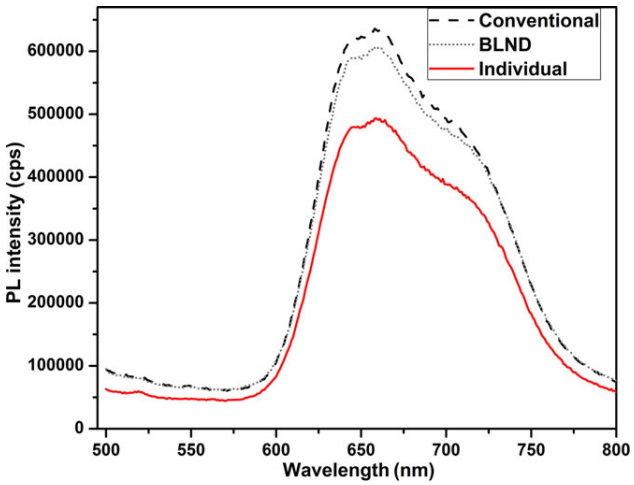

FIGURE 5. PL spectra of P3HT: PCBM films casted of solutions without any modification and modified by individually mixed and BLND CHN addition approach.

bulk of BLND cosolvent modified and individually mixed cosolvent modified films. In the same way, the two films prepared via two different routes of cosolvent modification were also discriminated in terms of PL emission, as the individually mixed modified film shows more quenching in PL signals than the BLND cosolvent modified film. Relating the PL signals of the films, we can state that the individually mixed cosolvent casted film provides the appropriate equilibrium phase separation for efficient excitons dissociation and free carrier generation. Remarkable PL quenching, in the case of larger grain-sized P3HT crystals formed in individually mixed cosolvent casted film, can be explained on the basis of the long-range interchain excitons quenching or self-quenching, in its more ordered and planar P3HT chains at a diffusion length larger than the normal excitons diffusion length in organic polymer (8–10 nm) and hence diminishing the possibility of PL radiative decay.[24] Although the BLND cosolvent modified film shows more quenched PL signals than the conventional film, however, the quenching in PL signal, that is a sign of efficient excitons dissociation at the interfaces of the donor and acceptor domain, is still much smaller when compared to the individually mixed modified film. Higher PL intensity in the blend cosolvent-mixed casted film recommends a coarser P3HT: PCBM mixture, so that not all the excitons generated in one polymer reach at the interface of the other polymer within the same film, i.e., unfavourable phase separation between the domains of larger sizes than the normal excitons diffusion length (~8 –10 nm).[25]

Conclusions

We recommend the individually mixed cosolvent addition method for preparing P3HT: PCBM composite, as this method benefits the casted film by providing optimum achievable P3HT crystallization and in this way, increasing the absorption of radiation in the UV–vis region. The intermixed domains of P3HT polymer and PCBM acceptor in individually mixed cosolvent casted films though a bit larger in size, however, have shown to be just close enough to be capable of long-range interchain excitons quenching interaction. Such a long-range quenching phenomena in the individually mixed cosolvent casted film is supported by more planarized and crystallized P3HT chains, so as to have electronic energy transfer at the donor–acceptor interface in the event of photoexcitation. This comprehensive study on individually mixed cosolvent modified P3HT: PCBM films shows that efficient P3HT crystallization, optimal phase separation, and vertical concentration gradient encourage the utilization of this modified film as an active layer in the inverted photovoltaic technology in the case of photovoltaic excitation. The individually mixed cosolvent modification method emphasized in our study is not only limited to P3HT/PCBM composite but can also be applied in other low band gap self-assembling polymer donor–acceptor mixtures.

Acknowledgments

Authors are thankful to Prof. P. B. Sharma, Vice-Chancellor, Delhi Technological University (formerly Delhi College of Engineering), Delhi, for encouragement and support. A financial support to one of the author, Sarita, is also greatly acknowledged. The authors are also grateful to Moserbaer India Ltd. for their assistance in performing the experiment and characterization.

References

1. Facchetti, A. Chem Mater 2011, 23, 733–758.
2. Chen, J.-T.; Hsu, C.-S. Polym Chem 2011, 2, 2707–2722.
3. Kraabel, B.; McBranch, D.; Sariciftci, N. S.; Moses, D.; Heeger, A. J. Phys Rev B 1994, 50, 18543–18552.
4. He, M.; Ge, J.; Fang, M.; Qiu, F.; Yang, Y. Polymer 2010, 51, 2236–2243.

5. Wang, Y.; Wei, W.; Liu, X.; Gu, Y. Sol Energy Mater Sol Cells 2012, 98, 129–145.
6. Kozub, D. R.; Vakhshouri, K.; Orme, L. M.; Wang, C.; Hexemer, A.; Gomez, E. D. Macromolecules 2011, 44, 5722–5726.
7. Zhao, Y.; Guo, X.; Xie, Z.; Qu, Y.; Geng, Y.; Wang, L. J Appl Polym Sci 2009, 111, 1799–1804.
8. Chen, D.; Nakahara, A.; Wei, D.; Nordlund, D.; Russell, T. P. Nano Lett 2011, 11, 561–567.
9. Liu, J.; Shao, S.; Wang, H.; Zhao, K.; Xue, L.; Gao, X.; Xie, Z.; Han, Y. Org Electron 2010, 11, 775–783.
10. Karagiannidis, P. G.; Georgiou, D.; Pitsalidis, C.; Laskarakis, A.; Logothetidis, S. Mater Chem Phys 2011, 129, 1207–1213.
11. Moulé, A. J.; Meerholz, K. Adv Mater 2008, 20, 240–245.
12. Park, Y. D.; Lee, H. S.; Choi, Y. J.; Kwak, D.; Cho, J. H.; Lee, S.; Cho, K. Adv Funct Mater 2009, 19, 1200–1206.
13. Li, L.; Tang, H.; Wu, H.; Lu, G.; Yang, X. Org Electron 2009, 10, 1334–1344.
14. Chen, K.-S.; Yip, H.-L.; Schlenker, C. W.; Ginger, D. S.; Jen, A. K.-Y. Org Electron 2012, 13, 2870–2878.
15. Treat, N. D.; Brady, M. A.; Smith, G.; Toney, M. F.; Kramer, E. J.; Hawker, C. J.; Chabinyc, M. L. Adv Energy Mater 2011, 1, 82–89.
16. Kayunkid, N.; Uttiya, S.; Brinkmann, M. Macromolecules 2010, 43, 4961–4967.
17. Sio, A. D.; Madena, T.; Huber, R.; Parisi, J.; Neyshtadt, S.; Deschler, F.; Como, E. D.; Esposito, S.; Hauff, E. Sol Energy Mater Sol Cells 2011, 95, 3536–3542.
18. Pavlopoulou, E.; Fleury, G.; Deribew, D.; Cousin, F.; Geoghegan, M.; Hadzioannou, G. Org Electron 2013, 14, 1249–1254.
19. Lu, H.; Akgun, B.; Russell, T. P. Adv Energy Mater 2011, 1, 870–878.
20. Wu, Z.; Song, T.; Jin, Y.; Sun, B.; Appl Phys Lett 2011, 99, 143306/1–3.
21. Samitsu, S.; Shimomura, T.; Ito, K. Thin Solid Films 2008, 516, 2478–2486.
22. Brown, P. J.; Thomas, D. S.; Köhler, A.; Wilson, J. S.; Kim, J.-S.; Ramsdale, C. M.; Sirringhaus, H.; Friend, R. H. Phys Rev B 2003, 67, 064203/1–16.
23. Malik, S.; Jana, T.; Nandi, A. K. Macromolecules 2001, 34, 275–282.
24. Ayzner, A. L.; Tassone, C. J.; Tolbert, S. H.; Schwartz, B. J. J Phys Chem C 2009, 113, 20050–20060.
25. Koeppe, R.; Sariciftci, N. S. Photochem Photobiol Sci 2006, 5, 1122–1131.

Microelectronics Journal 45 (2014) 1001–1007

Contents lists available at ScienceDirect

Microelectronics Journal

journal homepage: www.elsevier.com/locate/mejo

An efficient triple-tail cell based PFSCL D latch

Neeta Pandey [a,*], Kirti Gupta [a], Maneesha Gupta [b]

[a] Department of ECE, Delhi Technological University, Formerly Delhi College of Engineering, Bawana Road, Delhi 110042, India
[b] Division of ECE, Netaji Subhas Institute of Technology (NSIT), University of Delhi, Sector 3, Dwarka, New Delhi 110078, India

ARTICLE INFO

Article history:
Received 18 May 2013
Received in revised form
30 April 2014
Accepted 6 May 2014

Keywords:
PFSCL
D latch
Triple-tail cell

ABSTRACT

In this paper, an efficient positive feedback source-coupled logic (PFSCL) D latch topology is proposed. It uses triple-tail cell concept which results in lesser number of stages as well as gate count in comparison to the traditional PFSCL D latch. The operation of the proposed D latch is described and is supported with mathematical formulations. The functionality is verified through SPICE simulations using TSMC 0.18 μm CMOS technology parameters. It is found that the proposed D latch topology significantly reduces the power consumption and delay in comparison to the traditional PFSCL D latch. The impact of process variation on the proposed and traditional PFSCL D latch at different design corners shows similar variations.

© 2014 Elsevier Ltd. All rights reserved.

1. Introduction

The source-coupled logic (SCL) style is preferred over the traditional CMOS logic style in mixed signal applications for high speed digital circuit design due to its inherent characteristics of reduced switching noise and frequency independent power consumption [1–3]. The SCL gates are broadly classified as differential or single-ended [4–10]. The former is based on the stacking of the transistors pairs [4,5] whereas the transistors are connected in parallel and are source-coupled to a transistor whose gate is connected to reference voltage source [6] in the latter one.

An improved single-ended SCL style named as positive-feedback source-coupled logic (PFSCL) style has been suggested in literature [6–10]. The logic style replaces the reference voltage source used in traditional single-ended SCL gates with a positive feedback to improve their performance. It mainly uses NAND/NOR gates to implement a given logic function since no stacked transistor pairs are employed. Therefore, the traditional PFSCL D latch realization consist of multiple PFSCL NOR stages. In this paper, a new topology for PFSCL D latch employing lesser number of PFSCL stages than the traditional one is proposed. It uses triple-tail cell concept [11–15] to improve the overall performance of the gate.

The paper first briefly describes the PFSCL style in Section 2 and its usage in D latch implementation. Thereafter, the proposed PFSCL D latch architecture is explained in Section 3. The functionality of proposed gate and its effectiveness over traditional PFSCL D latch is illustrated through simulations using TSMC 0.18 μm CMOS technology parameters in Section 4. The impact of process variation at different design corners is also studied. Finally, the conclusions are drawn in Section 5.

2. PFSCL style

The PFSCL style works on the principle of current steering and uses a pull-down network (PDN), a constant current source and a load circuit in order to implement the logic gate. The realization of a generic N-input NOR based PFSCL gate is shown in Fig. 1a. The inputs are applied to the gates of N-NMOS transistors M_i ($i=1, 2,\ldots, N$) which share common source and drain terminals [6]. The input transistors are source-coupled with a feedback transistor M_f whose gate is connected to the output node Q. The constant current source M_S provides the bias current I_{SS} while the PMOS load transistor M_{L1} and M_{L2} performs the current to voltage conversion. The transistor M_{L2} (optional) is inserted to generate the complement of the output $\left(\overline{Q}\right)$ and can be substituted by a short circuit when it is not needed [6]. The NOR based realization can also be used for N-input NAND gate with help of De Morgan law. The inputs need to be applied in the inverted form, and the output is taken from M_{L2} as depicted in Fig. 1b. Thus it can be deduce that the PFSCL style does not require stacked transistor pairs [6].

To analyze the PFSCL circuits, the load transistors M_{L1}, M_{L2} is substituted by an equivalent linear resistance R_P model given as [6]

$$R_P = \frac{R_{\text{int}}}{1-\left(\left(R_{\text{DSW}}10^{-6}\right)/W_P\right)/R_{\text{int}}} \quad (1)$$

* Corresponding author.
E-mail addresses: n66pandey@rediffmail.com, neetapandey06@gmail.com (N. Pandey).

http://dx.doi.org/10.1016/j.mejo.2014.05.002
0026-2692/© 2014 Elsevier Ltd. All rights reserved.

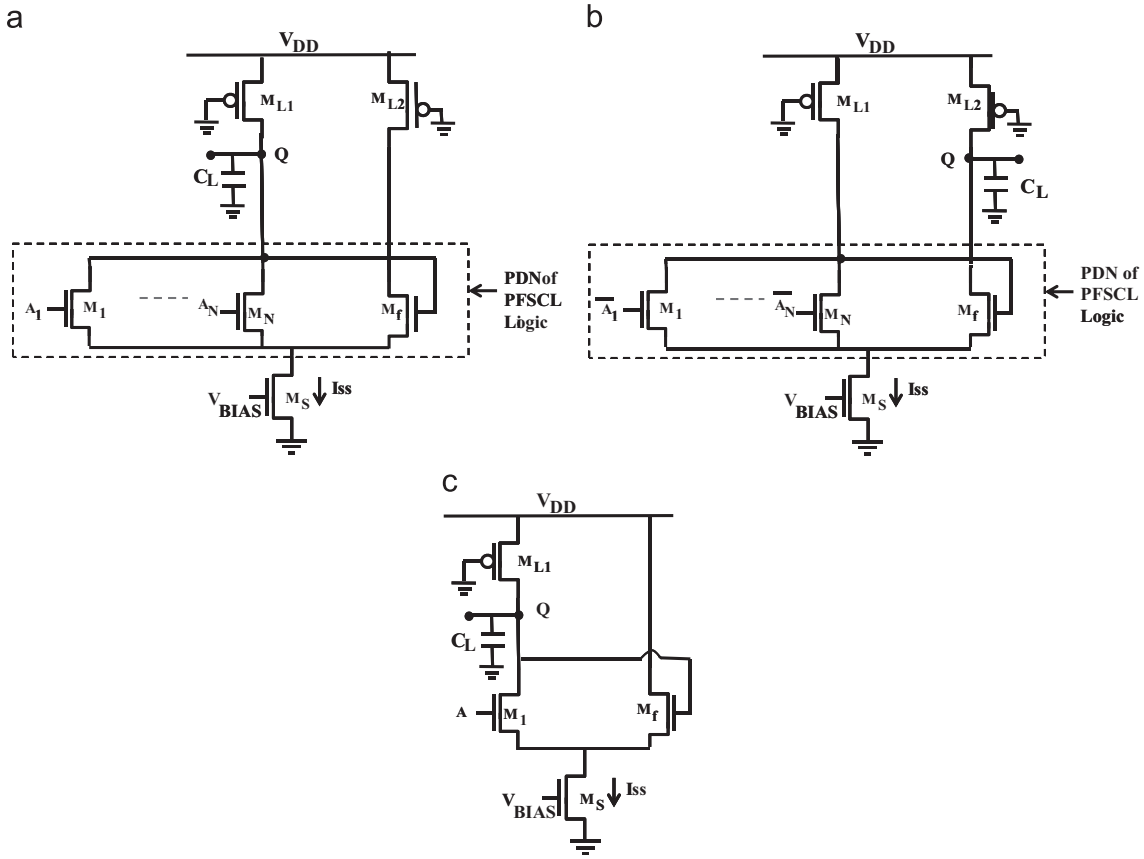

Fig. 1. (a) Generic N-input PFSCL circuit (NOR based implementation. (b) N-input PFSCL circuit (NAND based implementation. (c) PFSCL inverter.

where R_{DSW} is the empirical model parameter, W_P is the effective channel width of the load transistor and the parameter R_{int} is the intrinsic resistance of the PMOS load transistors in the linear region and is given as

$$R_{int} = \left[\mu_{eff,p} C_{ox} \frac{W_P}{L_P}(V_{DD} - |V_{T,p}|)\right]^{-1} \quad (2)$$

where C_{ox} is the oxide capacitance per unit area. The parameters $\mu_{eff,p}$, $V_{T,p}$ and L_P are the effective hole mobility, the threshold voltage, and the effective channel length of the load transistor, respectively.

The circuit of a PFSCL inverter with input A is shown in Fig. 1c. For high value at input A, the bias current I_{SS} is steered through transistor M_1 and produces a low output voltage ($V_{OL}=V_{DD}-R_P I_{SS}$) [6]. Similarly, the transistor M_1 is turned OFF for low value of input A, and a high voltage ($V_{OH}=V_{DD}$) is obtained at the output. The voltage swing for PFSCL circuits (V_{SWING}) is the difference between V_{OH} and V_{OL} and is computed as

$$V_{SWING} = R_P I_{SS} \quad (3)$$

In PFSCL gates the bias current I_{SS} flows throughout the operation and consumes power computed as:

$$P = V_{DD} I_{SS} \quad (4)$$

The NOR based realization of the traditional PFSCL D latch having three levels is shown in Fig. 2. The first level is responsible for generating the complement of the applied inputs whereas the subsequent two levels implements the SR latch. In all, it consist of six identical PFSCL NOR gates such that the total power consumption is six times the power consumed by a single PFSCL NOR gate. Hence, the traditional D latch may not be beneficial in many low-power applications. Therefore, in the next section a new D latch topology is proposed. The number of levels as well as the gate count is reduced which makes it more efficient than the traditional PFSCL D latch.

3. Proposed PFSCL D latch topology

The complete schematic of the proposed D latch comprise of two levels namely a single PFSCL inverter and a new fundamental cell as shown in Fig. 3. The PFSCL inverter generates the complement of CLK which is fed as the input to the fundamental cell. The new fundamental cell is based on the triple-tail cell concept [11–15]. It consists of two triple-tail cells (M_{X3}, M_{X4}, M_{X7}) and (M_{X5}, M_{X6}, M_{X8}) biased by separate current sources of $I_{SS}/2$ value such that the new cell draws the same current as that of the single traditional PFSCL gate (Fig. 1). A detailed analysis of the fundamental cell by configuring it as an AND gate is discussed in Appendix. To realize a D latch, the transistors M_{X7} and M_{X8} driven by the input clock (CLK) and its complement are connected between the supply terminal and the common source terminal of transistor pairs M_{X3}–M_{X4} and M_{X5}–M_{X6}, respectively, as shown in Fig. 3. A high voltage on CLK turns ON the transistor M_{X7}, and deactivates the transistor pair M_{X3}–M_{X4}. At the same time, the transistor M_{X8} turns OFF so that the transistor pair M_{X5}–M_{X6} generates the output according to the input D. Similarly, the transistor pair M_{X3}–M_{X4} gets activated for low voltage of CLK and preserves the previous output. Thus the proposed D-latch models the positive level sensitive D latch.

It may be noted that if equal aspect ratio of all transistors in the triple-tail cells is considered, then the transistors M_{X7} and M_{X8} will

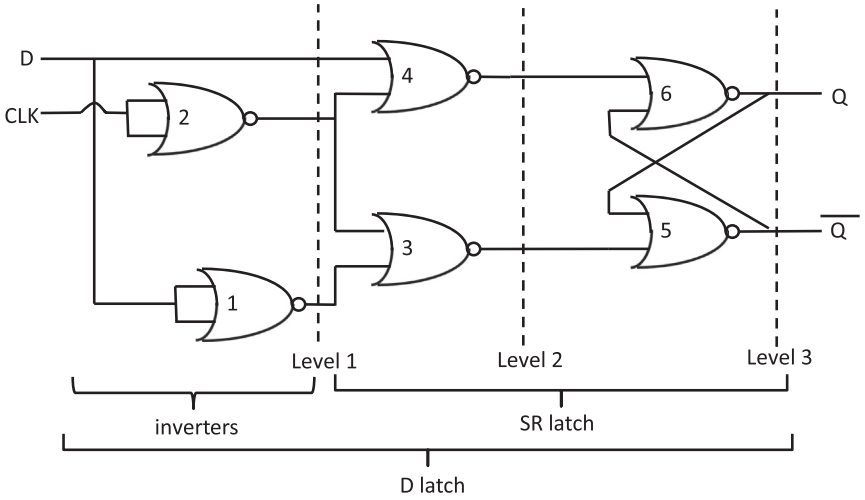

Fig. 2. Traditional PFSCL D latch.

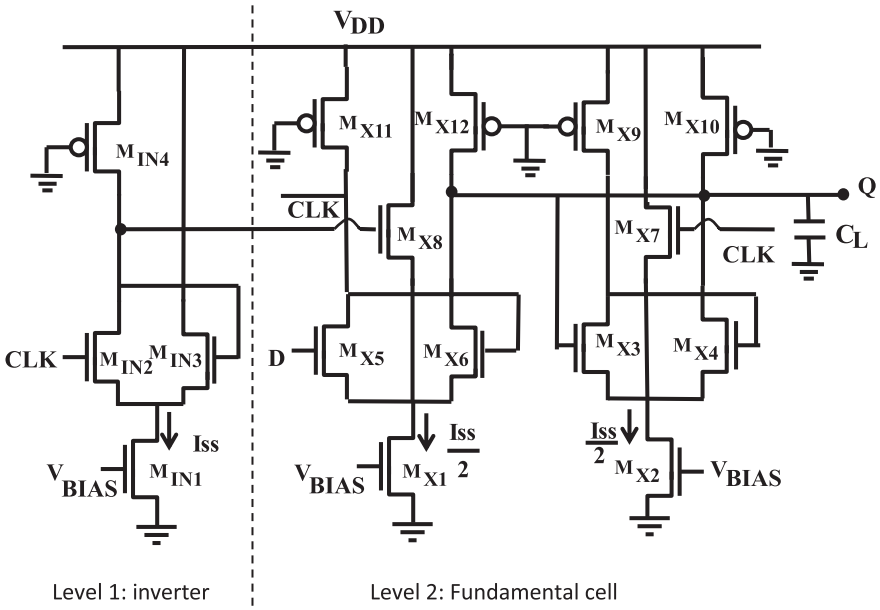

Fig. 3. Complete schematic of the proposed triple-tail cell based PFSCL D latch.

not be able to completely switch OFF the transistor pair M_{X3}–M_{X4} and M_{X5}–M_{X6}. For the case when both D and Q are high and CLK makes a transition from low to high, the transistors M_{X3} and M_{X7} draw the same current as their gate-source voltages are equal. However, the proper operation demands that transistor M_{X7} should draw all/maximum bias current of the triple-tail cell. To ensure this the aspect ratio of M_{X7} is made larger (say N times) than M_{X3}.In this case, the currents flowing through M_{X3} and M_{X7} can be written as:

$$i_{D,3} = \frac{I_{SS}}{2}\frac{1}{1+N} \tag{5a}$$

$$i_{D,7} = \frac{I_{SS}}{2}\frac{N}{1+N} \tag{5b}$$

The current through M_{X3} can be minimized by increasing factor N. This input condition produces the high output voltage V_{OH} as

$$V_{OH} = V_{DD} - R_P\left[(i_{D,4} + i_{D,6})\right] = V_{DD} \tag{6}$$

where $i_{D,4}$, $i_{D,6}$ are the currents through transistors M_{X4} and M_{X6}, respectively. The output voltages for various input combinations are enlisted in Table 1.

It can be observed from Table 1 that there are two values of both maximum output voltage V_{OH} and minimum output voltage V_{OL} for different combinations of D and Q. Consequently, the voltage swing, V_{SWING1} for the same value of the input D and the present state can be expressed as

$$V_{SWING1} = V_{OH1} - V_{OL1} = \frac{R_P I_{SS}}{2}\left(1 + \frac{N}{1+N}\right) \tag{7a}$$

where V_{OH1}, V_{OL1} are maximum output voltage and minimum output voltage, respectively, for the same inputs and the present state and the voltage swing, V_{SWING2} for the different value of the input D and the present state can be expressed as

$$V_{SWING2} = V_{OH2} - V_{OL2} = \frac{R_P I_{SS}}{2}\left(\frac{N}{1+N}\right) \tag{7b}$$

where V_{OH2}, V_{OL2} are maximum output voltage and minimum output voltage, respectively, for different inputs. As $V_{SWING2} < V_{SWING1}$, V_{SWING2} has been considered as the worst case voltage

Table 1
Differential output voltages for various input combinations.

Inputs		Previous state	Currents through the transistors						Output voltage of the next state V_Q	
CLK	D	Q	M_{X3}	M_{X4}	M_{X5}	M_{X6}	M_{X7}	M_{X8}	Level	$V_{DD}-R_P\,(i_{D,4}+\,i_{D,6})$
L	L	L	0	I_1	0	I_3	0	I_2	V_{OL1}	$V_{DD}-R_PI_{SS}/2(1+1/1+N)$
L	L	H	I_1	0	0	I_3	0	I_2	V_{OH2}	$V_{DD}-R_PI_{SS}/2(1/1+N)$
L	H	L	0	I_1	I_3	0	0	I_2	V_{OL2}	$V_{DD}-R_PI_{SS}/2$
L	H	H	I_1	0	I_3	0	0	I_2	V_{OH1}	V_{DD}
H	L	L	0	I_3	0	I_1	I_2	0	V_{OL1}	$V_{DD}-R_PI_{SS}/2(1+1/1+N)$
H	L	H	I_3	0	0	I_1	I_2	0	V_{OL2}	$V_{DD}-R_PI_{SS}/2$
H	H	L	0	I_3	I_1	0	I_2	0	V_{OH2}	$V_{DD}-R_PI_{SS}/2(1/1+N)$
H	H	H	I_3	0	I_1	0	I_2	0	V_{OH1}	V_{DD}

Where L/H=low/high input voltage, $I_1=I_{SS}/2$, $I_2=I_{SS}/2\ (N/1+N)$, $I_3=I_{SS}/2\ (1/1+N)$, V_{OL}/V_{OH}=low/high output voltage.

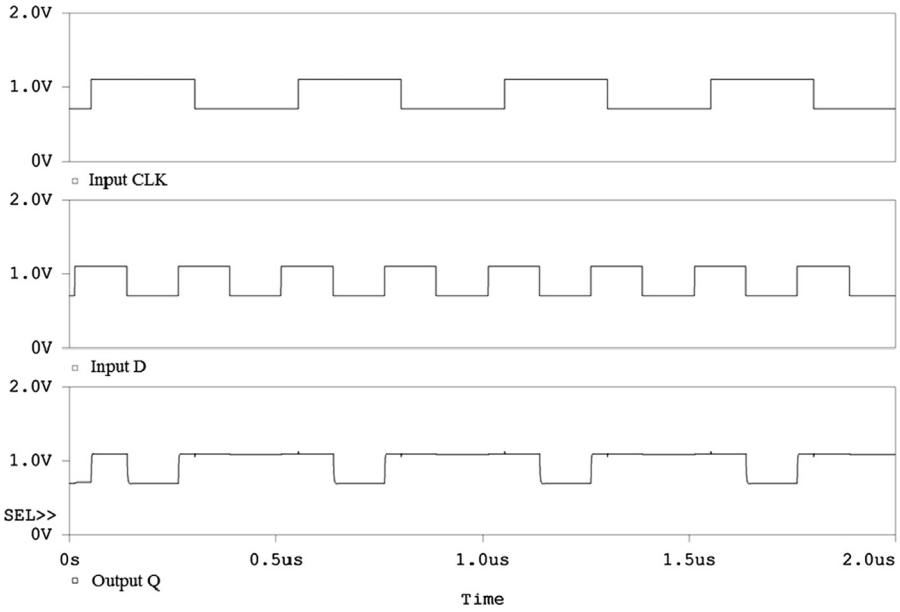

Fig. 4. Waveforms of the proposed PFSCL D latch.

Table 2
Impact of parameter variations on the performance of the proposed and the traditional D latches.

Parameter	**NMOS** **PMOS**	***T*** ***T***	***F*** ***F***	***S*** ***S***	***F*** ***S***	**S** **F**
Propagation delay(ps) (C_L=100 fF)	Proposed	658	628	953	631	640
	Traditional	1270	1036	1489	1203	1240
Power (μW)	Proposed	219	283	158	261	256
	Traditional	633	846	438	642	635

Where different design corners are denoted by T=typical, F=fast, S=slow.

swing, V_{SWING} and has been further approximated as

$$V_{SWING}=\frac{R_PI_{SS}}{2}\quad \text{for large values of } N \tag{8}$$

It may be noted from Eq. (8) that the voltage swing of the proposed D latch is half the voltage swing of the traditional PFSCL D latch. This can be compensated by keeping the value of the load resistance twice the resistance value of the traditional D latch.

4. Simulation section

This section verifies the functionality of the proposed D latch followed by its performance comparison with the traditional PFSCL D latch in terms of the power consumption and the propagation delay. Also, the effect of parameter variations is also studied for both the topologies. The voltage swing and bias current of 400 mV and 100 μA, respectively, are considered for both the types of gates. TSMC 0.18 μm CMOS technology parameters and a power supply of 1.1 V are taken in all the simulations.

The proposed D latch (Fig. 3) is simulated and the waveforms of the inputs (D and CLK), and the output node Q are shown in Fig. 4. It can be observed that for high values of the CLK signal the D latch is in the transparent state whereas it is in the hold state for low values of the CLK signal.

The performance of the proposed D latch is compared with the PFSCL counterpart. The power consumption of the proposed and the traditional D latch are 219 μW and 633 μW, respectively. The proposed gate saves 65% power in comparison to the traditional

one. This is due to the fact that the power consumed by the proposed D latch is given as the sum of the power consumed by the inverter and the fundamental cell whereas for the traditional D latch it is the sum of power consumed by all the gates six identical NOR gates in Fig. 2. Thus, the proposed D latch offers power saving due to the lesser number of gates in comparison to the traditional one. Similarly, the propagation delay for the proposed and the traditional gates are 658 ps and 1270 ps, respectively. This shows an improvement of 48% which can be attributed to the reduction in the number of levels involved in the implementation.

The impact of parameter variation on the proposed and the traditional D latch performance is studied at different design corners. The findings for various operating conditions are given in Table 2. It is found that the propagation delay and the power of the proposed D latch vary by a factor of 1.5 and 1.8, respectively, between the best and the worst cases whereas a factor of 1.43 and 1.9, respectively, are obtained for the traditional PFSCL D latch.

5. Conclusion

In this paper, an efficient triple-tail cell based positive feedback source-coupled logic (PFSCL) D latch topology is proposed. The topology has lesser number of stages as well as gates count in comparison to the traditional PFSCL D latch. The D latch has been implemented and simulated using TSMC 0.18 μm CMOS technology parameters. It is found that the proposed D latch topology is better than the traditional one in terms of speed and power. The study of impact of process variation at different design corners shows that both the gates show similar variations.

Appendix

The proposed D latch consists of a new fundamental cell employing two triple-tail cells as shown in Fig. 3. The behavior of the new fundamental cell can be analyzed by configuring it as a 2-input AND gate shown in Fig. A.1. When input B is high, the transistor M_{X7} is ON and the transistor pair M_{X3} and M_{X4} is deactivated. At the same time, the transistor M_{X8} is turned OFF and the output is generated according to the input A through the transistor pair M_{X5}–M_{X6}. Similarly, the transistor pair M_{X3}–M_{X4} gets activated for low voltage on B and a low voltage is obtained at the output. Thus, confirming to the functionality of the AND gate.

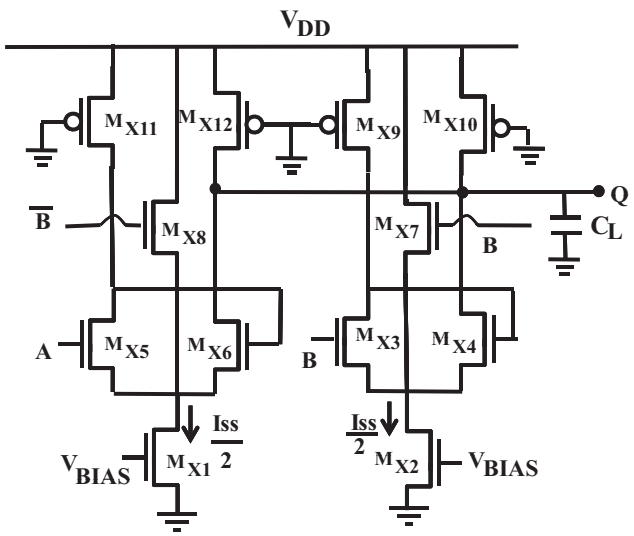

Fig. A.1. Fundamental cell configured as AND gate with inputs A and B .

It may be noted in the new fundamental cell that if equal aspect ratio of all transistors is considered, then the transistors M_{X7} and M_{X8} will not be able to completely switch OFF the transistor pair M_{X3}–M_{X4} and M_{X5}–M_{X6}. For the case when both the inputs are high, the transistors M_{X3}, M_{X5} and M_{X7} are ON while M_{X4}, M_{X6} and M_{X8} are OFF. A high to low transition at B makes transistor M_{X8} ON. In this case the transistors M_{X5} and M_{X8} will draw equal currents as their gate-source voltages are same. Hence the transistor M_{X8} is not able to completely deactivate the transistor pair M_{X5}–M_{X6}. Therefore to achieve proper operation, the aspect ratio of transistors M_{X7}, M_{X8} is made greater than other transistors' aspect ratio by a factor N. Thus, the currents flowing through M_{X5} and M_{X8} can be written as:

$$i_{D,5} = \frac{I_{SS}}{2}\frac{1}{1+N} \tag{A.1}$$

$$i_{D,8} = \frac{I_{SS}}{2}\frac{N}{1+N} \tag{A.2}$$

Based on this observation, the DC analysis of the AND gate for the different combinations of the inputs is discussed below:

Case 1. *Both inputs (A and B) are high*

When both the inputs are high, the transistors M_{X3}, M_{X5}, M_{X7} are ON and transistors M_{X4}, M_{X6} and M_{X8} are OFF. The current through the transistors M_{X3} $(i_{D,3})$, M_{X5} $(i_{D,5})$, M_{X7} $(i_{D,7})$ may be written as:

$$i_{D,3} = \frac{I_{SS}}{2}\frac{1}{1+N};\quad i_{D,5} = \frac{I_{SS}}{2};\quad i_{D,7} = \frac{I_{SS}}{2}\frac{N}{1+N} \tag{A.3}$$

This input condition produces the high output voltage V_{OH} as:

$$V_{OH} = V_{DD} - R_P\left[(i_{D,4} + i_{D,6})\right] = V_{DD} \tag{A.4}$$

Case 2. *Both inputs (A and B) are low*

When both the inputs are low, the transistors M_{X4}, M_{X6}, M_{X8} are ON and transistors M_{X3}, M_{X5} and M_{X7} are OFF. The current through the transistors M_{X4} $(i_{D,4})$, M_{X6} $(i_{D,6})$, M_{X8} $(i_{D,8})$ may be written as:

$$i_{D,4} = \frac{I_{SS}}{2};\quad i_{D,6} = \frac{1}{1+N}\frac{I_{SS}}{2};\quad i_{D,8} = \frac{I_{SS}}{2}\frac{N}{1+N} \tag{A.5}$$

This input condition produces the low output voltage V_{OL1} as:

$$V_{OL1} = V_{DD} - R_P\left[(i_{D,4} + i_{D,6})\right] = V_{DD} - \frac{R_P I_{SS}}{2}\left(1 + \frac{1}{1+N}\right) \tag{A.6}$$

Case 3. *A is high and B is low*

For this input condition, the transistors M_{X4}, M_{X5}, M_{X8} are ON and transistors M_{X3}, M_{X6} and M_{X7} are OFF. The current through the transistors M_{X4} $(i_{D,4})$, M_{X5} $(i_{D,5})$, M_{X8} $(i_{D,8})$ may be written as:

$$i_{D,4} = \frac{I_{SS}}{2};\quad i_{D,5} = \frac{1}{1+N}\frac{I_{SS}}{2};\quad i_{D,8} = \frac{I_{SS}}{2}\frac{N}{1+N} \tag{A.7}$$

This input condition produces the low output voltage V_{OL2} as:

$$V_{OL2} = V_{DD} - R_P\left[(i_{D,4} + i_{D,6})\right] = V_{DD} - \frac{R_P I_{SS}}{2} \tag{A.8}$$

Case 4. *A is low and B is high*

For this input condition, the transistors M_{X3}, M_{X6}, M_{X7} are ON while the transistors M_{X4}, M_{X5} and M_{X8} are OFF. The current through the transistors M_{X3} $(i_{D,3})$, M_{X5} $(i_{D,5})$, M_{X8} $(i_{D,7})$ may be

written as:

$$i_{D,3}=\frac{I_{SS}}{2}\frac{1}{1+N};\quad i_{D,6}=\frac{I_{SS}}{2};\quad i_{D,7}=\frac{I_{SS}}{2}\frac{N}{1+N} \tag{A.9}$$

This input condition produces the low output voltage given by (A.8)

It may be observed that there are two values of low output voltage V_{OL1} (Eq. (A.6)) and V_{OL2} (Eq. (A.8)) resulting in the two values of the voltage swing given as:

$$V_{SWING1}=V_{OH}-V_{OL1}=\frac{R_P I_{SS}}{2}\left(1+\frac{1}{1+N}\right) \tag{A.10}$$

$$V_{SWING2}=V_{OH}-V_{OL2}=\frac{R_P I_{SS}}{2} \tag{A.11}$$

For large values of N, the voltage swing V_{SWING} can be approximated as:

$$V_{SWING}=\frac{R_P I_{SS}}{2} \tag{A.12}$$

The small-signal voltage gain (A_v) and noise margin (NM) for the new fundamental cell are computed by the method outlined in [6] as

$$A_v=\frac{g_{m,n}R_P/2}{1-g_{m,n}R_P/2} \tag{A.13}$$

$$\mathrm{NM}=\frac{V_{SWING}}{2}\left[1-\frac{1}{A_v}\right] \tag{A.14}$$

where $g_{m,n}=\sqrt{\mu_{eff,n}C_{OX}(W_N/L_N)(I_{SS}/2)}$ is the transconductance of the transistors $M_{X3,4,5,6}$ and $\mu_{eff,n}$, W_N and L_N are the effective electron mobility, the effective channel width and length of the said transistors, respectively.

The expressions of small-signal voltage gain (A_v) and noise margin (NM) represented in (A.13) and (A.14), respectively, are valid for the cases wherein $g_{m,n}R_P/2$ is taken to be lower than unity whereas for the remaining case, the circuit exhibits hysteresis. So as recommended in [6], to avoid large sizes of the transistors, the PFSCL circuits with $g_{m,n}R_P/2$ values close to unity are considered. The DC behavior of the proposed fundamental cell is validated through SPICE simulations by using TSMC 0.18 μm CMOS process parameters and with a power supply of 1.1 V. The new fundamental gate was implemented and simulated for a voltage swing of 400 mV, $N=10$, and the bias current of 100 μA. The dc transfer characteristic of the fundamental cell for $g_{m,n}R_P/2=0.98$ and $g_{m,n}R_P/2=3$ by varying the two inputs simultaneously are shown in Figs. A.2 and A.3, respectively. The simulation results conform to the theoretical prepositions.

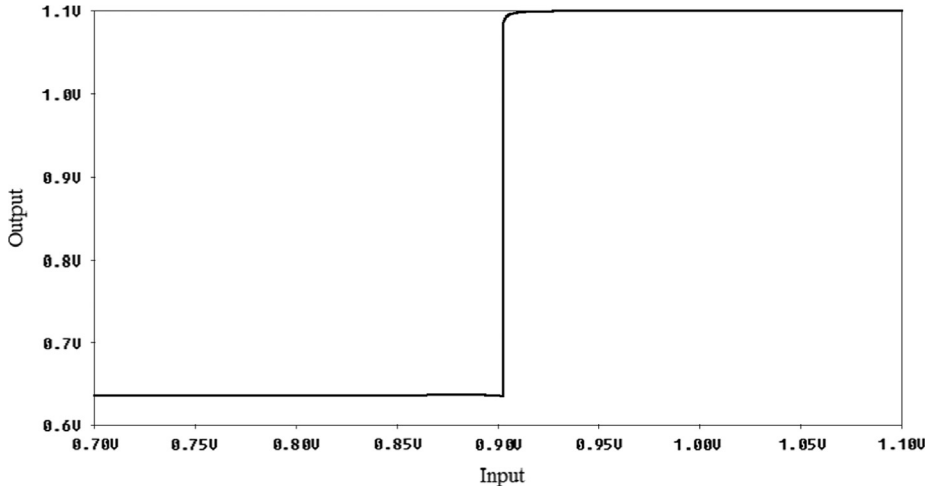

Fig. A.2. DC transfer characteristics of the fundamental cell configured as AND gate ($g_mR_D/=0.98$).

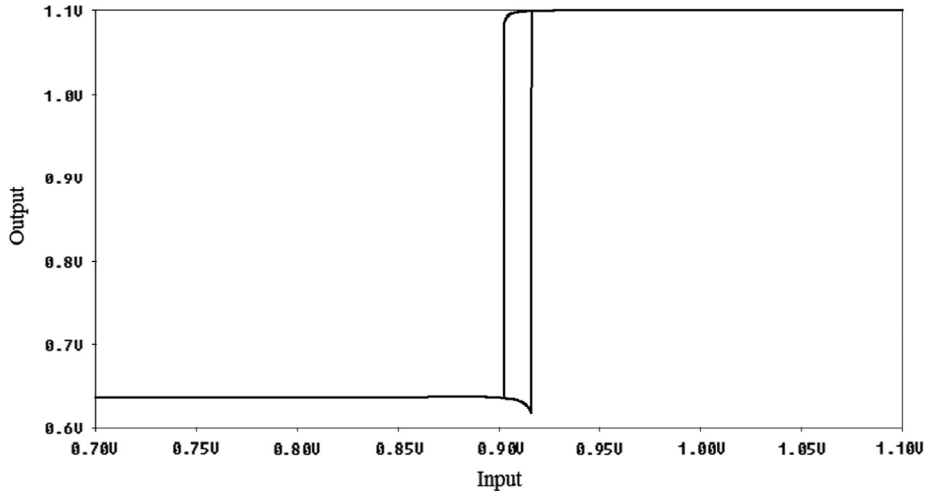

Fig. A.3. DC transfer characteristics of the fundamental cell configured as AND gate ($g_mR_D/2=3$).

References

[1] D. Allstot, S. Chee, S. Kiaei, M. Shristawa, Folded source-coupled logic vs. CMOS static logic for low-noise mixed-signal ICs, IEEE Trans. Circuits Syst. Regul. Pap. 40 (1993) 553–563.

[2] S. Masui, Simulation of substrate coupling in mixed-signal MOS circuits, in: Proceedings of International Symposium on VLSI Circuits, 1992, pp. 42–43.

[3] S. Kiaei, S. Chee, D. Allstot, CMOS source-coupled logic for mixed-mode VLSI, in: Proceedings of International Symposium on Circuits and Systems, 1990, pp. 1608–1611.

[4] M. Alioto, G. Palumbo, Model and Design of Bipolar and MOS Current-Mode logic (CML, ECL and SCL Digital Circuits), Springer, The Netherlands, 2005.

[5] O. Musa, An efficient delay model for MOS current-mode logic automated design and optimization, IEEE Trans. Circuits Syst. Regul. Pap. 57 (2010) 2041–2052.

[6] M. Alioto, L. Pancioni, S. Rocchi, V. Vignoli, Modeling and evaluation of positive-feedback source-coupled logic, IEEE Trans. Circuits Syst. Regul. Pap. 51 (2004) 2345–2355.

[7] M. Alioto, A. Fort, L. Pancioni, S. Rocchi, V. Vignoli, Positive-feedback source-coupled logic: a delay model, in: Proceedings of International Symposium on Circuits and Systems, 2004, pp. II/641–644.

[8] M. Alioto, A. Fort, L. Pancioni, S. Rocchi, V. Vignoli, An approach to the design of PFSCL gates, in: Proceedings of International Symposium on Circuits and Systems, 2005, pp. 2437–2440.

[9] M. Alioto, L. Pancioni, S. Rocchi, V. Vignoli, Power-delay-area-noise margin trade-offs in positive-feedback mos current-mode logic, IEEE Trans. Circuits Syst. Regul. Pap. 54 (2007) 1916–1928.

[10] M. Alioto, L. Pancioni, S. Rocchi, V. Vignoli, Exploiting hysteresys in MCML circuits, IEEE Trans. Circuits Syst. Express Briefs 53 (2006) 1170–1174.

[11] K. Kimura, Circuit design techniques for very low-voltage analog functional blocks using triple-tail cells, IEEE Trans. Circuits Syst. Fundam. Theor. Appl. 42 (1995) 873–885.

[12] F. Matsumoto, Y. Noguchi, Linear bipolar OTAs based on a triple-tail cell employing exponential circuits, IEEE Trans. Circuits Syst. Express Briefs 51 (2004) 670–674.

[13] M. Alioto, R. Mita, G. Palumbo, Performance evaluation of the low-voltage CML D-latch topology, Integr. VLSI J. 36 (2003) 191–209.

[14] K. Gupta, N. Pandey, M. Gupta, M.O.S. Low-Voltage, Current mode logic multiplexer, Radio Eng. J. 22 (2013) 259–268.

[15] K. Gupta, N. Pandey, M. Gupta, Analysis and design of MOS current mode logic exclusive-OR gate using triple-tail cells, Microelectron. J. (2013) 1–7 http://dx.doi.org/10.1016/j.mejo.2013.03.007.

Microelectronics Journal 45 (2014) 1001–1007

Contents lists available at ScienceDirect

Microelectronics Journal

journal homepage: www.elsevier.com/locate/mejo

An efficient triple-tail cell based PFSCL D latch

Neeta Pandey [a,*], Kirti Gupta [a], Maneesha Gupta [b]

[a] Department of ECE, Delhi Technological University, Formerly Delhi College of Engineering, Bawana Road, Delhi 110042, India
[b] Division of ECE, Netaji Subhas Institute of Technology (NSIT), University of Delhi, Sector 3, Dwarka, New Delhi 110078, India

ARTICLE INFO

Article history:
Received 18 May 2013
Received in revised form
30 April 2014
Accepted 6 May 2014

Keywords:
PFSCL
D latch
Triple-tail cell

ABSTRACT

In this paper, an efficient positive feedback source-coupled logic (PFSCL) D latch topology is proposed. It uses triple-tail cell concept which results in lesser number of stages as well as gate count in comparison to the traditional PFSCL D latch. The operation of the proposed D latch is described and is supported with mathematical formulations. The functionality is verified through SPICE simulations using TSMC 0.18 μm CMOS technology parameters. It is found that the proposed D latch topology significantly reduces the power consumption and delay in comparison to the traditional PFSCL D latch. The impact of process variation on the proposed and traditional PFSCL D latch at different design corners shows similar variations.

© 2014 Elsevier Ltd. All rights reserved.

1. Introduction

The source-coupled logic (SCL) style is preferred over the traditional CMOS logic style in mixed signal applications for high speed digital circuit design due to its inherent characteristics of reduced switching noise and frequency independent power consumption [1–3]. The SCL gates are broadly classified as differential or single-ended [4–10]. The former is based on the stacking of the transistors pairs [4,5] whereas the transistors are connected in parallel and are source-coupled to a transistor whose gate is connected to reference voltage source [6] in the latter one.

An improved single-ended SCL style named as positive-feedback source-coupled logic (PFSCL) style has been suggested in literature [6–10]. The logic style replaces the reference voltage source used in traditional single-ended SCL gates with a positive feedback to improve their performance. It mainly uses NAND/NOR gates to implement a given logic function since no stacked transistor pairs are employed. Therefore, the traditional PFSCL D latch realization consist of multiple PFSCL NOR stages. In this paper, a new topology for PFSCL D latch employing lesser number of PFSCL stages than the traditional one is proposed. It uses triple-tail cell concept [11–15] to improve the overall performance of the gate.

The paper first briefly describes the PFSCL style in Section 2 and its usage in D latch implementation. Thereafter, the proposed PFSCL D latch architecture is explained in Section 3. The functionality of proposed gate and its effectiveness over traditional PFSCL D latch is illustrated through simulations using TSMC 0.18 μm CMOS technology parameters in Section 4. The impact of process variation at different design corners is also studied. Finally, the conclusions are drawn in Section 5.

2. PFSCL style

The PFSCL style works on the principle of current steering and uses a pull-down network (PDN), a constant current source and a load circuit in order to implement the logic gate. The realization of a generic N-input NOR based PFSCL gate is shown in Fig. 1a. The inputs are applied to the gates of N-NMOS transistors M_i ($i=1, 2,\ldots, N$) which share common source and drain terminals [6]. The input transistors are source-coupled with a feedback transistor M_f whose gate is connected to the output node Q. The constant current source M_S provides the bias current I_{SS} while the PMOS load transistor M_{L1} and M_{L2} performs the current to voltage conversion. The transistor M_{L2} (optional) is inserted to generate the complement of the output $\left(\overline{Q}\right)$ and can be substituted by a short circuit when it is not needed [6]. The NOR based realization can also be used for N-input NAND gate with help of De Morgan law. The inputs need to be applied in the inverted form, and the output is taken from M_{L2} as depicted in Fig. 1b. Thus it can be deduce that the PFSCL style does not require stacked transistor pairs [6].

To analyze the PFSCL circuits, the load transistors M_{L1}, M_{L2} is substituted by an equivalent linear resistance R_P model given as [6]

$$R_P = \frac{R_{\text{int}}}{1-\left(\left(R_{\text{DSW}}10^{-6}\right)/W_P\right)/R_{\text{int}}} \quad (1)$$

* Corresponding author.
E-mail addresses: n66pandey@rediffmail.com, neetapandey06@gmail.com (N. Pandey).

http://dx.doi.org/10.1016/j.mejo.2014.05.002
0026-2692/© 2014 Elsevier Ltd. All rights reserved.

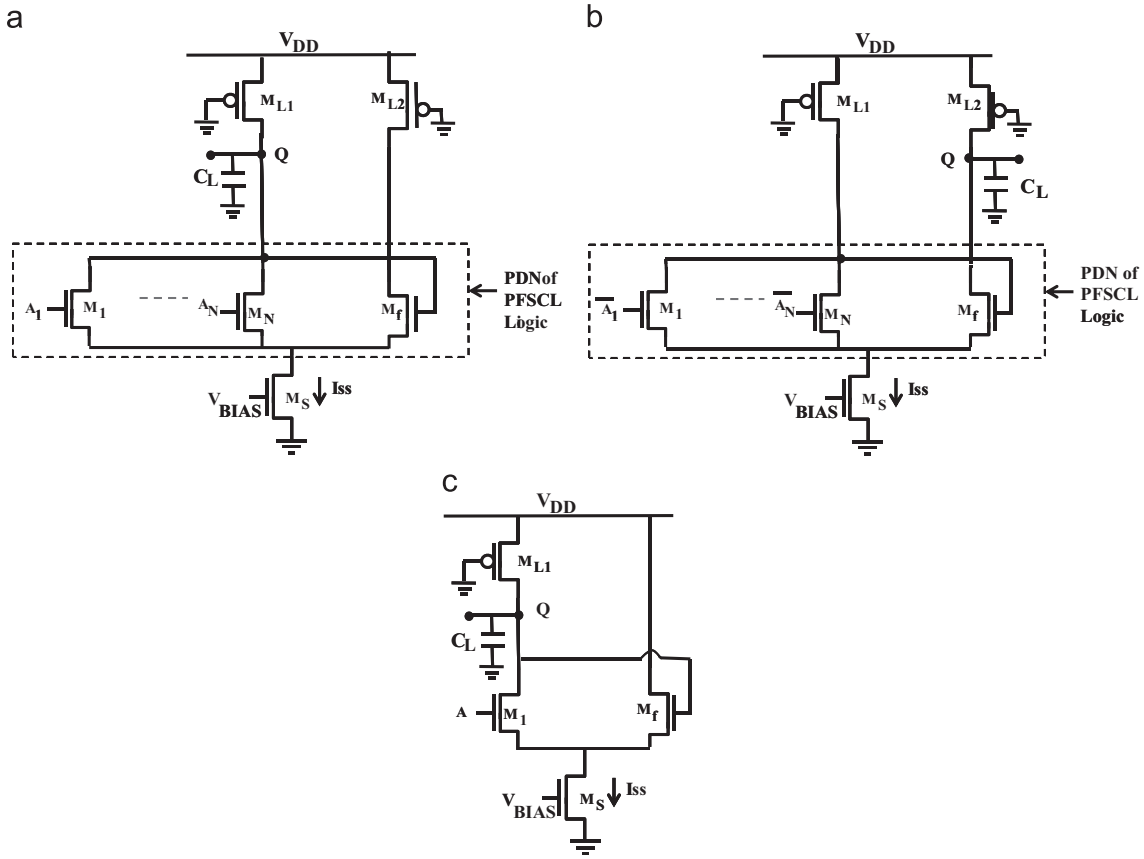

Fig. 1. (a) Generic N-input PFSCL circuit (NOR based implementation. (b) N-input PFSCL circuit (NAND based implementation. (c) PFSCL inverter.

where R_{DSW} is the empirical model parameter, W_P is the effective channel width of the load transistor and the parameter R_{int} is the intrinsic resistance of the PMOS load transistors in the linear region and is given as

$$R_{int} = \left[\mu_{eff,p} C_{ox} \frac{W_P}{L_P}(V_{DD} - |V_{T,p}|)\right]^{-1} \quad (2)$$

where C_{ox} is the oxide capacitance per unit area. The parameters $\mu_{eff,p}$, $V_{T,p}$ and L_P are the effective hole mobility, the threshold voltage, and the effective channel length of the load transistor, respectively.

The circuit of a PFSCL inverter with input A is shown in Fig. 1c. For high value at input A, the bias current I_{SS} is steered through transistor M_1 and produces a low output voltage ($V_{OL}=V_{DD}-R_P I_{SS}$) [6]. Similarly, the transistor M_1 is turned OFF for low value of input A, and a high voltage ($V_{OH}=V_{DD}$) is obtained at the output. The voltage swing for PFSCL circuits (V_{SWING}) is the difference between V_{OH} and V_{OL} and is computed as

$$V_{SWING} = R_P I_{SS} \quad (3)$$

In PFSCL gates the bias current I_{SS} flows throughout the operation and consumes power computed as:

$$P = V_{DD} I_{SS} \quad (4)$$

The NOR based realization of the traditional PFSCL D latch having three levels is shown in Fig. 2. The first level is responsible for generating the complement of the applied inputs whereas the subsequent two levels implements the SR latch. In all, it consist of six identical PFSCL NOR gates such that the total power consumption is six times the power consumed by a single PFSCL NOR gate. Hence, the traditional D latch may not be beneficial in many low-power applications. Therefore, in the next section a new D latch topology is proposed. The number of levels as well as the gate count is reduced which makes it more efficient than the traditional PFSCL D latch.

3. Proposed PFSCL D latch topology

The complete schematic of the proposed D latch comprise of two levels namely a single PFSCL inverter and a new fundamental cell as shown in Fig. 3. The PFSCL inverter generates the complement of CLK which is fed as the input to the fundamental cell. The new fundamental cell is based on the triple-tail cell concept [11–15]. It consists of two triple-tail cells (M_{X3}, M_{X4}, M_{X7}) and (M_{X5}, M_{X6}, M_{X8}) biased by separate current sources of $I_{SS}/2$ value such that the new cell draws the same current as that of the single traditional PFSCL gate (Fig. 1). A detailed analysis of the fundamental cell by configuring it as an AND gate is discussed in Appendix. To realize a D latch, the transistors M_{X7} and M_{X8} driven by the input clock (CLK) and its complement are connected between the supply terminal and the common source terminal of transistor pairs M_{X3}–M_{X4} and M_{X5}–M_{X6}, respectively, as shown in Fig. 3. A high voltage on CLK turns ON the transistor M_{X7}, and deactivates the transistor pair M_{X3}–M_{X4}. At the same time, the transistor M_{X8} turns OFF so that the transistor pair M_{X5}–M_{X6} generates the output according to the input D. Similarly, the transistor pair M_{X3}–M_{X4} gets activated for low voltage of CLK and preserves the previous output. Thus the proposed D-latch models the positive level sensitive D latch.

It may be noted that if equal aspect ratio of all transistors in the triple-tail cells is considered, then the transistors M_{X7} and M_{X8} will

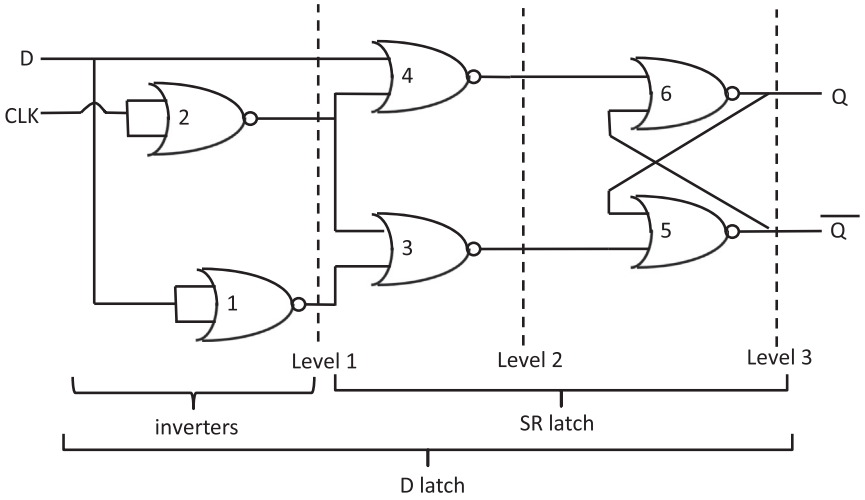

Fig. 2. Traditional PFSCL D latch.

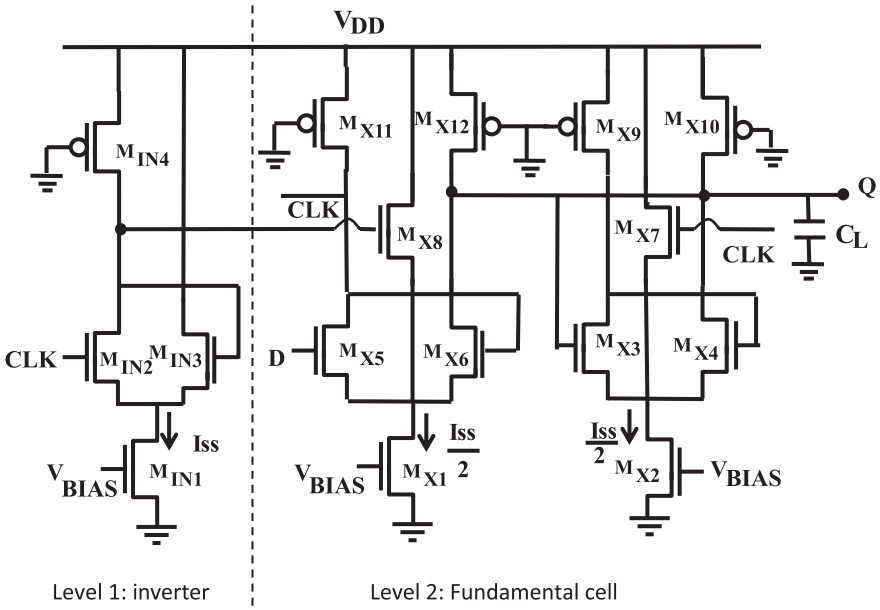

Fig. 3. Complete schematic of the proposed triple-tail cell based PFSCL D latch.

not be able to completely switch OFF the transistor pair M_{X3}–M_{X4} and M_{X5}–M_{X6}. For the case when both D and Q are high and CLK makes a transition from low to high, the transistors M_{X3} and M_{X7} draw the same current as their gate-source voltages are equal. However, the proper operation demands that transistor M_{X7} should draw all/maximum bias current of the triple-tail cell. To ensure this the aspect ratio of M_{X7} is made larger (say N times) than M_{X3}.In this case, the currents flowing through M_{X3} and M_{X7} can be written as:

$$i_{D,3} = \frac{I_{SS}}{2}\frac{1}{1+N} \tag{5a}$$

$$i_{D,7} = \frac{I_{SS}}{2}\frac{N}{1+N} \tag{5b}$$

The current through M_{X3} can be minimized by increasing factor N. This input condition produces the high output voltage V_{OH} as

$$V_{OH} = V_{DD} - R_P\left[(i_{D,4} + i_{D,6})\right] = V_{DD} \tag{6}$$

where $i_{D,4}$, $i_{D,6}$ are the currents through transistors M_{X4} and M_{X6}, respectively. The output voltages for various input combinations are enlisted in Table 1.

It can be observed from Table 1 that there are two values of both maximum output voltage V_{OH} and minimum output voltage V_{OL} for different combinations of D and Q. Consequently, the voltage swing, V_{SWING1} for the same value of the input D and the present state can be expressed as

$$V_{SWING1} = V_{OH1} - V_{OL1} = \frac{R_P I_{SS}}{2}\left(1 + \frac{N}{1+N}\right) \tag{7a}$$

where V_{OH1}, V_{OL1} are maximum output voltage and minimum output voltage, respectively, for the same inputs and the present state and the voltage swing, V_{SWING2} for the different value of the input D and the present state can be expressed as

$$V_{SWING2} = V_{OH2} - V_{OL2} = \frac{R_P I_{SS}}{2}\left(\frac{N}{1+N}\right) \tag{7b}$$

where V_{OH2}, V_{OL2} are maximum output voltage and minimum output voltage, respectively, for different inputs. As $V_{SWING2} < V_{SWING1}$, V_{SWING2} has been considered as the worst case voltage

Table 1
Differential output voltages for various input combinations.

Inputs		Previous state	Currents through the transistors						Output voltage of the next state V_Q	
CLK	D	Q	M_{X3}	M_{X4}	M_{X5}	M_{X6}	M_{X7}	M_{X8}	Level	$V_{DD}-R_P\,(i_{D,4}+\,i_{D,6})$
L	L	L	0	I_1	0	I_3	0	I_2	V_{OL1}	$V_{DD}-R_PI_{SS}/2(1+1/1+N)$
L	L	H	I_1	0	0	I_3	0	I_2	V_{OH2}	$V_{DD}-R_PI_{SS}/2(1/1+N)$
L	H	L	0	I_1	I_3	0	0	I_2	V_{OL2}	$V_{DD}-R_PI_{SS}/2$
L	H	H	I_1	0	I_3	0	0	I_2	V_{OH1}	V_{DD}
H	L	L	0	I_3	0	I_1	I_2	0	V_{OL1}	$V_{DD}-R_PI_{SS}/2(1+1/1+N)$
H	L	H	I_3	0	0	I_1	I_2	0	V_{OL2}	$V_{DD}-R_PI_{SS}/2$
H	H	L	0	I_3	I_1	0	I_2	0	V_{OH2}	$V_{DD}-R_PI_{SS}/2(1/1+N)$
H	H	H	I_3	0	I_1	0	I_2	0	V_{OH1}	V_{DD}

Where L/H=low/high input voltage, $I_1=I_{SS}/2$, $I_2=I_{SS}/2\ (N/1+N)$, $I_3=I_{SS}/2\ (1/1+N)$, V_{OL}/V_{OH}=low/high output voltage.

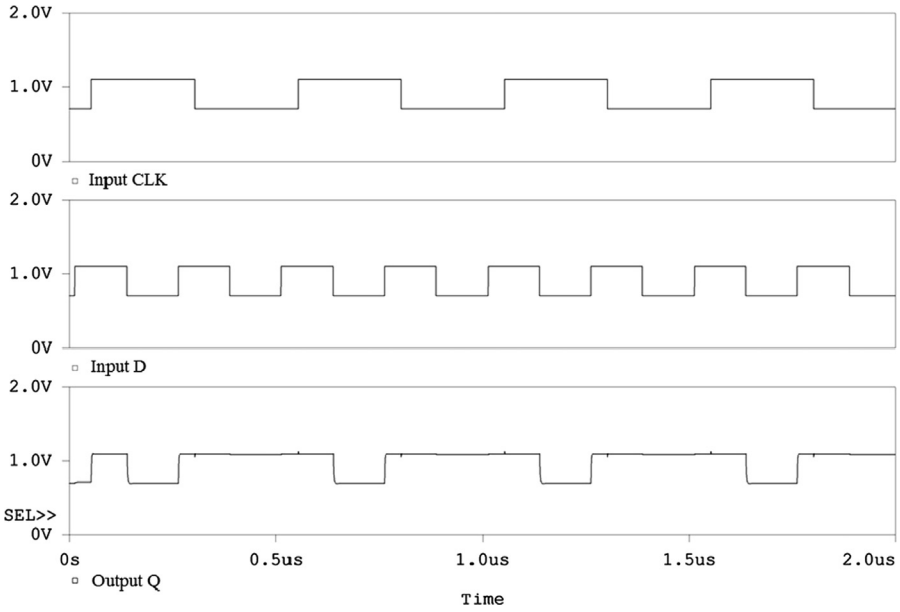

Fig. 4. Waveforms of the proposed PFSCL D latch.

Table 2
Impact of parameter variations on the performance of the proposed and the traditional D latches.

Parameter	**NMOS** **PMOS**	***T*** ***T***	***F*** ***F***	***S*** ***S***	***F*** ***S***	**S** **F**
Propagation delay(ps) (C_L=100 fF)	Proposed	658	628	953	631	640
	Traditional	1270	1036	1489	1203	1240
Power (μW)	Proposed	219	283	158	261	256
	Traditional	633	846	438	642	635

Where different design corners are denoted by T=typical, F=fast, S=slow.

swing, V_{SWING} and has been further approximated as

$$V_{SWING}=\frac{R_PI_{SS}}{2}\quad \text{for large values of } N \tag{8}$$

It may be noted from Eq. (8) that the voltage swing of the proposed D latch is half the voltage swing of the traditional PFSCL D latch. This can be compensated by keeping the value of the load resistance twice the resistance value of the traditional D latch.

4. Simulation section

This section verifies the functionality of the proposed D latch followed by its performance comparison with the traditional PFSCL D latch in terms of the power consumption and the propagation delay. Also, the effect of parameter variations is also studied for both the topologies. The voltage swing and bias current of 400 mV and 100 μA, respectively, are considered for both the types of gates. TSMC 0.18 μm CMOS technology parameters and a power supply of 1.1 V are taken in all the simulations.

The proposed D latch (Fig. 3) is simulated and the waveforms of the inputs (D and CLK), and the output node Q are shown in Fig. 4. It can be observed that for high values of the CLK signal the D latch is in the transparent state whereas it is in the hold state for low values of the CLK signal.

The performance of the proposed D latch is compared with the PFSCL counterpart. The power consumption of the proposed and the traditional D latch are 219 μW and 633 μW, respectively. The proposed gate saves 65% power in comparison to the traditional

one. This is due to the fact that the power consumed by the proposed D latch is given as the sum of the power consumed by the inverter and the fundamental cell whereas for the traditional D latch it is the sum of power consumed by all the gates six identical NOR gates in Fig. 2. Thus, the proposed D latch offers power saving due to the lesser number of gates in comparison to the traditional one. Similarly, the propagation delay for the proposed and the traditional gates are 658 ps and 1270 ps, respectively. This shows an improvement of 48% which can be attributed to the reduction in the number of levels involved in the implementation.

The impact of parameter variation on the proposed and the traditional D latch performance is studied at different design corners. The findings for various operating conditions are given in Table 2. It is found that the propagation delay and the power of the proposed D latch vary by a factor of 1.5 and 1.8, respectively, between the best and the worst cases whereas a factor of 1.43 and 1.9, respectively, are obtained for the traditional PFSCL D latch.

5. Conclusion

In this paper, an efficient triple-tail cell based positive feedback source-coupled logic (PFSCL) D latch topology is proposed. The topology has lesser number of stages as well as gates count in comparison to the traditional PFSCL D latch. The D latch has been implemented and simulated using TSMC 0.18 μm CMOS technology parameters. It is found that the proposed D latch topology is better than the traditional one in terms of speed and power. The study of impact of process variation at different design corners shows that both the gates show similar variations.

Appendix

The proposed D latch consists of a new fundamental cell employing two triple-tail cells as shown in Fig. 3. The behavior of the new fundamental cell can be analyzed by configuring it as a 2-input AND gate shown in Fig. A.1. When input B is high, the transistor M_{X7} is ON and the transistor pair M_{X3} and M_{X4} is deactivated. At the same time, the transistor M_{X8} is turned OFF and the output is generated according to the input A through the transistor pair M_{X5}–M_{X6}. Similarly, the transistor pair M_{X3}–M_{X4} gets activated for low voltage on B and a low voltage is obtained at the output. Thus, confirming to the functionality of the AND gate.

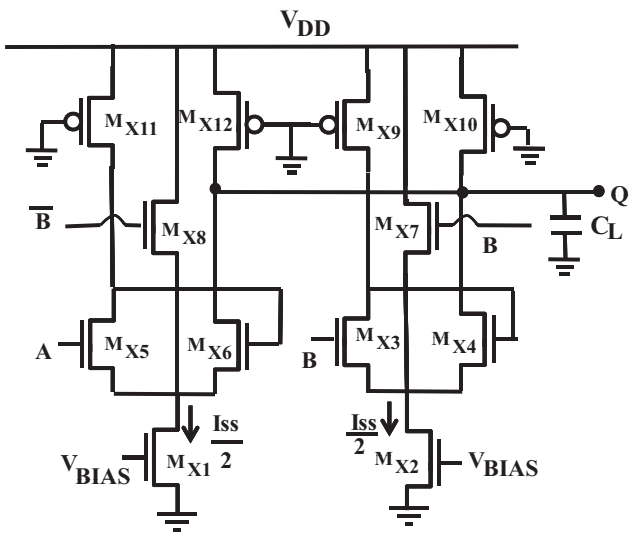

Fig. A.1. Fundamental cell configured as AND gate with inputs A and B .

It may be noted in the new fundamental cell that if equal aspect ratio of all transistors is considered, then the transistors M_{X7} and M_{X8} will not be able to completely switch OFF the transistor pair M_{X3}–M_{X4} and M_{X5}–M_{X6}. For the case when both the inputs are high, the transistors M_{X3}, M_{X5} and M_{X7} are ON while M_{X4}, M_{X6} and M_{X8} are OFF. A high to low transition at B makes transistor M_{X8} ON. In this case the transistors M_{X5} and M_{X8} will draw equal currents as their gate-source voltages are same. Hence the transistor M_{X8} is not able to completely deactivate the transistor pair M_{X5}–M_{X6}. Therefore to achieve proper operation, the aspect ratio of transistors M_{X7}, M_{X8} is made greater than other transistors' aspect ratio by a factor N. Thus, the currents flowing through M_{X5} and M_{X8} can be written as:

$$i_{D,5} = \frac{I_{SS}}{2}\frac{1}{1+N} \tag{A.1}$$

$$i_{D,8} = \frac{I_{SS}}{2}\frac{N}{1+N} \tag{A.2}$$

Based on this observation, the DC analysis of the AND gate for the different combinations of the inputs is discussed below:

Case 1. *Both inputs (A and B) are high*

When both the inputs are high, the transistors M_{X3}, M_{X5}, M_{X7} are ON and transistors M_{X4}, M_{X6} and M_{X8} are OFF. The current through the transistors M_{X3} $(i_{D,3})$, M_{X5} $(i_{D,5})$, M_{X7} $(i_{D,7})$ may be written as:

$$i_{D,3} = \frac{I_{SS}}{2}\frac{1}{1+N};\quad i_{D,5} = \frac{I_{SS}}{2};\quad i_{D,7} = \frac{I_{SS}}{2}\frac{N}{1+N} \tag{A.3}$$

This input condition produces the high output voltage V_{OH} as:

$$V_{OH} = V_{DD} - R_P\left[(i_{D,4} + i_{D,6})\right] = V_{DD} \tag{A.4}$$

Case 2. *Both inputs (A and B) are low*

When both the inputs are low, the transistors M_{X4}, M_{X6}, M_{X8} are ON and transistors M_{X3}, M_{X5} and M_{X7} are OFF. The current through the transistors M_{X4} $(i_{D,4})$, M_{X6} $(i_{D,6})$, M_{X8} $(i_{D,8})$ may be written as:

$$i_{D,4} = \frac{I_{SS}}{2};\quad i_{D,6} = \frac{1}{1+N}\frac{I_{SS}}{2};\quad i_{D,8} = \frac{I_{SS}}{2}\frac{N}{1+N} \tag{A.5}$$

This input condition produces the low output voltage V_{OL1} as:

$$V_{OL1} = V_{DD} - R_P\left[(i_{D,4} + i_{D,6})\right] = V_{DD} - \frac{R_P I_{SS}}{2}\left(1 + \frac{1}{1+N}\right) \tag{A.6}$$

Case 3. *A is high and B is low*

For this input condition, the transistors M_{X4}, M_{X5}, M_{X8} are ON and transistors M_{X3}, M_{X6} and M_{X7} are OFF. The current through the transistors M_{X4} $(i_{D,4})$, M_{X5} $(i_{D,5})$, M_{X8} $(i_{D,8})$ may be written as:

$$i_{D,4} = \frac{I_{SS}}{2};\quad i_{D,5} = \frac{1}{1+N}\frac{I_{SS}}{2};\quad i_{D,8} = \frac{I_{SS}}{2}\frac{N}{1+N} \tag{A.7}$$

This input condition produces the low output voltage V_{OL2} as:

$$V_{OL2} = V_{DD} - R_P\left[(i_{D,4} + i_{D,6})\right] = V_{DD} - \frac{R_P I_{SS}}{2} \tag{A.8}$$

Case 4. *A is low and B is high*

For this input condition, the transistors M_{X3}, M_{X6}, M_{X7} are ON while the transistors M_{X4}, M_{X5} and M_{X8} are OFF. The current through the transistors M_{X3} $(i_{D,3})$, M_{X5} $(i_{D,5})$, M_{X8} $(i_{D,7})$ may be

written as:

$$i_{D,3}=\frac{I_{SS}}{2}\frac{1}{1+N};\quad i_{D,6}=\frac{I_{SS}}{2};\quad i_{D,7}=\frac{I_{SS}}{2}\frac{N}{1+N} \tag{A.9}$$

This input condition produces the low output voltage given by (A.8)

It may be observed that there are two values of low output voltage V_{OL1} (Eq. (A.6)) and V_{OL2} (Eq. (A.8)) resulting in the two values of the voltage swing given as:

$$V_{SWING1}=V_{OH}-V_{OL1}=\frac{R_P I_{SS}}{2}\left(1+\frac{1}{1+N}\right) \tag{A.10}$$

$$V_{SWING2}=V_{OH}-V_{OL2}=\frac{R_P I_{SS}}{2} \tag{A.11}$$

For large values of N, the voltage swing V_{SWING} can be approximated as:

$$V_{SWING}=\frac{R_P I_{SS}}{2} \tag{A.12}$$

The small-signal voltage gain (A_v) and noise margin (NM) for the new fundamental cell are computed by the method outlined in [6] as

$$A_v=\frac{g_{m,n}R_P/2}{1-g_{m,n}R_P/2} \tag{A.13}$$

$$\mathrm{NM}=\frac{V_{SWING}}{2}\left[1-\frac{1}{A_v}\right] \tag{A.14}$$

where $g_{m,n}=\sqrt{\mu_{eff,n}C_{OX}(W_N/L_N)(I_{SS}/2)}$ is the transconductance of the transistors $M_{X3,4,5,6}$ and $\mu_{eff,n}$, W_N and L_N are the effective electron mobility, the effective channel width and length of the said transistors, respectively.

The expressions of small-signal voltage gain (A_v) and noise margin (NM) represented in (A.13) and (A.14), respectively, are valid for the cases wherein $g_{m,n}R_P/2$ is taken to be lower than unity whereas for the remaining case, the circuit exhibits hysteresis. So as recommended in [6], to avoid large sizes of the transistors, the PFSCL circuits with $g_{m,n}R_P/2$ values close to unity are considered. The DC behavior of the proposed fundamental cell is validated through SPICE simulations by using TSMC 0.18 μm CMOS process parameters and with a power supply of 1.1 V. The new fundamental gate was implemented and simulated for a voltage swing of 400 mV, $N=10$, and the bias current of 100 μA. The dc transfer characteristic of the fundamental cell for $g_{m,n}R_P/2=0.98$ and $g_{m,n}R_P/2=3$ by varying the two inputs simultaneously are shown in Figs. A.2 and A.3, respectively. The simulation results conform to the theoretical prepositions.

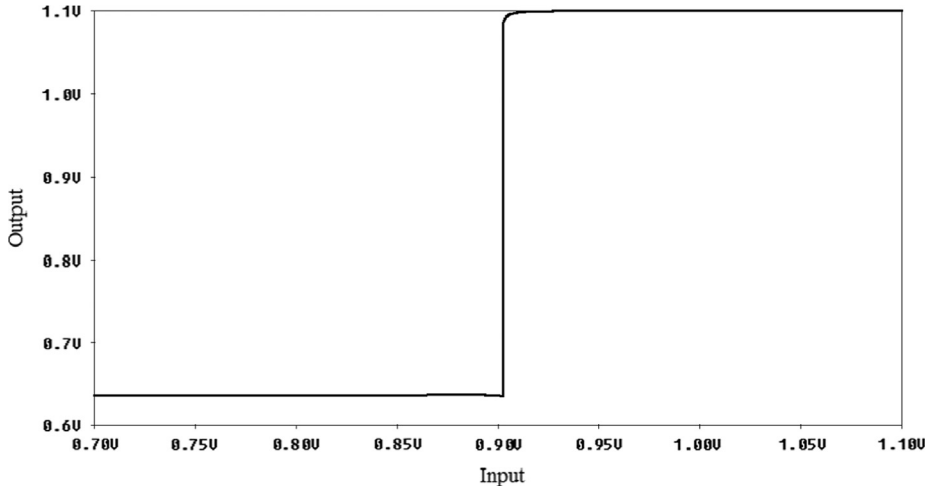

Fig. A.2. DC transfer characteristics of the fundamental cell configured as AND gate ($g_mR_D/=0.98$).

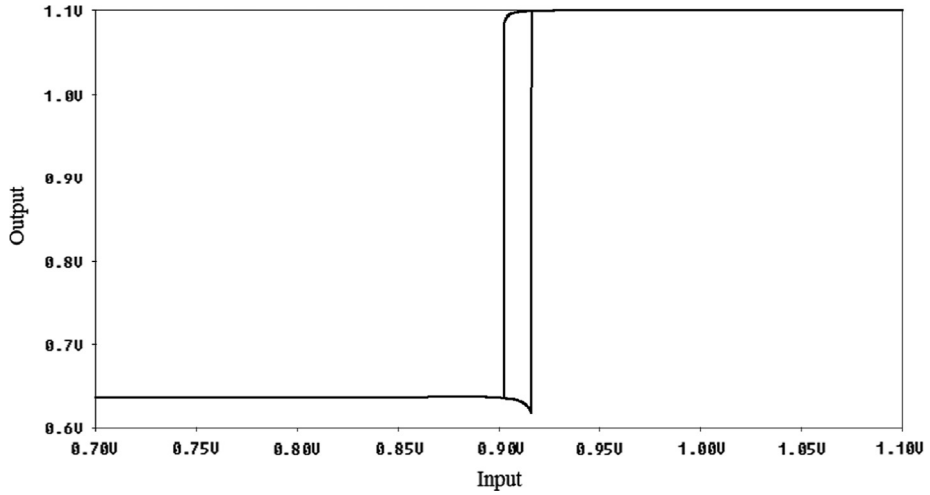

Fig. A.3. DC transfer characteristics of the fundamental cell configured as AND gate ($g_mR_D/2=3$).

References

[1] D. Allstot, S. Chee, S. Kiaei, M. Shristawa, Folded source-coupled logic vs. CMOS static logic for low-noise mixed-signal ICs, IEEE Trans. Circuits Syst. Regul. Pap. 40 (1993) 553–563.

[2] S. Masui, Simulation of substrate coupling in mixed-signal MOS circuits, in: Proceedings of International Symposium on VLSI Circuits, 1992, pp. 42–43.

[3] S. Kiaei, S. Chee, D. Allstot, CMOS source-coupled logic for mixed-mode VLSI, in: Proceedings of International Symposium on Circuits and Systems, 1990, pp. 1608–1611.

[4] M. Alioto, G. Palumbo, Model and Design of Bipolar and MOS Current-Mode logic (CML, ECL and SCL Digital Circuits), Springer, The Netherlands, 2005.

[5] O. Musa, An efficient delay model for MOS current-mode logic automated design and optimization, IEEE Trans. Circuits Syst. Regul. Pap. 57 (2010) 2041–2052.

[6] M. Alioto, L. Pancioni, S. Rocchi, V. Vignoli, Modeling and evaluation of positive-feedback source-coupled logic, IEEE Trans. Circuits Syst. Regul. Pap. 51 (2004) 2345–2355.

[7] M. Alioto, A. Fort, L. Pancioni, S. Rocchi, V. Vignoli, Positive-feedback source-coupled logic: a delay model, in: Proceedings of International Symposium on Circuits and Systems, 2004, pp. II/641–644.

[8] M. Alioto, A. Fort, L. Pancioni, S. Rocchi, V. Vignoli, An approach to the design of PFSCL gates, in: Proceedings of International Symposium on Circuits and Systems, 2005, pp. 2437–2440.

[9] M. Alioto, L. Pancioni, S. Rocchi, V. Vignoli, Power-delay-area-noise margin trade-offs in positive-feedback mos current-mode logic, IEEE Trans. Circuits Syst. Regul. Pap. 54 (2007) 1916–1928.

[10] M. Alioto, L. Pancioni, S. Rocchi, V. Vignoli, Exploiting hysteresys in MCML circuits, IEEE Trans. Circuits Syst. Express Briefs 53 (2006) 1170–1174.

[11] K. Kimura, Circuit design techniques for very low-voltage analog functional blocks using triple-tail cells, IEEE Trans. Circuits Syst. Fundam. Theor. Appl. 42 (1995) 873–885.

[12] F. Matsumoto, Y. Noguchi, Linear bipolar OTAs based on a triple-tail cell employing exponential circuits, IEEE Trans. Circuits Syst. Express Briefs 51 (2004) 670–674.

[13] M. Alioto, R. Mita, G. Palumbo, Performance evaluation of the low-voltage CML D-latch topology, Integr. VLSI J. 36 (2003) 191–209.

[14] K. Gupta, N. Pandey, M. Gupta, M.O.S. Low-Voltage, Current mode logic multiplexer, Radio Eng. J. 22 (2013) 259–268.

[15] K. Gupta, N. Pandey, M. Gupta, Analysis and design of MOS current mode logic exclusive-OR gate using triple-tail cells, Microelectron. J. (2013) 1–7 http://dx.doi.org/10.1016/j.mejo.2013.03.007.

Logistics Research
© The Author(s) 2014
10.1007/s12159-014-0117-9
Original Paper

Analysis of the skilled work force effect on the logistics performance index—case study from India

Amrita Jhawar1 , S. K. Garg1 and Shikha N. Khera1
(1)Delhi School of Management, Delhi Technological University, Shahbad Daulatapur, Main Bawana Road, New Delhi, 110042, India

Amrita Jhawar
Email: ajhawar1@gmail.com
Received: 14 October 2013
Accepted: 2 June 2014
Published online: 17 June 2014
Abstract
The purpose of this paper is to study the impact of development of skilled work force through investment in training, welfare, working conditions, and wages on the logistics performance index. It also discusses the effect of skilled labour on logistics cost, logistics time, reliability, flexibility, and safety of a logistics system. The paper is based on a case study conducted on an Indian Logistics Service provider. A causal loop diagram and the stock and flow diagram have been developed according to system dynamics modelling principles. The simulation result shows significant improvement in the logistics performance index. The reduction in logistics cost and logistics time is 12 % and 80 min, respectively. With training provided to 36 % employees of the company, the retention rate improved by 58 % and score of recruitment reached to 4.4 out of five. The paper shows that investment done in human resources in the Indian logistics sector will help the logistics service providers and their customers in terms of improved logistics performance and higher profits and will also improve the image attractiveness of the Indian logistics industry.
Keywords Human resources Indian logistics industry Logistics performance index System dynamics Causal loop diagram

1 Introduction

1.1 Importance of logistics

Over the past decades, globalization has caused an expansion in trade, leading to the growing strategic importance of the logistics function within the organization. At present, improvements in logistics have been the primary source of increased profits for companies, allowing them to maintain their competitive advantage [24]. Logistics have become important source of sustainable competitive advantage [8, 18, 39].

Logistics concern the efficient transfer of goods from the source of supply through the place of manufacture to the point of consumption in a cost-effective way while providing an acceptable service to the customer [21]. The chartered institute of logistics and transport (CILT) in the UK describes logistics as getting the right product to the right place in the right quantity at the right

time in the best condition and at an acceptable cost [26]. The Council of Supply Chain Management Professionals (2007) defines logistics management as that part of the supply chain management processes, which plans, implements, and controls the efficient, effective forward and reverse flow and storage of goods, services, and related information between the point of origin and the point of consumption in order to meet customers' requirements [17].

With the world economy changing and globalization is overpowering, world is becoming an open market. It becomes necessary for every company to response quickly to consumer demands, reduce lead times, maintain quality at the right cost, and be flexible to achieve the competitive advantage. And the solution to achieve this is to have and efficient logistics system. Having good logistics infrastructure and culture is becoming a prerequisite for attracting global manufacturing and service companies into the country [46]. Figure 1 shows the growth rate of the world economy. The Indian GDP is growing steadily at 5 to 6 % compared with the world GDP growth rate of 3 % (refer Fig. 2), which is one of the biggest motivation for India to improve its logistics infrastructure so as to attract foreign investors and enhance global trade.

/static-content/images/556/art%253A10.1007%252Fs12159-014-0117-9/MediaObjects/12159_2014_117_Fig1_HTML.gif

Fig. 1

World GDP growth rate [20]

/static-content/images/556/art%253A10.1007%252Fs12159-014-0117-9/MediaObjects/12159_2014_117_Fig2_HTML.gif

Fig. 2

Indian GDP growth rate [10]

Growth of any economy relies on the trade, exports, imports, manufacturing, primary and secondary industries, etc. With trade, it also relies on the infrastructure and facilities the country possesses. All these factors have a direct and huge impact on the businesses of the country. An investment of $1,025 billion is targeted over the duration of the twelfth five year plan (2012–17) in infrastructure development in order to sustain a real GDP growth rate of 9 per cent [10]. Despite this increase, the country's infrastructure network will be insufficient as freight movement increases about three fold in the coming years, and this shortfall will put India's growth at risk [28].

To run a well-knit and sophisticated logistics system, skilled human resources is required and proactive efforts need to be made to develop it. Human resource is a group of individuals working together towards a unique vision and mission to achieve a common goal for organizational growth [2]. Competitive advantage would be gained through the systemic benefits of shared HR practices such as selection, training, and performance management that improve overall supply chain performance [19].

The number of skilled personnel required in India to support the smooth functioning of the logistics network is likely to increase from less than10 million in 2011 to 20 million by 2020, including 100,000 warehouse managers, five million truck drivers, and 70,000 coastal seafarers [28].

Logistics, till recent times, was considered as operational function rather than strategic. Also, it is considered as a low-level job. The logistics job in India is still not an option for an educated person, because of the poor image of the industry and harsh-working conditions. The need of

the hour is to turnaround the image of the sector by investing in training, making it more organized, granting it the status of an industry, so that skilled professionals will be readily available to make the system more reliable and safe. The skill development of the employees can be attained by means of providing training and education to employee, maintaining safe and pleasant working environment, treating all employees fairly and consistently, encouraging participation through teambuilding, open communication and mutual respect [35].

The logistics performance index was the term coined by the World Bank [4]. It is a comprehensive index created to help countries identify the challenges and opportunities they face in trade logistics performance. The LPI assesses the performance of countries in the following areas and is an equally weighted average of these six components. They are namely customs, infrastructure, international shipments, logistics competence, tracking and tracing and timeliness, which affect the supply chain performance measures measured in terms of time, cost, reliability, and flexibility [5]. Also, as safety plays a major role in supply chain and logistics performance, the authors have added one more performance measure as safety (Fig. 3).
/static-content/images/556/art%253A10.1007%252Fs12159-014-0117-9/MediaObjects/12159_2014_117_Fig3_HTML.gif
Fig. 3
Relationship between Enablers, Results and LPI
The six factors discussed above can be broadly classified into infrastructure, government regulation and information technology, which cannot function independently without proficient human resources. Therefore, the paper identifies factors that influence the logistics performance and thus the competitiveness of organizations classifying them as enablers and results. Enablers will be the factors that enable to achieve the results or to improve the logistics performance to help organizations to achieve the competitive edge. Results are basically the competitiveness factors that influence the logistics cost and are influenced by the enablers. Thus, LPI is the summation of all factors classified as results. This paper considers one of the enablers' namely human resources to study the influence of this enabler on LPI. Further, the study also includes the variables that create the human resource namely investment in training, investment in improving the service conditions, leading to development of skilled work force.

1.2 Logistics Scenario in India

Logistics industry around the globe is valued about US$ 3.5 trillion, out of which India's share is US$ 90 billion [31]. The sector provides employment to about 45 million people in the country, which is more than the information technology (IT) and information technology enabled services (ITES) sectors put together [2]. In 2011, 7.3 million truck drivers were working in the logistics sector in India. It is predicted, that with growing trade this number will increase to 25 million in 2022 [47]. According to a report by KPMG [23], from a survey done on 80 logistics company, it was found that the manpower costs forms 8–10 % of overall cost in the sector (in case of road logistics it is 4 %). This roughly translates to about Rs. 500 billion spent on logistics manpower annually. Of this, only 13–14 % is spent on non-salary expenses such as manpower development items such as welfare, training, which is very less compared with global logistics countries, which spend more than 20 %.

The availability of skilled work force in the logistics sector is scarce, leading to improper handling of products, rash driving, losses, and separate person for each activity rather than multitasking, lower standard of living, etc. At management and mid-tier levels, the logistical sector in India suffers from organizational skills, lack of leadership, disjointed skills, and positions and lack of process-driven systems [25]. This shortage is present at all the three levels management, managerial, operational, and strategic. The industry is highly unattractive due to its poor image, extreme working conditions, lack of infrastructural facilities, low pay scale, and lack of clearly defined career path. Also, it severely lack institutionalized manpower creation environment, low or no investment in staff welfare, low participation of women, etc. This leads to less people opting for logistics jobs and high attrition rate, which results in improper and less recruitment. This has widened the gap between skill set required and skill set available for the industry. To have a world class logistics system, the prerequisite is the team that can run such system. Hence, it is required to improve the human resources available, which is influenced by the investment in human resources by government and the private sector. The most severe and immediate requirement for skill development is found to be in the road freight and warehousing segments [23].

1.3 Importance of HR and skills development for efficient logistics

A lot of studies have been conducted to study the role of human resources in logistics management and organizational performance. Delaney and Huselid [11] conducted a survey in 590 profit and non-profit firms and found that human resource management (HRM) practices like training, staff selectivity, and incentive compensation are positively related to perceptual measures of organizational performance. Sum [43] studied the effect and the role of training in business strategies and found that training function is a value-added source for sustained competitive advantage, and the training activities should be aligned with corporate objective and goals. Okeudo [33] conducted a study in Nigeria by collecting data from logistics service provider (LSP) and concluded that recruitment and selection, performance appraisal, training and development, health and safety of employee compensation and benefits have a significant and positive impact on firm performance. Also, that if these LSPs increase their human capital investment, by off and on job training, they will be able to improve their performance.

Ellinger et al. [12] conducted a study on 123 logistics service provider organization and concluded that employee-related activities such as service-related training and coaching influence both employee and organizational performance.

Wong and Karia [48] analysed profiles of fifteen LSPs through content analysis and concluded that it is not the number of employees that matter, but it is the competence and knowledge of human assets that deliver outstanding service and customer satisfaction. Ensuring continuous and desirable work outcomes of employees have strong relationship with their commitment to their organization; Acar [1] conducted a study on 344 employees of 37 Turkish logistics firms. This research supported the positive effect of organization culture on the organization commitment of the employee in the logistics industry. Gibson and Cook [14] surveyed 41 US 3PLs firm for hiring practices and recruiting, selection and compensation data, and recommending that the firms to use information to benchmark current practices. Kam et al. [22] explored the relationship between induction, recruitment and selection, performance

management, reward management, and training and development with logistics capabilities and concluded that reward management, performance management and training and development are likely to reduce staff turnover and strengthen LSP's capabilities.

Anastasiou [3] states that HRM practices such as: training, work motivation, employee commitment, adaptability, empowerment, leadership, and shared values can positively contribute to supply chain success and encourage innovation with recognition and reward for managers, teams and individuals, leading to successful attainment of organizational goals.
Pandey et al. [34] conducted a survey in 60 automobile component manufacturing organizations in India to study the importance of human resource (HR) practices such as (training, collaborative performance systems and reward alignment) in achieving high levels of supply chain (SC) integration. The results indicated that information sharing has a significant effect on SC integration, and the relationship between these two variables is found to be positively moderated by 'training' and 'reward alignment', while 'collaborative performance systems' does not emerge as a significant moderator in the proposed relationships. Gorane and Kant [15] identified employee motivation, organization culture, teamwork and trust among employees, employee involvement, information communication technology (ICT) infrastructure and employee education training as most important supply chain enablers affecting all other factors, so the management should address these enablers cautiously. Not many studies have been done in India to study the effect of human resource management on logistics management. This research is an attempt to fill this gap, and on the basis of the above literature review, the following hypotheses are formulated:
H 1 :
Skilled work force has a positive effect on corporate reputation building, recruitment, and retention of employees.
H 2 :
Skilled work force has a positive relationship with reduction in cost, reduction in time, improvement in reliability, flexibility, and safety of a logistics system.
H 3 :
Skilled work force has a positive relationship with logistics performance index.
H 4 :
Logistics performance index has a positive relationship with profit.
2 Methodology

2.1 Case description

ABC is an Indian based logistics company established in 1985 with an annual turnover of 1,200 crores. The company has a unified connectivity through air, road, and rail resulting in a plethora of offerings to its customers. It is the market leader in India and has a strong presence in Asia Pacific region and SAARC countries. It has a fleet of about 7,000 vehicles on road and 4,000 business partners in India. For services in India, the company relies heavily on the road transport segment.

With more and more multinational logistics service providers entering Indian market, the company is facing stiff competition and is striving hard to maintain its position. For reducing logistics cost, the company is trying to optimize its logistics process.
The company is facing huge losses through damages, high lead times and lower retention rate. After studying the various components of the process, it was found that major reasons for the increase in cost are improper handling, pilferage, redundant procedures, and lack of coordination. Also, there is a lack of proper procedure for recruitment of logistics staff. People switch to other jobs as soon as they get one because of improper working conditions. There is a lack of focus on the development of human resources and to tap the potential savings, which can be achieved through its improvement.
After a lot of brainstorming and convincing, the company has agreed to carry out this case study. To study the impact, it is necessary to develop a model that can show the dynamics between the enablers and results.

2.2 Development of system dynamics model

System dynamics is one of the efficient tools in real and dynamic conditions, which was developed by Forrester for the first time in 1950s and has grown rapidly in last 50 years [13]. It is a computer-based simulation method that allows the modeller to graphically represent a system of differential nonlinear equations and to have the computer do the discrete-step computational effort over a preset time frame [27]. It is an approach to discover nonlinear dynamic behaviour and study structure and parameters of the system. The other main objective of it is designing the effective and stable policies that modify system performance. It also provides the possibility of testing new procedures and policies before performance [42].
The system dynamics approach begins with defining complex problems and uses different tools to reach its goals and to support decision-making processes. The tools are both qualitative (diagramming tools, as causal loop diagrams, stock and flow diagrams) and quantitative (formal model based on rigorous mathematical language, equations). For the present study, system dynamics modelling has been found appropriate to develop dynamic model for a case LSP.

2.3 Causal loop diagram

Causal loop diagrams are very effective systems thinking tool, which shows relationships between variables and also help to convert mental model into systems model. Variables are connected to each other with the help of arrows, to which polarity either negative or positive is assigned. A positive sign '+' means that if the cause increases or decreases, then the effect will also increase or decrease in the same direction. It is also known as reinforcing loop, which is denoted by 'R'. A negative sign '−' means that if the cause increases or decreases, then the effect will increase or decrease in the opposite direction. It is also known as balancing loop, which is denoted by 'B'.
Figure 4 shows the causal loop diagram to study the impact of investment in human resources on development of skilled work force and its effect on LPI and Table 1 introduces all the variable used in development of causal loop diagram. The LSP will invest in human resources in training and improvement in service conditions. The training will be provided to office staff, truck drivers, warehouse managers, and loading staff. Through training, the skills of the worker will be improved. The service conditions will be improved by increased wages, improving

working conditions, and welfare of the employee. This will improve the attractiveness of the sector and will lead to corporate reputation building. Corporate reputation will attract people to continue their jobs leading to high retention rate, leading to more skilled labour. Corporate reputation building will attract people to take up jobs in the sector and will lead to better recruitment. Better recruitment will enhance the image of the sector, which will improve the corporate reputation. So, closed loop between better recruitment and corporate reputation building is reinforcing. Also, better recruitment will also lead to skilled work force.

/static-content/images/556/art%253A10.1007%252Fs12159-014-0117-9/MediaObjects/12159_2014_117_Fig4_HTML.gif

Fig. 4

Causal loop diagram for impact of investment in HR on Logistics Performance Index

Table 1

Introduction to variables used in causal loop diagram

Variable	References	Description
Investment in human resources	KPMG [23]	Investment done in human resources by 3PL to improve service conditions and provide training
Training	Chandra and Kumar [9], Gowen and Tallon [16]	Training imparted to truck drivers, loading supervisors, warehouse managers, office staff, logistics managers
Improvement in service conditions	Okeudo [33]	Improving the conditions under which the logistics personnel work which is the biggest hindrance for people not opting for logistical jobs
Welfare/wages/working conditions	Ellinger et. al [12], Prowse and Prowse [35], Vonder gracht et. al [47]	Investing money or forming policies for welfare of the employee, improving wages of the employees and the harsh and unhygienic conditions under which they work
Staff–truck drivers, loading staff, warehouse managers, office staff	KPMG [23]	Categories of people required for doing logistical work
Corporate reputation building	KPMG [23]	The positive image of the company which increases investment by shareholders, retain and attracts good talent
Retention	Min and Emam [29], Bhatnagar [6]	Reduction in employee turnover
Recruitment	Gibson and Cook [14]	Attracting suitable and skilled candidates to apply for logistical jobs.

Skilled work force
Mitra [30]
Workforce which is equipped with the skills required to perform the jobs better and in efficient manner
Logistics cost
Somuyiwa [40], Rahman [36]
Cost required to carry out logistics operations
Logistics time
Sauvage [38]
Total time required to carry out logistics services
Reliability in services
Islam et. al [21]
A consistent system which work effectively under different conditions
Flexibility in services
Zhang et. al [49], Naim et. al [32]
Ease with which the system can respond to uncertainty and quick response
Safety
Cantor [7]
A system which is less prone to accidents, damages and other losses
Profit
Stapleton et. al [41], Randall et. al [37]
A positive gain from a business after subtracting all the expenses
With the increase in the skill level of the workforce, cost will decrease. Since cost is an important factor in building the LPI, decrease in cost will lead to improvement in LPI. It is expected that improvement in LPI will generate more trade and thus revenue for LSP a part of which will be reinvested more in further training, development and welfare of human resources. Therefore, the loop between investments in HR, training or improvement in service conditions, skilled labour, cost, LPI and profit is balancing. Skilled work force will reduce the time for doing logistics activities, which will also improve the LPI. So, the loop between investments in HR, training or improvement in service conditions, skilled labour, time, LPI and profit is also balancing. Skilled labour will also improve the reliability, flexibility and safety of the system. Therefore, the loops between investment in HR, training or improvement in service conditions, skilled labour, reliability or flexibility or safety, LPI and profit are all reinforcing loops. There are four reinforcing loops and two balancing loops.

3 Result and discussions

The causal loop diagrams help to create the flow diagram, which are the ultimate diagramming aid that represents the feedback structure in terms of physical and information flows and stocks and are also known as stock and flow diagrams [44]. The important components used to develop the stock and flow diagram are shown in Table 2.

Table 2
Description of important system dynamics components Source [45]
S·No.
Variable name

Symbol
Description
1.
Level
/static-content/images/556/art%253A10.1007%252Fs12159-014-0117-9/MediaObjects/12159_2014_117_Figa_HTML.gif
It accumulates changes and is influenced by flows
2.
Auxiliary
/static-content/images/556/art%253A10.1007%252Fs12159-014-0117-9/MediaObjects/12159_2014_117_Figb_HTML.gif
A variable type, which contains calculations based on other variables
3.
Flow with rate
/static-content/images/556/art%253A10.1007%252Fs12159-014-0117-9/MediaObjects/12159_2014_117_Figc_HTML.gif
It influences levels. The flow is controlled by the connected rate variable, normally an auxiliary variable

The stock and flow diagram has been developed as shown in Fig. 5 using STELLA 9.1.3 software. After developing the stock and flow diagram, the model has been simulated by taking 2012 as a base year as this study was initiated in that year and simulation is run for next 12 years, taking the value of DT (Delta Time) as one. Delta time controls how frequently calculations are applied each unit of time and as their process will not change every unit of time, it is taken as one in this case. The company agreed to invest Rs. 10 crores for improving the conditions of human resources. Among which 20 % was invested in training and 80 % in welfare, wages and improvement in working conditions. The scores of all the parameters in calculated out of five. Score is the rating of the particular variable on the scale of one to five. Table 3 indicates the rating of each score for various variables studied in the paper.

/static-content/images/556/art%253A10.1007%252Fs12159-014-0117-9/MediaObjects/12159_2014_117_Fig5_HTML.gif

Fig. 5
Stock and Flow diagram for development of skilled work force and measurement of Logistics Performance Index

Table 3
Rating of score for variables

Factor	Score				
	1	2	3	4	5
Corporate reputation building	Extremely bad				

Quite bad
Good
Quite good
Extremely good
Recruitment
Extremely bad
Quite bad
Good
Quite good
Extremely good
Skilled work force
Introduced
Practiced
Skilled
Advanced
Expert
LPI
Poor
Fair
Good
Very good
Excellent
Figure 6 shows the relationship between skilled labour, retention, recruitment and corporate reputation building (CRB). The total labour trained is 18,168 out of about 50,000 employees i.e. 36 % employees were trained, taking average training cost per employee as Rs.12,000 only. The score of CRB is 2.8 out of five. Due to this, retention is improved by 58 % and the score of recruitment was 4.4. As the company started improving the working conditions, wages and welfare of the employees, people started opting for jobs in this company and better people were available for recruiting. As the attrition rate also reduced, so there is a high retention of skilled and experienced labour. With the focus on improving the working conditions and overall welfare of the employees, the company will get a facelift. Therefore, H1 stating skilled work force has a positive effect on corporate reputation building, recruitment and retention of employees can be accepted.
/static-content/images/556/art%253A10.1007%252Fs12159-014-0117-9/MediaObjects/12159_2014_117_Fig6_HTML.gif
Fig. 6
Improvement in skills, recruitment, retention and corporate reputation building due to skilled work force
Figure 7 discusses the improvement in results in the period of 12 years. With an investment of ten crores and in the period of 12 years, the score of cost reaches 2.87 and the reduction in cost is 12 %. The score for time is 3.2 and the reduction in time is 80 min a day. The score for reliability, flexibility and safety are 2.53, 2.02 and 4.05 respectively. Human resource is an important factor in logistics, but the logistical system is dependent on many other factors such as infrastructure, government regulations, use of information technology. Flexibility is

influenced by the logistics infrastructure and use of information technology more than human resources. Therefore, the score is the lowest. Proper training leads to reduction in accidents, maintenance of the vehicle, proper handling of the goods, etc. Also, due to improvement in the image of the sector, better qualified drivers will be recruited, which will also reduce the number of accidents. So the score of safety is highest and has major contribution in LPI. Therefore, we accept H2 stating skilled work force has a positive relationship with reduction in cost, reduction in time, improvement in reliability, flexibility and safety of a logistics system.

/static-content/images/556/art%253A10.1007%252Fs12159-014-0117-9/MediaObjects/12159_2014_117_Fig7_HTML.gif

Fig. 7

Improvement in logistics cost, logistics time, reliability, flexibility and safety due to skilled work force

Figure 8 shows the graph between skilled labour and logistics performance index. The score of LPI is 2.93 out of 5 and score of skilled work force is 2.7 out of 5. With more investment, these scores can be improved. This shows that development of skilled work force has a positive relationship with the LPI and H3 can be accepted that skilled work force has a positive impact on LPI.

/static-content/images/556/art%253A10.1007%252Fs12159-014-0117-9/MediaObjects/12159_2014_117_Fig8_HTML.gif

Fig. 8

Improvement in LPI due to skilled work force

Figure 9 shows the relationship between LPI and profit. With the improvement in LPI the profit also increases. The score of profit is in terms of percentage increase in profits. Increase in profit can be influenced by reduction in cost, improvement in safety thus increasing the revenues. Increase in profit will lead to more investment, leading to more skilled labours. So we accept H4 that logistics performance index has a positive relationship with profit.

/static-content/images/556/art%253A10.1007%252Fs12159-014-0117-9/MediaObjects/12159_2014_117_Fig9_HTML.gif

Fig. 9

Improvement in profit and logistics performance index due to investment in HR

As stated earlier, LPI is influenced by many other factors. Therefore, to improve the logistics performance index, other factors will also have to be involved. Although the index has considerably improved, but when other factors like use of information technology, reduction in taxes by the government, proper logistics policies will be involved, then the interplay of all these factors will give the highest LPI.

4 Conclusion

The present study demonstrates the effect of skilled work force on the logistics performance of an organization using system dynamics methodology. Skilled work force can also be developed by improving the service conditions and providing training to the employees. Improvement in service conditions will attract more people to join logistics industry and also will increase the retention rate. Attracting more people will provide better options for recruitment thereby increasing skilled labour.

Availability of skilled manpower can improve the logistics performance significantly leading to reduction in logistics cost, logistics time, and making the system more reliable and safe. Although flexibility is not directly affected by skilled labour, but to achieve flexibility, strong infrastructure and ICT backup is required, which would be difficult to run without skilled labour. Reduction in time, cost, losses, and accidents will improve the reliability of the logistics system and also improve the profits. More profits will help to invest more in development of human resources, which will lead to more improvement in LPI.

With the help of this case study, the authors try to prove that skilled work force has a strong relationship with the performance of any logistics system. Companies the world over are focussing on exploring the skills and competencies required by today's logistics professionals to tackle the information intensive and dynamic market conditions and still there is huge gap in the demand and supply of the professionals required. To cater to this, the logistics companies need to make sure that a strong commitment to addressing human resources challenges and commitment for improving the sector's comes should come straight from the top [47].

Managers should concentrate on training their workforce and recruiting skilled labour. Policy makers should concentrate on building training schools and forming policies so that the condition of human resources improves and more people opt for logistics jobs. Organizations should concentrate on improving the working condition and welfare of the employees to improve the image of the sector attracting better talent. The model can be simulated further to generate various scenarios under different investment plans and in different sector.

Open AccessThis article is distributed under the terms of the Creative Commons Attribution License which permits any use, distribution, and reproduction in any medium, provided the original author(s) and the source are credited.

References

1.
Acar A (2012) Organizational culture, leadership styles and organizational commitment in Turkish logistics industry. Procedia-Soc Behav Sci 58:217–226 Accessed 1 May 2014
CrossRef

2.
Alexander J, Goyal A, Dave A, Desai M, Vignesh P (2013) A speculative study on skill gaps in logistics industry—Indian perspective. Social science research network. Retrieved from http://ssrn.com/abstract=2241116

3.
Anastasiou S (2012) Critical human resources management functions for efficient logistics and supply chain management. In: Proceedings of the 2nd International Conference on Supply Chains, Katerini, Greece, 2012

4.
Arvis J, Mustra M, Panzer J, Ojala L, Naula T (2007) Connecting to compete: trade logistics in the global economy. http://siteresources.worldbank.org/INTTLF/Resources/lpireport.pdf. Accessed 12 June 2013

5.
Arvis J, Mustra M, Panzer J, Ojala L, Naula T (2012) Connecting to compete: trade logistics in the global economy. http://siteresources.worldbank.org/TRADE/Resources/2390701336654966193/LPI_2012_final.pdf. Accessed 12 June 2013

6.
Bhatnagar J (2007) Talent management strategy of employee engagement in Indian ITES employees: key to retention. Empl Relat 29(6):640–663
CrossRef
7.
Cantor D (2008) Workplace safety in the supply chain: a review of the literature and call for research. Int J Logist Manag 19(1):65–83
CrossRefMathSciNet
8.
Celebi D, Bayratkar D, Bingol L (2010) Analytical network process for logistics management: a case study in a small electronic appliances manufacturer. Comput Ind Eng 58(3):432–441
CrossRef
9.
Chandra C, Kumar S (2000) Supply chain management in theory and practice: a passing fad or a fundamental change. Ind Mana Data Syst 100(3):100–113
CrossRef
10.
Damadaran H (2013) India's GDP growth estimate. The Hindu Business Line. http://www.thehindubusinessline.com/opinion/columns/indias-gdp-growthestimate/article4375345.ece
11.
Delaney J, Huselid M (1996) The impact of human resource management practices on perceptions of organizational performance. Acad Manag J 39(4):949–969
CrossRef
12.
Ellinger A, Ketchen G, Hult G, Elmadag A, Richey R (2008) Market orientation, employee development practices, and performance in logistics service provider firms. Ind Mark Manag 37(4):353–366
CrossRef
13.
Forrester JW (2007) System dynamics: a personal view of the first fifty years. Syst Dyn Rev 23(2/3):345–358
CrossRef
14.
Gibson B, Cook R (2001) Hiring practices in US third-party logistics firm. Int J Phys Distrib Logist Manag 31(10):714–732
CrossRef
15.
Gorane S, Kant R (2013) Modelling the SCM enablers: an integrated ISM-fuzzy MICMAC approach. Asia Pac J Mark Logist 25(2):263–296
CrossRef
16.
Gowen C, Tallon W (2003) Enhancing supply chain practices through human resource management. J Manag Dev 22(1):32–44
CrossRef

17.
Green K, Whitten D, Inman R (2008) The impact of logistics performance on organizational performance in a supply chain context. Supply Chain Manag: An Int J 13(4):317–327
CrossRef
18.
Gunasekaran A, Ngai E (2003) The successful management of a small logistics company. Int J Phys Distrib Logist Manag 33(9):825–842
CrossRef
19.
Hall M, Hall C, Rigsbee C (2013) Strategic human resource management and supply chain orientation. Hum Resour Manag Rev 23(4):366–377
20.
Indexmundi (2011) Historical data graphs per year. http://www.indexmundi.com/g/g.aspx?c=xx&v=66. Accessed 1 May 2014
21.
Islam D, Meier J, Aditjandra P, Zunder T, Pace G (2013) Logistics and supply chain management. Res Transp Econ 41(1):3–16
CrossRef
22.
Kam B, Tsahuridu E, Ding M (2010) Does human resource management contribute to the development of logistics and supply chain capabilities? An empirical study of logistics service providers in China. Res Pract Hum Resour manag 18(2):15–34
23.
KPMG (2008) White paper on skill gaps in the Indian logistics. http://www.kpmg.de/docs/Skill_gaps_in_the_Indian_Logistics_Sector_A_white_paper.pdf. Accessed 1 May 2013
24.
Kunadhamraks P, Hanaoka S (2007) Evaluating the logistics performance of intermodal transportation in Thailand. Asia Pac J Mark Logist 20(3):323–342
CrossRef
25.
LCL Logistix (India) Pvt. Ltd (2011) Whitepaper on human resource shortfall in the Indian logistics sector. http://www.lcllogistix.com/pdf/white_paper.pdf. Accessed 25 July 2013
26.
Mangan J, Lalwani C, Butcher T (2008) Global logistics and supply chain management. Wiley, Wiltshire
27.
Marco A, Rafele C (2007) System dynamics simulation: an application to regional logistics policy making. Int J Math Mod Methods Appl Sci 1(4):253–260
28.
Mckinsey (2010) Building India transforming the nation's logistics infrastructure. http://www.mckinsey.com/locations/india/mckinseyonindia/pdf/Logistics_Infrastructure_by2020_fullreport.pdf. Accessed 25 April 2014
29.

Min H, Emam A (2003) Developing the profiles of truck drivers for their successful recruitment and retention. Int J Phys Distrib Logist Manag 33(2):149–162
CrossRef
30.
Mitra S (2006) A Survey of the third-party logistics (3PL) service providers in India. IIMB Manag Rev 18(2):159–183
31.
Mitra S (2008) Logistics industry: global and Indian perspectives. Glob Bus Econ Anthol Bus Econ Soc Int 2:130–138
32.
Naim M, Potter A, Mason R, Bateman N (2006) The role of transport flexibility in logistics provision. Int J Logist Manag 17(3):297–311
CrossRef
33.
Okeudo G (2012) The impact of human resources management in logistic service providers and supply chain capabilities: a case study. Br J Sci 4(1):57–71
34.
Pandey P, Bhattacharyya S, Kaur A (2012) Exploring the role of HR practices in supply chain. J Adv Manag Res 9(1):113–123
CrossRef
35.
Prowse P, Prowse J (2010) Whatever happened to human resource management performance. Int J Prod Perform Manag 59(2):145–162
CrossRef
36.
Rahman Z (2004) Use of internet in supply chain management: a study of Indian companies. Ind Manag Data Syst 104(1):31–41
CrossRef
37.
Randall W, Farris M (2009) Supply chain financing: using cash-to-cash variables to strengthen the supply chain. Int J Phys Distrib Logist Manag 39(8):669–689
CrossRef
38.
Sauvage T (2003) The relationship between technology and logistics third-party providers. Int J Phys Distrib Logist Manag 33(3):236–253
CrossRef
39.
Shang K, Marlow P (2007) Logistics capability and performance in Taiwan's major manufacturing firms. Transp Rep Part E 41:217–234
CrossRef
40.
Somuyiwa A (2010) Analysis of transportation cost in overall logistics cost management of manufacturing companies in southwestern, Nigeria. Eur J Sci Res 44(3):420–429
41.

Stapleton D, Hanna J, Yagla S, Johnson J, Markussen D (2002) Measuring logistics performance using strategic profit model. Int J Logist Manag 13(1):89–107
CrossRef
42.
Sterman JD (2010) Business dynamics (system thinking and modelling for a complex world). Mc Graw-Hill Higher Education, Delhi
43.
Sum V (2011) Integrating training in business strategies means greater impact of training on the firm's competitiveness. Res Bus Econ J 4:1–19
44.
Sushil (1993) System dynamics a practical approach for managerial problems. Wiley Eastern Limited, New Delhi
45.
Verma P (2004) Dynamic modelling for emission control policies in the delhi urban transport system. Dissertation Indian Institute of Technology Delhi
46.
Viswanadham N, Gaonkar R (2001) Whitepaper on industrial and logistics development strategy for India. The Logistics Institute-Asia Pacific, Singapore
47.
Von der Gracht H, Gnatzy T, Ecken P, Darkow I (2012) Transportation and logistics 2030. Eur Foresight Platf 60(39):59
48.
Wong C, Karia N (2009) Explain the competitive advantage of logistics service providers. Int Prod Econ 28:51–67
49.
Zhang Q, Vonderembse M, Lim J (2005) Logistics flexibility and its impact on customer satisfaction. Int J Logist Manag 16(1):71–95
CrossRef

ACS APPLIED MATERIALS & INTERFACES

Subscriber access provided by DELHI TECH UNIV

Article

Anisotropically Functionalized Carbon Nanotube Array Based Hygroscopic Scaffolds

Sehmus Ozden, Liehui Ge, Tharangattu N. Narayanan, Amelia H. C. Hart, Hyunseung Yang, Srividya Sridhar, Robert Vajtai, and Pulickel M Ajayan

ACS Appl. Mater. Interfaces, **Just Accepted Manuscript** • DOI: 10.1021/am5022717 • Publication Date (Web): 04 Jun 2014

Downloaded from http://pubs.acs.org on June 13, 2014

Just Accepted

"Just Accepted" manuscripts have been peer-reviewed and accepted for publication. They are posted online prior to technical editing, formatting for publication and author proofing. The American Chemical Society provides "Just Accepted" as a free service to the research community to expedite the dissemination of scientific material as soon as possible after acceptance. "Just Accepted" manuscripts appear in full in PDF format accompanied by an HTML abstract. "Just Accepted" manuscripts have been fully peer reviewed, but should not be considered the official version of record. They are accessible to all readers and citable by the Digital Object Identifier (DOI®). "Just Accepted" is an optional service offered to authors. Therefore, the "Just Accepted" Web site may not include all articles that will be published in the journal. After a manuscript is technically edited and formatted, it will be removed from the "Just Accepted" Web site and published as an ASAP article. Note that technical editing may introduce minor changes to the manuscript text and/or graphics which could affect content, and all legal disclaimers and ethical guidelines that apply to the journal pertain. ACS cannot be held responsible for errors or consequences arising from the use of information contained in these "Just Accepted" manuscripts.

ACS Publications
High quality. High impact.

ACS Applied Materials & Interfaces is published by the American Chemical Society.
1155 Sixteenth Street N.W., Washington, DC 20036

Published by American Chemical Society. Copyright © American Chemical Society. However, no copyright claim is made to original U.S. Government works, or works produced by employees of any Commonwealth realm Crown government in the course of their duties.

Anisotropically Functionalized Carbon Nanotube Array Based Hygroscopic Scaffolds

Sehmus Ozden[1], Liehui Ge[1], Tharangattu N. Narayanan[2], Amelia H. C. Hart[1], Hyunseung Yang[3], Srividya Sridhar[4], Robert Vajtai[1], Pulickel M. Ajayan[1]*

[1]Department of Material Science and NanoEngineering, Rice University, Houston, Texas 77005, USA
[2]CSIR-Central Electrochemical Research Institute, Karaikudi, 630006, India
[3]Department of Chemical and Biomolecular Engineering, Korea Institute of Science and Technology (KAIST), Daejeon, 305-701, Korea [4]Department of Physics, Delhi Technological University, Bawana Road, Delhi, 110042, India

KEYWORDS Carbon nanotubes, Water harvesting, Asymmetric Functionalization, Hydrophobic, Hydrophilic

ABSTRACT

Creating ordered microstructures with hydrophobic and hydrophilic moieties that enable the collection and storage of small water droplets from atmosphere, mimicking structures that exist in insects, such as the Stenocara beetle, which lives in environments with limited amounts of water. Inspired by this approach, vertically aligned multiwall carbon nanotube forests (NTF) are asymmetrically end-functionalized to create hygroscopic scaffolds for water harvesting and storage from atmospheric air. One side of the NTF is made hydrophilic, which captures water from atmosphere, and the other side is made superhydrophobic, which prevents water from escaping and the forest from collapsing. To understand how water penetrates into the NTF, the fundamentals of water/NTF surface interaction are discussed.

INTRODUCTION

Fresh water is an ever decreasing resource that can be found in small amounts in almost every environment. In nature, there are many organisms, such as the Stenocara beetle which lives in the Namib Desert survives by drinking fog-water that collects on its wing case[1]. The unique design of the Stenocara beetle's back involves randomly spaced bumps with hydrophilic peaks surrounded by hydrophobic areas the guide water into its mouth. The Stenocara beetle stands on a sand dune, facing into the morning wind at a forty-five degrees angle. With its head facing downward and its bottom upward, the minute water droplets from the fog collect on the superhydrophilic peak of each bump. When the water droplets grow big enough, they detach from the bump peaks, fall onto the superhydrophobic areas between the bump peaks and are guided downward to the beetle's mouth[1]. Additionally, Stipagrostis Sabulicola[2], and Cotula Fallax[3], are some other organisms that are able to effectively capture water droplets from the fog of the morning desert by using hydrophilic/hydrophobic combinations. In the recent past, a few efforts have been done using these and other hydrophilic/hydrophobic biomimetic mechanisms to capture and harvest atmospheric water[4-13] that doesn't require significant amounts of energy. Till now, several approaches have been reported to create hydrophilic/hydrophobic surfaces for water harvesting. In these reports polymers are extensively have been used. For example, L. Zei *et al*. mimicked Stenocara beetle by creating hydrophilic patterns on the superhydrophobic surfaces using hydrophilic and hydrophobic polymers[14].

The other material that can be used for water harvesting is carbon nanotubes (CNTs), known for their small size, mechanical, and physical strength, can be easily turned hydrophilic or super-hydrophobic by chemical functionalization[15-16]. Several kinds of CNT functionaliztions such as covalent[17] and non-covalent functionalization[18] have been reported extensively. Another type of CNT functionalization is asymmetric end-functinalization that brings two different functional at

their opposite ends[19]. Even some work has been reported, it is still a big challenge to functionalize their two end-tips with different functional groups[19-20]. For example Lee et. al. have used UV-irradiation to attach different functional group onto opposite end of individual CNTs[19]. In order to harvest water, the material must consist of both hydrophilic and hydrophobic surfaces. For example, Kinoshita and his co-worker used micro-patterning on CNT films to create superhydrophobic-hydrophilic heterogeneous surfaces using plasma-type hydrothermal atom beams[15]. Here we report a new approach for anisotrophically functionalized NTF as superhydrophilic/superhydrophobic. Due to combination of hydrophilic and hydrophobic surfaces, we were able to utilize the material for water collection from dry air and high humidity air. By this approach the water microparticles in air can be captured and stored in comparatively large amounts.

EXPERIMENTAL SECTION

The carbon nanotube forests (NTF) were synthesized *via* water-assisted chemical vapor deposition (WACVD) on a Si substrate, described elsewhere[21]; grown for 3 hours, resulting in a height of ~1 centimeter. Prior to CNT growth, 10 nm thick Al buffer layer and Fe catalyst layer were deposited on the Si wafer using electron-beam (E-beam) evaporation. The CNT synthesis takes place at 775 °C under Ar/H_2 with ethylene as the carbon source and water bubbler to aid the removal of amorphous carbon.

To create the hydrophobically-functionalized side of the NTF, 1H,1H,2H-heptadecaflouro-1-decene (HDFD) (99%, Sigma Aldrich) was coated onto the top surface of the as-grown NTF and plasma treated (700 V DC) for 2 minutes. After this, the NTF is then removed from the silica substrate, flipped over and transferred to a new silica substrate for further functionalization on the bottom surface. For the hydrophilic functionalization on the opposite side of the NTF, 0.5ml poly(ethylene glycol)methacrylate monomer (PEGMA) (average M_n, 360, Sigma Aldrich) was

coated onto the surface and the NTF was plasma treated (700 V DC) for 2 minutes (Figure 1). For comparison, one hydrophobic/hydrophillically functionalized NTF (PEGMA/HDFD-NTF), one NTF only hydrophilically PEGMA functionalized (PEGMA/PEGMA-NTF) on both top and bottom. One NTF only top side functionalized with PEGMA (PEGMA-NTF), and one non-functionalized NTF were all tested for water harvesting. Characterization was performed using scanning electron microscope (SEM, FEI Quanta 400 ESEM FEG), Raman spectroscopy, X-ray photoelectron spectroscopy (XPS), Thermogravimetric analysis (TGA), Fourier transform infrared spectroscopy (FT-IR), and contact angle measurements.

RESULTS AND DISCUSSION

To confirm that the NTF is actually hydrophilic/hydrophobic asymmetrically end-functionalized, the contact angle of each side is measured and discussed. The three different stages of functionalization, the as-grown NTF, the HDFD-NTF, and the PEGMA-NTF, can be seen in the SEM images shown in Figure 2 (a), (b), and (c), respectively. As seen in the inset of the three figures, the contact angle increases with HDFD treatment (118^o (as grown NTF) – 162^o (superhydrophobic)), and becomes completely hydrophilic after PEGMA treatment (0^o). As seen in Figure 2, the surface roughness of the end-functionalized NTF also affects the hydrophobicity and hydrophilicity of the surfaces[22]; a hydrophobic/hydrophilic surface becomes superhydrophobic/superhydrophilic with larger surface roughness[22]. It is also important to note that the infiltration of organic monomers and plasma treatment for polymerization only functionalizes the ends of the CNTs up to a few micrometers in depth (Figure 3a, b), which creates a CNT pot/container.

An additional way to evidence the success of the hydrophilic/hydrophobic functionalization of NTF is Raman spectroscopy, IR spectroscopy, XPS, and TGA. As seen in figure 4a, when

comparing the Raman spectra of the as-grown NTF to that of the PEGMA-CNT, and HDFD-NTF, the G-band, the in-plane vibration of the carbon-carbon bond, the D-band, shows the structural defects[23], and the G'-band, the second order overtone of the D-band, all upshifted due to the intercalation of the polymer with the CNT bundles[24]. In figure S1, the IR spectrum of the HDFD-NTF shows a characteristic perfluoroalkyl chain, -CF_2- stretching, between 1087 cm^{-1} and 1245 cm^{-1}, and CF_3 stretching band around 1350 cm^{-1}, [25]. On the PEGMA-NTF side, the IR spectrum shows the ether stretching band around 1735 cm^{-1} and alkyl chain CH_2 and CH_3 stretching at 2892 cm^{-1} and 2977 cm^{-1},respectively. The XPS analysis performed for quantitative chemical analysis, of the as-grown NTF (Figure 4b) shows sp^2 carbon atoms at approximately 284.6 eV and peaks at 284.9 eV and 285.4 eV represent C=O and C-O bonds respectively. A weak oxygen peak at around 532 eV is shown in Figure S8. In the XPS spectrum of the HDFD-NTF (Figure 4c) the C1s spectrum corresponds to graphitic carbon and the shoulder peak at 286.5 eV shows the C-CF bonding. The peak at 291.8 eV represents CF_2 bonding and CF_3 bonding is seen at around 294 eV. There are two C1s peaks in the XPS analysis of the PEGMA-NTF at 285 eV and 286.5 eV, corresponding to CO and CH_2 (Figure 4d), and a peak at 289 eV representing O-C=O bonding[26-27] . PEGMA-NTF has a larger amount of O atoms than the as-grown NTF due to the contribution of carbonyl(C=O) and ether (C-O) functional groups in PEGMA. TGA, conducted in Ar atmosphere (10 °C/min), (Figure S2) shows that the PEGMA-CNT side and HDFD-CNT side of the forest starts to decompose around 230 °C and 600 °C, respectively.

To demonstrate its water harvesting capabilities, the PEGMA/HDFD-NTF samples were exposed to dry and humid air at room temperature, and weighed before and throughout the experiment. During testing, the PEGMA/HDFD-NTF were orientated so that the hydrophilic

PEGMA-treated surface was kept facing upward, to capture the water, and the superhydrophobic HDFD-treated surface was kept facing downward, to hold the water. Four types of samples were tested: the PEGMA/HDFD-NTF, the PEGMA/PEGMA-NTF, the PEGMA-NTF, and the as grown NTF. The first test was performed in dry air (21% Relative Humidity (RH)) for 11 hours and weighed every hour. The second test was performed under very humid air (89% RH), generated by a water-bubbler (Figure S5), for 13 hours and weighed every hour.

To measure the water evaporation rate, 1mL of water was dropped onto the hydrophilic side of the PEGMA/HDFD-NTF and weight measurements were taken every hour at room temperature as well as under heating (40 °C). To compare this rate to the normal water evaporation rate, a separate glass vessel (0.5 cm diameter) was tested simultaneously. These results shows that the evaporation rate of water in the asymmetrically functionalized NTF is slower than the evaporation rate of water in a solid vessel because the asymmetrically functionalized NTF are able to isolate water from external environment.

It was found, during the first water harvesting and storage test, seen in Figure 5a, that the PEGMA/HDFD-NTF with a 0.5cmx0.5cm surface (~8 mg) harvests 27.4wt% (~2.27mg) of water from the air in 11 hours. In the second test performed under high relative humidity (RH), also seen in Figure 5a, the PEGMA/HDFD-NTF collected 80wt% (~6.4mg) of water in 13 hours. The PEGMA-NTF, tested under the same conditions, collected ~6.4mg of water in 13 hours but the non-functionalized side of the NTF collapsed leading to the destruction of the entire forest (Figure S3) . The HDFD and PEGMA polymers prevent the destruction of the NTF due to covalent bonding between the CNTs and the polymers. The PEGMA/PEGMA-NTF was not able to store water, the water was dropped onto the hydrophilic top of the escapes from bottom

hydrophilic side. After undergoing the same testing, the as-grown NTF shows no weight difference due to the hydrophobic nature of the entire forest.

In order to understand how water penetrates and stores in the NTF, it is important to understand the interactions between the water molecules and the hydrophilic PEGMA or the hydrophobic HDFD surfaces, respectively. Water is a polar molecule, where the hydrogen bonding keeps the atoms together is constantly breaking and forming bonds with new molecules. The hydrophilic PEGMA surface, consists of polar oxygen-containing functional groups (-OH, -C=O, C-O-C), which absorbs water due to hydrogen bonding, van der Waals forces and dipole-dipole interactions between the superhydrophilic surface and the water molecules. Water that is liquid, meaning it has a small contact angle on surfaces will spontaneously condense from vapor into pores on the superhydrophilic forest side[28]. Because the adhesive forces between the water molecules and the hydrophilic surface of the NTF are stronger than the cohesive forces, the water molecules are able to spread over the PEGMA-NTF surface. A water molecule attracts other molecules which surround it and in turn is attracted by them. Water molecules that are inside a liquid, the result of all these forces is neutral and the molecules are equally attracted to each other. When these molecules are on the surface, they are attracted by the water molecules that are below and by lateral ones. As a result of these attractions, water molecules directed inside the liquid[28] (Figure S6).

Capillary force, gravitational force and pressure balance models can be used to predict the penetration of water into the PEGMA/HDFD-NTF. The pressure balance model that can be effective for water penetration into the PEGMA/HDFD-NTF is based on the assumption that when water wets the PEGMA-NTF, the air in the NTF is not expelled but compressed[29-30] . At the liquid-air interface, a force balance exists between the force exerted by the compressed air

and the sum of the capillary force and gravitational forces[30]. The capillary force F_C can be expressed as,

$$F_C=\gamma\pi d \cos\theta \qquad (1)$$

where γ, d, and θ are the surface tension of the water, pore diameter and Young's contact angle respectively[31] . The gravitational force is relatively small compared to the capillary force, so the capillary force is balanced by the air resistance. The amount of absorbed vapor is dependent on the temperature and relative humidity (RH) in atmosphere. The lotus effect protects the superhydrophobic surface of the NTF from wetting as well as the hydrophobic side walls of the NTF, so the water is retained inside the forest. The asymmetrically functionalized ends of the NTF remain aligned because the CNTs are covalently bonded *via* polymer chains. As a result of all of the above, the asymmetrically functionalized NTF behaves as a container, the NTF holds water because of the innate hydrophobicity of the CNTs and the superhydrophobic non-wetting bottom surface of the functionalized NTF (Figure S7).

During the water evaporation measurements, seen in Figure 5b, it was found that the water evaporation rate in the end-functionalized NTF was less than in an open vessel. At room temperature, after 6 hours, the end-functionalized NTF lost ~8% of its weight compared to the 60% water weight lost by the vessel in 6 hours. At 40 °C, the end-functionalized NTF lost 40% of its weight in 6 hours. The reasons for this lower water evaporation rate are: the polymer from the functionalization prevents water from evaporating (Figure S4), and the NTF holds the water molecules captive preventing evaporation.

CONCLUSION

To conclude, a NTF was asymmetrically functionalized as hydrophilic and superhydrophobic *via* plasma treatment after coating with HDFD and PEGMA monomers on either side. The hydrophobic surface became more hydrophobic and the hydrophilic surface became more hydrophilic due to increased surface roughness. The asymmetrically functionalized NTF efficiently harvests and stores water from air humidity because of its superhydrophobic bottom surface, super hydrophilic top surface and innate hydrophobicity of center . In the future, it is possible to apply this unique system to arid lands if NTF productions become cheaper and scalable because this system, unlike other water collection devices, does not require external energy source for collecting water from humid ambient air.

AUTHOR INFORMATION

Corresponding Author

E-mail**:** ajayan@rice.edu

Acknowledgements

This work has been supported by U.S. Department of Defense: U.S. Air Force Office of Scientific Research for the Project MURI:"Synthesis and Characterization of 3-D Carbon Nanotube Solid Networks" Award No. FA9550-12-1-0035**.**

ASSOCIATED CONTENT

Supporting Information Available: FT-IR spectra of , as grown NTF, HDFD-NTF, PEGMA-NTF, Thermo gravimetric analysis of asymmetric functionalized NTF, images of asymmetrically functionalized NTF after water harvesting, schematic figure of water storage of asymmetrically end-functionalized NTF, schematic representation of water harvesting in the high humidity chamber, figure of interactions between water molecules and hydrophilic surfaces, schematic

representation that explains water storage mechanism in NTF, the survey scan of XPS characterization of NTF, HDFD-NTF and PEGMA-NTF. These materials are available free of charge via the Internet at http://pubs.acs.org.

REFERENCES

(1). Parker, A. R.; Lawrence, C.R. Water Capture by a Desert Beetle. *Nature* 2001, 414, 33-34.

(2). Ebner, M.; Miranda, T.; Roth-Nebelsick, A. Efficient Fog Harvesting by Stipagrostis Sabulicola (Namib Dune Bushman Grass). *J. Arid Environ.* **2011,** *75*, 524-531.

(3). Andrews, H. G. E., E. A.; Schofield, W. C.; Badyal, J. P. Three-Dimensional Hierarchical Structures For Fog Harvesting. *Langmuir* **2011,** *27*, 3798-802.

(4). Lee, A.; Moon, M. W.; Lim, H.; Kim, W. D.; Kim, H. Y. Water Harvest via Dewing. *Langmuir* **2012,** *28*, 10183-91.

(5). Thickett, S. C.; Neto, C.; Harris, A. T. Biomimetic Surface Coatings for Atmospheric Water Capture Prepared by Dewetting of Polymer Films. *Adv. Mater.* **2011,** *23*, 3718-3722.

(6). Bai, H.; Ju, J.; Zheng, Y. M.; Jiang, L. Functional Fibers with Unique Wettability Inspired by Spider Silks. *Adv. Mater.* **2012,** *24*, 2786-2791.

(7). Tian, X. L.; Chen, Y.; Zheng, Y. M.; Bai, H.; Jiang, L. Controlling Water Capture of Bioinspired Fibers with Hump Structures. *Adv. Mater.* **2011,** *23*, 5486-5491.

(8). Zheng, Y. M.; Bai, H.; Huang, Z. B.; Tian, X. L.; Nie, F. Q.; Zhao, Y.; Zhai, J.; Jiang, L. Directional Water Collection on Wetted spider Silk. *Nature* **2010,** *463*, 640-643.

(9). Hou, Y. P.; Chen, Y.; Xue, Y.; Zheng, Y. M.; Jiang, L. Water Collection Behavior and Hanging Ability of Bioinspired Fiber. *Langmuir* **2012,** *28*, 4737-4743.

(10). Gao, X. F.; Jiang, L. Water-Repellent Legs of Water Striders. *Nature* **2004,** *432*, 36-36.

(11). Norgaard, T.; Dacke, M. Fog-Basking Behaviour and Water Collection Efficiency in Namib Desert Darkling Beetles. *Front Zool.* **2010,** 7, 1-8.

(12). Feng, L.; Li, S. H.; Li, Y. S.; Li, H. J.; Zhang, L. J.; Zhai, J.; Song, Y. L.; Liu, B. Q.; Jiang, L.; Zhu, D. B. Super-Hydrophobic Surfaces: From Natural to Artificial. *Adv. Mater.* **2002,** *14*, 1857-1860.

(13). Rykaczewski, K.; Scott, J. H. J.; Rajauria, S.; Chinn, J.; Chinn, A. M.; Jones, W. Three Dimensional Aspects of Droplet Coalescence During Dropwise Condensation on Superhydrophobic Surfaces. *Soft Matter.* **2011,** *7*, 8749-8752.

(14). Zhai, L.; Berg, M. C.; Cebeci, F. C.; Kim, Y.; Milwid, J. M.; Rubner, M. F.; Cohen, R. E. Patterned Superhydrophobic surfaces: Toward a Synthetic Mimic of The Namib Desert Beetle. *Nano Lett.* **2006,** *6*, 1213-1217.

(15). Kinoshita, H.; Ogasahara, A.; Fukuda, Y.; Ohmae, N. Superhydrophobic/Superhydrophilic Micropatterning on a Carbon Nanotube Film Using a Laser Plasma-Type Hyperthermal Atom Beam Facility. *Carbon* **2010,** *48*, 4403-4408.

(16). Pastine, S. J.; Okawa, D.; Kessler, B.; Rolandi, M.; Llorente, M.; Zettl, A.; Frechet, J. M. J. A Facile and Patternable Method For The Surface Modification of Carbon Nanotube Forests Using Perfluoroarylazides. *J. Am. Chem. Soc.* **2008,** *130*, 4238-4239

(17). Singh, P.; Campidelli, S.; Giordani, S.; Bonifazi, D.; Bianco, A.; Prato, M. Organic Functionalisation and Characterisation of Single-Walled Carbon Nanotubes. *Chem. Soc. Rev.* **2009,** *38*, 2214-2230.

(18). Simmons, T. J.; Bult, J.; Hashim, D. P.; Linhardt, R. J.; Ajayan, P. M. Noncovalent Functionalization as an Alternative to Oxidative Acid Treatment of Single Wall Carbon Nanotubes With Applications for Polymer Composites. *Acs Nano* **2009,** *3*, 865-870.

(19). Lee, K. M.; Li, L.; Dai, L. Asymmetric End-Functionalization of Multi-Walled Carbon Nanotubes. *J. Am. Chem. Soc.* **2005,** *127,* 4122-3.

(20). Peng, Q.; Qu, L. T.; Dai, L. M.; Park, K.; Vaia, R. A. Asymmetrically Charged Carbon Nanotubes by Controlled Functionalization. *Acs Nano* **2008,** *2*, 1833-1840.

(21). Ci, L.; Vajtai, R.; Ajayan, P. M. Vertically Aligned Large-Diameter Double-Walled Carbon Nanotube Arrays Having Ultralow Density. *J. Phys. Chem. C* **2007,** *111*, 9077-9080.

(22). Quere, D. Rough Ideas on Wetting. *Physica A* **2002,** *313*, 32-46.

(23). Osswald, S.; Havel, M.; Gogotsi, Y. Monitoring Oxidation of Multiwalled Carbon Nanotubes by Raman Spectroscopy. *J. Raman Spectrosc.* **2007,** *38*, 728-736.

(24). Zhao, Q.; Wagner, H. D. Raman spectroscopy of carbon-nanotube-based composites. *Philos. T. Roy. Soc. A* **2004,** *362,* 2407-2424.

(25). Badge, I.; Sethi, S.; Dhinojwala, A. Carbon Nanotube-Based Robust Steamphobic Surfaces. *Langmuir* **2011,** *27*, 14726-14731.

(26). Akhtar, M. S.; Chun, J. M.; Yang, O. B. Advanced Composite Gel Electrolytes Prepared with Titania Nanotube Fillers in Polyethylene Glycol For the Solid-State Dye-Sensitized Solar Cell. *Electrochem. Commun.* **2007,** *9*, 2833-2837.

(27). Okpalugo, T. I. T.; Papakonstantinou, P.; Murphy, H.; McLaughlin, J.; Brown, N. M. D. High Resolution XPS Characterization of Chemical Functionalised MWCNTs and SWCNTs. *Carbon* **2005,** *43*, 153-161.

(28). Israelachvili, J. N. Intermolecular and Surface Forces, 3rd ed; *Academic Press is an imprint of Elsevier, London,* **2011.**

(29). Mateo, J. N.; Kulkarni, S. S.; Das, L.; Bandyopadhyay, S.; Tepper, G. C.; Wynne, K. J.; Bandyopadhyay, S. Wetting Behavior of Polymer Coated Nanoporous Anodic Alumina Films: Transition from Super-Hydrophilicity to Super-Hydrophobicity. *Nanotechnology* **2011,** *22,* 1-10.

(30). Buijnsters, J. G.; Zhong, R.; Tsyntsaru, N.; Celis, J. P. Surface Wettability of Macroporous Anodized Aluminum Oxide. *ACS Appl. Mater. Inter.* **2013,** *5*, 3224-3233.
(31). Kwok, D. Y.; Neumann, A. W. Contact Angle Measurement and Contact Angle interpretation. *Adv. Colloid Interface Sci.* **1999,** *81*, 167-249

For Table of Contents Only

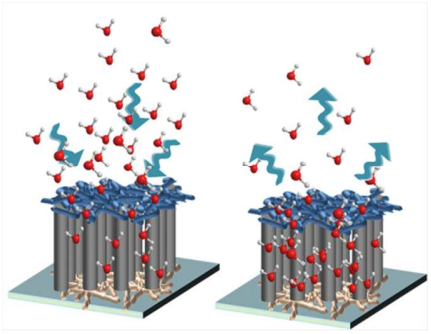

Anisotropically Functionalized Carbon Nanotube Array Based Hygroscopic Scaffolds

Sehmus Ozden[1], Liehui Ge[1], Tharangattu N. Narayanan[2], Amelia H. C. Hart[1], Hyunseung Yang[3], Srividya Sridhar[4], Robert Vajtai[1], Pulickel M. Ajayan[1]*

[1]Department of Material Science and NanoEngineering, Rice University, Houston, Texas 77005, USA
[2]CSIR-Central Electrochemical Research Institute, Karaikudi, 630006, India
[3]Department of Chemical and Biomolecular Engineering, Korea Institute of Science and Technology (KAIST), Daejeon, 305-701, Korea
[4]Department of Physics, Delhi Technological University, Bawana Road, Delhi, 110042, India

KEYWORDS Carbon nanotubes, Water harvesting, Asymmetric Functionalization,

Hydrophobic, Hydrophilic

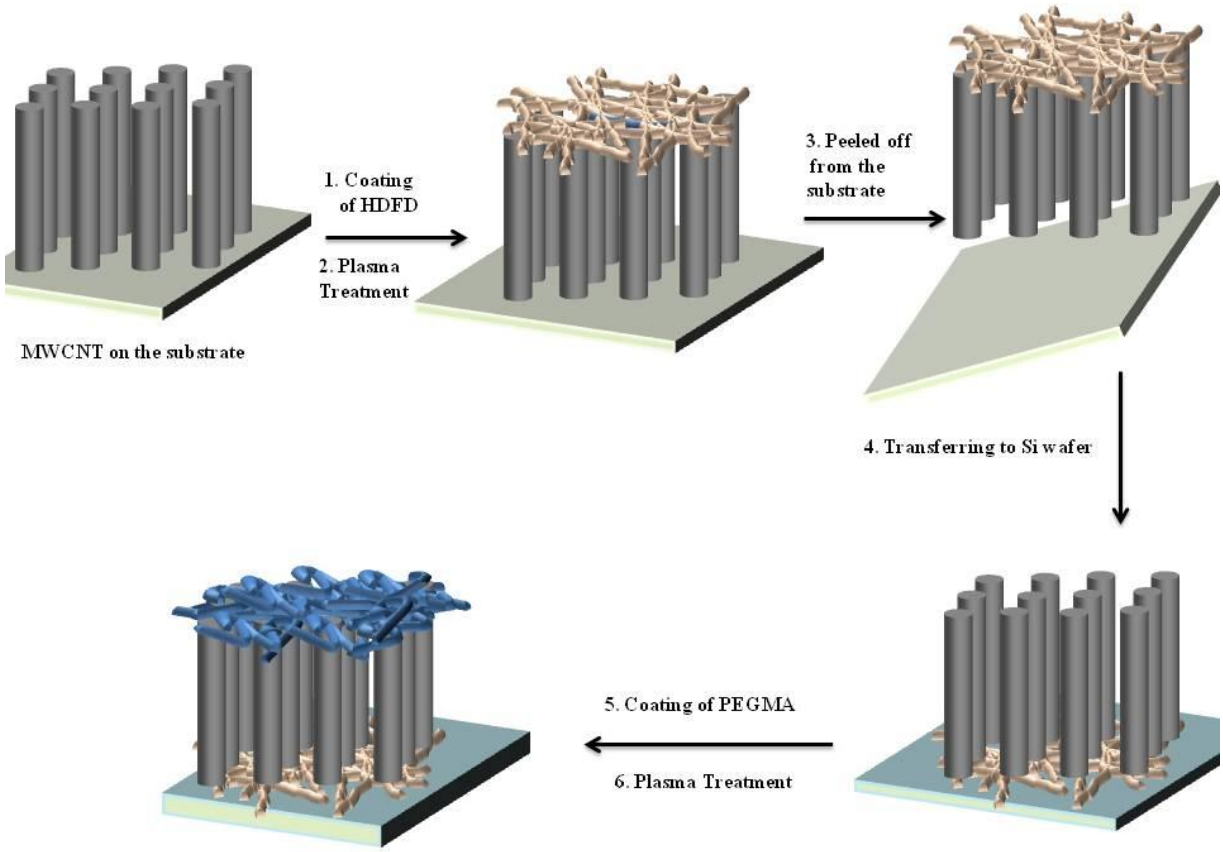

Figure 1. Schematic representation of asymmetric-end functionalization of NTF. The top surface of forest was coated with HDFD monomer and treated to plasma for 2min. NTF slip over to on the another subtrate and coated with PEGMA and treated to plasma for 2min.

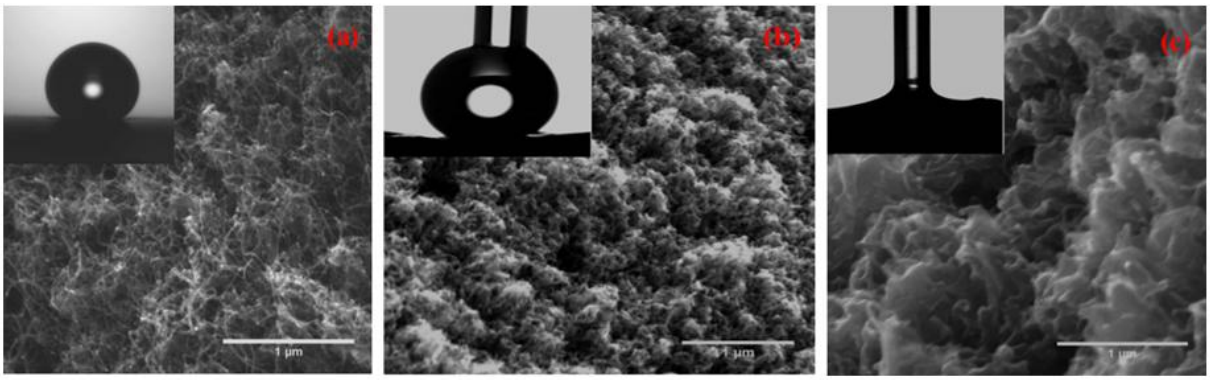

Figure 2. SEM images of a) as grown NTF and contact angle of the CNTs is 118°, b) HDFD-NTF and the contact angle is increased to 162° that is superhydrophobic surface, c) PEGMA-NTF and the contact angle decreased to 0° that is superhydrophobic. The polymerization on the surface clearly can be seen after plasma treatment.

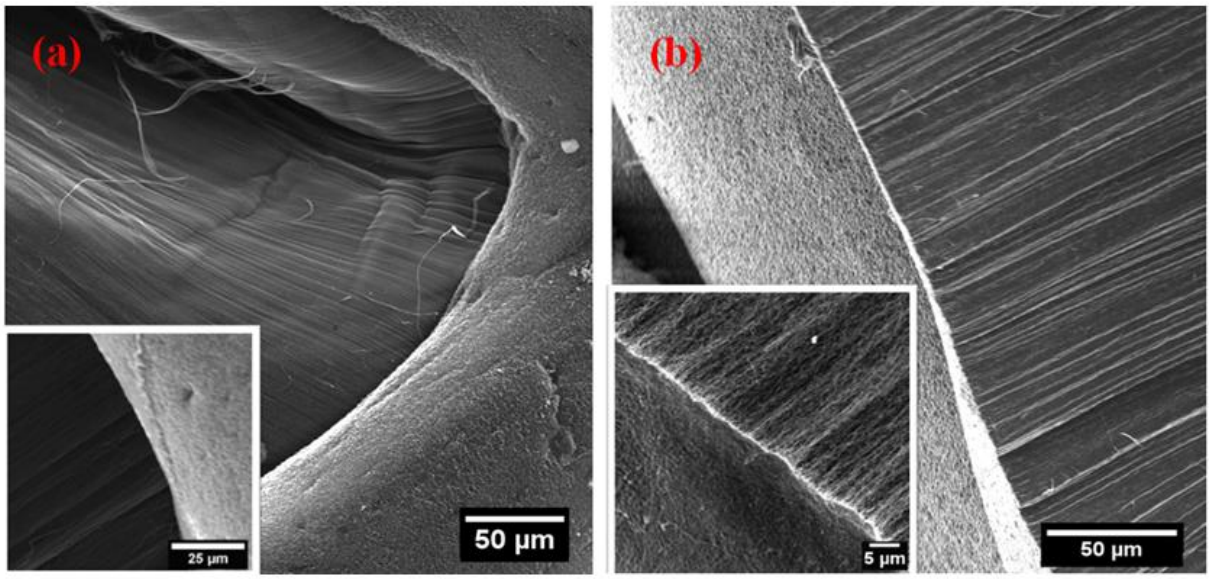

Figure 3. SEM images of a) HDFD-NTF (Superhydrophobic side), b) PEGMA-NTF (Superhydrophilic side). It can clearly seen polymers are penetrated a few micrometers into the CNT because monomers were penetrated into forest during coating. If the amount of monomers increase, penetration will be deeper.

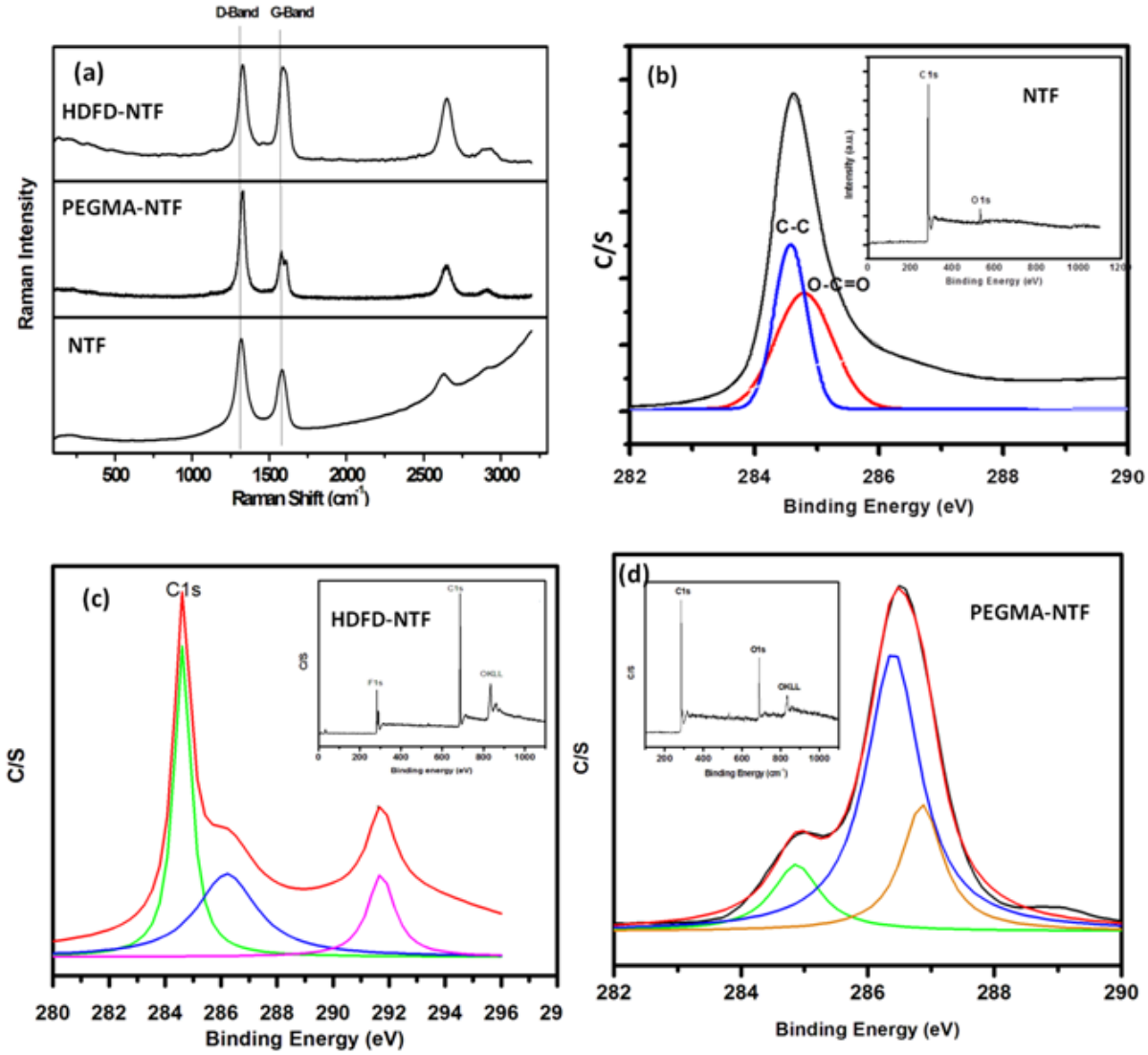

Figure 4. (a)Raman spectra of as grown and asymmetrically functionalized carbon nanotube forest (NTF), (b) XPS spectra of as grown NTF, c) XPS spectra of HDFD-NTF (superhydrophobic), d) XPS spectra of PEGMA-NTF (superhydrophilic)

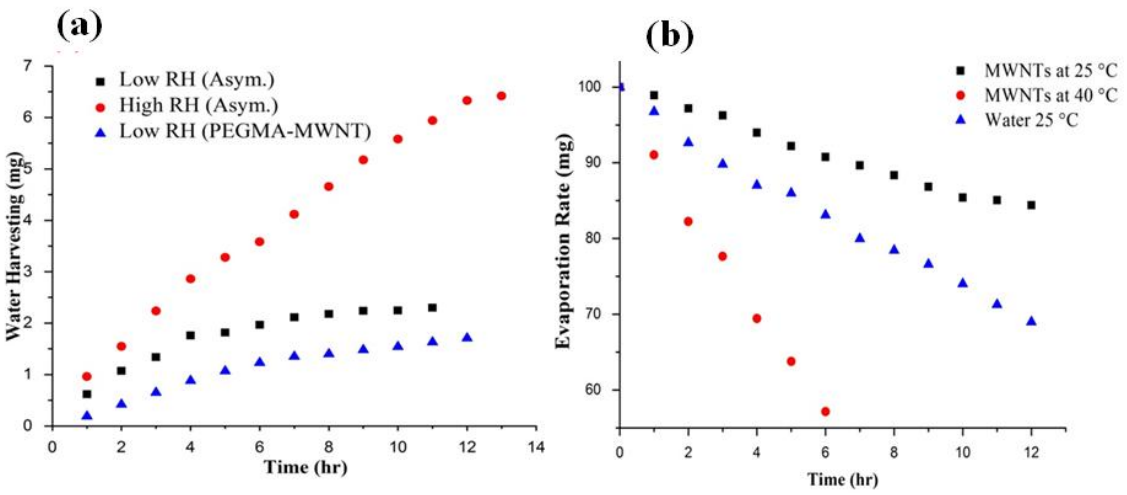

Figure 5. a) Harvesting water from low relative humidity rate (RH) and high humidity rate (RH), b) Water evaporation (WE) rate of water from asymmetrically functionalized NTF and from vessel.

Anisotropically Functionalized Carbon Nanotube Array Based Hygroscopic Scaffolds

Sehmus Ozden[1], Liehui Ge[1], Tharangattu N. Narayanan[2], Amelia H. C. Hart[1], Hyunseung Yang[3], Srividya Sridhar[4], Robert Vajtai[1], Pulickel M. Ajayan[1]*

[1]Department of Material Science and NanoEngineering, Rice University, Houston, Texas 77005, USA
[2]CSIR-Central Electrochemical Research Institute, Karaikudi, 630006, India
[3]Department of Chemical and Biomolecular Engineering, Korea Institute of Science and Technology (KAIST), Daejeon, 305-701, Korea
[4]Department of Physics, Delhi Technological University, Bawana Road, Delhi, 110042, India

KEYWORDS Carbon nanotubes, Water harvesting, Asymmetric Functionalization,

Hydrophobic, Hydrophilic

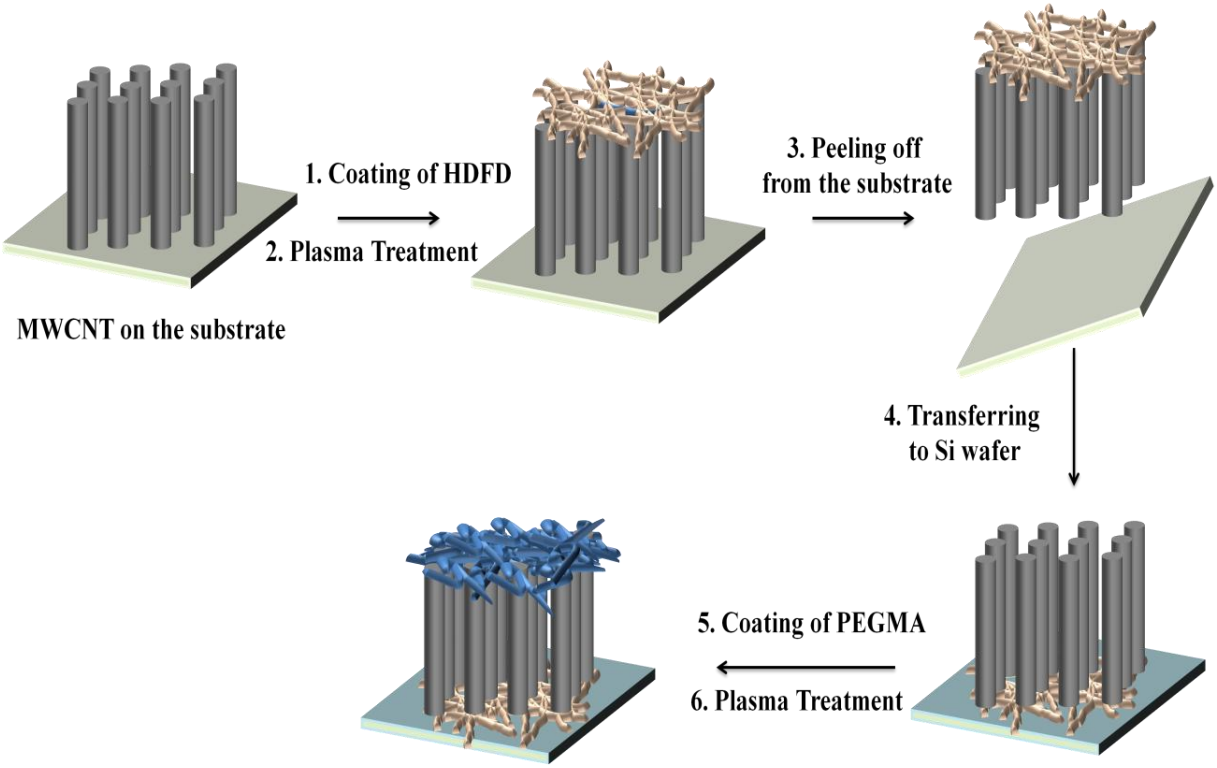

Figure 1. Schematic representation of asymmetric-end functionalization of NTF. The top surface of forest was coated with HDFD monomer and treated to plasma for 2min. The NTF was then flipped onto another subtrate and coated with PEGMA and treated to plasma for 2min.

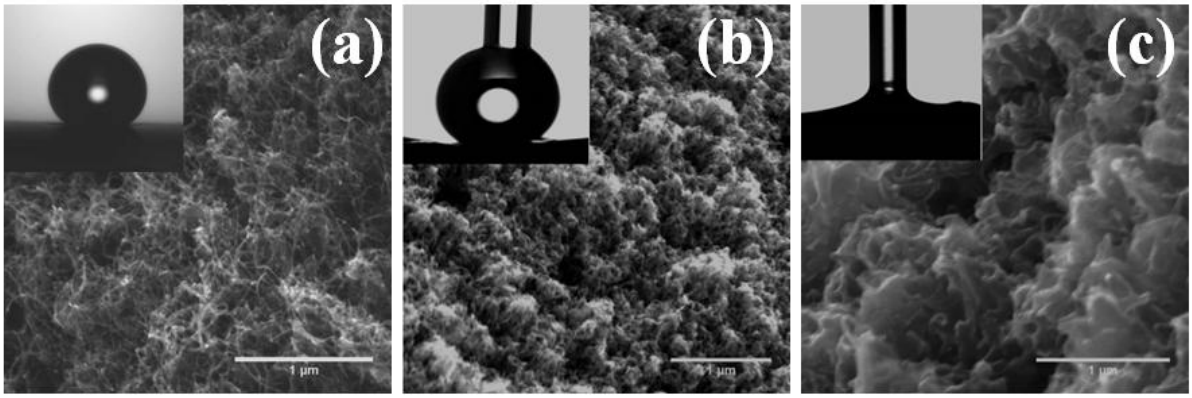

Figure 2. SEM images of a) as grown NTF and contact angle of the CNTs is 118°, b) HDFD-NTF and the contact angle is increased to 162° that is superhydrophobic surface, c) PEGMA-

NTF and the contact angle decreased to 0° that is superhydrophilic. The polymerization on the surface clearly can be seen after plasma treatment.

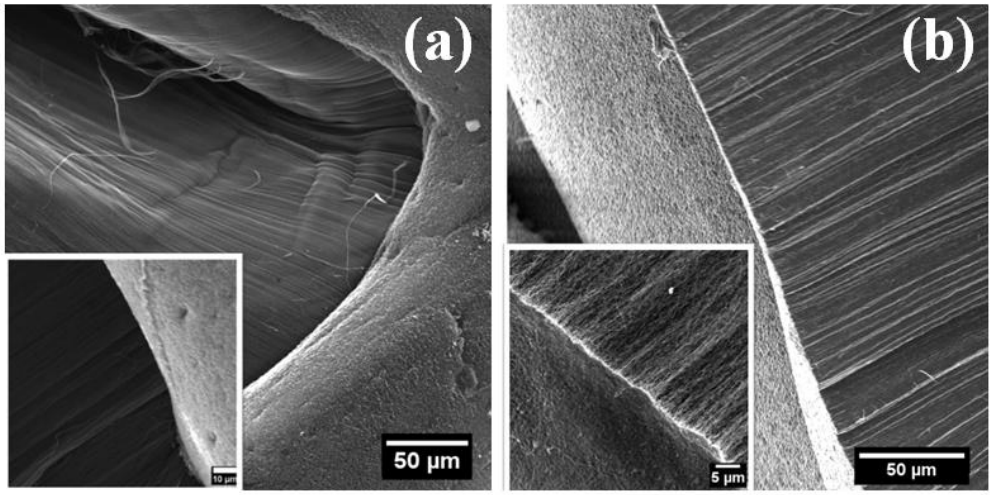

Figure 3. SEM images of a) HDFD-NTF (Superhydrophobic side), b) PEGMA-NTF (Superhydrophilic side). It can be clearly seen polymers are penetrated a few micrometers into the CNT because monomers were penetrated into forest during coating. If the amount of monomers increases, penetration will be deeper.

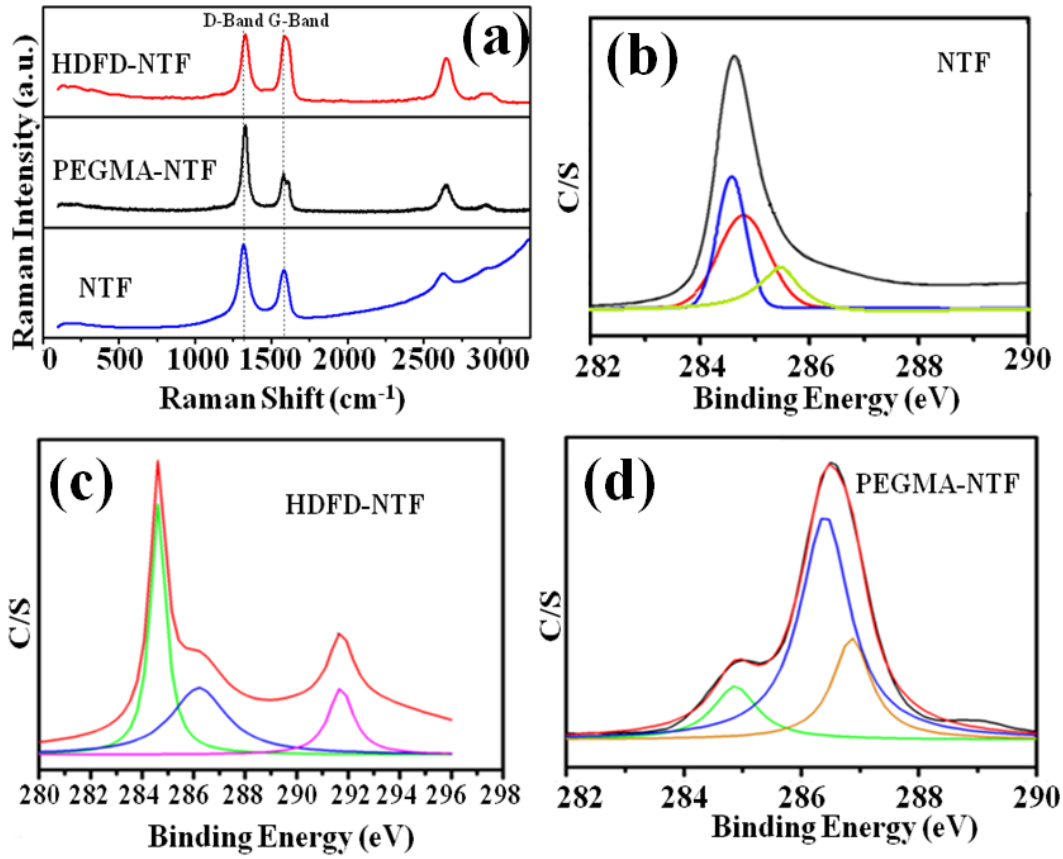

Figure 4. (a)Raman spectra of as grown and asymmetrically functionalized carbon nanotube forest (NTF), (b) XPS spectra of as grown NTF, c) XPS spectra of HDFD-NTF (superhydrophobic), d) XPS spectra of PEGMA-NTF (superhydrophilic)

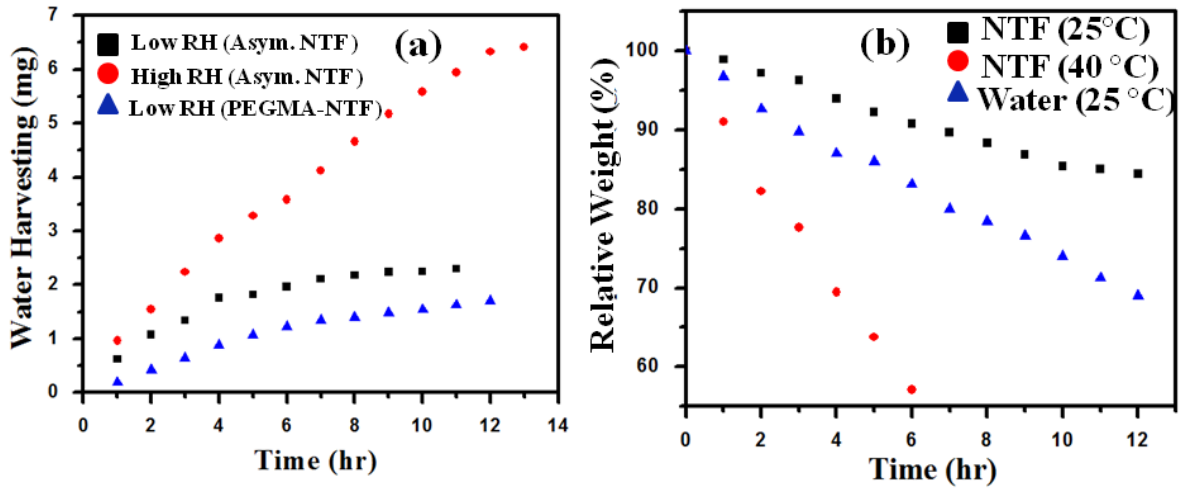

Figure 5. a) Harvesting water from low relative humidity (RH) and high humidity (RH), b) Water evaporation (WE) of water from asymmetrically functionalized NTF and from vessel.

Scientific Online

OPEN JOURNAL OF MOBILE COMPUTING AND CLOUD COMPUTING
In Press

OPEN JOURNAL OF MOBILE COMPUTING AND CLOUD COMPUTING

Comparative Study on Load Balancing Techniques in Cloud Computing

N. S. Raghava* and Deepti Singh

Department of Information Technology, Delhi Technological University, Delhi, India.
***Corresponding author**: nsraghava@gmail.com

Abstract:
The present era has witnessed tremendous growth of the internet and various applications that are running over it. Cloud computing is the internet based technology, emphasizing its utility and follows pay-as-you-go model, hence became so popular with high demanding features. Load balancing is one of the interesting and prominent research topics in cloud computing, which has gained a large attention recently. Users are demanding more services with better results. Many algorithms and approaches are proposed by various researchers throughout the world, with the aim of balancing the overall workload among given nodes, while attaining the maximum throughput and minimum time. In this paper, various proposed algorithms addressing the issue of load balancing in Cloud Computing are analyzed and compared to provide a gist of the latest approaches in this research area.

Keywords:
Cloud Computing; Green Computing; Load Balancing; Virtualization

1. INTRODUCTION

Cloud Computing is the most recent emerging paradigm promising to turn the vision of "computing utilities" into reality, it provides a flexible and easy way to store and retrieve huge data without worrying about the hardware needed. As the number of users on cloud increases, the existing resources decreases automatically which leads to the problem of delay between the users and the cloud service providers. Thus, the load balancing comes into the picture. The traffic over the network must be dealt smartly such that the situation in which some nodes are overloaded and some other are under loaded should never arise. To overcome this situation, many load balancing algorithms are proposed by researchers, with their own pros and cons.

In this paper,an overall review of the current load balancing algorithms in the Cloud Computing environment is presented. Theideas of each algorithm are discussed and finally summarized as an overview.

The rest of the paper is organized as follows. The issues related to load balancing in cloud computing environmentare discussed in Section 2. In Section 3, the current literature and the load balancing algorithm in cloud proposed by various researchers were discussed. In section 4, the proposed approacheswere discussed and compared. Finally, in Section 5 we concluded the paper and also presented some ideas which can be implemented in the future.

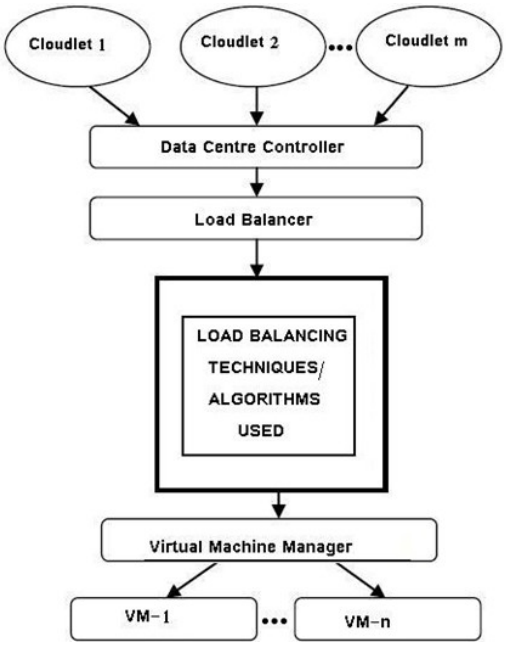

Figure 1. **Load Balancing Algorithms Execution**

2. ISSUE EFFECTING LOAD BALANCING IN CLOUD COMPUTING

There are various issues while dealing with load balancing in a cloud computing environment. Each load balancing algorithm must be such as to achieve the desired goal. Some algorithms aims at achieving higher throughput, some aims at achieving minimum response time, some other aims to achieve maximum resource utilization while some aims at achieving a trade-off between all these metrics. **Figure 1** presents a framework under which various load balancing algorithms work in a cloud computing environment.

Some major issues which must be considered while designing any load balancing algorithm are as follows:

2.1 Geographical distribution of nodes

The geographical distribution of the nodes matters a lot in the overall performance of any real time cloud computing systems, especially in case of the large scaled applications like Facebook, Twitter, etc. A well-distributed system of nodes in cloud environment is helpful in handling fault tolerance and maintaining the efficiency of the system.

2.2 Dynamic Vs Static behavior of algorithms

Any algorithm concerning load balancing is designed, based on the state or behavior of the system, which may be static or dynamic.

2.2.1 Static Algorithms

These algorithms do not depend upon the current state of the system and have prior knowledge regarding system resources and details of all tasks in an application. These kinds of algorithms face a major drawback in case of sudden failure of system resource and tasks.

2.2.2 Dynamic Algorithms

These algorithms take decisionsconcerning load balancing based upon the current state of the system and don't need any prior knowledge about the system. This approach is an improvement over the static approach. The algorithms in this category are considered complex, but have better fault tolerance and overall performance.

2.3 Algorithm Complexity

The complexity of any load balancing algorithm affects the overall performance of the system. Sometimes the algorithm is complex, but is better in terms of throughput and resource utilization. On the other hand, the algorithms which are simpler in terms of complexity may give poor performance in terms of fault tolerance, migration time and response time. Therefore, based on the system requirements, care should be taken to decide a better or suitable load balancing algorithm. A trade-off between all the parameters must be set wisely.

2.4 Traffic analyses over different geographical location.

For any load balancing algorithm, it is very important to analyze the traffic flow in real-time scenarios over different geographic regions, and then balance the overall workload accordingly. All regions over the globe have a different time zone and have certain peak hours during which the network load is supposed to be at its peak. Therefore, load balancer must be capable of handling the traffic in peak hours in every location so as to achieve maximum resource utilization and throughput.

3. EXISTING LOAD BALANCING TECHNIQUES IN CLOUD COMPUTING

In this section, some significant contributions on load balancing in cloud computing, as mentioned in the literature are discussed.A. Khiyaita *et al.* [1], in their paper gave an overview of load balancing in cloud computing, classification of load balancing algorithms based upon system load and system topology, examples of load balancing and different research challenges in load balancing. While in [2] authors discussed most of the existing techniques which are aimed at reducing the associated overhead, service response time and improving performance of the technique. The paper also provides details about various parameters, used to compare the existing techniques. D. A. Menasce *et al.* [3] discussed the concept of cloud computing, its advantages, disadvantages and described several existing cloud computing platforms. He also discussed the results of quantitative experiments carried out using PlanetLab, a cloud computing platform and capacity planning methods for cloud users and cloud service providers. To maintain the load balancing in the cloud computing system, Kuo-Qin Yan *et al.* [4] proposed a scheduling algorithm. Their algorithm combined the capabilities of both OLB (Opportunistic Load Balancing) [5] and LBMM (Load

Balance Min-Min) [6] scheduling algorithms, and is comparatively more efficient. In [7], idea is to find the best cloud resource while considering Co-operative Power aware Scheduled Load Balancing, solution to the Cloud load balancing challenge. The algorithm proposed in this paper, utilizes the benefits of both distributed and centralized approach of computing. Inherent efficiency of centralized approach as well as the energy efficiency and fault-tolerance nature of distributed approach is well used in this algorithm.

In PALB [8] approach, the utilization percentages of each compute node is estimated. This helps in deciding the number of compute nodes which must keep operating while other nodes completely shuts down. The algorithm has three sections: Balancing section, Upscale section and Downscale section. Balancing section is responsible for determining where virtual machines will be instantiated based on utilization percentages. The upscale section power-on's the additional compute nodes. And the downscale section shut-downs the idle compute nodes. This algorithm is guaranteed to decrease the overall power consumption while maintaining the availability of resources as compared to other load balancing algorithms. Raul Alonso-Calvo *et al.* [9] have discussed on managing large image collections in companies and institutions. A cloud computing service and its application for storage and analysis of very large images have been created and the data operations are adapted for working in a distributed mode by using different sub-images that can be stored and processed separately by different agents in the system, facilitating processing very-large images in a parallel manner. This work can be viewed as another way of load balancing in cloud computing. Apart from availability of resources, other factors like scaling of resources and power consumption are also important concerns in load balancing that cannot be ignored. Load balancing techniques should be such as to obtain measurable improvements in resource utilization and availability of resources in the cloud computing environment [10]. Alexandru Iosup *et al.* [11] Analyzed the performance of cloud computing services for scientific computing workloads and quantified the presence in real scientific computing workloads of Many-Task Computing (MTC) users, that is, of users who employ loosely coupled applications comprises many tasks to achieve their scientific goals. They also perform an empirical evaluation of the performance of four commercial cloud computing services.

Srinivas Sethi *et al.* [12] proposed a load balancing algorithm using fuzzy logic in a cloud computing environment. This algorithm uses two parameters processor speed and assigned a load of virtual machine, to balance the overall load through fuzzy logic,although in [13], the authors have introduced a new fuzzy logic based dynamic load balancing algorithm with additional parameters- memory usage, bandwidth usage, disk space usage and virtual machine status and named it as Fuzzy Active Monitoring Load Balancer (FAMLB). Milan E. Sokile [14], have discussed different load balancing techniques in a distributed environment, namely diffusive load, static, round robin and shortest queue in different client environments. Experimental analysis have been done showing diffusive load balancing is more efficient than static and round robin load balancing in a dynamic environment. Ankush P. Deshmukh and Prof. Kumarswamy Pamu [15], discussed on different load balancing strategies, algorithms and methods. The research also shows that the dynamic load balancing is more efficient than other static load balancing techniques. Efficient load balancing can clearly give major performance benefits [16]. A Network Processor consists of a number of on-chip processors to carry out packet level parallel processing operations, ensuring good load balancing among the processors. This process increases the throughput of the system. However, such type of multiprocessing increases out-of-order departure of processed packets. In this paper, the authors first propose an Ordered Round Robin (ORR) scheme to schedule packets in a heterogeneous network processor, assuming that the workload is perfectly divisible. The processed loads from the processors are perfectly ordered. This paper analyzes the throughput and derives expressions for the batch size, scheduling time and maximum number of schedulable processors. Jaspreet Kaur [17] has discussed active vm load balancer algorithm to find a suitable virtual machine in less time period. She has done simulation showing comparative analysis of round robin and equal spread current execution policies

of load balancing with varying service broker policies for data center in a cloud computing environment and comparedtheir response time and cost.

Zhang Bo *et al.* [18], proposed an algorithm which adds capacity to the dynamic balance mechanism for the cloud. The experiments demonstrate that the algorithm has obtained a better load balancing degree and used less time in loading all tasks. Soumya Ray and Ajanta De Sarkar [19] have discussed various algorithms of load balancing like Round robin algorithm, Central queuing algorithm and Randomized algorithm, their analysis is carried out on MIPS vs. VM and MIPS vs. HOST basis. Their results demonstrate that these algorithms can possibly improve the response time in order of magnitude, with respect to number of VMs in Datacenter. Execution analysis of the simulation shows that the change of MIPS will affect the response time. Increasing MIPS vs. VM decreases the response time. In order to handle the random selection based load distribution problem, dynamic load balancing algorithm can be implemented as the future course of work to evaluate various parameters. In [20], the authors have proposed an algorithm on load distribution of workloads among nodes of a cloud, by the use of Ant Colony Optimization (ACO). This algorithm uses the concept of the ant colony optimization method.

Shridhar G. Domanal and G. Ram Mohana Reddy [21] have proposed a local optimized load balancing approach for distributing incoming job request uniformly between the servers or virtual machines. They analyzed the performance of their algorithm using the Cloud Analyst simulator. Further, they also compared their approach with Round Robin [22] and Throttled algorithm [23]. A similar work was done by Shridhar G. Domanal and G. Ram Mohana [21] using CloudSim and Virtual Cloud simulators. In [24], the authors have analyzed various policies in combination with different load balancing algorithms using a tool called Cloud Analyst. They presented various variants of Round Robin load balancing algorithm, demonstrating the pros and cons of each. The Dynamic Round Robin algorithm is an improvement over static Round Robin algorithm [25], this paper analyzed the Dynamic Round Robin algorithm with varying parameters of host bandwidth, cloudlet length, VM image size and VM bandwidth. Results have been analyzed based upon the simulation carried in CloudSim simulator. In [26], the authors Ching-Chi Lin, Pangfeng Liu, Jan-Jan Wu, have proposed a new Dynamic Round Robin (DRR) algorithm for energy-aware virtual machine scheduling and consolidation. This algorithm is compared with other existing algorithms, namely Greedy, Round Robin and Powersave strategies used in Eucalyptus.

4. DISCUSSION AND COMPARISION

In the previous section different load balancing techniques proposed by various researchers have been discussed. **Table 1** gives a comparative analysis of different load balancing techniques with respect to different performance parameters.

In **Table 1** various metrics have been considered to compare different techniques. The metrics on which the existing load balancing techniques have been measured are discussed below:

1. *Throughput*

   This metric is used to estimate the total number of tasks, whose execution has been completed successfully. High throughput is necessary for overall system performance.

2. *Overhead*

   Overhead associated with any load balancing algorithm indicates the extra cost involved in implementing the algorithm. It should be as low as possible.

3. *Fault Tolerance*

Table 1. Comparison of existing Load Balancing Techniques

Metrics/ Techniques	Throughput	Overhead	Fault tolerance	Migration time	Response time	Resource Utilization	Scalability	Performance
Round Robin [22]	YES	YES	NO	NO	YES	YES	YES	YES
Dynamic Round Robin [26]	YES	YES	YES	YES	NO	YES	NO	NO
PALB [8]	YES	YES	YES	YES	YES	YES	NO	NO
Active Monitoring [23]	YES	YES	NO	YES	YES	YES	YES	NO
FAMLB [13]	YES	YES	YES	YES	NO	YES	YES	YES
Min-Min [6]	YES	YES	NO	NO	YES	YES	NO	YES
Max-Min [27]	YES	YES	NO	NO	YES	YES	NO	YES
OLB+LBMM [4]	NO	NO	NO	NO	NO	YES	NO	YES
Throttled [23]	NO	NO	YES	YES	YES	YES	YES	YES
Honeybee Foraging [28]	NO	NO	NO	NO	NO	YES	NO	NO
Active Clustering [28]	NO	YES	NO	YES	NO	YES	NO	NO
Biased Random Sampling [28]	NO	YES	NO	NO	NO	YES	NO	YES

It measures the capability of an algorithm to perform uniform load balancing in case of any failure. A good load balancing algorithm must be highly fault tolerable.

4. *Migration Time*

   It is defined as, the total time required in migrating the jobs or resources from one node to another. It should be minimized.

5. *Response Time*

   It can be measured as, the time interval between sending a request and receiving its response. It should be minimized to boost the overall performance.

6. *Resource Utilization*

   It is used to ensure the proper utilization of all those resources, which comprised the whole system. This factor must be optimized to have an efficient load balancing algorithm.

7. *Scalability*

   It is the ability of an algorithm to perform uniform load balancing in a system with the increase in the number of nodes, according to the requirements. Algorithm with higher scalability is preferred.

8. *Performance*

   It is used to check, how efficient the system is. This has to be improved at a reasonable cost, e.g., reducing the response time though keeping the acceptable delays.

5. CONCLUSION AND FUTURE WORK

In this paper, we have surveyed various load balancing algorithms in the Cloud Computing environment. We discussed major issues which must be taken into consideration while designing any load balancing algorithm. We have discussed the already proposed algorithms by various researchers in literature, their advantages and disadvantages. A comparison has been done on the basis of different criteria like scalability, network overhead, resource utilization, algorithm complexity, fault tolerance, response time, etc. In future we will focus on designing algorithms which will maintain a better trade-off among all performance parameters.

References

[1] A. Khiyaita, M. Zbakh, H. El Bakkali, and D. El Kettani, "Load balancing cloud computing: state of art," in *Network Security and Systems (JNS2), 2012 National Days of*, pp. 106–109, IEEE, 2012.

[2] N. J. Kansal and I. Chana, "Existing load balancing techniques in cloud computing: A systematic review.," *Journal of Information Systems & Communication*, vol. 3, no. 1, 2012.

[3] D. A. Menascé and P. Ngo, "Understanding cloud computing: Experimentation and capacity planning," in *Computer Measurement Group Conference*, 2009.

[4] S.-C. Wang, K.-Q. Yan, W.-P. Liao, and S.-S. Wang, "Towards a load balancing in a three-level cloud computing network," in *Computer Science and Information Technology (ICCSIT), 2010 3rd IEEE International Conference on*, vol. 1, pp. 108–113, IEEE, 2010.

[5] T. D. Braun, H. J. Siegel, N. Beck, L. L. Bölöni, M. Maheswaran, A. I. Reuther, J. P. Robertson, M. D. Theys, B. Yao, D. Hensgen, *et al.*, "A comparison of eleven static heuristics for mapping a class of independent tasks onto heterogeneous distributed computing systems," *Journal of Parallel and Distributed computing*, vol. 61, no. 6, pp. 810–837, 2001.

[6] T. Kokilavani and D. Amalarethinam, "Load balanced min-min algorithm for static meta-task scheduling in grid computing.," *International Journal of Computer Applications*, vol. 20, no. 2, 2011.

[7] T. Anandharajan and M. Bhagyaveni, "Co-operative scheduled energy aware load-balancing technique for an efficient computational cloud.," *International Journal of Computer Science Issues (IJCSI)*, vol. 8, no. 2, 2011.

[8] J. M. Galloway, K. L. Smith, and S. S. Vrbsky, "Power aware load balancing for cloud computing," in *Proceedings of the World Congress on Engineering and Computer Science*, vol. 1, pp. 19–21, 2011.

[9] R. Alonso-Calvo, J. Crespo, M. Garcia-Remesal, A. Anguita, and V. Maojo, "On distributing load in cloud computing: A real application for very-large image datasets," *Procedia Computer Science*, vol. 1, no. 1, pp. 2669–2677, 2010.

[10] Z. Chaczko, V. Mahadevan, S. Aslanzadeh, and C. Mcdermid, "Availability and load balancing in cloud computing," in *International Conference on Computer and Software Modeling, Singapore*, vol. 14, 2011.

[11] A. Iosup, S. Ostermann, M. N. Yigitbasi, R. Prodan, T. Fahringer, and D. H. Epema, "Performance analysis of cloud computing services for many-tasks scientific computing," *Parallel and Distributed Systems, IEEE Transactions on*, vol. 22, no. 6, pp. 931–945, 2011.

[12] S. Sethi, A. Sahu, and S. K. Jena, "Efficient load balancing in cloud computing using fuzzy logic," *IOSR Journal of Engineering*, vol. 2, no. 7, pp. 65–71, 2012.

[13] Z. Nine, M. SQ, M. Azad, A. Kalam, S. Abdullah, and R. M. Rahman, "Fuzzy logic based dynamic load balancing in virtualized data centers," in *Fuzzy Systems (FUZZ), 2013 IEEE International Conference on*, pp. 1–7, IEEE, 2013.

[14] M. E. Soklic, "Simulation of load balancing algorithms: a comparative study," *ACM SIGCSE Bulletin*, vol. 34, no. 4, pp. 138–141, 2002.

[15] A. P. Deshmukh and K. Pamu, "Applying load balancing: A dynamic approach," *International Journal*, vol. 2, no. 6, 2012.

[16] J. Yao, J. Guo, and L. N. Bhuyan, "Ordered round-robin: An efficient sequence preserving packet scheduler," *Computers, IEEE Transactions on*, vol. 57, no. 12, pp. 1690–1703, 2008.

[17] J. Kaur, "Comparison of load balancing algorithms in a cloud," *International Journal of Engineering Research and Applications*, vol. 2, no. 3, pp. 1169–173, 2012.

[18] Z. Bo, G. Ji, and A. Jieqing, "Cloud loading balance algorithm," in *Information Science and Engineering (ICISE), 2010 2nd International Conference on*, pp. 5001–5004, IEEE, 2010.

[19] S. Ray and A. De Sarkar, "Execution analysis of load balancing algorithms in cloud computing environment.," *International Journal on Cloud Computing: Services & Architecture*, vol. 2, no. 5, 2012.

[20] K. Nishant, P. Sharma, V. Krishna, C. Gupta, K. P. Singh, N. Nitin, and R. Rastogi, "Load balancing of nodes in cloud using ant colony optimization," in *Computer Modelling and Simulation (UKSim), 2012 UKSim 14th International Conference on*, pp. 3–8, IEEE, 2012.

[21] S. G. Domanal and G. R. M. Reddy, "Load balancing in cloud computing using modified throttled algorithm," 2013.

[22] S. Subramanian, G. Nitish Krishna, M. Kiran Kumar, P. Sreesh, and G. Karpagam, "An adaptive algorithm for dynamic priority based virtual machine scheduling in cloud.," *International Journal of Computer Science Issues (IJCSI)*, vol. 9, no. 6, 2012.

[23] B. Wickremasinghe, "Cloudanalyst: A cloudsim-based tool for modelling and analysis of large scale cloud computing environments," *MEDC Project Report*, vol. 22, no. 6, pp. 433–659, 2009.

[24] S. Mohapatra, S. Mohanty, and K. S. Rekha, "Analysis of different variants in round robin algorithms for load balancing in cloud computing," *International Journal of Computer Applications*, vol. 69, no. 22, 2013.

[25] A. Gulati and R. K. Chopra, "Dynamic round robin for load balancing in a cloud computing," 2013.

[26] C.-C. Lin, P. Liu, and J.-J. Wu, "Energy-aware virtual machine dynamic provision and scheduling for cloud computing," in *Cloud Computing (CLOUD), 2011 IEEE International Conference on*, pp. 736–737, IEEE, 2011.

[27] Y. Mao, X. Chen, and X. Li, "Max–min task scheduling algorithm for load balance in cloud computing," in *Proceedings of International Conference on Computer Science and Information Technology*, pp. 457–465, Springer, 2014.

[28] M. Randles, D. Lamb, and A. Taleb-Bendiab, "A comparative study into distributed load balancing algorithms for cloud computing," in *Advanced Information Networking and Applications Workshops (WAINA), 2010 IEEE 24th International Conference on*, pp. 551–556, IEEE, 2010.

CONVERSION OF WASTE COOKING OIL INTO BIODIESEL

Amit Pal &[*]S. S. Kachhwaha

Department of Mechanical Engineering, Delhi Technological University, Bawana Road, Delhi 110042, India

[*]Department of Mechanical Engineering, School of Technology, Pandit Deendayal Petreoleum University, Gandhinagar-382007, Gujrat, India

amitpal1@yahoo.com,* sskachhawaha@rediffmail.com

ABSTRACT

Due to the depletion of the world's petroleum reserves and the increasing environmental concerns, there is a great demand for alternative sources of fossil fuels. Biodiesel, a clean renewable and environment friendly fuel, has recently been considered as the best substitute for the diesel fuel because it can be used in any diesel engine out the need for any modification. Since the cost of biodiesel raw materials accounts about 60–80% of the total cost of production, choosing a right feedstock is very important. Waste Cooking Oil (WCO), which is not suitable for human consumption, and whose safe disposal is a challenge, may prove to be a potential feedstock for biodiesel production.

Biodiesel can be produced by various methods, such as: alkali catalysis, acid catalysis, lipase catalysis etc. Considering various limitations of these methods, there is a strong quest to develop an efficient, time-saving, and economically functional and environment friendly biodiesel production processes suitable to large scale biodiesel production. Keeping this aspect into consideration, some of the recently developed biodiesel production technologies are power ultrasound, hydrodynamic cavitation and supercritical methanol processes. Power ultrasound is a useful tool to strengthen mass transfer of liquid–liquid heterogeneous system. In this process cavities are created by the irradiation of power ultrasonic sufficient energy in the immiscible liquids. As a result micro fine bubbles are formed and the asymmetric collapse of the cavitation of these bubbles disrupts the phase boundary and impinging of the liquids creates micro jets, leading to intensive emulsification of system. Another cavitation technique, which is popularly known as hydrodynamic cavitation is a potential method for biodiesel production at industrial scale due to its easy scale-up property. This is a rapid technique for preparing alkyl esters from triglycerides at pilot plant scale operation. Supercritical methanol is a simple and fast process and produces high yield because of simultaneous transesterification of triglycerides and methyl esterification of fatty acids at critical state. Supercritical methanol a co-solvent process require relatively lower reaction temperature and pressures and hence energy, as compared to conventional supercritical methanol method. All these methods have future potential for biodiesel production at large industrial scale. The present paper deals the details of conversion of WCO into biodiesel through cavitation techniques followed by its performance testing on a diesel engine.

1. INTRODUCTION

Diesel fuel play important role in the industrial economy of developing countries, it is commonly used in transport of industrial and agricultural goods, etc. Economic growth is always accompanied by commensurate increase in the transport activities [1]. Majority of the world's energy needs are supplied through petrochemical sources, coal and natural gases, the exception of hydroelectricity and nuclear energy. All these sources are finite and at current usage rates they will be consumed shortly [2]. Also, petroleum fuels are currently the dominant global source of CO_2 emissions and their combustion is posing stronger threat to clean environment. This has stimulated the recent interest in alternative sources for petroleum-based fuels [3]. The prerequisite for an alternative fuel is that it should be easily available, renewable, environment friendly and techno-economically competitive.

India is a developing country and its energy demand is increasing day by day. Most of the country's oil demands are fulfilled by import from the foreign countries which is a major expense for the country. Therefore, there is a dire need of searching a viable alternative source of energy for long term energy security. Bio-diesel is an alternative to petroleum-based fuels derived from vegetable oils or animal fats [4]. It is named biodiesel because it is derived from biological products and matches petro-diesel in properties and performance.The glycerides present in vegetable oils can be separated in the transesterification reaction and used as a by-product [5]. Bio-diesel production is a very modern and technological area for researchers because of its relevance due to increase in the petroleum price and the environmental advantages [6]. Vegetable oils have good heating power and provide exhaust gas negligible sulphur and aromatic polycyclic compounds. It possesses high biodegradability and lubricating property which makes it even better fuel. As vegetable oils are produced from plants, their burning is completely recyclable as it produces carbon dioxide (CO_2), which is consumed by the plants in photosynthesis [7]. Waste cooking oil can be used as a biodiesel feedstock, as it is available in vast quantities and in its present form if it is used in engines, it will be big threat to the environment [8-10].

The biodiesel produced from vegetable oil or animal fat is usually more expensive than petroleum based diesel fuel from 10 to 50 %. This is a great concern to biodiesel producers, since the cost of feedstock comprises 70 to 95% of total operating cost of a biodiesel plant. Many vegetable oils like Soybean, Groundnut, Rapeseed, Palm, Olive etc are wildly used for frying a number of food items. But once they are heated above a critical temperature for deep frying, they become unfit for eating, as their further use may lead to cholesterol formation. Thus they need to be disposed in an environment friendly manner. Compared to neat vegetable oils the cost of WCO is anywhere from 60% less to totally free, depending upon the source and availability. Presently, the WCOs are still lower cost feedstock making biodiesel production more competitive to the production of petroleum based diesel fuel. In developing countries like India, the significant amount of WCOs is collected from catering industry. As if unused WCO, poured down the drain may create problems for waste water treatment plants and energy loss, or integrated into food chain of animal deeding, causing human health problems. Their use for biodiesel production offers solution to a growing problem of the increased WCO production from household and industrial sources all around the world.

Biodiesel can be produced by various conventional methods [11–14], such as: alkali catalysis, acid catalysis, lipase catalysis etc. Due to the fact that the transesterification is an equilibrium reaction, an excess of alcohol is used to displace the reaction towards ester formation. Non-edible oil and alcohols are immiscible, so that their reaction takes place at the interface in a very slow process. The reaction is catalyzed by alkali, acid or enzyme. Enzymes-catalyzed procedures, using lipase as catalyst, do not produce side reactions, but the lipases are very expensive for industrial scale production and a three-step process is required to achieve a 95% conversion. Acid catalyzed process is useful when a high amount of free fatty acids are present in the vegetable oil, but the reaction time is very long (48–96 h), even at the boiling point of the alcohol, and a high molar ratio of alcohol is needed (20:1 wt/wt to the oil). In the base catalyzed procedure, some soap is formed and it acts as phase transfer catalyst, thus helping the mixing of the reactants. Base catalyzed process is strongly affected by the mixing of the reactants and/or by efficient heating that produces tiny droplets, thus increasing the reaction contact area. Presently, mechanical stirring is the commonly adopted process in worldwide industrial applications. Considering these limitations, there is a strong quest to develop an efficient, time-saving, economically functional and environmental friendly biodiesel production process at industrial scale having superiority over the classical procedure. Keeping this aspect into consideration, some of the recently developed biodiesel production technologies are supercritical methanol processes, hydrodynamic cavitation and power ultrasound.

Saka and Kusdian [15] and Dembribas [16] have proposed that biodiesel fuels may be prepared from vegetables oil via non-catalytic transesterification supercritical methanol associated the two phase nature of normal methanol/oil mixtures by forming a single phase. As a result, the reaction was found to be complete in a very short time. Compared to the catalytic processes, purification of products (due to absence of catalyst) is much simpler and more environmental friendly. However the reaction requires very high temperatures and pressures which are not very viable and economical from industrial point of view due to very high production costs. Han et al. [17] succeeded in preparing biodiesel from soybean oil using supercritical methanol and CO_2 as co-solvent at relatively lower temperature and pressure.

Among recently developed techniques, hydrodynamic cavitation is a potential method for biodiesel production at industrial scale due to its easy scale-up property. Pal et al. [18] presented the details of thumba biodiesel production test rig based on hydrodynamic cavitation followed by results of experimental investigation carried out on a CI engine. The transesterification reaction of vegetable oils using base catalyst and short-chain alcohols was studied by Gogate et al. [19, 20] by the method of hydrodynamic cavitation. This is a rapid technique for preparing alkyl esters from triglycerides at pilot plant scale operation. As reported by Ji et al. [21] that cavitating conditions identical to acoustic cavitation could be generated in hydrodynamic cavitation (HC), which even had a better effect on mixing immiscible liquids. Furthermore, scale-up of hydrodynamic cavitation to meet industrial- scale operations had better opportunities due to its easier generating and less sensitivity to the geometric details of the reactor.

In the last decade ultrasound cavitation has seen diverse applications in a number of fields [22], such as synthesis of nanostructure material, processing of biomass, sonofusion, sonodynamic therapy, and sonochemical degradation of pollutants and hazardous chemicals. The ultrasound field is known to produce unique chemical and physical effects that arise from the collapse of the cavitation bubbles. Because oil and methanol are not completely miscible, the mixing efficiency was stated as one of the most important factors affecting the yield of the transesterification. Low frequency ultrasound irradiation is widely used in industry for emulsification of immiscible liquids. Stavarache et al. [23, 24] showed that by using ultrasounds the problems of efficient mixing could be overcome. During the collapse of cavitational bubbles of methanol supersonic jets are created generating nano sized drops that are efficiently mixed thus abundantly enhancing the reaction surface. Hoang et al. [22, 25, 26] investigated the transesterification of triolin ethanol to make biodiesel fuel under ultrasound irradiation to evaluate the effect of the amount of base catalyst, molar ratio, and temperature and concluded that alcoholysis of triolin by ultrasound irradiation has the potential for producing cheap biofuels, which could reduce pollution and protect the environment. He also studied the transesterification of triolin various alcohols under mechanical stirring conditions and found that the rate of the alkyl ester formation under the ultrasound irradiation condition was higher. Biodiesel production from canola oil methanol was performed by Thanh et al. [27] in the presence of a base-catalyst by an ultrasound assisted circulation process at room temperature. The conventional and ultrasound irradiation transesterification of beef tallow methanol were investigated by Teixeira el al. [28]. It was shown that the ultrasound process led to similar yields of alkyl esters as compared to the conventional procedure and effectively decreased the reaction time. In the open literature very few studies are available regarding production of biodiesel from WCO using recently developed ultrasound and hydrodynamic cavitation techniques in comparison to mechanical stirring methods. In the present study, these three methods are compared and in terms of transesterification reaction time, molar ratio, catalyst % and yield obtained at different time intervals followed by performance analysis. For this purpose a laboratory scale test rig for hydrodynamic cavitation is indigenously designed and fabricated.

2. BIODIESEL PRODUCTION THROUGH CAVITATION TECHNOLOGY

The chemical reactions requiring stringent conditions can be effectively carried out using cavitation at ambient conditions. Moreover, free radicals are generated in the process due to the dissociation of vapours trapped in the cavitating bubbles, which results in either intensification of the chemical reactions or in the propagation of certain unexpected reactions. Cavitation also results in the generation of local turbulence and liquid micro- circulation (acoustic streaming) in the reactor, enhancing the rates of transport processes. The generation, subsequent growth and collapse of cavities results in very high energy densities of the order of 1- 10^{18} kW/m^3. Cavitation can occur at millions of locations in a reactor simultaneously and generate conditions of very high temperatures and pressures locally, overall environment being that of ambient conditions. The two principle types of cavitations and their application for transesterification process are described below.

2.1 ULTRASONIC CAVITATION

Ultrasonic Cavitation is a useful tool for strengthening mass transfer of liquid-liquid heterogeneous system. In this process cavities are created by the irradiation of power ultrasonic sufficient energy in the immiscible liquids. As a result micro fine bubbles are formed. The asymmetric collapse of the cavitation bubbles disrupt the phase boundary and impinging of the liquids create micro jets,

leading to intensive emulsification of the system. The transesterification of vegetable oil short-chain alcohols in the presence of base-catalyst, by means of low frequency ultrasound (28 and 40 kHz) in order to obtain biodiesel fuel was studied by Stavarache et al. [22-23]. By using ultrasounds the reaction time observed was much shorter (10-40 min) as compared to mechanical stirring. The quantity of required catalyst was also lower.

2.2 HYDRODYNAMIC CAVITATION

Hydrodynamic cavitation is another technology developed recently, it allows the generation of cavity collapse conditions similar to acoustic cavitation, thereby enabling different applications requiring different cavitational intensities, which have been successfully carried out using acoustic cavitation phenomenon but at much lower energy inputs. Hydrodynamic cavitation is a potential method for biodiesel production at industrial scale due to its easy scale-up property. It is reported that hydrodynamic cavitation can be successfully applied to transesterification reaction more than 90% yield of the product according to stoichiometry is as low as 15 min of the reaction time.

3. EXPERIMENTAL WORK ON BIODIESEL PRODUCTION

3.1 CHEMISTRY OF BIODIESEL

Biodiesel is made using the process of transesterification. In the transesterification of different type of oils, triglycerides react an alcohol, generally methanol or ethanol, to produce esters and glycerin. To make it possible, a catalyst is added to the reaction [3].

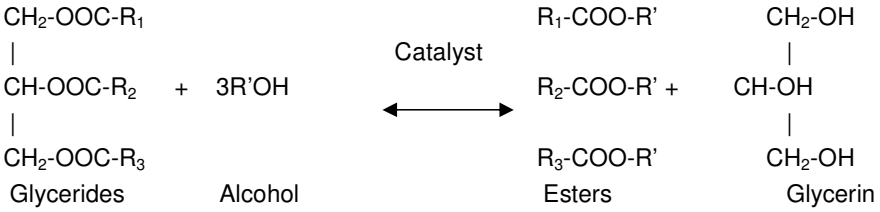

Where, term R represents to different alkyl groups. The overall process is normally a sequence of three consecutive steps, which are reversible reactions. In the first step from triglycerides, diglycerides are obtained. From diglyceride, monoglyceride is produced and in the last step from monoglycerides, glycerin is obtained. In all these reactions esters are produced. The stoichiometric ratio between alcohol and the oil is 3:1. However, an excess of alcohol is usually more appropriate to improve the reaction towards the desired product.

Triglycerides (TG) + R'OH $\longleftrightarrow$ Diglycerides (DG) + $R'COOR_1$

Diglycerides (DG) + R'OH $\longleftrightarrow$ Monoglycerides (MG) + $R'COOR_2$

Monoglycerides (MG) + R'OH $\longleftrightarrow$ Glycerin (GL) + $R'COOR_3$

The catalyst used for the reaction is mainly of three types which are given below.

Alkali Catalyst

This catalyst can be used methanol or ethanol as well as any kind of oils, refine, crude or frying. The main alkali catalysts are sodium hydroxide (NaOH) and potassium hydroxide (KOH).

Acidic Catalyst

Acid transesterification is a great way to make biodiesel if the sample has relatively high free fatty acid content. The main acidic catalysts are Sulfuric acid (H_2SO_4) and Sulfonic acid.

Enzymes-catalyzed

Enzymes-catalyzed procedures, using lipase as catalyst, but the lipases are very expensive for industrial scale production and there are three-step process was required to achieve a 95% conversion. Due to this three step process the reaction time is too large.

3.2 MATERIAL AND METHODS

In this work the WCO is collected from Hotel Maurya Sheraton of Delhi. It was fist properly filtered to separate out any kind of suspended impurities present. Then WCO (300g for mechanical stirring and ultrasonic cavitation and 3kg for hydrodynamic cavitation) is taken in a beaker and the oill is heated up to 120^0C in order to remove water content in the oil to avoid soap formation. This

oil is then allowed to cool up to 55^0C temperature so that after mixing the reactants the mixture temperature is limited to 50^0C. Simultaneously methyl alcohol (CH_3OH) is taken in molar ratio of (1:4.5 & 1:6) and Catalyst (KOH) is taken as (0.5%, 0.75% and 1% by weight of oil).The mixer of methyl alcohol and KOH is stirred until KOH dissolves in methyl alcohol. For mechanical stirring method this mixture is continuously rotated to mix on a magnetic stirrer. Temperature is controlled between 45^0C to 55^0C

The schematic diagram of the hydrodynamic cavitation test rig developed is shown in Fig. 1. The setup consists of a closed loop circuit comprising a feed tank approx. 12 liter volume, a reciprocating pump (7.36 kW), a control valve and a coupling to accommodate the orifice plate. The suction side of the pump is connected to the bottom of the feed tank. Discharge from the pump branches into two lines, which helps to control of the inlet pressure and inlet flow rate into the main line housing and the orifice. The main line consists of a coupling to accommodate the orifice plate. The cavitating conditions are generated just after the orifice plate in the main line and hence the intensity of the cavitating conditions strongly depends on the geometry of the orifice plate. When the liquid passes through the orifice plate, the velocities at the orifice increase due to the sudden reduction in the area offered for the flow, resulting in the decrease of the pressure. If the velocities are such that their increase is sufficient to allow the local pressure to go below the medium vapour pressure under operating conditions, cavities are formed. Cavitating conditions are generated just after the orifice plates in the main line and hence the intensity of the cavitating conditions are strongly depend on the geometry of the orifice plate. At the downstream of the orifice, however, due to an increase in the area of cross-section, the velocity decreases giving rise to increasing pressure and pressure fluctuations, which control the different states of cavitation, mainly formation, growth & collapse. The feed tank is provided a cooling jacket to control the temperature of the circulating liquid. Setup is capable of processing vegetable oil 2.5 to 10 kg.

Figure 2 shows an ultrasonic horn type biodiesel processor which consumes about 150Watt and produces ultrasonic frequencies from 32 to 40 kHz. This is suitable for preparing the biodiesel samples of 50 to 300grams. In present experiment it has been utilised for 300gram samples. The ultrasonic horn is dipped into the WCO and reactants mixture. The mixture is taken initially at 45^0C and it is monitored not to go beyond 55^0C.

Experiments have been conducted one of the main objectives of present study convert WCO in to biodiesel by both types of cavitation technique and to compare the same conventional magnetic stirring method in terms of biodiesel production time and yield (%). Table 1 present the details of ingredients used for biodiesel production using mechanical stirring and Hydrodynamic caviation. Experiments were carried out for molar ratio of 4.5:1 and 6:1. Results for biodiesel production yield and time for both the processes are shown in Fig 3 to Fig. 5 respectively. From the experimental results it is clear that there is a significant reduction in the reaction time for biodiesel production and an increase in yield (%) in cavitation techniques as compared to mechanical stirring method. Thus Hydrodynamic cavitation can be successfully applied to transesterification reactions, more than 90% yield of the product for molar ratio 4.5:1 and minimum catalyst percentage of 0.5%. Changing molar ratio to 6:1 does not give any appreciable increase in yield %. Therefore, with Hydrodynamic cavitation technique molar ratio of 4.5:1 appears to be a rapid and effective technique compared to the mechanical stirring method, for preparing alkyl esters from triglycerides at laboratory scale of operation. It can be seen that using cavitation methods reaction time is almost half compared to conventional method which is beneficial for industrial purpose.

Table 1: Oil, alcohol and catalyst used for mechanical stirring

Molar ratio (alcohol/oil)	**Quantity of WCO(g)**	**Quantity of methanol (g)**	**Catalyst (KOH)**		
			0.5%	**0.75%**	**1.0%**
6:1	300 g	66 g	1.5 g	2.25 g	3.0 g
4.5:1	300 g	49.18 g	1.5 g	2.25 g	3.0 g

3.3 CALCULATION OF MOLAR RATIO

Molecular weight of triglycerides from waste cooking oil = 870

Molecular weight of methanol = 32

Hence, 1 gm mole of waste cooking oil = 870 gm

and 1 gm mole of methanol = 32 gm

Catalyst (KOH) = 0.5%, 0.75% and 1% by weight of oil

Amount of methanol for 300 g of vegetable oil

- For 1:6 molar ratio = (32 / 870) ×300 × 6 = 66 g
- 1:4.5 molar ratio = (32 / 870) ×300 × 4.5 = 49.18 g

Yield % = (Quantity of biodiesel produced/Quantity of oil taken)*100

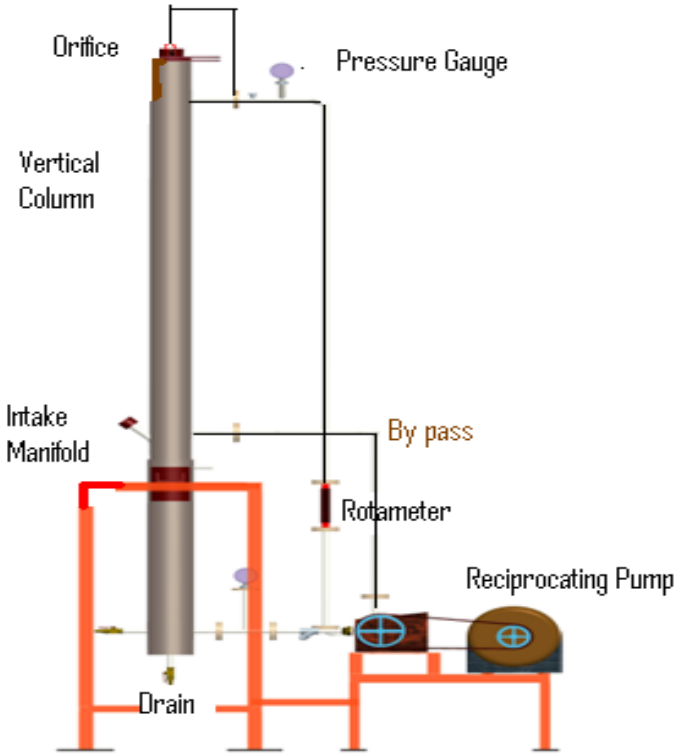

Figure 1: Schematic diagram of hydrodynamic cavitation system setup

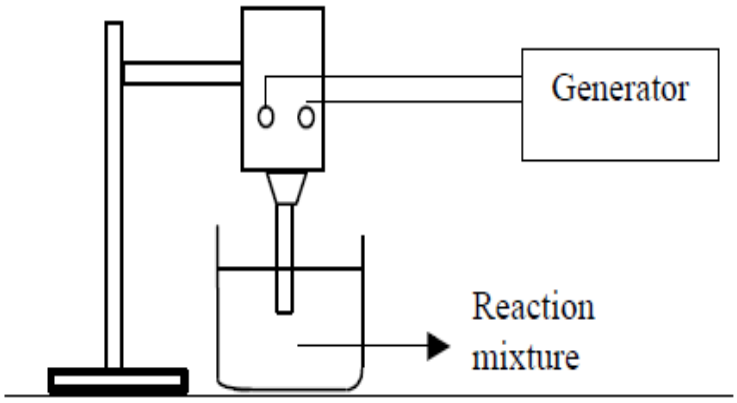

Figure 2: Schematic diagram of ultrasonic horn type reactor

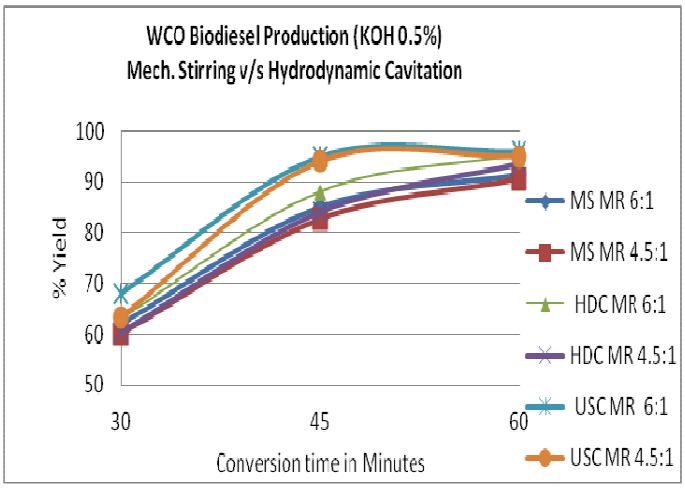

Figure 3: WCO Biodiesel production yield vs. time [KOH= 0.5%]

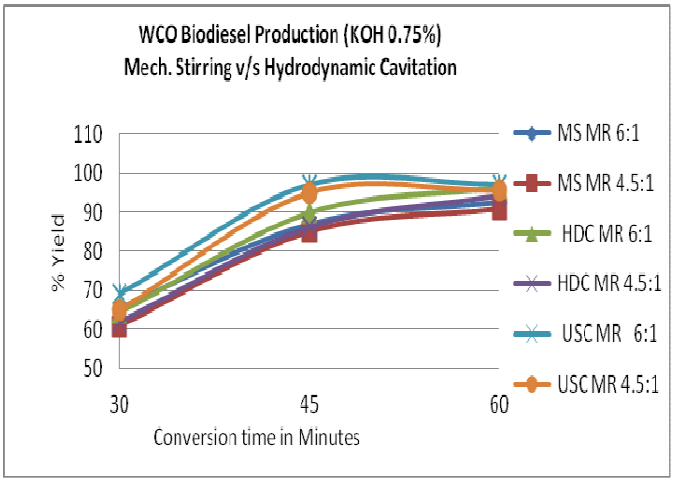

Figure 4: WCO Biodiesel production yield vs. time [KOH=0.75%]

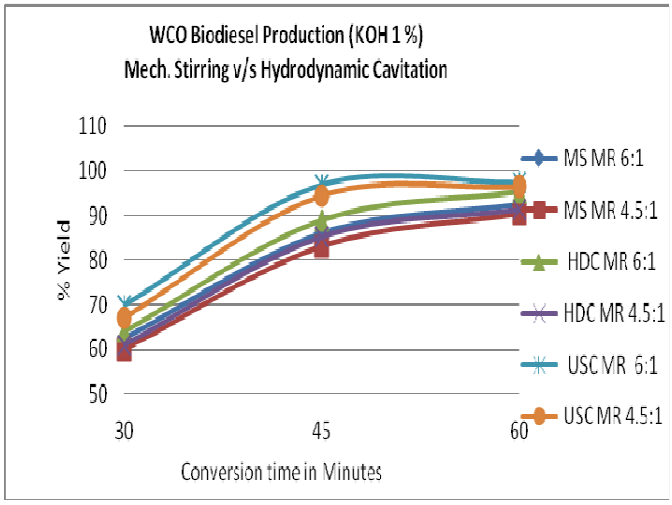

Figure 5: WCO Biodiesel production yield vs. time [KOH= 1%]

4. EXPERIMENTAL WORK ON PERFORMANCE AND EMISSION IN CI ENGINE

The biodiesel prepared from WCO is tested on a single cylinder, four strokes, constant speed (3.5 kW, 1500 RPM) Diesel engine which is equipped with eddy current type dynamometer for loading (test setup details are shown in Fig 6). Lab view based Engine performance Analysis software package "Engine soft LV" is used for on line performance evaluation. AVL 437C smoke meter is used for the smoke opacity measurement. Experiment has been performed by taking WCO biodiesel blends diesel in proportion of volume 20%, 40%, 60%, 80% and 100% respectively and following parameters has been obtained.

4.1 VARIATION OF BRAKE THERMAL EFFICIENCY WITH BRAKE POWER

Figure 7 shows the variation of BTE v/s brake power for WCO blends of B20, B40, B60, B80 and B100 respectively compared diesel. For all blends BTE increases increases power output. The gain in thermal efficiency as compared to diesel is due to presence of oxygen in biodiesel molecules and higher lubricity than diesel, which results in better combustion.

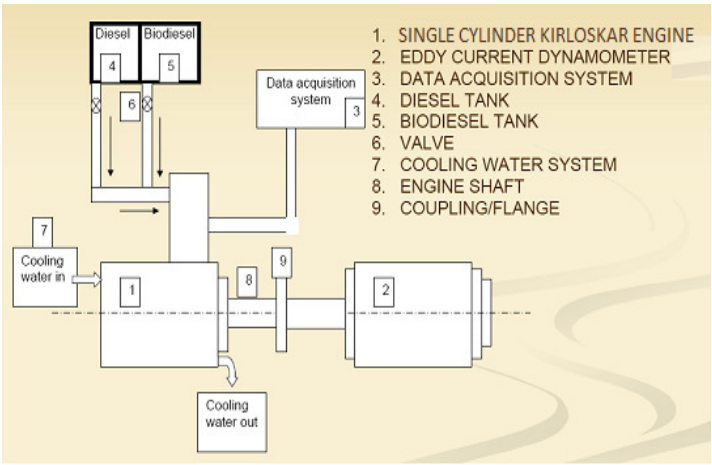

Figure 6: Experimental setup for performance and emission studies.

4.2 VARIATION OF BRAKE SPECIFIC FUEL CONSUMPTION WITH BRAKE POWER

BSFC v/s brake power are shown in Figure 7. The trend of WCO blends almost resembles with diesel for entire range of brake power. This is initially due to better combustion and later due to due to lower heating value of the biodiesel blend requires higher mass flow rate of blend to meet the engine loads. Increase of BSFC for WCO is less than 20% for 0.5 to 3.5 kWpower output range. BSFC remains almost constant for wide range of brake power (1-3.5 kW).

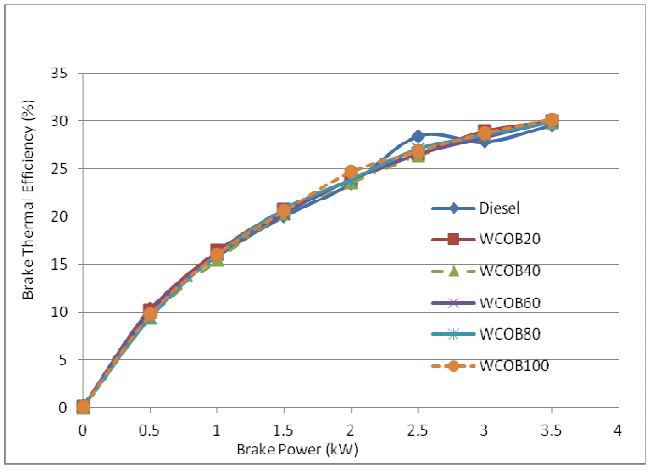

Figure 7: Variation of BTE v/s brake power for WCO biodiesel blends

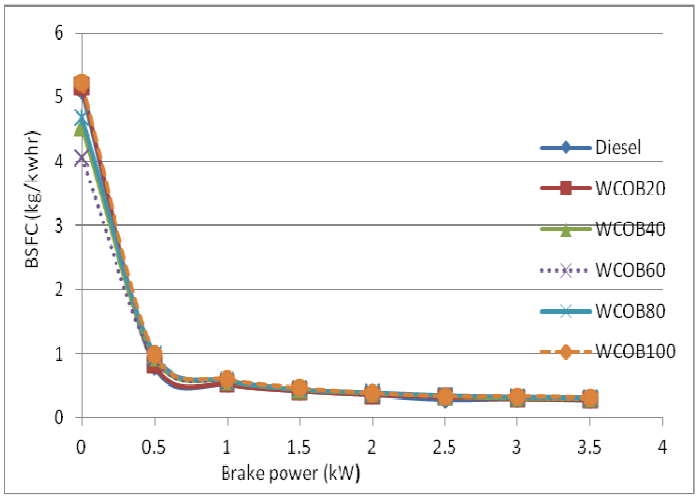

Figure 7: Variation of brake specific fuel consumption of WCO biodiesel blends

4.3 VARIATION OF BRAKE SPECIFIC ENERGY CONSUMPTION WITH BRAKE POWER

Figure 8 represents the variation of the brake specific energy consumption with brake power of WCO biodiesel blends of (B20, B40, B60, B80, B100) respectively and compared with diesel. Brake specific energy consumption (BSEC) is an ideal parameter for comparing engine performance of fuels having different calorific values. At idling the specific fuel energy consumption decreases for all blends of biodiesel. The specific energy consumption increases due to decrease in thermal efficiency and better combustion characteristics of WCO biodiesel.

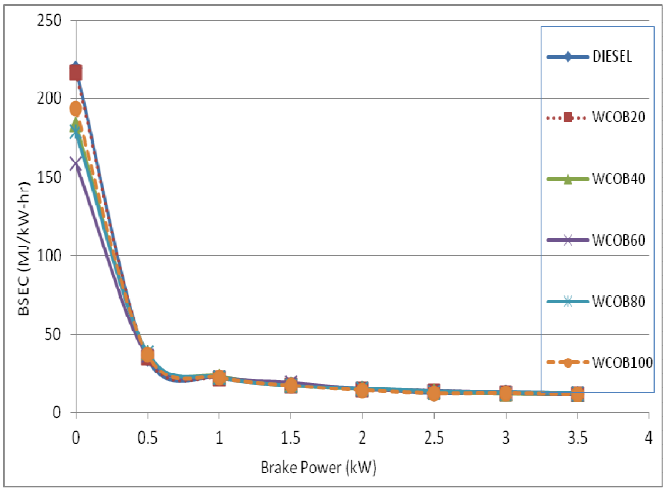

Figure 8: Variation of the brake specific energy consumption of WCO biodiesel blends

4.4 VARIATION OF EXHAUST GAS TEMPERATURE WITH BRAKE POWER

Figures 9 represents the variation of the exhaust gas temperature with brake power for different blends of WCO biodiesel compared with diesel. At all loads, diesel was found to have the highest temperature. The exhaust gas temperature increased with increase in load. It also initially marginally increases with blend % of biodiesel in the fuel but at higher blend % reduces. The exhaust gas temperature reflects on the status of combustion inside the combustion chamber. The reason for rise in the exhaust gas temperature may be due to ignition delay and increased quantity of fuel injected. The exhaust gas temperature can be reduced by adjusting the injection timing/injection pressure in to the diesel engine.

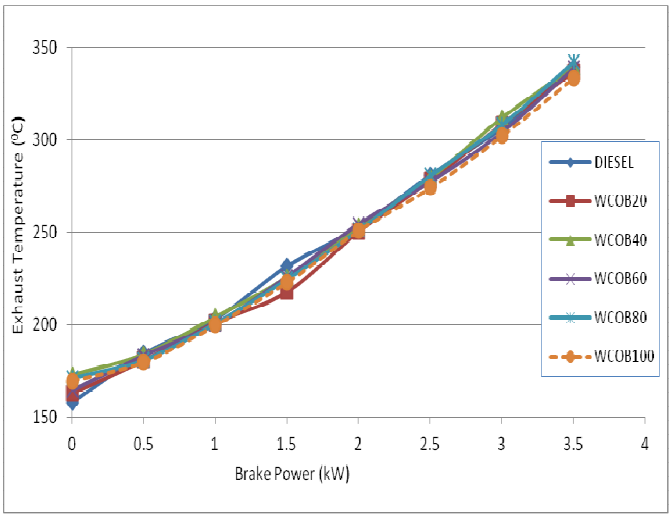

Figure : 9 Variation of exhaust gas temperature with WCO biodiesel blends

4.5 VARIATION OF A/F RATIO WITH BRAKE POWER

Figure 10 shows the variation of air fuel ratio versus brake power for WCO blends respectively. Air fuel ratio decreases with increases in brake power required of rich mixture at higher brake outputs. This is due to presence of oxygen in the biodiesel molecules. The maximum variation in the value of air fuel ratio is about -10% for various blends of WCO.

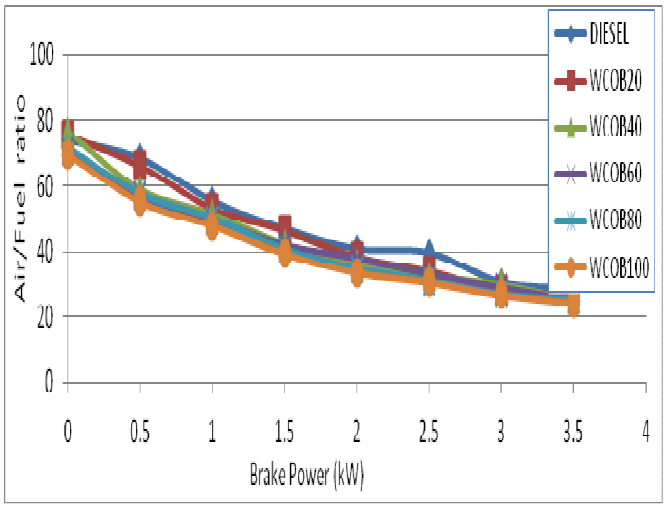

Figure 10: Variation of A/F ratio with WCO biodiesel blends with brake power

4.6 VARIATION OF SMOKE OPACITY WITH BRAKE POWER

Figures 11 represent the variation of the smoke opacity with brake power for different blends of WCO biodiesel to diesel. Smoke opacity is usually found to significantly decrease with biodiesel blends as compared to diesel. The smoke emissions were also sensitive to the oxygen content of the fuel and good combustion characteristics. Because of the heterogeneous nature of diesel combustion, fuel-air ratios, which affect smoke formation, tend to vary in the cylinder of a diesel engine. Smoke formation occurs primarily in the fuel-rich zone of the cylinder, at high temperatures and pressures. If the applied fuel is partially oxygenated, locally over-rich regions can be reduced and primary smoke formation can be limited. The % variation of smoke opacity has 40% reduction at wide range of loads.

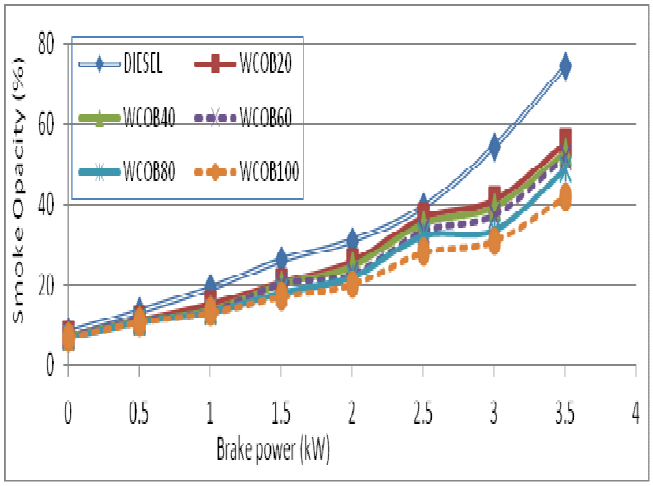

Figure 11: Variation of smoke opacity of WCO biodiesel blends with brake power

5. CONCLUSIONS

Hydrodynamic cavitation method is energy efficient, time saving and economically functional, offering a lot of advantages over the conventional mechanical stirring method. The relatively mild reaction conditions and high yield of methyl esters using this environmentally friendly method makes it viable for industry. All these methods have future potential for biodiesel production at industrial scale due to their easy scale up property. Experimental studies on performance and emissions prove that WCO biodiesel can be easily used through blending in existing diesel engines foe better combustion and greener exhaust emissions. Though for blends higher than 40% shall require long term test runs and analysis of its effect on various engine components.

6. REFERENCES

1. Hebbal, O. D., Reddy, V. K., Rajagopal, K, 2006. Performance characteristics of a diesel engine deccan hemp oil. Fuel 85, 2187–2194.
2. Srivastava, A., Prasad, R., 2000. Triglycerides based diesel fuels. Renew Sustain Energy Rev, 4, 111–133.
3. Agarwal, A. K., 2007. Biofuels (alcohols and biodiesel) applications as fuels for internal combustion engines. Progress in Energy and Combustion Science, 33, 233-271.
4. Murugesan, A., Umarani, C., Chinnusamy, T. R., Krishnan, M., Subramanian, R., Neduzchezhain, N., 2008. Production and analysis of bio-diesel from non-edible oils—A Review. Renewable and Sustainable Energy Reviews, 13(4), 825-834.
5. Wang, Y. D., Al-Shemmeri, T., Eames, P., McMullan, J., Hewit,t N., Huang, Y., 2006. An experimental investigation of the performance and gaseous exhaust emissions of a diesel engine using blends of a vegetable oil. Appl. Thermal Eng, 26, 1684–91.
6. Dmytryshyn, S. L, Dalai, A.K., Chaudhari, S. T., Mishra, H. K., Reaney, M. J., 2004. Synthesis and characterization of vegetable oil derived esters: evaluation for their diesel additive properties. Bioresource Technology. 92, 55–64.
7. Marchetti, J. M., Miguel, V. U., Errazu, A. F., 2005. Possible methods for biodiesel production. Renew Sustain Energy Rev., 11, 1300–1311.
8. *Achanai Buasri, Nattawut Chaiyut and Kowit Phongprasit, 2008. Production of biodiesel from waste cooking oil using mixed alcohol system. KMITL Sci. Vol. 8 No.2 (Section B) July- December 2008.*
9. Cigizoglu, K. B., Ozaktas, T., Karaosmanoglu, F., 1997. Used sunflower oil as an alternative fuel for diesel engines. Energy Sour, 19,559–566.
10. Kerschbaum, S., Rinke, G., 2004. Measurement of the temperature dependent viscosity of biodiesel fuels. Fuel, 83, 287–91.

11. Stavarache, C., Vinatoru, M., Nishimura, R., Maeda, Y., 2005. Fatty acids methyl esters from vegetable oil by means of ultrasound energy. Ultrason Sonochem, 12, 367–72.
12. Gerpen, J. V., 2005. Biodiesel processing and production. Fuel Processing Technology, 86, 1097–107.
13. Meher, L. C., Sagar, D. V., Naik, S. N., 2006. Technical aspects of biodiesel production by transesterification–a review. Renewable and Sustainable Energy Reviews, 10, 248-68.
14. Bouaid, A., Diaz, Y., Martinez, M., Aracil, J., 2005. Pilot plant studies of biodiesel production using Brassica carinata as raw material. Catalysis Today, 106, 193–6.
15. Saka, S., and Kusdiana, D., 2001. Biodiesel fuel form rapseed oil as prepared in supercritical methanol. Fuel, 80, 225-231.
16. Demirbas, A., 2000. Biodiesel from vegetable oils via transesterification in supercritical methanol. *Energy Conv Mgmt,,* 43, 2349–56.
17. Han, H., Cao, W., and Zhang, J., 2005. Preparation of biodiesel from soybean using supercritical methanol and CO_2 as co-solvent. Process Biochemistry, 40, 3148-3151.
18. Pal, A., Verma, A., Kachhwaha, S. S., Maji, S., 2010. Biodiesel production through hydrodynamic cavitation and performance testing. Renewable Energy, 35(3), 619–624.
19. Gogate, P. R., Pandit, A. B., 2005. A review and assessment of hydrodynamic cavitation as a technology for the future. Ultrasounds Sonochemistry, 12, 21–7.
20. Gogate, P. R., Tayal, R. K., Pandit, A. B., 2006. Cavitation: a technology on the horizon. Current Science, 91, 35–46.
21. Jianbing Ji, Jianli Wang, Yongchao Li, Yunliang Yu, Zhichao Xu, 2006. Preparation of biodiesel the help of ultrasound and hydrodynamic cavitation. Ultrasounds, 44, e411–e414.
22. Hoang Duc Hanh, Nguyen The Dong, Kenji Okitsu, Rokuro Nishimura, Yasuaki Maeda, 2009. Biodiesel production through transesterification of triolein various alcohols in an ultrasound field. Renewable Energy, 34, 766–768.
23. Stavarache, C., Vinatoru, M., Nishimura, R., Maeda, Y., 2005. Fatty acids methyl esters from vegetable oil by means of ultrasound energy. Ultrasound Sonochemistry, 12, 367–372.
24. Stavarache, C., Vinatoru, M., Maeda, Y., 2006. Aspects of ultrasoundally assisted transesterification of various Vegetable oils methanol. Ultrasounds Sonochemistry, 14(3), 380-386.
25. Hoang Duc Hanh, Nguyen The Dong, Kenji Okitsu, Yasuaki Maeda, and Rokuro Nishimura, 2007. Effect of Molar Ratio, Catalyst Concentration and temperature on transesterification of Triolein Ethanol under Ultrasound Irradiation. Journal of the Japan Petroleum Institute, 50(4), 195-199.
26. Hoang Duc Hanh, Nguyen The Dong, Kenji Okitsu, Rokuro Nishimura, Yasuaki Maeda, 2009. Biodiesel production by esterification of oleic acid short-chain alcohols under ultrasound irradiation condition. Renewable Energy, 34, 780–783.
27. Thanh, L. T., Okitsu, K., Sadanaga, Y., Takenaka, N., Maeda, Y., and Bandow, H., 2010. Ultasound assisted production of biodiesel fuel from vegetable oils in a small scale circulation process. Bioresource Technology, 101, 639-645.
28. Teixeira, L. S. G., Assis, J. C. R., Mendonca, D. R., Santaos, I. T. V., Guimaraes, P. R. B., Pontes, L. A. M., and Teixeira, J. S. R., 2009. Comparison between conventional and ultrasound preparation of beef tallow biodiesel. Fuel Processing Technology, 90, 1164-1166.

ISSN: 2319-5967
ISO 9001:2008 Certified
International Journal of Engineering Science and Innovative Technology (IJESIT)
Volume 3, Issue 3, May 2014

Decision Table based Model & implementation for Automatic prevention of Unauthorized Database Transactions by Trusted Database Users

Rohit Jain

Abstract*— Database security is one of the most important issues for any organization, especially for financial institutions such as banks. Protecting database from external threats is relatively easier and a number of effective security schemes are available in market. Existing security policies are inadequate to prevent the attacks from insiders (trusted users) and require human intervention in some form or other to detect unauthorized transactions.eg Oracle Vault. This paper addresses this issue and proposes an automated detection and prevention mechanism with minimal/nil human interaction. Each database (DB) user is authorized to do particular transactions by performing a sequence of queries. These queries perform operations (select, insert, update, delete) on various attributes of different tables in RDBMS. However the sequence of queries, attributes & tables authorized to User1 are not authorized to User2. User2 may be authorized to perform a different sequence and types of queries. If in a Database, User2 is able to deviate from its normal course of transaction queries and perform such a query for which it is not authorized then it is a serious breach in DB security. This paper proposes a Decision Table based methodology and a working model to protect DB from such security breaches and prevent trusted DB users from doing unauthorized Transactions. Our approach recommends creation of Decision tables with the help of TQLC (Transaction Queries Log Crawler), Authorized Query Indicator Arrays (AQIA), Transaction Query Sequence Analyzer Arrays (TQSAA); Query Weight Analysis and Quad Phase Verification Techniques. These decision tables automatically identify any malicious intent during Transaction initiated from a User thereby, suggesting and activating a particular action as specified in Decision Table. We have implemented this system model in Oracle-J2EE based environment. Our model is also equipped with the feature of "Customization in Implementation". During implementation, the Database owner has the choice to set the number of Verification phases to be used as per his wish. We will also allow the audience to generate arbitrary dummy transaction loads to measure the overall performance of our mechanism through graphical Dashboard.

***Index Terms*—Transaction Authorization, Decision Table, Transaction Queries Log Crawler (TQLC), Authorized Query Indicator Arrays (AQIA), Transaction Query Sequence Analyzer Arrays (TQSAA), Query Weight Analysis, Quad Phase Verifier**

I. INTRODUCTION

Data is an important asset for companies and organizations. Some of these data are worth lacs and crores. The organizations need to take great care at controlling access to such data, from the perspective of both internal users, within the organization, and external users, outside the organization. The organization reputation and client's beliefs lies with the confidentiality of these data. Thus, the development of Database Management Systems (DBMSs) with high-assurance security is always a hot & spicy research topic. Even though DBMSs provide access control mechanisms, these mechanisms alone are not enough to guarantee data security.

Each database (DB) user is authorized to do particular transactions by performing a sequence of queries. These queries perform operations (select, insert, update, delete) on various attributes of different tables in RDBMS. However the sequence of queries, attributes & tables authorized to User1 are not authorized to User2. User2 may be authorized to perform a different sequence and types of queries. For example, consider that a database user/application is authorized to access data related to HR tables and only non financial attributes of tables as EMPLOYEE_ID, FIRST_NAME, LAST_NAME, EMAIL, PHONE_NUMBER, HIRE_DATE, JOB_ID, etc. but suddenly that user/application submits a SQL command to the DBMS that accesses the records from the Finance Tables or access financial attributes as SALARY, LAST_PAY, GROSSPAY etc. of tables. Such anomalous access

ISSN: 2319-5967
ISO 9001:2008 Certified
International Journal of Engineering Science and Innovative Technology (IJESIT)
Volume 3, Issue 3, May 2014

pattern of the SQL command may be the result of an SQL Injection vulnerability or privilege abuse by an authorized user.

Even the database administrators (DBAs) be monitored, and responded to if deemed malicious. This is a difficult problem to address since the policies that specify a response action need to be created for the DBAs who are, in turn, responsible for managing the same policies. A Case study for the same is carried out for Oracle based applications databases of Indian Railways and the solutions adopted. *Oracle Vault* tool is used in which audit logs are maintained and administered by Oracle vault user and DBA roles are also performed by DBA user with the persuasion of one or more DBA users. Thus instead of one user, a combined persuasion of 2-3 users is required for access. But the fact is that there is no automated solution for catching an Unauthorized Transaction (UT) and responding to it with an Unauthorized Transaction Response (UTR) for Database security purposes.

Here, we have tried to propose an automated approach through Decision Tables created with the help of **TQLC(Transaction Queries Log Crawler), Authorized Query Indicator Array (AQIA), Transaction Query Sequence Analyzer Arrays(TQSAA), Query Weight Analysis Algorithm and Quad Phase Verification Techniques.**

II. RELATED WORK

In 2005 Marco and Henrique [1] proposed a Database Malicious Transaction Detector (DBMTD). DBMTD mechanism is a log based mechanism for the detection of malicious transactions in DBMS. The detection model proposed in [1] is used to detect the malicious transaction after the transaction has been committed. Lee et al.[2] propose an approach for detecting illegitimate database accesses by finger-printing every transaction, mainly by summarizing SQL statements into compact regular expression fingerprints. Mathew et al. [3] propose a data-centric approach for solving the AD problem in a DBMS. They model users' access patterns by profiling the used data points. [4] Signifies that Anomaly Detection mechanisms are essential to detect anomalies in data accesses by users. Such anomalies may be indicative of insider attacks or compromised database user accounts. [5,6] proposes a methodology for discovering user behavior from web log data. The concept of Log Data Usage has been derived from here. [7] Covers important aspects of Oracle based auditing; from basic configuration to advanced techniques which helped us in designing Log Crawler.[8] proposes a Role Based Access Control (RBAC) methodology which helps us in designing Parsing techniques for different arrays design.

To the best of our knowledge, no work demonstrating use of Decision Tables with the help of TQLC (Transaction Queries Log Crawler), Authorized Query Indicator Arrays (AQIA), Transaction Query Sequence Analyzer Arrays (TQSAA), Query Weight Analysis and Quad Phase Verification Techniques for prevention of UT and responding with UTR for DBMS exists

.

III. PROPOSED METHODOLOGY

Our methodology as shown in Fig 1 starts with the use of TQLC (Transaction Queries Log Crawler). TQLC is a utility (can be implemented using PL/SQL procedures or Java Code) which scans through the Database AUDIT logs and is responsible for creating valid User Transaction Profiles i.e. User Authorized Transactions. All available enterprise databases come bundled with some inbuilt audit mechanisms. Oracle database has certain Audit tables in System schema which keeps the track of executed queries for particular database users. TQLC collects last 6-10 transactions performed by a User and analyze the queries involved in those transactions. The authorized transactions will always have same set of queries in same sequence. TQLC looks for such transactions and declare them as Authorized Transactions (AT). Such ATs are identified user wise and an AT store is maintained. Each AT in AT store is taken one by one and each query of an AT is parsed in specific ways to generate AQIA and TQSAA. An example demonstrating the above discussed steps is presented for better understanding of concept. Suppose an Oracle RDBMS instance having an Employee centered schema with Relations (Tables) as EMPLOYEES, DEPARTMENTS, JOB_HISTORY, JOBS, etc. The trusted users for the Database are User1, User2 & User3. The Database Audit Tables are configured to store the Audit log records of all SELECT, INSERT, UPDATE and DELETE commands executed over any trusted user. TQLC reads the Audit Log Table records, recognize ATs and fill AT store. The sample Audit data for a user extracted from Audit log tables is shown as Table 1:

ISSN: 2319-5967
ISO 9001:2008 Certified
International Journal of Engineering Science and Innovative Technology (IJESIT)
Volume 3, Issue 3, May 2014

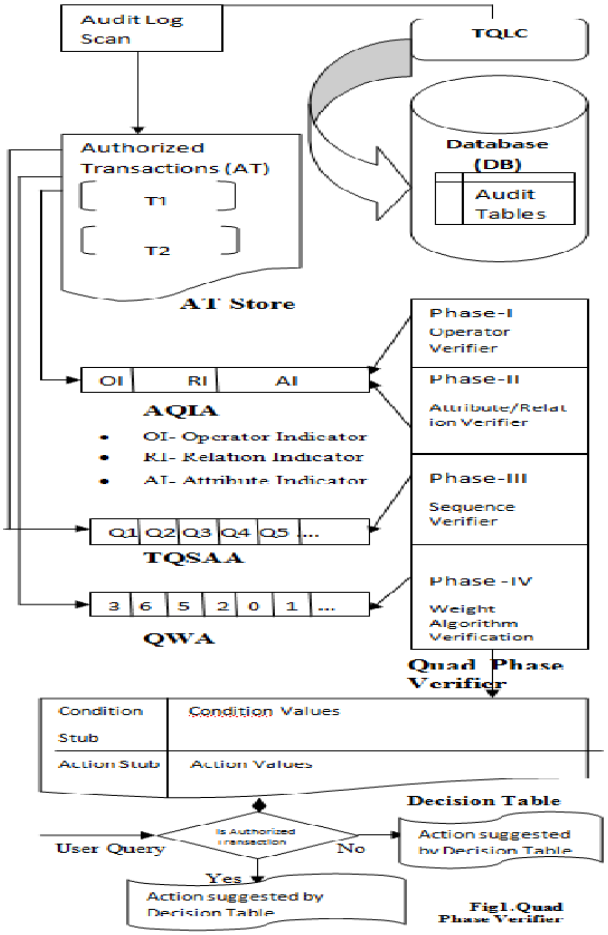

Fig1.Quad Phase Verifier

Operation	SQL Text	Object	User
SELECT	Select ……. From Employees	EMPLOYEES	User1
SELECT	Select ……. From JOB_History	JOB_HISTORY	User1
INSERT	Insert into JOB_History () values (….)	JOB_HISTORY	User1
INSERT	Insert into Employees () values (….)	EMPLOYEES	User1
SELECT	Select ……. From Employees	EMPLOYEES	User1
SELECT	Select ……. From Jobs	JOBS	User1

Table 1: Data from Audit Tables

The AT store entries populated with the help of above specified data extracted is shown as Table 2:

Operation	Referred Attributes	Objects	Query Serial in Transaction	User
SELECT	EmployeeID, FirstName, JobID…	Employees, Job	1	User1
SELECT	StartDate, JobID	JobHistory	2	User1
INSERT	Employee, Startdate…	JobHistory	3	User1

ISSN: 2319-5967
ISO 9001:2008 Certified
International Journal of Engineering Science and Innovative Technology (IJESIT)
Volume 3, Issue 3, May 2014

INSERT	EmployeeID, FirstName	Employees	4	User1
SELECT	EmployeeID, FirstName	Employees	5	User1
SELECT	JobID, JobTitle	Jobs	6	User1

Table 2: AT Store entries

Each entry in AT store for a Transaction is parsed to generate AQIA and TQSAA. AQIA (Authorized Query Indicator Array) is a two dimensional array representation of a Transaction. AQIA is an array of following arrays:-

1. OI (Operator Indicator)
2. RI (Relation Indicator)
3. AI (Attribute Indicator)

Suppose an AT taken from AT store consists of 6 queries in a particular sequence as shown in Table 2. The value of 2 dimensional array AQIA is shown in tabular form. Each AT store entry is represented in AQIA table e.g. First entry of AT store in Table 2 is:

Select -- EmployeeID, FirstName, JobID -- Employee, Job -- 1-- User1

The four DML (Data Manipulation Language) operators of SQL are – SELECT, INSERT, UPDATE, DELETE. For OI representation in AQIA table, these operators are symbolized as 0,1,2,3 respectively. Thus OI value for the sample query taken from AT is 0.

Suppose the total number of Relations (tables) in the schema is 4. The sample query taken uses two relations EMPLOYEES & JOBS. For RI representation, first of all a bit stream equal to total number of tables is initialized with value 0 as

0000

Now the bit values of those tables which are referred should be set ON. If EMPLOYEES & JOBS are the table numbers 2 and 4 in schema then bit representation now becomes

0101

Thus RI value for the sample query taken is 0101. The AI (Attribute Indicator) will indicate the attributes of relations referred in the query. In the sample query taken, there are two relations (tables) referred i.e. Employee (10 attributes) & Job (5 attributes). For AI representation, first of all a bit stream equal to total number of attributes in the table is initialized with value 0 as

0000000000 | 00000

Now the bit values of those attributes which are referred should be set ON. If EmployeeID, FirstName are the attribute number 1, 2 in EMPLOYEES table and JOB_ID is the attribute number 1 in Job table then bit representation now becomes

1100000000 | 10000

On applying the similar pattern to all the AT queries for one AT, the AQIA table obtained is shown as Table 3:-

OI	RI	AI
0	0101	1100000000|10000
0	0010	01010
1	0010	11000
1	0100	1100000000
0	0100	1100000000
0	0001	1100

Table 3: AQIA

Random Weights has already been defined for each operation type on each database schema table e.g. as shown in Table 4

Operation	Table	Weight
SELECT	EMPLOYEE	24
INSERT	EMPLOYEE	43
UPDATE	EMPLOYEE	54
DELETE	EMPLOYEE	20

Table 4: Weights Table

ISSN: 2319-5967
ISO 9001:2008 Certified
International Journal of Engineering Science and Innovative Technology (IJESIT)
Volume 3, Issue 3, May 2014

Each query in an AT is assigned a random weight during AT identification phase. After this phase each transaction can also be viewed as a strict sequence of weights.

TQSAA (Transaction Query Sequence Analyzer Array) stores the sequence of queries in ATs in the form of weights. Thus a TQSAA can look like

24	56	71	43	32	53

TQSAA

Where all numeric values are the weights of queries at serial number 1 to 6.
An algorithm has also been proposed based on query weights to keep a check over UTs and identify ATs. This algorithm is presented in next section.

Query Weight Analysis Algorithm

In this algorithm, there is a Hashed Query Weight Counter, Hash functions & Weighted Queries. Hashed Query Weight Counter is initialized with all zero bits. Each query in an AT has already been assigned a random weight during AT identification phase. A particular number of Hash functions are applied one by one to each query weight of AT. The corresponding hashed values are obtained and the obtained hashed value'th bit in Hashed Query Weight Counter is incremented. After applying all query weights, the counter reaches a particular value. This is called as Transaction Weight.
Suppose the counter is initialized as

0	0	0	0	0

The Hash functions used are:
H1(x) = x % 5
H2(x) = (2x + 5) % 5

The query weights for the selected queries in an AT taken above for example are
24, 56, 71, 43, 32, 53
Applying 24 to H1(x)→ 4
Applying 24 to H2(x)→ 3
Hence after applying first query weight (24), the counter value becomes

0	0	0	1	1

Applying 56 to H1(x)→ 1
Applying 56 to H2(x)→ 2
The counter value after applying second query weight (56) the counter value becomes

0	1	2	1	1

Applying 71 to H1(x)→ 1
Applying 71 to H2(x)→ 2
The counter value after applying second query weight (71) the counter value becomes

0	2	3	1	1

Applying 43 to H1(x)→ 3
Applying 43 to H2(x)→ 1
The counter value after applying second query weight (43) the counter value becomes

0	3	3	2	1

Applying 32 to H1(x)→ 2
Applying 32 to H2(x)→ 4
The counter value after applying second query weight (32) the counter value becomes

0	3	4	2	2

ISSN: 2319-5967
ISO 9001:2008 Certified
International Journal of Engineering Science and Innovative Technology (IJESIT)
Volume 3, Issue 3, May 2014

Applying 53 to H1(x)→ 3
Applying 53 to H2(x)→ 1
The counter value after applying second query weight (53) the counter value becomes

0	4	4	3	2

The number of hash functions & the number of bits in counter are kept at optimal level to achieve best output. Thus the transaction weight for AT-1 becomes as above.

IV. QUAD-PHASE VERIFIER

Quad-Phase Verifier is a vital component of the proposed model. This component is responsible for accepting the real time transaction from a trusted User, check the authorization of submitted transaction against the specified parameters and respond to it as mentioned in the Decision Tables.

An organization can design a Decision Table suitable to their policies & standards after discussions with Database owner, Security experts, Domain Analyzers, Technical experts, etc. This Decision Table will pave the way for Quad Phase Verifier usage and respond to UTs by suitable UTRs. A detailed description of Decision Tables will be covered in next section.

Quad-Phase Verifier, as the name suggests, comprises of four verification phases. These phases verify the submitted transaction by a user against the AT profile of that user and declare the transaction as UT or AT.

As mentioned in the Introduction section, our model is also equipped with the feature of "Customization in Implementation" i.e. during implementation of proposed model; an organization is not bound to use all the verification phases of Quad-Phase Verifier. The organizations can select to activate only those phases of Quad-Phase Verifier which they think are more suitable and worthy for their organizational needs. The Quad-Phase verifier will then suppress the unselected phases and continue to work on selected phases only.
The four phases of Quad-Phase Verifier are:-
1. Phase-I Operator Verifier
2. Phase-II Relations/Attributes Verifier
3. Phase-III Sequence Verifier
4. Phase-IV Weight Algorithm Verifier

Suppose a Trusted User submits a real time Transaction. Suppose the real time submitted transactions' query are

1. SELECT FIRST_NAME from EMPLOYEES;
2. INSERT into JOB_HISTORY values ('1750',sysdate,'J1');
3. UPDATE EMPLOYEES set PHONE_NUMBER='111111111';
4. SELECT EMPLOYEE_ID from JOB_HISTORY;
5. DELETE from EMPLOYEES where EMP_ID='001';
6. SELECT JOB_ID,JOB_TITLE from JOBS;

The queries from this transaction are parsed and needs to be verified to declare the transaction as AT/UT.

Phase-I

Phase-I is termed as the Operator Verifier phase. This phase verifies the submitted query in terms of Operators' correctness. This can be achieved by using the AQIA's OI array. For the example specified above, the OI array value for AT is

0
0
1
1
0
0

OI for AT

0
1
2
0
3
0

OI for Submitted Transaction

ISSN: 2319-5967
ISO 9001:2008 Certified
International Journal of Engineering Science and Innovative Technology (IJESIT)
Volume 3, Issue 3, May 2014

Now the OI array for the real time submitted transactions' query is also computed. Hence OI Array computed for this transaction is as shown in table 2. Thus OI array value for real time submitted transactions' query doesn't match with OI Array value of AT. Hence Phase-I will declare this submitted transaction as UT. However, if both OI arrays would have same values then it could have been declared as AT.

Phase-II

Phase-II is termed as the Relations/Attributes Verifier phase. This phase verifies the submitted query in terms of Relations' (Tables) & Attributes' correctness. This can be achieved by using the AQIA's RI & AI array. For the example specified above, the RI array & AI array values for AT are

RI
0101
0010
0010
0100
0100
0001

AI
1100000000|10000
01010
11000
1100000000
1100000000
1100

Now the RI & AI array for the real time submitted transactions' query is also computed Hence RI & AI Arrays computed for this transaction are

RI
0100
0010
0100
0010
0100
0001

AI
0100000000
11100
0000000001
1000000000
0000000000
1100

Thus RI & AI array value for real time submitted transactions' query doesn't match with RI & AI Array value of AT. Hence Phase-II will declare this submitted transaction as UT. However, if both RI & AI arrays would have same values then it could have been declared as AT.

Phase-III

Phase-III is termed as the Sequence Verifier phase. This phase verifies the submitted query in terms of Query Sequence correctness. This can be achieved by using the TQSAA array. For the example specified above, the TQSAA array value for AT is

24	56	71	43	32	53

Now the TQSAA array for the real time submitted transactions' query is also computed. Hence TQSAA Array value computed for this transaction is

12	29	25	43	31	53

Thus TQSAA array value for real time submitted transactions' query doesn't match with TQSAA Array value of AT. Hence Phase-III will declare this submitted transaction as UT. However, if both TQSAA arrays would have same values then it could have been declared as AT.

Phase-IV

Phase-IV is termed as the Weight Algorithm Verifier phase. This phase verifies the submitted query though a Query Weight based algorithm. This can be achieved by using the QWA array. For the example specified above, the QWA array values computed above for AT are

0	4	4	3	2

This is ultimately the hashed value representation of query weights. Now the Query Weight Analysis Algorithm is applied to the submitted transaction queries to declare a transaction as UT/AT.

QUERY_WEIGHT_ANALYSIS_ALGORITHM ***(ATWeight [], SubTWeight [], Hashfunctions [])***

1 Load ATWeight []

ISSN: 2319-5967
ISO 9001:2008 Certified
International Journal of Engineering Science and Innovative Technology (IJESIT)
Volume 3, Issue 3, May 2014

```
2  For 0 to SubTWeight.length
3   For 0 to Hashfunctions.length
4     hashedval <-Apply Hashfunction [index] to SubTWeight [index]
5     ATWeight [hashedval] = ATWeight [hashedval]-1
6   End For;
7  End For;
8  For 0 to ATWeight.length
9   IF ATweight [index]!=0
10    Declare Transaction is UT
11    Exit
13  ENDIF
14  Declare Transaction is AT
15  End For
16  End
```

Suppose the user enter correct sequence of commands then how QUERY_WEIGHT_ANALYSIS_ALGORITHM () algorithm with two hash functions will identify it is shown below.

ATWeight Loaded

0	4	4	3	2

Use 12: 0 0 1 0 1
AT Weight

0	4	3	3	1

Use 29: 0 0 0 1 1
AT Weight

0	4	3	2	0

Use 25: 2 0 0 0 0
AT Weight

-2	4	3	2	0

Use 43: 0 1 0 1 0
AT Weight

-2	3	3	1	0

Use 31: 0 1 1 0 0
AT Weight

-2	2	2	1	0

Use 53: 0 1 0 1 0
AT Weight

-2	1	2	0	0

At the end of Algorithm, if all the values of ATWeight array become zero, then it signifies that the submitted transaction is AT. But if, the ATWeight array is non zero, then the transaction is UT.

V. DECISION TABLE

A Decision table is basically a four quadrant structure

ISSN: 2319-5967
ISO 9001:2008 Certified
International Journal of Engineering Science and Innovative Technology (IJESIT)
Volume 3, Issue 3, May 2014

Conditions	Condition Alternatives
Actions	Action Entries

Each decision corresponds to a variable, relation or predicate whose possible values are listed among the condition alternatives. Each action is a procedure or operation to perform, and the entries specify whether (or in what order) the action is to be performed for the set of condition Many decision tables include in their condition alternatives the don't care symbol, a hyphen. Using don't cares can simplify decision tables, especially when a given condition has little influence on the actions to be performed alternatives the entry corresponds to. Decision Table works like an instructor in the proposed model. This Decision Table works like an Instruction Sheet to guide our model how to deal the real time submitted transaction queries.

As discussed above, the Quad-Phase Verifier consists of four phases that can be applied together, individually or in any combination to declare a submitted transaction as AT/UT. As mentioned in the Introduction section, our model is equipped with the feature of "Customization in Implementation" i.e. during implementation of proposed model; an organization is not bound to use all the verification phases of Quad-Phase Verifier. The organizations can select any combination of those phases of Quad-Phase Verifier which they think are more suitable and worthy for their organizational needs. The Quad-Phase verifier will then suppress the unselected phases and continue to work on selected phases only.

Our model proposes use of two decision tables-

1. **Decision Table 1** demonstrated as Fig2 indicates which array values to be computed for real time submitted transaction queries & compared with AT Arrays values based on the selected combination of phases of Quad-Phase verifier.
2. **Decision Table 2** demonstrated as Fig3 indicates what response to be generated (UTR or some other) based on the result of comparison of various array values of real time submitted transaction with AT arrays values.

The use of Decision tables is the basis of high performance of this model. In the absence of these decision tables, all the array values for real time submitted transaction queries would have been computed, and then according to the selected phases the required array values would be compared with AT array values and a customized message for different types of results to be generated as response by the system. All these activities would have been completed dynamically (at run time).

However, with the use of decision tables, first we have static guidance available that for a selected combination of phases, which array values to be computed and compared. Thus no need to compute all array values. Second, we have static guidance available that what response action to be taken for what phase and what comparison result. The use of static decision tables instead of Dynamic computation proves greatly time and cost effective in nature. Decision Tables 1 & 2 are shown on next page. Decision Table 1 has four conditions about selection of Verifier Phases. There are five actions specified in the table. Each combination of condition values (True or False) result in zero or more actions from the action list e.g. If condition values are FFFF i.e. no phase is selected then no action will be performed. If condition values are FTTT i.e. Phase I, II & III are selected and Phase IV not selected then action 1, 2, 3 & 4 will be performed and so on.

The output of Decision Table 1 is fed as input to the Decision Table 2. The output of Decision Table 1 will be a five bit value which indicates the Selected actions of Decision Table 1 e.g. If condition values for Decision Table 1 are FTTT i.e. Phase I, II & III are selected and Phase IV not selected then action 1, 2, 3 & 4 will be performed and the result obtained from Actions values will be like a bit stream as shown

* * * * -

This bit stream has first four bits as * and fifth bit as '-'. The '-'indicates "don't care" and the '*' indicates that this bit needs to be considered. This bit stream is the input to Decision Table 2.

Decision Table 2 has five conditions about selection of bits in the bit stream obtained from Decision Table 1. There are twelve actions specified in the table. Each combination of condition values (True or False) result in one or more actions from the action list e.g. If the bit stream obtained from decision table 1 is

---**

ISSN: 2319-5967
ISO 9001:2008 Certified
International Journal of Engineering Science and Innovative Technology (IJESIT)
Volume 3, Issue 3, May 2014

		Rules															
Conditions	Is Phase IV selected?	F	F	F	F	F	F	F	F	T	T	T	T	T	T	T	T
	Is Phase III selected?	F	F	F	F	T	T	T	T	F	F	F	F	T	T	T	T
	Is Phase II selected?	F	F	T	T	F	F	T	T	F	F	T	T	F	F	T	T
	Is Phase I selected?	F	T	F	T	F	T	F	T	F	T	F	T	F	T	F	T
Actions	Compute OI Array & Match with AT Store entry's OI Array		*		*		*		*		*		*		*		*
	Compute RI Array & Match with AT Store entry's RI Array			*	*			*	*			*	*			*	*
	Compute AI Array & Match with AT Store entry's AI Array			*	*			*	*			*	*			*	*
	Compute TQSAA Array & Match with AT Store entry's TQSAA Array					*	*	*	*					*	*	*	*
	Apply QWA Algorithm and Match final output array with zero.									*	*	*	*	*	*	*	*

Fig 2. Decision Table 1

		Rules															
		*----		-**--													*****
Conditions	Is Bit 1 selected?	T	F														T
	Is Bit 2 selected?			F	F	T	T										T
	Is Bit 3 selected?			F	T	F	T										T
	Is Bit 4 selected?																T
	Is Bit 5 selected?																T
Actions	Declare Transaction as AT	*					*										*
	Declare Transaction as UT		*	*	*	*											
	Declare OI phase as successful	*															*
	Declare OI phase as Failure		*														
	Declare AI phase as successful					*	*										*
	Declare AI phase as Failure			*	*												
	Declare RI phase as successful				*		*										*
	Declare RI phase as Failure			*		*											
	Declare TQSAA phase as successful																*
	Declare TQSAA phase as Failure																
	Declare QWA phase as successful																*
	Declare QWA phase as Failure																

Fig 3. Decision Table 2

It means bit 2 and 3 are * (to be considered) and bit 1, 4, 5 are – (don't care). Referring the Decision Table 2 for the bit stream mentioned, the values of * bit values are to be considered. Bit 2 and Bit 3 are * and there are four possible combinations of bit2 & bit 3 i.e. FF, FT, TF, TT. These are shown in Condition values of Decision Table 2 for bit stream -**--. Depending on the value of these bits, the particular actions from the Action list can be selected e.g. If the bit values are TT for bit stream -**--, then it means that RI & AI arrays have been matched perfectly for the Real time submitted transaction with that of AT, hence the action taken selected from the Action List of Decision Table 2 are

- Declare Transaction as AT
- Declare AI Phase as successful.
- Declare RI Phase as successful

Thus at the end of Decision Table 2, it can be stated whether Real time submitted transaction is AT/UT based on success of which phases verification.

ISSN: 2319-5967
ISO 9001:2008 Certified
International Journal of Engineering Science and Innovative Technology (IJESIT)
Volume 3, Issue 3, May 2014

VI. ORACLE-J2EE IMPLEMENTATION

We have implemented the proposed model using Oracle DBMS, integrated with a J2EE based application. During the implementation, our audience has been given the choice of selecting the Quad-Phase Verifier phases.

Auditing is a default feature of the Oracle RDBMS. Auditing is disabled by default, but can be enabled by setting the AUDIT_TRAIL static parameter.

The system table which keeps the Audit records is "DBA_AUDIT_TRAIL".
To enable auditing and direct audit records to the database audit trail, the commands executed are:

```
SQL> ALTER SYSTEM SET audit_trail=db SCOPE=SPFILE;

System altered.

SQL> SHUTDOWN
Database closed.
Database dismounted.
ORACLE instance shut down.
                                                SQL> STARTUP
ORACLE instance started.

Total System Global Area 289406976 bytes
Fixed Size                  1248600 bytes
Variable Size              71303848 bytes
Database Buffers          213909504 bytes
Redo Buffers                2945024 bytes
Database mounted.
Database opened.
SQL>
```

Suppose there are three users User1, User2, User3 created in Oracle. Now we need to Audit all DMLs (SELECT, INSERT, UPDATE, DELETE) executed by these users. To enable this, the commands executed are:

```
CONNECT sys/password AS SYSDBA

SQL> AUDIT SELECT TABLE, UPDATE TABLE, INSERT TABLE, DELETE TABLE BY User1 BY ACCESS;
SQL> AUDIT SELECT TABLE, UPDATE TABLE, INSERT TABLE, DELETE TABLE BY User2 BY ACCESS;
SQL> AUDIT SELECT TABLE, UPDATE TABLE, INSERT TABLE, DELETE TABLE BY User3 BY ACCESS;
```

Now all the DML activities performed by Users User1, User2 and User3 will be audited and recorded in table DBA_AUDIT_TRAIL.
TQLC (Transaction Query Log Crawler) utility is implemented using SQL queries executed through a JDBC connection from the J2EE Application. These queries perform a SELECT over DBA_AUDIT_TRAIL tables for the specified user and analyze them over different transaction ids.

```
CONNECT sys/password AS SYSDBA

SQL> SELECT OPERATIONTYPE, SQLTEXT, OBJECT, TRANSACTIONID FROM DBA_AUDIT_TRAIL WHERE USERNAME='USER1' ORDER BY
TRANSACTIONID;

SQL> SELECT OPERATIONTYPE, SQLTEXT, OBJECT, TRANSACTIONID FROM DBA_AUDIT_TRAIL WHERE USERNAME='USER2' ORDER BY
TRANSACTIONID;

SQL> SELECT OPERATIONTYPE, SQLTEXT, OBJECT, TRANSACTIONID FROM DBA_AUDIT_TRAIL WHERE USERNAME='USER3' ORDER BY
TRANSACTIONID;
```

AT store entries are created by the output analysis of these queries. For each AT store entry, the TQIA [OI, RI, AI] & TQSAA needs to be evaluated. OI array is computed by using `OPERATIONTYPE` attribute of AT store entry. For RI & AI, the total number of tables in the schema and total number of attributes in that table needs to be known. Following query is executed for this:

```
CONNECT sys/password AS SYSDBA

SQL> SELECT table_name FROM dba_tables where owner='USER1';

SQL> SELECT table_name FROM dba_tables where owner='USER2';

SQL> SELECT table name FROM dba tables where owner='USER3';

For each table_name obtained, the query executed is:
```

ISSN: 2319-5967
ISO 9001:2008 Certified
International Journal of Engineering Science and Innovative Technology (IJESIT)
Volume 3, Issue 3, May 2014

```
SQL> SELECT count (column_name) FROM USER_TAB_COLUMNS where TABLE_NAME=?
```

A database master table is created with records inserted for each operation type for each table in schema assigned with a random weight e.g.
SELECT EMPLOYEE 35
INSERT JOBS 54
Each AT store entry refers this table to create TQSAA array and QWA weights Array. The initial setup activities are completed now.
For evaluation of the proposed model and its implementation, a user specified number of random transactions is generated automatically through different combinations of Operators & Tables for different users. The user selects which phases of Quad-Phase verifier to be used. The decision table1 is referred accordingly and corresponding Arrays values are computed for each random generated transaction and matched with array values of AT computed during setup. The output of decision table 1 is referred to decision table 2 & final action is performed.

Decision tables are referred twice for each transaction. For optimal performance, Decision tables are made as Static Java Classes. These are loaded in memory once on start up and will be referred directly from there for every instance

VII. EXPERIMENTAL EVALUATION

The efficiency of our model can be characterized by following measures:

- **Decision Table Reference Time** (Time taken to refer decision table 1 + decision table 2 and generating final response) depicted in Fig 4.
- **False Negatives** (number of UTs identified as AT) depicted in Fig 5, 6, 7, 8
- **Coverage** (number of UTs detected * 100 / number of UTs submitted) depicted in Fig 9

For experimental evaluation, 1000 random dummy transactions are generated automatically and above mentioned parameters are calculated and a graphical comparison and evaluation is done.

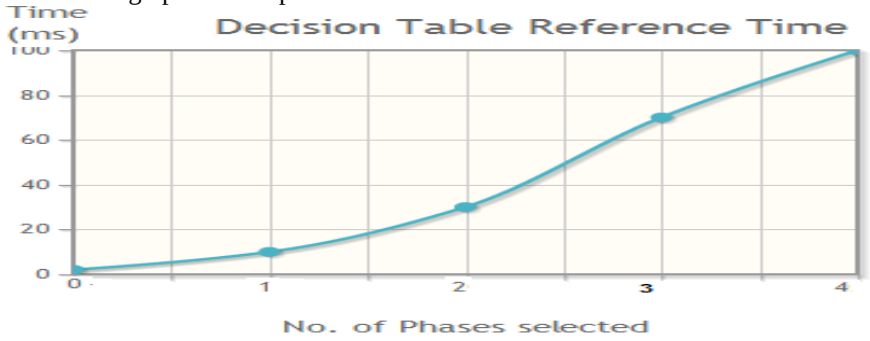

Fig 4 Decision Table Reference Time Vs No. of Phases

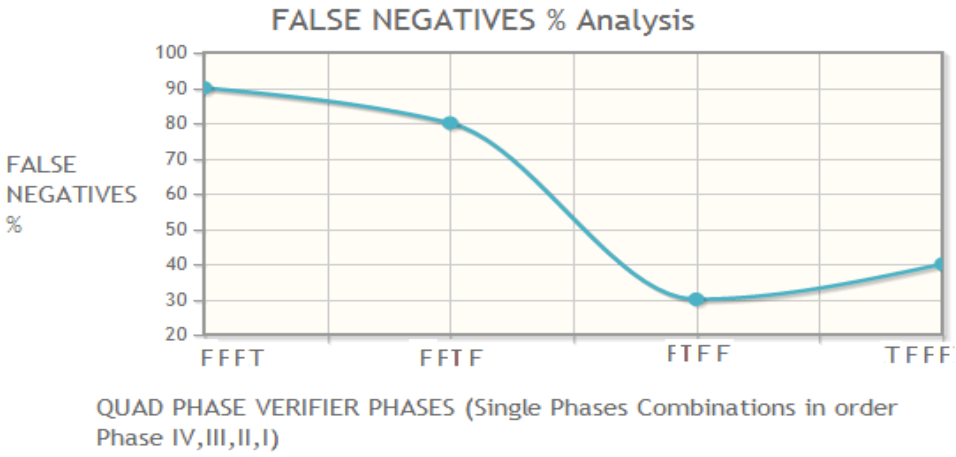

Fig 5 False Negatives % Vs Single Phases selection

ISSN: 2319-5967
ISO 9001:2008 Certified
International Journal of Engineering Science and Innovative Technology (IJESIT)
Volume 3, Issue 3, May 2014

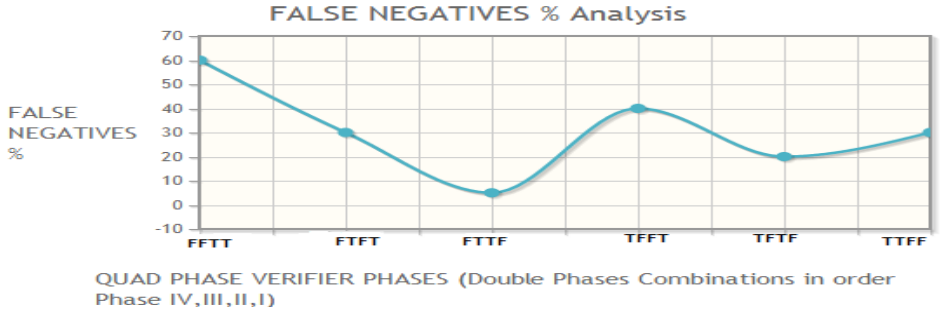

Fig 6 False Negatives % Vs Double Phases selection

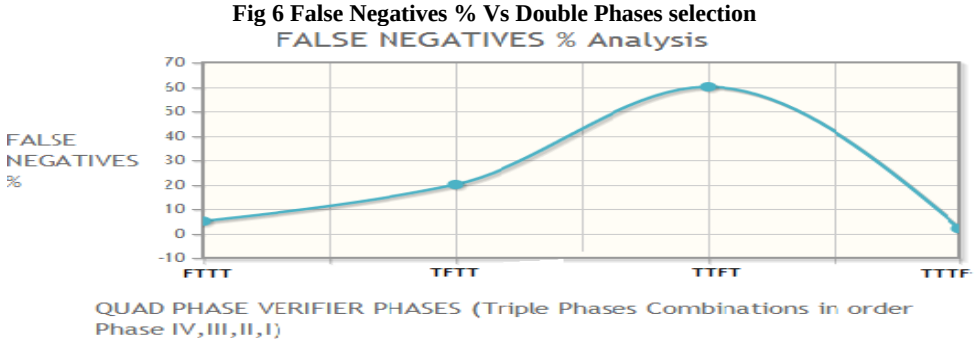

Fig 7 False Negatives % Vs Triple Phases selection

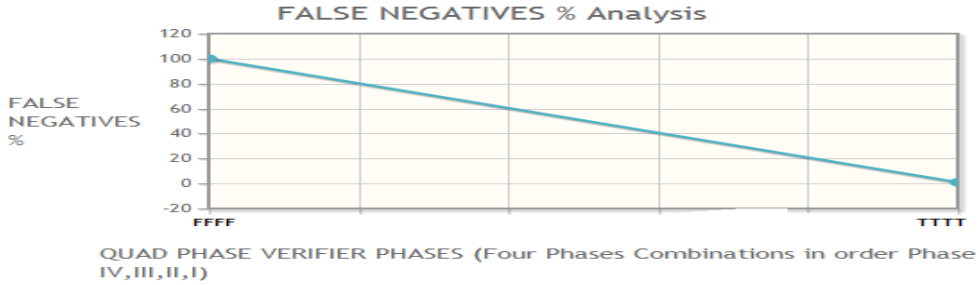

Fig 8 False Negatives % Vs Quad Phases selection

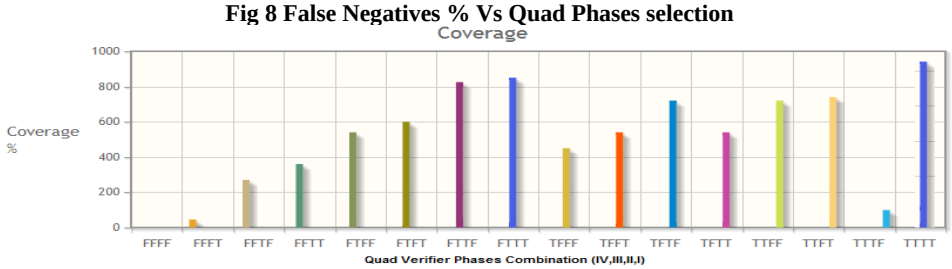

Fig 9 Coverage Vs Quad Phases phase selection

VIII. CONCLUSION & FUTURE WORK

In this paper, we have demonstrated the design and implementation of a Decision Table based model for automatic prevention of Unauthorized Database Transactions by trusted Database users. The model is implemented using J2EE & Oracle RDBMS. We have developed an application interface for the audience to interact and evaluate our system. Based on the experimental evaluation done in the previous section, it has been concluded that the Decision Table Reference Time is directly proportional to the number of phases. The results show that 99% of the UTs can be detected and responded if best combination of Quad Phase Verifier Phases is selected. Also the False Negatives (no. of UTs identified as ATs) can be kept close to 0.2% if all the four phases of Verifier are used. False Negatives can be kept between 3 to 8% by selected combinations of 2 to 3 phases also. Thus, organizations implementing the solution can implement with those combinations also thereby reducing the Decision Table Reference Time & computation involved. As future work, extension of this model to handle DDL statements is planned. Another

ISSN: 2319-5967
ISO 9001:2008 Certified
International Journal of Engineering Science and Innovative Technology (IJESIT)
Volume 3, Issue 3, May 2014

complementary area for future research is to enable this model for handling multiple joins, sub-queries, decode etc enable queries by assigning suitable weights for every component.

REFERENCES

[1] Marco Vieira and Henrique Madeira, "Detection of Malicious Transactions in DBMS", IEEE Proceedings- 11th Pacific Rim International Symposium on Dependable Computing, Dec 12-14, 2005.

[2] S. Y. Lee, W. L. Low, and P. Y. Wong. Learning fingerprints for a database intrusion detection system. In Proceedings of the 7th European Symposium on Research in Computer Security, ESORICS '02, pages 264–280, London, UK, UK, 2002. Springer-Verlag.

[3] S. Mathew, M. Petropoulos, H. Q. Ngo, and S. Upadhyaya. A data-centric approach to insider attack detection in database systems. In Proceedings of the 13th international conference on recent advances in intrusion detection, RAID'10, pages 382–401, Berlin, Heidelberg, 2010. Springer-Verlag.

[4] E. Bertino. Data Protection from Insider Threats. Synthesis Lectures on Data Management. Morgan & Claypool Publishers, 2012.

[5] Navin Kumar Tyagi and A.K. Solanki, "Prediction of Users Behavior through Correlation Rules", (IJACSA) International Journal of Advanced Computer Science and Applications, Vol. 2, No. 9, 2011.

[6] L.K.J. Grace, V. Maheshwari, D. Nagamalai "Analysis of web logs and web user in web mining" International journal of Network Security & its Applications (IJNSA), Vol.3, No1.January (2011).

[7] Mike Dean, "All about Oracle Auditing – A White Paper", February 2013.

[8] Ashish Kamra, Evimaria Terzi, Elisa Bertino, "Detecting anomalous access patterns in relational databases" The VLDB Journal Springer-Verlag 2007.

AUTHORS BIOGRAPHY

Rohit Jain is currently working as Project Engineer in CRIS (Centre for Railway Information Systems), New Delhi. He is also a final year M.Tech (Computer Science and Engineering) scholar in Delhi Technological University (formerly Delhi College of Engineering), New Delhi.

He has 9 years of Software industry experience. He is also a Sun Certified Java Programmer (SCJP). His areas of interest include Java, J2EE based Application Architecture Design, Relational Database Systems, Software Engineering & Data Structures

2014 Fourth International Conference on Communication Systems and Network Technologies

Dynamic Growth of Hidden-Layer Neurons Using the Non-extensive Entropy

Seba Susan and Mayank Dwivedi
Department of Information Technology,
Delhi Technological University, New Delhi, India
e-mail: seba_406@yahoo.in

Abstract—**In this paper we present a dynamic neural network that dynamically grows the number of the hidden-layer neurons based on an increase in the entropy of the weights during training. The weights are normalized to probability values prior to the computation of the entropy. The entropy being referred is the non-extensive entropy proposed recently by Susan and Hanmandlu for the representation of structured data. Incrementally growing the hidden layer as per requirement leads to better tuning of network weights and high classification performance as proved by the empirical results.**

Keywords— Hidden layer neurons; Dynamic Neural Network; Dynamic growth of neurons; Multi-layer perceptron; Susan and Hanmandlu entropy; Non-extensive entropy; Weighted sum of non-extensive entropies

I. INTRODUCTION

The advent of dynamic neural networks marks a significant advancement in the field of machine learning due to the manifold benefits it offers over the conventional neural network with a fixed architecture. The word dynamic refers to either dynamically changing the neural network architecture by adding or deleting neurons [1] or incorporating dynamic units [2]. The use of statistical probability theory for improvisation in the performance of neural networks has been investigated before [3-5]. The scope of using statistics in neural networks is due to the possibility of visualizing the neural network as a statistical model of non-linear regression and discriminant analysis. In [3] for instance the error entropy is minimized instead of the conventional mean square error for adaptive systems training. The Renyi entropy of order α and the Csiszar distance measure is used for the minimization. In [4] efficient training algorithms are devised using Information theoretic learning. The minimum error entropy was used recently in [5] for kernel adaptive filtering and a new kernel minimum error criterion algorithm was developed. The dynamic growth of hidden units and the pruning strategy has been sufficiently investigated in the case of the Radial Basis Function (RBF) neural network [6-9] but relatively less in the case of the feedforward Multi-layer Perceptron (MLP) due to the similarity in the hidden units in the MLP, though related research has picked up recently [10-12]. The growth or pruning of the number of hidden units is mostly decided by the weights emanating from the training process. In [10] the neurons are added and the weights are updated incrementally till the error is minimized. In [11] the neural network is likened to a linear regression model and the selection of optimal number of hidden units is based on the minimization of a risk estimation criterion. Dynamic fuzzy neural networks have also been proposed that perform the addition and deletion of RBF units as the learning progresses [13]. Our paper focuses on the dynamic growth of hidden units in the MLP neural network on a one by one basis as the training progresses, using the non-extensive entropy of weights as the yardstick for effecting a change. The paper is organized as follows: The significance of the hidden layer unit of a MLP neural network is described in brief in Section II. The Susan and Hanmandlu non-extensive entropy is described in Section III. The proposed dynamic growth of hidden layer neurons using the weighted sum of non-extensive entropies is described in Section IV. The empirical results are described in Section V and the overall conclusions are drawn in Section VI.

II. DETERMINING THE HIDDEN LAYER PARAMETERS OF A DYNAMIC NEURAL NETWORK

The feedforward neural network differs from the recurrent neural network in that there is no connection between the hidden units in a single layer. The first layer in a feedforward neural network is the input layer for feeding the inputs into the network, and the last layer is the output layer in which the overall output pertaining to the category or class is available. In between these two layers we have a number of internal or hidden layers each containing a number of hidden units or neurons. The main computing takes place in these layers. Associated with each hidden neuron is a set of weights that are the scales of the connections between the hidden layer neuron and the neurons in the input and output layers. These weights are significant since they are responsible for the fraction of the input that is fed into the activation function of the hidden neuron and thereby influences its output. The hidden layer units are significant due to their ability to interpret the data in a meaningful way. The internal or hidden layers remap the inputs to achieve a more linearly separable representation of the data and hence behave as "feature detectors" [14]. The choice of the number of hidden layers and the number of hidden neurons per layer is a topic of debate, with more the number the more accurate the result, at

978-1-4799-3070-8/14 $31.00 © 2014 IEEE
DOI 10.1109/CSNT.2014.104

IEEE computer society

a cost of increasing the training time and the network size. Usually the number of hidden neurons is kept lesser than the size of the training data for efficient results [10]. The single-hidden-layer-feedforward network (SLFN) that has several practical applications [15,16] and uses a random number of hidden nodes [17] was improvised by Huang *et al* in [18] to devise a three step learning method called the Extreme Learning Machine (ELM) that does not use back-propagation (BP) or other iterative techniques. Instead of tuning the hidden layer parameters as in traditional neural networks, the ELM generates the hidden layer parameters by calculating the output weights. In [10] the error minimized extreme learning machine (EM-ELM) is used for dynamically growing the hidden layer units in an ELM and updating the output weights simultaneously. In our paper we focus on the conventional SLFN architecture with random number of hidden neurons wherein the weights are first tuned iteratively by back-propagation and then evaluated for ambiguity or a state of chaos which implies an equal status for all connections. Since the entropy function is a measure of the chaos or uncertainty regarding an event, we use it to measure the state of chaos among the weights associated with the hidden layer in the neural network. We grow the hidden layer dynamically by incrementing the hidden neurons by one if the chaos among the weights increases after a training session. Since we desire a state of order or declining entropy as training progresses, we use the Susan and Hanmandlu non-extensive entropy to measure the chaos among the tuned weights, since it is proved successful for the representation of structured information in regular textures [19].

III. THE SUSAN AND HANMANDLU NON-EXTENSIVE ENTROPY

The Susan and Hanmandlu non-extensive entropy was proposed as a feature for texture identification and classification [19]. Its specialty lies in identifying regular textures containing repetitive patterns that translate to high co-occurrence probabilities. The non-extensive entropy function as defined by Susan and Hanmandlu is given below.

Consider a random variable $X=\{x_1,x_2,\ldots,x_n\}$ with the associated probabilities $P=\{p_1,p_2,\ldots p_n\}$. Assume that the probability distribution is complete i.e. $p_i \in [0,1]$ and $\sum_{i=1}^{n} p_i = 1$ for i=1,2,…n where, n is the number of probabilistic experiments.

Let the information gain on the ith event of X with an associated probability p_i be defined by the Gaussian function

$$I(p_i) = e^{-p_i^2} \tag{1}$$

The non-extensive entropy of X is then defined as

$$H(P) = E(I(p_i)) = \sum_{i=1}^{n} p_i I(p_i) = \sum_{i=1}^{n} p_i e^{-p_i^2} \tag{2}$$

The entropy in (2) is non-extensive due to its non-additive property which holds true under all conditions unlike Tsallis entropy [20] which is pseudo-additive and behaves like the extensive or additive Shannon entropy [21] under certain conditions. The normalized entropy H_N is of the form

$$H_N = \frac{H - H_{\min}}{H_{\max} - H_{\min}} \tag{3}$$

i.e.

$$H_N = \frac{H - e^{-1}}{e^{-\frac{1}{n^2}} - e^{-1}} \tag{4}$$

It is especially at an advantage when computing the entropy in a structured environment as opposed to Shannon entropy which serves best for finding the entropy in a chaotic environment, as proved in the fuzzy domain [22].

IV. DYNAMICAL GROWTH OF HIDDEN UNITS USING THE NON-EXTENSIVE ENTROPY OF NORMALIZED WEIGHTS

The weighted sum of non-extensive entropies over two consecutive frame pairs was used in [23] for the detection of video anomalies. The significance of this weighted sum is that any significant departure from the normal will result in a positive spike indicating an anomaly. In our work we compute over time the weighted sum of non-extensive entropies associated with the trained weights of a feedforward network, tuned by back-propagation. A positive spike or an increase in the weighted sum indicates an anomaly in training inputs and increments the number of hidden neurons by one. The weighted sum of non-extensive entropies, also called the entropy of the source $H(S)$ is defined as

$$H(S) = \sum_{x \in X} p(x) H(p(y|x)) \tag{5}$$

Solving for the entropy $H(p(y|x))$ using (2), we have

$$H(p(y|x)) = \sum_{y \in Y} p(y|x) e^{-p(y|x)^2} \tag{6}$$

Here $p(x)$ denotes the probability associated with the weight between the output neuron and the x^{th} hidden unit. The set $\{p(y|x)\}$ indicates the probabilities associated with the input connection weights of the x^{th} hidden unit, and $H(p(y|x))$ is the non-extensive entropy associated with $\{p(y|x)\}$ computed using (6).

The multi-layer perceptron architecture 4-3-1 with the actual weights associated with each layer is shown in Fig. 1. Let $w_{ki}^{\ t}$ denote the weight associated with the connection between the kth input dimension and the ith hidden layer neuron after the training of the tth training data sample. The computation of the entropy in (5) from the network weights $\{w_{ki}^{\ t}\}$ and $\{w_{ij}^{\ t}\}$ is explained below. The normalized weights $\{w_{kiN}^{\ t}\}$ are obtained from $\{w_{ki}^{\ t}\}$ by transforming the value of the weights $\{w_{ki}^{\ t}\}$ in the range of 0 to 1, and dividing by the total sum of weights as shown in (7) and (8).

$$w_{kip}^{\ t} = \frac{w_{ki}^{\ t} - \min_{\forall k}(w_{ki}^{\ t})}{\max_{\forall k}(w_{ki}^{\ t}) - \min_{\forall k}(w_{ki}^{\ t})}, \text{k=1,2,3,…,M} \tag{7}$$

$$w_{kiN}^{\ t} = \frac{w_{kip}^{\ t}}{\sum_{i=1}^{M} w_{kip}^{\ t}}, \text{k=1,2,3,…,M} \tag{8}$$

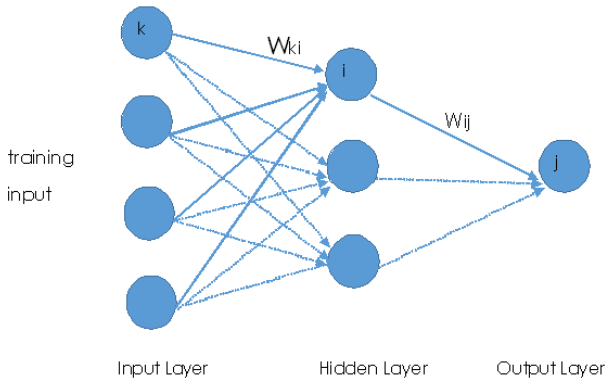

Fig. 1 The multi-layer perceptron (MLP) neural network and the connection weights during training

Here M is the number of connection weights between the input layer and the hidden neuron i. The normalized weights $\{w_{1iN}{}^t, w_{2iN}{}^t, ..., w_{MiN}{}^t\}$ are equal to probability values $\{p(y|x)\}$ for a given x, with values in the range of 0 to 1 and $\sum_{k=1}^{M} w_{kiN}{}^t = 1$. This probability distribution can be used for the computation of the entropy $H(p(y|x))$ using (6). The probabilities $\{p(x)\}$ associated with the H hidden neurons and the single output neuron $(j=1)$ are the normalized weights $\{w_{ijN}{}^t\}$ which are computed from $\{w_{ij}{}^t\}$ in a similar manner. The weighted sum of non-extensive entropies given by (5) is generalized for O equally significant outputs as

$$H(S) = \sum_{j=1}^{O} \frac{1}{O} \sum_{i=1}^{H} w_{ijN}{}^t \sum_{k=1}^{M} w_{kiN}{}^t e^{-w^2_{kiN}{}^t} \qquad (9)$$

In our example $O=1$. The entropy value computed using (9) for the t^{th} training sample is compared with the entropy value for the previous training data sample $t-1$. If a positive spike in entropy $H(S)$ is encountered, the number of hidden neurons is increased by one and the training proceeds for sample $t+1$. A single memory storage for the previous entropy value is only required for comparison purpose. The steps of the proposed method are summarized below.

1. Initialize the neural network architecture with 3 hidden neurons with all network weights initialized to 0.1.
2. Tune the weights for a training input using BP.
3. Calculate the probabilities of the tuned weights of each layer using (7) and (8).
4. Compute the weighted sum of non-extensive entropies of the tuned network using (9).
5. If this entropy value is greater than that for previous training sample then increment the number of hidden neurons by one, its weights being initialized to 0.1.
6. Repeat the training process for the next sample using the tuned weights of the existing neurons and the newly added neuron.
7. Repeat above steps 2-6 until the training is complete.

The highlight of our method is thus that a new computational unit is added whenever an unusual pattern occurs in the training. This trend was also observed before in the case of the Resource-allocating network in [24] which however requires memorizing of specific input patterns that perform poorly, in order to achieve desired accuracy.

V. EXPERIMENTAL RESULTS

The single hidden layer Multi-layer Perceptron 4-3-1 shown in Fig. 1 is used as the initial configuration for our experiments, with a learning rate η of 0.2 and an error threshold ε of 0.01. The number of hidden layer units is initialized to 3 at the beginning of the training procedure and is grown dynamically as explained in Section IV. The coding is done in the C++ platform on a 2.2 GHz Pentium processor. The experiments are conducted on a linearly separable synthetic dataset containing 100 data samples distributed into two classes shown in Fig. 2. The result of the dynamic growth of hidden neurons as training progresses is shown in Table 1 for both non-extensive and extensive entropy. As observed from the slow growth of hidden nodes in Table 1, when consecutive training patterns follow a similar pattern irrespective of the actual range of values, the non-extensive entropy of the weights decreases (or remains stable) indicating a decline in the chaos in the weights as some weights are assigned higher values than the others due to the higher significance of their connections. An unnatural training pattern is said to be encountered when it is different from its predecessors in its relationship between the features, training samples 9 and 34 in Table 1 being examples where feature 2 and 3 are closer than usual. The distinct training inputs are detected correctly by the non-extensive entropy (samples 4,9,34,36) while the Shannon entropy is highly sensitive and includes lots of false alarms (samples 2,5,7,18,33,35,39), for instance sample 2 is a normally occurring pattern in the dataset. This fact was also observed for the video anomaly example in [23] where Shannon entropy gives rise to false alarms due to random crowd movement. The results are summarized in Table 2 for the proposed dynamic neural network and the static neural network with fixed number of hidden neurons. We observe a slow and steady rise of the number of hidden neurons for the non-extensive entropy (hidden nodes=7), while Shannon entropy results in growth of 11 hidden neurons taking more training time than the non-extensive entropy. Apart from a reduced MLP architecture with only 7 hidden nodes, the overall training time required by the proposed method is much less than the equivalent fixed neuron architecture, while its classification performance (98.33%) is higher than any possible static neural network configuration. This suggests that the dynamic growth of hidden layer as proposed in our work not only gives the optimal number of hidden neurons for a dataset, at the same time it provides a better tuning of weights and faster training than any static neural network configuration.

VI. CONCLUSIONS

In this paper, the dynamical growth of hidden units is proposed that is based on the non-extensive entropy of the network weights that are normalized to probability values. A decrease in entropy of weights is observed as the training progresses and if this criterion is not met the number of hidden units is incrementally increased. The performance is improved as compared to the fixed architecture feedforward neural network in terms of convergence and testing accuracy. The highlight of our approach is that it can grow the hidden-layer dynamically while training and the weights are tuned better than any configuration of the static neural network leading to high classification performance.

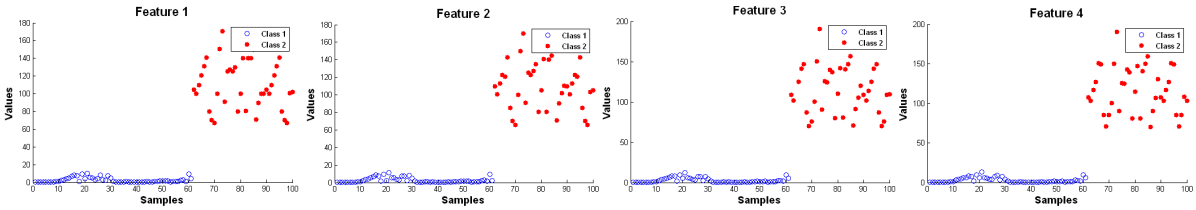

Fig. 2 The linearly separable four dimensional artificial dataset used for the experimentation

Table 1: Growth of hidden neurons dynamically using the proposed method for training set of 40 samples

Training input Sample number	Training Feature 1	Training Feature 2	Training Feature 3	Training Feature 4	Class	Growth of hidden neurons using the non-extensive Susan and Hanmandlu entropy	Growth of hidden neurons using the extensive Shannon entropy
1	0.01	0.02	0.03	0.04	1	3	3
2	0.4	0.5	0.6	0.7	1	3	**4**
3	0.10	0.11	0.12	0.13	1	3	4
4	**0.12**	**0.1**	**0.16**	**0.18**	1	**4**	4
5	0.35	0.25	0.45	0.55	1	4	**5**
6	0.55	0.40	0.56	0.65	1	4	5
7	0.05	0.06	0.07	0.08	1	4	**6**
8	0.61	0.63	0.67	0.69	1	4	6
9	**0.71**	**0.73**	**0.74**	**0.77**	1	**5**	6
10	0.94	0.91	0.93	0.95	1	5	**7**
11	2.3	2.5	2.57	2.9	1	5	7
12	3.1	3.25	3.7	3.9	1	5	7
13	4.3	4.5	4.7	4.9	1	5	7
14	5.1	5.4	5.6	5.9	1	5	7
15	6.7	6.9	6.4	6.45	1	5	7
16	8.0	8.5	8.3	8.4	1	5	7
17	7.5	7.7	7.9	7.2	1	5	7
18	1.2	1.3	1.5	1.7	1	5	**8**
19	9.2	9.3	9.5	9.7	1	5	8
20	3.9	2.4	5.4	5.9	1	5	8
21	10.0	11.1	12.2	13.3	1	5	8
22	5.2	5.5	5.7	5.9	1	5	8
23	5.1	5.3	5.4	5.7	1	5	8
24	3.2	3.4	3.6	3.8	1	5	8
25	3.9	3.1	3.5	3.7	1	5	8
26	7.9	7.4	7.2	7.5	1	5	8
27	3.2	7.7	7.5	9.2	1	5	8
28	2.3	2.5	2.7	2.9	1	5	8
29	7.3	7.9	7.7	7.5	1	5	8
30	4.7	4.55	4.3	4.1	1	5	8
31	1.2	1.9	1.59	1.7	1	5	8
32	104.5	109.6	108.7	107.8	2	5	8
33	100	101	102	103	2	5	**9**
34	**110**	**113**	**114**	**117**	2	**6**	9
35	121	123	125	127	2	6	**10**
36	**131**	**121**	**141**	**151**	2	**7**	10
37	141	143	147	149	2	7	10
38	80.1	85.11	87.2	84.9	2	7	10
39	70.0	70.2	70.3	70.7	2	7	**11**
40	67.2	65.5	75.5	85.0	2	7	11

Table 2: Performance analysis of the proposed dynamic neural network and various static neural network configurations, in terms of training time in secs (s), number of hidden nodes and the testing accuracy in (%). (Proposed method is shown in gray)

Methods	Dynamic growth of hidden neurons using Susan and Hanmandlu entropy	Dynamic growth of hidden neurons using Shannon entropy	Static 3 hidden neuron	Static 7 hidden neuron	Static 11 hidden neuron	Static 22 hidden neuron	Static 34 hidden neuron	Static 40 hidden neuron
Total training time (for 40 samples)	0.39s	0.78s	0.25s	0.51s	0.58s	0.6s	0.62s	0.62s
Number of hidden nodes	7	11	3	7	11	22	34	40
Testing Accuracy (for 60 samples)	98.33%	98.33%	83.4%	83.4%	93.4%	93.4%	83.4%	83.4%

REFERENCES

[1] Yang, Hong, and Jun Ni. "Dynamic neural network modeling for nonlinear, nonstationary machine tool thermally induced error." *International Journal of Machine Tools and Manufacture* 45.4 (2005): 455-465.

[2] Gupta, Madan M., Liang Jin, and Noriyasu Homma. *Static and dynamic neural networks: from fundamentals to advanced theory*. Wiley-IEEE Press, 2004.

[3] Erdogmus, Deniz, and Jose C. Principe. "An error-entropy minimization algorithm for supervised training of nonlinear adaptive systems." *Signal Processing, IEEE Transactions on* 50.7 (2002): 1780-1786.

[4] Ben-David, Arie. "Monotonicity maintenance in information-theoretic machine learning algorithms." *Machine Learning* 19.1 (1995): 29-43.

[5] Morejon, Rodney A., and Jose C. Principe. "Advanced search algorithms for information-theoretic learning with kernel-based estimators." *Neural Networks, IEEE Transactions on* 15.4 (2004): 874-884.

[6] Ciabattoni, Lucio, et al. "Supervisory control of PV-battery systems by online tuned neural networks." *Mechatronics (ICM), 2013 IEEE International Conference on*. IEEE, 2013.

[7] Yingwei, Lu, Narashiman Sundararajan, and Paramasivan Saratchandran. "Performance evaluation of a sequential minimal radial basis function (RBF) neural network learning algorithm." *Neural Networks, IEEE Transactions on* 9.2 (1998): 308-318.

[8] Huang, Guang-Bin, Paramasivan Saratchandran, and Narasimhan Sundararajan. "An efficient sequential learning algorithm for growing and pruning RBF (GAP-RBF) networks." *Systems, Man, and Cybernetics, Part B: Cybernetics, IEEE Transactions on* 34.6 (2004): 2284-2292.

[9] Wu, Shiqian, and Meng Joo Er. "Dynamic fuzzy neural networks-a novel approach to function approximation." *Systems, Man, and Cybernetics, Part B: Cybernetics, IEEE Transactions on* 30.2 (2000): 358-364.

[10] Feng, Guorui, et al. "Error minimized extreme learning machine with growth of hidden nodes and incremental learning." *Neural Networks, IEEE Transactions on* 20.8 (2009): 1352-1357.

[11] Lan, Yuan, Yeng Chai Soh, and Guang-Bin Huang. "Constructive hidden nodes selection of extreme learning machine for regression." *Neurocomputing* 73.16 (2010): 3191-3199.

[12] Kurino, Ryusuke, Masanori Sugisaka, and Katsunari Shibata. "Growing neural network with hidden neurons." *Proc. 9th Int. Symp. on Artificial Lifeand Robotics (AROB'04)*. Vol. 1. 2004.

[13] Wu, Shiqian, and Meng Joo Er. "Dynamic fuzzy neural networks-a novel approach to function approximation." *Systems, Man, and Cybernetics, Part B: Cybernetics, IEEE Transactions on* 30.2 (2000): 358-364.

[14] Robert J.Schalkoff, **Artificial Neural Networks**, McGraw-Hill, 2011.

[15] Singh, Rampal, and S. Balasundaram. "Application of extreme learning machine method for time series analysis." *International Journal of Intelligent Technology* 2.4 (2007): 256-262.

[16] Huynh, Hieu Trung, Jung-Ja Kim, and Yonggwan Won. "Performance comparison of SLFN training algorithms for DNA microarray classification." *Software Tools and Algorithms for Biological Systems*. Springer New York, 2011. 135-143.

[17] Huang, Guang-Bin, Lei Chen, and Chee-Kheong Siew. "Universal approximation using incremental constructive feedforward networks with random hidden nodes." *Neural Networks, IEEE Transactions on* 17.4 (2006): 879-892.

[18] Huang, Guang-Bin, Lei Chen, and Chee-Kheong Siew. "Universal approximation using incremental constructive feedforward networks with random hidden nodes." *Neural Networks, IEEE Transactions on* 17.4 (2006): 879-892.

[19] Seba Susan, Madasu Hanmandlu, "A Non-Extensive entropy feature and its application to texture classification", *Neurocomputing,* Volume 120, November 2013, pp. 214–225.

[20] Tsallis, Constantino. "Possible generalization of Boltzmann-Gibbs statistics." *Journal of statistical physics* 52.1-2 (1988): 479-487.

[21] C.E.Shannon, "A Mathematical theory of communication", *The Bell system Technical Journal*, Vol.27, pp.379-423 July,1948.

[22] Seba Susan, Madasu Hanmandlu," A novel Fuzzy Entropy based on the Non-Extensive Entropy and its application for feature selection"*, FUZZ-IEEE 2013*

[23] Susan, Seba, and Madasu Hanmandlu. "Unsupervised detection of nonlinearity in motion using weighted average of non-extensive entropies." *Signal, Image and Video Processing* (2013): 1-15.

[24] Platt, John. "A resource-allocating network for function interpolation." *Neural computation* 3.2 (1991): 213-225.

Full Paper Wiley Online Library ELECTROANALYSIS

DOI: 10.1002/elan.201400050

Electroactive Prussian Blue Encapsulated Iron Oxide Nanostructures for Mediator-Free Cholesterol Estimation

Rachna Sharma,[a, b] R. K. Sinha,[b] and Ved Varun Agrawal*[a]

Abstract: Iron oxide nanoparticles of size ~10 nm have been encapsulated into four nanometer thick shells of Prussian blue and were then electrophoretically deposited onto an indium tin oxide substrate. The immobilization of cholesterol oxidase has been done onto the nanostructured film to investigate the kinetic parameters and biosensing characteristics. The fabricated bioelectrode exhibits an electron transfer coefficient and a charge transfer rate constant of 0.45 and 45.15 s^{-1}, respectively. Direct electron transfer properties of the nanostructured film result in 3rd generation cholesterol biosensor. The bioelectrode exhibits high sensitivity (2.15 $mAM^{-1}cm^{-2}$), a low K_m^{app} value (0.07 mM), good stability and high selectivity towards cholesterol.

Keywords: Iron oxide · Prussian blue · Kinetic analysis · Direct electron transfer · Cholesterol biosensor

1 Introduction

Nanotechnology has recently become one of the most exciting forefronts in analytical chemistry. For realization of direct electron transfer at the biointerface, novel nanostructured redox materials are recently being employed for fabrication of electrochemical enzymatic biosensors [1,2]. Exploitation of nanostructured iron oxide for the fabrication of biosensors has recently gained momentum owing to its non-toxicity, biocompatibility and stability in physiological conditions [3]. The use of magnetic nanoparticles for biomedical applications offers a number of additional advantages such as transport of the bioassembly to a specific location onto the transducer surface. In addition, they can be retained and removed with a magnet without affecting the transducer surface, thus creating possibilities for regeneration and their reuse [4]. However, the inclination of Fe_3O_4 NPs towards oxidation and agglomeration limits its applications. Encasing Fe_3O_4 colloids in a shell of different material may prevent oxidation and agglomeration of Fe_3O_4 NPs [5]. In particular, capping of Fe_3O_4 NPs with Prussian blue (PB), an electroactive material, can prevent oxidation and agglomeration of NPs alongwith enhancing their electrochemical activity. Prussian blue is a prototype of metal hexacyanoferrates with well-known electrochromic, electrochemical, photophysical, and magnetic properties and potential analytical applications [6]. Due to its excellent electrocatalysis and its analogy with peroxidase enzymes, PB has been widely used as an electron-transfer mediator in the amperometric biosensors [7]. Several hydrogen peroxide sensors and enzymatic biosensors have been fabricated using bulk form of PB and its composites [8,9]. However, very few reports on the utilization of nanosized PB for application in biosensors are available. Zhang et al. have reported the fabrication of glucose biosensor based on direct assembly of PB modified electrode with the Ionic Liquid-Chitosan matrix assisted glucose oxidase immobilization [10]. Zhu et al. have reported the fabrication of amperometric glucose biosensor using nanosized PB-carbon nanotubes composite and excellent biosensing characteristics were obtained due to improved electrocatalytic activity towards the reduction of hydrogen peroxide [11]. Thus, encapsulation of PB onto Fe_3O_4 NPs may prove significant for the fabrication of an electrochemical biosensor which enroutes direct electron transfer across the interface due to its extraordinary electrocatalytic activity.

Electrical communication of redox enzymes to the electrode has been a subject of extensive research and an essential prerequisite for the development of effective electrochemical biosensors [12,13]. Direct exchange of electrons from enzymes to the electrode is prohibited due to the insulating protein barrier which surrounds the redox centers of enzyme molecules. This limits the performance of a biosensor [14]. Diffusional redox mediators, the tethering of redox relay units to the enzymes, incorporation of enzymes into redox polymers and redox hydrogels are the common practices to establish electrical contact between redox group of enzymes with the electrode and shuttle electrons from the enzymes [15,16]. The incorporation of NPs with coating of redox active material with appropriate dimensions and functionalization onto the electrode surface can act as a current collector and an electron relay to the immobilized enzyme [17]. This

[a] R. Sharma, V. V. Agrawal
Biomedical Instrumentation Section, National Physical Laboratory
New Delhi – 110012
phone: +91-11-45609489
*e-mail: ved.varun@gmail.com

[b] R. Sharma, R. K. Sinha
Department of Applied Physics, Delhi Technological University
New Delhi – 110042

Supporting information for this article is available on the WWW under http://dx.doi.org/10.1002/elan.201400050.

 © 2014 Wiley-VCH Verlag GmbH & Co. KGaA, Weinheim

shortens the electron transfer distance and establishes an electronic pathway for efficient electron transfer.

For biosensing application, a precise control over the spatial arrangement and distribution of the NPs onto the substrate is of utmost importance [18]. Among the various techniques, electrophoretic deposition provides tunable control over the degree of deposition of the charged colloidal particles onto an electrode surface under the influence of an applied electric field. It offers rapid deposition of desired materials and their composites with a simple laboratory setup and uniform films can be obtained by optimizing parameters such as solution concentration, applied potential, pH etc. [19]. The utilization of the orderly arranged PB-Fe_3O_4 NPs on the ITO electrode for the immobilization of the enzyme molecules may result in improved biosensing performance due to the facilitation of direct electron transfer from redox centers of biomolecules to the electrode.

In this paper, we report the formation of PB shell onto the Fe_3O_4 NPs. We have investigated the electrocatalytic properties of the PB-modified Fe_3O_4 NPs which have been utilized for the development of cholesterol biosensor. Kinetic parameters and biosensing characteristics of the ChOx/PB-Fe_3O_4 NPs/ITO bioelectrode have been investigated using cyclic voltammetry in the absence of any artificial redox mediator. The excellent sensitivity, low value of K_m^{app} and high charge transfer rate constant (k_s) have been observed for the bioelectrode due to facile and direct electron transfer properties of PB-Fe_3O_4 NPs.

2 Experimental

2.1 Materials and Methods

Ferrous chloride ($FeCl_2$), ferric chloride ($FeCl_3$), sodium hydroxide (NaOH), 1-Ethyl-3-(3-dimethylaminopropyl)-carbodiimide, *N*-hydroxysuccinimide, triton X-100, tween-20, potassium ferricyanide ($K_3[Fe(CN)_6]$), cholesterol and cholesterol oxidase (specific activity, 26 Umg^{-1}) have been purchased from Sigma-Aldrich. All reagents were of analytical grade and used without further purification. De-ionized water (Milli Q 10 TS) with resistivity $>18.2\,M\Omega\,cm$ has been used for preparing all aqueous solutions. The stock solution of cholesterol has been prepared in 10% triton X-100 and stored at 4 °C.

High resolution transmission electron microscopy (HR-TEM) and scanning electron microscopy (SEM) studies were carried out using Tecnaii-G2F30 STWIN and FEI Nova 600 microscopes, respectively. The optical absorption studies were conducted on Perkin Elmer Lambda 950 UV/Vis/NIR spectrophotometer. Fourier transform infrared (FT-IR) studies in the infrared region were carried out on Perkin Elmer, Spectrum BX II spectrophotometer. X-ray diffraction patterns were recorded on XRD Rigaku with Cu-Kα radiations ($\lambda = 1.5406$ Å). Electrochemical experiments were conducted on Autolab PGSTAT 302N System (Ecochemie, The Netherlands) in three electrodes system with platinum as auxiliary, Ag/AgCl as reference and ITO substrate as working electrode.

2.2 Synthesis of Prussian Blue Encapsulated Fe_3O_4 NPs

The Fe_3O_4 NPs have been prepared via hydrolytic reaction based on chemical co-precipitation of metal salts with an alkali as reported earlier [5]. Briefly, 0.32 M $FeCl_2$ and 0.64 M $FeCl_3$ were added to 2 mL of deoxygenated water (containing 12.1 N HCl) with continuous stirring at 30 °C. Solution containing iron salts was dropwise added to 20 mL of NaOH solution (1.5 M) with vigorous stirring at 30 °C. Mixture was then stirred for additional 30 min resulting in appearance of a black precipitate. The particles were washed by centrifugation at 3500 rpm for 30 min and supernatant was removed by decantation.

To encapsulate Fe_3O_4 NPs with PB, 1 mmol of $K_3[Fe(CN)_6]$ and 0.5 mmol of citric acid was mixed with 30 ml of Fe_3O_4 NPs solution (0.5 $mg\,mL^{-1}$) while stirring for 30 min. Solution containing 1 mmol of $FeCl_2$ and 0.5 mmol of citric acid was then dropwise added to the mixture. The resultant mixture was stirred for additional 30 min. Immediate appearance of blue color indicated the formation of PB-Fe_3O_4 NPs [20]. Citrate ions induced carboxyl groups at the surface of NPs which were utilized for covalent attachment of ChOx molecules.

The synthesized Fe_3O_4 NPs carry positive charge in 0.1 M HCl solution (zeta potential ~38.5 mV) [Figure S1; Supporting Information]. Addition of $K_3[Fe(CN)_6]$ (zeta potential ~−27.3 mV) results in the electrostatic adsorption of $[Fe(CN)_6]^{3-}$ ions onto the positive surface of Fe_3O_4 NPs. Also, CN^- ions can form complex with Fe^{3+} ions onto the surface of NPs resulting in adsorption of $[Fe(CN)_6]^{3-}$. Further, addition of Fe^{2+} ions into the solution result in the formation of PB shell on the surface of Fe_3O_4 NPs [21]. The pH of the suspension was recorded as 2.0.

2.3 Electrophoretic Deposition of PB Encapsulated Fe_3O_4 NPs

The nanocrystalline films of PB encapsulated Fe_3O_4 NPs have been obtained using two-electrodes system with platinum plate as auxiliary electrode and ITO substrate as the deposition electrode. The PB-Fe_3O_4 NPs carry positive charge at pH 2.0. Thus, ITO substrate was connected to cathode terminal while platinum electrode was made anode. Concentration of PB encapsulated Fe_3O_4 NPs was adjusted to obtain current of 1 mA and uniform films of PB-Fe_3O_4 NPs were obtained on ITO surface by applying 5 V for 60 s.

2.4 Enzyme Immobilization

Prior to enzyme immobilization, the PB-Fe_3O_4 NPs/ITO electrode was dipped in PBS containing 0.4 M 1-ethyl-3-(3-dimethylaminopropyl)carbodiimide (EDC)and 0.1 M *N*-hydroxysuccinimide (NHS) for 4 h at 30 °C. The NHS

 © 2014 Wiley-VCH Verlag GmbH & Co. KGaA, Weinheim

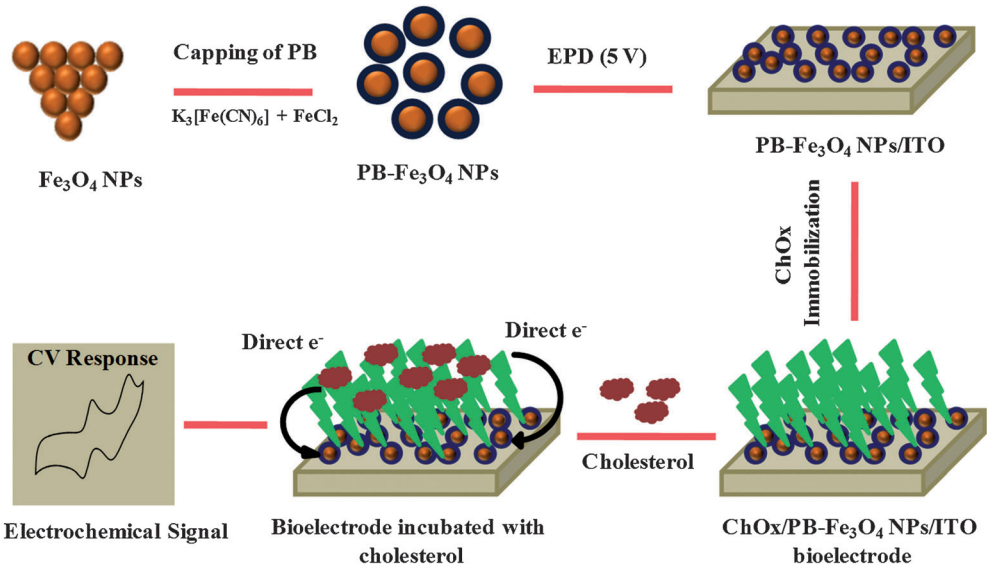

Scheme 1. Schematic illustration of the preparation of PB encapsulated Fe_3O_4 NPs, formation of the bioelectrode and its application for mediator-free cholesterol detection.

acts as an activator for the carboxyl groups present at the surface of PB-Fe_3O_4 NPs/ITO electrode and EDC acts as the coupling agent. The modified electrode was then incubated with 20 mL of ChOx solution (1 mg mL^{-1}) at 4 °C for overnight. The NH_2 groups of the enzymes form covalent amide bond (CO–NH) with the activated carboxyl groups at the surface of PB-Fe_3O_4 NPs/ITO electrode and result in the formation of ChOx/PB-Fe_3O_4 NPs/ITO bioelectrode (Scheme 1). The loosely bound enzymes were washed off using 100 mM PBS containing 0.05 % tween-20.

3 Results and Discussion

3.1 TEM Studies

Figure 1a shows TEM micrograph of Fe_3O_4 NPs indicating the average size of 10 nm. The lattice fringe of ~2.60 Å obtained from fringe pattern (Inset) match with d-value (2.56 Å) corresponding to (311) *hkl* plane of Fe_3O_4 nanocrystals (JCPDS file: 890951). On encapsulation of Fe_3O_4 NPs with PB (Figure 1b), the average size of NPs increases to 18 nm, suggesting the shell thickness of four nm. Due to the formation of thick shell of PB, magnetic interaction among NPs has been considerably reduced resulting in highly dispersed and stable NPs. However, formation of dimers and trimers on capping of PB over Fe_3O_4 NPs can be observed.

3.2 UV-Visible Studies

Figure 2A shows the optical absorption spectra from Fe_3O_4 NPs and PB encapsulated Fe_3O_4 NPs. The absorption onset of Fe_3O_4 NPs is at ~600 nm (Figure 2Aa). Because of the quantum size effect, this onset value is blue-shifted by 100 nm as compared to that of the bulk Fe_3O_4. The band near 300 nm corresponds to ligand field transitions of Fe^{3+} and the shoulder peak around 480 nm corresponds to excitation of Fe–Fe pair [22].

On addition of $K_3[Fe(CN)_6]$ to Fe_3O_4 NPs, absorption from Fe_3O_4 NPs is masked by the characteristic peaks of $K_3[Fe(CN)_6]$ at 260 nm, 301 nm and 412 nm [23] (Figure 2Ab). On further addition of $FeCl_2$, sharp absorption occurs around 700 nm which marks the formation of PB over Fe_3O_4 NPs [20] (Figure 2Ac). Absorption band starts at 500 nm and extends to 900 nm with the maximum absorption at 700 nm which is ascribed to the mixed-valence charge transfer of the polymeric complex [Fe(II)–C–N–Fe(III)] confirming the formation of PB on the surface of Fe_3O_4 NPs [21].

3.3 FTIR Studies

Figure 2B shows the transmittance spectra of iron oxide NPs and PB encapsulated iron oxide NPs. Peak at 618 cm^{-1} corresponds to the vibrations of Fe-O from Fe_3O_4 NPs [24] (Figure 2Ba). The peak at 1587 cm^{-1} corresponding to the H–O–H bending mode and the band at 3400 cm^{-1} corresponding to the O–H stretching vibrations indicate the presence of hydroxyl groups at the surface of Fe_3O_4 NPs.

In case of PB encapsulated Fe_3O_4 NPs (Figure 2Bb), the peak at 609 cm^{-1} corresponds to Fe-O vibrations of Fe_3O_4 NPs. The sharp peak at 2082 cm^{-1} is the characteristic of PB and its analogues and corresponds to C–N stretching vibrations. The peak at 498 cm^{-1} corresponds to the formation of [Fe(II)–C–N–Fe(III)] complex confirming encapsulation of PB onto Fe_3O_4 NPs [25]. The band at 3323 cm^{-1} and peak at 1602 cm^{-1} corresponding to O–H stretching and H–O–H bending modes, respectively, indicates presence of water molecules in the NPs.

© 2014 Wiley-VCH Verlag GmbH & Co. KGaA, Weinheim

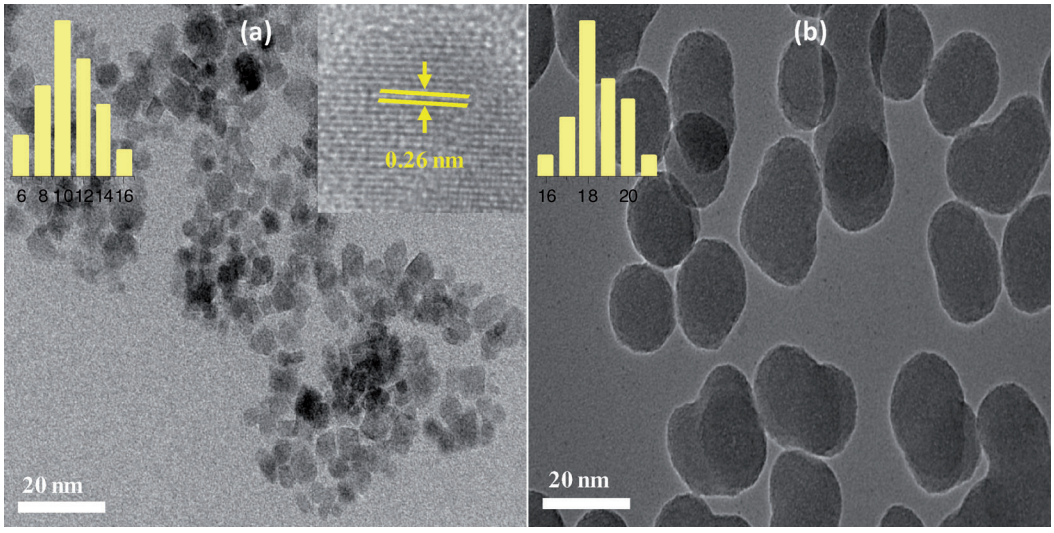

Fig. 1. TEM micrographs of (a) Fe_3O_4 NPs, (b) Prussian blue modified Fe_3O_4 NPs.

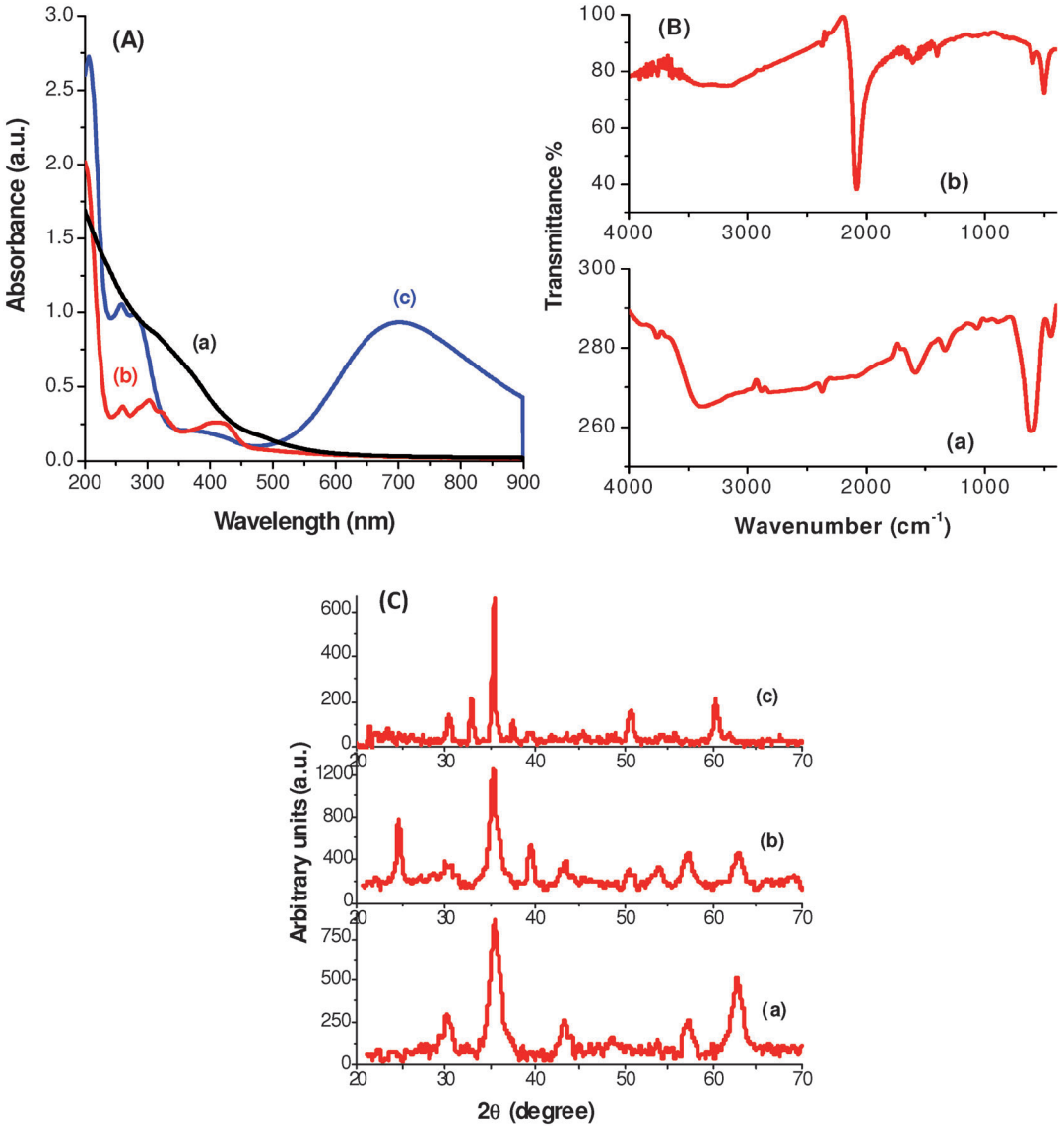

Fig. 2. (A) UV-vis absorption spectra of (a) Fe_3O_4 NPs; (b) Fe_3O_4 NPs + $K_3[Fe(CN)_6]$; (c) PB modified Fe_3O_4 NPs. (B) FTIR spectra of (a) Fe_3O_4 NPs; (b) PB modified Fe_3O_4 NPs. (C) XRD of (a) Fe_3O_4 NPs; (b) PB modified Fe_3O_4 NPs; (c) PB-Fe_3O_4 film on ITO.

© 2014 Wiley-VCH Verlag GmbH & Co. KGaA, Weinheim

3.4 X-Ray Diffraction Studies

Figure 2Ca shows X-ray diffraction pattern from Fe_3O_4 NPs. The peaks match with those of magnetite (Fe_3O_4) suggesting NPs have cubic spinel structure. The peaks obtained at $2\theta = 30.07^\circ$, 35.67°, 43.35°, 52.65°, 57.35°, 62.86° corresponds to (*hkl*) planes of (220), (311), (400), (422), (511) and (440), respectively (JCPDS file: 890599). Except for the broadening of the peaks, all the position and relative intensity of diffraction peaks are identical with the standard spectrum for bulk magnetite. The average size of NPs has been calculated using Debye–Scherrer formula and is found to be ~6 nm from the most intense peak at $2\theta = 35.50^\circ$.

In Figure 2Cb, the additional peaks at $2\theta = 24.73^\circ$, 39.42°, 50.69°, 65.98°, 68.97° match with those of PB and correspond to (*hkl*) planes (220), (420), (440), (640) and (642), respectively [26]. The average size of PB encapsulated Fe_3O_4 NPs (calculated from the diffraction peak at $2\theta = 35.25^\circ$) is ~10 nm. The increase in average size of NPs from 6 nm to 10 nm confirms capping of Fe_3O_4 NPs with PB. Figure 2Cc shows XRD pattern from the nanocrystalline film of PB encapsulated Fe_3O_4 NPs onto ITO substrate where peaks from ITO at $2\theta = 32.95^\circ$ and 45.48° alongwith peaks from PB-Fe_3O_4 NPs also contribute to the spectrum. The decrease in the broadening of peaks is indicative of the aggregation of NPs while deposition.

3.5 SEM Studies

Figure 3 shows the morphological changes of nanocrystalline film of PB-Fe_3O_4 after enzyme immobilization. SEM micrograph reveals dense packing of PB-Fe_3O_4 NPs onto the ITO substrate (Figure 3a). However, the irregular size of the NPs reveals agglomeration during deposition. Densely packed globular structure in the nanoscale provides conductive environment for immobilization of the biomolecules. Figure 3b shows the uniform and complete coverage of ChOx molecules onto the surface of PB-Fe_3O_4 NPs/ITO electrode. The covered and packed granular structure indicates immobilization of ChOx molecules onto the nanocrystalline film of PB-Fe_3O_4 resulting in the formation of ChOx/PB-Fe_3O_4 NPs/ITO bioelectrode.

3.6 Electrochemistry and Kinetic Analysis

The CV curves for the PB-Fe_3O_4 NPs/ITO electrode and ChOx/PB-Fe_3O_4 NPs/ITO bioelectrode have been recorded as a function of scan rate (10–100 $mV\,s^{-1}$) to investigate the interfacial kinetics. The shift of the anodic peak towards positive potential and the shift of cathodic peak towards negative potential have been observed with the increase of scan rate suggesting the redox process to be quasi-reversible. The linear variation of peak potential (anodic and cathodic) as a logarithmic function of scan rate in accordance with Laviron theory is depicted in Figure 4A and the slopes of two straight lines give $2.303RT/(1-\alpha)nF$ and $-2.303RT/\alpha nF$, respectively. The value of electron transfer coefficient (α), for n number of electrons, has been obtained as 0.38 and 0.45 for PB-Fe_3O_4 NPs/ITO electrode and ChOx/PB-Fe_3O_4 NPs/ITO bioelectrode, respectively. The charge transfer rate constant (k_s) can be determined from the following equation:

$$\ln k_s = \alpha \ln(1-\alpha) + (1-\alpha) \ln \alpha - \ln(RT/nFv) \\ -\alpha/(1-\alpha)(nF\Delta E_p/RT) \quad (1)$$

where, n is number of electrons appearing in half-reaction for the redox couple, R is the ideal gas constant ($8.314\ J\,K^{-1}\,mol^{-1}$), T is thermodynamic temperature (K), F is the faraday constant, v is the scan rate and ΔE_p is the

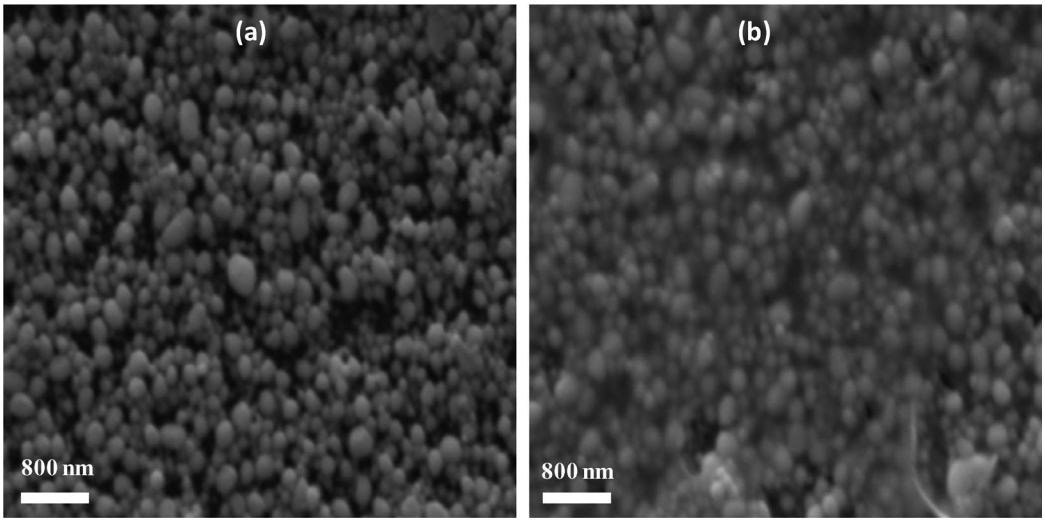

Fig. 3. SEM images of (a) PB-Fe_3O_4 NPs/ITO electrode, (b) ChOx/PB-Fe_3O_4 NPs/ITO bioelectrode.

© 2014 Wiley-VCH Verlag GmbH & Co. KGaA, Weinheim

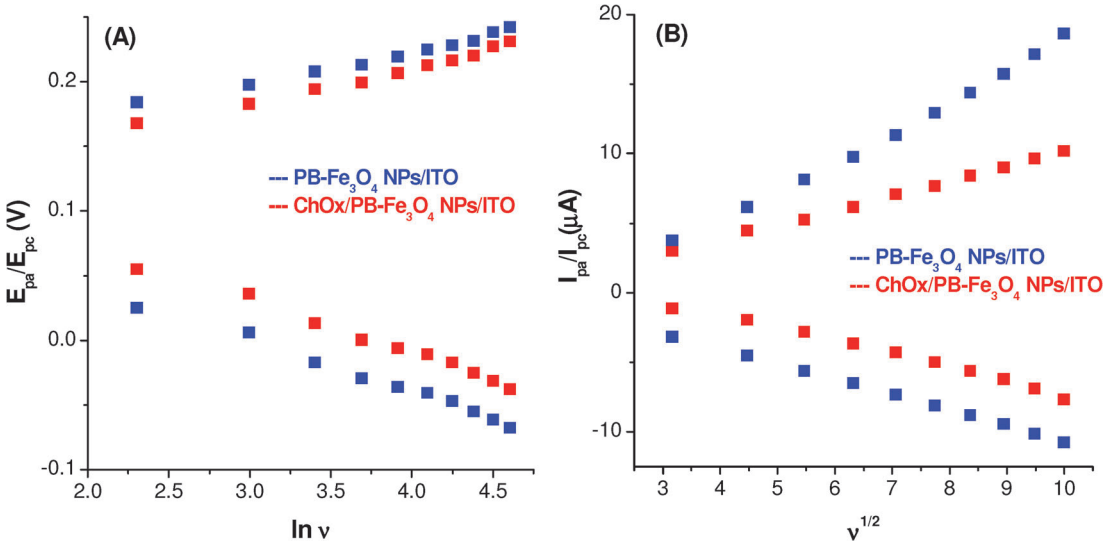

Fig. 4. (A) Anodic and cathodic peak potential as a function of the logarithm of the scan rate for the PB-Fe_3O_4 NPs/ITO electrode and ChOx/PB-Fe_3O_4 NPs/ITO bioelectrode. (B) Anodic current and cathodic current as a function of square root of the scan rate for the PB-Fe_3O_4 NPs/ITO electrode and ChOx/PB-Fe_3O_4 NPs/ITO bioelectrode.

Table 1. Values of α, k_s, Γ, D and A for the PB-Fe_3O_4 NPs/ITO electrode and ChOx/PB-Fe_3O_4 NPs/ITO bioelectrode.

Electrode	α	k_s (s^{-1})	Γ (mol cm^{-2})	D ($cm^2 s^{-1}$)	A (cm^2)
PB-Fe_3O_4 NPs/ITO	0.38	17.12	3.68×10^{-13}	0.23×10^{8}	0.22
ChOx/PB-Fe_3O_4 NPs/ITO	0.45	45.15	1.23×10^{-12}	0.97×10^{8}	0.31

potential difference between oxidation peak potential and reduction peak potential [27]. The value of k_s has been found to increase from 17.12 s^{-1} to 45.15 s^{-1} on immobilization of ChOx molecules (Table 1). This shows that the redox centers (FAD) of ChOx molecules are in close proximity of the nanostructured PB-Fe_3O_4 surface, resulting in facile electron transport across the interface.

For a surface-controlled process, the surface concentration of the absorbed electroactive species (Γ) can be estimated from a plot of anodic peak current (I_p) versus scan rate (ν) in accordance with the Brown–Anson model using following Equation 2:

$$I_p = n^2F^2\nu A\Gamma(4RT)^{-1} \quad (2)$$

where, A is area of the electrode (0.5 cm^2). The anodic and cathodic current for the PB-Fe_3O_4 NPs/ITO electrode and the ChOx/PB-Fe_3O_4 NPs/ITO bioelectrode are proportional to square rate of the scan rate (Figure 4B). This indicates that the ionic transport from the bulk solution to the electrode occurs exclusively by diffusion [28]. Diffusion coefficient (D) is determined by the concentration gradient of ionic species between the bulk and the interface and can be calculated using Randles–Sevcik Equation [29]:

$$I_p = 2.687\times10^5\, n^{3/2}AD^{1/2}\nu^{1/2}\Gamma \quad (3)$$

The electroactive surface area of the electrode can further be obtained by using the calculated diffusion coefficient. The surface concentration of ionic species for the PB-Fe_3O_4 NPs/ITO electrode has been calculated as 3.68×10^{-13} mol cm^{-2} which increases to 1.23×10^{-12} mol cm^{-2} for the ChOx/PB-Fe_3O_4 NPs/ITO bioelectrode. The diffusion coefficient increases from 0.23×10^8 $cm^2 s^{-1}$ to 0.97×10^8 $cm^2 s^{-1}$ and the electrochemical surface area increases from 0.22 cm^2 to 0.31 cm^2 on immobilization of the enzyme molecules onto PB-Fe_3O_4 NPs/ITO electrode (Table 1). The higher electroactive surface area and higher surface concentration is in accordance with the enhanced redox currents on immobilization of ChOx molecules.

The fabrication of the ChOx/PB-Fe_3O_4 NPs/ITO bioelectrode has been investigated electrochemically at each modification step in PBS (pH 6.5) without any redox mediator. Figure 5A shows the cyclic voltammograms (CV) of ITO electrode, PB-Fe_3O_4 NPs/ITO electrode and ChOx/PB-Fe_3O_4 NPs/ITO bioelectrode. The ITO electrode shows an oxidation peak at 0.76 V in slight acidic conditions. The ITO electrode modified with PB-Fe_3O_4 NPs shows additional set of redox peaks at +0.2 V and +0.1 V corresponding to the transition of PB to Prussian white and Prussian white to PB, respectively [6]. Thus, PB-Fe_3O_4 NPs/ITO electrode acts as a self mediated electrode due to the facile charge propagation inside the film. The immobilization of ChOx molecules onto PB-Fe_3O_4 NPs/ITO electrode results in enhanced oxidation current due to the direct transfer of electrons between the enzyme and the electrode. The enzyme molecules are attached to the electrode surface in such a way that their redox centers are in close proximity, this may result in

© 2014 Wiley-VCH Verlag GmbH & Co. KGaA, Weinheim

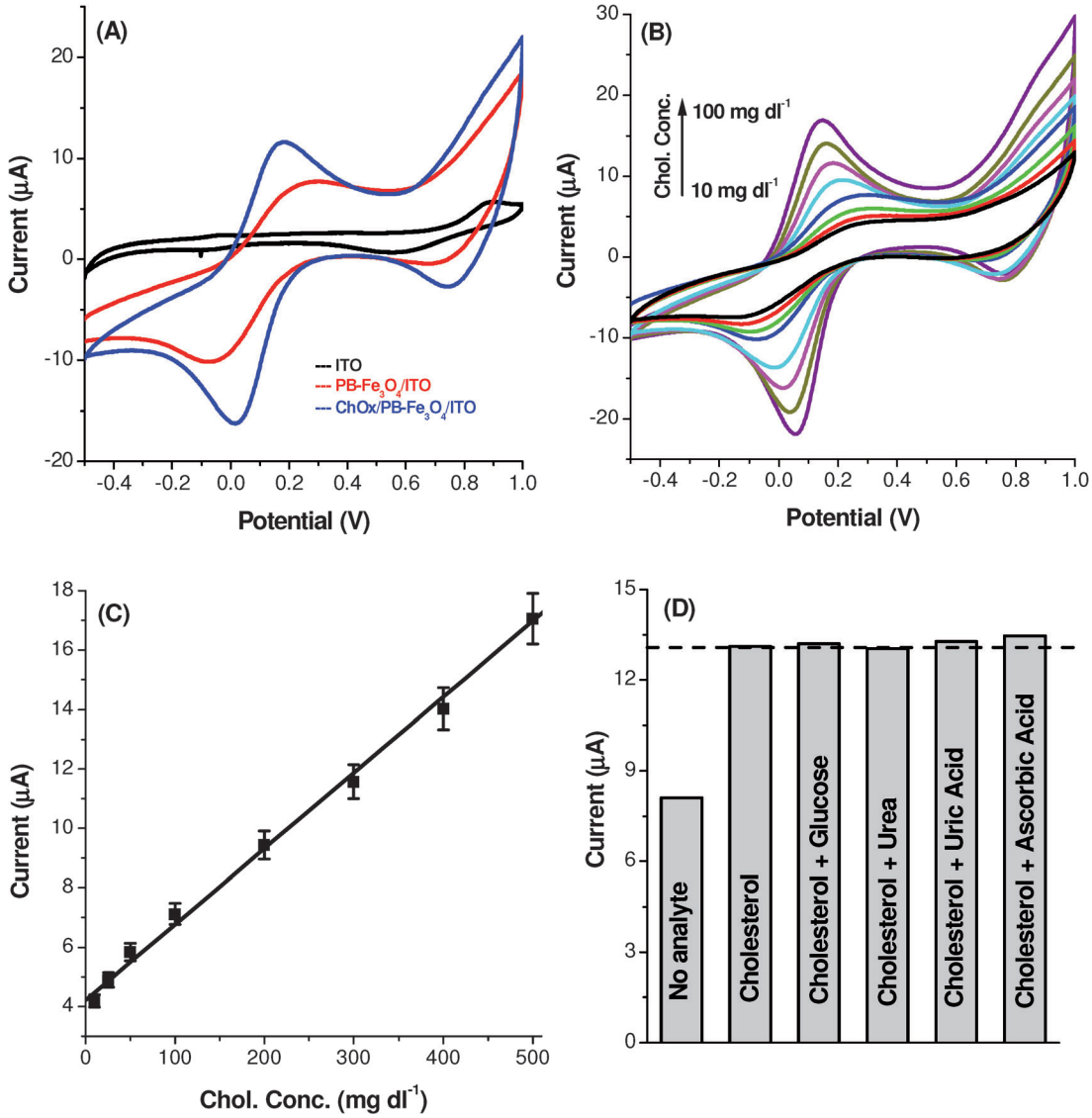

Fig. 5. (A) Cyclic voltammograms of ITO electrode, PB-Fe_3O_4 NPs/ITO electrode and ChOx/PB-Fe_3O_4 NPs/ITO bioelectrode in PBS (100 mM) at scan rate of 50 mV s^{-1}. (B) Cyclic voltammetric response of ChOx/PB-Fe_3O_4 NPs/ITO bioelectrode for varying concentrations of cholesterol (10–400 mg dL^{-1}) in PBS (100 mM) at scan rate of 50 mV s^{-1}. (C) Anodic peak current as a function of cholesterol concentration. (D) Current response of ChOx/PB-Fe_3O_4 NPs/ITO bioelectrode towards cholesterol (100 mg dL^{-1}) in presence of different interferents.

direct electron transfer between the enzyme and the electrode.

3.7 Cholesterol Detection

To show the potential application of enhanced electrochemical properties of Fe_3O_4 NPs on incorporation of the electroactive PB, CV response studies of ChOx/PB-Fe_3O_4 NPs/ITO bioelectrode towards different concentrations of cholesterol have been carried out in PBS. Anodic peak current at ~0.2 V has been found to increase with the increasing concentrations of cholesterol (Figure 5B). ChOx catalyzes the oxidation of cholesterol to cholest-5-en-3-one and then isomerization to cholest-4-en-3-one and the FAD cofactor reduces to $FADH_2$ in the process [30]. In order to reoxidize, the reduced cofactor of ChOx molecules undergo direct exchange of electrons with the nanostructured PB-Fe_3O_4 electrode and results in increase in peak current with the increasing concentrations of cholesterol (Scheme 2). The buffer solution has been deoxygenated by purging of nitrogen gas prior to the electrochemi-

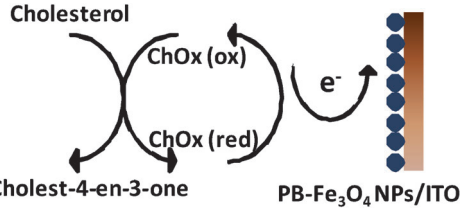

Scheme 2. Enzymatic reaction of cholesterol oxidase and cholesterol onto PB-Fe_3O_4 NPs/ITO electrode.

© 2014 Wiley-VCH Verlag GmbH & Co. KGaA, Weinheim

Table 2. Comparison table summarizing response characteristics of present mediator free cholesterol biosensors alongwith those reported in literature.

Electrode	Sensitivity	Detection limit	Linear range (mM)	K_m^{app} value (mM)	Shelf life (days)	Response time (s)	Reference
Pt/SAM/PB/Ppy-ChOx/Nf	$0.6–8.5\times10^{-3}$ AM^{-1}	8 μM	0.05–0.30	0.09	25	–	[31]
PB silicic sol-gel/GCE	0.329 AM^{-1}	0.12 μM	0.001–0.080	–	35	–	[32]
PANI-CdS/ITO	1.015×10^{-3} AM^{-1}	1.19 mM	1.25–12.5	0.82	–	20	[33]
PANI-PB/GCE	–	0.18 μM	0.001–0.080	0.54	30	20–30	[34]
PPy-PB/GCE	0.039×10^{-3} AM^{-1}	0.60 μM	0.01–0.1	–	30	30	[35]
PB-Fe_3O_4 NPs/ITO	2.15×10^{-3} $AM^{-1}cm^{-2}$	0.92 mM	0.62–12.5	0.07	65	15	Present work

cal studies to ensure that there is no production of H_2O_2 during the enzymatic reaction and the current results from the direct electron transfer phenomenon.

The ChOx/PB-Fe_3O_4 NPs/ITO bioelectrode exhibits linear increase in current in the range of 10–500 mg dL^{-1} (0.25–12.5 mM) (Figure 5C) and exhibits the response time of 15 s indicating facile electron transfer from enzyme molecules to the electrode. The sensitivity has been calculated from the linear region of the calibration plot and is found to be as 53.94 nA mg^{-1} $dL\,cm^{-2}$ (2.15 mA $M^{-1}\,cm^{-2}$) with regression coefficient of 0.99 and standard deviation of 0.65 μA. The detection limit of the bioelectrode ($DL=3\times SD$/Sensitivity) is calculated to be as 36.78 mg dL^{-1} (0.92 mM). The high sensitivity, low response time and low detection limit of the fabricated mediator-free cholesterol biosensor reveals the enhanced bioelectrocatalytic activity of the enzyme onto PB-Fe_3O_4 NPs/ITO electrode and facile direct charge transport properties of PB-Fe_3O_4 NPs. The apparent Michaelis–Menten kinetic parameter (K_m^{app}) has been calculated using Lineweaver Burk plot and is estimated to be as 2.82 mg dL^{-1} (0.07 mM). The low value of K_m^{app} signifies the high catalytic efficiency of enzyme onto nanostructured PB-Fe_3O_4 electrode resulting in better interaction of ChOx with cholesterol.

The effect of potential interferents on the cholesterol measurements has been investigated by taking the solution containing 1:1 ratio of cholesterol (100 mg dL^{-1}) and interferents such as glucose (5 mM), urea (1 mM), uric acid (0.1 mM) and ascorbic acid (0.05 mM) (Figure 5D). In the presence of interferents, 1–2% change of current has been observed from the CV response of the ChOx/PB-Fe_3O_4 NPs/ITO bioelectrode which has been calculated using following equation:

$$\%inter = I_{chol} - I_{Int}/I_{chol},$$

where I_{chol} and I_{int} are the changes in current corresponding to the cholesterol and the1:1 mixture of cholesterol with interferent. The interferents present in blood samples may get easily oxidized at high potentials. Thus, the proposed biosensor with low detection potential (~0.15 V) can avoid the effect of other analytes present in blood and is thus highly selective towards cholesterol. The reproducibility of the ChOx/PB-Fe_3O_4 NPs/ITO bioelectrode has also been investigated with cholesterol concentration of 100 mg dL^{-1}. The bioelectrode can be used upto 15 times without appreciable loss of the signal (< 5%). In addition, the ChOx/PB-Fe_3O_4 NPs/ITO bioelectrode retained 97% of the current response after 9–10 weeks (when stored at 4 °C) indicating good stability (Figure S2; Supporting Information). Comparison of the response characteristics of present mediator-free cholesterol biosensor with those reported in literature shows that electroactive Prussian blue encapsulated iron oxide nanostructures results in high sensitivity and specificity towards cholesterol detection and low K_m^{app} value shows the high enzymatic activity of ChOx molecules towards cholesterol onto electroactive Prussian blue encapsulated iron oxide nanostructures [31–35] (Table 2).

4 Conclusions

Iron oxide nanoparticles with an average diameter of 10 nm were encapsulated in four nm thick shells of Prussian blue, which is evident from TEM analysis of the particles. The capping of Prussian blue onto Fe_3O_4 NPs reduces the magnetic interaction among Fe_3O_4 NPs and imparts monodispersity and stability to the NPs. The electrophoretically deposited PB-Fe_3O_4 NPs onto the ITO substrate exhibit excellent electrocatalytic activity and enroute direct electron transfer from the immobilized enzyme molecules to the nanostructured PB-Fe_3O_4 film resulting in the fabrication of mediator-free cholesterol biosensor. The proposed cholesterol biosensor exhibits high sensitivity, low detection limit and low K_m^{app} value due to facile charge transport through the PB-Fe_3O_4 film. The low operating potential (~0.15 V) of the fabricated cholesterol biosensor circumvents the effect of potential interferents, rendering the biosensor to be highly selective for cholesterol detection. Also, the biosensor shows good reproducibility and stability and thus can be utilized for healthcare diagnostics application. Further, results of these studies have implications that electroactive Prussian blue encapsulated Fe_3O_4 NPs may find applications in DNA immobilization, cell imaging, drug delivery etc.

© 2014 Wiley-VCH Verlag GmbH & Co. KGaA, Weinheim

Supporting Information

Zeta potential graphs of Fe_3O_4 NPs and $K_3[Fe(CN)_6]$, shelf-life curve of ChOx/PB-Fe_3O_4 NPs/ITO bioelectrode showing reduction in peak current with time, preparation details of cholesterol solution.

Acknowledgement

We thank Prof. *R. C. Budhani* (Director, NPL), Dr. *A. M. Biradar* and Prof. *B. D. Malhotra* for providing support and facilities, Dr. *K. N. Sood* for SEM measurements. R. S. is thankful to *UGC-CSIR* for the award of a Junior Research Fellowship. Financial support received from *DST and CSIR Empower projects* is sincerely acknowledged.

References

[1] Y. Liu, M. Wang, F. Zhao, Z. Xu, S. Dong, *Biosens. Bioelectron.* **2005**, *21*, 984.
[2] Z. Wang, S. Liu, P. Wu, C. Cai, *Anal. Chem.* **2009**, *81*, 1638.
[3] H. Li, Q. Wei, J. He, T. Li, Y. Zhao, Y. Cai, B. Du, Z. Qian, M. Yang, *Biosens. Bioelectron.* **2011**, *26*, 3590.
[4] J. Wang, A. N. Kawde, A. Erdem, M. Salazar, *Analyst* **2001**, *126*, 2020.
[5] R. Sharma, V. V. Agrawal, A. K. Srivastava, Govind, L. Nain, M. Imran, S. R. Kabi, R. K. Sinha, B. D. Malhotra, *J. Mater. Chem. B* **2013**, *1*, 464.
[6] A. A. Karyakin, *Electroanalysis* **2001**, *13*, 813.
[7] H. Wang, Y. Huang, *J. Hazard. Mater.* **2011**, *191*, 163.
[8] C. Wang, S. Chen, Y. Xiang, W. Li, X. Zhong, X. Che, J. Li, *J. Mol. Catal. B, Enzym.* **2011**, *69*, 1.
[9] G. Fu, X. Yue, Z. Dai, *Biosens. Bioelectron.* **2011**, *26*, 3973.
[10] Y. Zhang, Y. Liu, Z. Chu, L. Shi, W. Jin, *Sens.Actuators B, Chem.* **2013**, *176*, 978.
[11] L. Zhu, J. Zhai, Y. Guo, C. Tian, R. Yang, *Electroanalysis* **2006**, *18*, 1842.
[12] I. Baravik, R. Tel Vered, O. Ovits, I. Willner, *Langmuir* **2009**, *25*, 13978.
[13] L. Gorton, A. Lindgren, T. Larsson, F. D. Munteanu, T. Ruzgas, I. Gazaryan, *Anal. Chim. Acta* **1999**, *400*, 91.
[14] A. Heller, *Nat. Biotech.* **2003**, *21*, 631.
[15] P. D. Hale, T. Inagaki, H. I. Karan, Y. Okamoto, T. A. Skotheim, *J. Am. Chem. Soc.* **1989**, *111*, 3482.
[16] A. Ramanavicius, K. Habermuller, E. Csoregi, V. Laurinavicius, W. Schuhmann, *Anal. Chem.* **1999**, *71*, 3581.
[17] Y. Xiao, F. Patolsky, E. Katz, J. F. Hainfeld, I. Willner, *Science* **2003**, *299*, 1877.
[18] Z. Matharu, A. J. Bandodkar, V. Gupta, B. D. Malhotra, *Chem. Soc. Rev.* **2012**, *41*, 1363.
[19] L. Besra, M. Liu, *Prog. Mater Sci.* **2007**, *52*, 1.
[20] X. Q. Zhang, S. W. Gong, Y. Zhang, T. Yang, C. Y. Wang, N. Gu, *J. Mater. Chem.* **2010**, *20*, 5110.
[21] G. Zhao, J. J. Feng, Q. L. Zhang, S. P. Li, H. Y. Chen, *Chem. Mater.* **2005**, *17*, 3154.
[22] L. H. Huo, W. Li, L. H. Lu, H. N. Cui, S. Q. Xi, J. Wang, B. Zhao, Y. C. Shen, Z. H. Lu, *Chem. Mater.* **2000**, *12*, 790.
[23] F. H. Getman, *J. Phys. Chem.* **1920**, *25*, 147.
[24] M. Ma, Y. Zhang, W. Yu, H. Shen, H. Zhang, N. Gu, *Coll. Surfaces A, Physicochem. Engin. Aspects* **2003**, *212*, 219.
[25] M. Pyrasch, A. Toutianoush, W. Jin, J. Schnepf, B. Tieke, *Chem. Mater.* **2002**, *15*, 245.
[26] F. Shiba, *Coll. Surf. A, Physicochem. Eng. Aspects* **2010**, *366*, 178.
[27] E. Laviron, *J. Electroanal. Chem. Inter. Electrochem.* **1979**, *100*, 263.
[28] M. Yang, Y. Yang, H. Yang, G. Shen, R. Yu, *Biomaterials* **2006**, *27*, 246.
[29] V. Gau, S. C. Ma, H. Wang, J. Tsukuda, J. Kibler, D. A. Haake, *Methods* **2005**, *37*, 73.
[30] J. R. Harris, A. Vrielink , *Cholesterol Binding and Cholesterol Transport Proteins*, Vol. 51, Springer, Heidelberg **2010**, p. 137.
[31] J. C. Vidal, J. Espuelas, E. Garcia Ruiz, J. R. Castillo, *Talanta* **2004**, *64*, 655.
[32] J. Li, T. Peng, Y. Peng, *Electroanalysis* **2003**, *15*, 1031.
[33] H. Dhyani, C. Dhand, B. D. Malhotra, P. Sen, *J. Biosens. Bioelectron.* **2011**, *3*, 112.
[34] J. P. Li, T. Z. Peng, *Chin. J. Chem* . **2002**, *20*, 1038.
[35] J. P. Li, H. N. Gu, *J. Chin. Chem. Soc.* **2006**, *53*, 575.

Received: January 30, 2014
Accepted: March 31, 2014
Published online: ■■ ■■, 2014

 © 2014 Wiley-VCH Verlag GmbH & Co. KGaA, Weinheim

Volume 2 (2014) 337-341 ISSN 2347 - 3258
International Journal of Advance Research and Innovation

Friction Stir Processing of Aluminum alloys for Defense Applications

V. Jeganathan Arulmoni, R. S. Mishra
Department of Mechanical & Production Engineering, Delhi Technological University, New Delhi, India

Article Info
Article history:
Received 2 March 2014
Received in revised form
10 April 2014
Accepted 20 May 2014
Available online 15 June 2014

Keywords
Friction Stir Processing,
Aluminium Alloys,
Process Parameters

Abstract
Friction stir processing (FSP) is a surface modifying Technique, which was developed, based on the basic principles of friction stir welding (FSW), but FSP is used to modify the local microstructure and does not join metals together..A rotating tool with pin and shoulder is inserted into a single piece of material and traversed along the desired path to cover the region of interest. Friction between the shoulder and workpiece results in localized heating which raises the temperature of the material to the range where it is plastically deformed. During this process, the severe plastic deformation and thermal exposure of material, results in a significant evolution in the local microstructure. FSP has been successfully used for formation of nanograin, increase the surface hardness and also enhances the wear resistance, tensile strength and fatigue strength of the material. This review paper, the current scenario and development of FSP of various materials mainly (a) formation of nanograins, microstructure and mechanical properties. (b) Effect of FSP/W process parameters.

1. Introduction

FSP was developed by Mishra et al, 6 for improving the surface modification based on the principles of new solid state welding Technique. In this process a special non consumable rotating tool is used; the shoulder of the tool rubs the surface and gives enough load and generating sufficient heat to soften the material. The pin plunged in to the material producing refined microstructure due to 'stirring' action. The purpose of this article is to review the process parameters and tools used in FSP/W of ferrous materials and Al/Mg Alloys. The advantages using FSP are as follows:

1. It is used to transform a heterogeneous microstructure to homogeneous, refined microstructure.
2. It is used to form nanostructure surface as a result increases the hardness of the base metal.
3. To improve the tensile properties, fatigue properties and wear characteristics of the surface material.

During FSP no gases involved, no smoke is produced, no secondary materials are used, due to this reason it is called "green-efficient technology" and it not changes the size and shape of the processed components. FSP can be

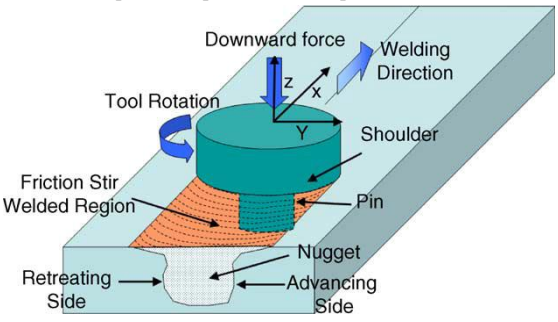

Fig: 1. Working Principle of friction stir processing (Mishra[6])

accurately described as a forging and extrusion, or metal working process. The resulting microstructure is composed three primary zones: the heat-affected zone (HAZ), the thermo-mechanically-affected zone (TMAZ), and the nugget zone (NZ). As a result of intense plastic deformation at elevated temperature, grain refinement to a size range from 0.8 to 12 lm can be achieved. It is well known that the nugget zone consists of fine and equiaxed grains produced due to the dynamic recrystallization. FSP has proven to be successful in the modification of various properties such as formability, hardness, and yield strength, fatigue and corrosion resistance. The current developments in process modelling, microstructure and properties, material specific issues, applications of friction stir processing have been discussed in detail. Because Tool geometry is very important factor for producing sound welds and it is known that a cylindrical threaded pin and concave shoulder are widely used welding tool features.. Processing parameters, including tool rotation rate, traverse speed, spindle tilt angle, and target depth, are crucial to produce sound and defect-free processed region. It has been suggested by some researchers that FSP can be generally described as an in situ extrusion process and the stirring and mixing of material occurred only at the surface layer of the processed zone adjacent to the rotating shoulder. FSP results in significant temperature rise within and around the weld. A temperature rise of 400–500oC has been recorded within the stirred zone for aluminium alloys. Intense plastic deformation and temperature rise result in significant micro structural evolution, i.e., fine recrystallized grains of 0.1–18 mm, texture, precipitate dissolution and coarsening, and residual stress with a much lower magnitude. Three different micro structural zones have been identified in friction stir processed region, i.e., nugget region experiencing intense plastic deformation and high-temperature exposure and characterized by fine and equiaxed recrystallized grains, thermo-mechanically affected region experiencing medium temperature and deformation and characterized by deformed and un-recrystallized grains, and heat-affected region

Corresponding Author,
E-mail address: professor-rsmishra@yahoo.co.in
All rights reserved: http://www.ijari.org

experiencing only temperature and characterized by precipitate coarsening. FSP exhibits a considerable improvement in strength, ductility, and fatigue and fracture toughness. FSP has found several applications for micro structural modification in metallic materials, including micro structural refinement for high- strain rate super plasticity, fabrication of surface composite on aluminium substrates, and homogenization of microstructure in nano phase aluminium alloys, metal matrix composites, and cast Al–Si alloys. Despite considerable interests in the FSP technology in past decade, the basic physical understanding of the process is lacking. Some important aspects, including material flow, tool geometry design, wear of welding tool, micro structural stability, welding of dissimilar alloys and metals, Friction stir processing is a novel surface modification technique and resulted in significant grain refinement in Aluminum alloy. The microstructure is characterized by equiaxed fine grains with well-defined grain boundaries. The microstructure evolved through dynamic recovery and dynamic recrystallization process. The strength of the FSP material improved significantly and at the same time the ductility was also retained, the hardness also improved substantially. FSP was found to be beneficial in improving wear resistance. The high wear behavior in the stir zone is attributed to a lower coefficient of friction and the improved micro-hardness in this region.

2. Literature Review

L. Karthikeyan, V. S. Senthil Kumar [1.] discussed the relationship between process parameters and mechanical properties of friction stir processed AA6063-T6 aluminium alloy plate in T6 temper condition was single pass FSP. Processing was carried out at different axial forces (8, 10 and 12KN), tool feeds (22.2, 40.4 and 75 mm/min) and tool rotational speeds (800, 1000, 12000, 14000 and 16000 rpm). And found that at lower axial forces, friction stir processed material exhibits lower tensile and ductility properties and . on increasing the axial force, they attain peak values but fall with further increases. The depth to which the tool pin plunges into the process zone and the accompanied material flow is controlled by the shoulder force, which in turn is influencing by the axial force. And also found that Lower axial forces result in both poorer stirring as well as insufficient consolidation of material. Besides the insufficient downward force result in absence of vertical flow giving rise to defects and reduced tensile and ductility properties. And concluded that by increase in axial load increases the heat input and reducing flow stress due to the pressure developed to consolidate the material in process zone. He is found that very high axial forces lead to higher tan optimal temperatures which causing excessive thinning of material accompanied by micro voids and tunnel defects due to excessive heat input. As increase of approximately 46.5% compared to parent material in the tensile strength of specimens processed at an axial force of 10KN, tool feed of 40.2 mm/min and a tool rotational speed of 1400 rpm and also found that ductility increases in the processed specimens ranged from 3% to 133%. And hardness followed the same trend as that of tensile properties. In his experiments, all the specimens processed with an axial force of 8KN yielded process defects and multivariate non linear regression equations are used to predict the mechanical properties such as yield, tensile, ductility and micro hardness. In the multivariate case, with more than one independent variable, regression line is articulated as a function of axial force, tool feed and the tool rotational speed. A second order polynomial curve is found to best fit the experimental values. K. Elangovan, V. Balasubramanian [2.] did experiments on for finding the Influences of tool pin profile and tool shoulder diameter on the formation of friction stir zone in rolled plates of 6mm thickness AA6061 aluminium alloy cut into 300x150 mm were prepared in butt joint configuration and followed single pass welding procedure with high carbon steel tool for five different tool profiles (i.e. cylindrical, threaded cylindrical, tapered cylindrical, square, triangle) and each profile with three different shoulder diameters (15, 18 and 21mm) is employed for fabricating 15 joints. They considered welding parameters (i.e. rotational speed of 1200rpm, weld speed of 1.25mm/s and axial force of 7KN and tool dimensions (i.e.5.5mm pin length and 6mm pin diameter in the experiments and joints were fabricated by square pin profiled tool exhibited superior tensile properties irrespective of tool shoulder diameter and triangular pin profiled tool fabricated joints showed almost matching tensile properties and rest profile tools produced inferior joints. The flat faces of profiles were associated with eccentricity which allowed incompressible material to pass around pin profile and triangular and square pin profiles produce a pulsating stirring action in flowing material, about 80 pulses/s for square pin and 60pulses/s for triangular pin with 1200 rpm. This pulsating action yields very fine equiaxed microstructure with high hardness and strength. The joints fabricated by tools with shoulder diameter of 18mm have shown higher tensile strength and elongation and this trend is common for all tool pin profiles. In their experiments, the tool shoulder diameter is having directly proportional relationship with the heat generation due to friction and larger shoulder diameter leads to wider contact area and hence the wider TMAZ and HAZ subsequently deteriorating tensile properties of the materials. They found the less shoulder diameter resulted in less heat generation and hence weld metal consolidation is not good in FSP region. With optimum diameter of 18mm, the fabricated joint consisted of fine equiaxed grains with uniform distribution of fine strengthening precipitates throughout the matrix causing higher tensile strength and hardness and 15 joints were fabricated using square pin profiled tool with shoulder diameter of 18mm showed superior tensile properties. K. Elangovan, V. Balasubramanian [3.] did experiments for finding the Influence of tool pin profile and welding speed on the formation of friction stir processing zone They used rolled plates of 6mm thickness AA2219 aluminium alloy cut into 300 x 150 mm in butt joint configuration. Single pass welding procedure normal to rolling direction was followed with high carbon steel tool. five different tool profiles (cylindrical, threaded cylindrical, tapered cylindrical, square, triangle), each with three different welding speeds (0.37, 0.76 and 1.25 mm/s) were employed to fabricate 15 joints and welding parameters like rotational speed of 1600 rpm and axial force of 12kN with used tool dimensions like 5.7mm pin length and 6mm pin diameter .They carried out macrostructure analysis and found the formation of

defect free FSP zone is a function of tool profile and used welding speeds. In their experiments, the joints were fabricated by square tool profile exhibited superior tensile properties with joint efficiency of 61% as compared to other joints irrespective of welding speed and triangular pin profiled tool fabricated joints showed almost matching tensile properties and rest profile tools produced inferior joints irrespective of welding speeds used and found that the flat faces of profiles are associated with eccentricity which allows incompressible material to pass around pin profile. Also triangular and square pin profiles produce a pulsating stirring action in flowing material, about 100 pulses/s for square pin and 75pulses/s for triangular pin with 1500 rpm. This pulsating action yields very fine grained microstructure with uniformly distributed precipitates (CuAl2) and in turn yields higher strength and hardness and found that constant rotational speed of 1600 rpm, higher welding speed resulted in lower heat input per unit length of the weld causing lack of stirring in the friction stir processing zone. Lower weld speed resulted in higher temperature and slower cooling rate in the weld zone causing grain growth and severing clustering of CuAl2 precipitates. They also observed that the material on retreating side never enters into rotational zone but the material on advancing side form the fluidized bed near the pin and rotates around it. Hence the weld zone is heterogeneous and there is variation in flow of material on retreating and advancing sides evident with lower hardness on retreating side which is the major fracture site and 15 joints, the joint fabricated using square pin profiled tool at a welding speed of 0.76 mm/s exhibited maximum tensile strength and higher hardness- K. N. Ramesh, S. Pradeep and Vivek Pancholi[4] studied Multipass Friction Stir Processing and its effect on Mechanical Properties of Aluminium Alloy 5086and conducted experiments on, 6mm plates of commercial AA 5086 alloy cut into 150 mm x 110 mm were used for single and multipass FSP and non consumable hot die steel tool with flat shoulder of 24mm diameter, a cylindrical pin of 6 mm diameter and 3 mm length. The separation between subsequent passes during multipass FSP was 3mm and 12 passes in all were carried out by them and two processing methods were employed (i) intermittent multipass processing in which the material was allowed to cool back to room temperature after each pass and (ii) continuous multipass processing in which FSP was continuously performed for 12 passes without any cooling between passes and found that the grain size increases with a traverse speed (TS) of up to 80 mm/min and then start decreasing at higher speed. up to TS of 110 mm/min, grain size obtained after CMP is coarser than IMP and single pass processing and for higher TSs, obtained grain sizes for all processing variants lie within narrow region. The CMP material processed in initial passes at low traverse speed is exposed to a temperature of 0.3 Tm for a sufficiently long time and may cause grain growth (cause of coarse grains). In IMP, the material does not experience any preheating of the processed area and is cooled to room temperature causing comparatively finer grains, bulk properties like yield strength and UTS showing a significant reduction after multipass FSP compared to Single pass and base metal because of dissolution of precipitates. However, hardness after single and multipass are found to be higher than the base metal as grain size is reduced. micro structural inhomogeneity caused by multipass processing is reason for decrease in strength compared to single pass and base metal. They found that the yield and ultimate tensile strength to decrease up to the traverse speed of 110 mm/min and then increase at 150 mm/min. At traverse speed of 150 mm/min, lower heat input and higher strain rate result in grain refinement and hence better strength. Ductility values are found to be better in multipass and single pass processed material than the base material under all processing conditions used. Adem Kurt, Ilyas Uygur and Eren Cete [5] carried out work on surface modification of aluminium by friction stir processing used cold-rolled plates of 1050 aluminium alloy were used average size of the SiC particles about 10micrometers and added a small amount of methanol and mixed, and then applied to surface of the plates to form a thin SiC particle layer without any binder in the mixture. The experimental dimensions of the work piece were 50mx100mmx5mm and AISI 1050 steel tool was made with the rotating shoulder 0.1mm inserted into the work piece. The tool was rotated clockwise at rotation speed of 500–700–1000 rpm. They kept travelling or transverse speeds of 15–20–30 mm/min and the tool spindle angle of 2°. They performed micro structural observations and vickers micro hardness test on the treated surfaces with a load of 100g on a specimen of dimension 10mmx100mmx5mm **and** found the effect of travelling speed was that the thickness of the modified surface significantly decreased due to the heat input. An increase in rotation speed caused thicker surface thickness compared with slow rotation speed rates. At high travelling speed (30 mm/min), the surface composite layer SiC, was usually weakly bonded with the aluminium alloy substrate.

3. Experimental Results

B. Zahmatkesh [8] observed hardness profile that on increased travelling speeds caused significant increment on the hardness values for all rotational speeds for the plain specimens and found the highest hardness value was 80 and the lowest was 37 for the plain specimens however, increased rotation speeds resulted in lower hardness values at the same travelling speeds and observed in the bend test that the plain FSP treated surface was much more ductile and had lower yield strength as compared with SiC added specimen. Three point yield strength of plain specimen was 60MPa for plain specimen, but it was 84MPa for the SiC added specimen. While analysing the processed specimen they have observed that there are three distinct regions on the microstructure:

1. Upper surface where SiC particles are homogenously distributed. The thickness of this region can be adjusted by rotational and travelling speed or pin height.
2. Lower surface where extremely small fine grains, broken inclusions and redistributed fine precipitations occur as a result of recrystallization.
3. Beneath the surface where elongated grains can be seen due to the material flow caused by the rotating shoulder that includes high plastic deformation in this zone.
4. Base metal, where no micro structural changes occurred.

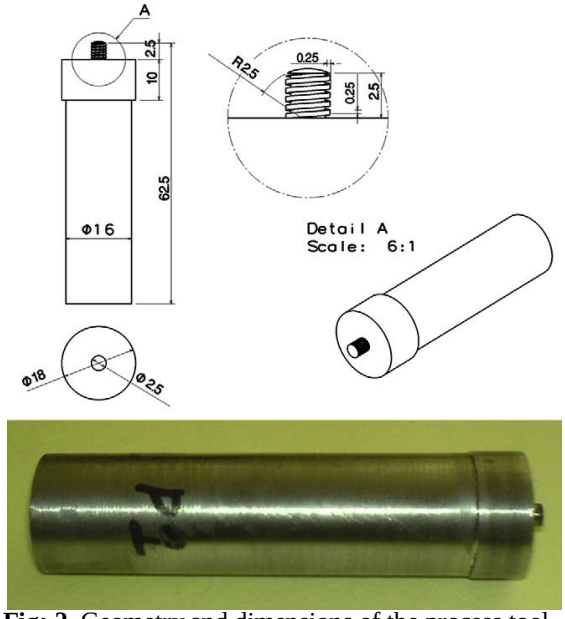

Fig: 2. Geometry and dimensions of the process tool (B. Zahmatkesh [8])

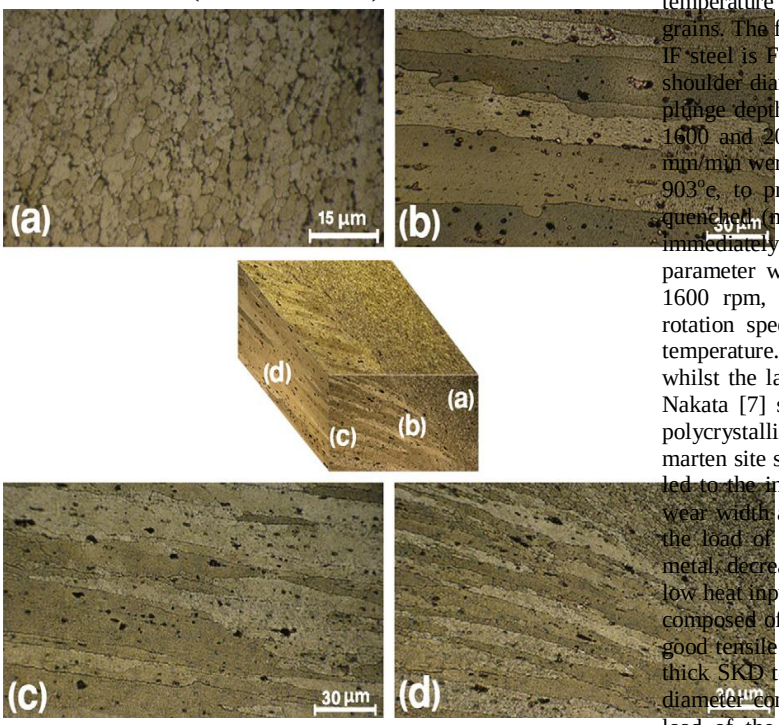

Fig: 3. Optical micrographs of different zones of FSP sample: (a) NZ, (b) TMAZ, (c) HAZ, and (d) BM (B. Zahmatkesh[8])

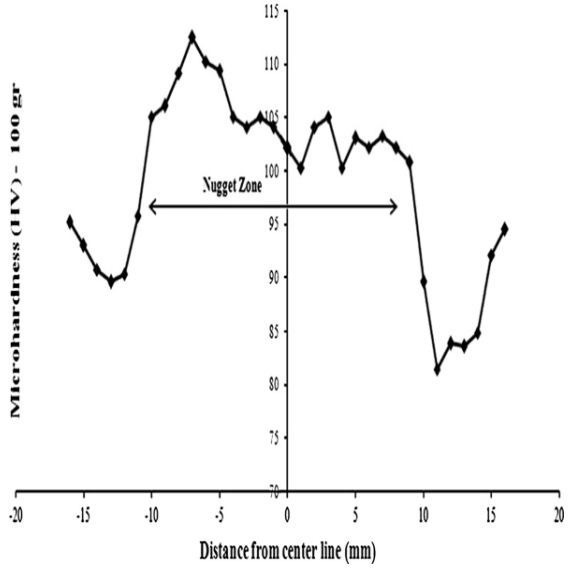

Fig: 3. Micro-hardness profile measured on the cross section of the FSP zone B. Zahmatkesh [8]

The main parameters the effect of strain rate and temperature on the nanograins and formation of ultrafine grains. The full annealed 1.5 mm thick sheet (20cmx 20 cm) IF steel is FSP by using tungsten carbide tool with 16 mm shoulder diameter without any pin. The tool angle is 3° and plunge depth is 0.5 mm. The rotational speeds (800, 1250, 1600 and 2000rpm) and two traverse speeds 31.5 and 63 mm/min were tried. The temperature during FSP was 876 to 903°e, to prevent any grain growth the work piece was quenched (mixture of ice & water at 600°C cooling rate) immediately after the FSP. The strain rate is the controlling parameter when the rotation speed increases from 800 to 1600 rpm, leading to finer grains. For increase in the rotation speed results in strain rate as well as in higher temperature. The former leads to a reduction in grain size, whilst the latter promotes the grain growth. Chen YC and Nakata [7] studied the SKD61 tool steel by FSP using a polycrystalline cubic boron nitride. Fine grains with a marten site structure were produced in the FSP zone, which led to the increase of the micro indentation hardness. The wear width and depth of the friction stir processed zone at the load of 1.96 N were 339µm and 42 µm of the base metal, decreased by 62% and 86%.His studies suggests that low heat input is an effective method to produce a FSP zone composed of relatively fine grain marten site structure with good tensile properties and wear characteristic .The 10 mm thick SKD tool steel FSP by PCBN consists of a 22mm in diameter convex shoulder a 5mm long probe. The forging load of the tool was 30KN. The rotational speeds were within the range of 200 to 800 rpm and the travel speeds were 0.5, 1.0 and 1.25mm/s. The hardness is the FSP zones is higher (890Hv) higher than that in the base metal (220Hv), which is caused by marten site transformation. The wear width and wear depth of the base metal are 888µm and 42µm respectively. After FSP the wear width and wear depth of the base metal is decreased to 339µm and 6µm respectively. The average coefficient of the FSP zone

(0.73) is slightly higher than that of the base metal (0.66). It is known that by the abrasive wear mechanism, the wear of the material decreases with the increasing hardness.

4. Results and Discussions

Current developments in process modelling, microstructure and properties, material specific issues, applications of friction stir processing have been addressed. Tool geometry is very important factor for producing sound welds. From the open literature, it is known that a cylindrical threaded pin and concave shoulder are widely used welding tool features. Besides, tri-fluted pins such as MX TrifuteTM and Flared-TrifuteTM have also been developed. Processing parameters, including tool rotation rate, traverse speed, spindle tilt angle, and target depth, are crucial to produce sound and defect-free processed region. It has been suggested by some researchers that FSP can be generally described as an in situ extrusion process and the stirring and mixing of material occurred only at the surface layer of the processed zone adjacent to the rotating shoulder. FSP results in significant temperature rise within and around the weld. A temperature rise of 400–500^{o}C has been recorded within the stirred zone for aluminium alloys. Intense plastic deformation and temperature rise result in significant micro structural evolution, i.e., fine recrystallized grains of 0.1–18 mm, texture, precipitate dissolution and coarsening, and residual stress with a much lower magnitude. Three different micro structural zones have been identified in friction stir processed region, i.e., nugget region experiencing intense plastic deformation and high-temperature exposure and characterized by fine and equiaxed recrystallized grains, thermo-mechanically affected region experiencing medium temperature and deformation and characterized by deformed and un-recrystallized grains, and heat-affected region experiencing only temperature and characterized by precipitate coarsening.FSP exhibits a considerable improvement in strength, ductility, fatigue and fracture toughness. FSP has found several applications for micro structural modification in metallic materials, including micro structural refinement for high- strain rate super plasticity, fabrication of surface composite on aluminium substrates, and homogenization of microstructure in nanophase aluminium alloys, metal matrix composites, and cast Al–Si alloys. Despite considerable interests in the FSP technology in past decade, the basic physical understanding of the process is lacking. Some important aspects, including material flow, tool geometry design, wear of welding tool, microstructural stability, welding of dissimilar alloys and metals, require understanding. Phases during FSP. The processing parameters exhibit significant effects on formation of surface composite layer.

1. It was observed that when the target depth is too large, the shoulder of tool pushes way all the preplaced SiC particles, and basically no surface composite is formed.
2. Too small depth was also ineffective to mix SiC particles into aluminium alloy.
3. A target depth of 2.03 mm resulted in incorporation of SiC particles into aluminium matrix.
4. The bonding of surface composite layer and substrate plate was influenced by the transverse speed. At higher transverse speed, the surface composite layer was usually separated from the aluminium ally substrate and the bonding was poor.
5. The surface composite layer appears to be very well bonded to the aluminium alloy substrate, and no defects were visible.
6. With same processing parameters and increasing the amount of preplaced SiC particles, surface composite with higher particle content were generated.
7. There are several advantages of FSP as compared to laser processing, high- energy electron beam irradiation, and casting sinter- firstly the FSP is carried out in solid state, so interfacial reaction and formation of detrimental phases are avoided, secondly, the FSP results in significant grain refinement in surface layer. Thirdly, FSP operation is relatively simple and easily controlled because no complicate high energy laser device or high- voltage electron accelerator is needed.
8. In addition, curved surfaces can be handled by changing the tool shoulder geometry.
9. Alternatively, the tool-spindle angle can be changed during processing to follow the surface curvature using a multi-axis computer- controlled machine with feedback loop.

References

[1] L. Karthikeyan, V. S. Senthilkumar, K. A. Padmanabhan, On the role of process variables in the friction stir processing of cast aluminum A319 alloy, Materials and Design. 31, 2010, 761–772

[2] K. Elangovan, V. Balasubramanian, Influences of tool pin profile and tool shoulder diameter on the formation of friction stir processing zone in AA6061 aluminium alloy, Materials and Design. 29, 2008, 362–373

[3] K. Elangovan, V. Balasubramanian, Influences of tool pin profile and welding speed on the formation of friction stir processing zone in AA2219 aluminium alloy, Journal of material processing Technology. 200, 2008 163-175.

[4] K. N. Ramesh, S. Pradeep, Vivek Pancholi, Multipass Friction-Stir Processing and its Effect on Mechanical Properties of Aluminum Alloy 5086, Metallurgical and Materials Transactions A., 2012

[5] Adem Kurt, Ilyas Uygur, ErenCete, Surface modification of aluminium by friction stir processing,Journal of Materials Processing Technology. 211, 2011, 313–317

[6] R.S. Mishra , Z.Y. Ma, I. Charit, Letter Friction stir processing: a novel technique for fabrication of surface composite, Materials Science and Engineering A 341, 2003, 307-310

[7] Y. C., K. Nakata, Evaluation of microstructure and mechanical properties in FSP SKD61 tool steel, Materials Characterization.60:1471-1475, 2009

[8] B. Zahmatkesh, M. H. Enayati, F. Karimzadeh, Tribological and microstructural evaluation of friction stir processed Al2024 alloy, Materials and Design. 31, 2010, 4891–4896

Friedmann model with viscous cosmology in modified $f(R,T)$ gravity theory

C. P. Singh [1], **Pankaj Kumar** [2]

[1,2]Department of Applied Mathematics,
Delhi Technological University (Formerly Delhi College of Engineering)
Bawana Road, Delhi-110 042, India.
[1]cpsphd@rediffmail.com
[2]pankaj.11dtu@gmail.com

arXiv:1406.4258v1 [gr-qc] 17 Jun 2014

Abstract In this paper, we introduce bulk viscosity in the formalism of modified gravity theory in which the gravitational action contains a general function $f(R,T)$, where R and T denote the Ricci scalar and the trace of the energy-momentum tensor, respectively within the framework of a flat Friedmann-Robertson-Walker model. As equation of state for prefect fluid, we take $p = (\gamma - 1)\rho$, where $0 \leq \gamma \leq 2$ and viscous term as a bulk viscosity due to isotropic model, of the form $\zeta = \zeta_0 + \zeta_1 H$, where ζ_0 and ζ_1 are constant, and H is the Hubble parameter. The exact non-singular solutions of field equations are obtained by assuming a particular form of $f(R,T) = R + 2f(T)$ with constant and time-dependent bulk viscosity. A big-rip singularity is also observed for $\gamma < 0$ at a finite value of cosmic time under certain constraints. We study all possible scenarios to analyze the behavior of the scale factor and matter density, and discuss the expansion history of the universe with deceleration parameter. It is observed that the universe accelerates or exhibits transition from decelerated phase to accelerated phase under certain constraints due to the presence of bulk viscosity.

[1]Corresponding author

1 Introduction

Recently, the modified theory of gravity has become one of the most popular candidate to understand the problem of dark energy. In literature, a number of modified theories have been discussed to explain early and late time expansion of the universe. In this context, $f(R)$ theory (R being the Ricci scalar) is the simplest and most popular modification of General Relativity (GR). The $f(R)$ theory was first introduced in [1] and later used to find a non-singular isotropic de -Sitter type cosmological solution [2](for a recent reviews of $f(R)$ gravity, see refs. [3-6]). In $f(R)$ theory, it has been suggested that the cosmic acceleration can be achieved by replacing Einstein-Hilbert action of GR with a general function $f(R)$. Many authors [7-11] have investigated several aspects of $f(R)$ gravity. The $f(R)$ theory can produce cosmic inflation, mimic behavior of dark matter and current cosmic acceleration, compatible with the observational data [12-14]. Other modified gravities like scalar Gauss-Bonnet $f(G)$ gravity [15], $f(T)$ theory [16], where T is the torsion have been proposed to overcome many problems in cosmology. Therefore, modifying the law of gravity is a possible way to explain the acceleration mechanism of the universe.

Bertolami et al. [17] generalized $f(R)$ theory by introducing an explicit coupling between arbitrary function of the Ricci scalar R and the matter Lagrangian density $\mathcal{L}_m$. It provides a non-minimal coupling between matter and geometry in a more general manner at the action level. A maximal extension of the Einstein-Hilbert Lagrangian was introduced in [18], where the Lagrangian of the gravitational field was considered to be a general function of R and $\mathcal{L}_m$. In $f(R, \mathcal{L}_m)$ theory, it is assumed that all the properties of the matter are encoded in the matter Lagrangian $\mathcal{L}_m$. Harko and Lobo [19] generalized this concept to the arbitrary coupling between matter and geometry.

Recently, Harko et al. [20] introduced another extension of GR, so called the $f(R,T)$ modified theory of gravity, where the gravitational Lagrangian is given by an arbitrary function of the Ricci scalar R and of the trace T of the stress-energy tensor. The authors suggested that the coupling of matter and geometry leads to the model to be depend on a source term representing the variation of the matter-stress-energy tensor with respect to the metric. Houndjo et al. [21] investigated $f(R,T)$ gravity models to reproduce the four known types of future finite-time singularities. Alvarenga et al. [22] tested some $f(R,T)$ gravity models through energy conditions. Pasqua et al. [23] studied a particular model $f(R,T) = \mu R + \nu T$ which describes a quintessence-like behavior and exhibits transition from decelerated to accelerated phase. Sharif and Zubair [24] considered two forms of the energy-momentum tensor of dark components and demonstrated that the equilibrium description of thermodynamics can not be achieve at the apparent horizon of Friedmann-Robertson-Walker (FRW) universe in $f(R,T)$ gravity. Azizi [25] showed the matter threading of the wormhole may satisfy the energy conditions and the effective stress-energy is responsible for violation of the null energy condition in $f(R,T)$ gravity. Chakraborty [26] incorporated conservation of stress-energy momentum tensor in the field equations and discussed the energy conditions in $f(R,T)$ gravity with perfect fluid. Recently, Singh and Singh [27] have presented the reconstruction of $f(R,T)$ gravity with perfect fluid in the framework of FRW model for two well-known scale factors.

In recent years the observations like type Ia supernovae [28-31], cosmic microwave back-

ground [32,33] and large scale structure [34,35] indicate an accelerated expansion of the universe. The investigation of cosmological models usually has the energy-momentum tensor of matter described by perfect fluid. It is important to investigate more realistic models that take into account dissipative processes due to viscosity. It is known that when neutrino decoupling occurred, the matter behaved like a viscous fluid in the early stage of the universe. The first suggestion was investigated by Misner [36] who proposed that the neutrino viscosity acting in the early era might have considerably reduced the present anisotropy of the black-body radiation during the process of evolution. Murphy [37] showed that the bulk viscosity can push the initial singularity in FRW model to the infinite past. In the context of inflation of the very early universe, it has been known since long time ago that an imperfect fluid with bulk viscosity in cosmology can produce an acceleration without the need of a cosmological constant or some scalar field. Thus, the bulk viscosity plays a very important role in the history of the universe. In the framework of homogeneous and isotropic universe, for a sufficiently large bulk viscosity, the effective pressure become negative and can explain late time acceleration of the universe. Indeed, it has been shown that for right viscosity coefficient, an accelerating cosmology can be achieved without the need of a cosmological constant [38-43]. In refs.[44-48], the bulk viscosity in cosmology has been studied in various aspects. Therefore, dissipative processes are thought to be present in any realistic theory of the evolution of the universe. At the late times, since we do not know the nature of the universe content (dark matter and dark energy components) very clearly, concerning about the bulk viscosity is reasonable and practical.

In the present paper, we study FRW model with bulk viscosity in modified $f(R,T)$ gravity theory and investigate the effect of bulk viscosity in explaining for the early and late time acceleration of the universe. The model contains the perfect fluid with bulk viscosity of the form $\zeta = \zeta_0 + \zeta_1 H$, where ζ_0 and ζ_1 are constant, and H is the Hubble parameter. The exact solutions of field equations are obtained by assuming a particular form of $f(R,T) = R + 2f(T)$, where $f(T) = \alpha T$, with constant and varying bulk viscosity. We study all possible scenarios to analyze the behavior of the scale factor and matter density and discuss the expansion history of the universe.

The paper is organized as follows. In section 2 we present the brief review of the modified $f(R,T)$ gravity theory as proposed by Harko et al. [22]. Section 3 presents the cosmological model and its field equations with a bulk viscous fluid. Section 4 is divided into two subsections 4.1 and 4.2. In 4.1 we present the solution with constant bulk viscosity for two cases 4.1.1 and 4.1.2 and the solutions with time-dependent bulk viscosity is presented in 4.2.1, 4.2.2 and 4.2.3 of section 4.2. In Section 5 we summarize our results in detail.

2 Brief review of modified $f(R,T)$ gravity theory

The $f(R,T)$ theory is a modified theory of gravity, in which the Einstein-Hilbert Lagrangian, i.e., R is replaced by an arbitrary function of the scalar curvature R and the trace T of energy-momentum tensor. So the action for $f(R,T)$ modified theory of gravity [20] in the unit $8\pi G = 1 = c$ takes the following form:

$$S = \frac{1}{2}\int d^4x\sqrt{-g}[f(R,T) + 2\mathcal{L}_m], \tag{1}$$

where g is the determinant of the metric tensor $g_{\mu\nu}$ and $\mathcal{L}_m$ the matter Lagrangian density. The energy-momentum tensor $T_{\mu\nu}$, defined from matter Lagrangian density $\mathcal{L}_m$ is given by

$$T_{\mu\nu} = -\frac{2}{\sqrt{-g}}\frac{\delta(\sqrt{-g}\,\mathcal{L}_m)}{\delta g^{\mu\nu}}, \tag{2}$$

and its trace by $T = g^{\mu\nu}T_{\mu\nu}$. By assuming that the matter Lagrangian density $\mathcal{L}_m$ depends only on the metric tensor components $g_{\mu\nu}$, not on its derivatives, we obtain

$$T_{\mu\nu} = g_{\mu\nu}\mathcal{L}_m - 2\frac{\partial\mathcal{L}_m}{\partial g^{\mu\nu}}. \tag{3}$$

The equations of motion by varying the action(1) with respect to metric tensor are

$$f_R(R,T)R_{\mu\nu} - \frac{1}{2}f(R,T)g_{\mu\nu} + (g_{\mu\nu}\Box - \nabla_\mu\nabla_\nu)f_R(R,T) = T_{\mu\nu} - f_T(R,T)T_{\mu\nu} - f_T(R,T)\ominus_{\mu\nu}, \tag{4}$$

where f_R and f_T denote the derivatives of $f(R,T)$ with respect to R and T, respectively. Here, ∇_μ is covariant derivative and $\Box \equiv \nabla_\mu\nabla^\mu$ is the d'Alembert operator and $\ominus_{\mu\nu}$ is defined by

$$\ominus_{\mu\nu} \equiv g^{\alpha\beta}\frac{\delta T_{\alpha\beta}}{\delta g^{\mu\nu}}. \tag{5}$$

Using (3) into (5), we obtain

$$\ominus_{\mu\nu} = -2T_{\mu\nu} + g_{\mu\nu}\mathcal{L}_m - 2g^{\alpha\beta}\frac{\partial^2\mathcal{L}_m}{\partial g^{\mu\nu}\partial g^{\alpha\beta}}. \tag{6}$$

Since, the field equations of $f(R,T)$ depend on $\ominus_{\mu\nu}$, i.e., on the physical nature of the matter, therefore, several models corresponding to different form of $f(R,T)$ would generate depending on the nature of the matter source. In what follows, we assume

$$f(R,T) = R + 2f(T). \tag{7}$$

where $f(T)$ is an arbitrary function of the trace of energy-momentum tensor of matter. Using (7), one can re-write the gravitational field equations defined in (4) as

$$R_{\mu\nu} - \frac{1}{2}Rg_{\mu\nu} = T_{\mu\nu} - 2(T_{\mu\nu} + \ominus_{\mu\nu})f'(T) + f(T)g_{\mu\nu}, \tag{8}$$

which is considered as the field equations of $f(R,T)$ gravity. Here, a prime stands for derivative of $f(T)$ with respect to T.

The main issue now arises on the content of the universe through the energy-momentum tensor and consequently on the matter Lagrangian $\mathcal{L}_m$ and the trace of the energy-momentum tensor.

3 Metric and field equations

We assume the spatially flat Friedmann-Robertson-Walker (FRW) metric

$$ds^2 = dt^2 - a^2(t)(dx^2 + dy^2 + dz^2), \tag{9}$$

where $a(t)$ is the cosmic scale factor.

In comoving coordinates, the components of the four-velocity u^μ are $u^0 = 1$, $u^i = 0$. With the help of the projection tensor $h_{\mu\nu} = g_{\mu\nu} + u_\mu u_\nu$, we have the energy momentum tensor for a viscous fluid [49, 50]

$$T_{\mu\nu} = \rho u_\mu u_\nu - \bar{p} h_{\mu\nu}, \tag{10}$$

where $\bar{p}$ denotes the effective pressure. In the first order thermodynamics theory of Eckart [51], $\bar{p}$ is given by

$$\bar{p} = p - 3H\zeta. \tag{11}$$

Thus, for large ζ it is possible for negative pressure term to dominate and an accelerating cosmology to ensue. Here, $H = \dot{a}/a$ is Hubble parameter, where an overdot means differentiation with respect to t, and ρ, p and ζ are the energy density, the isotropic pressure and coefficient of bulk viscosity, respectively. Therefore, the Lagrangian density may be chosen as $\mathcal{L}_m = -\bar{p}$, and the tensor $\ominus_{\mu\nu}$ in (6) is given by

$$\ominus_{\mu\nu} = -2T_{\mu\nu} - \bar{p} g_{\mu\nu}. \tag{12}$$

Using (10) and (12), the field equations (8) for bulk viscous fluid become

$$R_{\mu\nu} - \frac{1}{2} R g_{\mu\nu} = T_{\mu\nu} + 2f'(T)T_{\mu\nu} + \left(2\bar{p}f'(T) + f(T)\right)\, g_{\mu\nu}. \tag{13}$$

The field equations (13) with the particular choice of the function $f(T) = \alpha T$, where α is a constant [see, Harko et al.[20]] for the metric (9) yield

$$3H^2 = \rho + 2\alpha(\rho + \bar{p}) + \alpha T, \tag{14}$$

$$2\dot{H} + 3H^2 = -\bar{p} + \alpha T, \tag{15}$$

where $T = \rho - 3\bar{p}$. We have two independent equations (14) and (15), and four unknown variables, namely H, ρ, p and ζ to be solved as functions of time. In the following section we choose equation of state and bulk viscosity and try to solve for H.

4 Solution of field equations

From (14) and (15) we get a single evolution equation for H:

$$2\dot{H} + (1 + 2\alpha)(\rho + p) - 3(1 + 2\alpha)\zeta H = 0. \tag{16}$$

Thus, if an equation of state (EoS) connecting p and ρ is chosen in the form

$$p = (\gamma - 1)\rho, \tag{17}$$

where γ is a constant known as the EoS parameter lying in the range $0 \leq \gamma \leq 2$, then equation (16) can be solved for any particular choice of ζ.

Let us assume the bulk viscosity ζ of the form [48, 52, 53]:

$$\zeta = \zeta_0 + \zeta_1 H, \tag{18}$$

where ζ_0 and ζ_1 are constant. Using (11), (17) and (18) into (14), we have

$$\rho = \frac{3H[(1-\alpha\zeta_1)H - \alpha\zeta_0]}{1+4\alpha-\alpha\gamma}. \tag{19}$$

4.1 Cosmology with non-viscous fluid

In this case, where $\zeta = 0$, equation (16), with the help of (17), (18) and (19), reduces to

$$\dot{H} + \frac{3}{2}\frac{\gamma(1+2\alpha)H^2}{(1+4\alpha-\alpha\gamma)} = 0. \tag{20}$$

On solving (20) for $\gamma \neq 0$, we get

$$H = \frac{1}{[C + \frac{3(1+2\alpha)\gamma}{2(1+4\alpha-\alpha\gamma)}\, t]}, \tag{21}$$

where C is a constant of integration. Using $H = \dot{a}/a$, equation (21) gives the power-law expansion for the scale factor of the form

$$a = D\left[C + \frac{3\gamma(1+2\alpha)}{2(1+4\alpha-\alpha\gamma)}\, t\right]^{\frac{2(1+4\alpha-\alpha\gamma)}{3\gamma(1+2\alpha)}}, \quad (\alpha \neq -1/2), \tag{22}$$

where D is another constant of integration. This scale factor can be rewritten as

$$a = a_0\left[1 + \frac{3\gamma(1+2\alpha)H_0}{2(1+4\alpha-\alpha\gamma)}\, t\right]^{\frac{2(1+4\alpha-\alpha\gamma)}{3\gamma(1+2\alpha)}}, \tag{23}$$

where $H = H_0 > 0$ at $t = t_0$. The cosmic time t_0 corresponds to the time where dark component begins to become dominant. The energy density is given by

$$\rho = \rho_0\left[1 + \frac{3\gamma(1+2\alpha)H_0}{2(1+4\alpha-\alpha\gamma)}\, t\right]^{-2}, \tag{24}$$

where $\rho_0 = 3H_0^2/(1+4\alpha-\alpha\gamma)$. For $\gamma < 0$ we get a big rip singularity at finite time $t_{br} = -2(1+4\alpha-\alpha\gamma)/3\gamma(1+2\alpha)H_0 > t_0$ as the scale factor and energy density tend to infinite at this time.

The cosmological inflation or the accelerated expansion of the universe is characterized by the deceleration parameter q defined by $q = -\frac{\ddot{a}a}{\dot{a}^2}$. In this case, we get

$$q = \frac{3\gamma(1+2\alpha)}{2(1+4\alpha-\alpha\gamma)} - 1, \tag{25}$$

which is constant through out the evolution of the universe. As we know that $q > 0$ determines expansion of universe with decelerated rate, $q < 0$ describes the accelerated expansion of the universe and $q = 0$ gives the coasting or marginal inflation. Thus, for suitable values of α and γ we can obtain decelerated and accelerated expansion of the universe. In this case, the model does not exhibit phase transition due to constant value of q.

For $\gamma = 0$ i.e. $p = -\rho$, equation (20) gives $H = H_0$, which corresponds to $a = a_0 e^{H_0 t}$ i.e. de-Sitter type expansion of universe. Both ρ and p are constant and $q = -1$ through out the evolution of the universe.

4.2 Cosmology with viscous fluid

On the thermodynamical grounds, ζ in (18) is conventionally chosen to be a positive quantity and may depend on the cosmic time t, or the scale factor a, or the energy density ρ. Therefore, different forms of viscosity can be used to make (16) solvable numerically or exactly. We investigate in the following some different choices for ζ.

4.2.1 Solution with constant bulk viscosity

From bulk viscosity point of view, the simplest case is thought to be a constant bulk viscosity. Therefore, assuming $\zeta_1 = 0$ in (18), we get $\zeta = \zeta_0$. In this case (19) reduces to

$$\rho = \frac{3H^2 - 3\alpha\zeta_0 H}{(1 + 4\alpha - \alpha\gamma)}. \tag{26}$$

Substituting (17) and (26) into (16), we get

$$\dot{H} + \frac{3}{2}\frac{\gamma(1+2\alpha)H}{(1+4\alpha-\alpha\gamma)}\left[H - \frac{\zeta_0(1+4\alpha)}{\gamma}\right] = 0. \tag{27}$$

In what follows we solve (27) for $\gamma \neq 0$ and $\gamma = 0$ separately.

Case I: Solution for $\gamma \neq 0$

Solving (27) for $\gamma \neq 0$, we find

$$H = \frac{e^{\frac{3}{2}\frac{(1+2\alpha)(1+4\alpha)\zeta_0}{(1+4\alpha-\alpha\gamma)}\,t}}{c_0 + \frac{\gamma}{(1+4\alpha)\zeta_0}\,e^{\frac{3}{2}\frac{(1+2\alpha)(1+4\alpha)\zeta_0}{(1+4\alpha-\alpha\gamma)}\,t}}, \tag{28}$$

where c_0 is a constant of integration. Using $H = \dot{a}/a$, the scale factor in terms of t is given by

$$a = c_1\left[c_0 + \frac{\gamma}{(1+4\alpha)\zeta_0}\,e^{\frac{3}{2}\frac{(1+2\alpha)(1+4\alpha)\zeta_0}{(1+4\alpha-\alpha\gamma)}\,t}\right]^{\frac{2}{3}\frac{(1+4\alpha-\alpha\gamma)}{\gamma(1+2\alpha)}}, \tag{29}$$

where $c_1 > 0$ is another integration constant. This scale factor may be rewritten as

$$a(t) = a_0\left[1 + \frac{\gamma H_0}{(1+4\alpha)\zeta_0}\left(e^{\frac{3}{2}\frac{(1+2\alpha)(1+4\alpha)\zeta_0}{(1+4\alpha-\alpha\gamma)}\,t} - 1\right)\right]^{\frac{2}{3}\frac{(1+4\alpha-\alpha\gamma)}{\gamma(1+2\alpha)}}. \tag{30}$$

The energy density can be calculated as

$$\rho = \frac{3H_0}{(1+4\alpha-\alpha\gamma)}\left[\frac{e^{\frac{3}{2}\frac{(1+2\alpha)(1+4\alpha)\zeta_0}{(1+4\alpha-\alpha\gamma)}\,t}}{1+\frac{\gamma H_0}{(1+4\alpha)\zeta_0}\left(e^{\frac{3}{2}\frac{(1+2\alpha)(1+4\alpha)\zeta_0}{(1+4\alpha-\alpha\gamma)}\,t}-1\right)}\right]$$
$$\left[\frac{H_0\, e^{\frac{3}{2}\frac{(1+2\alpha)(1+4\alpha)\zeta_0}{(1+4\alpha-\alpha\gamma)}\,t}}{1+\frac{\gamma H_0}{(1+4\alpha)\zeta_0}\left(e^{\frac{3}{2}\frac{(1+2\alpha)(1+4\alpha)\zeta_0}{(1+4\alpha-\alpha\gamma)}\,t}-1\right)}-\alpha\,\zeta_0\right]. \tag{31}$$

For $0 \leq \gamma \leq 2$, viscous solution satisfies the dominant energy condition (DEC), i.e., $\rho+p \geq 0$. If $\gamma < 0$ we have a big rip singularity at a finite value of cosmic time

$$t_{br} = \frac{2(1+4\alpha-\alpha\gamma)}{3(1+2\alpha)(1+4\alpha)\zeta_0}\, ln\left(1-\frac{(1+4\alpha)\zeta_0}{\gamma H_0}\right) > t_0. \tag{32}$$

One may observe that there is a violation of DEC. The energy density grows up to infinity at a finite time $t > t_0$, which leads to a big rip singularity characterized by the scale factor and Hubble parameter blowing up to infinity at this finite time. Therefore, there are cosmological models with viscous fluid which present in the development of this sudden future singularity.

The deceleration parameter is given by

$$q = \frac{\frac{3}{2}\frac{(1+2\alpha)}{(1+4\alpha-\alpha\gamma)}[\gamma-\frac{(1+4\alpha)\zeta_0}{H_0}]}{e^{\frac{3}{2}\frac{(1+2\alpha)(1+4\alpha)\zeta_0}{(1+4\alpha-\alpha\gamma)}\,t}}-1, \tag{33}$$

which is time-dependent in contrast to perfect fluid. Thus, the constant bulk viscous coefficient generates time-dependent q which may also describes the transition phases of the universe along with deceleration or acceleration of the universe. Let us observe the variation of q with bulk viscous coefficient ζ_0 for various ranges of α in different phases of evolution of the universe for $\gamma > 0$, which are presented in the following tables 1-3.

Table. 1 : Variation of q for $\gamma = 2/3$.

Range of α	Constraints on ζ_0	q	Evolution of Universe
$\alpha > 0$	for all $\zeta_0 > 0$	negative	accelerated expansion
$-0.25 < \alpha < 0$	$0 < \zeta_0 < \frac{-8\alpha H_0}{9(1+2\alpha)(1+4\alpha)}$	+ve to -ve	transition from dec. to acc.
	$\zeta_0 \geq \frac{-8\alpha H_0}{9(1+2\alpha)(1+4\alpha)}$	negative	accelerated expansion
$-0.30 < \alpha \leq -0.25$	for all $\zeta_0 > 0$	positive	decelerated expansion
$-0.50 \leq \alpha < -0.30$	for all $\zeta_0 > 0$	negative	accelerated expansion
$\alpha < -0.50$	$0 < \zeta_0 < \frac{-8\alpha H_0}{9(1+2\alpha)(1+4\alpha)}$	-ve to +ve	transition from acc. to dec.
	$\zeta_0 \geq \frac{-8\alpha H_0}{9(1+2\alpha)(1+4\alpha)}$	positive	decelerated expansion

Table. 2 : Variation of q for $\gamma = 4/3$.

Range of α	Constraints on ζ_0	q	Evolution of Universe
$\alpha > -0.25$ $(\alpha \neq 0)$	$0 < \zeta_0 < \frac{2(3+4\alpha)H_0}{9(1+4\alpha)(1+2\alpha)}$	+ve to -ve	transition from dec. to acc.
	$\zeta_0 \geq \frac{2(3+4\alpha)H_0}{9(1+4\alpha)(1+2\alpha)}$	negative	accelerated expantion
$-0.375 < \alpha \leq -0.25$	for all $\zeta_0 > 0$	positive	decelerated expansion
$-.50 \leq \alpha < -0.375$	for all $\zeta_0 > 0$	negative	accelerated expansion
$\alpha < -0.50$	$0 < \zeta_0 < \frac{2(3+4\alpha)H_0}{9(1+4\alpha)(1+2\alpha)}$	-ve to +ve	transition from acc. to dec.
	$\zeta_0 \geq \frac{2(3+4\alpha)H_0}{9(1+4\alpha)(1+2\alpha)}$	positive	decelerated expansion

Table. 3 : Variation of q for $\gamma = 1$.

Range of α	Constraints on ζ_0	q	Evolution of Universe
$\alpha > -0.25$ $(\alpha \neq 0)$	$0 < \zeta_0 < \frac{H_0}{3(1+2\alpha)(1+4\alpha)}$	+ve to -ve	transition from dec. to acc.
	$\zeta_0 \geq \frac{H_0}{3(1+2\alpha)(1+4\alpha)}$	negative	accelerated expantion
$-0.33 < \alpha \leq -0.25$	for all $\zeta_0 > 0$	positive	decelerated expansion
$-0.50 \leq \alpha < -0.33$	for all $\zeta_0 > 0$	negative	accelerated expansion
$\alpha < -0.50$	$0 < \zeta_0 < \frac{H_0}{3(1+2\alpha)(1+4\alpha)}$	-ve to +ve	transition from acc. to dec.
	$\zeta_0 \geq \frac{H_0}{3(1+2\alpha)(1+4\alpha)}$	positive	decelerated expansion

We observe from the above tables 1-3 that the universe accelerates through out the evolution when $\alpha > 0$ for any $\zeta_0 > 0$ in inflationary phase where as it shows transition from decelerated phase to accelerated phase when $\alpha > -0.25$ for smaller values of ζ_0 and acceleration for larger values of ζ_0 in radiation and matter-dominated phases. It is to be noted here that the larger values of ζ_0 makes the effective pressure more negative to accelerate the universe through out the evolution. We find that the universe decelerates in $-0.33 < \alpha \leq -0.25$ and accelerates in $-0.50 \leq \alpha < -0.33$ for $\zeta_0 > 0$ in all the three phases. When $\alpha < -0.50$, then model shows transition from acceleration to deceleration phase for small values of ζ_0 and decelerates for large values of ζ_0. In conclusion we can say that the universe accelerates or shows transition from decelerated phase to accelerated phase for $\alpha > -0.25$ with constant viscous term in all phases of its evolution.

For $\gamma < 0$ where the solution has big rip singularity, q is always negative for $\alpha > 0$ during any cosmic time.

Case II: Solution for $\gamma = 0$

In this case, (27) reduces to

$$\dot{H} - \frac{3}{2}(1 + 2\alpha)\zeta_0 H = 0, \tag{34}$$

which gives the solution for H in terms of t as

$$H = c_2 e^{\frac{3}{2}(1+2\alpha)\zeta_0 t}, \tag{35}$$

where c_2 is a constant of integration. The scale factor in terms of t is given by

$$a = c_3 e^{\frac{2c_2}{3(1+2\alpha)\zeta_0} e^{\frac{3}{2}(1+2\alpha)\zeta_0 t}}, \tag{36}$$

where $c_3 > 0$ is another constant of integration. This scale factor may be rewritten as

$$a = a_0 e^{\frac{2H_0}{3(1+2\alpha)\zeta_0}(e^{\frac{3}{2}(1+2\alpha)\zeta_0 t}-1)}. \tag{37}$$

We find that the scale factor shows the superinflation in the presence of constant bulk viscous coefficient where as it has de-Sitter expansion in non-viscous case. The energy density is given by

$$\rho = \frac{3H_0 e^{\frac{3}{2}(1+2\alpha)\zeta_0 t}}{(1+4\alpha)}\left[H_0 e^{\frac{3}{2}(1+2\alpha)\zeta_0 t} - \alpha\zeta_0\right]. \tag{38}$$

We observe that ρ varies with time in contrast to perfect fluid solution where it is constant. Both $a(t)$ and ρ tend to constant at $t = 0$ and tend to infinity at $t \to \infty$. In this case the deceleration parameter is given by

$$q = -\frac{3\zeta_0(1+2\alpha)}{2H_0}\, e^{-\frac{3}{2}(1+2\alpha)\zeta_0 t} - 1, \tag{39}$$

which is time-dependent. We study the variation of q with bulk viscous coefficient ζ_0 for various ranges of α, which are summarized in table 4. From table 4 we observe that q is always negative for $\alpha \geq -0.50$ and the universe accelerates for all values of $\zeta_0 > 0$. The value of q varies from negative to positive, that is, the universe shows transition from accelerated phase to decelerated phase for small values of ζ_0 and always decelerate for large values of ζ_0.

Table. 4 : Variation of q for $\gamma = 0$.

Range of α	Constraints on ζ_0	q	Evolution of Universe
$\alpha \geq -0.50$ $(\alpha \neq 0)$	for all $\zeta_0 > 0$	negative	accelerated expansion
$\alpha < -0.50$	$0 < \zeta_0 < \frac{-2H_0}{3(1+2\alpha)}$	-ve to +ve	transition from acc. to dec.
	$\zeta_0 \geq \frac{2H_0}{3(1+2\alpha)}$	positive	decelerated expansion

4.2.2 Solution with variable bulk viscosity

In this section, we present the solution for $\zeta_0 = 0$ and $\zeta_0 \neq 0$.

Case I: $\zeta_0 = 0$

For $\zeta_0 = 0$, the form of bulk viscosity assumed in (18) reduces to $\zeta = \zeta_1 H$ [54]. This is the most interesting case. As ζ is assumed to be positive, and for this the constant ζ_1 must be positive.

Using (17) and (19) into (16) we get

$$\dot{H} + \frac{3}{2}\frac{(1+2\alpha)(\gamma - \zeta_1 - 4\alpha\zeta_1)}{(1+4\alpha-\alpha\gamma)}H^2 = 0. \tag{40}$$

Solving (40), the Hubble parameter can be obtained in terms of t for any value of γ in the range $0 \leq \gamma \leq 2$, except $\gamma \neq (1+4\alpha)\zeta_1$ and $\alpha \neq -1/2$ as

$$H = \frac{1}{[\frac{3(1+2\alpha)(\gamma-\zeta_1-4\alpha\zeta_1)}{2(1+4\alpha-\alpha\gamma)}\ t + c_4]}, \tag{41}$$

where c_4 is a constant of integration. Correspondingly, the scale factor in terms of t is given by

$$a = c_5 \left[c_4 + \frac{3(1+2\alpha)(\gamma-\zeta_1-4\alpha\zeta_1)}{2(1+4\alpha-\alpha\gamma)}\ t\right]^{\frac{2(1+4\alpha-\alpha\gamma)}{3(1+2\alpha)(\gamma-\zeta_1-4\alpha\zeta_1)}}, \tag{42}$$

where $c_5 > 0$ is another constant of integration. We find that the form $\zeta = \zeta_1 H$ yields a power-law expansion for the scale factor. This scale factor may be rewritten as

$$a = a_0 \left[1 + \frac{3(1+2\alpha)(\gamma-\zeta_1-4\alpha\zeta_1)H_0}{2(1+4\alpha-\alpha\gamma)}\ (t-t_0)\right]^{\frac{2(1+4\alpha-\alpha\gamma)}{3(1+2\alpha)(\gamma-\zeta_1-4\alpha\zeta_1)}}, \tag{43}$$

where $H = H_0$ at $t = t_0$ and t_0 corresponds to the time where dark component begins to dominant, i.e., describes the present value. The energy density and bulk viscous coefficient are respectively given by

$$\rho = \frac{3(1-\alpha\zeta_1)H_0^2}{(1+4\alpha-\alpha\gamma)} \left[1 + \frac{3(1+2\alpha)(\gamma-\zeta_1-4\alpha\zeta_1)H_0}{2(1+4\alpha-\alpha\gamma)}\ (t-t_0)\right]^{-2}, \tag{44}$$

$$\zeta = \zeta_1 H_0 \left[1 + \frac{3(1+2\alpha)(\gamma-\zeta_1-4\alpha\zeta_1)H_0}{2(1+4\alpha-\alpha\gamma)}\ (t-t_0)\right]^{-1}. \tag{45}$$

In this case we get deceleration parameter as

$$q = \frac{3(1+2\alpha)(\gamma-\zeta_1-4\alpha\zeta_1)}{2(1+4\alpha-\alpha\gamma)} - 1, \tag{46}$$

which is constant. The sign of q depends on the values of parameters γ, α and ζ_1. It is always negative for $\gamma \leq 0$, $\alpha > 0$ and $\zeta_1 > 0$.

If we demand to have the occurrence of a big rip in the future cosmic time then we have the following constraints on the parameters α, ζ_1 and γ

$$\zeta_1(1+4\alpha) > \gamma, \tag{47}$$

which leads the scale factor and energy density tending to infinity at a finite time

$$t_{br} = \frac{2(1+4\alpha-\alpha\gamma)}{3(1+2\alpha)(\zeta_1+4\alpha\zeta_1-\gamma)} H_0^{-1}. \tag{48}$$

We can observe from (43) and (44) that energy density of the dark component increases with scale factor for $\zeta_1(1+4\alpha) > \gamma$.

Case II: $\zeta_0 \neq 0$

Using (17), (18) and (19) into (16) we get

$$\dot{H} + \frac{3}{2}\frac{(1+2\alpha)(\gamma-\zeta_1-4\alpha\zeta_1)}{1+4\alpha-\alpha\gamma}H\left[H - \frac{(1+4\alpha)\zeta_0}{\gamma-\zeta_1-4\alpha\zeta_1}\right] = 0. \tag{49}$$

Solving (49), we find the following solution for any value of γ in the range $0 \leq \gamma \leq 2$, except $\gamma \neq (\zeta_1 + 4\alpha\zeta_1)$ and $\alpha \neq -1/2$ as

$$H = \frac{e^{\frac{3\zeta_0(1+4\alpha)(1+2\alpha)}{2(1+4\alpha-\alpha\gamma)}t}}{c_6 + \frac{(\gamma-\zeta_1-4\alpha\zeta_1)}{(1+4\alpha)\zeta_0}e^{\frac{3\zeta_0(1+4\alpha)(1+2\alpha)}{2(1+4\alpha-\alpha\gamma)}t}}, \tag{50}$$

where c_6 is constant of integration. The scale factor in terms of t is given by

$$a = c_7\left[c_6 + \frac{(\gamma-\zeta_1-4\alpha\zeta_1)}{(1+4\alpha)\zeta_0}\, e^{\frac{3}{2}\frac{(1+2\alpha)(1+4\alpha)\zeta_0}{(1+4\alpha-\alpha\gamma)}\,t}\right]^{\frac{2(1+4\alpha-\alpha\gamma)}{3(\gamma-\zeta_1-4\alpha\zeta_1)(1+2\alpha)}}, \tag{51}$$

where $c_7 > 0$ is a constant of integration. This scale factor may be rewritten as

$$a = a_0\left[1 + \frac{H_0(\gamma-\zeta_1-4\alpha\zeta_1)}{(1+4\alpha)\zeta_0}\,\left(e^{\frac{3}{2}\frac{(1+2\alpha)(1+4\alpha)\zeta_0}{(1+4\alpha-\alpha\gamma)}\,t} - 1\right)\right]^{\frac{2(1+4\alpha-\alpha\gamma)}{3(\gamma-\zeta_1-4\alpha\zeta_1)(1+2\alpha)}}. \tag{52}$$

The energy density ρ and bulk viscosity ζ can be calculated as

$$\begin{aligned}\rho &= \frac{3H_0}{(1+4\alpha-\alpha\gamma)}\frac{e^{\frac{3}{2}\frac{(1+2\alpha)(1+4\alpha)\zeta_0}{(1+4\alpha-\alpha\gamma)}\,t}}{\left[1 + \frac{(\gamma-\zeta_1-4\alpha\zeta_1)H_0}{(1+4\alpha)\zeta_0}\,\left(e^{\frac{3}{2}\frac{(1+2\alpha)(1+4\alpha)\zeta_0}{(1+4\alpha-\alpha\gamma)}\,t} - 1\right)\right]} \\ &\left[\frac{(1-\alpha\zeta_0)H_0\, e^{\frac{3}{2}\frac{(1+2\alpha)(1+4\alpha)\zeta_0}{(1+4\alpha-\alpha\gamma)}\,t}}{1 + \frac{(\gamma-\zeta_1-4\alpha\zeta_1)H_0}{(1+4\alpha)\zeta_0}\,\left(e^{\frac{3}{2}\frac{(1+2\alpha)(1+4\alpha)\zeta_0}{(1+4\alpha-\alpha\gamma)}\,t} - 1\right)} - \alpha\,\zeta_0\right],\end{aligned} \tag{53}$$

$$\zeta = \zeta_0 + \zeta_1\left[\frac{H_0\, e^{\frac{3\zeta_0(1+4\alpha)(1+2\alpha)}{2(1+4\alpha-\alpha\gamma)}t}}{1 + \frac{H_0(\gamma-\zeta_1-4\alpha\zeta_1)}{(1+4\alpha)\zeta_0}\left(e^{\frac{3\zeta_0(1+4\alpha)(1+2\alpha)}{2(1+4\alpha-\alpha\gamma)}t} - 1\right)}\right]. \tag{54}$$

With the constraint given in (47) we get big rip singularity at

$$t_{br} = \frac{2(1+4\alpha-\alpha\gamma)}{3(1+2\alpha)(1+4\alpha)\zeta_0}\; ln\left(1 + \frac{(1+4\alpha)\zeta_0}{H_0(\zeta_1+4\alpha\zeta_1-\gamma)}\right). \tag{55}$$

In this case the deceleration parameter is given by

$$q = \frac{\frac{3}{2}\frac{(1+2\alpha)}{(1+4\alpha-\alpha\gamma)}[(\gamma-\zeta_1-4\alpha\zeta_1) - \frac{(1+4\alpha)\zeta_0}{H_0}]}{e^{\frac{3}{2}\frac{(1+2\alpha)(1+4\alpha)\zeta_0}{(1+4\alpha-\alpha\gamma)}\,t}} - 1, \tag{56}$$

which shows that q is time-dependent. Therefore, we study the variation of q with bulk viscous coefficient $\zeta_0 + \zeta_1 H$ for various ranges of α in different phases of evolution of the universe, which are summarized in tables 5-8.

Table. 5 : Variation of q for $\gamma = 2/3$.

Range of α	Constraints on ζ_0 and ζ_1	q	Evolution of Universe
$\alpha > 0$	for all $\zeta_0 > 0$ and $\zeta_1 > 0$	negative	accelerated expansion
$-0.25 < \alpha < 0$	$0 < (\zeta_0 + H_0\zeta_1) < \frac{-8\alpha H_0}{9(1+2\alpha)(1+4\alpha)}$	+ve to -ve	transition from dec. to acc.
	$0 < (\zeta_0 + H_0\zeta_1) \geq \frac{-8\alpha H_0}{9(1+2\alpha)(1+4\alpha)}$	negative	accelerated expansion
$-0.30 < \alpha \leq -0.25$	for all $\zeta_0 > 0$ and $\zeta_1 > 0$	positive	decelerated expansion
$-0.50 \leq \alpha < -0.30$	for all $\zeta_0 > 0$ and $\zeta_1 > 0$	negative	accelerated expansion
$\alpha < -0.50$	$0 < (\zeta_0 + H_0\zeta_1) < \frac{-8\alpha H_0}{9(1+2\alpha)(1+4\alpha)}$	-ve to +ve	transition from acc. to dec.
	$0 < (\zeta_0 + H_0\zeta_1) \geq \frac{-8\alpha H_0}{9(1+2\alpha)(1+4\alpha)}$	positive	decelerated expansion

Table. 6 : Variation of q for $\gamma = 4/3$.

Range of α	Constraints on ζ_0 and ζ_1	q	Evolution of Universe
$\alpha > -0.25$ $(\alpha \neq 0)$	$0 < (\zeta_0 + H_0\zeta_1) < \frac{2(3+4\alpha)H_0}{9(1+2\alpha)(1+4\alpha)}$	+ve to -ve	transition from dec. to acc.
	$0 < (\zeta_0 + H_0\zeta_1) \geq \frac{2(3+4\alpha)H_0}{9(1+2\alpha)(1+4\alpha)}$	negative	accelerated expantion
$-0.375 < \alpha \leq -0.25$	for all $0 < (\zeta_0 + H_0\zeta_1)$	positive	decelerated expansion
$-0.50 \leq \alpha < -0.375$	for all $0 < (\zeta_0 + H_0\zeta_1)$	negative	accelerated expansion
$\alpha < -0.50$	$0 < (\zeta_0 + H_0\zeta_1) < \frac{2(3+4\alpha)H_0}{9(1+2\alpha)(1+4\alpha)}$	-ve to +ve	transition from acc. to dec.
	$0 < (\zeta_0 + H_0\zeta_1) \geq \frac{2(3+4\alpha)H_0}{9(1+2\alpha)(1+4\alpha)}$	positive	decelerated expansion

Table. 7 : Variation of q for $\gamma = 1$.

Range of α	Constraints on ζ_0 and ζ_1	q	Evolution of Universe
$\alpha > -0.25$ $(\alpha \neq 0)$	$0 < (\zeta_0 + H_0\zeta_1) < \frac{H_0}{3(1+2\alpha)(1+4\alpha)}$	+ve to -ve	transition from dec. to acc.
	$(\zeta_0 + H_0\zeta_1) \geq \frac{H_0}{3(1+2\alpha)(1+4\alpha)}$	negative	accelerated expantion
$-0.33 < \alpha \leq -0.25$	for all $\zeta_0 > 0$ and $\zeta_1 > 0$	positive	decelerated expansion
$-0.50 \leq \alpha < -0.33$	for all $\zeta_0 > 0$ and $\zeta_1 > 0$	negative	accelerated expansion
$\alpha < -0.50$	$0 < (\zeta_0 + H_0\zeta_1) < \frac{H_0}{3(1+2\alpha)(1+4\alpha)}$	-ve to +ve	transition from acc. to dec.
	$(\zeta_0 + H_0\zeta_1) \geq \frac{H_0}{3(1+2\alpha)(1+4\alpha)}$	positive	decelerated expansion

Table. 8 : Variation of q for $\gamma = 0$.

Range of α	Constraints on ζ_0 and ζ_1	q	Evolution of Universe
$\alpha \geq -0.50$ $(\alpha \neq 0)$	for all $\zeta_0 > 0$ and $\zeta_1 > 0$	negative	accelerated expansion
$\alpha < -0.50$	$0 < \zeta_0 + H_0\zeta_1 < -\frac{2H_0}{3(1+2\alpha)}$	-ve to +ve	transition from acc. to dec.
	$0 < \zeta_0 + H_0\zeta_1 \geq -\frac{2H_0}{3(1+2\alpha)}$	positive	decelerated expansion

We observe from the above tables 5-8 that the universe accelerates through out the evolution when $\alpha > 0$ for any positive values of ζ_0 and ζ_1 in inflationary phase where as it shows

transition from decelerated phase to accelerated phase when $\alpha > -0.25$ for smaller values of $(\zeta_0 + H_0\zeta_1)$ and shows acceleration for larger values of $(\zeta_0 + H_0\zeta_1)$ in radiation and matter-dominated phases. It is due to the fact that the larger values of ζ_0 or ζ_1 or both make the effective pressure more negative to accelerate the universe through out the evolution. We find that the universe decelerates in $-0.33 < \alpha \leq -0.25$ and accelerates in $-0.50 \leq \alpha < -0.33$ for positive values of ζ_0 and ζ_1 in the phases where $\gamma = 1,\ 2/3,$ and $4/3$. For $\gamma = 0$ we observe that universe shows accelerated expansion for positive values of $\zeta_0,\ \zeta_1$ and $\alpha \geq -0.50$. When $\alpha < -0.50$, then model shows transition from acceleration to deceleration phase for small values of $\zeta_0 + H_0\zeta_1$ and decelerates for large values of $\zeta_0 + H_0\zeta_1$ for all phases.

For $\zeta_1(1+4\alpha) > \gamma$ where the model has big rip singularity, q is always negative for $\alpha > 0$ during any cosmic time. We also see from (40) and (49) that $\dot{H} = 0$ for $\zeta_1(1 + 4\alpha) = \gamma$ or $\alpha = -1/2$, which shows de -Sitter expansion of scale factor in both cases. The solutions for $\gamma = 0$ can be obtained directly from (43) and (52), and the big rip singularity can be observed at $t_{br} = 2/[3(1 + 2\alpha)\zeta_1 H_0] > t_0$ in case I and $t_{br} = \frac{2}{3(1+2\alpha)\zeta_0}\ ln\left(1 + \frac{\zeta_0}{H_0\zeta_1}\right) > t_0$ in case II, respectively.

5 Conclusion

In this paper, we have extensively studied the effects of viscous fluid in $f(R,T)$ gravity within the framework of a flat FRW model. We have investigated the dissipative processes of the standard Eckart theory of relativistic irreversible thermodynamics. We have studied all possible scenarios to analyze the behavior of the scale factor and matter density. We have discussed the expansion history of the universe with and without bulk viscosity. We summarize the results as follows:

In case of perfect fluid distribution as presented in section 4.1, a power-law expansion for the scale factor has been obtained for $\gamma \neq 0$. It has found that the energy density decreases with time and the deceleration parameter is constant throughout the evolution. For $\gamma = 0$ i.e. $p = -\rho$, we have de Sitter solution of scale factor and both p and ρ are constant. For $\gamma < 0$ there is a big rip singularity at a finite value of cosmic time describing the phantom cosmology.

In case of viscous cosmology, we have explored bulk viscous model composed by perfect fluid with bulk viscosity of the form $\zeta = \zeta_0 + \zeta_1 H$. We have discussed three different cases depending on the composition of the bulk viscosity. In case of constant coefficient of bulk viscosity, the scale factor varies exponentially for $\gamma \neq 0$, which avoids the big-bang singularity. We have observed that the constant viscous term generates the time-dependent deceleration parameter, which describes the different phases of the universe and transition to accelerated phase. We have shown the variation of q and the corresponding evolution of the universe in tables 1-4 for various ranges of α. In this case we also have the big rip singularity at finite value of cosmic time for $\gamma < 0$. When $\gamma = 0$, a superinflation for the scale factor has been found whereas it has de Sitter solution in non-viscous case.

In case where the bulk viscosity is proportional to Hubble parameter, we have obtained a power-law expansion for the scale factor similar to the perfect fluid model. The energy density varies inversely as the square of the cosmic time whereas the bulk viscosity decreases

linearly with time. In this case the value of q is constant and the sign of q depends on γ, α and ζ_1. This form of bulk viscosity generates big rip singularity when the constraint given in (47) holds.

In case of $\zeta = \zeta_0 + \zeta_1 H$, we again have obtained exponential form of expansion for the scale factor which is similar to the form with constant bulk viscous term. It has been observed that the deceleration parameter is time-dependent which can explain the expansion history of the universe and the transition to accelerated or decelerated phase (see tables 5-8).

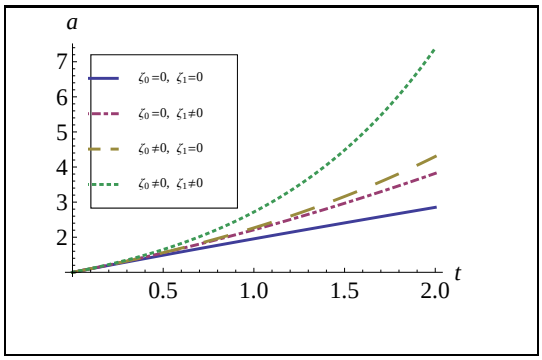

Fig. 1(a) Scale factor in terms of cosmic time for $\alpha > 0$. Here $\gamma = \alpha = a_0 = H_0 = 1$ and $\zeta_0 = \zeta_1 = 0.1$.

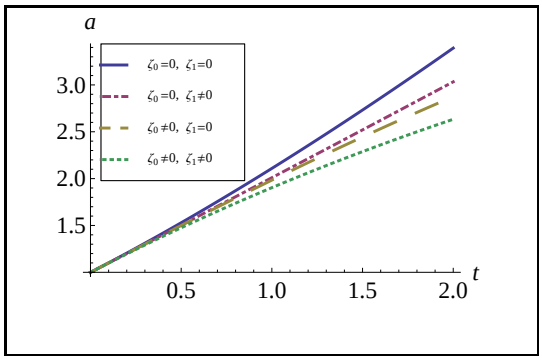

Fig. 1(b) Scale factor in terms of cosmic time for $\alpha < 0$. Here $\alpha = -1$, $\gamma = a_0 = H_0 = 1$ and $\zeta_0 = \zeta_1 = 0.1$

The behavior of scale factor with cosmic time has been shown in Figures 1a and 1b for different models with the particular choices of bulk viscosity. It has been observed that the scale factor increases rapidly in all viscous models as compared to the non-viscous model(perfect fluid model) for any positive values of α as shown in figure 1a. The rate of expansion depends on the bulk viscous coefficient. The scale factor varies very close to non-viscous model when bulk viscous coefficient is assumed to be small. Figure 1a shows that the expansion of scale factors deviate more rapidly from the perfect fluid expansion rate for larger bulk viscous coefficient and the rate of expansion is very fast when the bulk viscosity is considered in the form $\zeta = \zeta_0 + \zeta_1 H$. The behavior of scale factor for different models is reverse for $\alpha < 0$ as shown in figure 1b. The variation of deceleration parameter with cosmic time has been shown in figure 2 for different models. The models with $\zeta = 0$ (perfect fluid) and $\zeta = \zeta_1 H$ where the scale factor vary as power-law of cosmic time, the values of q are constant. On the other hand, in models $\zeta = \zeta_0$ and $\zeta = \zeta_0 + \zeta_1 H$ where the scale factors vary exponentially, q is time-dependent and transitions from positive to negative values are observed.

The main conclusion, in the context of the bulk viscous, is that the form of $\zeta = \zeta_0 + \zeta_1 H$ is suitable to describe the power-law and exponential expansion for the scale factor. It is also possible to obtain big rip type solutions under certain constraints. Therefore, we can explore the possibility that the present acceleration of the universe is driven by a kind of viscous fluid by assuming this form of bulk viscous term. Though the viscous dark energy form is simple, the results are better. We emphasize that perfect fluid is just a limiting case of a general viscosity media that is more practical in the astrophysics sense. Therefore, it is worthy to

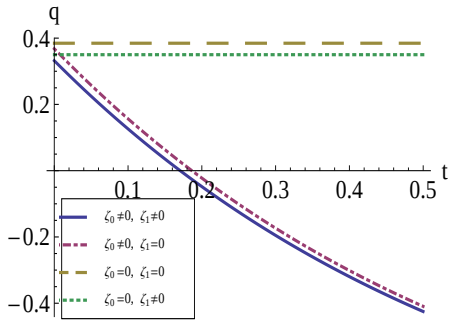

Fig. 2 Deceleration parameter in terms of cosmic time for $\alpha > 0$. Here $\gamma = H_0 = 1, \alpha = 0.1, \zeta_0 = 0.01$ and $\zeta_1 = 0.02$.

study the early and late time evolution of the universe with viscous fluid.

Acknowledgement

PK would like to express his sincere thank to University Grants Commission (UGC), India for providing Junior Research Fellowship scheme.

References

1. H.A. Buchdahl, Mon. Not. R. Astro. Soc. **150**, 1 (1970)
1. A.A. Starobinsky, Phys. Lett. B **91**, 99 (1980)
3. S. Nojiri, S.D. Odintsov, Phys. Rev. D **68**, 123512 (2003)
4. T.P. Sotiriou, V. Faraoni, Rev. Mod. Phys. **82**, 451 (2010)
5. S. Capozziello, M. De Laurents, Phys. Rept. **509**, 167 (2011)
6. T. Clifton, P.G. Ferreira, A. Padilla, C. Skordis, Phys. Rept. **513**, 1 (2012)
7. S. Nojiri, S.D. Odintsov, Phys. Lett. B **562**, 147 (2003)
8. S. Nojiri, S.D. Odintsov, Phys. Lett. A **19**, 627 (2004)
9. S. Nojiri, S.D. Odintsov, Int. J. Geom. Meth. Mod. Phys. **4**, 115 (2007)
10. S.M. Carrol, V. Duwuri, M. Trodden, M.S. Turner, Phys. Rev. D **70**, 043528 (2004)
11. T. Chiba, A.L. Erichcek, Phys. Rev. D **75**, 124014 (2007)
12. A.A. Starobinsky, J. Exp. Theor. Phys. Lett. **86**, 157 (2007)
13. S. Nojiri, S.D. Odintsov, Phys. Rep. **505**, 59 (2011)
14. K. Bamba, S. Nojiri, S.D. Odintsov, J. Cosmol. Astropart. Phys. **0180**, 045 (2008)
15. S. Nojiri, S.D. Odintsov, M. Sami, Phys. Rev. D **74**, 046004 (2006)
16. R. Femaro, F. Fiorini, Phys. Rev. D **75**, 084031 (2007)
17. O. Bertolami, C.G. Bochmer, T. Harko, F.S.N. Lobo, Phys. Rev. D **75**, 104016 (2007)
18. T. Harko, Phys. Lett. B **669**, 376 (2008)
19. T. Harko, F.S.N. Lobo, Eur. Phys. J. C **70**, 373 (2010)
20. T. Harko, F.S.N. Lobo, S. Nojiri, S.D. Odintsov, Phys. Rev. D **84**, 024020 (2011),

[arXiv:gr-qc/1104.2669].
21. M.J.S. Houndjo, C.E.M. Batista, J.P. Campos, O.F. Piattella, Canadian J. Phys. **91**, 548 (2013), [arXiv:gr-qc/1203.6084]
22. F.G. Alvarenga, M.J.S. Houndjo, A.V. Monwanou, J.B. Chobi Oron, J. Mod. Phys. **4**, 130 (2013), [arXiv:gr-qc/1205.4678]
23. A. Pasqua, S. Chattopadhyay, I. Khomenkoc, Canadian J. Phys. **91**, 632 (2013)
24. M. Sharif, M. Zubair, J. Cosmol. Astropart. Phys. **21**, 28 (2012), [arXiv:gr-qc/1204.0848]
25. T. Azizi, Int J. Theor. Phys. **52**, 3486 (2013), [arXiv:gr-qc/1205.6957]
26. S. Chakraborty, Gen. Relativ. Grav. **45**, 2039 (2013), [arXiv:gen-ph/1212.3050]
27. C.P. Singh and V. Singh, Gen. Relativ. Grav. **46**, 1696 (2014)
28. A.G. Riess, et al., Astron. J. **116**, 1009 (1998)
29. S. Perlmutter, et al., Astrophys. J. **517**, 565 (1999)
30. A.G. Riess, et al., Astrophys. J. **607**, 665 (2004)
31. A.G. Riess, et al., Astrophys. J. **659**, 98 (2007)
32. E. Komatsu, et al., Astrophys. J. Suppl. **192**, 18 (2011)
33. C.L. Bennett, et al., Astrophys. J. **148**, 1 (2003)
34. K. Abazajian, et al., Astron. j. **128**, 502 (2004)
35. M. Tegmark et al., Phys. Rev. D **69**, 103501 (2004)
36. W. Misner, Astrophysical J. **151**, 431 (1968)
37. G.L. Murphy, Phys. Rev. D **8**, 4231 (1973)
38. J.C. Fabris, S.V.B. Goncalves, R. de Sa Ribeiro, Gen. Relativ. Gravit. **38**, 495 (2006)
39. I. Brevik, O. Gorbunova, Gen. Relativ. Gravit. **37**, 2039 (2005)
40. Ming-Guang Hu, Xin-He Meng, Phys. Lett. B **635**, 186 (2006), [arXiv:astro-ph/0511615]
41. Jie Ren and Xin-He Meng, Phys. Lett. B **633**, 1 (2006)
42. Jie Ren and Xin-He Meng, Phys. Lett. B **636**, 5 (2006)
43. J.S. Gagnon, J. Lesgourgues, J. Cosmol. Astropart. Phys. **09**, 026 (2011), [arXiv:astro-ph/1107.1503v2]
44. A.A. Sen et al., Phys. Rev. D **63**, 107501 (2001)
45. M.K. Mak and T. Harko, *Int. J. Mod. Phys. D* **12**, 925 (2003)
46. C.P. Singh, S. Kumar, A. Pradhan, Class. Quantum Grav. **24**, 455 (2007)
47. C.P. Singh, Pramana J. Phys. **72**, 429 (2008)
48. X.H. Meng, X. Dou, Commun. Theor. Phys. **52**, 377 (2009), [arXiv:astro-ph/0812.4904]
49. S. Weinberg, Astrophys. J. **168**, 175 (1972)
50. I. Brevik, Phys. Rev. D **65**, 127302 (2002)
51. C. Eckart, Phys. Rev. **58**, 919 (1940)
52. Xin-He Meng, Jie Ren, Ming-Gaung Hu, Commun. Theor. Phys. **47**, 379 (2007)
53. A. Avelino, U. Nucamendi, J. Cosmol. Astropart. Phys. **9**, 1008 (2010), [arXiv:gr-qc/1002.3605]
54. Ø. Grøn, Astrophys. space Sci. **173**, 191 (1990)
55. M. Cataldo, N. Cruz, S. Lepe, Phys. Lett. B **619**, 5 (2005)
56. I. Brevik, O. Gorbunova, Y. A. Shaido, Int. J. Mod. Phys. D **14**, 1899 (2005)

Scientific Online

SOP TRANSACTIONS ON WIRELESS COMMUNICATIONS
In Press

SOP TRANSACTIONS ON WIRELESS COMMUNICATIONS

High Gain Patch Antenna for WBAN Applications

N.S. Raghava[1]*, Asok De[2], Rishik Bazaz[3], Pushkar Arora[4], Aman Samaiyar[5] and Deepender Dabas[6]

[1] *Department of Electronics and Communication Engineering, Delhi Technological University, India.*
[2] *Director, NIT, Patna, India.*
[3] *Intel Corporation, Chandler Arizona, USA.*
[4] *University of Michigan Ann Arbor, USA.*
[5] *Department of EEE, Delhi Technological University, Delhi, India.*
[6] *Department of ECE, JIIT Noida, India.*
***Corresponding author**: nsraghava@gmail.com

Abstract:
This paper proposes a Rectangular Circularly Polarized Microstrip Patch Antenna (RCPPA) that can be used for WBAN applications. The antenna is operating at 869.3 MHz, with enhanced gain, directivity and efficiency. With truncations on diagonally opposite sides and coaxial feed on Y axis a right hand circular polarization has been achieved. The antenna also shows reduction in surface waves, has no back radiation and is thinner in physical size, which makes it more suitable for WBAN applications. The properties of proposed antenna is then compared with Compact Slot Loaded Patch Antenna (CSLPA), which is already being used for WBAN applications.

Keywords:
Compact Slot Loaded Patch Antenna (CSLPA); Rectangular Circularly Polarized Patch Antenna (RCPPA); Circular Polarization (CP); Antenna Efficiency; High Gain

1. INTRODUCTION

Wireless body area network (WBAN) is a wireless network of wearable computing devices. They provide great opportunity for on-body and in-body services like remote health monitoring. They are generally capable of sensing physiological signals, processing the data and transmitting them to a centralized WBAN monitoring server, which in turn can send reports to medical experts [1]. WBAN is a new emerging technology in the field of medical science with a capability to revolutionize health care [2, 3].

A WBAN system consists of a number of inexpensive, lightweight and miniature sensors that collects the physiological signals from human body. A range of expensive and inexpensive wearable monitoring sensors are available in the market such as pedometers, accelerometers and gyroscopes that can be located on different characteristic points on the body (ankle, arm, waist, thigh, etc.) [3, 4]. Some WBAN systems have on-sensor signal processing and in some cases processing is done in the centralized server. Increased sensor intelligence reduces the need for communication, therefore minimizing power consumption and extending battery life. A detailed analysis on implementation of WBAN system for remote health

monitoring has been done in [5, 6]. A certain rules of engagement are applied to WBAN antennas [7]. They should be capable of utilizing effective WBAN security mechanisms. There antenna should not be any interfere between antenna and the lossy dielectric tissue cells. Antenna should be preferable planar and less bulky and a circular polarization is preferred for antennas near human body [8]. A work on use of cross slotted circular polarized antenna for medical implants can be found in [9]. Considering the reasons stated above, a microstrip patch antenna is a suitable antennas for WBAN systems. Microstrip patch type antennas has already been used for on-body communications [10].

Microstrip antennas are planar printed antennas. A Microstrip patch antenna has a conducting metal patch suspended over a grounded microwave substrate. Low cost, ease of fabrication, light weight and mechanically robust have made them very popular. Apart from these advantages there are certain limitations of microstrip antennas such as low gain, low directivity and low impedance bandwidth. Wide research is being conducted in the field of microstrip antenna to overcome these limitations and successfully tap its advantages. Microstrip patch antennas have a number of wireless applications such as mobile communications, Radio Frequency Identification (RFID) etc.

In this letter, we are proposing an efficient Rectangular Circularly Polarized Microstrip Patch Antenna (RCPPA) that can be used to transmit the data collected and (or) processed by the sensor platforms and custom sensor modules. The operating frequency of this antenna can be easily regulated for different frequencies to enable implementation of different communication architectures for wireless body area network apart from standard IEEE 802.15.6TM-2012 [11]. The antenna is simulated on IE3D and the obtained results are compared with the experimental results taken from a RHODE and SCHWARZ ZVB 20 Vector Network Analyzer. The radiation patterns obtained from IE3D is also compared with the experimental results measured in an anechoic chamber. An ETS Lindgren Model 3115 double ridged horn antenna was used as a reference antenna for transmission. The antenna is then compared with a compact slot-loaded patch antenna (CSLPA) which is already being used for WBAN applications [12]. A further improvement on the proposed antenna can be done by implementation of photonic band gap structures in the substrate as discussed in [13].

The rest of the paper is organized as follows. Section 2 discusses the designing and functionality of the proposed RCPP antenna. Section 3 describes the results obtained from the simulation and measurement of the proposed antenna. Section 4 lays out the comparison between RCPPA and CSLPA. Section 5 concludes the paper. High Gain Patch Antenna for WBAN Applications

2. ANTENNA DESIGN

The microstrip antenna designed is shown in **Figure 1** . The substrate consists of one layer each of foam and FR4 [14]. The antenna has a rectangular patch of 132×138 mm. Truncations at the corners have been made to achieve Circular Polarization (CP). Since circular polarized antennas send and receive in all planes, the signal strength is not lost. In circularly-polarized systems the reflected signal is returned in the opposite orientation thus largely avoiding conflict with the propagating signal and making circularly polarized antennas highly advantageous over linearly polarized antennas.

The truncations on the opposite corners of the antenna produce Circular Polarization by excitation of the two near-degenerate orthogonal modes of operation along the diagonal of the patch. The size of the truncation (D) determines the axial ratio of the antenna.

The dimensions of the antenna are shown in **Table 1** [15]. Two consecutive substrate layers are placed on the ground layer. Foam layer with permittivity of 1.05 is placed above ground. A FR4 layer with relative permittivity of 4.4 and loss tangent of .018 is placed above the previous layer. The probe is placed at the distance F from the center of patch and its radius is 0.5mm. The photographs of actual circuit are

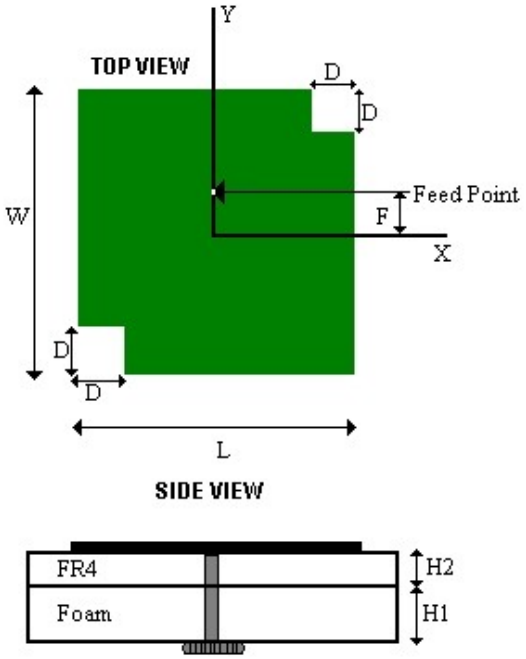

Figure 1. **Microstrip antenna design**

Table 1. **DIMENSIONS OF ANTENNA**

Dimension	Length[a]
W	138
L	132
D	18
F	32
H1	3.9
H2	1.6

[a]All dimensions are in millimeters.

shown in **Figure 6** .

3. RESULTS AND DISCUSSION

The newly proposed structure is compatible with microstrip circuits and has been implemented for practical uses. The various parameters of the proposed RCPPA were found using IE3D simulation software. The simulated results were compared with the experimental results taken from a RHODE and SCHWARZ ZVB 20 Vector Network Analyzer.

The return loss characteristics of obtained from the simulation has been shown in **Figure 2** and have been compared with experimentation results. The figure shows that frequency of operation of proposed antenna is 869.3 MHz. Frequency of operation of RCPPA can be changed easily by adjusting the dimensions of the truncations and the position of the feed. **Figure 2** shows an Impedance Bandwidth of 22.9 MHz i.e. 2.64%. The measured results show good conformity with the simulated results. The 3-D radiation/gain pattern of the proposed antenna has been illustrated in **Figure 3** . The Gain achieved

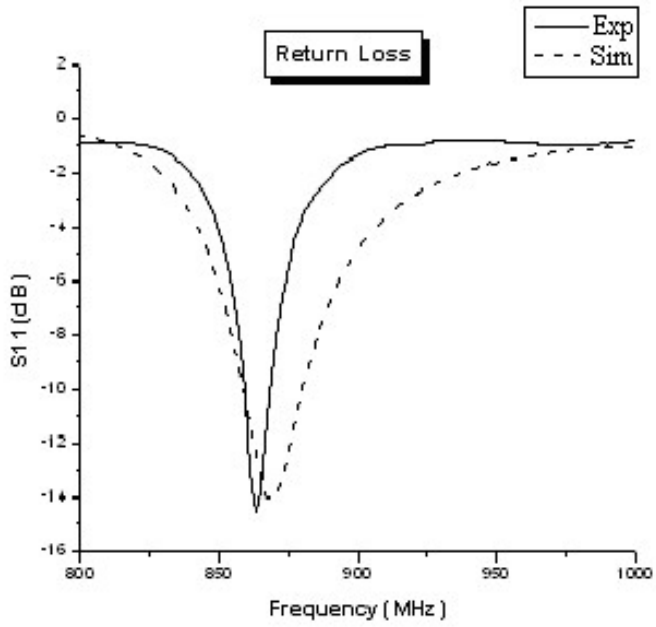

Figure 2. **Return Loss of RCPPA**

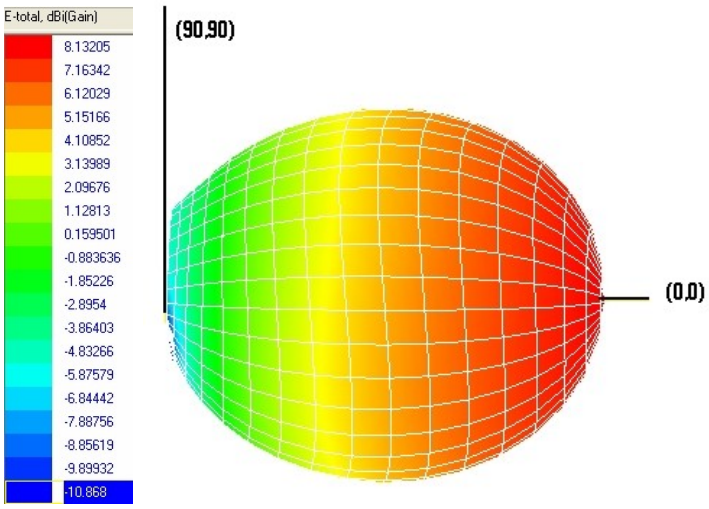

Figure 3. **Microstrip Antenna Radiation Pattern**

with the proposed antenna is very high and is equal to 8.13dBi. Radiation efficiency of RCPPA is 87%. Apart from the simulation results, the E and H field radiation patterns were also measured in an anechoic chamber. An ETS Lindgren Model 3115 double ridged horn antenna was used as a reference antenna for transmission. The comparison between simulated and observed radiation patterns is shown in **Figure 4** and 5. The E- Plane pattern shows a slight back lobe less than -20dB. This can be on the account of feed impedance mismatch or copper losses. Overall both patterns show acceptable similarity in the simulated and measured values.

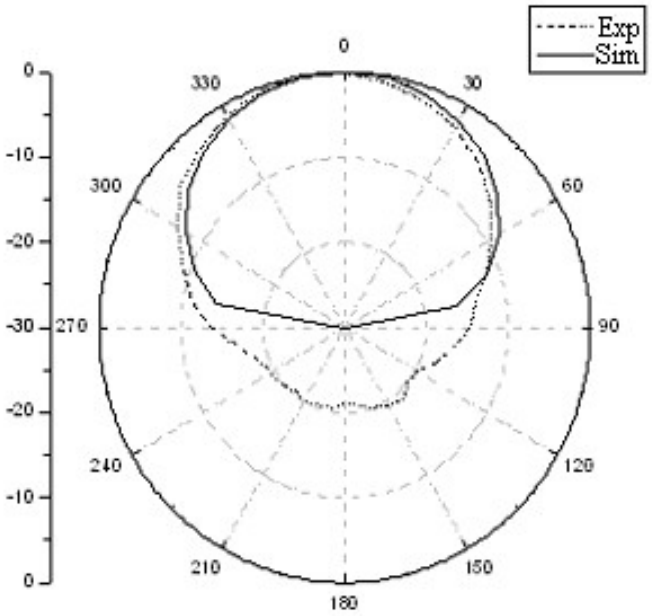

Figure 4. **E Plane Radiation Pattern (893 MHz)**

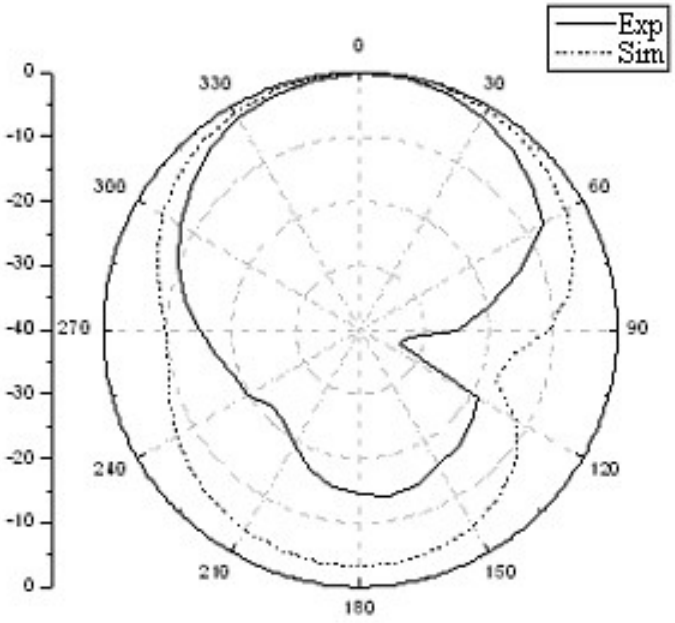

Figure 5. **H Plane Radiation Pattern (893 MHz)**

4. COMPARISON BETWEEN RCCPA AND CSLPA

The frequency of operation for CSLPA [12] is 868 MHz while that of the proposed antenna is 869.3MHz. The total height of the proposed antenna is 5.5 mm which is thinner as compared to 10.5 mm of CSLPA [12] and it can be easily placed on the body. Impedance Bandwidth has been increased from 4 MHz

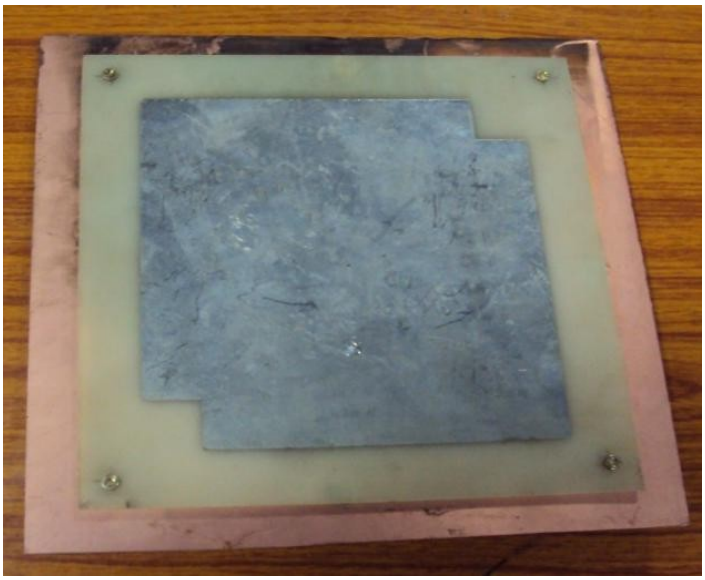

(a) Top View

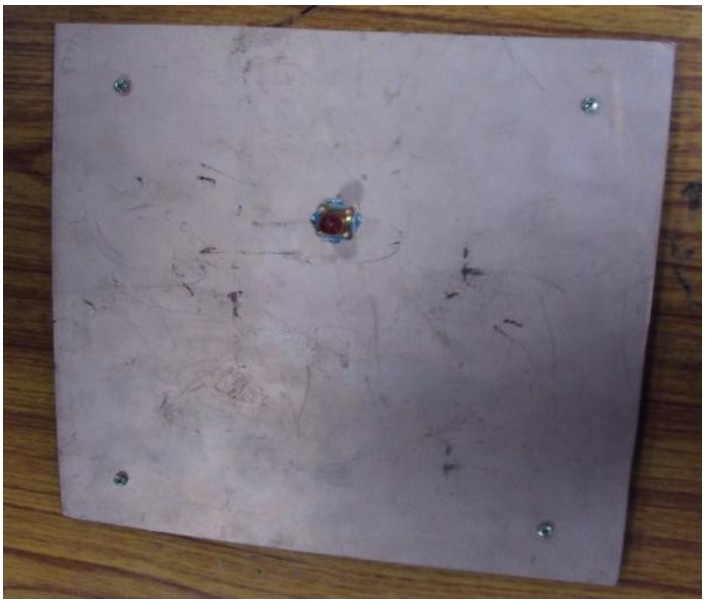

(b) Bottom View

Figure 6. **Photograph of proposed antenna**

to 22.9 MHz i.e. 0.4% to 2.64%. It is also observed that with RCPPA there is a 5.34 times increase in directivity from 1.64dBi to 8.77dBi with respect to the CSLPA. The radiation efficiency of the CSLPA is 88.6% while that of the RCPPA is 87%.This shows that RCPPA provides a high gain and directivity without any significant change in efficiency as compared to CSLPA.

5. CONCLUSION

An economical and easy to fabricate patch antenna with high gain and directivity has been proposed. There is no back radiation as seen from **Figure 3** , which results in high gain and directivity. The measured and simulated E Plane and H Plane radiation patterns have been shown in **Figure 4** and **Figure 5** . Use of a substrate of low permittivity i.e. foam (permittivity=1.05) has resulted in the decrease in surface waves over the patch which results in increased gain and efficiency.

References

[1] B. G. Steele, B. Belza, K. Cain, C. Warms, J. Coppersmith, and J. Howard, "Bodies in motion: Monitoring daily activity and exercise with motion sensors in people with chronic pulmonary disease," *Journal of Rehabilitation Research & Development*, vol. 40, no. 5, 2003.

[2] R. S. Istepanian, E. Jovanov, and Y. Zhang, "Guest editorial introduction to the special section on m-health: Beyond seamless mobility and global wireless health-care connectivity," *Information Technology in Biomedicine, IEEE Transactions on*, vol. 8, no. 4, pp. 405–414, 2004.

[3] D. Raskovic, T. Martin, and E. Jovanov, "Medical monitoring applications for wearable computing," *The Computer Journal*, vol. 47, no. 4, pp. 495–504, 2004.

[4] S.-W. Lee and K. Mase, "Activity and location recognition using wearable sensors," *IEEE pervasive computing*, vol. 1, no. 3, pp. 24–32, 2002.

[5] E. Jovanov, A. Milenkovic, C. Otto, P. De Groen, B. Johnson, S. Warren, and G. Taibi, "A WBAN system for ambulatory monitoring of physical activity and health status: applications and challenges," in *Engineering in Medicine and Biology Society, 2005. IEEE-EMBS 2005. 27th Annual International Conference of the*, pp. 3810–3813, IEEE, 2006.

[6] C. A. Otto, E. Jovanov, and A. Milenkovic, "A WBAN-based system for health monitoring at home," in *Medical Devices and Biosensors, 2006. 3rd IEEE/EMBS International Summer School on*, pp. 20–23, IEEE, 2006.

[7] S. Warren and E. Jovanov, "The need for rules of engagement applied to wireless body area networks," in *Proc. of the IEEE consumer communications and networking conference, CCNC*, 2006.

[8] M. F. Iskander, Z. Yun, and R. Quintero-Illera, "Polarization and human body effects on the microwave absorption in a human head exposed to radiation from handheld devices," *Microwave Theory and Techniques, IEEE Transactions on*, vol. 48, no. 11, pp. 1979–1987, 2000.

[9] N. Raghava, P. R. Chadha, and D. D. Asok De, "A Compact Circular Microstrip Antenna with Cross Shaped Slot," 2012.

[10] P. Salonen, Y. Rahmat-Samii, and M. Kivikoski, "Wearable antennas in the vicinity of human body," in *Antennas and Propagation Society International Symposium, 2004. IEEE*, vol. 1, pp. 467–470, IEEE, 2004.

[11] C. Li, H.-B. Li, and R. Kohno, "Performance evaluation of IEEE 802.15. 4 for wireless body area network (WBAN)," in *Communications Workshops, 2009. ICC Workshops 2009. IEEE International Conference on*, pp. 1–5, IEEE, 2009.

[12] A. R. Chandran, G. A. Conway, and W. G. Scanlon, "Compact slot-loaded patch antenna for 868 mhz wireless body area networks," in *Antennas and Propagation Conference, 2008. LAPC 2008. Loughborough*, pp. 433–436, IEEE, 2008.

[13] N. Raghava and A. De, "Photonic bandgap stacked rectangular microstrip antenna for road vehicle communication," *Antennas and Wireless Propagation Letters, IEEE*, vol. 5, no. 1, pp. 421–423, 2006.

[14] C. A. Balanis, *Antenna theory: analysis and design*. John Wiley & Sons, 2012.

[15] S.-Y. Ke, "Efficiency improvement of a circularly polarized microstrip antenna using a two-layer substrate," *WHAMPOA–An Interdisciplinary Journal*, vol. 53, pp. 19–24, 2007.

IMPROVED SYNTHESIS OF INDOLYLCHALCONES AND 2-AMINO-3-CYANO-4-INDOLYL-6-ARYLPYRIDINES USING ULTRASONIC IRRADIATION

Anshu Jain[a], Yogita Madan[b], Davendra Kumar[a*]
[a]Department of Applied Chemistry and Polymer Technology, Delhi Technological University, Delhi-110042, *India*
E-Mail: anshujaindtu@gmail.com
[b]Malaviya National Institute of Technology, Jaipur-302017, *India*

ABSTRACT
Various indolylchalcones are synthesized by Claisen- Schmidt condensation of aryl ketones and 3-formylindoles to give 2-amino-3-cyano-4-indolyl-6-arylpyridines by the coupling reaction of indolylchalcone, ammonium acetate and malanonitrile. The reaction is carried out under ultrasonic irradiation in lesser time with higher yields as compared to conventional heating methods. All the synthesized compounds were characterized on the basis of their elemental analyses and spectral data (IR, ^{1}H NMR, ^{13}C NMR and Mass).

KEYWORDS
Indolylchalcones, 2-Amino-3-cyano-4-indolyl-6-arylpyridines, Claisen- Schmidt condensation, Ultrasonic irradiation

INTRODUCTION

Indole nucleus annulated to heterocyclic ring(s) is one of the most important scaffolds found in various natural or synthetic alkaloids [1] , pharmaceuticals [2] , agrochemicals [3] showing various bioactivities *viz* anti-inflammatory [4], antioxidant [5], antimicrobial [6], antiviral and antitumor etc [7-10]. These heterocycles are also useful in the treatment of fibromyalgia, chronic fatigue and irritable bowel syndrome [11-13]. In particular, indolylchalcones exhibit versatile bioactivities such as anti-inflammatory, antiproteolytic, antithelmintic, anticancer and antiproliferative [14]. These compounds are synthesized by Claisen Schmidt condensation of 3-formylindole and aromatic ketones in the presence of bases such as NaOH, KOH etc [15]. Besides being biologically active, they are also used extensively as synthons in organic synthesis that possess potentially reactive site for a variety of chemical reactions [16]. Indolylchalcone are also important intermediate product in this synthesis.
Pyridine functionalities have been widely studied [17-18] and widely used [19-21] but still generate much interest due to their wide range of application in medicinal chemistry [22-25]. Cyanopyridine derivatives were found to show antimicrobial, antihypertensive, cardiovascular, anti-inflammatory, analgesic, antipyretic activities [26-28]. Some bifunctional pyridines are used as non linear optical materials [29], electrical materials [30], chelating agents in metal-ligand chemistry [31], and as fluorescent liquid crystals [32]. Among them, 2-amino-3-cyanopyridines have been identified as IKK-β inhibitors [33] and also inhibit two metalloenzyme human carbonic anhydrase isozymes hCA I and hCA II [34]. Therefore, the synthesis of 2-amino-3-cyano-4-indolyl-6-arylpyridines attracts much interest in organic chemistry. There are a variety of methods described in literature [35-36] to synthesize similar skeleton. In our earlier work we have synthesized 2-amino-3-cyano-4,6-diarylpyridines using various green chemical methods [37].

The presence of two or more different heterocyclic moieties in a single molecule often enhances the biocidal profile remarkably. Encouraged by all the above facts, we have synthesized various 2-amino-3-cyano-4-indolyl-6-arylpyridines which incorporates both indole and pyridine moieties in a single molecule under ultrasonic irradiation.

RESULTS AND DISCUSSION

As part of our interest in heterocycles and development of eco-friendly methods [37-38], we have synthesized various indolylchalcones and 2-amino-3-cyano-4-indolyl-6-aryl pyridines **(4a-f)** under ultrasonic irradiation. In this method indolylchalcone **3**, malanonitrile and ammonium acetate were grinded together with pestle and mortar and then placed in ultrasonic bath using ethanol as solvent for 25-30 mins which provided a yellow solid product in good to excellent yields.

The key intermediate indolylchalcones **(3a-f)** were prepared by Claisen-Schmidt condensation of aryl ketones and 3-formylindoles **1** with KOH using ethanol as solvent under ultrasonic irradiation **(Scheme 1)**.

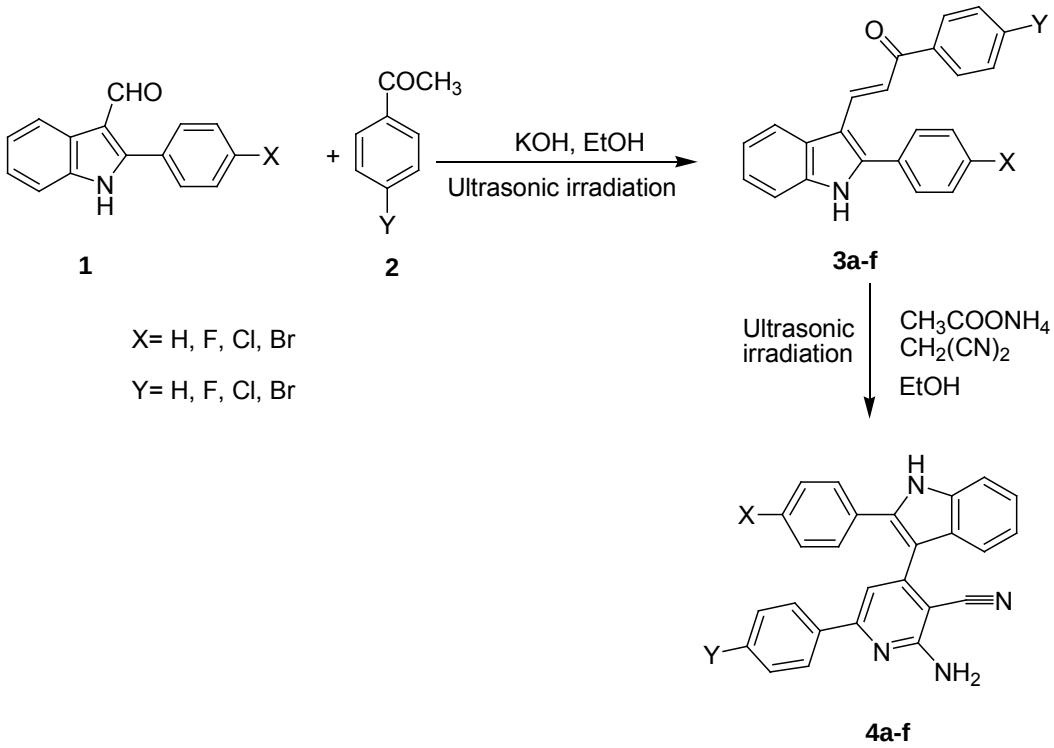

SCHEME 1: Synthesis of indolylchalcones (3a-f) and 2-amino-3-cyano-4-indolyl-6-dipyridines (4a-f)

In the IR spectra of indolylchalcones **(3a-f)**, a characteristic absorption band is observed in the region 1680-1660 cm^{-1} due to conjugated carbonyl group which disappears in the IR spectra of 2-amino-3-cyano-4-indolyl-6-arylpyridine derivatives **(4a-f)**. Besides this, the stretching

vibration of $-NH_2$ group appears as two stretching vibration corresponding to asymmetric and symmetric vibrations in the region 3500-3430 cm^{-1} and 3410-3310 cm^{-1}, respectively. Appearance of a characteristic peak of -CN group in the region 2215-2200 cm^{-1} confirmed the formation of desired compounds **(4a-f)**.

TABLE 1: Synthesis of indolylchalcones (3a-f) and 2-amino-3-cyano-4-indolyl-6-arylpyridines (4a-f)

Compound	X	Y	Ultrasonic irradiation		M.P. (°C)
			Time (min)	Yield (%)	
3a	H	H	18	78	250
3b	H	F	17	86	265
3c	F	Cl	19	86	278
3d	Cl	Br	18	75	302
3e	Br	H	21	80	290
3f	F	Br	17	82	286
4a	H	H	28	85	315
4b	H	F	26	80	290
4c	F	Cl	29	82	298
4d	Cl	Br	30	84	305
4e	Br	H	28	82	307
4f	F	Br	26	85	301

In the ^1H NMR spectra of indolylchalcones **(3a-f)** the two olefinic protons constitute an AB system and appear as a pair of doublets; the downfield doublet centered at δ 7.75-7.78 ppm is due to CO-C*H*= and the doublet centered at δ 7.90-7.92 ppm is due to >CH=C*H*, which are merged with aromatic protons in the region δ 6.82-8.25 ppm. This AB pattern disappears in the ^1H NMR spectra of 2-amino-3-cyano-4-indolyl-6-arylpyridine derivatives **(4a-f)**. A characteristic singlet is observed in the region δ 5.58-5.73 ppm due to presence of NH_2 group, which is D_2O exchangeable. Aromatic protons are obtained as multiplets in the region δ 6.81-8.31 ppm. Most downfield shift in the region δ 8.20-8.31 ppm is attributed due to 5-*H* of pyridine moiety.
In the ^{13}C NMR of 2-amino-3-cyano-4-indolyl-6-arylpyridine derivatives **(4a-f)**, various characteristic peaks at 115.92 (CN), 157.75, 164.62 ppm are observed. Aromatic region is obtained from 109.77-145.79 ppm.
Final confirmation was obtained from FAB mass spectra which showed an accurate M^+/M+2 peaks at m/z 323/325 **(3a)**, 341/343 **(3b)**, 375/377 **(3c)**, 435/437 **(3d)**, 401/403 **(3e)**, 419/421 **(3f)**, 386/388 **(4a)**, 404/406 **(4b)**, 438/440 **(4c)**, 498/500 **(4d)**, 464/466 **(4e)**, and 482/484 **(4f)**, that agreed well with their corresponding molecular formula.

EXPERIMENTAL

Melting points were determined in open glass capillaries and are uncorrected. The IR spectra (υ_{max} in cm^{-1}) were recorded on FT-IR SHIMADZU-8400S Spectrophotometer using KBr

pellets. ^{1}H NMR spectra were recorded on JEOL-AL 300 spectrophotometer (300 MHz) using $CDCl_3$/DMSO-d_6 as solvents. TMS was taken as internal standard. FAB mass spectra were recorded on JEOL SX-102/DA-6000 (FAB) mass spectrometer/data system using Argon/Xenon (6 kV, 10 mA) as the FAB gas at Central Drug Research Institute (CDRI), Lucknow using *m*-nitrobenzyl alcohol as matrix. Elentar Vario EL III automatic CHN analyzer was used for elemental analyses. The FAB mass spectra and CHN analyses were recorded at central drug research institute (CDRI), Lucknow, India. Sonication was performed in a Toshcon model SW 4 cleaner (with a frequency of 37 KHz and operating at maximum power of 150 W). The purity of compounds was checked by TLC using silica gel (60-120 mesh) as adsorbent, UV light, or iodine accomplished visualization. All common reagents and solvents were used as obtained from commercial suppliers without further purification. Starting materials were **(1)** prepared by method given in literature [39].

General Procedure for the Synthesis of Indolylchalcones (3a-f)

The compound was prepared by following the method of Gupta *et al*. [37] A mixture of 3-formylindole (**1**, 2.9 mmol), aryl ketone (**2**, 2.9 mmol), ethanol (30 mL) and 2N KOH solution (15 mL) were taken into a 100 mL conical flask which was irradiated by ultrasonic irradiation in an ultrasonic bath at 30-35 °C temperature for 15-20 mins. The solid product so formed was diluted with water and neutralized with 2N HCl solution. Then it was filtered, washed with cold water (2 x 25 mL) and recrystallized from ethanol to afford yellow shiny crystals **(3a-f)**.

General Procedure for the Synthesis of 2-Amino-3-Cyano-4-Indolyl-6-Arylpyridines (4a-f)

The compound was prepared by the method of Gupta *et al.* [37]. In this method, indolylchalcone **(3a-f)** (1 mmol), malanonitrile (1 mmol), and ammonium acetate (8 mmol) were grinded together in a mortar. Then this mixture was transferred into a 100 mL round bottom flask with the addition of ethanol (15-20 mL). The reaction flask was then placed in the maximum energy area in an ultrasonic cleaning bath (observation of the surface of the reaction solution during vertical adjustment of flask depth shows the optimum position by the point at which maximum surface disturbance occurs). The bath temperature was controlled (30-35 °C) by addition or removal of water. The progress of the reaction was monitored by TLC using C_6H_6 : EtOAc :: 95:5 as solvent system. Sonication was continued until starting reactants disappeared as indicated by TLC. A yellow solid product was obtained within 25-30 min of irradiation **(Table-1)**. After the completion of the reaction, the mixture was poured into crushed ice with constant stirring to obtain a yellow solid mass, which was dried and recrystallized from 95% ethanol.

1-Phenyl-3-(2-phenyl-1H-indol-3-yl)prop-2-en-1-one (3a)

Yellow solid, Yield: 78%, Mp 250 °C. IR (cm^{-1}): 3360, (NH), 3210 (ArH), 1685 (>CO), 1630, 1575. MS (m/z): 323. ^{1}H NMR (300 MHz, $CDCl_3$) δ 6.82-8.23 (m, ArH, 14H), 7.75 (d, >CO-CH, 1H, *J=15 Hz*), 7.90 (d, >CH=CH, 1H, J=15 Hz), 8.45 (s, Indole NH, 1H). ^{13}C NMR (75.45 MHz, $CDCl_3$):δ 102.11, 110.25, 116.25, 119.65, 121.35, 122.36, 123.25, 126.85, 127.65, 128.65, 129.54, 132.24, 133.56, 134.85, 135.26, 145.67, 168.25, 189.54. Anal. calcd. for $C_{23}H_{17}NO$: C, 85.42; H, 5.30; N, 4.33; Found: C, 85.40; H, 5.31; N, 4.32.

1-(4-Fluorophenyl)-3-(2-phenyl-1H-indol-3-yl)prop-2-en-1-one (3b)

Yellow solid, Yield: 86%, Mp 265 °C. IR (cm^{-1}): 3365, (NH), 3215 (ArH), 1675 (>CO), 1635, 1570, 1240. MS (m/z): 341. ^{1}H NMR (300 MHz, $CDCl_3$) δ 6.85-8.23 (m, ArH, 13H), 7.76 (d, >CO-CH, 1H, *J=15 Hz*), 7.91 (d, >CH=CH, 1H, *J=15 Hz*), 8.46 (s, Indole NH, 1H). ^{13}C NMR (75.45 MHz, $CDCl_3$):δ 102.11, 110.25, 116.25, 119.65, 121.35, 122.36, 123.25, 126.85, 127.65, 128.65, 129.54, 132.24, 133.56, 134.85, 135.26, 145.67, 168.25, 189.54. Anal. calcd. for $C_{23}H_{16}FNO$: C, 80.92; H, 4.72; N, 4.10; found: C, 80.91; H, 4.70; N, 4.08.

1-(4-Chlorophenyl)-3-(2-(4-fluorophenyl)-1H-indol-3-yl)prop-2-en-1-one (3c)

Yellow solid, Yield: 86%, Mp 278 °C. IR (cm^{-1}): 3369, (NH), 3210 (ArH), 1670 (>CO), 1635, 1570, 1240, 750. MS (m/z): 341. ^{1}H NMR (300 MHz, $CDCl_3$) δ 6.83-8.24 (m, ArH, 12H), 7.77 (d, >CO-CH, 1H, *J=15 Hz*), 7.92 (d, >CH=CH, 1H, *J=15 Hz*), 8.47 (s, Indole NH, 1H). ^{13}C NMR (75.45 MHz, $CDCl_3$):δ 102.11, 110.25, 116.25, 119.65, 121.35, 122.36, 123.25, 126.85, 127.65, 128.65, 129.54, 132.24, 133.56, 134.85, 135.26, 145.67, 168.25, 189.54. Anal. calcd. for $C_{23}H_{15}ClFNO$: C, 73.50; H, 4.02; N, 3.73; found: C, 73.53; H, 4.01; N, 3.72.

1-(4-Bromophenyl)-3-(2-(4-chlorophenyl)-1H-indol-3-yl)prop-2-en-1-one (3d)

Yellow solid, Yield: 75%, Mp 302 °C. IR (cm^{-1}): 3375, (NH), 3210 (ArH), 1670 (>CO), 1635, 1570, 1240, 550. MS (m/z): 436. ^{1}H NMR (300 MHz, $CDCl_3$) δ 6.82-8.25 (m, ArH, 12H), 7.75 (d, >CO-CH, 1H, *J=15 Hz*), 7.92 (d, >CH=CH, 1H, *J=15 Hz*), 8.49 (s, Indole NH, 1H). ^{13}C NMR (75.45 MHz, $CDCl_3$): δ 102.11, 110.25, 116.25, 119.65, 121.35, 122.36, 123.25, 126.85, 127.65, 128.65, 129.54, 132.24, 133.56, 134.85, 135.26, 145.67, 168.25, 189.54. Anal. calcd. for $C_{23}H_{15}BrClNO$: C, 63.25; H, 3.46; N, 3.21; found: C, 63.23; H, 3.45; N, 3.20.

3-(2-(4-Bromophenyl)-1H-indol-3-yl)-1-phenylprop-2-en-1-one (3e)

Yellow solid, Yield: 80%, Mp 290 °C. IR (cm^{-1}): 3373, (NH), 3210 (ArH), 1665 (>CO), 1632, 1574, 1243, 540. MS (m/z): 402. ^{1}H NMR (300 MHz, $CDCl_3$) δ 6.86-8.25 (m, ArH, 13H), 7.78 (d, >CO-CH, 1H, *J=15 Hz*), 7.90 (d, >CH=CH, 1H, *J=15 Hz*), 8.48 (s, Indole NH, 1H). ^{13}C NMR (75.45 MHz, $CDCl_3$): δ 102.11, 110.25, 116.25, 119.65, 121.35, 122.36, 123.25, 126.85, 127.65, 128.65, 129.54, 132.24, 133.56, 134.85, 135.26, 145.67, 168.25, 189.54. Anal. calcd. for $C_{23}H_{16}BrNO$: C, 68.67; H, 4.01; N, 3.48; found: C, 68.65; H, 4.02; N, 3.45.

1-(4-Bromophenyl)-3-(2-(4-fluorophenyl)-1H-indol-3-yl)prop-2-en-1-one (3f)

Yellow solid, Yield: 82%, Mp 286 °C. IR (cm^{-1}): 3373, (NH), 3210 (ArH), 1660 (>CO), 1632, 1574, 1243, 540. MS (m/z): 420. ^{1}H NMR (300 MHz, $CDCl_3$) δ 6.85-8.24 (m, ArH, 12H), 7.76 (d, >CO-CH, 1H, *J=15 Hz*), 7.91 (d, >CH=CH, 1H, *J=15 Hz*), 8.48 (s, Indole NH, 1H). ^{13}C NMR (75.45 MHz, $CDCl_3$): δ 102.11, 110.25, 116.25, 119.65, 121.35, 122.36, 123.25, 126.85, 127.65, 128.65, 129.54, 132.24, 133.56, 134.85, 135.26, 145.67, 168.25, 189.54. Anal. calcd. for $C_{23}H_{15}BrFNO$: C, 65.73; H, 3.60; N, 3.33 found: C, 65.72; H, 3.61; N, 3.31.

2-Amino-3-cyano-6-phenyl-4-(2-phenyl-1H-indol-3-yl)pyridine (4a)

Yellow solid, Yield: 85%, mp 315 °C. IR (cm^{-1}): 3430, 3370, 3310 (NH_2, NH), 3200 (ArH), 2200 (CN), 1625, 1575, 1550, 1510, 1250, 1175, 1025, 820. MS (m/z): 386. ^{1}H NMR (300 MHz, $CDCl_3$) δ 5.61 (s, NH_2, 2H), 6.92-8.20 (m, ArH, 15H), 8.45 (s, Indole NH, 1H). ^{13}C NMR (75.45 MHz, $CDCl_3$):δ 90.77, 110.64, 115.92, 117.25, 118.65, 119.22, 121.23, 122.36, 126.98, 127.48, 128.65, 128.82, 130.31, 132.25, 133.52, 135.77, 136.58, 157.75, 164.62. Anal. calcd. for $C_{26}H_{18}N_4$: C, 80.81; H, 4.69; N, 14.50 found: C, 80.81; H, 4.69; N, 14.50.

2-Amino-3-cyano-6-(4-fluorophenyl)-4-(2-phenyl-1H-indol-3-yl)pyridine (4b)

Yellow solid, Yield: 80%, mp 290 °C. IR (cm^{-1}): 3433, 3365, 3313 (NH_2, NH), 3199 (ArH), 2207 (CN), 1628, 1574, 1551, 1512, 1250, 1175, 1025, 820. MS (m/z): 404. ^{1}H NMR (300 MHz, $CDCl_3$) δ 5.64 (s, NH_2, 2H), 6.89-8.29 (m, ArH, 14H), 8.46 (s, Indole NH, 1H). ^{13}C NMR (75.45 MHz, $CDCl_3$):δ 90.89, 111.64, 115.79, 117.29, 118.85, 119.42, 120.46, 122.69, 127.04, 127.54, 128.69, 128.65, 131.39, 132.38, 133.35, 135.79, 136.88, 157.57, 164.68. Anal. calcd. for $C_{26}H_{17}FN_4$: C, 77.21; H, 4.24; N, 13.85 Found: C, 77.20; H, 4.23; N, 13.84.

2-Amino-3-cyano-6-(4-chlorophenyl)-4-(2-(4-fluorophenyl)-1H-indol-3-yl)pyridine (4c)

Yellow solid, Yield: 82%, mp 298 °C. IR (cm^{-1}): 3438, 3369, 3314 (NH_2, NH), 3205 (ArH), 2210 (CN), 1630, 1578, 1556, 1515, 1252, 1176, 1025, 820. MS (m/z): 438. ^{1}H NMR (300 MHz, $CDCl_3$) δ 5.67 (s, NH_2, 2H), 6.92-8.20 (m, ArH, 13H), 8.46 (s, Indole NH, 1H). ^{13}C NMR (75.45 MHz, $CDCl_3$):δ 90.81, 110.69, 115.98, 117.29, 118.61, 119.15, 121.09, 122.38, 126.91, 127.47, 128.67, 128.86, 130.35, 132.19, 133.39, 135.45, 136.61, 157.87, 164.81. Anal. calcd. for $C_{26}H_{16}ClFN_4$: C, 71.15; H, 3.67; N, 12.77 Found: C, 71.14; H, 3.66; N, 12.75.

2-Amino-3-cyano-6-(4-bromophenyl)-4-(2-(4-chlorophenyl)-1H-indol-3-yl)pyridine (4d)

Yellow solid, Yield: 84%, mp 305 °C. IR (cm^{-1}): 3428, 3374, 3307 (NH_2, NH), 3206 (ArH), 2207 (CN), 1626, 1579, 1548, 1507, 1248, 1173, 1025, 820. MS (m/z): 499. ^{1}H NMR (300 MHz, $CDCl_3$) δ 5.70 (s, NH_2, 2H), 6.98-8.29 (m, ArH, 13H), 8.45 (s, Indole NH, 1H). ^{13}C NMR (75.45 MHz, $CDCl_3$):δ 90.65, 110.74,115.72, 116.01, 117.29, 118.71, 119.32, 121.17, 122.39, 126.92, 127.51, 128.72, 128.76, 130.29, 132.28, 133.53, 135.79, 136.61, 157.79, 164.67. Anal. calcd. for $C_{26}H_{16}BrClN_4$: C, 62.48; H, 3.23; N, 11.21 Found: C, 62.48; H, 3.23; N, 11.21.

2-Amino-3-cyano-4-(2-(4-bromophenyl)-1H-indol-3-yl)-6-phenylpyridine (4e)

Yellow solid, Yield: 82%, mp 307 °C. IR (cm^{-1}): 3425, 3373, 3313 (NH_2, NH), 3209 (ArH), 2210 (CN), 1618, 1568, 1555, 1508, 1250, 1175, 1025, 820. MS (m/z): 465. ^{1}H NMR (300 MHz, $CDCl_3$) δ 5.73 (s, NH_2, 2H), 7.02-8.28 (m, ArH, 14H), 8.49 (s, Indole NH, 1H). ^{13}C NMR (75.45 MHz, $CDCl_3$):δ 90.65, 110.77, 115.76, 117.45, 118.05, 119.31, 121.34, 122.36, 126.98, 127.48, 128.65, 128.79, 130.21, 132.41, 133.59, 135.78, 136.65, 157.80, 164.61. Anal. calcd. for $C_{26}H_{17}BrN_4$: C, 67.11; H, 3.68; N, 12.04 found: C, 67.12; H, 3.67; N, 12.03.

2-Amino-3-cyano-6-(4-bromophenyl)-4-(2-(4-fluorophenyl)-1H-indol-3-yl)pyridine (4f)

Yellow solid, Yield: 85%, mp 301 °C. IR (cm^{-1}): 3423, 3369, 3315 (NH_2, NH), 3196 (ArH), 2215 (CN), 1631, 1568, 1553, 1510, 1250, 1175, 1025, 820. MS (m/z): 482. ^{1}H NMR (300 MHz, $CDCl_3$) δ 5.72 (s, NH_2, 2H), 6.99-8.31 (m, ArH, 13H), 8.51 (s, Indole NH, 1H). ^{13}C NMR (75.45 MHz, $CDCl_3$):δ 90.63, 110.74, 115.90, 117.28, 118.49, 119.31, 121.19, 122.12, 126.99, 127.53, 128.69, 128.89, 130.39, 132.22, 133.45, 135.81, 136.67, 157.79, 164.48. Anal. calcd. for $C_{26}H_{16}BrFN$: C, 64.61; H, 3.34; N, 11.59 found: C, 64.62; H, 3.33; N, 11.58.

REFERENCES

1. K. H. Lim, O. Hiraku, K. Komiyama, T. Koyano, M. Hayashi, T. S. Kam, Biologically Active Indole Alkaloids from Kopsia arborea, ***J. Nat. Prod.*** 70, 2007, 1302-1307.
2. I. Ninomiya, Recent Progress in the Synthesis of Indole Alkaloids, ***J. Nat. Prod.*** 55,1992, 541-564.
3. D. Faulkner, ***J. Nat. Prod. Rep.*** 18, 2001, 1-49.
4. V. Lather, P. V. Chowdary, Synthesis And Antimicrobial Activity Of N1- (Arylidine Hydrazidomethyl)-Indoles, 2-(Substituted Aryl)-3-(N1-Indolyl Acetamidyl)-4-Oxo-Thiazolidines And 5-Benzylidine Derivatives Of Thiazolidinones, ***Indian J. Pharm. Sci.*** 65, 2003, 576-579.
5. S. S. Panda, P. V. R. Chowdary, Synthesis of Novel Indolyl-Pyrimidine Antiinflammatory, Antioxidant and Antibacterial Agents, ***Indian J. Pharm. Sci.*** 70 (2), 2008, 208-215.
6. G. S. Adaginamath, A. S. Shyadligeri, R. R. Kavali, Chemoselectivity of indole-dicarboxylates towards hydrazine hydrate, ***Indian J. Chem.*** 38, 1999, 156-159.
7. Arlette Longeon, Brent R. Copp, Elodie Quévrain, Mélanie Roué, Betty Kientz, Thierry Cresteil, Sylvain Petek, Cécile Debitus, and Marie-Lise Bourguet-Kondracki, Bioactive Indole Derivatives from the South Pacific Marine Sponges Rhopaloeides odorabile and Hyrtios sp., ***Mar Drugs.*** 9(5), 2011, 879–888.
8. Min Chen, Chang-Lun Shao, Xiu-Mei Fu, Ru-Fang Xu, Juan-Juan Zheng, Dong-Lin Zhao, Zhi-Gang She, and Chang-Yun Wang, Bioactive Indole Alkaloids and Phenyl Ether Derivatives from a Marine-Derived Aspergillus sp. Fungus, J. Nat. Prod. 76 (4), 2013, 547–553.
9. Yu Li, Rong-Jie Zeng, Qing Lu, Shui-Sheng Wu and Jian-Zhong Chen, Ultrasound/microwave-assisted extraction and comparative analysis of bioactive/toxic indole alkaloids in different medicinal parts of Gelsemium elegans Benth by ultra-high performance liquid chromatography with MS/MS, Journal of Separation Science 37 (3),2014, 308–313.
10. Amnat Eamvijarna, Nelson M. Gomesa, Tida Dethoupa, Jamrearn Buaruangc, Leka Manochb, Artur Silvad, Madalena Pedroe, Ioulia Marinig, Vasilios Roussisg, Anake Kijjoaa, Bioactive meroditerpenes and indole alkaloids from the soil fungus Neosartorya fischeri (KUFC 6344), and the marine-derived fungi Neosartorya laciniosa (KUFC 7896) and Neosartorya tsunodae (KUFC 9213), Tetrahedron 69 (40),2013, 8583–8591.
11. A. Kathleen, A. G. Merrill, PCT. Int. Appl. WO 99, Chem. Abstr. 130, 1999, 276-765.

12. C. A. Bradfield, L. F. Bjeldanes, Structure-activity relationships of dietary indoles: a proposed mechanism of action as modifiers of xenobiotic metabolism, J. Toxicol. Environ. Health 21 (3), 1987, 311-323.
13. R. H. Da shwood, L. Uyetake, A. T. Fong, J. D. Hendricks, G. S. Bailey, Food Chem. Toxicol. 27, 1987, 385-392.
14. Dalip Kumar, N. Maruthi Kumar, Kanako Akamatsu, Eriko Kusaka, Hiroshi Harada, Takeo Ito, Synthesis and biological evaluation of indolyl chalcones as antitumor agents, Bioorganic & Medicinal Chemistry Letters 20 (13), 2010, 3916-3919.
15. V. Calvino, M. Picallo, A. J. López-Peinado, R. M. Martín-Aranda, C. J. Durán-Valle, Ultrasound accelerated Claisen–Schmidt condensation: A green route to chalcones, Applied Surface Science 252 (17),2006, 6071-6074.
16. Zeba N. Siddiqui*, Farheen Farooq and T. N. Mohammed Musthafa, A highly efficient, simple, and ecofriendly microwave-induced synthesis of indolyl chalcones and Pyrazolines, Green Chemistry Letters and Reviews 4, (1), 2011, 63-68.
17. K. Krohnke, The Specific Synthesis of Pyridines and Oligopyridines, Synthesis 1, 1976, 1-24.
18. A. R. Katritzky, E. M. Elisseou, R. C. Patel, B. Plau, Coenzyme models. Part 29. On the unusual spectroscopic behaviour of 10-dodecyl-3-methylisoalloxazine (amphiphilic flavin analogue) in aqueous solution, J. Chem. Soc., Perkin Trans. 2 1982, 125-133.
19. P. Steenwinkel, S. L. James, D. M. Grove, H. Kooijman, A. L. Spek, G. V. Koten, Double cyclometalation via carbon-silicon bond cleavage by palladium(II) acetate. X-ray structure of a cationic 1,4-dipalladated benzene ring and selective synthesis of heterobimetallic 1,4-phenylene-bridged platinum(II)-palladium(II) complexes, Organometallics 16,1997, 513-515.
20. F. Neve, S. Campagna, A. Crispini, Anisometric Cyclometalated Palladium(II) and Platinum(II) Complexes. Structural and Photophysical Studies, Inorg. Chem. 36, 1997, 6150-6156.
21. G. W. V. Cave, J. Hallett, W. Errington, J. P. Rourke, Angew. Chem. 23, 1998, 3466 (Angew. Chem., Int. Ed. 37, 1998, 3270).
22. E. C. Constable, C. E. Housecroft, M. Neuburger, A. G. Schneider, B. Springler, M. Zehnder, Inorg. Chim. Acta 49, 2000, 300.
23. Li, Y.; Liu, Y.; Bu, W.; Guo, J.; Y.Wang, A mixed pyridine–phenol boron complex as an organic electroluminescent material, Chem. Commun. 16, 2000, 1551-1552.
24. C. R. Rice, M. D. Ward, M. K. Nazeeruddin, M. Grazel, Catechol as an efficient anchoring group for attachment of ruthenium–polypyridine photosensitisers to solar cells based on nanocrystalline TiO2 films, New J. Chem. 24 (9), 2000, 651-652.
25. G. W. V. Cave, F. P. Fanizzi, R. J. Deeth, W. Errington, J. P. Rourke, Organometallics 19, 2000, 1801-1803.
26. Thomas J. Delia, John B. Kanaar and Elizabeth Knefel kamp, Diarylthiopyrimidines and pyridines: Synthesis and biological activity, Journal of Heterocyclic Chemistry, 39 (2), 2002, 347–350.
27. K. A. Vishnumurthy, M. S. Sunitha, Adhikari A. Vasudeva, New optical limiting polymeric materials with different π–electron conjugation bridge structures: Synthesis and Characterisation, European Polymer Journal, 48 (9), 2012, 1575-1585.

28. Ludwik Bukowski and Roman Kaliszan, Imidazo[4,5-b]pyridine derivatives of potential tuberculostatic activity, II: Synthesis and bioactivity of designed and some other 2-cyanomethylimidazo[4,5-b]pyridine derivatives, Archiv der Pharmazie 324 (9),1991, 537–542.
29. Gemma O'Donnell, Rosemarie Poeschl, Oren Zimhony, Mekala Gunaratnam, Joao B. C. Moreira, Stephen Neidle, Dimitrios Evangelopoulos, Sanjib Bhakta, Bioactive pyridine-N-oxide disulfides from Allium stipitatum, Journal of Natural Products, 72 (3), 2009, 360-365.
30. P. Patel, S. Koregaokar, M. Shah, H. Parekh, Synthesis of some novel pyrazoline and cyanopyridine derivatives as antimicrobial agents, Farmaco. 51 (1), 1996, 59-63.
31. N. Kumar, A. Chauhan, S. Drabu, Synthesis of cyanopyridine and pyrimidine analogues as new anti-inflammatory and antimicrobial agents, Biomed Pharmacother 65 (5), 2011, 375-380.
32. K. A. Vishnumurthy, M. S. Sunitha, K. Safakath, Reji Philip, Airody Vasudeva Adhikari, Synthesis, electrochemical and optical studies of new cyanopyridine based conjugated polymers as potential fluorescent materials, Polymer 52, 2012, 19.
33. T. Murata, M. Shimada, S. Sakakibara, T. Yoshino, H. Kadono, T. Masuda, M. Shimazaki, T. Shintani, K. Fuchikami, K. Sakai, H. Inbe, K. Takeshita, T. Niki, M. Umeda, K. B. Bacon, K. B. Ziegelbauer, T. B. Lowinger, Discovery of novel and selective IKK-β serine-threonine protein kinase inhibitors. Part 1, Bioorg. Med. Chem. Lett. 13 (5), 2003, 913-918.
34. S. Ayvaz, M. Çankaya, A. Atasever, A. Altuntas, R. A. Janis, P. J. Silver, D. Triggle, 2-Amino-3-cyanopyridine derivatives as carbonic anhydrase inhibitors. J. Adv. Drug Res. 16, 1987, 309-591.
35. D. V. Tyndall, T. A. Nakib, M. J. Meegan, A novel synthetic route to phenyl-substituted pyridines synthesis of benzopyrano[4,3-b]pyridines, benzothiopyrano[4,3-b]pyridines and pyrido[3,2-b][1,4]benzothiazines(1-azaphenothiazines), Tetrahedron Lett. 29 (22), 1988, 2703-2706.
36. M. M. Al-Arab, A facile synthesis of 6-alkoxy-2,4-diaryl-5-cyanopyridine, J. Heterocycl. Chem. 26 (6), 1989, 1665-1673.
37. R. Gupta, A. Jain, M. Jain, R. Joshi, ‘One Pot’ Synthesis of 2-Amino-3-cyano-4,6-diarylpyridines under Ultrasonic Irradiation and Grindstone Technology, Bull. Korean Chem. Soc. 31, 2010, 3080-3082.
38. R. Gupta, A. Jain, M. Jain, R. Joshi, Eco friendly solvent less synthesis of 5-indolyl pyrimido[4,5-d]pyrimidinones, Bull. Korean Chem. Soc., 32, 2011, 899-904.
39. K. C. Joshi, V. N. Pathak, P. Chand, Synthesis of some fluorine containing indole and related compounds, J. Prakt. Chemie. 320 (4),1978, 701-704.

International Journal of Emerging Technology and Advanced Engineering
Website: www.ijetae.com (ISSN 2250-2459, ISO 9001:2008 Certified Journal, Volume 4, Issue 5, May 2014)

Indian Energy Crises and Biodiesel as Renewable Alternative Fuel

Shashank Mohan[1], Manish Jain[2], Amit Pal[3]
[1,3]Department of Mechanical Engineering, Delhi Technological University, Bawana Road, Delhi 110042, India
[2]Department of Mechanical Engineering, RJIT, BSF Academy, Takenpur, Gwalior, India

***Abstract*--In this research paper we found that in order to meet the growing energy needs as a consequence of spiraling demand and diminishing supply, in today's world renewable energy and biomass sources mostly bio-fuels are receiving more attention. The demand for energy has been phenomenon due to the rapid development of certain growing economies, especially in developing countries. Also because of the environmental pollution from internal combustion engines, the increasing global concern has compelled the researcher's worldwide to focus on the renewable alternative fuels. Various research studies to replace petroleum based diesel fuel with the vegetable oils or their derivations suggested that biodiesel can be produced from various vegetable oils, waste cooking oils and animal fats.**

***Keywords*-- Energy crises, Biodiesel, Diesel engine, Pollution, Environment**

I. Introduction

Energy is one of the most significant inputs for growth of all sectors including agricultural, industrial service and transport sectors. Energy has been at the centre stage of national & global economic development for several decades. The demand for energy, around the world is increasing exponentially, specifically the demand for petroleum-based energy. Petroleum derived fuels, actually, exceeds the demand of any other fuels or energy resources. The world consumption for petroleum and other liquid fuel will grow from 85 million barrels/day in 2006 to 107 million barrels/day in 2030. Under these growth assumptions, approximately half of the world's total resources would be exhausted by 2030. Also, as per many studies, the world oil production would peak sometime between 2007 and 2030 [1]. Therefore, the future energy availability is a serious global. Another, major global concern is environmental degradation or climate change such as global warming. Global warming is related with the greenhouse gases which are mostly emitted from the combustion of petroleum fuels. In order to control the emissions of greenhouse gases, Kyoto Protocol targets to reduce the greenhouse gas emission by a collective average of 5% below 1990 level of respective countries.

The Intergovernmental Panel on Climate Change (IPCC) concludes in the Climate Change 2007 that, because of global warming effect the global surface temperatures are likely to increase by 1.1°C to 6.4°C between 1990 and 2100 [1].

II. Energy Crisis

There is a realization throughout the world that the petroleum resources which are non-renewable, are limited and are being consumed at an alarming rate. The growing demand for energy and gradual extinction of fossil fuels has lead to an energy crisis. Most of the power in industries and transportation is derived from oil and coal. Special mention is needed for automobiles where almost all of the fuels for combustion engine today are derived from petroleum, a nonrenewable source of energy, which is nearing its end at an unprecedented pace. The grave name of the energy problem was sharply brought into focus by the oil crisis of 1973. Since then, several price hikes have taken place, upsetting economy of most of the nation. The globe today uses about 147 trillion kWh of energy which is expected to rise in the coming future [2]. A major chunk of this rise will be due to the developing countries, which are bound to grow by leaps and bounds.

Energy Scenario: Indian Context

India had experienced robust growth for the past few years, and after an impressive 9.6 per cent gross domestic product (GDP) growth in 2006-07 the Indian economy is headed towards 8.7 per cent growth in the current fiscal [3]. The energy needs of India are also rising to cope up the growth rate Of the 156.1 million tonnes of crude oil that India consumed in 2007-08; it produced only 34.12 million tonnes [4]. Indian economy is mainly agriculture based and modern agriculture system is heavily dependent upon internal combustion engines for running farm machinery, irrigation pump sets, and other equipments. Indian growth is mainly based on energy, produced by "oil-burning" in IC engines. It is very difficult to find clear blue sky in Indian metropolis. Petroleum fuels are major contributor to ecological imbalance in India.

International Journal of Emerging Technology and Advanced Engineering
Website: www.ijetae.com (ISSN 2250-2459, ISO 9001:2008 Certified Journal, Volume 4, Issue 5, May 2014)

As Indian economy is heavily based upon IC engines, it is not possible in any case to discard them and some other, easily available renewable fuels in India. These renewable fuels must be sought to lease new life to existing engines in order to curb the twin problems of fuel scarcity and air pollution. Various national emission standards have been set by the Government of India through which the fleets are facing greater pressures to switch to cleaner alternative fuels. The alternative fuels are desirable from the fact that they are the only fuels used with recent engine developments, which can meet the stringent EURO-IV emission norms, which are expected to be enforced in India from 2010. India being richer in flora and fauna can look forward to use fuels from bio origin as the suitable alternatives. The prominent bio fuels from Indian perspective are ethanol and biodiesel. India, the world's second most populous nation, has seen its population exploding from 300 million in 1947 to around 1.2 billion today. This rapidly growing population has placed a strain not only on India's infrastructure, but also on its environment. According to the World Health Organization, New Delhi is one of the top ten most polluted cities in the world. Two primary sources of air pollution in India are vehicular emissions and untreated industrial smoke. The number of vehicles has registered a sharp increase more so, during the last decade. In Delhi alone, the vehicle number has crossed about 4.6 million. Today, the vehicular pollution contributes roughly 64 % of total air pollution in Delhi, followed closely by Mumbai at 52% and somewhat controlled figure of 30% for Kolkata. About 50% of the total petroleum products consumed in the country go into the transport sector mainly in the form of high-speed diesel and gasoline [5]. India's per capita energy use and carbon emissions, while lower than the world average, result in a substantial percentage of world energy use and carbon emissions, due to the country's large population and heavy reliance on fossil fuels. Increased use of renewable energy is one means of reducing carbon emissions.

III. Energy Demand And Supply

Energy Security is driven by the demand and supply behaviour. India ranks sixth in the world in terms of energy demand accounting for 3.64% of world commercial energy demand in 2007. Although India ranks fifth in total energy consumption in the world (404.4 MTOE (million tones of oil equivalent), this is only 17.12% of the energy consumed by the largest consumer, i.e. USA (2361.4 MTOE). In per capita terms, its consumption is only about 20% of the global average. Rapid Industrialization and Globalization have pushed the demand of energy to new heights.

In the year 2011, India will have a total population of about 1.3 billion people of which 68% will be living in rural areas. Since diesel constitutes 37 % of total petroleum consumption mainly for transportation and other purposes, its demand is integrally related to economic growth and is seen as a growth inducing factor. Stress of the over-burdening population will augment the strain in terms of the volume of fuel required, but the picture of proven oil reserves distribution doesn't reflect the pleasant sight at all. The share with respect to the energy distribution of the remaining oil reserves across the world is shown in Figure 1.

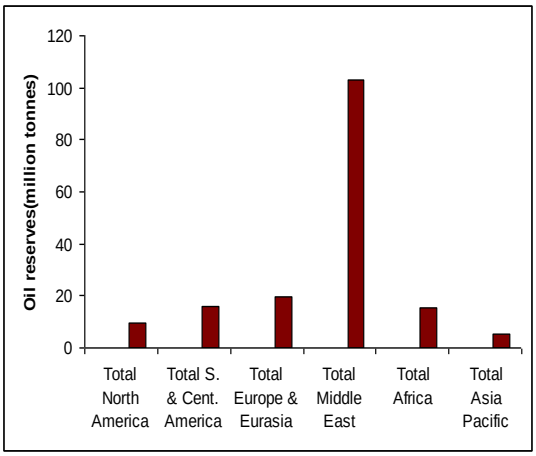

Figure 1: World Oil Reserves, 2008 [6]

It can be observed, that bulk of the reserves are with Middle East. The condition of the Asia Pacific countries presents a dismal trend, presently, only 3.3%of the total share is in their buckets. Therefore, it is apparent that the Asian countries have to change their fuel strategy or live with the escalating burdens of oil imports or with joint venture abroad with the hope to meet their requirement. At present, India imports about 77.94 % of its crude oil required. Net import of crude oil has increased from 74.10 MMT in 2000-01 to 121.67 MMT in 2007-08. India paid Rs.272,699 Crores for importing crude oil in 2007-08. This import comprised about 30 % of the total value of Indian imports in 2007-08 [4]. Heavy dependence on import of crude oil is a subject of serious concern. As per The World Energy out Look, India's dependence on oil import would grow to 91.6 % by the year 2020. The trend of import of crude oil in India is shown in table 1.

As already evident from above discussion that the self reliance of our country is declining and has reached to a very low figure of 21.86% in year 2007-08 as shown in table 2.

International Journal of Emerging Technology and Advanced Engineering
Website: www.ijetae.com (ISSN 2250-2459, ISO 9001:2008 Certified Journal, Volume 4, Issue 5, May 2014)

Although, India has invested considerable resources in petroleum sector, the crude oil production has stagnated around 32-33 million metric tonnes per year over the past decade. The majority of India's roughly 5.4 billion barrels in oil reserves are located in the Bombay High, Upper Assam, Cambay, Krishna-Godavari, and Cauvery basins. India's average oil production level for 2007 was 801000 barrels per day [4]. But the consumption continues to outstrip production. Over the years, the domestic availability of the crude oil has not kept pace with the demand. Table 2 summarises the trends of demand and supply of crude petroleum in the preceding years.

Table 1
Import of Crude Oil in India [4]

Year	Crude Oil	
	Qty MMT	Value (Rs. In Crores)
1996-97	33.91	18538
1997-98	34.49	15897
1999-99	39.81	14876
1999-00	57.80	30695
2000-01	74.10	65932
2001-02	78.70	60397
2002-03	85.81	62876
2003-04	90.43	83528
2004-05	95.86	117003
2005-06	99.41	171702
2006-07	110.86	219991
2007-08	121.67	272699

Table 2
Consumption and Domestic Availability of Crude Oil [4]

Year	Domestic Production (Mt)	Demand (Mt)	(%)Self Reliance
1990-91	33.02	53.72	61.4
1995-96	35.17	62.51	56.2
2000-01	32.43	106.523	30.4
2001-02	32.03	110.738	28.92
2002-03	33.04	115.031	28.72
2003-04	33.38	123.815	26.96
2004-05	33.98	129.84	26.17
2005-06	32.19	131.6	24.4
2006-07	33.99	144.85	23.46
2007-08	34.12	156.1	21.86

IV. Alternate Fuels

To solve dual problems of fossil fuel depletion and environmental degradation, the renewable fuels with lower environmental impact are necessary. Nowadays, many new fuels have been used and biomass derived fuels are among them. Some of the well known biomass derived fuels are ethanol for gasoline engines and bio-diesel for compression ignition engines. Biodiesel is a renewable and environmental friendly alternative fuel for diesel engine which is produced from variety of vegetable oils and animal fats by the trans-esterification process. Transesterification is a chemical reaction in which vegetable oils and animal fats are reacted with alcohol in the presence of a catalyst. The products of reaction are fatty acid alkyl ester and glycerine, and the fatty acid alkyl ester is known as biodiesel. Bio-diesel is an oxygenated fuel containing 10% to 11% oxygen by weight. Also it is a sulphur-free fuel. These lead biodiesel to more complete combustion and less harmful exhaust emissions. However, biodiesel fuel has higher viscosity, density, pour point, flash point and cetane number than diesel fuel. Also the energy content or net calorific value of biodiesel is about 12% lower than that of diesel fuel on a mass basis. Using biodiesel can help in reducing the world's dependence on fossil fuels and also has significant environmental benefits. Using biodiesel instead of the conventional diesel fuel reduces exhaust emissions such as the overall life circle carbon dioxide (CO_2), particulate matter (PM), carbon monoxide (CO), sulphur oxides (SO_x), volatile organic compounds (VOCs), and unburned hydrocarbons (UBHC). However, most of the biodiesels give 10% to 15% higher oxides of nitrogen (NO_x) when fuelling with 100% biodiesel [7]. Depending on the abundantly availability of feedstock in local region, the different feedstocks are tried for the biodiesel production. In the United States, the primary sources for biodiesel production is soy bean oil, while EU nations prefer to utilize rapeseed oil, and in South East Asia regions, palm oil, coconut oil and Jatropha oil are used for biodiesel productions. Growing the production of biodiesel in many countries around the world has been accompanied by the development of standards to ensure high fuel quality. The biodiesel standards are ASTM D6751 in the United States and EN 14214 in EU Nations. The properties of biodiesel are mainly determined by the structure of fatty acids alkyl esters which constitutes it, particularly, the combustion characteristics such as ignition quality, and the fuel properties such as density, viscosity, pour point and oxidation stability of biodiesel are mostly affected by the structure of fatty acids alkyl esters [8].

International Journal of Emerging Technology and Advanced Engineering
Website: www.ijetae.com (ISSN 2250-2459, ISO 9001:2008 Certified Journal, Volume 4, Issue 5, May 2014)

V. Alternative Fuel Attributes

There are some very important parameters which should be considered before adaptation of an alternative fuel in an existing engine. These include:

- No or minimum engine modification
- Use of same storage and transportation infrastructure.
- Biodegradable and non-toxic assuring safe handling and transportation.
- Capability of being produced locally and low investment cost. [2, 3].

The economic benefits of the fuels like vegetable oils, compressed natural gas, ethanol, and methanol etc. compared to the traditional petroleum resources are marginal but the environmental benefits are enormous, thus public policies need to be revised to encourage the development of these resources for which:

- Land for production need to be explored
- An efficient extraction of oil from oil seeds and transesterification plant would be required
- Distribution and storage facilities constructed
- Monitoring of major users for detection of problems
- Large scale use are needed before the technology can be recommended for general use
- The magnitude of our energy needs provides an inexhaustible market of our total agriculture production capacity at the highest possible level
- Farm back to work providing for our food needs and also growing crops and livestock for energy. Energy is the only crop that we could never grow in surplus [4,9].

VI. Biodiesel As An Alternative

Biodiesel is an organic, non-toxic and biodegradable fuel made from everyday renewable resources, like vegetable oils or animal fats. It can power your car's engine and help the environment at the same time. It doesn't contain any petroleum, so forget about escalating gas prices. Biodiesel cuts down on CO2 emissions; in fact, it's the only alternative fuel to have fully completed the health effects testing requirements of the US Clean Air Act. Biodiesel can be purchased at a growing number of fuelling stations around the world but you can also make it in your own backyard. Even if you don't like chemistry, you can brew your own.

Use of Biodiesel in Railways

Indian Railways has set up a biodiesel production unit at Loco Workshops Perambur in Chennai which is successfully manufacturing biodiesel for the past 8 years. Similar plants are being established at Raipur in Chattisgarh and Tondiarpet near Chennai. Biodiesel is being used in blends of B5, B10 and B20 for diesel engines of transport vehicles and locomotives. These locomotives have 2600 hp diesel engines and are mostly underutilized. Similarly both these workshops invariably use diesel engine operated fork lift trucks as the components handled are quite heavy. As already Biodiesel is successfully introduced it can also be tried out in both of these workshops in days to come. [10-11]

Waste Vegetable Oil

Restaurants use many different oils for frying foods. These oils are subjected to very high temperatures as well as fats and water from various foods. The process of frying food changes the physical and chemical make-up of the oil increasing the acidity and water content. This affects the Transesterification Process - the chemical process of making of biodiesel. Higher FFA's require more catalyst and alcohol, which in turn increases production costs. Other problems may arise from oils high in water or FFA's, such as poor fuel from incomplete reaction and the formation of emulsions from a water washing process due to excess soap formation or shortened life of ION exchange resins. WVO with the least amount of water ("under 1%") and low FFA'S (fewer than 5%") are desirable. Biodiesel Chemically known as Fatty Acid Methyl Ester (FAME) refers to any vegetable oil or animal fat that has been altered through a process called transesterification, a process in which oil, (an ester) gets converted to biodiesel, (another ester) and glycerin a byproduct. Biodiesel is a clean burning renewable fuel that mimics the properties of petroleum diesel, but with increased lubricity and lower emissions. Biodiesel can be mixed in any ratio with petroleum diesel to create a blend. Common blends are B2 and B20.

Places to look for high quality oil would be restaurants that fry low fat foods, vegetables, fish, chicken, and potato chips. Example: Oriental restaurants and shrimp boats etc. The types of WVO to look for are Canola, Soy, Sunflower and Corn Oil in this order from thin to thick. The thickness or viscosity of the oil becomes a concern in cold climates as biodiesel made from heavier oil has "higher viscosity" and poor cold weather performance.

International Journal of Emerging Technology and Advanced Engineering
Website: www.ijetae.com (ISSN 2250-2459, ISO 9001:2008 Certified Journal, Volume 4, Issue 5, May 2014)

Thinner oils will have better cold flow properties and better cold weather performance. Biodiesel made from WVO will usually have a higher viscosity than biodiesel made from virgin oil due to the physical and chemical changes made to WVO in the frying process. This will not be a large temperature difference, but you should expect a few degrees difference. Hotels and restaurants use many different oils for frying foods. These oils are subjected to very high temperatures as well as fats and water from various foods. The process of frying food changes the physical and chemical make-up of the oil increasing the acidity and water content. This affects the Transesterification Process - the chemical process of making of biodiesel. Higher FFA's require more catalyst and alcohol, which in turn increases production costs. Other problems may arise from oils high in water or FFA's, such as poor fuel from incomplete reaction and the formation of emulsions from a water washing process due to excess soap formation or shortened life of ION exchange resins. WVO with the least amount of water ("under 1%") and low FFA'S (fewer than 5%") are desirable look for high quality oil would be restaurants that fry low fat foods, vegetables, fish, chicken, and potato chips. Example: Oriental restaurants and shrimp boats etc. The types of WVO to look for are Canola, Soy, Sunflower and Corn Oil in this order from thin to thick. The thickness or viscosity of the oil becomes a concern in cold climates as biodiesel made from heavier oil has "higher viscosity" and poor cold weather performance. Thinner oils will have better cold flow properties and better cold weather performance. Biodiesel made from WVO will usually have a higher viscosity than biodiesel made from virgin oil due to the physical and chemical changes made to WVO in the frying process. This will not be a large temperature difference, but you should expect a few degrees difference.

Non-hydrogenated or partially hydrogenated oils will be the most common type of oils used in restaurants. Some will use completely hydrogenated oil that is solid at room temperature and should be avoided. Non-hydrogenated oil will have better cold flow properties, but will not store as well without adding stabilizers.

Partially hydrogenated oil has a higher "cloud point" but will not oxidize as fast. The difference between non-hydrogenated and partially hydrogenated oil is small and both are treated the same when making biodiesel. Hydrogenation results in the conversion of liquid vegetable oils to solid or semi-solid fats. Complete hydrogenation converts unsaturated fatty acids to saturated ones. Changing the degree of saturation of the fat changes some important physical properties such as the melting point, which is why liquid oils become semi-solid. Since partially hydrogenated vegetable oils are cheaper than animal source fats and are available in a wide range of consistencies, and have other desirable characteristics (e.g., increased oxidative stability). Table 3 gives the summary of proposed BIS (Bureau of Indian Standards) standards for biodiesel.

Most restaurants tend to use partially hydrogenated oil due to cost and longer life of Non-hydrogenated or partially hydrogenated oils will be the most common type of oils used in restaurants. Some will use completely hydrogenated oil that is solid at room temperature and should be avoided. Non-hydrogenated oil will have better cold flow properties, but will not store as well without adding stabilizers. Partially hydrogenated oil has a higher "cloud point" but will not oxidize as fast. The difference between non-hydrogenated and partially hydrogenated oil is small and both are treated the same when making biodiesel. Hydrogenation results in the conversion of liquid vegetable oils to solid or semi-solid fats. Complete hydrogenation converts unsaturated fatty acids to saturated ones.

Changing the degree of saturation of the fat changes some important physical properties such as the melting point, which is why liquid oils become semi-solid. Since partially hydrogenated vegetable oils are cheaper than animal source fats and are available in a wide range of consistencies, and have other desirable characteristics (e.g., increased oxidative stability. Most restaurants tend to use partially hydrogenated oil due to cost and longer life of oil. Table 4 gives the Properties of biodiesel from different oils.

International Journal of Emerging Technology and Advanced Engineering
Website: www.ijetae.com (ISSN 2250-2459, ISO 9001:2008 Certified Journal, Volume 4, Issue 5, May 2014)

Table 3
summary of proposed BIS(Bureau of Indian Standards) standards for biodiesel [9]

Standard / specification	Unit	Proposed BIS
Density @ 15°C	g/cm^3	0.87 –
Viscosity @ 40°C	mm^2/s	3.5 -
Flash point	°C	>=100
Sulphur, max.	%mass	0.035
CCR,100%distilation	%mass	0.05
Sulphated ash,max,	%mass	0.02
Water.max	mg/kg	500
Total contamination,	mg/kg	20
Cetane no	-	>=51
Acid no	mg	<=0.8
Methanol	%mass	<=0.02
Ester content	%mass	>=96.5
Diglyceride	%mass	<=0.2
Triglyceride	%mass	<=0.2
Free glycerol	%mass	<=0.02
Total glycerol	%mass	<=0.25
Iodine no		<=115
Phosphorus	ppm	<=10
Alkaline matter(Na,K)		<=10
Distillation, T 95%	°C	<=360

Table 4
Properties of biodiesel from different feedstocks [9]

Vegetable oil methyl esters	Kinematic viscosity mm^2/s	Cetane no.	LHV MJ /kg	Cloud point (°C)	Pour point (°C)	Flash point °C	Density (kg/l)
Peanut	4.9	54	33.6	5	–	176	0.883
Soya bean	4.5	45	33.5	1	-7	178	0.885
Babassu	3.6	63	31.8	4	–	127	0.875
Palm	5.7	62	33.5	13	–	164	0.880
Sunflower	4.6	49	33.5	1	–	183	0.860
Tallow	–	–	–	12	9	96	–
Diesel	3.06	50	43.8	–	-16	76	0.855
20% Bid-d blend	3.2	51	43.2	–	-16		0.859

VII. CONCLUSIONS

In this work it is observed that the fuel properties of biodiesel need to be monitored when different feedstocks are used. If the fuel properties of biodiesel are compared to petroleum diesel fuel, it can be seen that biodiesel has higher viscosity, density, pour point, flash point and cetane number, near-zero aromatic compound, and no sulphur link make it more suitable than petro-diesel. Keeping the large wasteland available in India a tangible planning is needed to use the vegetable oil biodiesel as a supplement/ substitute for the petro-diesel.

REFERENCES

[1] B. Ghobadian A, H. Rahimi, A.M. Nikbakht,G. Najafi ,T.F. Yusaf. "Diesel engine performance and exhaust emission analysis using waste cooking biodiesel fuel with an artificial neural network". Renewable Energy 976–982,34 (2009).

[2] Yinnan YUAN, Deqing MEI, Zhong WANG, Tian ZHANG. "Combustion and emissions of the diesel engine using bio-diesel fuel." Front. Mech. Eng. China,: 189–192,3(2008).

[3] Jehad A. A. Yamin,Nina Sakhnini,Ahmad Sakhrieh, M Hamdan. "Performance of CI engines using Biodiesel as fuel." Amman-Jordan, March 31st – April 2nd(2009).

[4] Sukumar Puhan, A. Gopinath,G. Nagarajan. "Combustion, performance and emission characteristics of a DI CI engine using biodiesel with varied fatty acid composition." Renewable Energy Technology, Vol. 1, No. 1,(2009).

[5] O. M. I. Nwafor, G. Rice, A. I.Ogbonna. "Effect of advanced injection timing on the performance of rapeseed oil in diesel engines." Renewable Energy Renewable Energy 21(2000),433–444,

[6] Md. Nurun Nabi, Md. Shamim Akhter, Mhia Md. Zaglul Shahadat. "Improvement of engine emissions with conventional diesel fuel and diesel–biodiesel blends." Bioresource Technology 97 (2006),372–378.

[7] D.H. Qi,L.M. Geng, H. Chen,Y.ZH. Bian, J. Liu, X.CH. Ren. "Combustion and performance evaluation of a diesel engine fuelled with biodiesel produced from soybean crude oil." Renewable Energy 34 (2009), 2706–2713

[8] Avinash Kumar Agarwal. "Biofuels (alcohols and biodiesel) applications as fuels for internal combustion engines." Progress in Energy and Combustion Science 33 (2007), 233–271.

[9] D. N. Tewari, Report of the committee on development of BIO-FUEL, New Delhi, 2003 (43 - 109)

[10] B. K. Barnwal, M.P. Sharma, Prospects of biodiesel production from vegetable oils in India, Renewable and Sustainable Energy Reviews, 9 (2005) 363–378.

[11] Suresh D. Mane and N. Nagesha, "Renewable Energy Technologies for Carriage Repair Shops: A Case Study of Two Workshops" The International Journal of Engineering And Science|Vol. 1(2) (2012), 324-331

frontiers in
CELL AND DEVELOPMENTAL BIOLOGY

REVIEW ARTICLE
published: 11 June 2014
doi: 10.3389/fcell.2014.00026

Manufacturing blood *ex vivo*: a futuristic approach to deal with the supply and safety concerns

Vimal K. Singh[1]*, Abhishek Saini[1], Kohichiro Tsuji[2], P. B. Sharma[1] and Ramesh Chandra[3]

[1] *Stem Cell Research Laboratory, Department of Biotechnology, Delhi Technological University, Delhi, India*
[2] *Departments of Pediatric Hematology/Oncology, Research Hospital, The Institute of Medical Science, The University of Tokyo Hospital, Tokyo, Japan*
[3] *Dr B. R. Ambedkar Center for Biomedical Research, University of Delhi, Delhi, India*

Edited by:
Cedric Viero, Saarland University Medical Faculty, Germany

Reviewed by:
Joao Mario Martins Bigares, Cardiff University, UK
Tomo Saric, University of Cologne, Germany

****Correspondence:***
Vimal K. Singh, Stem Cell Research Laboratory, Department of Biotechnology, Delhi Technological University, Shahbad Daulatpur, Bawana Road, Delhi-110042, India
e-mail: vim_kissor@yahoo.co.in; vimalkishorsingh@gmail.com

Blood transfusions are routinely done in every medical regimen and a worldwide established collection, processing/storage centers provide their services for the same. There have been extreme global demands for both raising the current collections and supply of safe/adequate blood due to increasingly demanding population. With, various risks remain associated with the donor derived blood, and a number of post collection blood screening and processing methods put extreme constraints on supply system especially in the underdeveloped countries. A logistic approach to manufacture erythrocytes *ex-vivo* by using modern tissue culture techniques have surfaced in the past few years. There are several reports showing the possibilities of RBCs (and even platelets/neutrophils) expansion under tightly regulated conditions. In fact, *ex vivo* synthesis of the few units of clinical grade RBCs from a single dose of starting material such as umbilical cord blood (CB) has been well established. Similarly, many different sources are also being explored for the same purpose, such as embryonic stem cells, induced pluripotent stem cells. However, the major concerns remain elusive before the manufacture and clinical use of different blood components may be used to successfully replace the present system of donor derived blood transfusion. The most important factor shall include the large scale of RBCs production from each donated unit within a limited time period and cost of their production, both of these issues need to be handled carefully since many of the recipients among developing countries are unable to pay even for the freely available donor derived blood. Anyways, keeping these issues in mind, present article shall be focused on the possibilities of blood production and their use in the near future.

Keywords: RBCs, *ex-vivo* erythrocytes, manufacturing blood, hematopoietic stem cells, induced pluripotent stem cells

INTRODUCTION

Initially, started by Harvey's studies of blood circulation system, blood transfusion began in the 17th century with animal blood transfusion experiments. The first fully documented report on blood transfusion in humans was from Dr. Jean-Baptiste Denys, who in 1665 successfully transfused blood from a sheep in a 15 years old boy. Though, he could not succeed in later transfusions as recipients died after transfusions were made. In similar studies, Dr. Richard Lower demonstrated the effects of changes in blood volume in circulatory function and developed methods for cross-circulatory study of animals. The first successful human blood transfusion was reported by Dr. James Blundel (1818) between a married couple for a postpartum hemorrhage. However, in 1901, the breakthrough was achieved in human transfusion with the discovery of blood group antigen by Austrian researcher Karl Landsteiner, who discovered that red blood cells got clumped when incompatible blood types were mixed and immunological reaction occurred if the recipient of a blood transfusion had antibodies against the donor blood cells. This "Nobel Prize" (1930) winning discovery made it possible to determine blood type and paved the way for safe blood transfusions. Since then many other blood groups have been discovered. Following to these discoveries a number of blood banks were established during 1940–1950s and it is an inevitable part of all the modern clinical modalities (Alter and Klein, 2008).

The global blood collection was reported to be about 103 million units (www.who.int/worldblooddonorday/en/) (Department of Health and Human Services, 2010, 2013; World Health Organization, 2011). The quality and quantity of donor derived blood collection remain unevenly scattered in economically developed and developing countries. Almost 50% of these blood collections is made in developed countries, which accommodate only a mere 15% fraction of the world's population. Presently, the blood collection seems to be sufficient in economically developed countries. It is supported by reports showing 30,000 annual blood donations on an average per blood center through ∼8000 blood centers scattered in 159 high-income countries (Department of Health and Human

Services, 2010, 2013). For example, in U.S. the total no. of blood unit collected were 5% more than the actual transfusion made during year 2011 (Department of Health and Human Services, 2013). On the contrary, this number of collections/per center is very less (3700) in developing countries. As per WHO report 82 low income and middle income countries have only 10 donations per 1000 people in the population that would remain highly insufficient to supply a comparable large population residing in these countries (World Health Organization, 2011). Further, the screening facilities are very much inefficient in most of the developing countries. As per WHO record, 39 countries are not able to screen all blood donations for one or more of the following transfusion-transmissible infections (TTIs): HIV, hepatitis B, hepatitis C, and syphilis (Department of Health and Human Services, 2013). Again, there are only 106 countries which have national guidelines on the appropriate clinical use of blood. It would be worth noticing that only 13% of low-income countries have a national haemovigilance system to monitor and improve the safety of the transfusion process. Moreover, the blood supply may look sufficient for the time being in developed countries, it likely becomes inefficient to keep supporting a rapidly growing proportion of elderly population (>60 years age) and burgeoning demand for blood transfusions for surgical treatments by the year of 2050 (U.S. Census Bureau, 2004; Ali et al., 2010).

One of the major challenges in clinical settings is to find blood group compatibility for more than 30 blood group system (308 recognized antigens) including ABO & Rh antigens (Daniels et al., 2009).

There are a number of situations such as rare phenotypes, hemoglobinopathies, polytransfusion patients and polyimmunization that may result in significant complications (World Health Organization, 2011) adding more complexity to the supply constraints. Recent technologies such as antigen masking and enzymatic cleavage to generate universal donor blood groups (O and RhD antigens) have been proposed. But these methods are yet to be developed (Bagnis et al., 2011). While keeping these issues in mind, it is worth noticing that the donated blood is tested for various kinds of infections before any transfusion could be made [e.g., HIV-1, HIV-2, HTLV-1, HTLV-2, Hepatitis B, Hepatitis C, Syphilis (*T pallidum*), Chagas disease (*T cruzi*), and West Nile Virus, Cytomegalovirus (CMV)], and a number of precautionary measures are followed during transfusion procedures. Even then blood transfusions are often associated with several complications (Alter and Klein, 2008; World Health Organization, 2011). These complications not only compromise the quality of treatment, but may add to the overall cost of the regime also which remain associated with it in any clinical setting (Department of Health and Human Services, 2010). This is true even in the developed countries where 0.24 % transfusion has been reported to be associated with adverse reactions (Department of Health and Human Services, 2013). For example, adverse events from transfusions in the US only may account for approximately $17 Billion every year. These complications depend upon the patient status or specific transfusion quantity involved. These situations have evoked researchers to develop alternate methods to get blood from various non-donor derived sources. In the search of blood alternates researchers have developed various artificial molecules mimicking functionalities of blood RBCs. The majority of these molecules is either hemoglobin based oxygen carriers or perfluorocarbon solutions. Hemoglobin based carriers are reported to be inefficient as compared to the oxygen carrying capacity of native RBCs. Whereas, perflorocarbons could not become popular due to their limited functional applications (Winslow, 2006; Henkel-Honke and Oleck, 2007; Natanson et al., 2008; Silverman and Weiskopf, 2009; Castro and Briceno, 2010).

Ex vivo expansion of erythrocytes or manufacturing blood from stem cell is the most attracting approach among the global research community for the last few years. The basis for the principle that *ex vivo* cultivated RBCs (or other blood cells) may be of clinical use was provided by Nakamura and his colleagues who have demonstrated that RBCs derived from the immobilized ESCs cell line can protect mice from lethal anemia (Hiroyama et al., 2008). Recently, the proof-of-concept was described by first in-human blood transfusion using *ex-vivo* generated RBCs (Giarratana et al., 2011). In a major landmark study, Giarratana et al. shown the survival capacity of *ex vivo* cultivated RBCs in humans. As described by them, the $CD34^+$ cells obtained from volunteer donors as an aphaeresis product were cultured in a serum free media (with the addition of Stem cell factor (SCF), Interleukin-3 (IL-3), and Erythropoietin (EPO) resulting into 2 ml of blood RBCs equivalent (10^{10} cells) under GMP conditions. The *ex vivo* expanded RBCs were labeled with ^{51}Cs to trace their fate in patients as approved by FDA U.S. (Giarratana et al., 2011) and demonstrated to be comparable with any native RBCs transfusion. These findings established the proof-of-concept for clinical utilization of *ex vivo* generated RBCs globally. As discussed in the next section, a number of methods have been demonstrated so far (**Figure 2**), which ensure the feasibilities of *ex vivo* RBCs expansion from various source materials (e.g., $CD34^+$ HSCs, Embryonic stem cells, and IPSCs) (**Figure 3**). There are various factors which essentially regulate the yield and the level of RBCs maturation through these protocols. Reports are there, showing numerical expansion of erythrocyte precursors up to ∼0.5 transfusion unit/donation from UCB $CD34^+$ cells, and approximately 2 million fold expansions of enucleated erythrocytes functionally comparable to native RBCs through slight modification of culturing techniques (Neildez-Nguyen et al., 2002). Further, large scale production (up to 10 transfusion unit) from two units of UCB have been demonstrated by technically complex protocols (described in later sections) which presently may appear ill suited from the commercial scale production point of view but strengthen the concept that with the advancement of techniques sufficient transfusable units may be produced (Fujimi et al., 2008). Besides that, RBCs precursors, cellular intermediates/nucleated erythroid precursors are generated through these protocols, which may also be of use if transfused. It is expected that these cells are likely to become functionally matured *in vivo* while interacting with internal factors governing their maturation. The same has been reported both in human and animal models (Ende and Ende, 1972; Neildez-Nguyen et al., 2002). Conceptually, the maturing cells along with functionally matured cells may aid to maintain the cellular content at the time of transfusion. These maturing cells may proliferate and each cell may give rise to 4–64 cells before they get enucleated and functionally

matured *in vivo*. This hypothesis is supported by the data available from clinical observations in developing countries where 40–80 ml of compatible CB blood (containing 4–7 $\times 10^{10}$ RBCs and 2–8 $\times 10^{9}$ erythroblast cells) is occasionally used for transfusion in emergent conditions (Ende and Ende, 1972). Together, these reports strengthen the concept that *ex vivo* RBCs expansion likely support the different clinical short-comes to exist due to limited supply and various rare blood based disorder.

However, a number of factors such as technological barriers associated with large scale production and per unit production cost remain to be considered in order to support a large population. The present scale of RBCs production would require to be enhanced several times in a more cost-effective and timely manner. Commercial production of blood may lack essential background financial support in developing countries which are suffering from even more sensitive issues. Moreover, in the absence of more realistic, achievable goals it may become hard even in the capitalistic developed countries. Present article focuses on various issues related to current methods and their feasibilities to realize limited "blood pharming" in near future.

ERYTHROPOIESIS *IN VIVO*

Hematopoiesis, a dynamic process, is regulated both temporally and spatially. It may be classified as "*primitive hematopoiesis*" in featus where specified cells termed as "blood islands" are generated by yolk sac (YS). In YS, nucleated RBCs exclusively expresses embryonic Hbs (Gower-1, Gower-2, and Hb Portland) are generated for a small period of time. Following to that, a second wave of hematopoiesis or "*definitive hematopoiesis*" produce hematopoietic stem cells, which have the potential of transfusion and includes enucleated RBCs along with various other hematopoietic cells. This event takes place largely in the fetal liver and up to a little extent in YS. In later stages of featus development Definitive hematopoiesis occurs in bone marrow (BM) and that serves as the only site of hematopoiesis in adults through their life. The hematopoietic cells from fetal and adult definitive hematopoietic stages may be differentiated on the basis of their HB contents. In the fetus hematopoiesis α and γ globins, (the components of fetal Hb) (Hb F), are expressed, and in the later β globins (the components of adult-type) (HbA), are expressed (Palis, 2008; Baron et al., 2012).

Erythropoiesis or generation of RBCs includes hematopoietic progenitor cells, which are first differentiated into committed erythroid progenitors and thereafter proliferate/converted to functional red blood cells in a highly regulated hierarchal manner. This dynamic process is tightly regulated through a number of growth factors which ensure the maintenance of regular homeostasis of the RBCs mass.

The entire process of erythropoiesis may be defined to occur in three stages: (1) Erythropoietic commitment of HSCs: this includes development of erythroid committed blast cells from multipotent hematopoietic progenitors; (2) Division and differentiation of these morphologically identifiable erythroid progenitor cells; and (3) Terminal differentiation including cellular morphological changes such as enucleation, to produce reticulocytes and ultimately maturation: of RBCs (**Figure 1**).

The Hematopoietic stem cells are generated in YS and may be differentiated into a common myeloid progenitor that, in turn, gives rise to bipotent progenitors restricted to either the granulocyte/macrophage or the erythroid/megakaryocytic pathways (Suda et al., 1983; Debili et al., 1996; McLeod et al., 1996; Akashi et al., 2000). A comparable stage of development defined *in vitro* using cytokine containing semisolid medium (**Figure 1**) is the colony-forming unit granulocyte, erythroid, macrophage, megakaryocytic (CFU-GEMM) precursor that gives rise to bipotent progenitors restricted to either granulocyte/macrophage or erythroid/megakaryocytic pathways (Suda et al., 1983; Debili et al., 1996; McLeod et al., 1996). Those progenitors which express erythropoietin receptor (EPOR) remain responsive to erythropoietin (EPO) and are committed to the erythroid/megakaryocytic pathway.

On the other hand, EPOR deficient progenitor cells are committed to the myeloid pathway. The burst-forming unit–erythroid (BFU–E), which gives rise to colony-forming unit–erythroid (CFU–E) is termed as the most immature erythroid-restricted progenitor. Among them, early BFU–E (blast-like cells) are highly proliferative, and give rise to clustered burst colonies of up to 20,000 cells in semisolid culture assays.

However, BFU–E bear comparatively small number of EPOR but later progenies (daughter cells) derived from them acquire a high expression level of EPOR and become EPO responsive, transferrin receptor positive, and begin to express hemoglobin (Heath et al., 1976; Lichtman et al., 2007). Later on, CFU–E are derived from these cells, which are highly responsive to EPO, but generate smaller colonies, and express many of the gene products required for definitive erythroid development (**Figure 1**). There are reports describing a cell division stimulating anti-apoptotic role of EPO in late-stage erythroid cells derived from CFU–E. At this stage of development cells may start the synthesis of hemoglobin and acquire cytoskeletal proteins in tissue culture systems. Moreover, cellular adhesion molecules are expressed in these cells that help define them as nucleated erythroblasts. Thereafter morphologically identifiable nucleated erythroid precursor become visible, which progress from the pro-erythroblast to basophilic, polychromatophilic, and orthochromatic cell forms leading to the reticulocyte (**Figure 1**) (Stephenson et al., 1971; Lichtman et al., 2007; Jing et al., 2013).

Erythroid differentiation encompasses four distinct major cellular processes such as, (1) the accumulation of hemoglobin that participates in driving the basophilic to acidophilic cytoplasmic changes seen during maturation, (2) limited erythroblast expansion, (3) a continued decrease in cell size, (4) and nuclear condensation leading to their final enucleation. These highly regulated developmental changes take place in the microenvironment of BM niche where "erythroblast islands" are closely associated with macrophages that serve as stromal or nurse cells (Bessis et al., 1978; Manwani and Bieker, 2008; Rhodes et al., 2008). These erythroid development stages end up with the exit of reticulocytes from the marrow, which now enter the circulation and get matured into erythrocytes. The characteristic features of this stage include disassembly of ribosomes, Golgi bodies, and other cellular machinery, removal of organelles, enucleation, changes in

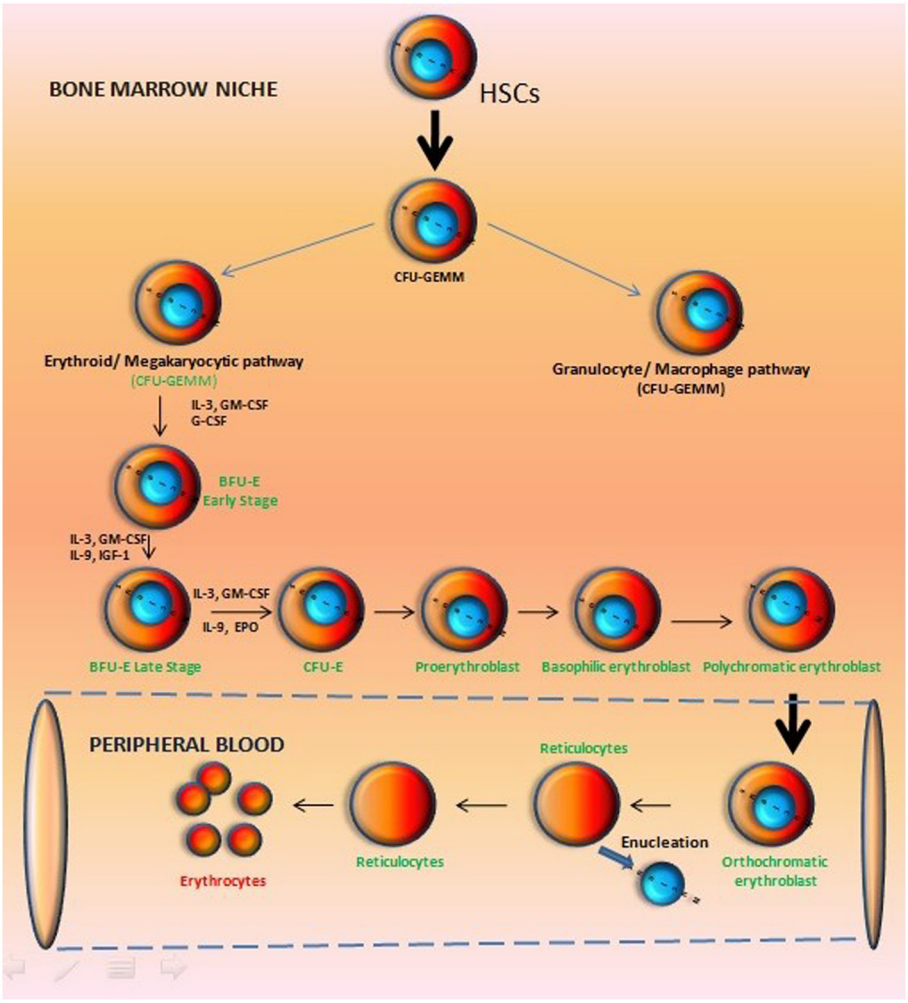

FIGURE 1 | Hierarchy of erythropoietic development in vertebrates. In adult Bone Marrow, committed progenitors arising from hematopoietic stem cells give rise to erythroblasts, and as the progeny of a stem cell progress through development, there is a loss of their multipotency while increasing lineage restriction. The various cellular stages in erythrocyte development are identified by their ability to form colonies in semisolid medium supplemented with specific cytokines and by cell surface markers.

the cytoskeleton leading to the classic biconcave discoid shape, and then release into the circulation (Department of Health and Human Services, 2013). Terminal maturation takes place in the erythroblast islands, which involves participation macrophages of with maturing erythrocytes (Bessis et al., 1978; Manwani and Bieker, 2008; Rhodes et al., 2008).

The mature erythrocyte have a life span of 120 days in blood circulation, and afterwards "senescence" occurs reflected through changes in surface antigen expression or physical characteristics of the cell triggering their removal from the blood by macrophages/reticuloendothelial system (Gifford et al., 2006). Thus, hematopoiesis is regulated through changes in body compartments during mammalian development, from embryo to adult, and depending on the age of development, specialized microenvirnmental niches precisely regulate hematopoietic development (Migliaccio et al., 1986; Palis and Yoder, 2001; Baron and Fraser, 2005; Mikkola et al., 2005; McGrath and Palis, 2008).

EX VIVO ERYTHROPOIESIS: AN OVERVIEW

There has been considerable progress in the field of developing biological control over the expansion of erythrocytes to generate terminally differentiated, fully functional RBCs (Migliaccio et al., 2012). The *in vivo* hematopoietic development process have been studied (**Figure 1**) and an in depth knowledge of the generation of erythroblast regulated through various growth factors have paved the way to mimic the process *in vitro* (Lodish et al., 2010). Altogether, these reports demonstrated the enormous potential inherited by three major cell types including (i) $CD34^{+}$ HSPCs, (II) Embryonic stem cells/induced pluripotent stem cells, and (III) immortalized erythroid precursors which can be differentiated into erythroid lineages by using almost similar/overlapping protocols (**Figure 2**) (**Table 1**). Regardless of their types, stem cells are promoted to become erythroid progenitor in three basic steps viz. commitment, expansion, and maturation. There are a number of reports showing use of various cytokines/growth factors

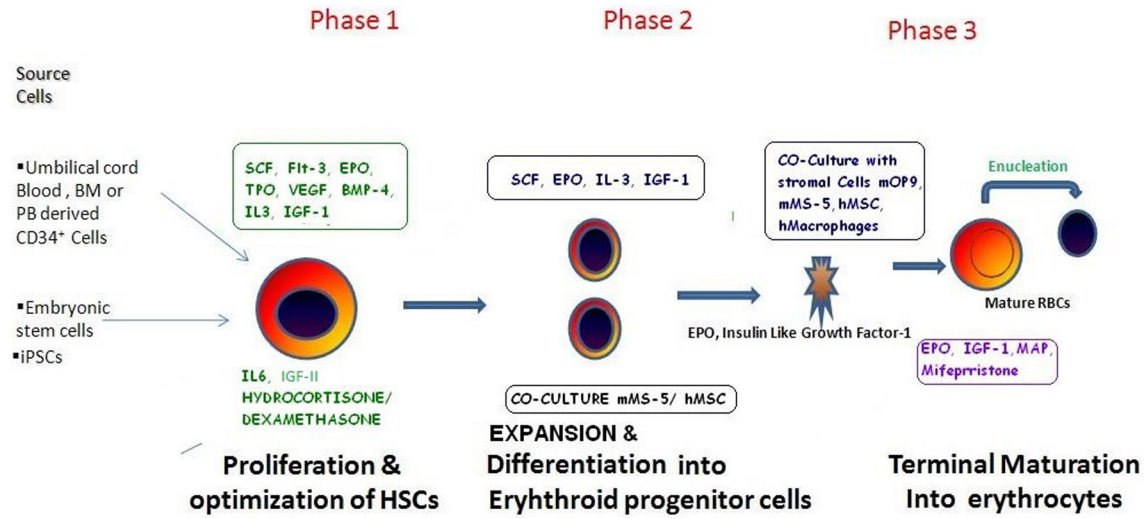

FIGURE 2 | The various methods/protocols described so far for the *ex vivo* RBCs expansion. As discussed in the main text, manufacturing blood may involve various step which are to be categorized in three main phases as depicted in the figure. In phase 1: initial source material is to be collected from a variety of source material(s) on the basis of their availability, suitability, and expansion potential and grown in medium generally supplemented with growth factors to enhance HSCs proliferation: subsequently these cells are cultured in the presence of Erythropoietin to induce their differentiation and maintenance into erythropoietic progenitor stage. Finally, in Phase 3 cultures these Erythropoietic progenitors may be co cultured with murine/human stromal cell line support to induce their maturation and enucleation resulting into mature RBCs. These RBCs are evaluated for their biochemical properties and various antigenic profiles to ensure their nativeness.

(SCF and EPO are most common) to generate variable yields of immature progenitors or mature RBCs with or without using animal/human derived feeder coculture system (**Figure 2**). Recently, a new concept of transdifferentiation (directly differentiating human fibroblast cells into erythroblasts) has been shown to bypass the HSPC state (**Figure 3**) (Szabo et al., 2010). Although promising, but the technique remains to be evaluated for their potential to generate large scale RBCs. Most of these protocols suffer from similar problems such as degree of enucleation or erythrocyte formation, predominate form of Hb expressed by them, use of animal derived products such as serum and feeder cell coculture, and clinical transfusion related problems such as blood type matching and unavailability of sufficient number of RBCs for transfusion. All these issues can be summarized in the following sections.

CD34$^+$ HEMATOPOIETIC CELLS FROM VARIOUS SOURCES AND THEIR USE FOR *EX VIVO* RBCs CULTURE

CD34$^+$ cells from peripheral blood (PB), cord blood (CB), and BM have been in use for clinical transplantations for more than two decades (Carmelo et al., 1995). Initialed by Fibach et al. the methods to generate RBCs from CD34$^+$ HSPCs have been existing for a long time (Fibach et al., 1989, 1991; Wada et al., 1990). Douay et al. were quick to demonstrate functional characteristics of the erythrocytes generated by CB derived CD34$^+$ HSPCs (Douay, 2001; Neildez-Nguyen et al., 2002). Their studies confirmed a higher erythrocyte generating potential in comparison to myeloid precursors with low (4%) enucleation efficiency (Neildez-Nguyen et al., 2002). Giarratana et al. further modified the protocol and demonstrated 90% enucleation efficiency in a similar 3 step method for adult blood/BM derived CD34$^+$ cells (Giarratana et al., 2005) by co-culturing them with murine stromal cell line (MS5) or Human mesenchymal stem cells (HuMSC). The procedure resulted in, 20,000 fold, 30000 fold and 2×10^5 fold increment in the erythrocytic cell generation when BM, GM-CSF mobilized PB, and CB derived CD34$^+$ cells were used respectively (Douay and Andreu, 2007; Douay and Giarratana, 2009; Douay et al., 2009). This group further reported 5–10 units of blood cells on prolonged culture with feeder cell coculture system (Douay and Andreu, 2007; Douay and Giarratana, 2009; Douay et al., 2009). The cells were reported to have native RBCs like functional characteristics as described by normal glucose-6-phosphate dehydrogenase (G6PD) and Pyruvate Kinase (PK) enzyme levels, membrane deformability and oxygen dissociation characteristics. This was also evident by their similar survival rate in non-obese diabetic/severe combined immunodeficient (NOD/SCID) mice following to intraperitoneal infusion of carboxyfluorescein diacetate succinidyl acetate (CFSE) labeled cells.

These methods suffer from two major drawbacks such as (i) use of animal serum and co-culture system and (ii) low yield of functionally matured RBCs per unit of blood cells, which tempted researchers to identify more defined cocktail of growth factors to achieve a better control over erythrocytes proliferation and differentiation. Malik et al. demonstrated generation of ∼10–40% enucleated erythrocytes by enriched CD34$^+$ cells from CB, PB, and BM (Malik et al., 1998) in a serum free liquid culture system (with Flt-3, GM-CSF, EPO). This report indicated the possibilities of generating erythrocytic progenitors in the absence of animal derived serum that is strongly recommended by most clinicians. Following to these reports $10^5 - 1.5 \times 10^8$ folds erythroid cell expansion have been reported in similar serum free environment. (Panzenböck et al., 1998; Freyssinier et al., 1999).

Table 1 | Progression in the field of *ex vivo* RBCs expansion during last two decades.

S. no.	Cell source and culture time	Growth factors	Co-culture	Expansion	Units of blood	Enucleation rate	Animal or human serum/plasma	Key points	References
1	CB CD34+ 21 days	FLT-3, SCF, TPO, EPO, IGF-1	NO	NA	NA	4% *in vitro* 99% *in vivo*	No	Basis for transfusion potential of *ex vivo* cultured RBCs in animal model	Neildez-Nguyen et al., 2002
2	Cord blood 21 days	SCF, IL-3, EPO hydrocortisone	Murine stromal mMS-5	1.95×10^6	4.6/CB	95%	No	First *in vitro* production of RBCs	Giarratana et al., 2005
3	Cord blood 60 days	EPO, SCF, IGF-1 dex and lipid mix	No	10^9	-NA	−100%	Yes	Prolonged expansion protocol up to 60 days for adult globin switching	Leberbauer et al., 2005
4	Cord blood 20 days	SCF, IL-3, EPO VEGF, IGF-2	No	7.2×10^5	10^4/CB	77.5%	Yes	Low expansion and enucleation rates	Miharada et al., 2006
5	Cord blood 21 days	SCF, IL-3, EPO, TPO, Flt-3	Human MSCs	8×10^3	0.02/CB	64%	No	Less allogenicity, lower expansion, and enucleation rates, replaced BM derived feeder cells with UCB derived cells	Baek et al., 2008
6	Cord blood 38 days	SCF+Flt-3+TPO IL-3+EPO	hTERT+ Macrophages	3.5×10^6	8.8/CB	100%	Yes	Impossible to scale up	Fujimi et al., 2008
7	hESCs 59 days	Hydrocortisone, IL3, BMP-4, SCF, EPO, IGF-1	hMSCs, mMS-5 FH-B-hTERT	4×10^7 cells	NA	(6.5%, starting from CD34+ cells)	Yes	Globin switching	Qiu et al., 2008
8	hESCs 42 days	SCF, Epo, BMP-4, VEGF, bFGF, TPO, FLT3 L	MEFs, OP9	10^{10}–10^{11} cells/6-well plate of hESCs	NA	10–65%	No	Functional oxygen carrying capacity of ESCs derived RBCs	Lu et al., 2008
10	hiPSCs,(MR90, FD-136) hESCs(H1I) 46 days	SCF,TPO, FLT3-L, TPO, BMP-4; VEGF- IL-3, IL-6		hIPSCs 4.4×10^8 hESCs 35×10^8	NA	4–10% 52–66%	No	First time complete differentiation of hiPSCs cells into definitive erythrocytes capable of maturation up to enucleated RBCs (fetal hemoglobin in a functional tetrameric form)	Lapillonne et al., 2010
11	Cord blood 33 days	SCF, IL-3, EPO hydrocortisone	No	2.25×10^8	−500 units/UCB	>90%	No	First serum-free culture, first demonstration of RBC culture in a large-scale bioreactor	Timmins et al., 2011

(Continued)

Table 1 | Continued

S. no.	Cell source and culture time	Growth factors	Co-culture	Expansion	Units of blood	Enucleation rate	Animal or human serum/plasma	Key points	References
12	Cord blood 18 days	SCF, EPO hydrocortisone	No	4.3×10^7	75/CB	70%	Yes	Best yield to date	Giarratana et al., 2011
13	hiPSCs 59 days	Hydrocortisone, IL-3 BMP-4, Flt3L, SCF, EPO, IGF-1	hMSCs/Matrigel. hTERT immortalized fetal liver cells	$0.5–8 \times 10^6$	NA	NA	Yes	Production of large number of erythroid cells with embryonic and fetal-like characteristics regardless of the age of donor tissue	Chang et al., 2011
14	hESCs hiPSCs 60–125 days	Iron saturated transferrin, dexamethasone, insulin, SCF, EPO, TPO, IL-3, IL-6	MEFs, mOP9 mMS-5	2×10^5 ESCs	NA	2–10%	Yes	RBCs production from transgenic and transgene-free iPSCs using the OP9 coculture method with efficiency comparable to hESCs	Dias et al., 2011
15	hiPSCs 52 days	holo-human transferrin recombinant human insulin heparin, and 5% human plasma SCF, TPO, FLT3 ligand, BMP4, VEGF- n-3, IL-Epo	MEFs	$15–28.3 \times 10^8$	NA	20–26% RBC and 74–80% orthochromatic erythroblasts	5–10% Hu plasma	First time in a normal and a pathological erythropoietic differentiation models that hiPSC are intrinsically able to mature into adult hemoglobin synthesizing cells	Kobari et al., 2012

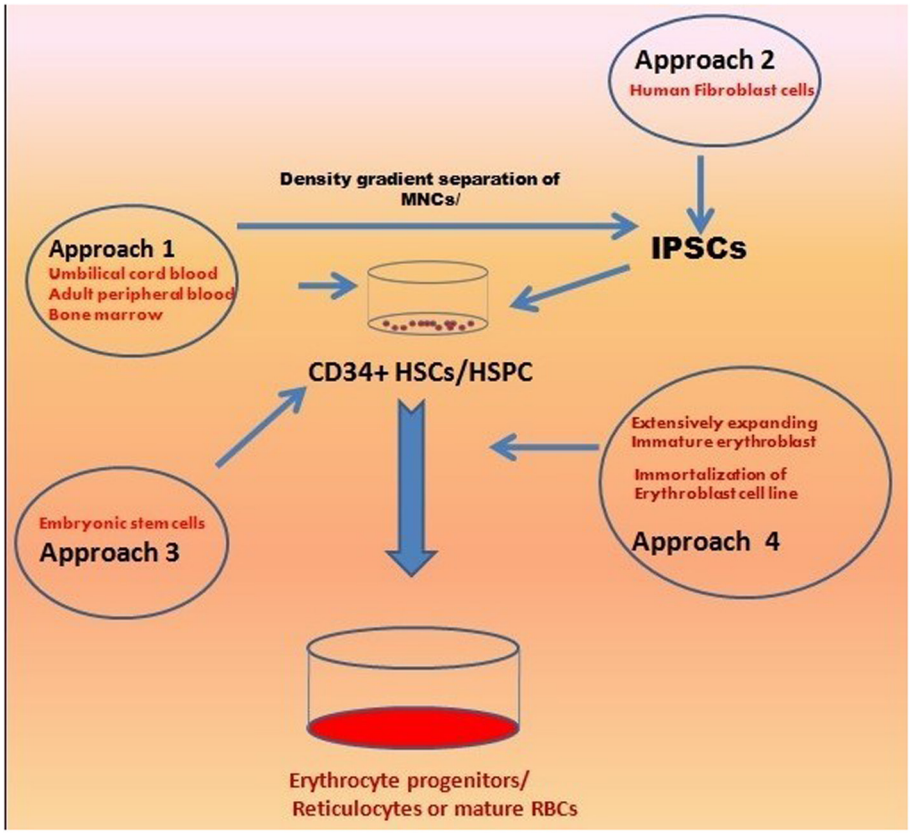

FIGURE 3 | An overview of the various approaches used for *ex vivo* Erythropoiesis. The different approaches are in use for developing large amount of transfusable clinical grade RBCs include $CD34^+$ HSPCs (from CB, PB, BM), ESCs/IPSCs derived erythroid progenitors, and highly expanding erythroid progenitors due to stress erythropoiesis. All these approaches has been discussed in detail in text.

Fujimi et al. demonstrated massive production of terminally matured erythrocytes from $CD34^+$ CB cells in the serum free environment while avoiding xenogenic feeder by using hTERT transduced human stromal cell line (Fujimi et al., 2008). These methods could result in massive growth of 6×10^{12} RBCs from one unit of CB and also the highest RBC number per starting cell (3.52×10^6) in any static culture. However, use of the AB blood group, serum to derive macrophages in a 14 days culture and an additional step of magnetic separation leaves this method ill-suited for the scaling up purposes. Beak et al. showed up to 64% enucleation efficiency by using CB or BM derived mesenchymal stem cells as feeder layer which would require an additional MSCs donor for the feeder cells and thus may not be suitable for large scale production procedures (Baek et al., 2008). Xi et al. has demonstrated an *in vitro* model of human erythropoiesis to study the erythroid differentiation in normal and pathological conditions (Xi et al., 2013). $CD34^+$ cells were shown to undergo up to 35 doublings in a prolonged 50 days culture in serum free media supplemented with EPO, synthetic glucocorticoid Dex, IGF-1, SCF, and iron saturated human transferrin. In a subsequent step, matured RBCs could be generated by coculturing erythroid progenitors with human fetal liver stromal cells. The procedure resulted in 10^9 fold expansion of erythrocytes (Xi et al., 2013).

Recent findings have indicated a significant erythropoietic potential in the CD34neg cell fraction which should also be exploited to enhance the production (Leberbauer et al., 2005; Van den Akker et al., 2010; Tirelli et al., 2011a). Leberbauer et al. described a culture method which exploited the signal transduction cascades of stress erythropoiesis, achieving a 10^9-fold expansion of erythroblasts of CB cells without prior CD34+ isolation (Leberbauer et al., 2005). Akker et al. describe a culture method modified from Leberbauer et al, and obtained a homogenous population of erythroblasts from peripheral blood mononuclear cells (PBMC) without prior purification of CD34+ cells. This pure population of immature erythroblasts can be expanded to obtain 4×10^8 erythroblasts from 1×10^8 PBMC after 13–14 days in culture. Upon synchronizing differentiation, high levels of enucleation (80–90%) and low levels of cell death (<10%) are achieved. These studies indicated $CD34^{Neg}$ cells as most significant early erythroid progenitor population (Van den Akker et al., 2010). Tirelli et al. also demonstrated significant enhancement (log scale) in the erythroid cell generation by using total MNC in Human Erythroid Massive Culture (HEMA) (Tirelli et al., 2011a). The careful phenotypes examination showed a significantly more erythropoietic potential of $CD34^{neg}$ population as compared to $CD34^+$ cells (Tirelli et al., 2011a).

One of the major criteria for calculating efficiency of various *ex vivo* expansion protocols remains to describe the degree of enucleation of these maturing erythrocytic cells. The interactions with macrophages/stromal cells play a crucial role in developing high degree of enucleated erythrocytes as described through various researchers (Kawano et al., 2003). However, most of the stromal cells support used by various researchers are of animal origin and may conflict with the interests of the few clinicians to describe these cells as clinical grade blood products. These issues raised the interest of the research community to define methods without a need for animal based products. Miharada et al. who showed generation of 4.5×10^{12} erythroid cells from 5×10^6 $CD34^+$ cells in the absence of any feeder cell layer or macrophage cells by using VEGF-1, TGF-1 and a glucocorticoid antagonist Mifepriostone to avoid dependence of these methods on feeder cells (Miharada et al., 2006). Maggakis-Kelemen et al. also reported similar results to improve the yield by using DMSO, Ferrous Citrate and Transferrin in the culture medium (Maggakis-Kelemen et al., 2003). Though these factors significantly increased the yield, but precursor cells shown higher degree of deformability and reticulocytes/erythrocytes were demonstrated to have reduced shear modulus. Beak et al. demonstrated the use of a polymer Poloxamer 188 to yield >95% enucleated RBCs in similar protocols without using any feeder cell support (Baek et al., 2009). Poloxamer 188 enhances the production by protecting cellular lysis during nucleation due to hydrodynamic stress. It provides support to the membranes and protects fragile cells from lysis at the time of enucleation. Thus, it seems that a large number of terminally matured clinical grade RBCs may be obtained regularly with the advent of similar protocol, while introducing newer alternatives at different levels of their expansion. Earlier, similar results were reported by Timmins et al. who demonstrated feeder free culture system by using a bioreactor and resulted in a massive 500 units (10^8 fold) per UCB donations (Timmins et al., 2011).

While considering these findings, it seems that both CB and PB derived $CD34^+$ cells possess enormous expansion potential with some marginal differences such as the predominant form of Hb expressed and % yield of enucleated RBCs. For example, RBCs from CB derived cells are predominantly rich in fetal Hb (Neildez-Nguyen et al., 2002; Giarratana et al., 2005, 2011), whereas, RBCs from PB derived cells majorly express adult Hb (Giarratana et al., 2005, 2011). Apart from that, there have been a significant difference in the expansion potential of CB/PB derived HSPCs. With the current technologies available for their expansion PB derived cells have shown comparatively low (120,000 fold) yields (Giarratana et al., 2005). In contrast, CB derived cells are reported to expand up to 2 million folds. Even more, a single unit of CB derived cells can result into 500 units of transfusable RBCs (Timmins et al., 2011). However, the later method has not been applied for the PB derived cells so far. Thus, it seems that CB shall provide a better option for initial source to be selected under present circumstances, and, if presence of fetal Hb is acceptable (Conley et al., 1963; Weatherall and Clegg, 1975; Thomson et al., 1998; Foeken et al., 2010), it shall remain the most attractive alternate for RBCs expansion protocols. The infrastructure for CB collection is well developed. According to a report in 2010, about 4,50,000 CB units were collected through 131 CB Banks worldwide (Foeken et al., 2010). There is enough information available through these blood bank registries regarding the blood types and combinations of the antigen present on these blood groups for each CB donation. Though, the exact percentage for each rare blood type may not be available and even if the specialized donor could be found for each rare antigen combination, it may be difficult to fulfill a regular demand of transfusion in every 3–4 weeks due to the limited life span of these cells. However, even then a large fraction of the population may be benefitted from the existing technologies without any risk for rare antigen combinations.

EMBRYONIC STEM CELLS AND INDUCED PLURIPOTENT STEM CELLS

Embryonic stem cells (Thomson et al., 1998) and induced pluripotent stem cells (Takahashi and Yamanaka, 2006; Takahashi et al., 2007) are defined as immortal cells with the self-renewing capacity and if the requisite growth environment is made available have potential to differentiate into all kinds of cells of the organism. Embryonic stem cells were first isolated from 3–4 days old Blastocysts (Takahashi et al., 2007), and subsequent studies by various research groups described their capabilities to be maintained indefinitely in cultures due to high telomerase activities. Takahashi and Yamanaka's group firstly demonstrated iPSCs or ESC-like cells that may be generated by reprogramming somatic cells. They showed the transformation of murine fibroblast cells in to ESC by transfection of transcription factors such as POUSF-1, KLF-4, SOX-2,and Myc (Takahashi and Yamanaka, 2006; Takahashi et al., 2007). These cells were further demonstrated to form teratoma on infusion in NOD-SCID mice and differentiation into cells from all the three germ cell lines respectively (Okita et al., 2007; Wernig et al., 2007). Generation of Human IPSCs (hips) was also defined by transformation of human neonatal or adult fibroblast by the same set of genes (Takahashi et al., 2007). Yu et al. also generated of hIPSCs from fibroblast cell by using lentivirus mediated transfection of Nanog and LIN28 to reduce the undesired effects of c-Myc (Yu et al., 2007). Subsequently, other methods of generating IPSCs have been reported such as ectopic expression of the same set of transcription factors (Stadtfeld et al., 2008) and use of excisable transposons (Lacoste et al., 2009). Alternatively, these factors could also be provided from outside attached to a cell penetrating peptide sequence (Zhou et al., 2009). Together these cells provide an alternate to generate HSPC. The mononuclear cells (CB/PB) may be reprogrammed in IPSCs and in subsequent procedure human IPSCs could be differentiated into $CD34^+CD45^+$ HSPC by using similar protocols used for ESCs (Ng et al., 2005; Choi et al., 2009).

There are a number of groups who have demonstrated hematopoietic differentiation of hESCs/IPSCs (Lu et al., 2008; Chang et al., 2011; Kobari et al., 2012) (**Table 1**). These methods can largely be grouped into two categories of (1) Embryoid body formation through suspension culture of hESCs without feeder cells, and (2) co culture of hESCs with murine stromal cell lines such as S17 or OP9 (Chadwick et al., 2003; Vodyanik et al., 2005, 2006; Chang et al., 2006). In the first approach, cells grow in suspension culture resulting in 3-dimensional structured aggregates of differentiating cells called Erythroid Bodies (EBs) (Vodyanik

et al., 2005). Chang et al. described a method of generating erythroid cells from embryoid bodies (Vodyanik et al., 2006). Nakamura's group described a method for the generation of enucleated erythrocytes from mouse ESCs (Hiroyama et al., 2008) which was followed by several researchers who demonstrated procedures for the generation of enucleated erythrocytes by using human ESCs (Lu et al., 2008; Qiu et al., 2008; Lapillonne et al., 2010; Dias et al., 2011)

During last 10–11 years significant development has occurred in the procedure to develop hESCs/iPSCs and high yields of approximately up to 10^{11}–10^{12} erythrocytic cells have been achieved from a single plate of hESCs (Lu et al., 2008). While comparing these reports, most procedures have indicated an important role of erythropoietin (along with other growth factors BMP-4, VEGF, bFGF etc.) and coculturing them with a feeder cell to derive sufficient yield of enucleated RBCs (Kaufman et al., 2001; Keller, 2005; Ng et al., 2005; Ledran et al., 2008; Zambidis et al., 2008). His can be a Co cultured with a number of feeder cells available, including mesenchymal cell Murine stromal cell line S17, OP9 (Vodyanik et al., 2005, 2006). YS endothelial cell lines (Kaufman et al., 2001), cell lines derived from murine AGM stroma, liver or other developmental niche (Ledran et al., 2008) (Murine AGM derived AM20-1B4 cells) are described as best supporting cells providing higher yields.

In order to achieve animal cell free clinical grade blood products efforts have been made by various researchers. It has been described that the use of feeder cell layer derived from human tissue itself e.g., human foreskin derived fibroblast cells support to generate similar results (Amit et al., 2003; Hovatta et al., 2003; Koivisto et al., 2004). Genbacey and his colleagues, has reported expansion of hESCs in serum free conditions by growing them on cells derived from human early gestation placental fibroblast cells or human placental laminin substrates (Genbacev et al., 2005). hESCs can also be grown in serum free and feeder free conditions by using fibronectin, TGF beta 1, bFGF, and leukemia inhibitory factor (Amit et al., 2003). Bouhasara's group demonstrated hESCs culture on hTERT cell line and their subsequent differentiation into erythrocytic cells in suspension culture method (Qiu et al., 2005; Olivier et al., 2006).

However, there have been ambiguities about the role of EPO/feeder layer played in erythrocytic enucleation; their presence in the final step of most protocols seems to remain inevitable. This is evident from the results obtained by growing these cells in the absence of both the above mentioned factors that result to meager 10% enucleating efficiency (Qiu et al., 2008; Dias et al., 2011). Whereas, inclusion of both EPO/feeder cells has been shown to yield remarkable up to 65% enucleation efficiency of these methods (Lu et al., 2008; Lapillonne et al., 2010). Similarly, IPSCS derived erythrocytes have been shown to depend on a feeder layer for their enucleation in final steps of maturation (Lapillonne et al., 2010; Chang et al., 2011; Dias et al., 2011; Kobari et al., 2012). Recently, heparin and insulin have been reported to enhance enucleation efficiency of IPSCs derived erythrocytes in a feeder free system, but that also remains only 26% (Kobari et al., 2012)

Another important factor is the expression of fetal Hb as a predominant form of protein by the erythrocytes generated in almost all these protocols (Lu et al., 2008; Lapillonne et al., 2010; Chang et al., 2011; Dias et al., 2011; Kobari et al., 2012). This is quite obvious because of the embryonic state of development of both ESCs/IPSc and a more primary route of hematopoietic development (indefinitive) likely to yield predominant expression of fetal/embryonic Hb through these protocols. However, researchers have demonstrated the possibilities of selective expression of adult Hb in erythrocytes by either increasing the time length for coculture (Qiu et al., 2008), or enforced transgene expression of RUNX1a to enhance hematopoiesis from human ESCs and iPSCs (Tirelli et al., 2011a) reporting a higher level of β-globin expression in differentiated erythrocytes (Ran et al., 2013).

So far, there has been no significant difference in the erythroid expansion potential of ESCs and IPSC lines (Dias et al., 2011). The findings reported by Douay's group about 7–8 fold higher erythrocytic expansion potential of human H1 ESC line in comparison to the human IPSCs line (IMR90-16) may be attributed to the viral vectors used for deriving IPSC that has been reported to decrease hematopoietic and erythrocytic expansion potential (Feng et al., 2010). Further, epigenetic variation (integration of viral genomes at different loci) associated with IPSCs generating methods could also contribute to these variations. Similarly, altered hematopoietic potential have been reported for various hESCs lines (Chang et al., 2008).

IPSCs may be advantageous in the conditions where no other alternate in present of generating rare blood group such as $O^{-}Rh^{-}$ type of blood group. It has been postulated that only three selected human IPSC lines may be sufficient to generate required blood groups for almost 95.5% of patients in France (Peyrard et al., 2011). While, no such ESC line lines with universal blood donor group has been identified so far in the current list of NIH-approved-for-research (Lu et al., 2008). In addition, IPSCs can be helpful to support autologous transfusion which is highly recommended for alloimmune patients. On the other hand, it has promising reports to generate functional RBCs to cure rare hemoglobinopathies such as sickle cell anemia and β-Thalassemia (Hanna et al., 2007; Zou et al., 2011).

ERYTHROID PRECURSOR FROM STRESS ERYTHROPOIESIS

In addition to the above mentioned stem cells, researchers have shown a significant RBCs generation potential in the extensively proliferating erythroid precursors which are developed due to stress conditions such as erythrolysis or hypoxia (**Figure 3**). The process, generally termed as "stress erythropoiesis," relies upon glucocorticoids and their counter receptor interactions. There are reports showing up to 10^{10}-fold expansion of CB-derived erythroid precursors using Dexamethasone as a glucocorticoid agonist along with other growth factors, e.g., SCF, EPO, and IGF-1 (Bauer et al., 1999; Von Lindern et al., 1999; Leberbauer et al., 2005). Similar results could be obtained for the PB derived erythroid precursors with the use of IL-3 along with above mentioned cytokines (Migliaccio et al., 2002). However, these approaches were reported to be of limited use due to their minimal fold expansion (<20 fold) which remain insufficient as per clinical transfusion is concerned (Migliaccio et al., 2010).

In contrast, there have been advancements in generating immortalized or extensively expanding erythroblast cell lines

from embryonic stem cells with the ability to produce enucleated erythrocytes in mouse (Carotta et al., 2004; Hiroyama et al., 2008). Similar extensive expansion potential has been demonstrated by mouse embryos (England et al., 2011), which indicated a higher proliferation potential of embryonic erythroid progenitors than postnatal cells. It is hypothesized that if postnatal erythroid cells could be reprogrammed by using existing techniques to the state of embryonic erythroid progenitor cells they could also proliferate up to a similar extent. In fact, it has been demonstrated by Cheng's group (Huang et al., 2013), who has demonstrated immortalization of human CB-derived erythroblast by using similar reprogramming factors defined by Yamasaki's group (Takahashi and Yamanaka, 2006). The Author has demonstrated a significant 10^{68}-fold expansion of CB-derived erythroblasts (in∼12 months) in a serum-free culture. The ectopic expression of three genetic factors Sox2, c-Myc, and a shRNA against TP53 gene enabled these cells to undergo an expanded expansion in similar culture condition. These cells showed normal erythroblast phenotypes and morphology, a normal diploid karyotype and dependence on a specific combination of growth factors for proliferation throughout the expansion period. The coculture of these cells with irradiated mouse OP9 cell line in the presence of serum yield to 30% enucleation efficiency with increased fetal Hb expression level. Similarly, Kurita et al, demonstrated immortalization of human IPSC or CB derived cells by inducible expression of TAL-1 and HPV-16-E6/E7 viral gene (Kurita et al., 2013). Thus, it is expected that with more advancements in the reprogramming technology such as the use of nonviral episomal plasmids, synthetic RNA, and small molecules, development of more donor cell line would facilitate generation of all blood types (Chou et al., 2011; Hou et al., 2013; Yoshioka et al., 2013).

EX-VIVO CULTURING OF OTHER BLOOD COMPONENTS

PLATELETS

Platelets are small anuleated, discoid shaped, 1–2 μm cell fragments that play essential role in the maintenance of homeostasis, stopping bleeding, or wound healing (thrombosis), inflammation, and innate immunity. There is a burgeoning use of plasma transfusions to control massive bleeding in clinics. The combination of red blood cells, platelet concentrates, and plasma is used for the same Platelets are present in much higher densities in vertebrate blood (5.5 platelets × 10^{10}/unit) that are generated from megakaryocytes and their precursor cells in BM (Machlus and Italiano, 2013).

Platelets are generated from megakaryocytic cells in the BM niche under the regulation of various growth factors. Unlike RBCs, committed HPCs can be easily recruited into megakaryocytic lineage differentiation pathways by their induction through a single growth factor TPO. This straight forward mechanism has tempted many researchers to mimic similar differentiation under research settings. Like RBCs, there have been efforts to generate platelets from all different sources, including CD34+ HSPC., ESCs/iPSCs and immature megakaryotic precursor cells. Christian et al. have demonstrated the generation of platelet precursor cells from human $CD34^+$ cells by using SCF, TPO, IL-3/IL-11, and Fetal Liver Tyrosine kinase-3 ligand (Flt-3L) in the liquid culture system (Christian et al., 2010). However, these precursors were shown to undergo recirculation in hematopoietic tissues on transfusion in mice. Proulx et al. demonstrated ∼300 fold expansion of MK/$CD34^+$ by growing UCB derived $CD34^+$ cells with SCF, Flt-3L, TPO, and IL-6 at high concentrations (Proulx et al., 2003, 2004). Growth of MK/$CD34^+$ may further be improved by optimizing culture conditions such as temp (39°C), O_2 tension and addition of additional factors such as SDF-1α and Nicotinamide (Guerriero et al., 2001; Mostafa et al., 2001; Cortin et al., 2005; Giamniona et al., 2006). Matsunaga et al. (2006), demonstrated generation of 3.4 unit platelets from UCB-$CD34^+$ cells by using hTERT mesenchymal cell coculture method in 33 days (Matsunaga et al., 2006). Sullenberger, also reported a 3D cartridge based perfusion bioreactor with the capacity of continuously producing platelets over a period of 30 days (Sullenharger et al., 2009). Moreover, the efforts described so far for producing platelets from UCB derived cells remain largely insufficient to fulfill even a fraction of global demand.

Recent advancements have demonstrated enormous *in vitro* platelets generation potential in pluripotent stem cells (including iPSCs/ESCs), and a comparatively new type of cells called induced MKs (iMKs) (Masuda et al., 2013). Matsubara et al. showed a direct conversion of fibroblasts (mouse/human) into megakaryocytes (MKs) by using three factors p45NF-E2, Maf G, and Maf K, which subsequently can release platelets (Ono et al., 2012). The authors identified significance of these factors in generating abundant MKs and platelets from human subcutaneous adipose tissues (Matsubara et al., 2009, 2010; Ono et al., 2012).

In another approach, ESCs/IPSC mediated generation of platelets in humans has been reported (Takayama et al., 2008, 2010). Eto et al. showed that c-Myc expression (essential for reprogramming of IPSCs) must be reactivated transiently and then shut-off (Takayama et al., 2010) and to ensure efficient platelet production from human IPSCs. This transient expression might be essential because continuous excessive c-Myc expression in IPSCs derived MKs was shown to increase p14 (ARF) and p16 (INK4A) expression, and decreased GATA1 and NF-E2 expression, which eventually resulted MK senescence and apoptosis, as well as impaired production of functional platelets (Takayama et al., 2010).

More recently, Eto and colleagues have established an immortalized MK cell line (MKCL) derived from human IPSCs (Masuda et al., 2013). The immortalized MKCL could potentially provide a stable supply of high quality platelets for transfusion medicine. However, this method remains elusive and a detailed protocol suitable for commercial production is yet to come.

Thus, recent findings indicate strong possibilities of a regular non donor derived platelet supply in near future. However, there are several factors that shall be discussed to compare existing approaches. While comparing with IPSCs/ESCs based methods, the iMK cells (derived in these studies) are rapidly converted (2 weeks) into MKs cells, but yield remain poor as fewer platelets (5–10 platelets per iMK cell was generated. In contrast, single MKs may give rise to up to 2000 platelets under *in vivo* conditions. Hence, one of the important factors shall remain to be discussed is the total number of cells that can be obtained from each cultural setting. For example, Matsubara et al reported generation of 8–10 $\times 10^5$ iMKs from 20×10^6 Human Derived Fibroblasts

(HDFs) (Ono et al., 2012). HDFs are easily expanded following to their initiation of direct conversion with limited number of transfected cells, whereas, 200–300 IPS clones from 10^5 HDFs were reported by Eto and colleagues in their studies. Further, 1×10^5 cultured IPSCs gave rise to 17×10^5 MKs (Takayama et al., 2010). Thus, these results indicated low platelet production efficiency per MK in both strategies.

Another important issue is the time taken for the production of MKs and platelets through these protocols. iMKs and iPSC-mediated MKs are induced in approximately 2 weeks and 2 months, respectively. However, it is yet to be established, but MKCLs may be a much faster approach to generate platelet sources for platelet production due to their direct expandability into MKs.

Further IPSC-mediated MKs are not completely free from the possible risk of some residual undifferentiated cells However, a possible approach may be to avoid transfusion of MKs while preferring fully matured platelets derived from these methods. Platelets (anucleated cells) may be irradiated before transfusion and thus may become free of any contamination of residual undifferentiated cells.

IPSCs and MKCLs are immortal cell lines and thus are comparatively easy to freeze down. Similarly, HDFs are also suitable for cryopreservationm from where they can be taken out and used as starting materials for iMK induction. HDFs in comparison to platelets show better suitability for cryopreservation. The functionality of iMKs has been assessed through their infusion into irradiated immunodeficient NOD/Shi-scid/IL-2Rγ^{null} (NOG) mice showing normal release of human platelets *in vivo* (5–10 platelets per infused IMK) cells and equal capabilities of forming a thrombus in *ex vivo* conditions formation under flow condition (Ono et al., 2012).

The iMKs are reported very recently and the early outcomes indicate them as a valuable option for transfusion medicine. However, there are some important issue which shall be considered in much detail such as the molecular mechanism by which iMKs are induced through the p45NF-E2 transcriptional complex, and identification of most suitable cells for direct conversion into iMKs (or for establishment of MKCLs).

One of the important issues to be discussed here is to explore the necessity of generating autologous iMKs through direct conversion for clinical transfusion. Under most clinical settings, platelet transfusion is done without any prior matching of human leukocyte antigen (HLA) between the donor and recipient. However, in rare conditions repeated platelet transfusions can elicit undesired production of anti-HLA antibodies against transfused platelets leading to an inevitable demand to identify HLA-matched platelet donor (Stroncek and Rebulla, 2007). A possible alternate may be provided by using autologous iMKs based strategies. In addition, establishment of iPSC banks shall be an alternative approach to deal with this problem. These banks shall store homozygous HLA-typed iPSCs which would be deposited for HLA-matched tissue transplantation (Taylor et al., 2012). It has been demonstrated that a tissue bank from 150 selected homozygous HLA-typed volunteers could match 93% of the UK population (Taylor et al., 2012). Yamanaka et al has also postulated that 140 unique HLA homozygous donors shall remain sufficient for 90% of the Japanese population (Okita et al., 2011).

NEUTROPHILS

Neutrophils play important role in cellular immunity, but unlike RBCs and Platelets they are not routinely collected in clinics. Neutrophils are need to be transfused in relatively large amount, i.e., $>10^{10}$ calls every day in neutropenic patients. *Ex vivo* expansion of neutrophils has been reported by some groups showing ∼400 fold expansion from single units of UCB-CD34$^+$ cells (5×10^6 CD34$^+$ cells), which equivalents to a mere 20% of the required daily dose. Although, sufficient cells may be produced by using PB mobilized by cytokines as demonstrated by Dick et al. (2008), who showed ∼534 × fold (equivalent to 10 neutrophil units) expansion on *ex vivo* culture of these cells. But this would mean one donor per recipient and supply constraints largely remain unsolved. Similar efforts to generate neutrophils from hESCs have also resulted in very low yields (Saeki et al., 2008). These reports indicated the need for developing more efficient and simple procedures to be developed first for the generation of neutrophils from either UCB-CD34$^+$, BM derived cells and/or houses before their commercial manufacturing could be planned.

FACTORS REGULATING THE FATE OF COMMERCIAL BLOOD MANUFACTURE AND FUTURE PROSPECTS

SOURCE MATERIAL SUITABILITY AND AVAILABILITY

Scientists have been trying to develop a consensus on the different variables controlling the fate of *ex vivo* RBCs expansion and clinical use. The most important of them is the source materials for various methods being explored to expand RBCs in large scale. Ideally, a source material should be a discarded material so that no extra cost would be aided in the commercial production process. At the same time, if a regular supply chain of *ex vivo* manufactured blood has to be maintained the source material would also be required on a regular basis i.e., unlimited availability of the source material should be ensured. The most important factor is the capability of the source cells to get developed into the finally matured RBCs cells with absolute efficiency without raising any immune response in the host i.e., it should be non-immunogenic. The criterion fits well with umbilical CB, which is available abundantly and is a waste product in all the maternity hospitals. In fact, a significant number of transfusion can be made for the patients who are suffering from rare hemoglobinopathies (∼ 1%) by using *ex vivo* cultivated RBCs units that might be obtained from these sub threshold units of CB (>90 ml) discarded regularly. Each discarded unit of CB may generate 10–75 RBCs products which might be useful in transfusions for rare hemoglobinopathies (Peyrard et al., 2011). Similarly, Leukopheresis is routinely done in clinical centers where transfusions are made to treat various leukemia patients. In these protocols the leuko-reduction buffy coat is produced as a byproduct and this contains significant amounts of RBCs producing cells (equivalent to umbilical CB) (Zhou et al., 2009).The proof-of-the concept that these *ex-vivo* cultivated cells may be of clinical use was provided by demonstrating successful transfusion of CD34$^+$ cells which were obtained from a G-CSF mobilized donor

(Migliaccio et al., 2010). Apart from UCB derived $CD34^+$ cells, ESCs, and hiPSCs as described in previous sections might serve as a potential source for regular manufacturing processes with the advancement in technologies.

QUANTITATIVE ISSUES

The most frequently transfused blood component, RBCs, are present in 2×10^{12} cells/unit (200 ml of blood) with an expected cell density of 3×10^6 cells/ml. According to the WHO data >100 million units of blood is collected every year worldwide. In order to replace this huge volume with synthetic blood/blood components, an extremely large amount of ingredients along with skilled manpower would be an inevitable requirement. It is hypothesized that a cell density of 5×10^7 cells/ml would be essential to produce regularly to support this much demand. Further, according to an assumption, manufacturing of a single unit of blood by using present static culture methods, would require 660 liters of culturing medium and 9500 lab scale 175 cm^2 culturing flasks (70 ml medium/flask) (Timmins and Nielsen, 2009; Zeuner et al., 2012).

Ensuring such a high concentration of RBCs would attract development of more automated methods like bioreactors that might be helpful in reducing the culturing assets and associated labor. Fortunately a wealth of information regarding the use of various types of bioreactors for HSCs expansion has been accumulating during the last two decades. This could help researchers achieve required cell density. It was reported by Timmins et al that similar density of RBCs as in static culture can be produced in a wave bioreactor (Timmins et al., 2011). A maximum cell density of 10^7 cells/ml was also reported in a stirred small scale bioreactor (Ratcliffe et al., 2012). Housler et al, reported a massive yield of 2×10^8 cells/ml in a hollow fiber bioreactor (Housler et al., 2012). These 3D bioreactors can be scaled up with current design to produce 1–2 units of RBCs in 3–4 weeks of time. These reports indicate possibilities of ensuring a regular production of large amounts of RBCs, however, a number of factors such as degree of cell maturation and various cultural parameters are yet to be defined in a more elaborated manner.

Further, an important achievement could be the development of methods to commit the source material directly into the erythropoietic lineages reducing both the time and cost of production. There are few preliminary reports about various efforts to define alternate sources such as (i) generation of erythropoietic cell lines from ESCs/IPSCc (i) reprogramming any somatic cells directly into erythroblasts by passing the pluripotent state through over expression of suitable genes.

This has been reported for megakaryocytic differentiation also where human fibroblast cells are directed to differentiate directly into megakaryocytic cells through over expression of p45NF and E2/MaF transcription factors (England et al., 2011; Wang et al., 2011). Cheng's group reported in humans the differentiated erythroid cells obtained from human embryo might be used as a potential initial source for RBCs production (Huang et al., 2013; Kurita et al., 2013). Thus, it is conceivable that with more advancements in the culture methods and initial source material a significant amount of RBCs could be produced for limited clinical uses.

GROWTH FACTORS

Growth factors used in various phases of *ex vivo* culturing should also be explored to regulate the fate of commercial manufacturing. Both the "*concentration*" and "*time*" of their administration would play an important role in the optimization of the expansion process. It is also to be noticed that there are various growth factors which express gene polymorphism, for example, >260 isoforms of human glucocorticoids receptors are expressed which are likely to differ in their potency and effects. In order to secure a large scale production of RBCs, it is conceivable to determine an in depth knowledge about the functioning and efficiency of various isoforms through high throughput screening methods regularly. A good example might be the use of reverse phase proteomic analysis of $CD34^+$ cells to define molecular mechanism of signaling pathways activated during erythroid differentiation. Recently, similar studies have been reported by various groups showing activation of different set of gene(s) in $CD34^+$ cells and erythroblasts. Genes that are involved in the inhibition of apoptosis, transcription, and proliferation are more active in $CD34^+$ cells, whereas erythroblasts predominantly express those genes which play important roles in regulation of cell cycle, transcription and translation (Ratcliffe et al., 2012). This information may be of use if specific pharmacological agents enhancing erythrocytic pathways and blocking apoptotic pathways may be introduced at various phases of *ex vivo* expansion.

BIOPHYSICAL AND BIOCHEMICAL PARAMETERS

Generation of clinical grade RBCs would require development of stringent quality checks for *ex vivo* expanded RBCs. The major parameters would include determination of antigenic profiles, hemoglobin contents and physical progenies derived from these culture processes. As described by various laboratories *ex vivo* generated RBCs are slightly macrocytic but normal in size. These RBCs also expresses a great level of α-hemoglobin stabilizing proteins (AHSP), BCL11A and globin gene with great donor to donor heterogeneity (Keel et al., 2008). It is also reported that *ex vivo* generated erythroblasts contain γ-globin in a slightly greater amount in comparison to RBCS which are generated *in vivo* (0.12–0.20 pg/cell with respect to total protein content of 18.723.7 per cell) (Lu et al., 2008).

ANTIGENIC PROFILE

Surface antigens are vital for the function of RBCs and a large number of surface antigen have been identified on the surface of mature RBCs. *Ex vivo* generated RBCs are reported to express normal level of antigens present on both the Ankyrin A (GPA, M/N, Ena FS, RhAO, and band 3/4.1 R) and Glycophorin B complex, the urea transporter, the complement receptor, and receptors that protect RBCs from complement mediated lysis Recent reports about the surface antigenic analysis of the *ex vivo* generated RBCs ensured that appropriate level of surface antigen such as band 3 and Rh antigen is assured at the beginning of the maturation process (Satchwell et al., 2011).

ETHNICITY

Recently, there have been some reports demonstrating effects of ethnicity on the source material used for *ex vivo* expansion.

African-American donor derived MNC were found to be found to be more useful as per as fold expansion is concerned since they could be expanded up to 14–40 fold in comparison to the Caucasian population derived MNCs which give rise to 1.7–30 fold expansion (Tirelli et al., 2011b; Carilli et al., 2012)

ENUCLEATION OF RBCs

Since, *Ex vivo* expanded RBCs shall essentially be evaluated for their degree of terminal maturation in all the production units. Hence, high level of enucleation of maturing erythroblast is an inevitable requirement. Erythroblasts derived from ESCs are demonstrated to yield >60% enucleated RBCs (Lu et al., 2008) while the nucleation efficiency of maturing erythroblast from ups could be demonstrated to a mere 4–10% of RBCs produced (Lapillonne et al., 2010). Recently, there have been efforts to define the factors regulating enucleation efficiency of RBCs indicating the significance of proteins such as Huston deacetylase (specifically HDAC-2 isoform) which are required for chromatin condensation and enucleation in mice fetal erythroblast (Chang et al., 2011). Since, glucocorticoids play important negative regulators for these proteins as mentioned above, application of molecular agents which specifically activates HDACs could be employed in phase-3 cultures to enhance the enucleation yields. As mentioned in a number of reports, co -culturing of maturating erythroblast along with stromal cells may enhance their terminal maturation, but on the other hand it might impose an additional risk of poorly defined potentially immunogenic and/or infectious agent which may compromise the production of GMP for RBCs in the developmental process. These issues indicate the need for the development of biochemical alternatives to avoid the use of stromal co-cultures in these protocols. There are preliminary reports on the use of drugs like Mifepristone and plasmanate which are defined to have similar effects on promoting enucleation efficiency during *ex vivo* expansion of RBCs (Miharada et al., 2006). In addition, factors promoting the functioning of proteins involved in vesicle trafficking such as "vaccuoline" may also be used to improve the enucleation efficiency if phase-3 cultures (Keerthivasan et al., 2010).

PRODUCTION COST

The regular commercial production of RBCs would be heavily affected by their cost of production. According to a hypothetical estimation, producing RBCs in desired range would cost approximately $8000–15000 per unit (Timmins and Nielsen, 2009; Zeuner et al., 2012). Whereas, the hospital cost for leuco-reduced RBCs is only $225 that is significantly lower in comparison to synthetic product. There are situations such as matching of rare phenotypes of RBCs and the present cost of a phenotypically matched unit of RBCs is ∼$700–1200. Producing blood on a commercial scale would require a huge monetary investment and it will be difficult to keep the momentum in the direction of R&D for developing more and more efficient protocols due to lack of money especially in low income grade countries. It would be important to find out immediate goals which can be achieved from the outcomes of the existing research findings to generate alternate sources of money. For example, immediate use of these small scale products may be useful in developing various immediately achievable goals. There are few promising examples, such as the use of *ex vivo* cultured cells for Reagent RBCs diagnostics in specifically alloimmunized patients and they can be used as drug delivery vehicles for personalized therapies. The requirement of relatively small no. of RBCs in these methods makes them most suitable for these kinds of assays, for example, $\sim 2 \times 10^8$ RBCs will be sufficient to perform 100× s of these assays in clinical settings and with the present methodologies 10^9–10^{10} RBCs can be expanded regularly.

SUMMARY

In brief, it seems feasible that commercial production of RBCs may take place in near future. There are enough technological evidences available supporting the concept and with the advent of newer source materials, optimal methods for *ex vivo* cultivation of RBCs and highly stringent, comprehensive quality control, analytical measures, the regular production of blood may take place to support a smaller fraction of the population at least. All the three major sources of like $CD34^{+-}$ HSCs (UCB, PB, and BM derived cells), hESCs and, iPSCs have enough potential of generating huge amounts of RBCs and if more sophisticated methods are generated such as development of erythropoietic hESC cell lines, it would be possible to generate an unlimited source of initial source material for the production measures.

Moreover, with the development of more in depth knowledge about the molecular mechanisms involved in various stages of *ex vivo* erythropoiesis. It would become more efficient to support even larger population's blood demands. The fundamental information shall also be helpful in developing pharmacological alternates for the various stages of erythropoietic development which presently depend upon their interactions with feeder cell support systems in most of the protocols. Development of pharmacological alternates is essential to simplify the production processes for clinical grade blood. Avoiding the need of feeder cells may also help in reducing the unexpected risks associated with their use due to undefined immunogenic and infectious exposures which are likely imposed to the recipients by animal derived feeder cell support methods. The omission of feeder cells from *ex vivo* RBCs expansion protocols would also simplify the commercial scale production methods and may also be helpful in reducing the cost of production. As per as cost is concerned, a small fraction of the population may be capable of bearing the cost of commercially produced blood in economically developed countries. However, more liberal government policies such as lowering both the sale and services taxes, provisions for subsidized input materials (like electricity, water, etc.), direct subsidy offered for the products may be helpful in supporting the low cost production of blood. Besides that, a small amount of remuneration may also be generated from the various smaller/specific products such as reagent RBCs, RBCs for the specific drug delivery targets to cure rare hemoglobinopathies and that might support the ongoing research and development in the same direction.

ACKNOWLEDGMENTS

We thank the Honorable Chairman and the Honorable Vice-Chancellor of the Delhi Technological University, Shahbad Daulatput, Bawana road, Delhi-42, for support. Dr. Vimal

K. Singh particularly thanks the Department of Science and Technology and Indian National Science Academy (INSA), INDIA, for the research grant.

REFERENCES

Akashi, K., Traver, D., Miyamoto, T., and Weissman, I. L. (2000). A clonogenic common myeloid progenitor that gives rise to all myeloid lineages. *Nature* 404, 193–197. doi: 10.1038/35004599

Ali, A., Auvinen, M. K., and Rautonen, J. (2010). The aging population poses a global challenge for blood services. *Transfusion* 50, 584–588. doi: 10.1111/j.1537-2995.2009.02490.x

Alter, H. J., and Klein, H. G. (2008). The hazards of blood transfusion in historical perspective. *Blood* 112, 2617–2626. doi: 10.1182/blood-2008-07-077370

Amit, M., Margulets, V., Segev, H., Shariki, K., Laevsky, I., Coleman, R., et al. (2003). Human feeder layers for human embryonic stem cells. *Biol. Reprod.* 68, 2150–2156. doi: 10.1095/biolreprod.102.012583

Baek, E. J., Kim, H. S., Kim, J. H., Kim, N. J., and Kim, H. O. (2009). Stroma-free mass production of clinical-grade red blood cells (RBCs) by using poloxamer 188 as an RBC survival enhancer. *Transfusion* 49, 2285–2295. doi: 10.1111/j.1537-2995.2009.02303.x

Baek, E. J., Kim, H. S., Kim, S., Jin, H., Choi, T. Y., and Kim, H. O. (2008). *In vitro* clinical grade generation of red blood cells from human umbilical cord blood $CD34^+$ cells. *Transfusion* 48, 2235–2245. doi: 10.1111/j.1537-2995.2008.01828.x

Bagnis, C., Chiaroni, J., and Bailly, P. (2011). Elimination of blood group antigens: Hope and reality. *Br. J. Haematol.* 152, 392–400. doi: 10.1111/j.1365-2141.2010.08561.x

Baron, M. H., and Fraser, S. T. (2005). The specification of early hematopoiesis in the mammal. *Curr. Opin. Hematol.* 12, 217–221. doi: 10.1097/01.moh.0000163217.14462.58

Baron, M. H., Isern, J., and Fraser, S. T. (2012). The embryonic origins of erythropoiesis in mammals. *Blood* 119, 4828–4837. doi: 10.1182/blood-2012-01-153486

Bauer, A., Tronche, F., Wessely, O., Kellendonk, C., Reichardt, H. M., Steinlein, P., et al. (1999). The glucocorticoid receptor is required for stress erythropoiesis. *Genes Dev.* 13, 2996–3002. doi: 10.1101/gad.13.22.2996

Bessis, M., Mize, C., and Prenant, M. (1978). Erythropoiesis: comparison of *in vivo* and *in vitro* amplification. *Blood. Cells* 4, 155–174.

Carilli, A. R., Sugrue, M. W., Rosenau, E. H., Chang, M., Fisk, D., Medei-Hill, M., et al. (2012). African American adult apheresis donors respond to granulocyte-colony-stimulatiflg factor with neutrophil and progenitor cell yields comparable to those of Cauc asian and Hispanic donors. *Transfusion* 52, 166–172. doi: 10.1111/j.1537-2995.2011.03253.x

Carmelo, C. S., Mario, C., Paolo, D. F., Armando, D. V., Lessandro, M. G., Francesco, L., et al. (1995). CD34-positive cells: biology and clinical relevance *Haematologica* 80, 367–387.

Carotta, S., Pilat, S., Mairhofer, A., Schmidt, U., Dolznig, H., Steinlein, P., et al. (2004). Directed differentiation and mass cultivation of pure erythroid progenitors from mouse embryonic stem cells. *Blood* 104, 1873–1880. doi: 10.1182/blood-2004-02-0570

Castro, C. I., and Briceno, J. C. (2010). Perfluorocarbonbased oxygen carriers: Review of products and trials. *Artif. Organs* 34, 622–634. doi: 10.1111/j.1525-1594.2009.00944.x

Chadwick, K., Wang, L., Li, L., Menendez, P., Murdoch, P., Rouleau, A., et al. (2003). Cytokines and BMP-4 promote hematopoietic differentiation of human embryonic stem cells. *Blood* 102, 906–915. doi: 10.1182/blood-2003-03-0832

Chang, C. J., Mitra, K., Koya, M., Velho, M., Desprat, R., Lenz, J., et al. (2011). Production of embryonic and fetal-like red blood cells from human induced pluripotent stem cells. *PLoS ONE* 6:10. doi: 10.1371/journal.pone.0025761

Chang, K. H., Nelson, A. M., Cao, H., Wang, L., Nakamoto, B., Ware, C. B., et al. (2006). Definitive-like erythroid cells derived from human embryonic stem cells coexpress high levels of embryonic and fetal globins with little or no adult globin. *Blood* 108, 1515–1523. doi: 10.1182/blood-2005-11-011874

Chang, K. H., Nelson, A. M., Fields, P. A., Hesson, J. L., Ulyanova, T., Cao, H., et al. (2008). Diverse hematopoietic potentials of five human embryonic stem cell lines. *Exp. Cell. Res.* 314, 2930–2940. doi: 10.1016/j.yexcr.2008.07.019

Choi, K. D., Yu, J., Smuga-Otto, K., Salvagiotto, G., Rehrauer, W., Vodyanik, M., et al. (2009). Hematopoietic and endothelial differentiation of human induced pluripotent stem cells. *Stem Cells* 27, 559–567. doi: 10.1634/stemcells.2008-0922

Chou, B. K., Mali, P., Huang, X., Ye, Z., Dowey, S. N., Resar, L. M., et al. (2011). Efficient human iPS cell derivation by a non-integrating plasmid from blood cells with unique epigenetic and gene expression signatures. *Cell Res.* 21, 518–529. doi: 10.1038/cr.2011.12

Christian, H., Rüster, B., Seifried, E., and Henschler, R. (2010). Platelet precursor cells can be generated from cultured human CD34+ progenitor cells but display recirculation into hematopoietic tissue upon transfusion in mice. *Transfus. Med. Hemother.* 37, 185–190. doi: 10.1159/000316975

Conley, C. L., Weatherall, D. J., Richardson, S. N., Shepard, M. K., and Charache, S. (1963). Hereditary persistence of fetal hemoglobin: a study of 79 affected persons in 15 Negro families in Baltimore. *Blood* 21, 261–281.

Cortin, V., Garnier, A., Pineault, N., Lemieux, R., Boyer, L., and Proulx, C. (2005). Efficient *in vitro* megakaryocyte maturation using cytokine cocktails optimized by statistical experimental design. *Exp. Hematol.* 33, 1182–1191. doi: 10.1016/j.exphem.2005.06.020

Daniels, G., Castilho, L., Flegel, W. A., Fletcher, A., Garratty, G., Levene, C., et al. (2009). International society of blood transfusion committee on terminology for red blood cell surface antigens: macao report. *Vox. Sang.* 96, 153–156. doi: 10.1111/j.1423-0410.2008.01133.x

Debili, N., Coulombel, L., Croisille, L., Katz, A., Guichardv, J., Breton-Gorius, J., et al. (1996). Characterization of a bipotent erythro megakaryocyticprogenitor in human bone marrow. *Blood* 88, 1284–1296.

Department of Health and Human Services. (2010). *The 2009 National Blood Collection and Utilization Survey Report.* Washington, DC: DHHS. Available online at: http://www.aabb.org/programs/biovigilance/nbcus/Documents/09-nbcus-report.pdf (Accessed May 4, 2014).

Department of Health and Human Services. (2013). *The 2011 National Blood Collection and Utilization Survey Report.* Washington, DC: DHHS. Available online at: http://www.aabb.org/programs/biovigilance/nbcus/Documents/11-nbcus-report.pdf (Accessed May 4, 2014).

Dias, J., Gumenyuk, M., Kang, H., Vodyanik, M., Yu, J., Thomson, J. A., et al. (2011). Generation of red blood cells from human induced pluripotent stem cells. *Stem Cells Dev.* 20, 1639–1647. doi: 10.1089/scd.2011.0078

Dick, E. P., Rebecca, L., and Sabroe, P. I. (2008). *Ex vivo*-expanded bone marrow $cd34^+$ derived neutrophils have limited bactericidal ability. *Stem Cells* 26, 2552–2563. doi: 10.1634/stemcells.2008-0328

Douay, L. (2001). Experimental culture conditions are critical for *ex vivo* expansion of hematopoietic cells. *J. Hematother. Stem. Cell. Res.* 10, 341–346. doi: 10.1089/152581601750288948

Douay, L., and Andreu, G. (2007). *Ex vivo* production of human red blood cells from hematopoietic stem cells: what is the future in transfusion? *Transfus. Med. Rev.* 21, 91–100. doi: 10.1016/j.tmrv.2006.11.004

Douay, L., and Giarratana, M. C. (2009). *Ex vivo* production of human red blood cells: a newadvance in stem cell engineering. *Methods Mol. Biol.* 482, 127–140. doi: 10.1007/978-1-59745-060-7_8

Douay, L., Lapillonne, H., and Turhan, A. G. (2009). Stem cells-A source of adult red blood cells for transfusion purposes: present and future. *Crit. Care Clinics* 25, 383–398. doi: 10.1016/j.ccc.2008.12.008

Ende, M., and Ende, N. (1972). Hematopoietic transplantation by means of fetal (cord) blood. A new method. *Va. Med. Mon.* 99, 276–280.

England, S. J., McGrath, K. E., Frame, J. M., and Palis, J. (2011). Immature erythroblasts with extensive *ex vivo* self-renewal capacity emerge from the early mammalian fetus. *Blood* 117, 2708–2717. doi: 10.1182/blood-2010-07-299743

Feng, Q., Lu, S. J., Klimanskaya, I., Gomes, I., Kim, D., Chung, Y., et al. (2010). Hemangioblastic derivatives from human induced pluripotent stem cells exhibit limited expansion and early senescence. *Stem Cells* 28, 704–712. doi: 10.1002/stem.321

Fibach, E., Manor, D., Oppenheim, A., and Rachmilewitz, E. A. (1989). Proliferation and maturation of human erythroid progenitors in liquid culture. *Blood* 73, 100–103.

Fibach, E., Manor, D., Oppenheim, A., and Rachmilewitz, E. A. (1991). Growth of human normal erythroid progenitors in liquid culture: a comparison with colony growth in semisolid culture. *Int. J. Cell. Cloning* 9, 57–64 doi: 10.1002/stem.5530090108

Foeken, L. M., Green, A., Hurley, C. K., Marry, E., Wiegand, T., and Oudshoorn, M. (2010). Monitoring the international use of unrelated donors for transplantation: The WMDA annual reports. *Bone Marrow Transplant.* 45, 811–818. doi: 10.1038/bmt.2010.9

Freyssinier, J. M., Lecoq-Lafon, C., Amsellem, S., Picard, F., Ducrocq, R., Mayeux, P., et al. (1999). Purification, amplification and characterization of a population of human erythroid progenitors. *J. Haematol.* 106, 912–922. doi: 10.1046/j.1365-2141.1999.01639.x

Fujimi, A., Matsunaga, T., Kobune, M., Kawano, Y., Nagaya, T., Tanaka, I., et al. (2008). *Ex vivo* large-scale generation of human red blood cells from cord blood $CD34^+$ cells by co-culturing with macrophages. *Int. J. Hematol.* 87, 339–350. doi: 10.1007/s12185-008-0062-y

Genbacev, O., Krtolica, A., Zdravkovic, T., Brunette, E., Powell, S., Nath, A., et al. (2005). Serum-free derivation of human embryonic stem cell lines on human placental fibroblast feeders. *Fertil. Steril.* 83, 1517–1529. doi: 10.1016/j.fertnstert.2005.01.086

Giamniona, L. M., Fuhrken, P. G., Papoustsakis, E. T., and Miller, W. M. (2006). Nicotinamide (vitamin B3) increases the polyploidisation and propletelet formation of cultured primary human megakaryocytes. *Br. J. Haemotol.* 135, 554–566. doi: 10.1111/j.1365-2141.2006.06341.x

Giarratana, M. C., Kobari, L., Lapillonne, H., Chalmers, D., Kiger, L., Cynober, T., et al. (2005). *Ex vivo* generation of fully mature human red blood cells from hematopoietic stem cells. *Nat. Biotechnol.* 23, 69–74. doi: 10.1038/nbt1047

Giarratana, M. C., Rouard, H., Dumont, A., Kiger, L., Safeukui, I., Le Pennec, P. Y., et al. (2011). Proof of principle for transfusion of *in vitro*-generated red blood cells. *Blood* 118, 5071–5079. doi: 10.1182/blood-2011-06-362038

Gifford, S. C., Derganc, J., Shevkoplyas, S. S., Yoshida, T., and Bitensky, M. W. (2006). A detailed study of time-dependent changes in human red blood cells: from reticulocyte maturation to erythrocyte senescence. *Br. J. Haematol.* 135, 395–404. doi: 10.1111/j.1365-2141.2006.06279.x

Guerriero, R., Mattia, G., Testa, U., Chelucci, C., Macioce, G., Casella, I., et al. (2001). Stromal cell-derived factor in increases polyploidization of megakaryocytes generated by human hematopoietic progenitor cells. *Blood* 97, 2587–2595. doi: 10.1182/blood.V97.9.2587

Hanna, J., Wernig, M., Markoulaki, S., Sun, C. W., Meissner, A., Cassady, J. P., et al. (2007). Treatment of sickle cell anemia mouse model with iPS cells generated from autologous skin. *Science* 318, 1920–1923. doi: 10.1126/science.1152092

Heath, D. S., Axelrad, A. A., McLeod, D. L., and Shreeve, M. M. (1976). Separation of the erythropoietin-responsive progenitors BFU–E and CFU–E in mouse bone marrow by unit gravity sedimentation. *Blood* 47, 777–792.

Henkel-Honke, T., and Oleck, M. (2007). Artificial oxygen carriers: a current review. *AANA. J.* 75, 205–211.

Hiroyama, T., Miharada, K., Sudo, K., Danjo, I., Aoki, N., and Nakamura, Y. (2008). Establishment of mouse embryonic stem cell-derived erythroid progenitor cell lines able to produce functional red blood cells. *PLoS ONE* 6:3. doi: 10.1371/journal.pone.0001544

Hou, P., Li, Y., Zhang, X., Liu, C., Guan, J., Li, H., et al. (2013). Pluripotent stem cells induced from mouse somatic cells by small-molecule compounds. *Science* 341, 651–654. doi: 10.1126/science.1239278

Housler, G. J., Miki, T., Schmelzer, E., Pekor, C., Zhang, X., Kang, L., et al. (2012). Compart- mental hollow fiber capillary membrane-based bioreactor technology for *in vitro* studies on red blood cell lineage direction of hematopoietic stem cells. *Tissue Eng. Part. C Methods* 18, 133–142. doi: 10.1089/ten.tec.2011.0305

Hovatta, O., Mikkola, M., Gertow, K., Stromberg, A. M., Inzunza, J., Hreinsson, J., et al. (2003). A culture system using human foreskin fibroblasts as feeder cells allows production of human embryonic stem cells. *Hum. Reprod.* 18, 1–6. doi: 10.1093/humrep/deg290

Huang, X., Shah, S., Wang, J., Ye, Z., Dowey, S. N., Tsang, K. M., et al. (2013). Extensive *ex vivo* expansion of functional human erythroid precursors established from umbilical cord blood cells by defined factors. *Mol. Ther.* 22, 451–463. doi: 10.1038/mt.2013.201

Jing, L., Jianhua, Z., Yelena, G., Huihui, L., Fumin, X., Lucia, D. F., et al. (2013). An: quantitative analysis of murine terminal erythroid differentiation *in vivo*: novel method to study normal and disordered erythropoiesis. *Blood* 121, e43–e49. doi: 10.1182/blood-2012-09-456079

Kaufman, D. S., Hanson, E. T., Lewis, R. L., Auerbach, R., and Thomson J. A. (2001). Hematopoietic colony-forming cells derived from human embryonic stem cells. *Proc. Natl. Acad. Sci. U.S.A.* 98, 10716–10721. doi: 10.1073/pnas.191362598

Kawano, Y., Kobune, M., Yamaguchi, M., Nakamura, K., Ito, Y., Sasaki, K., et al. (2003). *Ex vivo* expansion of human umbilical cord hematopoietic progenitor cells using a coculture system with human telomerase catalytic subunit (hTERT)-transfected human stromal cells. *Blood* 101, 532–540. doi: 10.1182/blood-2002-04-1268

Keel, S. B., Doty, R. T., Yang, Z., Quigley, J. G., Chen, J., Knoblaugh, S., et al. (2008). A heme export protein is required for red blood cell differentiation and iron homeosiasis. *Science* 319, 825–828. doi: 10.1126/science.1151133

Keerthivasan, G., Small, S., Liu, H., Wickrema, A., and Crispino, J. D. (2010). Vesicle trafficking plays a novel role in erythroblast enucleation. *Blood* 116, 3331–3340. doi: 10.1182/blood-2010-03-277426

Keller, G. (2005). Embryonic stem cell differentiation: emergence of a new era in biology and medicine.*Genes Dev.* 19, 1129–1155. doi: 10.1101/gad.1303605

Kobari, L., Yates, F., Oudrhiri, N., Francina, A., Kiger, L., Mazurier, C., et al. (2012). Human induced pluripotent stem cells can reach complete terminal maturation: *in vivo* and *in vitro* evidence in the erythropoietic differentiation model. *Haematologica* 97, 1795–1803. doi: 10.3324/haematol.2011.055566

Koivisto, H., Hyvärinen, M., Strömberg, A. M., Inzunza, J., Matilainen, E., Mikkola, M., et al. (2004). Cultures of human embryonic stem cells: serum replacement medium or serum-containing media and the effect of basic fibroblast growth factor. *Reprod. Biomed. Online* 9, 330–337. doi: 10.1016/S1472-6483(10)62150-5

Kurita, R., Suda, N., Sudo, K., Miharada, K., Hiroyama, T., Miyoshi, H., et al. (2013). Establishment of immortalized human erythroid progenitor cell lines able to produce enucleated red blood cells. *PLoS ONE* 8:3 doi: 10.1371/journal.pone.0059890

Lacoste, A., Berenshteyn, F., and Brivanlou, A. H. (2009). An efficient and reversible transposable system for gene delivery and lineage-specific differentiation in human embryonic stem cells. *Cell Stem Cell* 5, 332–342. doi: 10.1016/j.stem.2009.07.011

Lapillonne, H., Kobari, L., Mazurier, C., Tropel, P., Giarratana, M. C., Cleon, I. Z., et al. (2010). Red blood cell generation from human induced pluripotent stem cells: perspectives for transfusion medicine. *Haematologica* 95, 1651–1659. doi: 10.3324/haematol.2010.023556

Leberbauer, C., Boulme, F., Unfried, G., Huber, J., Beug, H., and Mullner, E. W. (2005). Different steroids coregulate long-term expansion versus terminal differentiation in primary human erythroid progenitors. *Blood* 105, 85–94. doi: 10.1182/blood-2004-03-1002

Ledran, M. H., Krassowska, A., Armstrong, L., Dimmick, I., Renstrom, J., Lang, R., et al. (2008). Efficient hematopoietic differentiation of human embryonic stem cells on stromal cells derived from hematopoietic niches. *Cell Stem Cell* 3, 85–98. doi: 10.1016/j.stem.2008.06.001

Lichtman, M. A., Beutler, E., Kipps, T. J., Kaushansky, K., Seligsohn, U., and Prchal, J. (2007). *Williams Hematology*. New York, NY: McGraw-Hill.

Lodish, H., Flygare, J., and Chou, S. (2010). From stem cell to erythroblast: regulation of red cell production at multiple levels by multiple hormones. *IUBMB Life* 62, 492–496. doi: 10.1002/iub.322

Lu, S. J., Feng, Q., Park, J. S., Vida, L., Lee, B. S., Strausbauch, M., et al. (2008). Biologic properties and enucleation of red blood cells from human embryonic stem cells. *Blood* 112, 4475–4484. doi: 10.1182/blood-2008-05-157198

Machlus, K. R., and Italiano, J. E. (2013). The incredible journey: from megakaryocyte development to platelet formation. *J. Cell Biol.* 201, 785–796. doi: 10.1083/jcb.201304054

Maggakis-Kelemen, C., Bork, M., Kayser, P., Biselli, M., and Artmann, G. M. (2003). Biological and mechanical quality of red blood cells cultured from human umbilical cord blood stem cells. *Med. Biol. Eng. Compuz.* 41, 350–356 doi: 10.1007/BF02348442

Malik, P., Fisher, T. C., Barsky, L. L. W., Zeng, L., Izadi, P., Hiti, A. L., et al. (1998). An *in vitro* model of human red blood cell production from hematopoietic progenitor cells. *Blood* 91, 2664–2671.

Manwani, D., and Bieker, J. J. (2008). The erythroblastic island. *Curr. Top. Dev. Biol.* 82, 23–53. doi: 10.1016/S0070-2153(07)00002-6

Masuda, S., Li, M., and Izpisua Belmonte, J. C. (2013). *In vitro* generation of platelets through direct conversion: first report in My Knowledge (iMK). *Cell. Res.* 23, 176–178. doi: 10.1038/cr.2012.142

Matsubara, Y., Saito, E., Suzuki, H., Watanabe, N., Murata, M., and Ikeda, Y. (2009). Generation of megakaryocytes and platelets from human subcutaneous adipose tissues. *Biochem. Biophys. Res. Commun.* 378, 716–720. doi: 10.1016/j.bbrc.2008.11.117

Matsubara, Y., Suzuki, H., Ikeda, Y., and Murata, M. (2010). Generation of megakaryocytes and platelets from preadipocyte cell line 3T3-L1, but not the

parent cell line 3T3, *in vitro*. *Biochem. Biophys. Res. Commun*. 402, 768–800. doi: 10.1016/j.bbrc.2010.10.120

Matsunaga, T., Tanaka, I., Kobune, M., Kawano, Y., Tanaka, M., Kuribayashi, K., et al. (2006). *Ex vivo* large-scale generation of human platelets from cord blood $CD34^+$. *Cells Stem Cells* 24, 2877–2887. doi: 10.1634/stemcells.2006-0309

McGrath, K., and Palis, J. (2008). Ontogeny of erythropoiesis in the mammalian embryo. *Curr. Top. Dev. Biol.* 82, 1–22. doi: 10.1016/S0070-2153(07)00001-4

McLeod, D. L., Shreve, M. M., and Axelrad, A. A. (1996). Induction of megakaryocyte colonies with platelet formation *in vitro*. *Nature* 88, 492–494.

Migliaccio, A. R., Masselli, E., Varricchio, L., and Whitsett, C. (2012). *Ex-vivo* expansion of red blood cells: how real for transfusion in humans? *Blood Rev.* 26, 81–95. doi: 10.1016/j.blre.2011.11.002

Migliaccio, G., Di Pietro, R., Di Giacomo, V., Di Baldassarre, A., Migliaccio, A. R., Maccioni, L., et al. (2002). *In vitro* mass production of human erythroid cells from the blood of normal donors and of thalassemic patients. *Blood Cells Mol. Dis.* 28, 169–180. doi: 10.1006/bcmd.2002.0502

Migliaccio, G., Migliaccio, A. R., Petti, S., Mavilio, F., Russo, G., Lazzaro, D., et al. (1986). Human embryonic hemopoiesis. Kinetics of progenitors and precursors underlying the yolk sac – liver transition. *J. Clin. Invest.* 78, 51–60. doi: 10.1172/JCI112572

Migliaccio, G., Sanchez, M., Masiello, F., Tirelli, V., Varricchio, L., Whitsett, C., et al. (2010). Humanized culture medium for clinical expansion of human erythroblasts. *Cell Transplant.* 19, 453–469. doi: 10.3727/096368909X485049

Miharada, K., Hiroyama, T., Sudo, K., Nagasawa, T., and Nakamura, Y. (2006). Efficient enucleation of eryth' roblasts differentiated *in vitro* from hematopoietic stem and progenitor cells. *Nat. Biotechnol.* 24, 1255–1256. doi: 10.1038/nbt1245

Mikkola, H. K., Gekas, C., Orkin, S. H., and Dieterlen-Lievre, F. (2005). Placenta as a site for hematopoietic stem cell development. *Exp. Hematol.* 33, 1048–1054. doi: 10.1016/j.exphem.2005.06.011

Mostafa, S. S., Papoutsakis, E. T., and Miller, W. M. (2001). Oxygen tension modulates the expression of cytokine receptors, transcription factors and lineage-specific markers in cultured human megakaryocytes. *Exp. Hematol.* 29, 873–883. doi: 10.1016/S0301-472X(01)00658-0

Natanson, C., Kern, S. J., Lurie, P., Banks, S. M., and Wolfe, S. M. (2008).Cell-free hemoglobin-based blood substitutes and risk of myocardial infarction and death: a meta-analysis. *J. Am. Med. Assoc.* 299, 2304–2312. doi: 10.1001/jama.299.19.jrv80007

Neildez-Nguyen, T. M., Wajcman, H., Marden, M. C., Bensidhoum, M., Moncollin, V., Giarratana, M. C., et al. (2002). Human erythroid cells produced cx vivo at large scale differentiate into red blood cells *in vivo*. *Nat. Biotechnol.* 20, 467–472. doi: 10.1038/nbt0502-467

Ng, E. S., Davis, R. P., Azzola, L., Stanley, E. G., and Elefanty, A. G. (2005). Forced aggregation of defined numbers of human embryonicstem cells into embryoid bodies fosters robust, reproducible hematopoietic differentiation. *Blood* 106, 1601–1603. doi: 10.1182/blood-2005-03-0987

Okita, K., Ichisaka, T., and Yamanaka, S. (2007). Generation of germlilne-competent induced pluripotent stem cells. *Nature* 448, 313–317. doi: 10.1038/nature05934

Okita, K., Matsumura, Y., Sato, Y., Okada, A., Morizane, A., Okamoto, S., et al. (2011). More efficient method to generate integration-free human iPS cells. *Nat. Methods* 8, 409–412. doi: 10.1038/nmeth.1591

Olivier, E. N., Qiu, C., Velho, M., Hirsch, R. E., and Bouhassira, E. E. (2006). Large-scale production of embryonic red blood cells from human embryonic stem cells. *Exp. Hematol.* 34, 1635–1642. doi: 10.1016/j.exphem.2006.07.003

Ono, Y., Wang, Y., Suzuki, H., Okamoto, S., Ikeda, Y., Murata, M., et al. (2012). Induction of functional platelets from mouse and human fibroblasts by p45NF-E2/Maf. *Blood* 120, 3812–3821. doi: 10.1182/blood-2012-02-413617

Palis, J. (2008). Ontogeny of erythropoiesis. *Curr. Opin. Hematol.* 15, 155–161 doi: 10.1097/MOH.0b013e3282f97ae1

Palis, J., and Yoder, M. C. (2001). Yolk-sac hematopoiesis: the first blood cells of mouse and man. *Exp. Hematol.* 29, 927–936. doi: 10.1016/S0301-472X(01)00669-5

Panzenböck, B., Bartunek, P., Mapara, M. Y., and Zenke, M. (1998). Growth and differentiation of human stem cell factor/erythropoietin-dependent erythroid progenitor cells *in vitro*. *Blood* 15, 3658–3668.

Peyrard, T., Bardiaux, L., Krause, C., Kobari, L., Lapillonne, H., Andreu, G., et al. (2011). Banking of pluripotent adult stem cells as an unlimited source for red blood cell production; Potential applications for alloimmunized patients and rare blood challenges. *Transfus. Med. Rev.* 25, 206–216. doi: 10.1016/j.tmrv.2011.01.002

Proulx, C., Boyer, L., Humanen, D. R., and Lemieux, R. (2003). Preferential *ex vivo* expansion of megakaryocytes from human cord blood CD34+-enriched cells in the presence of thrombopoietin and limiting amounts of stem cell factor and Flt-3 ligand. *J. Hematother. Stem. Cell. Res.* 12, 179–188. doi: 10.1089/152581603321628322

Proulx, C., Dupuis, N., Amour, I. S., Boyer, L., and Lemieux, R. (2004). Increased megakaryopoiesis in cultures of CD34-enriched cord blood cells maintained at 39 degrees C. *Biotechnol. Bioeng.* 88, 675–680. doi: 10.1002/bit.20288

Qiu, C., Hanson, E., Olivier, E., Inada, M., Kaufman, D. S., Gupta, S., et al. (2005). Differentiation of human embryonic stem cells into hematopoietic cells by coculture with human fetal liver cells recapitulates the globin switch that occurs early in development. *Exp. Hematol.* 33, 1450–1458. doi: 10.1016/j.exphem.2005.09.003

Qiu, C., Olivier, E. N., Velho, M., and Bouhassira, E. E. (2008). Globin switches in yolk sac-like primitive and fetal like definitive red blood cells produced from human embryonic stem cells. *Blood* 111, 2400–2408 doi: 10.1182/blood-2007-07-102087

Ran, D., Shia, W. J., Lo, M. C., Fan, J. B., Knorr, D. A., Ferrell, P. I., et al. (2013). RUNX1a enhances hematopoietic lineage commitment from human embryonic stem cells and inducible pluripotent stem cells. *Blood* 121, 2882–2890. doi: 10.1182/blood-2012-08-451641

Ratcliffe, E^1., Glen, K. E., Workman, V. L., Stacey, A. J., and Thomas, R. J. (2012). A novel automated bioreactor for scalable process optimisation of haematopoietic stem cell culture. *J. Biotechnol.* 161, 387–390. doi: 10.1016/j.jbiotec.2012.06.025

Rhodes, M. M., Kopsombut, P., Bondurant, M. C., Price, J. O., and Koury, M. J. (2008). Adherence to macrophages in erythroblastic islands enhances erythroblast proliferation and increases erythrocyte production by a different mechanism than erythropoietin. *Blood* 111, 1700–1708. doi: 10.1182/blood-2007-06-098178

Saeki, K., Nakahara, M., Matsuyama, S., Nakamura, N., Yogiashi, Y., Yoneda, A., et al. (2008). A feeder-free and efficient production of functional neutrophils from human embryonic stem cells. *Stem Cells* 27, 59–67. doi: 10.1634/stemcells.2007-0980

Satchwell, T. J., Bell, A. J., Pellegrin, S., Kuziq, S., Ridgwell, K., Daniels, G., et al. (2011). Critical band 3 multiprotein complex interactions establish early during human erythropoiesis. *Blood* 118, 182–191. doi: 10.1182/blood-2010-10-314187

Silverman, T. A., and Weiskopf, R. B. (2009). Hemoglobinbased oxygen carriers: Current status and future directions. *Transfusion* 49, 2495–2515. doi: 10.1111/j.1537-2995.2009.02356.x

Stadtfeld, M., Nagaya, M., Utikal, J., Weir, G., and Hochedlinger, K. (2008). Induced pluripotent stem cells generated without viral integration. *Science* 322, 945–949. doi: 10.1126/science.1162494

Stephenson, J. R., Axelrad, A. A., McLeod, D. L., and Shreevel, M. M. (1971). Induction of colonies of hemoglobin-synthesizing cells by erythropoietin *in vitro*. *Proc. Natl. Acad. Sci. U.S.A.* 68, 1542–1546. doi: 10.1073/pnas.68.7.1542

Stroncek, D. F., and Rebulla, P. (2007). Platelet transfusions. *Lancet* 370, 427–438. doi: 10.1016/S0140-6736(07)61198-2

Suda, T., Suda, J., and Ogawa, M. (1983). Single-cell origin of mouse hemopoietic colonies expressing multiplelineages in variable combinations. *Proc. Natl. Acad. Sci. U.S.A.* 80, 6689–6693. doi: 10.1073/pnas.80.21.6689

Sullenharger, B., Bhang, J. H., Gruner, R., Kotov, N., and Lasky, L. C. (2009). Prolonged continuous *in vitro* human platelet production using three-dimensional scaffolds. *Exp. Hematol.* 37, 101–110. doi: 10.1016/j.exphem.2008.09.009

Szabo, E., Rampalli, S., Risueno, R. M., Schnerch, A., Mitchell, R., Fiebig-Comyn, A., et al. (2010). Direct conversion of human fibroblasts to multilineage blood progenitors. *Nature* 468, 521–526. doi: 10.1038/nature09591

Takahashi, K., Tanabe, K., Ohnuki, M., Narita, M., Ichisaka, T., Tomoda, K., et al. (2007). Induction of pluripotent stem cells from adult human fibroblasts by defined factors. *Cell* 131, 861–872. doi: 10.1016/j.cell.2007.11.019

Takahashi, K., and Yamanaka, S. (2006). Induction of pluripotent stem cells from mouse embryonic and adult fibroblast cultures by defined factors. *Cell* 126, 663–676. doi: 10.1016/j.cell.2006.07.024

Takayama, N., Nishikii, H., Usui, J., Tsukui, H., Sawaguchi, A., Hiroyama, T., et al. (2008). Generation of functional platelets from human embryonic

stem cells *in vitro* via ES-sacs, VEGF-promoted structures that concentrate hematopoietic progenitors. *Blood* 111, 5298–5306. doi: 10.1182/blood-2007-10-117622

Takayama, N., Nishimura, S., Nakamura, S., Shimizu,T., Ohnishi, R., Endo, H., et al. (2010). Transient activation of c-MYC expression is critical for efficient platelet generation from human induced pluripotent stem cells. *J. Exp. Med.* 207, 2817–2830. doi: 10.1084/jem.20100844

Taylor, C. J., Peacock, S., Chaudhry, A. N., Bradley, J. A., and Bolton, E. M. (2012). Generating an iPSC bank for HLA-matched tissue transplantation based on known donor and recipient HLA types. *Cell Stem Cell* 11, 147–152. doi: 10.1016/j.stem.2012.07.014

Thomson, J. A., Itskovitz-Eldor, J., Shapiro, S. S., Waknitz, M. A., Swiergiel, J. J., Marshall, V. S., et al. (1998). Embryonic stem cell lines derived from human blastocysts. *Science* 282, 1145–1147.

Timmins, N. E., Athanasas, S., Günther, M., Buntine, P., and Nielsen, L. K. (2011). Ultrahigh-yield manufacture of red blood cells from hematopoietic stem cells. *Tissue Eng. Part. C Methods* 17, 1131–1137. doi: 10.1089/ten.tec.2011.0207

Timmins, N. E., and Nielsen, L. K.,(2009). Blood cell manufacture: current methods and future challenges. *Trends Biotechnol.* 27, 415–422. doi: 10.1016/j.tibtech.2009.03.008

Tirelli, V., Ghinassi, B., Migliaccio, A. R., Whitsett, C., Masiello, F., Sanchez, M., et al. (2011a). Phenotypic definition of the progenitor cells with erythroid differentiation potential present in human adult blood. *Stem Cells Int.* 2011:602483. doi: 10.4061/2011/602483

Tirelli, V., Masiello, F., Sanchez, M., Ghinassi, B., Whitsett, C., Migliaccio, G., et al. (2011b). Effects of ontogeny, ethnicity, gender and loss of companion cells on *ex-vivo* expansion of erythroid cells for transfusion. *Blood* 118, 563.

U.S. Census Bureau. (2004). *Global Population Composition.* Available online at: http://www.census.gov/population/international/files/wp02/wp-02004.pdf (Accessed September 14, 2012).

Van den Akker, E., Satchwell, T. J., Pellegrin, S., Daniels, G., and Toye, A. M. (2010). The majority of the *in vitro* erythroid expansion potential resides in CD34 (-) cells, outweighing the contribution of CD34 (+) cells and significantly increasing the erythroblast yield from peripheral blood samples. *Haematologica* 95, 1594–1598. doi: 10.3324/haematol.2009.019828

Vodyanik, M. A., Bork, J. A., Thomson, J. A., and Slukvin, I. I. (2005). Human embryonic stem cell-derived CD34+cells: efficient production in the coculture with OP9 stromal cells and analysis of lymphohematopoietic potential. *Blood* 105, 617–626. doi: 10.1182/blood-2004-04-1649

Vodyanik, M. A., Thomson, J. A., and Slukvin, I. I. (2006). Leukosialin (CD43) defines hematopoietic progenitors in human embryonic stem cell differentiation cultures. *Blood* 108, 2095–2105. doi: 10.1182/blood-2006-02-003327

Von Lindern, M., Zauner, W., Mellitzer, G., Steinlein, P., Fritsch, G., Huber, K., et al. (1999). The glucocorticoid receptor cooperates with the erythropoietin receptor and c-Kit to enhance and sustain proliferation of erythroid progenitors *in vitro*. *Blood* 94, 550–559.

Wada, H., Suda, T., Miura, Y., Kajii, E., Ikemoto, S., and Yawata, Y. (1990). Expression of major blood group antigens on human erythroid cells in a two phase liquid culture system. *Blood* 75, 505–511.

Wang, Y., Ono, Y., and Ikeda, Y. (2011). Induction of megakaryocytes from fibroblasts by p45NF-E2fMaf. *Blood* 11:908.

Weatherall, D. J., and Clegg, J. B. (1975). Hereditary persistence of fetal haemoglobin. *Br. J Haematol.* 29, 191–198 doi: 10.1111/j.1365-2141.1975.tb01813.xx

Wernig, M., Meissner, A., Foreman, R., Brambrink, T., Ku, M., Hochedlinger, K., et al. (2007). *In vitro* reprogramming of fibroblasts into a pluripotent ES-cell-like state. *Nature* 448, 318–324. doi: 10.1038/nature05944

Winslow, R. M. (2006). Current status of oxygen carriers ("blood substitutes"): 2006. *Vox Sang.* 91, 102–110. doi: 10.1111/j.1423-0410.2006.00789.x

World Health Organization. (2011). *Global Database on Blood Safety: Summary Report 2011.* Available online at: http://www.who.int/bloodsafety/global_database/GDBS_Summary_Report_2011.pdf (Accessed May 4, 2014).

Xi, J., Li, Y., Wang, R., Wang, Y., Nan, X., He, L., et al. (2013). *In vitro* large scale production of human mature red blood cells from hematopoietic stem cells by coculturing with human fetal liver stromal cells. *Biomed. Res. Int.* 2013:807863. doi: 10.1155/2013/807863

Yoshioka, N., Gros, E., Li, H. R., Kumar, S., Deacon, D. C., Maron, C., et al. (2013). Efficient generation of human iPSCs by a synthetic self-replicative RNA. *Cell Stem Cell* 13, 246–254. doi: 10.1016/j.stem.2013.06.001

Yu, J., Vodyanik, M. A., Smuga-Otto, K., Antosiewicz-Bourrget, J., Frane, J. L., Tian, S., et al. (2007). Induced pluripotent stem cell lines derived from human somatic cells. *Science* 318, 1917–1920. doi: 10.1126/science.1151526

Zambidis, E. T., Park, T. S., Yu, W., Tam, A., Levine, M., Yuan, X., et al. (2008). Expression of angiotensin-converting enzyme (CD143) identifies and regulates primitive hemangioblasts derived from human pluripotent stem cells. *Blood* 112, 3601–3614. doi: 10.1182/blood-2008-03-144766

Zeuner, A., Martelli, F., Vaglio, S., Federici, G., Whitsett, C., and Migliaccio, A. R. (2012). Concise review: stem cell-derived erythrocytes as upcoming players in blood trans- fusion. *Stem Cells* 30, 1587–1596. doi: 10.1002/stem.1136

Zhou, H., Wu, S., Joo, J. Y., Zhu, S., Han, D. W., Lin, T., et al. (2009). Generation of induced pluripotent stem cells using recombinant proteins. *Cell Stem Cell* 4, 381–384. doi: 10.1016/j.stem.2009.04.005

Zou, J., Mali, P., Huang, X., Dowey, S. N., and Cheng, L. (2011). Site-specific gene correction of a point mutation in human iPS cells derived from an adult patient with sickle cell disease. *Blood* 118, 4599–4608. doi: 10.1182/blood-2011-02-335554

Conflict of Interest Statement: The authors declare that the research was conducted in the absence of any commercial or financial relationships that could be construed as a potential conflict of interest.

Received: 25 January 2014; accepted: 26 May 2014; published online: 11 June 2014.
Citation: Singh VK, Saini A, Tsuji K, Sharma PB and Chandra R (2014) Manufacturing blood ex vivo: a futuristic approach to deal with the supply and safety concerns. Front. Cell Dev. Biol. ***2****:26. doi: 10.3389/fcell.2014.00026*
This article was submitted to Stem Cell Treatments, a section of the journal Frontiers in Cell and Developmental Biology.
Copyright © 2014 Singh, Saini, Tsuji, Sharma and Chandra. This is an open-access article distributed under the terms of the Creative Commons Attribution License (CC BY). The use, distribution or reproduction in other forums is permitted, provided the original author(s) or licensor are credited and that the original publication in this journal is cited, in accordance with accepted academic practice. No use, distribution or reproduction is permitted which does not comply with these terms.

AIP | Physics of Plasmas

Modeling carbon nanotube growth on the catalyst-substrate surface subjected to reactive plasma

Aarti Tewari and Suresh C. Sharma

Citation: Physics of Plasmas (1994-present) **21**, 063512 (2014); doi: 10.1063/1.4885104
View online: http://dx.doi.org/10.1063/1.4885104
View Table of Contents: http://scitation.aip.org/content/aip/journal/pop/21/6?ver=pdfcov
Published by the AIP Publishing

Articles you may be interested in

Effect of hydrogen plasma irradiation of catalyst films on growth of carbon nanotubes filled with iron nanowires
J. Vac. Sci. Technol. A **32**, 02B102 (2014); 10.1116/1.4827822

Role of negatively charged ions in plasma on the growth and field emission properties of spherical carbon nanotube tip
Phys. Plasmas **19**, 013502 (2012); 10.1063/1.3671968

Publisher's Note: "Effect of plasma parameters on growth and field emission properties of spherical carbon nanotube tip" [Phys. Plasmas18, 063503 (2011)]
Phys. Plasmas **18**, 109902 (2011); 10.1063/1.3641489

Effect of plasma parameters on growth and field emission properties of spherical carbon nanotube tip
Phys. Plasmas **18**, 063503 (2011); 10.1063/1.3595636

Use of plasma treatment to grow carbon nanotube forests on TiN substrate
J. Appl. Phys. **109**, 114312 (2011); 10.1063/1.3587234

Vacuum Solutions from a Single Source
- Turbopumps
- Backing pumps
- Leak detectors
- Measurement and analysis equipment
- Chambers and components

PFEIFFER VACUUM

This article is copyrighted as indicated in the article. Reuse of AIP content is subject to the terms at: http://scitation.aip.org/termsconditions. Downloaded to IP: 14.139.251.100 On: Tue, 01 Jul 2014 06:02:09

PHYSICS OF PLASMAS **21**, 063512 (2014)

Modeling carbon nanotube growth on the catalyst-substrate surface subjected to reactive plasma

Aarti Tewari and Suresh C. Sharma
Department of Applied Physics, Delhi Technological University (DTU), Shahbad Daulatpur, Bawana Road, Delhi 110 042, India

(Received 27 February 2014; accepted 9 June 2014; published online 26 June 2014)

The paper presents a theoretical model to study the growth of the carbon nanotube (CNT) on the catalyst substrate surface subjected to reactive plasma. The charging rate of the CNT, kinetics of electron, ions and neutral atoms, the growth rate of the CNT because of diffusion and accretion of ions on the catalyst nanoparticle inclusion of the issue of the plasma sheath is undertaken in the present model. Numerical calculations on the effect of ion density and temperature and the substrate bias on the growth of the CNT have been carried out for typical glow discharge plasma parameters. It is found that the height of CNT increases with the ion density of carbon ions and radius of CNT decreases with hydrogen ion density. The substrate bias also affects the growth rate of the CNT. The field emission characteristics from the CNTs can be analyzed from the results obtained. © *2014 AIP Publishing LLC*. [http://dx.doi.org/10.1063/1.4885104]

I. INTRODUCTION

Low temperature plasmas are beneficial to the synthesis of carbon-based nanostructures. For nanofabrication, either solid particle float in the plasma or some nanoscale objects grow on a solid surface exposed to plasma. The second method is the area of pursuit of recent years where plasma assisted syntheses of nanostructures have been the major area of concern. In plasma assisted synthesis of nanostructures, the particles in ionized gas phase nucleate, crystallize, and are taken through the plasma sheath eventually to deposit on the surface.[1]

Numerous works have been performed to study the CNT growth of plasma, the consequent effects of rf power density, temperature, gas flow rate on the growth rate, and dimensions of resulting CNTs.[2–7]

Choi *et al.*[2] have grown vertically aligned CNTs on Ni-coated silicon substrates using microwave plasma-enhanced chemical vapor deposition (MPECVD) technique. They establish that the growth rate and the density of CNTs increase with the reduction of the rf power density.

Aksak *et al.*[3] have demonstrated the effect of temperature along the increment of carbon nanotubes (CNTs) in methane CVD. At temperatures over and above 850 °C, they observed CNT formation with average radius and radii distribution, decreasing while their length is increased with temperature. They also noticed that the temperature affected the as-grown CNTs diameter inversely.

Loffler *et al.*[4] have optimized the growth of the CNT by plasma enhanced chemical vapor deposition (PECVD) for field emitters and observed the effect of growth parameters on the growth rate of the CNT. They confirmed that CNTs are better aligned at high power, but the etch rate increased due to strong ion bombardment. As a result, the catalytic particle is sputtered during the PECVD process so that the diameter of the CNT decreases and hence this effect can be used to sharpen the tip of the CNT by an adapted growth time.

Abdi *et al.*[5] have studied the effects of plasma powers on the growth of carbon nanotubes in the PECVD method and found that as the plasma power of the Ni layer was increased, the grain size of nickel nanoparticle decreased and consequently; nanotubes of smaller diameter were obtained.

Cho *et al.*[6] have investigated the effect of NH_3 gas on the growth of the CNTs using thermal CVD. They observed that the CNT length increased while CNT radius decreased with the NH_3 flow (cf. Fig. 5 of Cho *et al.*[6]). Moreover, the CNTs were etched back by dc plasma of N_2 to reduce the population density and radius of curvatures of CNTs, which resulted in a considerable improvement of the field emission characteristics.

Srivastava *et al.*[7] have studied the effect of hydrogen plasma treatment on oxide films on the growth and microstructures of MWCNTs and reported that the oxide films without H_2 plasma pretreatment or treated for lesser time resulted in CNT films with the high percentage of carbonaceous particles, and with embedded particles/nanorods distributed discontinuously in the cavity of the nanotubes.

Many theoretical models have evolved to study the nanostructure growth in plasma. Plasma environment processes, such as ion bombardment, atomic hydrogen effects, electron number density, sheath thickness, and surface potential on the growth rate, have been extensively examined.[8–12]

Denysenko *et al.*[8] have studied the growth of single walled carbon nanotubes (SWCNTs) in a PECVD using the surface deposition model. In this case, it was shown that at low substrate temperatures (1000 K), the atomic hydrogen and ion fluxes from the plasma could strongly affect the nanotube growth.

Levchenko *et al.*[9] have suggested that the plasma-aided process, in comparison to the neutral flux deposition, is a very efficient tool to control the nanotube aspect ratio. They highlight that an increased influx and controllable deposition of ionic Building Blocks (BBs) directly onto the nanotube lateral surfaces can be used to deterministically control the geometric configuration of the nanotips.

 © 2014 AIP Publishing LLC

This article is copyrighted as indicated in the article. Reuse of AIP content is subject to the terms at: http://scitation.aip.org/termsconditions. Downloaded to IP: 14.139.251.100 On: Tue, 01 Jul 2014 06:02:09

Mehdipour *et al.*[10] have analytically studied the effect of electron number density, sheath thickness, gas pressure, surface potentials, etching gas density on the growth rate of carbon nanofibres. They calculated the exact temperature of the catalyst nanoparticle with respect to the substrate temperature. They also establish that the growth parameters like (total gas pressure), the relative concentrations of hydrocarbon and etching gas can be used to obtain high aspect ratio nanostructures.

Ostrikov *et al.*[11] have highlighted the plasma based process during nanostructures growth, including sheath effects and the various processes involved during nanostructure growth like an ion induced dissociation, ion decomposition, hydrogen recombination; ion induced neutralization, adsorption of hydrogen atoms, adsorption and desorption of hydrocarbon radicals, and surface diffusion of carbon atoms and several others.

However, the studies have hitherto not fully followed the exact processes in SWCNT growth in a plasma environment where innumerable complex processes take place. Thus, we try to model the CNT growth on the catalyst substrate surface in reactive plasma by including sheath kinetics, the balance equation of the various plasma species like neutrals, ions, electrons and finally numerically solve for the radius and height of the CNT due to accretion and surface diffusion processes.

In recent years, most of the research publications on nanostructure synthesis do feature information on field emission properties. This partly may be ascribable to the reason that carbon nanostructures have emerged as potential field emitter devices.[12–18]

In the present paper, we study the development of CNT on the catalyst–substrate surface subjected to reactive plasma. In Sec. II, we develop a theoretical model, including the charging rate of the CNT, kinetics of electron, ions, and neutral atoms, the growth rate of the CNT on account of diffusion and accretion of ions on catalyst nanoparticle. The plasma sheath kinetics of the development process of the CNT have also been brought into account. Result and discussions are given in Sec. III. Conclusion is given in Sec. IV.

II. MODEL

In the present model, we consider the growth of the CNT on the catalyst–substrate surface subjected to reactive plasma containing electrons, positively charged ions of methyl (CH_3^+, CH_2^+) denoted as ions A and hydrogen ions (H^+) denoted as ions B, neutral atoms of type A methane (CH_4), and neutral atoms of type B hydrogen (H_2). A substrate of silicon (Si) over which catalyst of nickel (Ni) is taken. The reactive plasma of Ar + H_2 + CH_4 is considered and CH_4 acts as a carbon source gas. Since the catalyst-substrate surface is in contact with the plasma, we shall consider sheath kinetics in our present example. The electric field created due to charge separation within the sheath region is taken along the z-axis.

The sheath equations are:

First, the continuity equation (Lieberman *et al.*[19])

$$\frac{\partial n}{\partial \tau} + \nabla.(nu) = G - L,$$

where G and L are the left over terms of collisions part of the Boltzmann equation (Eq. (2.3.3) of Lieberman *et al.*[19]) when integrated over velocities. They denote collisions that create or destroy particles, respectively, i.e., either recombination or ionization, where $G = \nu_{iz} n_e$ and L = volume loss rate.

Finally, the continuity equation reduces to

$$\nabla.(nu) = \nu_{iz} n_e, \tag{1}$$

where n_e = number density of electron, ν_{iZ} = ionization frequency, n and u denote the number density and fluid velocity of electrons, CH_3^+, CH_2^+, Ar^+ and H^+.

Second, ion momentum balance equation[19]

$$Mn_j u_j \frac{du_j}{dz} = en_j E - Mn_j \nu_{jn} u_j, \tag{2}$$

where M is the mass of ions in plasma, u_j are their fluid velocity, n_j is their number density, ν_{jn} is the collision frequency, and E is the electric field.

For determining potential within the sheath, we use Poisson's equation (Mehdipour *et al.*[10])

$$\frac{d^2\phi}{dz^2} = -4\pi \sum q_j \delta_j n_j, \tag{3}$$

δ_j is the jth ion to electron number density ratio and ϕ is the electrostatic potential, $\sum_j \delta_j = 1$ and $0 < \delta_j < 1$ as electron density is greater in plasma bulk than in sheath.[19]

For the CNT growth over the catalyst-substrate surface in plasma, the following steps take place:

1. First, the applied plasma power dissociates the catalyst particle thereby forming catalyst nanoparticle.
2. The methyl ions (CH_3^+, CH_2^+) adsorb on the catalyst-substrate surface with adsorption flux[20] J_{ai}.
3. Some of the ions desorp with desorption energy E_{ai} with desorption flux[20] J_{desi}.
4. Therefore, there is thermal dehydrogenation (removal of hydrogen) of ion induced dissociated methyl ions to produce C ions.
5. While a big fraction of carbon atoms diffuses into catalyst particle contributing to nanotube growth, some of the carbon atoms evaporate from the surface with evaporation energy E_{ev}.
6. Ultimately, the growth of the CNT occurs due to two main processes, surface diffusion of carbon ions into the catalyst surface and sticking of neutrals onto the catalyst surface. The hydrogen ions effectively shape nanoparticles by etching effects.

A. Charging of the CNT

The equation describes the charge developed on the entire CNT (i.e., a spherical tip over the cylindrical surface), due to accretion of electrons and accretion and diffusion of positively charged ions on the surface of the CNT (a spherical tip over the cylindrical surface)

$$\frac{dZ}{d\tau} = n_{iActs} + n_{iActcys} + n_{iBcts} + n_{iBctcys} - \gamma_e (n_{ects} + n_{ictcys}), \tag{4}$$

This article is copyrighted as indicated in the article. Reuse of AIP content is subject to the terms at: http://scitation.aip.org/termsconditions. Downloaded to IP: 14.139.251.100 On: Tue, 01 Jul 2014 06:02:09

where Z is the charge over the entire CNT (i.e., a spherical tip over the cylindrical surface), $n_{ects} = \pi {r_{ct}}^2 (\frac{8k_BT_e}{\pi m_e})^{\frac{1}{2}} n_e(x) \exp[Z\alpha_e + \frac{eU_s}{k_BT_s}]$ is the electron collection current at the surface of the spherical CNT tip and $\alpha_e = (\frac{e^2}{r_{ct}k_BT_e})$, r_{ct} is the nanoparticle radius, U_s is the substrate bias and k_B is the Boltzmann constant, $n_e(x) = n_{e0}\exp[\frac{|e|\phi(x)}{k_BT_e}]$ is the electron density in plasma sheath,[1] $\phi(x)$ is the electrostatic potential, n_{e0} is plasma density in bulk and it decreases towards the substrate. T_e is the electron temperature, $\phi(x) = \phi_0 \exp(-\frac{|x|}{\lambda_d})$, ϕ_0 is the negative potential at the surface and $\lambda_d = \sqrt{\frac{k_BT_e}{n_e e^2}}$ is Debye length,[1] $n_{ectcys} = n_e(x) r_{ct} h (\frac{2\pi k_BT_e}{m_e})^{\frac{1}{2}} \exp[\frac{eV_s}{k_BT_e} + \frac{eU_s}{k_BT_s}]$ is the electron collection current on the cylindrical surface of the CNT and V_s is the surface potential on the cylindrical surface of the CNT and h is the height of cylindrical surface of the CNT, m_e is the mass of electron,

$$n_{ijctcys} = n_{ij}(x) r_{ct} h \left(\frac{2\pi k_B T_i}{m_{ij}}\right)^{\frac{1}{2}} \left\{ \frac{2}{\sqrt{\pi}} \left(\frac{eV_s}{k_BT_i}\right)^{\frac{1}{2}} + \exp\left[\frac{eV_s}{k_BT_i}\right] erfc\left[\left(\frac{eV_s}{k_BT_i}\right)^{\frac{1}{2}}\right] \right\} \times \exp\left[-\frac{E_b}{k_BT_s}\right] \exp\left[-\frac{eU_s}{k_BT_s}\right]$$

is the ion collection current on the cylindrical surface of CNT, T_i is the ion temperature, m_{ij} is the ion mass (j refers to either A or B positively charged ion as explained earlier), E_b is the energy barrier for bulk diffusion (≈1.6 eV), T_s is the substrate or catalyst temperature, $n_{ijcts} = \pi {r_{ct}}^2 (\frac{8k_BT_i}{\pi m_{ij}})^{\frac{1}{2}} n_{ij}(x)\ [1 - Z\alpha_i] \exp[-\frac{E_b}{k_BT_s}] \exp[-\frac{eU_s}{k_BT_s}]$ is the ion collection current to spherical CNT, where $n_{ij}(x) = n_{ijo}(1 - \frac{2e\phi(x)}{m_i {v_{i0}}^2})$ is the ion density in plasma sheath, v_{io} is the ion velocity at any point within the plasma and $\alpha_i (= \frac{e^2}{r_{ct}k_BT_i})$.

The substrate bias is an essential factor when the charge on CNT is considered as increasing the negative substrate bias, goes to more negative charge developing on the CNT surface which final results an increase in the thickness of plasma sheath.[1] Moreover, increasing the negative substrate bias accelerates the positive ion species.

B. Balance equation of electron density

The equation describes the balance of electron number density in the plasma bulk on account of ionization, recombination, and electron collection current

$$\frac{dn_e}{d\tau} = (\beta_A n_A + \beta_B n_B) - (\alpha_A n_e n_{iA} + \alpha_B n_e n_{iB}) - \gamma_e n_{ct}(n_{ects} + n_{ectcys}), \quad (5)$$

where β_j is the coefficient of ionization of the constituent neutral atoms due to external field, $\alpha_j(T_e) = \alpha_{j0}(\frac{300}{T_e})^k \mathrm{cm}^3/\mathrm{s}$ is the coefficient of recombination of electrons and positively charged ions. n_e is the electron number density and n_{iA} and n_{iB} are the ion number density of ions A and B, respectively, and $\kappa = -1.2$ is a constant (Tewari and Sharma[14]).

The first term on the right side of Eq. (5) is the rate of gain in electron density per unit time because of ionization of neutral atoms; the second term is the decaying rate of the electron density due to electron–ion recombination. The third term is the electron collection current at the surface of the CNT (spherical tip over the cylindrical surface) (Tewari and Sharma[14]).

C. Balance equation of positively charged ion density

The equation describes the balance of positively charged ions in plasma bulk due to ionization of neutral atoms, recombination of electrons and ions, ion collection current at CNT surface, their adsorption, desorption, and thermal dehydrogenation

$$\frac{dn_{iA}}{d\tau} = \beta_A n_A - \alpha_A n_e n_{iA} - n_{ct}(n_{iActs} + n_{iActcys}) - J_{aiA} + J_{desorptionA}, \quad (6)$$

$$\frac{dn_{iB}}{d\tau} = \beta_B n_B - \alpha_B n_e n_{iB} - n_{ct}(n_{iBcts} + n_{iBctcys}) - J_{aiB} + J_{desorptionB} + J_{th}, \quad (7)$$

$J_{aij} = \frac{P_i \nu}{(2\pi m_{ij} k_B T_{ij})^{\frac{1}{2}}}$ is the adsorption flux onto the catalyst -substrate surface, P_i is the partial pressure of adsorbing species,[20] $J_{desorptionj} = j_{ij}\nu \exp(\frac{-\varepsilon_{ai}}{k_BT_{ij}})$ is the desorption flux from the catalyst-substrate surface, j refers to either A or B ions, ν is the thermal vibrational frequency, E_{ai} is the adsorption energy,[20] j_{ij} is the ion flux on the catalyst substrate surface.

$J_{th} = j_H \nu \exp(\frac{-\delta\varepsilon_{th}}{k_BT_s})$ is the flux of type B ion (namely hydrogen) on account of thermal dehydrogenation. $\delta\varepsilon_{th}$ is the activation energy of thermal dehydrogenation, j_H is the hydrogen ion flux at catalyst-substrate surface.

The first term in Eqs. (6) and (7) is the gain in ion density per unit time on account of ionization of neutral atoms, the second term is the electron-ion recombination. The third term is the ion collection current to the surface of the CNT (spherical tip over the cylindrical surface) (Tewari and Sharma[14]). The fourth term is the loss of ions on account of their adsorption to the catalyst-substrate surface and fifth term is the gain of ion density due to the desorption ion of ions from the catalyst-substrate surface into plasma. The last term in Eq. (7) Describes the increase of hydrogen ion number density in plasma because of thermal dehydrogenation.

D. Balance equation of neutral atoms

The equation describes the balance of neutral particles in plasma due to recombination of electrons-ions, ionization of neutral molecules, ion and neutral collection current on the CNT surface

$$\frac{dn_A}{d\tau} = \alpha_A n_e n_{iA} - \beta_A n_A + n_{ct}(1 - \gamma_{iA})(n_{iActs} + n_{iActys}) - n_{ct}\gamma_A(n_{Acts} + n_{Actcys}), \quad (8)$$

This article is copyrighted as indicated in the article. Reuse of AIP content is subject to the terms at: http://scitation.aip.org/termsconditions. Downloaded to IP: 14.139.251.100 On: Tue, 01 Jul 2014 06:02:09

$$\frac{dn_B}{d\tau} = \alpha_B n_e n_{iB} - \beta_B n_B + n_{ct}(1-\gamma_{iB})(n_{iBcts} + n_{iBctcys}) - n_{ct}\gamma_B(n_{Bcts} + n_{Bctcys}), \quad (9)$$

where $n_{jcts} = \pi r_{ct}{}^2(\frac{8k_BT_n}{\pi m_j})^{\frac{1}{2}}n_j$ is the neutral collection current at the surface of spherical CNT tip, $n_{jctcys} = \pi r_{ct}h(\frac{2k_BT_n}{m_j})^{\frac{1}{2}}n_j$ is the neutral collection current on the cylindrical surface of CNT.

γ_{iA} is the ion sticking coefficient and γ_A is the neutral atom sticking coefficient, T_n is the neutral atom temperature, n_j is the neutral atom density, and m_j is the neutral atom mass.

The first term in Eqs. (8) and (9) is the gain in neutral atom density per unit time due to electron–ion recombination, the second term is the decrease in neutral density due to ionization. The third term is the gain in neutral density due to neutralization of the particles collected at the open of the CNT. The last term is the accumulation of neutral atoms of species A and B on the surface of the CNT (Tewari and Sharma[14]).

E. Rate equation for energy of catalyst particle

$$\text{rf power} = C_pT_S\frac{d}{d\tau}(m_p) = \left(\frac{3}{2}k_B\right) \times \left[n_{iActP}\left(\varepsilon^S{}_{iAc} + I_{pA}\right) + n_{iBctP}\left(\varepsilon^S{}_{iBc} + I_{pB}\right)\right] - \left(\frac{3}{2}k_B\right)[(1-\gamma_{Ai})n_{iActP} + n_{iBctP}]T_S, \quad (10)$$

where $m_P = \frac{4}{3}\pi r_P{}^3\rho_P$ is the mass of catalyst particle, r_p is the radius of catalyst particle whose initial value is 50 nm.[10] ρ_P is the mass density of catalyst particle. C_p is the specific heat of catalyst particle (Ni) and is 0.44 kJ/kg ^{0}K and T_s is the substrate temperature. I_{pA} and I_{pB} are the ionization energies of atoms A and B, respectively (Tewari and Sharma[14]), $\varepsilon^s_{ijc}(Z) = (\frac{(2-Z\gamma_{ji})}{(1-Z\gamma_{ji})} - Z\gamma_{ji})k_BT_{ij}$ are the mean energy collected by the ions j (where j refers to ion A or B) at the surface of the catalyst particle and $\gamma_{ji} = (\frac{e^2}{r_Pk_BT_{ij}})$ $n_{ijctP} = \pi r_P{}^2(\frac{8k_BT_i}{\pi m_{ij}})^{\frac{1}{2}}n_{ij}(x)[1-Z\gamma_i]\exp[-\frac{E_b}{k_BT_S}]\exp[-\frac{eU_S}{k_BT_S}]$ is the ion collection current at the surface of catalyst particle, j (where j refers to ion A or B) and $\gamma_i = (\frac{e^2}{r_Pk_BT_{ij}})$.

Equation (10) denotes the influence of rf power on the mass of catalyst particle for constant specific heat and substrate temperature. The first term on the right side of Eq. (10) is the rate of energy transferred to the catalyst particle due to the ion collected at the surface of catalyst particle on account of ionization of neutral atoms A and B and mean energy collected by the ions at the surface of catalyst particle, and the second term is due to the sticking accretion of ions A and B at the catalyst particle site.

We assume that as the applied rf power increases, it ionizes the gas more which creates more energetic ions, which thereby increase the density of plasma species of relatively higher energy, i.e., the number density and temperature of ions A and B increase. We assume that the rf power affects the radius of catalyst particle and the temperature or the specific heat is unaffected by applying rf power as most researches done highlight the variation of size of particles with rf power only (cf. Choi *et al.*,[2] Srivastava *et al.*,[7] and Abdi *et al.*[5]).

In Solving Eq. (10), we consider different rf power, i.e., 50 W, 100 W, 150 W, and 200 W. The substrate temperature T_S is taken as 500 °C, Substrate bias $U_s = -50$ V.

$n_{iB0} = n_{iA0} = 10^8\,\text{cm}^{-3}$, $T_{i0} = 1900$ K, $\varepsilon^s_{iAc} = \varepsilon^s_{iBc} = 2.648$ eV, $I_{pA} = 10.27$ eV, and $I_{pB} = 12$ eV. Substituting all the above value for a fixed rf power at 50 W, we can calculate n_{iActP}, n_{iBctP}. Now, for higher plasma power, we consider slightly different ion density and ion temperatures and calculate n_{iActP} and n_{iBctP} and consequently, the catalyst particle radius (r_p). The other parameters are same as in result and discussion section.

The resulting value of catalyst nanoparticle at time τ serves as the initial radius of nanotube (r_{ct}).

F. Growth rate equation of the curved surface area of CNT

Following, Denysenko *et al.*,[8] Mehdipour *et al.*,[10] Tewari and Sharma,[14] and Denysenko and Ostrikov,[26]

$$rct\frac{d(2\pi h)}{d\tau} = \left[\left\{2n_{CH}\nu\exp\left(\frac{-\delta E_t}{k_BT_S}\right) + 2\theta_{CH}j_{iA}y_d + 2j_{iA} + j_{iA}\sigma_{ads}j_{iB} + j_c\nu\right\}m_c + \left\{j_{iA}(1-\theta_t) + j_{iA}\sigma_{ads}j_H + j_{iA}\nu\exp\left(\frac{-\delta E_t}{k_BT_S}\right)\right\}m_{iA}\right] \times \frac{D_S\times 2\pi r_{ct}}{\pi r_{ct}^2\rho_p}(n_{iActcys}) + \gamma_{CH_3}\pi r_{ct}^2 n_{CH_3ctcys} \quad (11)$$

$$\frac{d(\pi r_{ct}^2)}{d\tau} = \left\{j_{iB}\nu\exp\left(\frac{-E_b}{k_BT_S}\right) + j_{iB}\nu\exp\left(\frac{-\delta E_{th}}{k_BT_S}\right) + j_{iB}(i-\theta_t) + j_{iB} + \theta_{CH} \times \left(j_{iB}y_d + \nu_0\nu\exp\left(\frac{-\delta E_i}{k_BT_S}\right)\right)\right\}\frac{h(\tau)}{n_{iB}}, \quad (12)$$

where $n_{CH} = \theta_{CH}\nu_0$ is the number density, concentration of CH (Mehdipour *et al.*[10]), $\nu_0 \approx 1.3\times 10^{15}\text{cm}^{-2}$ is the number of adsorption sites per unit area (Mehdipour *et al.*[10]), θ_{CH} is the total surface coverage (Mehdipour *et al.*[10]) of either C_2H_2 or CH_4 in our case, $j_C = n_{CH}v_{thC}/4$ is the ion flux of carbon ions and v_{thC} is the thermal velocity of C ions (Mehdipour *et al.*[10]), δE_t is thermal energy barrier (Denysenko *et al.*[26]), $j_{iA} = n_{iA}(k_BT_i/m_{iA})$ and $j_{iB} = n_{iB}(k_BT_i/m_{iB})$ are the ion flux of type A and B, respectively (Denysenko *et al.*[26]), $y_d \approx \varepsilon_{icH}/\varepsilon_{dis}$, where ε_{icH} is kinetic energy associated with the motion of hydrocarbon ions impinging on the substrate (Mehdipour *et al.*[10]), ε_{dis} is the dissociation energy[10] of C_2H_2 or CH_4 in our case, σ_{ads} is the cross section for the reactions of atomic hydrogen $\approx(6.8\times 10^{-16}\text{cm}^2)$ (Denysenko *et al.*[26]), E_b is the energy barrier for bulk diffusion $\approx(1.6\,\text{eV})$ (Denysenko *et al.*[26]), D_s is the surface diffusion coefficient $[D_S = D_{S0}\exp(-E_S/k_BT_S)]$, E_s is the energy barrier for diffusion of carbon (C) on the catalyst and is 0.3 eV (Ref. 10) and

This article is copyrighted as indicated in the article. Reuse of AIP content is subject to the terms at: http://scitation.aip.org/termsconditions. Downloaded to IP: 14.139.251.100 On: Tue, 01 Jul 2014 06:02:09

$D_{S0} = \nu a_0^2$ where a_0 is inter atomic distance (Mehdipour *et al.*[10]), θ_t is the total surface coverage (Mehdipour *et al.*[10]), ε_{th} is the energy due to thermal dehydrogenation, $\delta\varepsilon_t$ is the energy due to thermal dissociation (Mehdipour *et al.*[10]), γ_{CH_3} is the sticking coefficient of CH_3 molecules, (Tewari and Sharma[14]), m_C is the mass of a carbon atom ($=12$ a.m.u.), m_{iA} is the mass of type A ions (15 a.m.u. for CH_3^+ and 14 a.m.u. for CH_2^+).

Equations (11) and (12) trace the development of the CNT on catalyst nanoparticle. The height of CNT is obtained from Eq. (11) in which we consider the growth of the cylindrical part of the CNT and the value of the height of the cylindrical part of the CNT at time τ is then fed into Eq. (12) to determine the CNT radius CNT (r_{ct}). Equation (12) specifically calculates the curved surface of the spherical CNT tip.

In Eq. (11), the first term in the first bracket (Denysenko *et al.*[26]) describes the generation of carbon atoms on the catalyst surface due to thermal dissociation of methyl ions (with energy barrier δE_t), second term (Mehdipour *et al.*[10]) describes the ion induced dissociation of CH_4. The third term (Denysenko *et al.*[26]) denotes the decomposition of positively charged ions of type A (either $C_2H_2^+$ in Mehdipour *et al.*[10] or CH_4^+ in our case). The fourth term (Mehdipour *et al.*[10]) is the interaction of ions with atomic hydrogen from the plasma, fifth term (Mehdipour *et al.*[10]) accounts for the incoming flux of carbon atoms per unit time onto the catalyst particle. Likewise, the sixth term denotes the adsorption of type A ions to the surface, seventh term is the interaction of adsorbed type A ions with atomic hydrogen from plasma, and the eighth term is due to thermal dissociation of carbon source gas (C_2H_2 in Mehdipour *et al.*[10] or CH_4 in our case). The factor $n_{iActcys}$ accounts for the ion collection current on the growing cylindrical part of the CNT (Tewari and Sharma[14]). The term $\frac{D_S \times 2\pi r_{ct}}{\pi r_{ct}^2 \rho_p}$ denotes the surface diffusion of species onto the catalyst surface across the catalyst nanoparticle per unit area mass density. Finally, the last term denotes the sticking of neutral atoms of methane to the cylindrical surface of the CNT (Tewari and Sharma[14]).

In Eq. (12), the first term (Mehdipour *et al.*[10]) denotes hydrogen atom diffusing into the catalyst-substrate surface, second term (Mehdipour *et al.*[10]) accounts for the incoming flux of hydrogen ion due to thermal dehydrogenation of type A ions, third term (Denysenko *et al.*[26]) is adsorption of type B ions to the surface. The fourth term (Denysenko *et al.*[26])is the decomposition of positively charged ions of type B, fifth term (Denysenko *et al.*[8]) is due to ion induced dissociation of CH_4, sixth term (Denysenko *et al.*[8]) is due to the incorporation of hydrogen ions due to thermal dissociation of methyl ions).

Equation (12) accounts only for the nanoparticle tip radius as bottom area is already determined by the catalyst nanoparticle because they seed nanoparticle growth on them. $h(\tau)$ is the height of the CNT at a time τ.

III. NUMERICAL RESULT AND DISCUSSIONS

This report introduces a theoretical model for the intellect of the CNT growth on the catalyst-substrate surface in reactive plasma. Reactive plasma is composed of multiple reactive species that continually transform into each other and new species as a consequence of numerous chemical reactions in the ionized form. Since during nanostructure synthesis there are numerous processes involved like ionization, recombination, dissociation, etc., we, therefore, consider reactive plasma in our present model instead of the multi component plasma.

We assume that, first, the applied plasma power creates active species plasma, which dissociates the catalyst particle into nanoclusters needed for CNTs nucleation and growth. In a plasma medium, following processes takes place, namely ionization (in which a neutral atom gives rise to an ion) and recombination (of an ion with an electron results in a neutral molecule), adsorption (absorption on the surface), desorption of ionic species, thermal dehydrogenation (removal of hydrogen), evaporation and their diffusion (surface) into catalyst surface and sticking of neutral atoms to the CNT surface. Since, the substrate-catalyst surface is in contact with the plasma, the inevitable plasma sheath is molded close to the surface in contact with the plasma. Due to plasma sheath, the electric field is directed from plasma bulk towards the surface that accelerates the ions towards the surface, and then the effect of the sheath on electron and ion collection current to the CNT surface has been taken into account in the present example. The CNT considered in the present paper is SWCNT.

The calculations have been formed to investigate the dependence of the height and radius of the CNT on the plasma parameters (i.e., ion density of both type A and B ions and temperature and pressure) by simultaneous solution of Eqs. (1)–(12) at appropriate boundary conditions, viz., for CH_4 plasma, using values from Herrebout *et al.*,[21] boundary conditions $\tau = 0$, ion number density ($n_{iA0} = 0.6\ n_{e0}$) and $n_{iB0} = 0.4 n_{e0}$, neutral atom density ($n_{A0} = n_{B0} = 1 \times 10^{15}\ cm^{-3}$), electron number density($n_{e0} = 1.12 \times 10^{10}\ cm^{-3}$), electron temperature $T_{e0} = 1.15\,eV$, ion temperature $T_{i0} = 2100\,K$, neutral temperature $T_{n0} = 2000K$, mass of ion A(m_{iA}) = 15 amu and 14 amu (e.g., methyl (CH_3^+ or CH_2^+)), mass of ion B (m_{iB}) = 1amu, coefficient of recombination of electrons and ions ($\alpha_{A0} \approx \alpha_{B0}$) $= 1.12 \times 10^{-7} cm^3/s$, $\kappa = -1.2$ and density of Ni(ρ_P) $= 8.908\ g/cm^3$. Other parameters used in the calculation are substrate temperature (T_s) $= 500\,°C$, thermal energy barrier on the catalyst surface (δE_t) $= 1.3\,eV$, the energy barrier for bulk diffusion $E_b = 1.6\,eV$, energy due to thermal dissociation of methyl ions (δE_t) $= 300\,eV$, dissociation energy E_{dis} of C_2H_2 (Mehdipour *et al.*[10]) or CH_4 in our case $E_{dis} = 4.5\,eV$.

Fig. 1 sketches the schematic of the processes involved during the carbon nanotube growth on the catalyst-substrate surface in reactive plasma. It illustrates the various phenomena that occur during the CNT growth in plasma. The vignette represents all the participating species in the plasma, i.e., electrons, ions, neutral atoms, and the processes involved during the CNT growth.

Fig. 2 illustrates the time evolution of the height of the CNT for different ion density and temperature of type A (i.e., $n_{iA0} = 10^9\ cm^{-3}$ and $T_{i0} = 1800\,K$, $n_{iA0} = 5 \times 10^{10}\ cm^{-3}$ and $T_{i0} = 2000\,K$ and $n_{iA0} = 10^{11}\ cm^{-3}$ and $T_{i0} = 2100\,K$). Fig. 2 indicates that the height of the CNT increases as ion density

This article is copyrighted as indicated in the article. Reuse of AIP content is subject to the terms at: http://scitation.aip.org/termsconditions. Downloaded to IP: 14.139.251.100 On: Tue, 01 Jul 2014 06:02:09

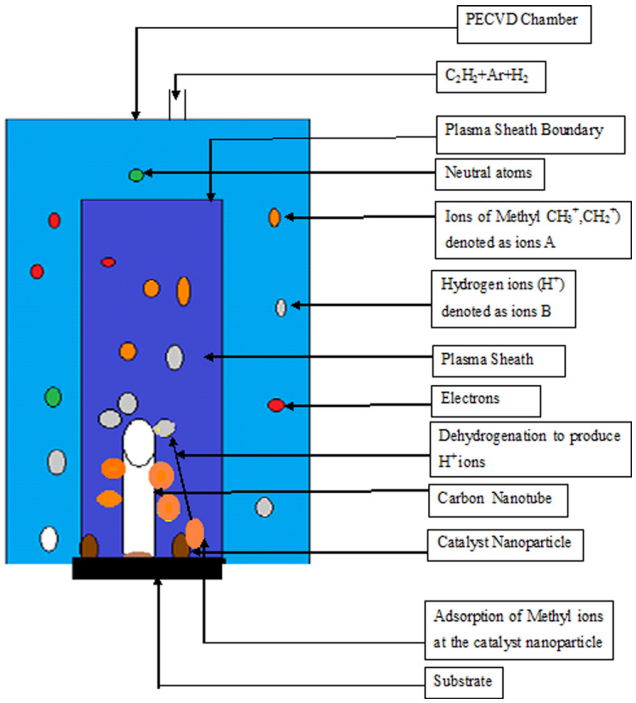

FIG. 1. Schematic of the processes involved during the carbon nanotube growth on the catalyst substrate surface in reactive plasma.

and temperature increases. This is imputable to the fact that as temperature T_{i0} and density n_{i0} increase, the plasma sheath thickness increases and ions gain more energy on communicating through the sheath, consequently, the energized ion diffusion to catalyst particle increase thereby giving to its peak. The similar pattern of variance of the height of the CNT with time in Fig. 2 has also been obtained by Futaba *et al.*[22] (cf. Fig. 2(a) of Futaba *et al.*[22]) and Loffler *et al.*[4] (cf. Fig. 4 of Loffler *et al.*[4]).The observations of Fig. 2 are in principle with the experimental observations of Aksak *et al.*[4]

Fig. 3 illustrates the time evolution of the radius of the spherical CNT tip for the different ion density and temperature of type B ions (i.e., to $n_{iB0} = 10^9\,cm^{-3}$ and $T_{i0} = 1800\,K$, $n_{iB0} = 5 \times 10^{10}\,cm^{-3}$ and $T_{i0} = 2000\,K$ and $n_{iB0} = 10^{11}\,cm^{-3}$ and $T_{i0} = 2100\,K$). Fig. 3 indicates that the radius of CNT

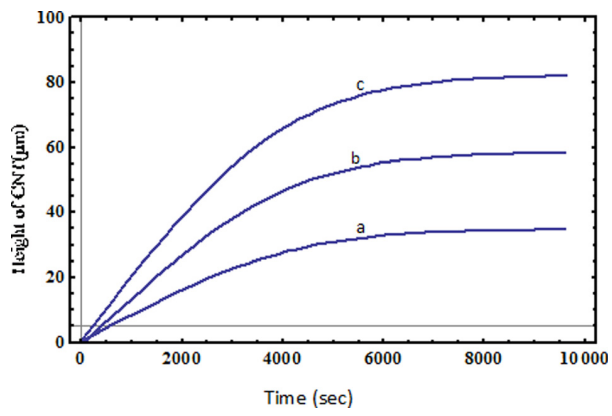

FIG. 2. Depicts the time evolution of the height of CNT for different ion density and temperature of type A (where a, b, and c correspond to $n_{iA0} = 10^9\,cm^{-3}$ and $T_{i0} = 1800\,K$, $n_{iA0} = 5 \times 10^{10}\,cm^{-3}$ and $T_{i0} = 2000\,K$ and $n_{iA0} = 10^{11}\,cm^{-3}$ and $T_{i0} = 2100\,K$). The other parameters are given in the text.

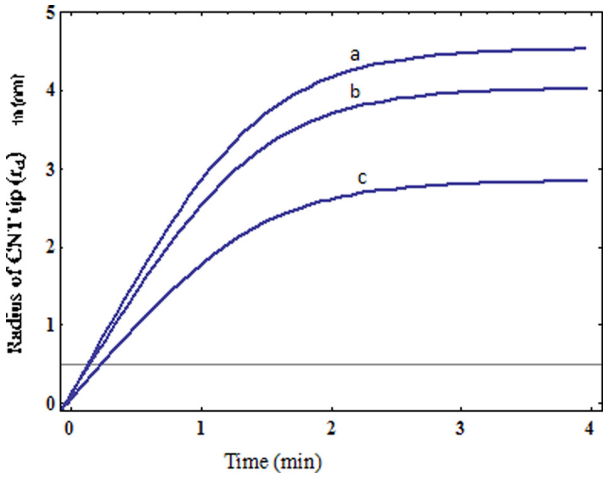

FIG. 3. Depicts the time evolution of the radius of the CNT tip for different ion density and temperature of type B (where a, b, and c correspond to $n_{iB0} = 10^9\,cm^{-3}$ and $T_{i0} = 1800\,K$, $n_{iB0} = 5 \times 10^{10}\,cm^{-3}$ and $T_{i0} = 2000\,K$ and $n_{iB0} = 10^{11}\,cm^{-3}$ and $T_{i0} = 2100\,K$). The other parameters are given in the text.

decreases as ion density and temperature of hydrogen ions increases. This is imputable to the fact that the tip of CNT is bombarded by incoming hydrogen ions, which etches up the tip of the CNT, and thus shortening the radius of the spherical CNT tip. At higher temperatures and density, energy is sufficient to dissociate methane gas into carbon and hydrogen ions, where carbon contributes to the length of CNTs, hydrogen effectively shapes the nanoparticle tip radius. The reason why we have not looked at the surface diffusion of hydrogen onto catalyst nanoparticle is that the activation energy for surface diffusion of hydrogen to Ni is greater than the activation energy in PECVD (~0.23 eV) (Hoffmann *et al.*[23]). The results of Fig. 3 comply with Denysenko *et al.*[8] and Mehdipour *et al.*[12]

Fig. 4 illustrates the time evolution of the height of CNT for different substrate bias U_s (e.g., $U_s = -50\,V$, $-100\,V$, and $-200\,V$). As the negative substrate bias is increased, more negative charge develops on the CNT (see Fig. 5 of the present paper) which in turn thickens the plasma sheath and therefore increases the diffusion and accretion of ions on CNT surface.

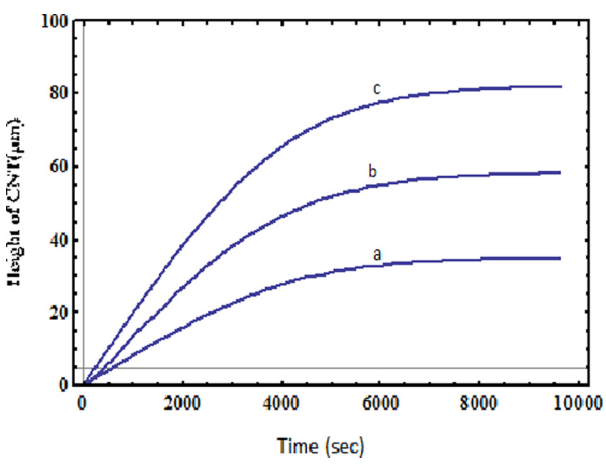

FIG. 4. Depicts the time evolution of the height of CNT for different substrate bias (where a, b, and c correspond to $U_s = -50\,V$, $-100\,V$, and $-200\,V$).

This article is copyrighted as indicated in the article. Reuse of AIP content is subject to the terms at: http://scitation.aip.org/termsconditions. Downloaded to IP: 14.139.251.100 On: Tue, 01 Jul 2014 06:02:09

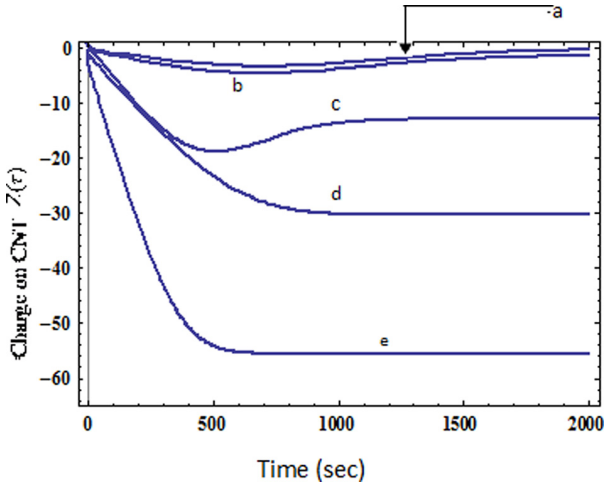

FIG. 5. Depicts the time evolution of charge on CNT for different substrate bias (where a, b, c, d, and e correspond to $U_s = -25$ V, -50 V, -100 V, -150 V, and -200 V).

Fig. 5 depicts the time evolution of charge on the CNT for different substrate bias (e.g., $U_s = -25$ V, -50 V, -100 V, -150 V, and -200 V). From Fig. 5, we see that the charge developed on the CNT increases with the substrate bias. The importance of charge variation effects on particles in plasma has also been discussed by Ostrikov *et al.*[25]

Fig. 6 illustrates the variation of the radius of catalyst particle with rf power (i.e., rf power = 50 W, 100 W, 150 W, and 200 W). From Fig. 6, it can be seen that as the rf power is increased the catalyst nanoparticle of smaller radii is observed. The fluctuation could be explained as with increasing plasma power the electric field in the plasma sheath increases, which in turn increases the ion bombardment to the catalyst particle and thereby etching up the catalyst particle. The increased plasma power dissociates the hydrocarbon gas in the plasma bulk rather than at the catalyst particle site. The above observation has been validated by the works of Choi *et al.*[2] (cf. Fig. 1(d) of Choi *et al.*[2]), Abdi *et al.*,[5] and Srivastava *et al.*[24]

As plasma treatments better the field emission characteristics,[12–14] from the present study, we can conclude

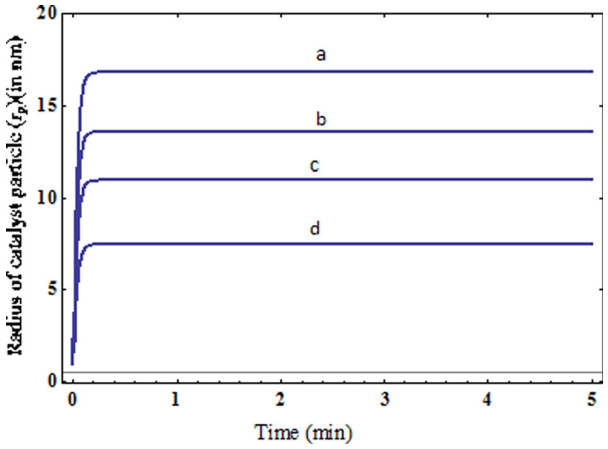

FIG. 6. Depicts the time evolution of the radius of catalyst particle for different rf plasma power (where a, b, c, and d correspond to rf power = 50 W, 100 W, 150 W, and 200 W).

that by suitably varying ion density and temperature, substrate bias, we can obtain more heighted and lesser radii of nanotubes, i.e., high aspect nanostructures. Hence, the results can be extended to better the field emission characteristics of CNTs.

IV. CONCLUSION

A theoretical model, including the charging rate of the CNT, kinetics of electron, ions and neutral atoms, the growth rate of the CNT because of diffusion and accretion of ions on catalyst nanoparticle inclusion of the subject of the plasma sheath is developed. It is described that the applied plasma power affects the radius of Ni catalyst nanoparticle inversely, which serves as the seed for nanotube growth. The issue of the ion density and temperature on the radius and height of the CNT has been examined. The effect of the substrate bias on the charge of CNT is also studied. Our work could serve as a tool for fabricating high aspect ratio nanotubes desirable for field emission devices.

[1]K. Ostrikov and S. Xu, *Plasma Aided Nanofabrication: From Plasma Sources to Nanoassembly* (Wiley-VCH, Weinheim, Germany, 2007).
[2]Y. C. Choi, Y. M. Shin, Y. H. Lee, B. S. Lee, G.-S. Park, W. B. Choi, N. S. Lee, and J. M. Kim, Appl. Phys. Lett. **76**, 2367 (2000).
[3]M. Aksak, S. Kir, and Y. Selamet, J. Optoelectron. Adv. Mater. Symposia **1**, 281 (2009).
[4]R. Loffler, M. Haffner, G. Visanescu, H. Weigand, X. Wang, D. Zhang, M. Fleischer, A. J. Meixner, J. Fortagh, and D. P. Kern, Carbon **49**, 4197 (2011).
[5]Y. Abdi, E. Arzi, and S. Mohajerzadeh, Eur. Phys. J. Appl. Phys. **44**, 149 (2008).
[6]H. Jin Cho, N. Lee, I. Jang, H. Soo Uh, and J. Pyo Hong, J. Korean Phys. Soc. **50**, 1848 (2007).
[7]S. K. Srivastava, V. D. Vankar, and V. Kumar, Nano-Micro Lett. **2**, 46 (2010).
[8]I. Denysenko, K. Ostrikov, M. Y. Yu, and N. A. Azarenkov, J. Appl. Phys. **102**, 074308 (2007).
[9]I. Levchenko, K. Ostrikov, J. Khachan, and S. V. Valdimirov, Phys. Plasmas **15**, 103501 (2008).
[10]H. Mehdipour, K. Ostrikov, and A. E. Rider, Nanotechnology **21**, 455605 (2010).
[11]K. Ostrikov, E. C. Neyts, and M. Meyyappan, Adv. Phys. **62**, 113 (2013).
[12]T. Feng, J. Zhang, and Q. Li, Physica E **36**, 28 (2007).
[13]S. F. Lee, Y. P. Chang, and L. Y. Lee, J. Mater. Sci. Mater. Electron **20**, 851 (2009).
[14]A. Tewari and S. C. Sharma, J. Plasma Phys. **79**, 939 (2013).
[15]V. I. Merkulov, D. H. Lowndes, Y. Y. Wei, G. Eres, and E. Voelkl, Appl. Phys. Lett. **76**, 3555 (2000).
[16]W. A. De Heer, A. Chatelain, and D. Ugarte, Science **270**, 1179 (1995).
[17]J. M. Kim, W. B. Choi, N. S. Lee, and J. E. Jung, Diamond Relat. Mater. **9**, 1184 (2000).
[18]L. Yukui, Z. Changchun, and L. Xinghui, Diamond Relat. Mater. **11**, 1845 (2002).
[19]M. A. Lieberman and A. J. Lichtenberg, *Principles of Plasma Discharges and Materials Processing* (Wiley Interscience Publication, USA, 1994).
[20]O. A. Louchev, C. Dussarrat, and Y. Sato, J. Appl. Phys. **86**, 1736 (1999).
[21]D. Herrebout, A. Bogaerts, M. Yan, and R. Gijbels, J. Appl. Phys. **90**, 570 (2001).
[22]D. N. Futaba, K. Hata, T. Yamada, K. Mizuno, M. Yumura, and S. Iijima, Phys. Rev. Lett. **95**, 056104 (2005).
[23]S. Hofmann, C. Ducati, J. Robertson, and B. Kleinsorge, Appl. Phys. Lett. **83**, 135 (2003).
[24]S. K. Srivastava, A. K. Shukla, V. D. Vankar, and V. Kumar, Thin Solid Films **492**, 124 (2005).
[25]K. N. Ostrikov, M. Y. Yu, S. V. Vladimirov, and O. Ishihara, Phys. Plasmas **6**, 737 (1999).
[26]I. Denysenko and K. Ostrikov, J. Phys. D: Appl. Phys. **42**, 015208 (2009).

This article is copyrighted as indicated in the article. Reuse of AIP content is subject to the terms at: http://scitation.aip.org/termsconditions. Downloaded to IP: 14.139.251.100 On: Tue, 01 Jul 2014 06:02:09

Multi-Response Optimization of Manual Material Handling Tasks through Utility Concept

Jaswinder Singh, P. Kalra and R.S. Walia

Abstract--- *In this work six Manual Material Handling (MMH) task parameters such as box size, Body Mass Index (BMI), frequency of lift, load lifted, vertical distance of lift, and asymmetric angle were chosen for multi response optimization of task parameters. Most of the existing approaches for multi response optimization of process parameters focus upon the subjective and practical knowledge available about the process. This is particularly true in case of Taguchi based optimization. however, this approach introduces some uncertainties and confusions in overall decision-making process. keeping in view these limitations, an approach based on a utility theory and Taguchi quality loss function (TQLF) has been applied to MMH tasks for simultaneous optimization of more than one response characteristics.*

Keywords--- *MMH Tasks, Multi Response Optimization, Taguchi Approach, Utility Concept, Heart Rate and Oxygen Consumption*

I. INTRODUCTION

MANUAL Material Handling (MMH) includes a wide variety of activities such as loading and unloading boxes, removing materials from a conveyor belt, stacking items in a warehouse, etc. As a result, workers may suffer from musculoskeletal disorders (MSDs). Various short and long term health effects are attributed due to MMH tasks. MMH tasks are very common in workplaces. MMH tasks are the main cause of severe injuries all over the world. More than a quarter of all injuries related to industrial work are directly associated with MMH activities. The cost associated with these injuries is very high. In order to control these occupational injuries various research and design guidelines have been proposed [1-3]. There are many physiological parameters (Heart rate, Oxygen consumption, Blood pressure etc.) which affect the MMH tasks. To reduce the occupational injuries due to MMH tasks performed at high frequencies, the MMH task parameters should be selected carefully and then optimized. In the MMH task scenario, it is most vital to optimize the physiological parameters of task to exploit its full utility. Practically, it is seen that one particular setting of input parameters for a response characteristics may not be suitable for other characteristics of MMH tasks. In most of the MMH tasks, more than one quality characteristics has to be considered for optimization of process parameters making it necessary that several response characteristics have to be simultaneously optimized. Therefore, in the situations involving many measurable response characteristics of a product/ process, an optimization strategy is required that can provide a unified criterion to represent the overall optimal setting of process parameters with respect to all the responses. These types of optimization problems need to be handled by multi-response optimization techniques. In the past, the applications of Taguchi method and Response Surface Methodology (RSM) have mainly dealt with single response problems [4-7] and only very few applications are reported for multi-response problems [8-9]. Shiau solved the Multi-response problem by assigning the weights to S/N ratio of each quality characteristic and than summing up the weighted S/N ratios for the measurement of overall performance of a process [10]. Tai et. al. used empirical loss functions for evaluating multi response problem by involving six parameters and nine responses for the surface mount process [11]. Singh studied the optimization of the quality characteristics of Magnetically Assisted Abrasive Flow Machining (MAAFM) process by using multi-response optimization through utility concept and Taguchi method [12]. Walia *et al.* studied Multi-response optimization of centrifugal Force Assisted Abrasive Flow Machining (CFAAFM) process through Taguchi method and Utility Concept [13]. Goyal *et al.* studied optimization of Low- pressure cold sprayed coatings process parameter using Taguchi multi-response [14]. Singh *et al.* studied the parametric optimization of Hybrid Electric Discharge Machining process with continuous and discontinuous ultrasonic vibrations on work piece [15]. Based on the foregoing discussions, in this paper, Taguchi method is briefly reviewed for the multi-response optimization. The multi-response optimization of the response parameters of MMH tasks is then presented by using the experimental data. Optimization models have been developed by combination of the Taguchi Method and the Utility concept. Two response parameters i.e., Heart rate, Oxygen consumption has been taken in this study for Multi response optimization.

II. WORKERS DETAILS

Body Mass Index (BMI) is used to indicate if an individual is underweight, normal or overweight. WHO (2003) categorized persons in three types namely underweight, normal weight and overweight based on their BMI [16]. A normal weight person BMI score is between 18.5 and 25 kg/m^2. A score below 18.5 indicates that a person is

Jaswinder Singh, Assistant Professor, Department of Production Engineering, PEC University of Technology, Chandigarh, India. E-mail:jaswindersingh_11@rediffmail.com

P. Kalra, Professor, Department of Production Engineering, PEC University of Technology, Chandigarh, India

R .S. Walia, Associate Professor, Department of Mechanical and Production Engineering, Delhi Technological University, Delhi, India

DOI : 10.9756/BIJIEMS.6034

underweight; a value above 25 indicates that a person is overweight. Eighteen male workers with different BMI and having 10 years of experience were selected for this laboratory study. An anthropometric kit was used to measure anthropometrical data. Height of workers was measured without shoes using an anthropometer. Body weight was measured without shoes using a portable digital scale. The BMI was calculated by dividing body mass of a person in kilogram to square of his height in meter. The anthropometric details of the workers in shown in Table 1.

Table 1: Anthropometric details of the Workers

Parameter of workers	Underweight workers BMI (kg/m^2)< 18 (Total number of workers=6)		Normal weight workers BMI (kg/m^2)=18-24.9 (Total number of workers=6)		Over weight workers BMI (kg/m^2)>24.9 (Total number of workers=6)	
	Mean	SD	Mean	SD	Mean	SD
Age (years)	26.7	4.23	27.17	2.86	26.5	3.94
Weight (kg)	45.5	5	55.7	4.81	67.27	3.28
Stature height (cm)	165.13	9.26	162.22	6.49	158.47	3.34
BMI (Kg/m^2)	16.66	0.48	21.23	2.30	26.84	0.86

III. Measuring Equipment Details

Cosmed Fitmate Pro equipment was used to measure the Heart rate and the Oxygen consumption responses. The equipment gives two response curves one for Oxygen consumption and another for Heart rate simultaneously on same time frame. For getting the Oxygen consumption readings a face mask was attached to the face of worker. A head cap with connectors was used for properly securing of the mask to a fixed position on worker's face during experiments. The measurement is made through a wired turbine one end of which is connected to the mask and other end connected to the equipment. For getting Heart rate readings a Polar belt was put around the chest of the worker. For transferring Heart rate signals to equipment a probe was attached near the polar belt with the help of clamp provided on the probe and other end of probe was attached to equipment through a wire. Time of experiment was noted with a stop watch.

IV. Multi-Response Optimization Through Utility Concept and Taguchi Method of MMH Task Parameters

The experiments were designed using Taguchi fractional factorial technique to study the effect of six factors: box size, BMI, frequency of lift, load lifted, vertical distance of lift, and asymmetric angle on response parameters such as oxygen uptake and Heart rate of workers. Taguchi L18 orthogonal array (OA) has been adopted for conducting the experiments [17-18]. Factors like horizontal distance, origin of lifting, room temperature were kept constant during the experimental study. The ranges of the selected MMH task parameters were based on the pilot study in laboratory and observation of the manual lifting tasks in industries. For representing each BMI level six workers per BMI level were taken, so total of eighteen workers participated in this work.

Table 2: MMH task Parameters at Different Levels

S. No	Symbol	Factors	Levels			Units
			Level-1	Level-2	Level-3	
1	A	Box size	Small	Large	-------	cm^3
2	B	BMI	Under weight	Normal weight	Over weight	Kg/m^2
3	C	Frequency of lift	2	4	6	lifts/min
4	D	Load lifted	15	19	23	kg
5	E	Vertical distance	Knee	Waist	Shoulder	cm
6	F	Asymmetric angle	0	30	60	deg
Horizontal distance: 25cm, Environment conditions : 32 ± 2^0C						

Lifting frequency was set at three levels of 2,4 and 6 lifts/min. Workers were lifting the weight from 14 to 20 kg in industries. Therefore weight is taken at three levels 15, 19 and 23kg. 23 Kg of higher load limit is set because it is the maximum load allowed to be lifted by NIOSH 1991. Vertical distance was varied at three levels which were set at knee, waist and shoulder respectively of the workers. Two wooden boxes of small and large size were used for the experiments. The dimension of small box is 60x40x17.5 cm^3 and that of large box is 60x40x27.5 cm^3. These box sizes are used in the industries for manual lifting tasks. Asymmetric angle was varied at three levels mainly 0, 30 and 60 degree respectively. Horizontal distance was fixed at 25cm for all experiments. All the experiments were performed at room temperature of 32 ± 2^0C. In this research work Taguchi's mixed level design was selected as it was decided to keep two levels of box size. The remaining five factors were studied at three levels. The selected number of factors and their levels are given in Table 2. Two level factor has 1 DOF and each of three level factors have 2 DOF, i.e., the total DOF required will be 11(=1×1+5×2).The most appropriate orthogonal array in this case is Taguchi L18 OA with (18-1) DOF. The unassigned columns were treated as error. Excel sheet was used for analyzing the results. To reduce error for each trial, experiments were repeated three times. All the experiments were conducted on experimental setup design and developed in Human Engineering laboratory of PEC University of Technology, Chandigarh, India. Experimental setup was made in such a way that it could be adjusted to various heights. To determine which factors significantly affect the response characteristics, main effect for raw data and S/N data had been calculated. In addition, plots of the various factors were developed to show significance. For the both Oxygen consumption and Heart rate lower the better response characteristic were taken for calculation of S/N data.

A mixture of sand and pebbles were used as the load material for the experiments. Free style lifting technique was used during experiments. Lifting of the boxes was done as per the experiment array by the worker on the experimental setup while lowering of the boxes was done by volunteers. In each of the trial conditions and for every replication, Heart rate and

the oxygen uptake were measured. The effect of selected MMH task parameters was studied on the following response characteristics:

- Heart rate (HR)
- Oxygen consumption (VO_2)

Heart rate and Oxygen consumption are "smaller the better" type of quality characteristic. A simplified multi-criterion methodology based on Taguchi's approach and utility concept (given below) is used to achieve the objective of this study. A product or a process is normally evaluated on the basis of certain number of quality characteristics, sometimes conflicting in nature. Therefore, a combined measure is necessary to gauge its overall performance, which must take into account the relative contribution of all the quality characteristics. In the following, a methodology based upon Utility concept and Taguchi method is developed for determining the optimal settings of process or parameters for multi-response/ multi-characteristics process or product. The multi-response optimization of quality characteristic of MMH tasks has been carried out by using this methodology given in this section.

A. Utility Concept

Utility can be defined as the usefulness of a product or a process in reference to the expectations of the users. The overall usefulness of a process/product can be represented by a unified index termed as Utility which is the sum of the individual utilities of various quality characteristics of the process/product. The methodological basis for Utility approach is to transform the estimated response of each quality characteristic into a common index.

If Xi is the measure of effectiveness of an attribute (or quality characteristic) i and there are n attributes evaluating the outcome space, than the joint Utility function can be expressed as [19]:

$$U(X_1, X_2, \ldots X_n) = f(U_1(X_1), U_2(X_2) \ldots U_n(X_n)) \quad (1)$$

where Ui(Xi) is the utility of the ith attribute.

The overall Utility function is the sum of individual utilities if the attributes are independent, and is given as follows:

$$U(X_1, X_2, \ldots X_n) = \sum_{i=1}^{n} U_i(X_i) \quad (2)$$

The attributes may be assigned weights depending upon the relative importance or priorities of the characteristics. The overall utility function after assigning weights to the attributes can be expressed as:

$$U(X_1, X_2, \ldots X_n) = \sum_{i=1}^{n} W_i U_i(X_i) \quad (3)$$

where Wi is the weight assigned to the attribute i. The sum of the weights for all the attributes must be equal to 1.

B. Determination of Utility Value

A preference scale for each quality characteristic is constructed for determining its utility value. Two arbitrary numerical values (preference number) 0 and 9 are assigned to the just acceptable and the best value of the quality characteristic respectively. The preference number (Pi) can be expressed on a logarithmic scale as follow [20-21]:

$$P_i = A \times \log\left(\frac{X_i}{X_i'}\right) \quad (4)$$

Where, Xi = value of any quality characteristic or attribute i

X_i' = just acceptable value of quality characteristic or attribute i

A = constant

The value of A can be found by the condition that if Xi = X* (where X* is the optimal or best value), then Pi = 9

Therefore,

$$A = \frac{9}{\log \frac{X^*}{X_i'}}$$

The overall utility can be calculated as follows:

$$U = \sum_{i=1}^{n} W_i P_i \quad (5)$$

Subject to the condition: $\sum_{i=1}^{n} W_i = 1$

Among various quality characteristics type viz. smaller the better, higher the better, and nominal the better suggested by Taguchi, the Utility function would be higher the better type. Therefore, if the Utility function is maximized, the quality characteristics considered for its evaluation will automatically be optimized (maximized or minimized as the case may be). The stepwise procedure for carrying out multi-response optimization with Utility concept and Taguchi method is illustrated in a Table 3.

Table 3: Methodology for Multi-Response Optimization by Utility Concept and Taguchi method

Step 1	Using Taguchi Parametric design approach, determined the optimal values and setting of each of response characteristic of VO_2 and HR, for the manual lifting task responses.
Step 2	Constructed a preference scale for each response characteristic, based on their optimal values and minimum acceptable level (Equation 5.4).
Step 3	Assigned weights (W_i) to the selected quality characteristics based upon the importance, experience or any other constraint, keeping in view that the total sum of weights is equal to 1.
Step 4	Determined the overall utility values corresponding to each experimental trial conditions (based on L_{18} OA for present investigation, Equation 5).
Step 5	Used these values and the calculated S/N ratio as responses for the trial conditions of the selected L_{18} OA. S/N ratio of higher-the-better type is selected as the utility is a higher-the-better type characteristic [17].
Step 6	Analyse the results using the Taguchi Method.
Step 7	Find the optimal settings of manual lifting task parameters for optimal utility based on the analysis performed in step 6.
Step 8	Predicted the values of different response characteristics based upon the optimal significant parameters determined by the previous step.
Step 9	Performed the confirmation experiments at the

	optimal settings to verify the optimal results.

V. Multi-Response Optimization for MMH Task Response Parameters

To obtain the optimal settings of the process parameters of MMH tasks for predicting the optimal values of combined responses, both the quality characteristics (HR and VO_2) have been included in utility response.

A. Heart Rate (HR) and Oxygen Consumption (VO2)

Taguchi L18 orthogonal array (OA) has been adopted for conducting the experiments [17-18]. Box size (A), BMI (B), Frequency of lift (C), Load lifted (D), Vertical distance (E) and Asymmetric angle (F) were selected as input parameters. Response parameters (quality characteristics) were Heart rate (HR) and Oxygen consumption (VO_2), when they are optimized individually, the summary of results is produced in Table 4.

Table 4: Optimal Setting and Values of Manual Lifting Task Parameters (Individual Quality Characteristic Optimization)

Response characteristics	Optimal level of MMH task parameters	Significant MMH task parameters	Predicted optimal value of quality characteristics
Oxygen consumption	A1,B2,C1,D1,E1	A, B, C, D, E	6.36 ml/kg/min
Heart rate	A1,B2,C1,D1,E1	A, B, C, D, E	91.50 beats/min

Following is the stepwise procedure for transforming experimental data into utility data.

B. Construction of Preference Scales

i. Preference Scale for HR (Heart Rate)

- X* = Optimal value of HR = 91.51 beats/min (refer Table 4)
- $X_i^{'}$ = Just acceptable value of HR = 146 (All the observed values of HR are less than 146)
- Following equation is obtained from equation 4:

$$P_{HR} = -44.36 \times \log\left(\frac{X_{HR}}{146}\right) \quad (6)$$

ii. Preference Scale for VO2 (Oxygen Consumption)

- X* = Optimal value of VO2 = 6.36 ml/kg/min (refer Table 4)
- $X_i^{'}$ = Just acceptable value of VO2 = 21 (All the observed values of VO2 are less than 21)
- Following equation is obtained from equation 4:

$$P_{VO_2} = -17.34 \times \log\left(\frac{X_{VO_2}}{21}\right) \quad (7)$$

C. Calculation of Utility Value

Equal weights (1/2 each) have been assigned to the selected quality characteristics assuming all the quality characteristics, are equally important. However, these weights can be varied depending upon the case or user requirements, if any.

The following relation was used to calculate the utility function based upon the experimental trials:

$$U(n,r) = P_{HR}(n,r) \times W_{HR} + P_{VO_2}(n,r) \times W_{VO_2} \quad (8)$$

Where n is the trial number (n = 1,2,3,….,18) and r is the repetition number (r = 1,2,3). The calculated Utility values are shown in Table 5.

Table 5: Calculated Utility Data Based on Responses Heart Rate and Oxygen Consumption

Trial Number	Utility Values			S/N Ratio (dB)
	R1	R2	R3	
1	8.19	7.65	7.76	-17.92
2	4.09	4.75	4.46	-12.95
3	1.15	1.14	1.32	-1.64
4	7.78	7.27	7.70	-17.60
5	3.73	3.49	3.67	-11.21
6	4.24	4.39	4.27	-12.67
7	5.12	4.47	4.42	-13.40
8	2.17	1.97	1.98	-6.22
9	1.18	1.16	1.17	-1.36
10	4.01	4.12	3.79	-11.99
11	4.38	4.66	4.56	-13.12
12	2.30	1.91	2.23	-6.66
13	5.40	5.22	5.28	-14.49
14	4.47	4.03	4.05	-12.44
15	3.19	3.17	3.12	-9.99
16	2.71	2.77	2.65	-8.66
17	1.05	0.99	1.12	-0.45
18	1.10	1.08	0.81	-0.03
R1, R2, R3 = repetitions of experiments against each of the trial conditions				

D. Analysis of Utility Data for Optimal Setting of MMH Task Parameters

The main effects in terms of Utility values for S/N ratio and Raw data (Tables 6 and 7) are plotted in Figure 1. It can be observed from Figure 2 that the 1st Box size (A1), 2nd level of BMI (B2), 1st level of Frequency of lift (C1), 1st level of Load lifted (D1), 1st level of Vertical distance (E1) and 1st level of Asymmetric angle (F1) are expected to yield a maximum values of the utility and S/N ratio within the experimental space.

Table 6: Main Effects of Heart Rate and Oxygen Consumption (S/N Ratio)

LEVEL	Box size	BMI	Frequency of lift	Load lifted	Vertical distance	Asymmetric angle
L1	-10.55	-10.71	-14.01	-10.07	-11.60	-9.73
L2	-8.65	-13.07	-9.40	-9.79	-10.35	-9.40
L3	--	-5.02	-5.39	-8.94	-6.85	-9.67
L2-L1	1.90	-2.35	4.61	0.28	1.25	0.34
L3-L2	--	8.05	4.01	0.85	3.49	-0.27
L1, L2 and L3 represent levels 1, 2 and 3 respectively of parameters. L2-L1 is the average main effect when the corresponding parameter changes from level 1 to level 2. L3-L2 is the average main effect when the corresponding parameter changes from level 2 to level 3.						

Table 7: Main Effects of Heart rate and Oxygen Consumption (Raw Data)

LEVEL	Box size	BMI	Frequency of lift	Load lifted	Vertical distance	Asymmetric angle
L1	4.10	4.03	5.35	4.23	4.42	3.78
L2	3.12	4.69	3.31	3.53	3.68	3.72
L3	--	2.11	2.16	3.07	2.72	3.32
L2-L1	-0.98	0.67	-2.04	-0.70	-0.74	-0.06
L3-L2	--	-2.59	-1.15	-0.46	-0.96	-0.41
L1, L2 and L3 represent levels 1, 2 and 3 respectively of parameters. L2-L1 is the average main effect when the corresponding parameter changes from level 1 to level 2. L3-L2 is the average main effect when the corresponding parameter changes from level 2 to level 3.						

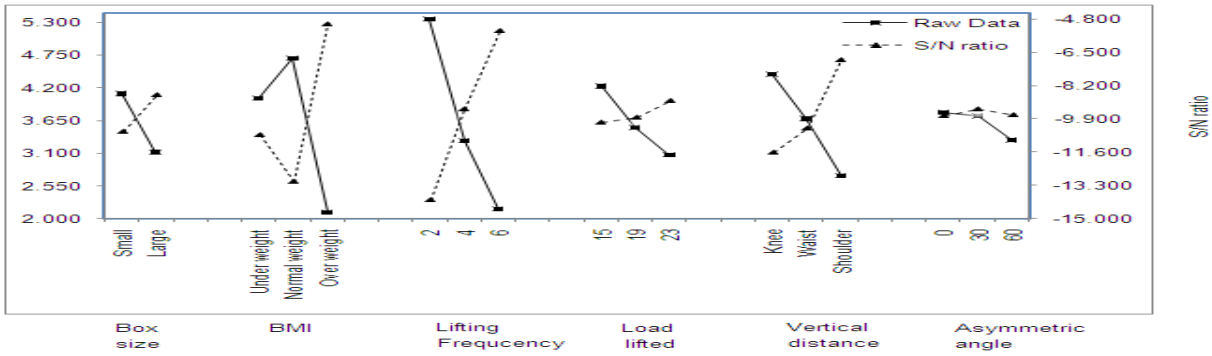

Figure 1: The Main Effects in Terms of Utility Values for S/N ratio and Raw Data

The pooled version of ANOVA of utility values for Raw data and S/N ratio are given in Tables 8 and 9 respectively. It can be noticed from Table 8 that all the input parameters has a significant effect (at 95% confidence level) on the Raw data of utility function. On the other hand, from Table 9 BMI and frequency of lift has significant effect on the S/N ratio of utility function. So, other insignificant parameters for S/N ratio can be taken as economy factor.

Table 8: Pooled ANOVA (Raw data) _ Heart Rate and Oxygen Consumption

SOURCE	SS	DOF	V	F-Ratio	SS'	P %
Box size	13.04	1	13.04	275.29*	12.99	6.06
BMI	64.92	2	32.46	685.17*	64.83	30.22
Frequency of lift	93.85	2	46.92	990.48*	93.75	43.70
Load lifted	12.21	2	6.11	128.91*	12.12	5.65
Vertical distance	26.21	2	13.10	276.60*	26.11	12.17
Asymmetric angle	2.32	2	1.16	24.52*	2.23	1.04
Error	1.99	42	0.05	--	2.51	1.17
Total	214.55	53	--	--	214.5469	100
*Significant at 95% confidence level, F_{Table} (Box size);4.07, F_{Table} (Others);3.22; SS: Sum of squares; DOF: Degree of Freedom; V: Variance; SS': Pure Sum of Squares						

Table 9: Pooled ANOVA (S/N ratio) _ Heart Rate and Oxygen Consumption

SOURCE	SS	DOF	V	F-Ratio	SS'	P %
Box size	16.26	1	16.26	3.65	--	--
BMI	205.35	2	102.68	23.07*	196.45	35.80
Frequency of lift	223.23	2	111.62	25.07*	214.33	39.06
Load lifted	4.20	2	2.10	0.47	--	--
Vertical distance	72.54	2	36.27	8.15*	63.64	11.60
Asymmetric angle	0.39	2	0.19	0.04	--	--
Error	26.71	6	4.45	--	74.27	13.54
Total	548.69	17	--	--	548.69	100
*Significant at 95% confidence level, F_{Table} (Box size);5.99, F_{Table} (Others);5.14; SS: Sum of squares; DOF: Degree of Freedom; V: Variance; SS': Pure Sum of Squares						

E. Optimal Values of Quality Characteristics (Predicted Means)

The average values of all the response characteristics at the optimum levels of significant parameters with respect to Utility function are recorded in Table 10.

The optimal values of the predicted means (μ) of different response characteristics can be obtained from the following equation:

$$\mu = A1 + B2 + C1 + D1 + E1 + F1 - 5T \quad (9)$$

where, A1-First level of Box size, B2- Second level of BMI, C1- First level of Frequency, D1- First level of Load lifted, E1- First level of Vertical distance and F1- First level of Asymmetric angle

The 95% confidence interval of confirmation experiments (CI_{CE}) can be computed [Roy (1990)] by using the following equation:

$$CI_{CE} = \sqrt{F_{\alpha}(1, f_e) V_e \left[\frac{1}{n_{eff}} + \frac{1}{R}\right]} \quad (10)$$

where, $F_{\alpha}(1, f_e)$ = The F-ratio at the confidence level of (1-α) against DOF 1 and error degree of freedom f_e., R = Sample size for conformation experiments, V_e = Error variance, $n_{eff} = \frac{N}{1+DOF}$, N= total number of trials, and DOF= Total degrees of freedom associated in the estimate of mean response.

i. For Heat Rate (HR)

- $\mu_{HR} = A1 + B2 + C1 + D1 + E1 + F1 - 5T_{HR} = 90.95$ where A1 = 119.71, B2 = 114.34, C1 = 111.56, D1= 119.61, E1 = 115.54, F1 = 121.75 (Table 10):

Table 10: Average Values of Various Responses at Optimal Levels

Levels	Heart rate (beats/min)	Oxygen consumption (ml/kg/min)
A1	119.71	12.56
B2	114.34	11.59
C1	111.56	10.54
D1	119.61	12.44
E1	115.54	12.47
F1	121.75	12.97
Note:The above average values are taken from experimental Data		

- T_{HR} = 122.31

The following values have been obtained by the ANOVA:

- N = 54, fe = 42; ve = 8.92, neff = 4.5, R= 3, F0.05 (1, 42) = 4.0764
- From equation 10, $CI_{CE} = \pm 4.49$
- The predicted optimal range (for conformation runs of three experiments) for HR is given by
- CI_{CE}: 86.46< μHR <95.44

ii. *For Oxygen Consumption (VO2)*

- $\mu_{VO_2} = A1 + B2 + C1 + D1 + E1 + F1 - 5T_{VO_2} = 6.01$ where A1 = 12.56, B3 = 11.59, C2 = 10.54, D2= 12.44, E3 = 12.47, F3 = 12.97 (Table 10):
- $T_{vo2 = 13.31}$
- The following values have been obtained by the ANOVA:
- N = 54, f_e = 42; v_e = 0.80, n_{eff} = 4.5, R= 3, $F_{0.05}$ (1, 42) = 4.0764
- From equation 10, $CI_{CE} = \pm 1.34$
- The predicted optimal range (for conformation runs of three experiments) for VO_2 is given by
- CI_{CE}:4.67< μ_{VO2}<7.35

VI. Confirmation Experiment

For confirmation of experimental results, three experiments were performed at optimal settings as suggested by Taguchi analysis of Utility data. The average Heart rate and Oxygen consumption were found to be 93.21bpm and 7.23ml/kg/min, which fall within the 95% CI_{CE} of the optimal range of the respective response characteristic.

VII. Conclusion

A simplified model based on the Taguchi method and Utility concept was used to analyze the multi response optimization of MMH tasks. Following conclusions can be drawn from this study:

- A simplified model based on Taguchi's approach and utility concept is used to determine the optimal setting of the MMH tasks parameters for multi-characteristics. The model is used to predict an optimal setting of the MMH tasks parameters to achieve the optimal quality characteristics (Heart rate and Oxygen consumption).

- All the input parameters significantly improve the Utility function comprising of two quality characteristics (Heart rate and Oxygen consumption).

REFERENCES

[1] National Institute of Occupational Safety and Health, NIOSH, "Work practices guide for manual lifting", NIOSH Technical Report No. 81 – 122, 1981.

[2] T.R. Waters, A.V. Putz, A. Garg, L.J Fine, "Revised NIOSH equation for the design and evaluation of manual lifting tasks", Ergonomics, vol. 36, pp. 749 – 776, 1993.

[3] T.R. Waters, A.V. Putz, A. Garg, "Application Manual for the Revised NIOSH Lifting Equation", National Institute for Occupational Safety and Health, Cincinnati, 1994.

[4] R. Creese, P. Kumar, "Effect of fly ash (as an additive to green sand) on the surface roughness of Al-7%Si alloy castings using Taguchi technique", AFS Transations, USA, 2001.

[5] P. Kumar, P.B. Barua, J.L. Gaindher, "Quality of V-process method through the Taguchi technique", Quality and Reliability Engineering International, vol. 12, pp. 421 – 427,1996.

[6] P. Kumar, R. Creese, "Effect of Zircon sand on surface finish of Al-7% Si alloy V-process castings", AFS Transactions, USA, pp. 95 – 98, 1999.

[7] H.T. Lee, J.P. Yur, "Characteristic analysis of EDMed surfaces using Taguchi approach", Materials and Manufacturing Processes, vol. 15 (6), pp. 781-806, 2000.

[8] J. Antony, "Multi-response optimization in industrial experiments using Taguchi quality loss function and principle component analysis", Quality and Reliability Engineering International, vol. 16, 3 – 8, 2000.

[9] C.T. Su, L.I. Tong, "Optimizing multi-response problems in the Taguchi method by fuzzy multiple attribute decision making", Quality and Reliability Engineering International, vol. 13, pp. 25 – 34, 1997.

[10] G.H. Shiau, "A study of the sintering properties of iron ores using the Taguchi's parameter design", Journal of Chinese Statistical Association vol. 28, pp. 253–275, 1990.

[11] C.Y. Tai, T.S. Chen, M.C. Wu, "An enhancement of Taguchi method for optimizing SMT processes", Journal of Electronics Manufacturing vol. 2, pp. 91–100, 1992.

[12] S. Singh, "Studies in metal finishing with magnetically assisted abrasive flow machining", PhD thesis IIT Roorkee, 2002.

[13] R.S. Walia, H.S. Shan, P. Kumar, "Multi-response optimization of centrifugal force assisted abrasive flow machining (CFAAFM) process through Taguchi method and Utility Concept", Journal of Materials and Manufacturing Processes, vol. 21, pp. 907 – 914, 2006.

[14] T. Goyal, R.S. Walia, T.S. Sidhu, "Low- pressure cold sprayed coatings process parameter optimization using Taguchi multi-response", International Journal of Surface Engineering and Materials Technology, vol. 1, pp. 5-11, 2011.

[15] J. Singh, P.S. Satsangi, R.S. Walia, V.P. Singh, "Parametric Optimization Of Hybrid Electric Discharge Machining Process With Continuous And Discontinuous Ultrasonic Vibrations On Workpiece", International Journal of Materials Science and Engineering, vol. 2(1-2), pp. 47 – 53, 2011.

[16] WHO, "Diet, nutrition and the prevention of chronic diseases", WHO technical report series 916, World Health Organization, Geneva, 2003.

[17] P.J. Ross, "Taguchi Techniques for quality engineering," McGraw Hill, New York, 1996.

[18] D. Montgomery, "Design and analysis of experiments," John Willey and Sons, New York, 2001.

[19] B. W. Derek, "Analysis for Optimal Decisions", New York, John Wiley and Sons, pp. 275, 1982.

[20] V. Gupta, P. N. Murthy, "An introduction to Engineering Design Methods", Tata McGraw Hill, New Delhi, pp. 78 – 98, 1980.

[21] P. Kumar, P.B. Barua, J.L. Gaindhar, "Quality optimization (Multi-Characteristics) through Taguchi Technique and Utility Concept", Quality and Reliability Engineering International, vol. 16, pp. 475 – 485, 2000.

First A. Jaswinder Singh is working as Assistant Professor in the Production and Industrial Engineering department of PEC University of Technology, Chandigarh, India. He received BE Degree from BBSEC Engineering College, Fathegarh sahib and ME Degree from PEC University of Technology, Chandigarh, India in the year 2002 and 2010, respectively. He has supervised several MTech Thesis. He has currently submitted his PhD in the Department of Production and Industrial Engineering at PEC, Chandigarh. His research interests include Ergonomics, CAD/CAM and product design. He has published/accepted for publication several papers in Journal Conference Proceedings.

Second B. P. Kalra is working as Professor in the Production and Industrial Engineering department of PEC University of Technology, Chandigarh, India. He received BE Degree in from PEC University of Technology, Chandigarh, India, and MS from Memorial University Canada in the year 1987 and 1990 respectively. He received PhD from Punjab University, Chandigarh, India in the year 2005. He has supervised several PhD and MTech Thesis. His area is in the field is Ergonomics, CAD/CAM, FEM, product design and Robotics. He has published/accepted for publication several papers in Journal/Conference Proceedings.

Third C. R S Walia is working as Associate Professor in the Mechanical and Production Engineering Department of Delhi College of Engineering, Delhi, India. He received BE Degree from GND Engineering College, Ludhiana and ME Degree with Honours from Thapar Institute of Engineering and Technology, Patiala and PhD from IIT Roorkee India in the year 2000, 2002 and 2006 respectively. He has supervised several PhD and MTech Thesis. His research interests include advance manufacturing process, work system design and quality engineering. He has published/accepted for publication several papers in Journal/Conference Proceedings.

Hasan et al. SpringerPlus 2014, 3:275
http://www.springerplus.com/content/3/1/275

SpringerPlus
a SpringerOpen Journal

CASE STUDY Open Access

Optimization of CCGT power plant and performance analysis using MATLAB/Simulink with actual operational data

Naimul Hasan[1], Jitendra Nath Rai[2,3*] and Bharat Bhushan Arora[2,3]

Abstract

In the Modern scenario, the naturally available resources for power generation are being depleted at an alarming rate; *firstly* due to wastage of power at consumer end, *secondly* due to inefficiency of various power system components. A Combined Cycle Gas Turbine (CCGT) integrates two cycles- Brayton cycle (Gas Turbine) and Rankine cycle (Steam Turbine) with the objective of increasing overall plant efficiency. This is accomplished by utilising the exhaust of Gas Turbine through a waste-heat recovery boiler to run a Steam Turbine. The efficiency of a gas turbine which ranges from 28% to 33% can hence be raised to about 60% by recovering some of the low grade thermal energy from the exhaust gas for steam turbine process. This paper is a study for the modelling of CCGT and comparing it with actual operational data. The performance model for CCGT plant was developed in MATLAB/*Simulink*.

Keywords: Combined cycle; Optimization; Model; Gas turbine; Efficiency

Introduction

With the advent of technological advancement, the dependency of human race on electricity has increased manifolds and keeping in mind the uncontrollable power requirement in almost every minute human activity methods are being taken up to exploit the present natural resources like coal, solar etc. Moreover, necessary up-gradation can be done so as to generate more power than the plant used to do in its normal running time.

A CCGT is one such advancement in the field of power generation. It consists of two units (a) the steam turbine unit and (b) the gas turbine unit. The net power output is the summation of both the independent units.

The two units while being physically independent, depend on each other for their operation. The gas turbine unit is fired first. This results in hot exhaust gases from the turbine. This hot exhaust gas is used to operate the boiler of the steam turbine generating steam. Once steam is generated the operation of the steam turbine starts.

As the above explanation shows, the steam turbine operates from the energy wasted at the exhaust of the gas turbine. Consequently no separate fuel or energy is required to operate the steam turbine. This results in considerable saving of energy while increasing the power generated.

Conversion of hot gases from the exhaust of the gas turbine to heat required for the boiler is done by the Heat Recovery Steam Generator (HRSG) unit.

The input temperature to a steam turbine is about 540°C and the exhaust can be maintained at the atmospheric pressure, due to design consideration the input temperature is limited and the efficiency of the about 40%. The input temperature of the gas turbine can be as high as 1100°C but the exhaust temperature can be lowered to about 500-600°C, the efficiency of a gas turbine is about 33%. It can be seen that to obtain higher efficiencies the exhaust of the gas turbine can used to drive the steam turbine giving efficiency up to 60% (Black & Veatch 1996).

The plant consists of a compressor, combustor, gas turbine, waste heat recovery boiler, steam turbine, and generator(s).

The air is provided in the compressor which compresses the air and passes it to the combustion chamber, where the compressed air is mixed with the fuel and

* Correspondence: jnrai.phd@gmail.com
[2]Department of Electrical Engineering, Delhi Technological University, Delhi, India
[3]Department of Mechanical Engineering, Delhi Technological University, Delhi, India
Full list of author information is available at the end of the article

Springer

© 2014 Hasan et al.; licensee Springer. This is an Open Access article distributed under the terms of the Creative Commons Attribution License (http://creativecommons.org/licenses/by/2.0), which permits unrestricted use, distribution, and reproduction in any medium, provided the original work is properly credited.

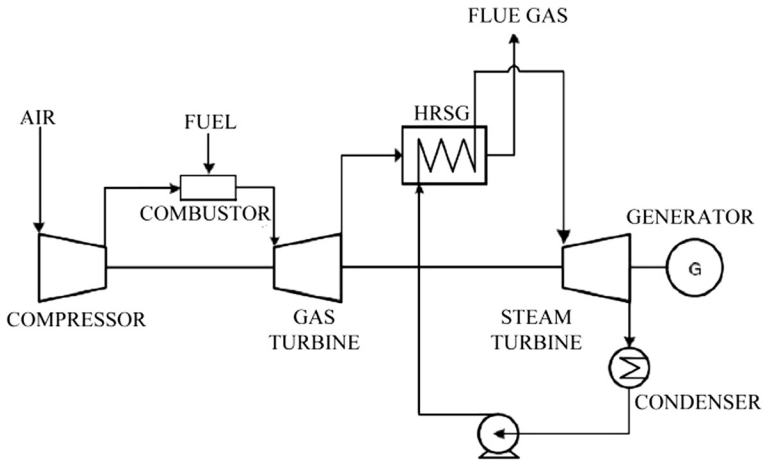

Figure 1 Combined cycle gas turbine.

burnt. The mixture is then sent to the gas turbine where it expands and rotates the turbine (Figure 1). The heat of the flue gas is recovered in HRSG (Heat Recovery Steam Generator) which is used to supply steam to the steam turbine at proper temperature and pressure. Plant power output is the sum of the gas turbine and the steam turbine outputs (Horlock 2003; Kehlhofer et al. 2009; Drbal Lawrence et al. 1996; Lalor & O'Malley 2003).

CCGT thermodynamics

The airflow (W) in the gas turbine is given as

$$W = W_a \frac{P_a}{P_{ao}} \frac{T_{io}}{T_i} \tag{1}$$

Where Ti is ambient temperature and P_a denotes the atmospheric pressure. W_a is air flow with the assumption that $P_a = P_{a0}$.

The compressor discharge temperature is given as

$$T_d = T_i\left(1 + \frac{x-1}{\eta_c}\right) \tag{2}$$

$$x = (P_{ro}W)^{\gamma-\frac{1}{\gamma}} \tag{3}$$

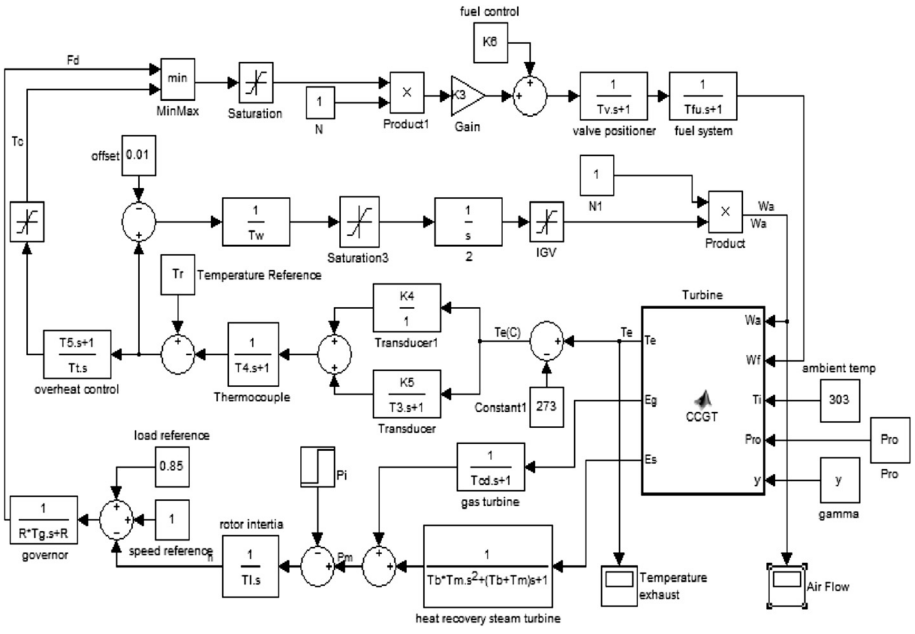

Figure 2 Simulink model of combined cycle gas turbine.

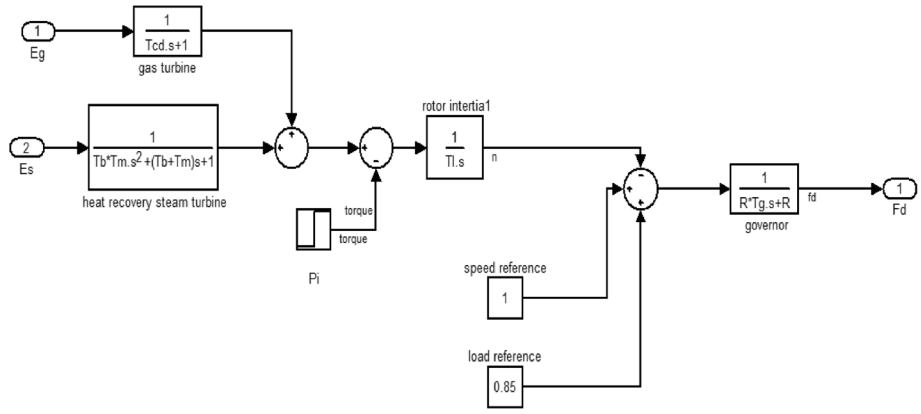

Figure 3 Speed/Load control block.

P_{ro} is the design compressor pressure ratio and y is the ratio of specific heats.

The gas turbine inlet temperature T_f (K) is given by (Kakimoto & Baba 2003)

$$T_f = T_d + \left(T_{fo} - T_{do}\right)\frac{W_f}{W} \tag{4}$$

Where W_f is fuel flow per unit its rated value, 'o' denotes rated value, W denotes the airflow and T_d denotes the compressor discharge temperature.

Gas Turbine exhaust temperature T_e (K) is given by (Kakimoto & Baba 2003)

$$T_e = T_f\left[1 - \left(1 - \frac{1}{x}\right)\eta_t\right] \tag{5}$$

Where η_t is turbine efficiency. The exhaust gas flow is practically equal to the airflow.

The efficiency of a combined cycle (unfired) is given as, Horlock (Horlock 2003)

$$\eta_{cc} = \eta_{gt} + \eta_{st}\left(1 - \eta_{gt}\right) \tag{6}$$

Where $\eta_{cc}$is the efficiency of the combined cycle, η_{gt} is the efficiency of Gas Turbine and η_{st} is the efficiency of Steam Turbine. The thermal efficiency of the simple gas turbine cycle is given as (Al-Zubaidy & Bhinder 1996)

$$\eta = \frac{\left(1 - \frac{1}{p_p}\right)\left(a - p_p\right)}{\eta_c(k_1 - 1) - p_p + 1} \tag{7}$$

Where, $a = \eta_c\eta_t k_1$.

Where p_p is the isentropic temperature ratio (T_2/T_1), k_1 is the cycle maximum temperature ratio (T_3/T_1).

Differentiating (6) gives (Kehlhofer et al. 2009)

$$\frac{\partial \eta_{cc}}{\partial \eta_{gt}} = 1 + \frac{\partial \eta_{st}}{\partial \eta_{gt}}\left(1 - \eta_{gt}\right) - \eta_{st} \tag{8}$$

The overall efficiency improves with the increase in gas turbine efficiency if

$$\frac{\partial \eta_{cc}}{\partial \eta_{gt}} > 0 \tag{9}$$

From equation (8) and (9) one obtains:

$$-\frac{\partial \eta_{st}}{\partial \eta_{gt}} < \left(\frac{1 - \eta_{st}}{1 - \eta_{gt}}\right) \tag{10}$$

The above calculations were done using the following parameters: Pressure Ratio: 8 to 16; Air Fuel Ratio: 50 to 65; Plant Rating: 122 MW for Steam Turbine and 104 MW for Gas turbine.

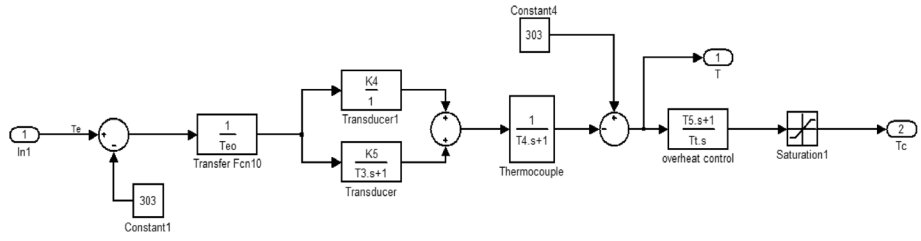

Figure 4 Temperature control block.

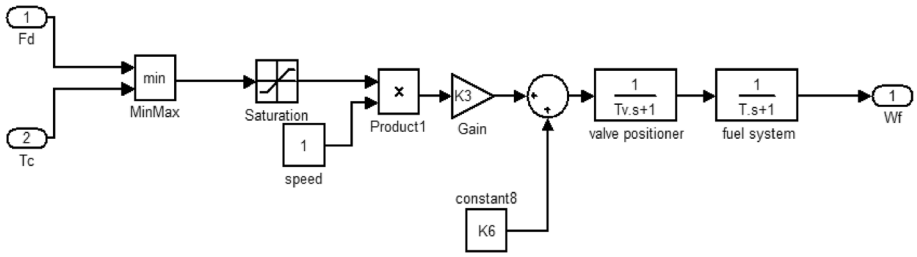

Figure 5 Fuel control block.

Description of simulink model

Several CCGT models have been developed in past few decades with to describe the behavior of gas turbine. The basic gas turbine model equations (Rowen Model II) (Rowen 1983; de Mello & Ahner 1994) for a single shaft system were given by Rowen in 1992. Figures 2, 3, 4, 5 and 6 shows a dynamic model of a combined cycle gas turbine.

This model consists of various blocks describing various parameters whose variations have to be studied in order to optimize the performance of combined cycle. There are blocks related with speed/load, temperature control, fuel control, air control and other blocks for gas turbine, waste heat recovery boiler/steam turbine, rotor shaft, and temperature transducer.

Speed/Load control block

The speed/load control block (Kunitomi et al. 2001) is used to determine the fuel demand F_d in accordance with a reference load reference and rotor speed reference (1-n). The value of n is determined with the help of blocks representing the net energy supplied to the gas turbine E_g andthe energy collected by the heat recovery boiler and steam turbine E_s. The output of these blocks is the power P_g and P_s respectively which when summed up gives the plant power output P_m. The rotor speed varies if there is any difference between power output P_m and load power P_l represented by the reference block of torque. After the value of n is obtained it is compared with the speed reference block and load reference blocks whose output when applied to governor gives the fuel demand $F_{d.}$ (Figure 7).

Temperature control block

The temperature control block (overheat control) is for controlling the exhaust temperature (T_e^0C) of the gas turbine so that the gas turbine does not get injured. The temperature is measured with the help of various transducers and thermocouple as shown in block diagram. The output of the thermocouple (electrical signals) is compared with a reference value (constant 4) (Rai et al. 2013a). According to the difference in values of thermocouple output and reference value the temperature control (Overheat control and Saturation 1) produces temperature control signal T_c. Then the output of the temperature control is combined with speed/load control to determine the fuel demand (using low select value) (Figure 8).

Fuel control block

The fuel control block (valve positioner and fuel control) performs according to the minimum value provided by the speed/load control and temperature control and determines the fuel flow W_f. The Min-Max block selects the minimum value between speed/load control and temperature control and the saturation controls the maximum value of the fuel flow. The output of the saturation is modified by various control blocks and then is input to the valve positioner block which controls the positioning of the valve for the fuel flow. The output

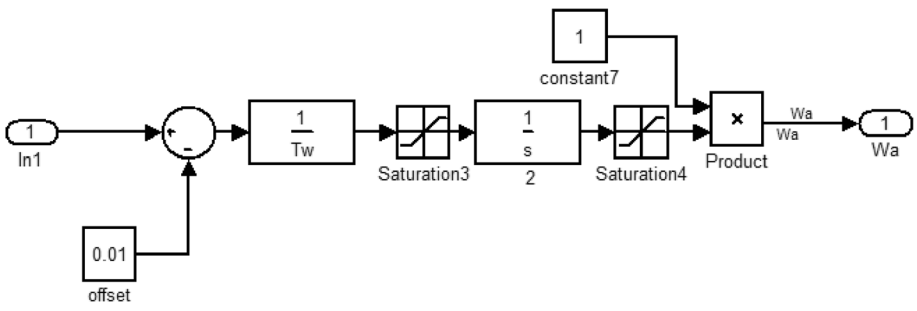

Figure 6 Air control block.

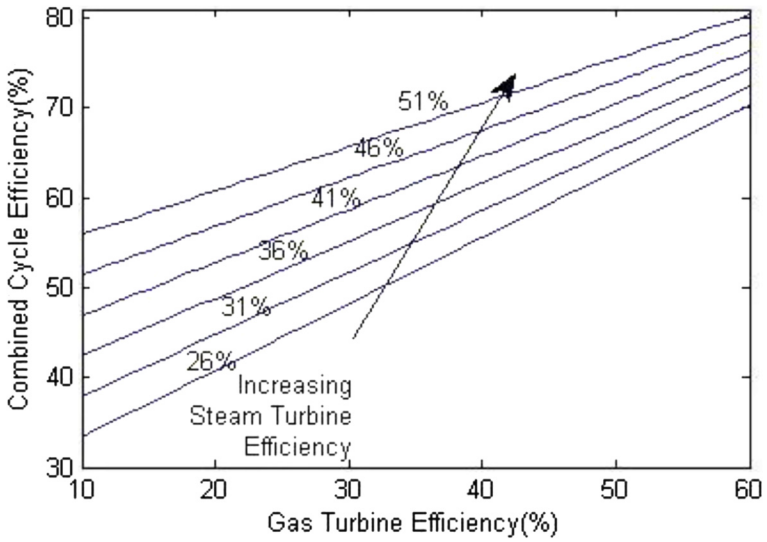

Figure 7 Combined cycle efficiency versus Gas turbine efficiency.

of the valve positioner is then input a fuel system control block which gives the value of the fuel flow W_f.

Air control block

The air control block (saturation 3 and saturation 4) is to adjust the air flow in the gas turbine to attain a desired exhaust temperature so that the temperature is kept below a reference temperature by an appropriate offset. This arrangement is used to control the compressor inlet guide vanes (IGV). The exhaust temperature of gas turbine T_e is compared with a reference temperature which gives the value in ln1. The value of ln1 is compared with offset block and then the output is sent to the air control blocks. The air control blocks adjust the opening of IGV according to the exhaust temperature of the gas turbine. The air flow in gas turbine is used to control the exhaust temperature in the gas turbine.

Results and discussions

Figure 7 shows the plot between overall efficiency and gas turbine efficiency with varying steam turbine efficiency as per the equation (6) (Rai et al. 2013b). It can be seen that combined cycle efficiency increases with the increase of both gas turbine efficiency and the steam turbine efficiency.

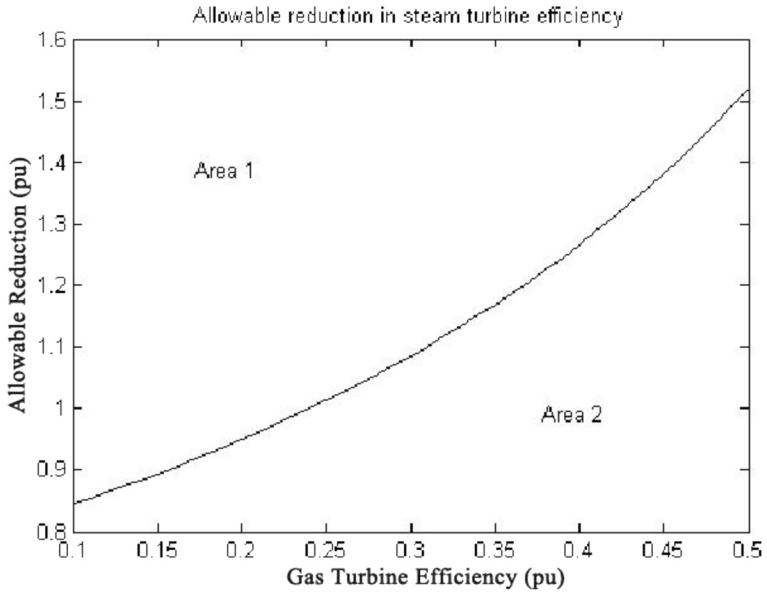

Figure 8 Gas Turbine efficiency versus rate of change of steam turbine efficiency.

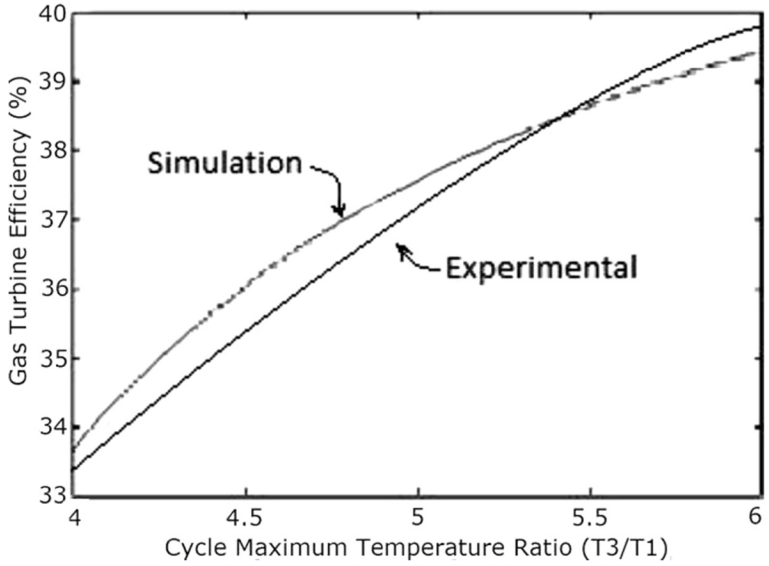

Figure 9 Gas turbine efficiency versus Maximum cycle temperature ratio.

The graph in Figure 8 shows the change in gas turbine efficiency for various rate of change in steam turbine with gas turbine efficiency keeping steam turbine efficiency constant = 24%. It shows that if the efficiency of steam turbine is kept constant and the efficiency of gas turbine is varied, the overall efficiency of the combined cycle can be increased but if the value of derivative falls below the R.H.S. the efficiency of combined cycle would drop. The area I shows the region in which there is allowable reduction in steam turbine efficiency with respect to the gas turbine efficiency.

Figure 9 shows the variation of gas turbine efficiency with cycle maximum temperature ratio (T3/T1) keeping the pressure ratio constant in accordance to equation (7). It shows that the turbine efficiency can be increased by increasing the maximum temperature ratio of Brayton cycle. The optimal value of T3/T1 observed as 5.5 This matches with the safe limit of operation of the plant beyond which the plant starts overheating.

The plot (Figure 10) shows how exhaust temperature of the gas turbine varies with the fuel flow as per equation (5). It can be seen that the exhaust temperature increases with

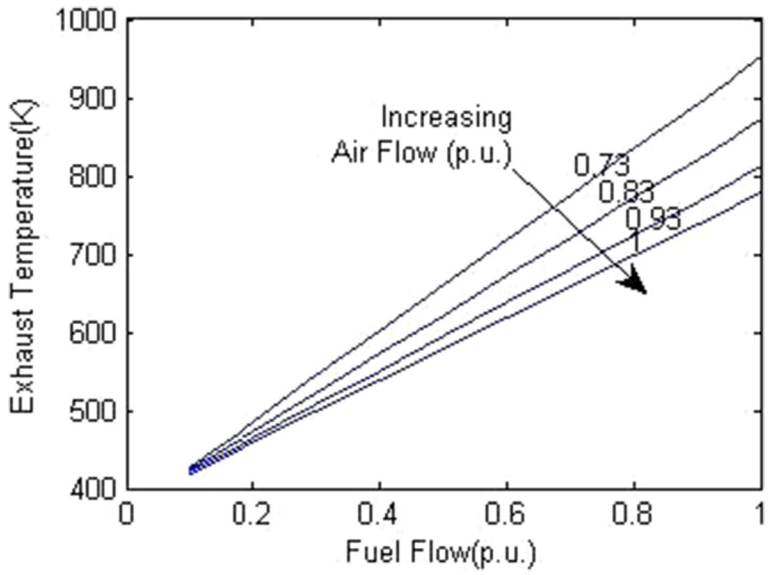

Figure 10 Exhaust temperature versus Fuel flow.

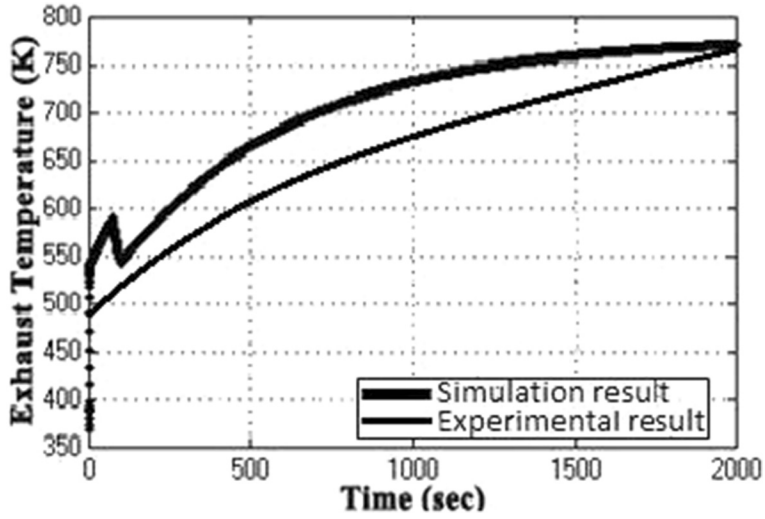

Figure 11 Exhaust temperature (K) versus Time.

the increase in fuel flow. As more energy is supplied temperature increases.

Figure 11 shows the variation of exhaust temperature with time. The exhaust temperature first increases due to more fuel flow till a reference temperature where it is controlled by air flow so that it does not rise any further as it would damage the turbine. From Figure 12 it can be seen that the IGV (Inlet Guide Vanes) start opening to allow more flow of air and thus reducing the exhaust temperature as can be seen by the drop in the exhaust temperature.

The difference in the plots (Figure 11 and Figure 12) of the experimental graph and the simulation is explained by the following:

- Simulation is based on numerical analysis which results in prediction errors while experimental result is the what is actually obtained
- Simulation is based on parameters which do not get affected during the simulation process while the parameters provided during experiment can change due to factors beyond the control of the researcher.

The results on reports were generated based on the following plant ratings and the parameters provided in Table 1 along with gas turbine model described in Appendix.

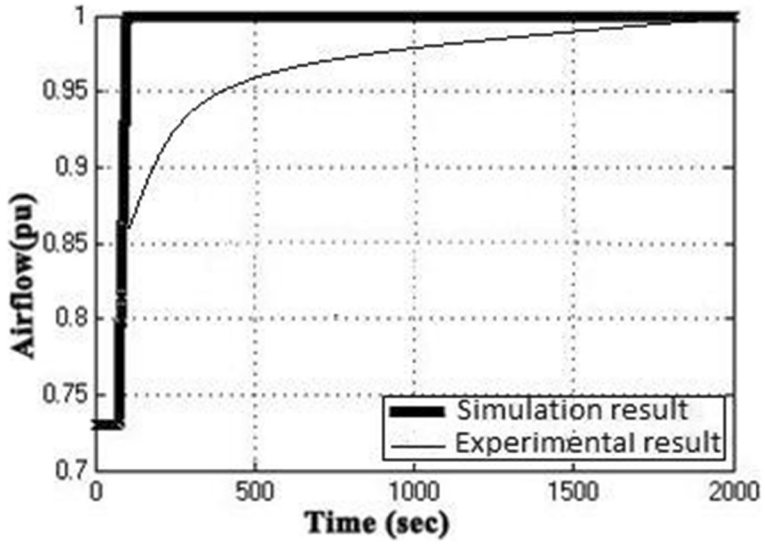

Figure 12 Air flow (p.u.) versus Time.

Table 1 System parameters

Symbol	Description	Value
T_i	Compressor inlet temperature	30°C
T_{do}	Compressor discharge temperature	390°C
T_{fo}	Gas turbine inlet temperature	1085°C
T_{eo}	Gas turbine exhaust temperature	535°C
P_{ro}	Compressor pressure ratio	11.5
γ	Ratio of specific heat	1.4
η_c	Compressor efficiency	0.85
η_t	Turbine efficiency	0.85
R	Speed Regulation	0.04
T_t	Temperature control integration rate	0.469
T_{cmax}	Temperature control upper limit	1.1
T_{cmin}	Temperature control lower limit	0
F_{dmax}	Fuel control upper limit	1.5
F_{dmin}	Fuel control lower limit	0
T_v	Valve positioner time constant	0.05
T_{fu}	Fuel system time constant	0.4
T_w	Air control time constant	0.4669
T_{cd}	Compressor volume time constant	0.2
K_0	Gas turbine output coefficient	0.0033
K_1	Steam turbine output coefficient	0.00043
T_g	Governor time constant	0.05
K_4	Gain of radiation shield	0.8
K_5	Gain of radiation shield	0.2
T_3	Radiation shield time constant	15
T_4	Thermocouple time constant	2.5
T_5	Temperature control time constant	3.3
K_3	Ratio of fuel adjustment	0.77
K_6	Fuel valve lower limit	0.23
T_m	Tube metal heat capacitance time constant of waste heat recovery boiler	5
T_b	Boiler storage time constant of waste heat recovery boiler	20
T_i	Turbine rotor time constant	18.5
W	Air flow	1.0

- A multi shaft CCGT was considered
- CCGT consisted of two gas turbines and one steam turbine
- Both gas turbines were of 104 MW
- The steam turbine was of 122 MW
- HRSG 330 MW

Conclusion

A model of CCGT was developed and variation of efficiency by varying various parameters was studied. The results of which can be summarized as follows:-

(1) The efficiency of Gas Turbine increases with the maximum cycle temperature ratio. The exhaust temperature of the Gas turbine can be increased up to a limit only due to structural limitations. But inlet Temperature (T1) can be lowered which increases the maximum cycle temperature ratio (T3/T1) which in turn will increase the Gas turbine efficiency (Figure 9).

(2) Improving the gas turbine efficiency alone does not necessarily mean the increase in the overall efficiency of the combined cycle (Figure 7). Increasing the gas turbine efficiency would cause lower input steam temperature for steam turbine for given output temperature so the efficiency of the steam turbine would decrease causing the drop in the overall efficiency of the combined cycle (Figure 8).

(3) The temperature exhaust of the gas turbine is also an important parameter which has to be maintained as by increasing fuel flow more power output can be obtained but it would cause a rise in the temperature but since the temperature has to be limited below a safe value as an increase in temperature can cause the turbine components to get damaged. The temperature is controlled by more air flow in the turbine (Figure 10, Figure 11 and Figure 12).

(4) With the rise in the ambient temperature of the atmosphere the output of the gas turbine falls and the output of the gas turbine can be increased by reducing the inlet temperature of the compressor by cooling of the air that is being fed to the compressor.

(5) When the fuel input to the turbine is increased, for increasing the output, the air flow has also to be adjusted accordingly to prevent the turbine temperature to go above a reference temperature. There is a linear rise in air flow with the fuel flow when the turbine is being operated near its rated value.

Appendix

Gas Turbine Model – Frame 6, MS9000 series units, 50 Hz application (rotational speed 3000 rpm).

Competing interests

The authors declare that there is no competing interest.

Authors' contributions

JNR conducted the research work at an operating power plant in New Delhi, India. The data presented is the actual data that was obtained during the experiment. The article was then written by JNR and was reviewed by BBA and NH. The authors have read and approved the final manuscript.

Acknowledgement

The authors wish to acknowledge the help provided by the staff of Pragati Power Corporation Ltd, New Delhi, India, in providing the necessary experimental data. Special thanks to Prof. Ibraheem, Jamia Millia Islamia, New Delhi, India for extending his guidance during the experiment. The author

wishes to thank Rahul Kapoor, Rajesh Garai and Rishabh Kumar Gupta for their contribution in the experiment.

Author details
[1]Department of Electrical Engineering, Jamia Millia Islamia, New Delhi, India. [2]Department of Electrical Engineering, Delhi Technological University, Delhi, India. [3]Department of Mechanical Engineering, Delhi Technological University, Delhi, India.

Received: 24 January 2014 Accepted: 13 May 2014
Published: 1 June 2014

References

Al-Zubaidy S, Bhinder FS (1996) Towards optimizing the efficiency of electrical power generation. Energy Conversion Engineering Conference 3:1857–1862
Black & Veatch (1996) Power plant engineering. Chapman & Hall, New York
de Mello FP, Ahner DJ (1994) Dynamic models for combined cycle plants in power system studies. IEEE Trans Power Syst 9:1698–1708
Drbal Lawrence F, Boston Patricia G, Westra Kayla L, Black& Veatch (1996) Power Plant Engineering. Springer, p 241
Horlock JH (2003) Advanced Gas Turbine Cycles. Pergamon Press, Pergamon
Kakimoto N, Baba K (2003) Performance of gas turbine-based plants during frequency drops. IEEE Transactions on Power Systems 18:1110–1115
Kehlhofer R, Bert R, Frank H, Franz S (2009) Combined-Cycle Gas & Steam Turbine Power Plants. PennWell,
Kunitomi K, Kurita A, Okamoto H, Tada Y, Ihara S, Pourbeik P, Price WW, Leirbukt AB, Sanchez-Gasca JJ (2001) Modeling frequency dependency of gas turbine output. Proc IEEE/Power Eng Soc Winter Meeting
Lalor G, O'Malley M (2003) Frequency control on an island power system with increasing proportions of combined cycle gas turbines. IEEE Power Tech Conference Proceedings, Bologna 4:7
Rai JN, Naimul H, Arora BB, Rajesh G, Gupta RK, Rahul K (2013a) Study the effect of temperature control on the performance of the output of combined cycle gas turbine. International Journal of Theoretical and Applied Mechanics 8 (1):15–23, ISSN 0973–6085
Rai JN, Naimul H, Arora BB, Rajesh G, Rahul K, Ibraheem (2013b) Performance analysis of CCGT power plant using MATLAB/Simulink based simulation. International Journal of Advancements in Research & Technology 2(5):285–290
Rowen WI (1983) Simplified mathematical representations of heavy-duty gas turbines. Trans Amer Soc Mech Eng 105:865–869

doi:10.1186/2193-1801-3-275
Cite this article as: Hasan *et al.*: Optimization of CCGT power plant and performance analysis using MATLAB/Simulink with actual operational data. *SpringerPlus* 2014 **3**:275.

Submit your manuscript to a SpringerOpen journal and benefit from:

► Convenient online submission
► Rigorous peer review
► Immediate publication on acceptance
► Open access: articles freely available online
► High visibility within the field
► Retaining the copyright to your article

Submit your next manuscript at ► springeropen.com

PERFORMANCE AND EMISSIONS ANALYSIS OF ETHANOL-DIESEL BLENDS

***Amit Pal, Prem Kumar, S Maji & #S S Kachhawaha**

Delhi Technological University, Delhi
* Email: amitpal1@yahoo.com

#Department of Mechanical Engineering, Pandit Deendayal Petroleum University, Gandhinagar, India

ABSTRACT

In this work an experimental investigation on performance and emissions analysis of the various blends of ethanol with diesel on a variable compression ratio diesel engine was carried out. The blends of ethanol, diesel and n-butanol are prepared in the volume percentages of 5 to 30% of ethanol with diesel, and with a fixed five percentage of n-butanol are used as a solvent. The experimental tests were carried out to study the performance and emissions of the engine fuelled with these blends of ethanol and diesel at different compression ratios 14, 16 and 18 at different loads. The test results show that the thermal efficiencies of the engine fuelled by these blends were comparable with that fuelled by diesel. However fuel consumption is increased slightly with ethanol diesel, which is due to the lower heating value of ethanol.

The emissions characteristics were also studied and it is found that the smoke opacity from the engine fuelled by the blends were all lower than diesel at particular fixed compression ratio but emissions relatively increases at lower compression ratio 16 and 14. The carbon monoxide (CO) emissions were reduced when the engine is operated at its half capacity loads and above, but increased at lower than half capacity loads and low speed; the hydrocarbon (HC) emissions were all higher except for the top loads at high speed.

Keywords: Ethanol, smoke opacity, Performance, Emissions, n-butanol

1. INTRODUCTION

Rising petroleum prices, increasing threat to the environment from vehicle exhaust emissions and fastly depleting stock of fossil fuels have generated an intense international interest in developing alternative renewable fuels for IC engines. Ethanol is an oxygenated fuel which increases the combustion and makes reduce exhaust emission. It can be produced from crops with high sugar or starch content. Some of these crops include; sugarcane, sorghum, corn, barley, cassava, sugar beets etc. Besides being a biomass based renewable fuel, ethanol has cleaner burning and higher octane rating than the various vegetable oils [1-5]. Jason and Marc (2002) presented the exergetic environmental assessment of lifecycle emissions from M-85, E-85 (used for the gasoline engine) and other alternative fuels[6]. Diesel exhaust is a major contributor to various types of air pollution, including particulate matter (PM), oxides of nitrogen (NOx), and carbon monoxide (CO) [7]. It has been demonstrated that the formation of these air pollutants can be significantly reduced by incorporating or blending oxygenates into the fossil fuels matrix [8]. Diesel engines are an important part of the public and private transportation sector and their use will continue and grow into the future. But their smoke has become biggest threat to health and environment [9]. Keeping in mind the higher octane number of the ethanol, variable compression ratio engine is a good option in this direction using the ethanol diesel blend as fuel; Shaik et al. (2007) demonstrated VCR engine has great potential for improving part-load thermal efficiency and reducing greenhouse gas emissions [10].

There were many attempts made to use ethanol in compression ignition (CI) engine. Huang et al. (2008) carried out tests to study the performance and emissions of the engine fuelled with the ethanol

diesel blends [11]. They found it feasible and applicable for the blends with n-butanol to replace pure diesel as the fuel for diesel engine. Bhattacharya and Mishra (2002) evaluated the feasibility of preparing diesel-ethanol blends using 200° (anhydrous ethanol) and ethanol lower proof [12]. They found that ethanol blends indicated power producing capability of the engine similar to that of diesel. Hansen et al. (2001) found that the properties of ethanol-diesel blends have a significant effect on safety, engine performance, durability and emissions [13]. Wang et al. (2003) analysed that the most noteworthy benefits of E-diesel use lie with petroleum fuel reductions and reductions in urban PM_{10} and CO emissions by heavy vehicle operations [11]. Ajav and Akingbehin (2002) experimentally determined some fuel properties of local ethanol blended with diesel to establish their suitability for use in compression ignition engines [14]. Eckland et al. (1984) presented, State-of-the-Art Report on the Use of Alcohols in Diesel Engines [15].

Techniques that have been evaluated for concurrent use of diesel and alcohols in a compression-ignition engine include (1) alcohol fumigation, (2) dual injection (3) alcohol/diesel fuel emulsions, and (4) alcohol/diesel fuel solutions. Heisey and Lestz (1981) reported significant reductions in particulate generation; however, NOx generation increases [16]. Likos et al. (1982) reported increased NOx and hydrocarbon emissions for diesel-ethanol emulsions [17]. Khan and Gollahalli (1981) reported decreased NOx and hydrocarbon emissions with increased particulate emissions for diesel-ethanol emulsions [18]. Lawson et al. (1981) reported increased NOx and decreased particulate emissions with diesel methanol emulsions [19]. This type of inconsistent performance is what has hindered the use of ethanol in diesel. Baker (1981) reported diesel-ethanol emulsions produce similar NOx, hydrocarbon, and particulate emulsions as compared to baseline runs with straight diesel [20]. Ahmed (2001) found Diesel engines are major contributors of various types of air polluting exhaust gasses such as particulate matter (PM), carbon monoxide (CO), oxides of nitrogen (NOx), sulfur, and other harmful compounds [21]. Ethanol blended diesel (e-diesel) is a cleaner burning alternative to regular diesel for both heavy-duty (HD) and light-duty (LD) compression ignition (CI) engines used in buses, trucks, off-road equipment, and passenger cars. Karabektas and Murat Hosoz (2009) reported the increase of fuel consumption with increase in percentage of ethanol in the blends [22]. Rao et al. (2008) carried out experiment in order to found out optimum compression ratio, experiments were carried out on a single cylinder four stroke variable compression ratio diesel engine [23].

2. EXPERIMENTAL WORK

BLEND PREPARATION:

Blends of ethanol with diesel fuel are prepared in the International Combustion Engines Laboratory of Delhi Technological University, (formerly Delhi College of engineering). Blends are prepared on the volume percentage base of ethanol and diesel. Ethanol percentage varied from 5 to 30 percent with n-butanol as co-solvent. Blends prepared are as-Z5E10D85, Z5E15D80, Z5E20D75, Z5E25D70, and Z5E30D65. Z represents the volume percentage of n-butanol, E represents the volume percentage of ethanol and D represents the volume percentage of diesel. Here Z5 represents use of 5% n-butanol as surfactant. Fuel properties for different blends are shown in the Table 1.

EXPERIMENTAL SETUP:

The setup consists of a Kirloskar, single cylinder, four stroke, 3.5 kW, 1500 RPM, diesel engine connected to eddy current type dynamometer for loading. The engine is modified to change the Compression ratio from 18 to 14 without stopping the engine and without altering the combustion chamber geometry by specially designed tilting cylinder block arrangement. Figure 1 shows the actual experimental setup.

Table 1: Fuel Blends Properties

Fuel/ properties	Diesel	Ethanol	n-butanol	Z5E10D85	Z5E15D80	Z5E20D75	Z5E25D70	Z5E30D65
Mole weight	190 - 220	46.07	74.12	182.56	174.61	166.67	158.72	150.77
Density at 20%°c	0.840	0.789	0.810	.8334	.83085	.8283	.82575	.8232
Oxygen Content (Wt %)	0	34.8	21.58	30.393	31.495	32.156	32.596	32.91
Carbon content (Wt %)	86	52.2	64.82	81.561	79.871	78.181	76.491	72.191
Hydrogen content (Wt %)	14	13	13.60	16.83	13.83	13.78	13.73	13.68
Viscosity at 20% °c Ns/m^2	3.35	1.2	3.0	3.1175	3.01	2.9025	2.795	2.6875

Figure 1: Layout of VCR Engine Test Set Up

3. DISCUSSION ON VARIATION OF PERFORMANCE AND EMISSIONS PARAMETERS

A set of reading was obtained first by running the engine with diesel at CR of 18 and varying the load from idle to rated load of 3.5 kW in steps of 1 up to 3 kW and then to 3.5 kW. The engine performance characteristics were recorded by using the software Engine Soft and instrumentation provided by the National Instruments. The emissions were recorded for each load by using Gas Analyzer AVL Di Gas 444 and the opacity was recorded by smoke meter (AVL 437). Then, the engine was run on blends of

ethanol-diesel and the parameters were recorded as above. The calorific value and density values of the fuels were entered accordingly in the Engine Soft. Similar sets of readings were recorded for the compression ratio of 16 and 14. For this purpose, the engine was started at compression ratio of 18 and then the compression ratio was changed by using the tilting head arrangement.

3.1 DISCUSSION ON PRESSURE- CRANK ANGLE (P-Θ) CURVES

Figure 2.1 (a) to 2.1 (c) show the combustion chamber pressure data with the variation of crank angle. It is found from these curves that for all the blends the maximum pressure attained in the combustion chamber is for the blend of Z5E15D85 which is closely followed by Z5E10D85 and Z5E20D75 blends. The trends are same for all the compression ratios used in the experiment. But it is also observed that there is significant maximum pressure loss with the reduction of the compression ratio. Trends for P-theta from all the fuels used are different, addition of ethanol in diesel results in more effective combustion due to its higher oxygen content but its significantly lower calorific value reduces the combustion pressure and thus as a combined effect causes higher combustion pressure. In this experiment highest pressure is observed with blend E-15, which may be attributed to the oxygenating effect of ethanol, while for higher blends it show a reducing trend which is due to very low calorific value of the ethanol. For blends lower than E-15, combustion improvement effect supersedes the effect of lower calorific value of ethanol than diesel and pressure developed increases with increase in blend percentage up to 15%. On reducing the compression ratio from 18 to 16 and then to 14 resulted in similar trends but with lower peak pressures.

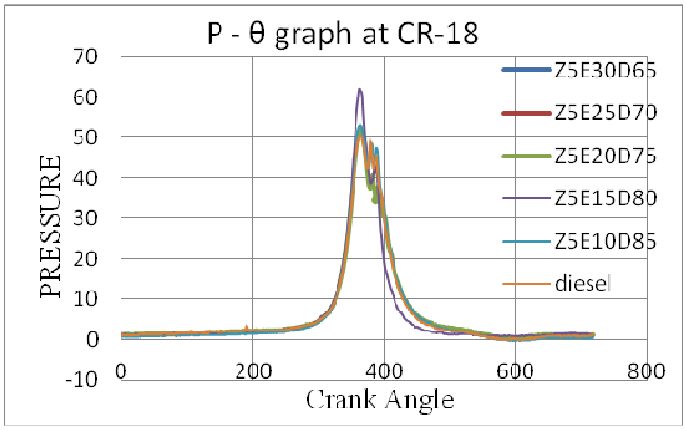

Fig. 2(a): p-θ Vs Crank angle at different Compression Ratios

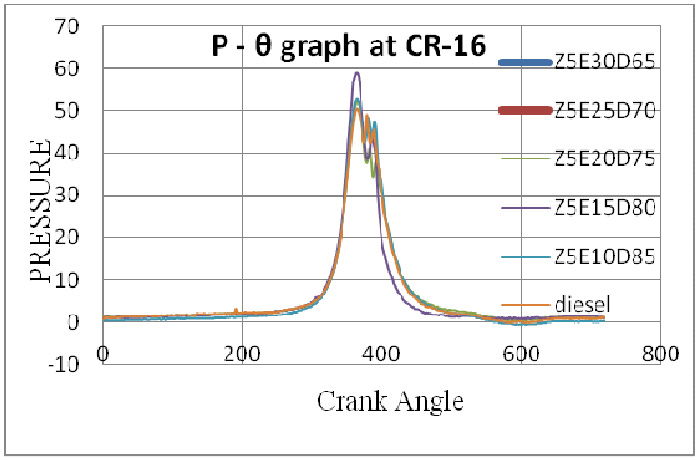

Fig. 2(b): p-θ Vs Crank angle at different Compression Ratios

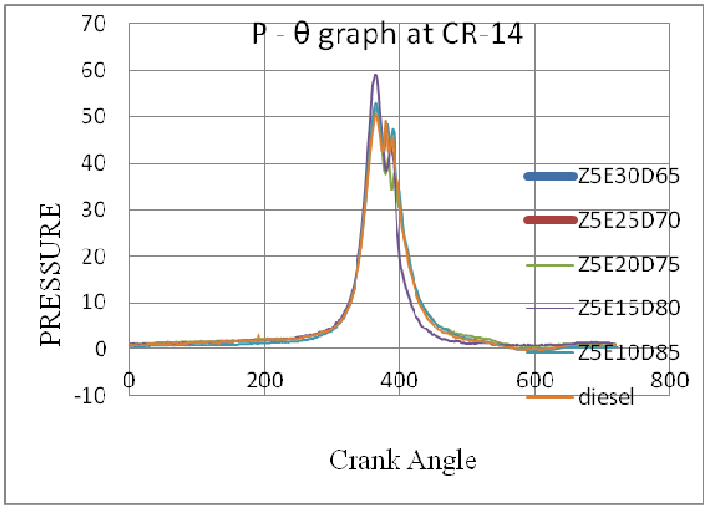

Fig. 2(c): p-θ Vs Crank angle at different Compression Ratios

3.2 DISCUSSION ON VARIATION OF PERFORMANCE PARAMETERS

BRAKE THERMAL EFFICIENCY V/S BRAKE POWER

Figure 3(a) to 3(c) show the results of the thermal efficiencies of engine with the engine power when fuelled by different fuel blends and the pure diesel at CR-18. The test results show that there are some differences for the brake thermal efficiencies for different blends compared with those of diesel. When the engine is operated at the different brake power, from 0 to 2 kW for the different blend, the thermal efficiency were decreased. But at higher loads of 2.5 kW to 3.5 kW, efficiency increased as we increase the percentage of ethanol into diesel up to 30% blending of ethanol into diesel therefore addition of ethanol in diesel results in more effective combustion due to its higher oxygen content. Similar trend was found at different compression ratio with substantial decrease in efficiency for lower compression ratio 16 and 14.

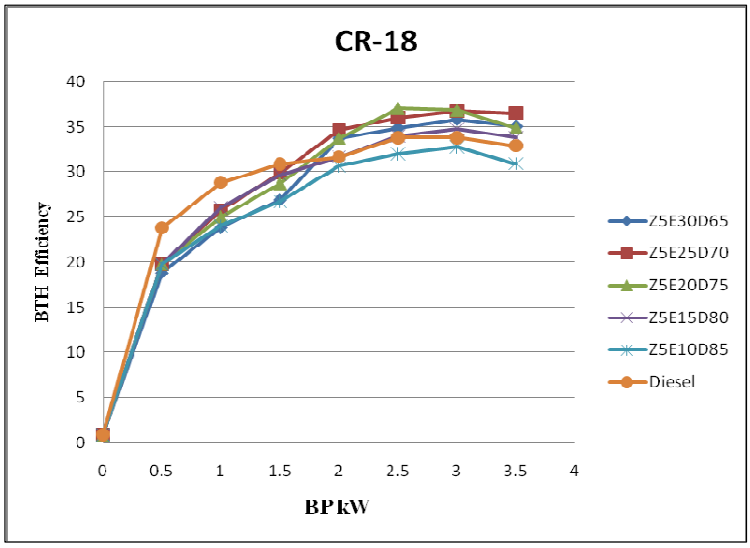

Figure 3(a): Brake Thermal Efficiency v/s Brake Power at CR-18

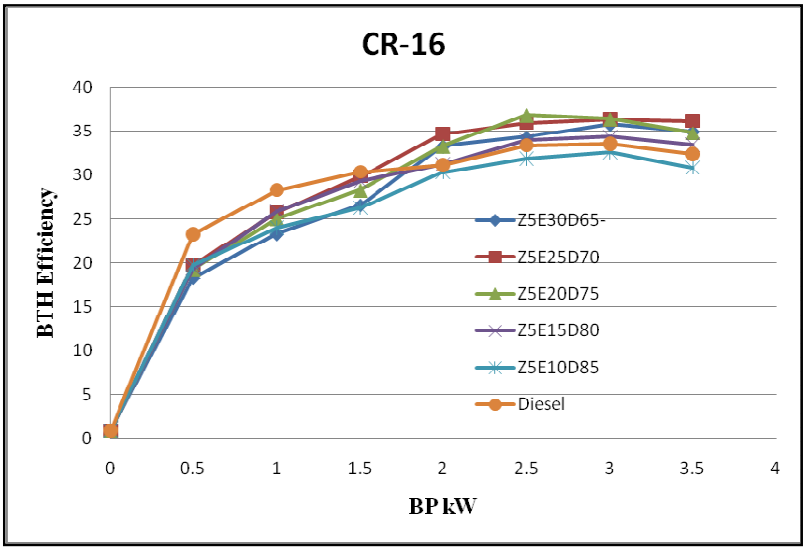

Figure 3(b): Brake Thermal Efficiency v/s Brake Power at CR-16

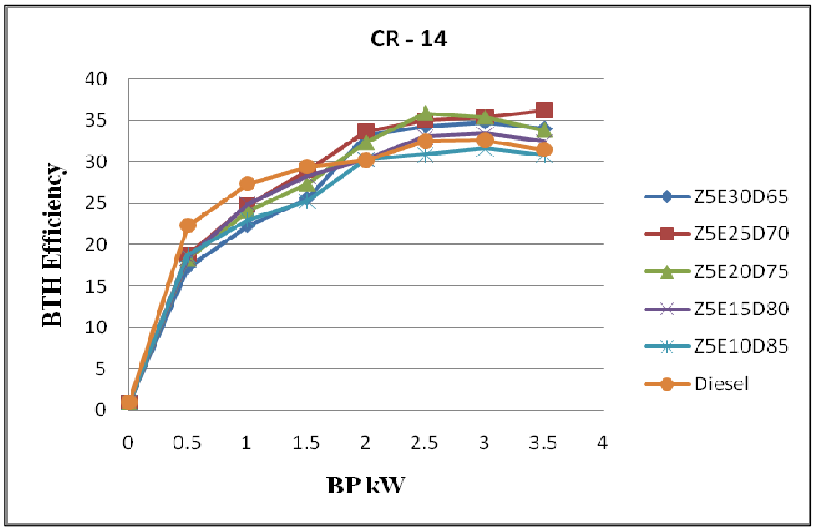

Figure 3(c): Brake Thermal Efficiency v/s Brake Power at CR-14

SPECIFIC FUEL CONSUMPTION V/S BRAKE POWER

Figure 4(a) to 4(c) show the test results of the brake specific fuel consumptions (BSFCs) with the engine power outputs, when the engine fuelled by different fuel blends and diesel. From the results, it can be seen that the engine power could be maintained at the same level when fuelled by different fuel blends with some extent increases of fuel consumption; the more ethanol was added in, the more fuel consumption was found, compared with pure diesel. These increases of fuel consumption are due to the lower heating value of ethanol than that of pure diesel. The results show the trend of the increase of fuel consumption with the increase percentage of ethanol in the blends. Similar results and trend can be seen when the engine is operated at lower compression ratio 14 and 16 on different engine loads with some decrease in fuel consumption.

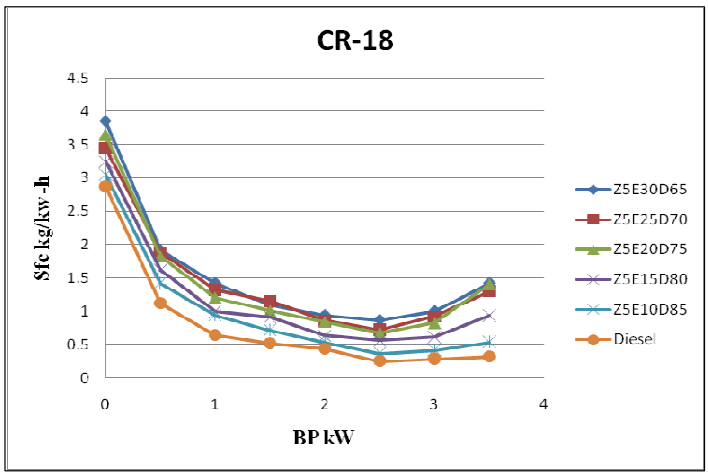

Figure 4(a): Specific Fuel Consumption v/s Brake Power at CR-18

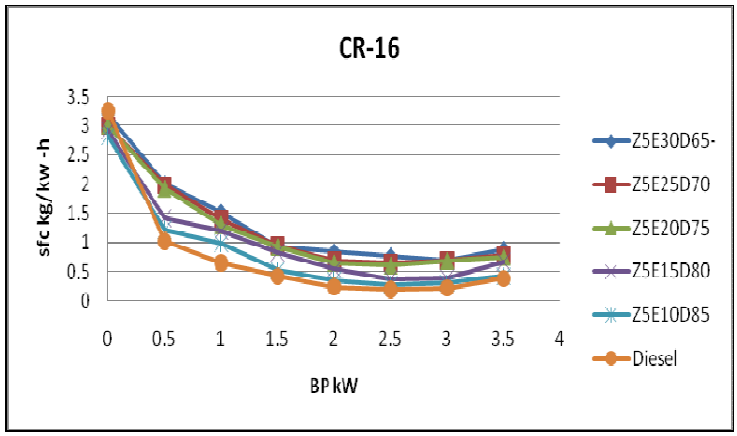

Figure 4(b): Specific Fuel Consumption v/s Brake Power at CR-16

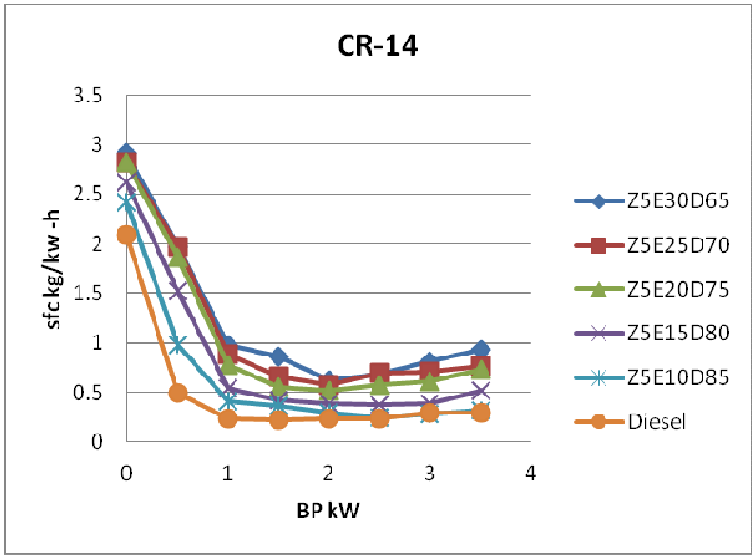

Figure 4(c): Specific Fuel Consumption v/s Brake Power at CR-14

3.3 DISCUSSION ON VARIATION OF EXHAUST EMISSIONS

THE NITROGEN OXIDES (NOX) EMISSIONS FROM THE ENGINE

The test results for the NOx emissions from the engine are shown in Figure 5 (a) to 5(c). When the engine is operated at CR 18 and above half of the engine load (2 kW); the NOx emissions from the engine were higher than those of diesel when fuelled by Z5E10D85, when the engine loads were less than 2 kW, the NOx emissions were reduced. The NOx emissions from the engine were all lower than those of diesel when fuelled by the other blends. When fuelled by Z5E25D70, the NOx emissions from the engine were not stable, at different engine loads. Similar trend were found at lower compression ratio with slight increase in the NOx.

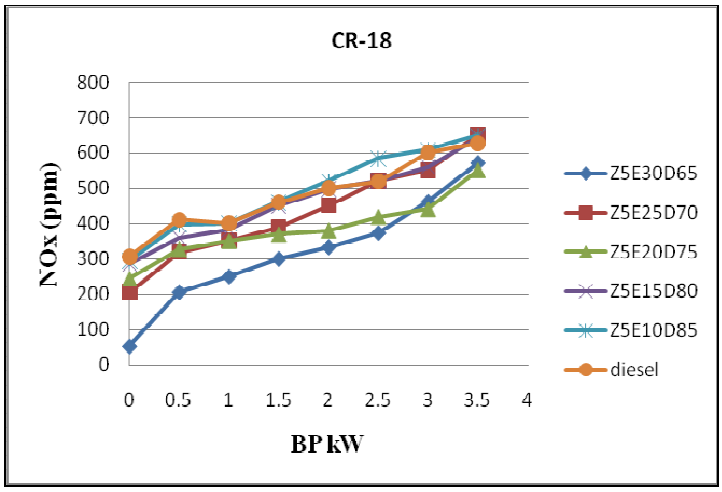

Figure 5(a): NOx Emissions v/s Brake Power at CR-18

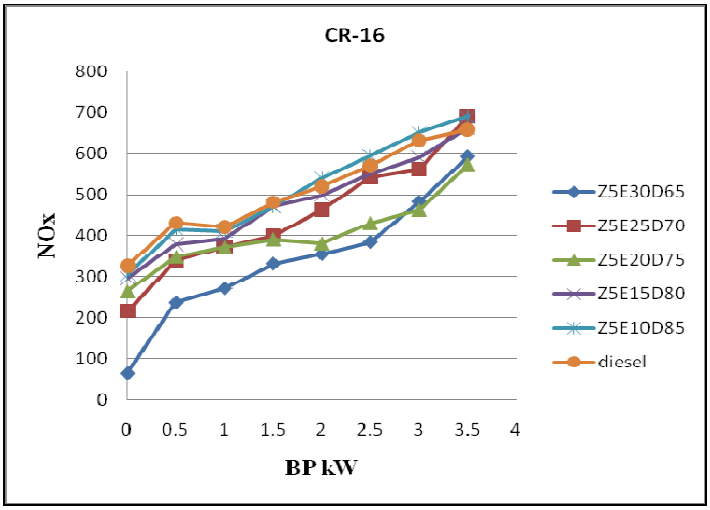

Figure 5(b): NOx Emissions v/s Brake Power at CR-16

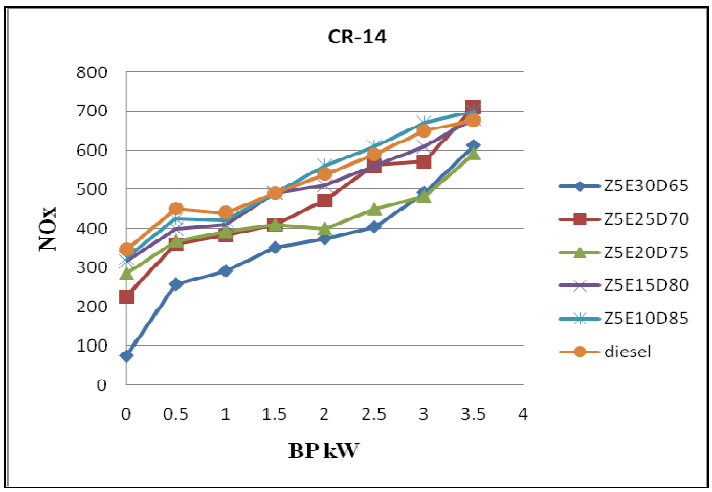

Figure 5(c): NOx Emissions v/s Brake Power at CR-14

THE UNBURNT HYDROCARBON (HC) EMISSIONS FROM THE ENGINE

The test results for the unburned HC from the engine are shown in Figures 6(a) to 6(c). The results showed that the HC emissions from the engine for the blend fuels were all higher when the engine is operated on the 14 and 16 compression ratio; and the HC emissions became less as the loads increased. A similar trend can be seen for the engine is operated on 18 compression ratio, except at the point of top power output. At this point, the HC emissions for all blends were lower than that when fuelled by diesel; this is due to the high temperature in the engine cylinder to make the fuel to react easily with oxygen when the engine is operated at the top load and high speed. There is a marginal increase in HC emissions with reduction in the compression ratio. Similar trend were found at lower compression ratio with further increase in the HC.

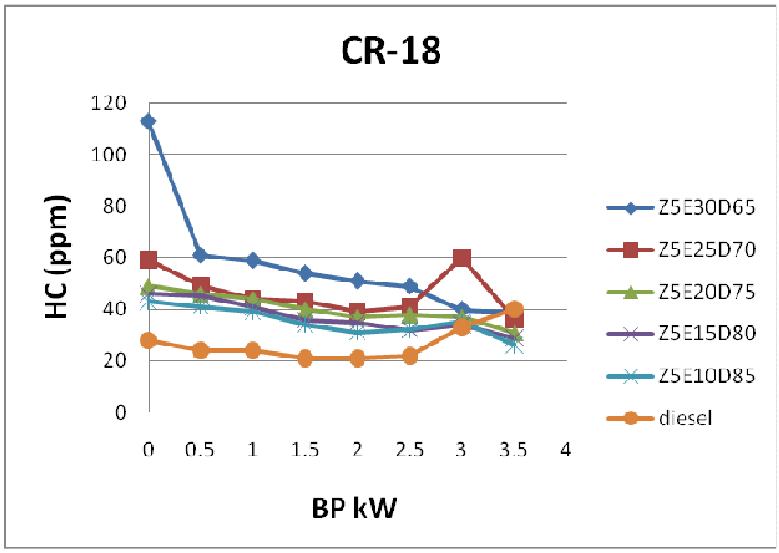

Figure 6(a): Unburnt hydrocarbon (HC) emissions v/s Brake Power at CR-18

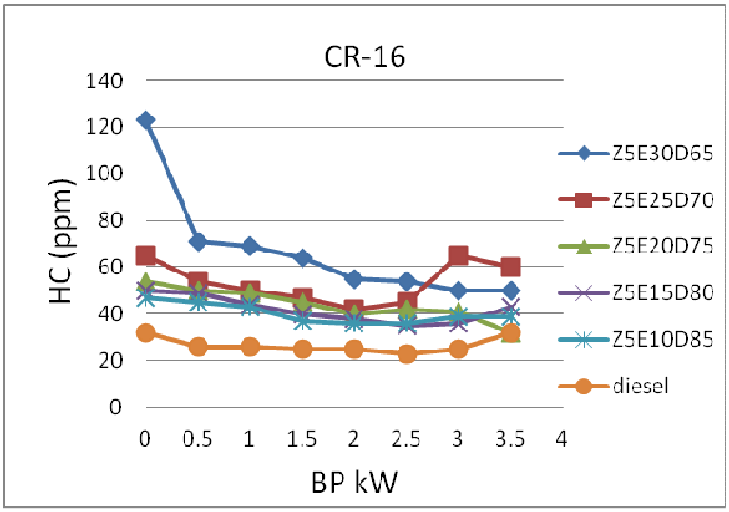

Figure 6(b): Unburnt Hydrocarbon (HC) Emissions v/s Brake Power at CR-16

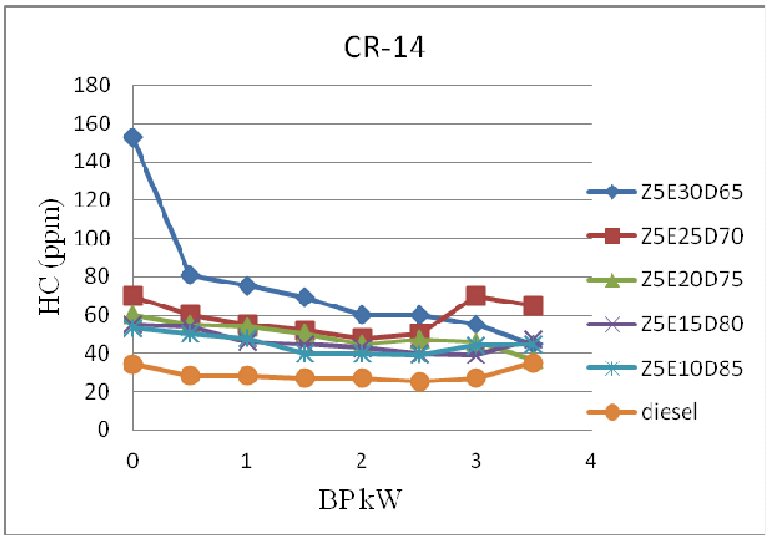

Figure 6(c): Unburned hydrocarbon emissions v/s break power at CR-14

THE CARBON MONOXIDE (CO) EMISSIONS FROM THE ENGINE

Figure 7(a) to 7(c) show the CO emissions from the engine exhaust at the compression ratio 14, 16 and 18 when fuelled by different fuels. When the engine is operated at CR 18 and at lower loads, the CO emissions from the engine fuelled by the ethanol blends were higher than those fuelled by pure diesel. The higher the percentages of the ethanol, there are higher CO emissions. But at the engine higher loads which were about above half of the maximum engine load, the CO emissions became lower than that fuelled by diesel for all the blend fuels. This may be attributed to the oxygenating effect of the ethanol, while at part loads the burning remains incomplete. The CO emission observed to be increasing with the reduction in the compression ratio.

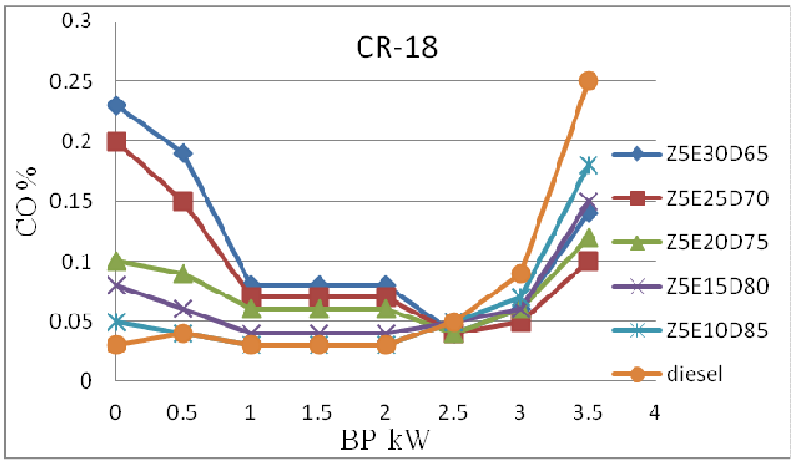

Figure 7(a): Carbon Monoxide (CO) Emissions v/s Brake Power at CR-18

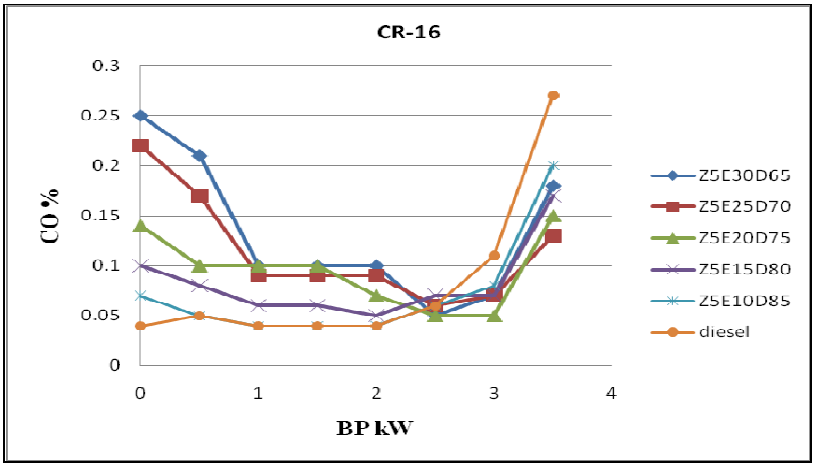

Figure 7(b): Carbon Monoxide (CO) Emissions v/s Brake Power at CR-16

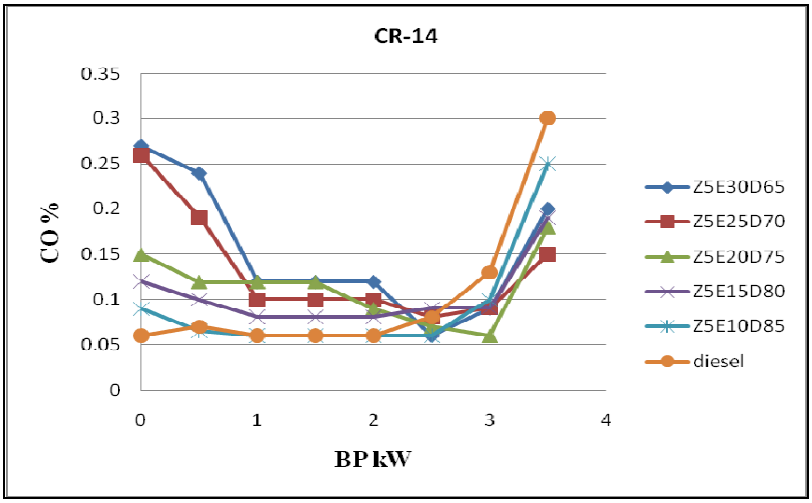

Figure 7(c): Carbon Monoxide (CO) Emissions v/s Brake Power at CR-14

SMOKE OPACITY V/S BRAKE POWER

Figure 8(a) to 8(c) show the test results of smoke emissions from the engine when fuelled by different fuels. The results show that the smokes from the engine were all lowered down using blends at the 18 compression ratio. A similar trend can be found on compression ratio 14 and 16 for the different blends and pure diesel but a significant increase in the smoke opacity on reducing the compression ratio with reference to the CR 18 is observed.

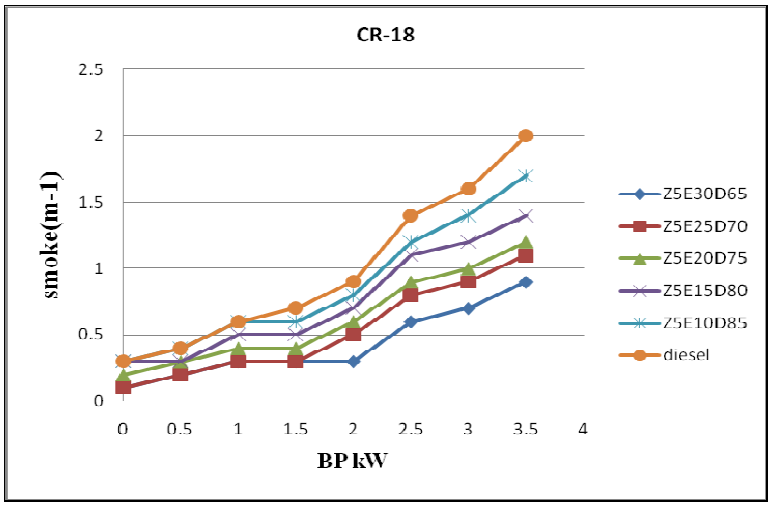

Figure 8(a): Smoke Opacity v/s Brake Power at CR-18

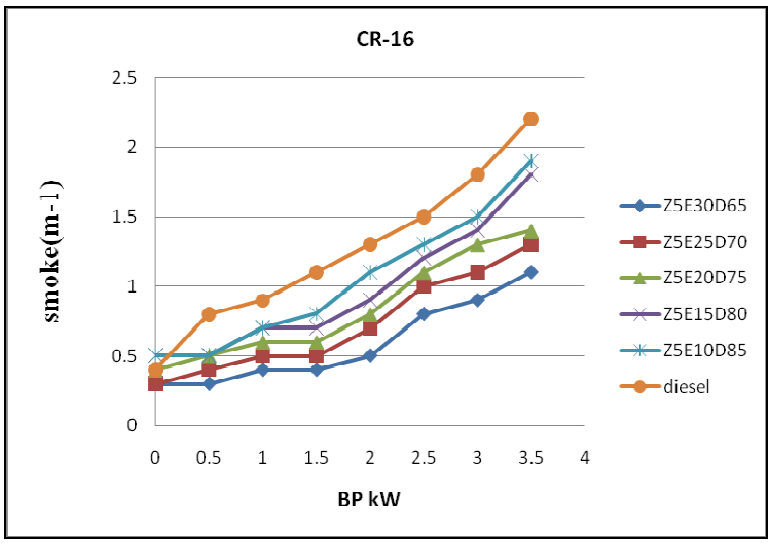

Figure 8(b): Smoke Opacity v/s Brake Power at CR-16

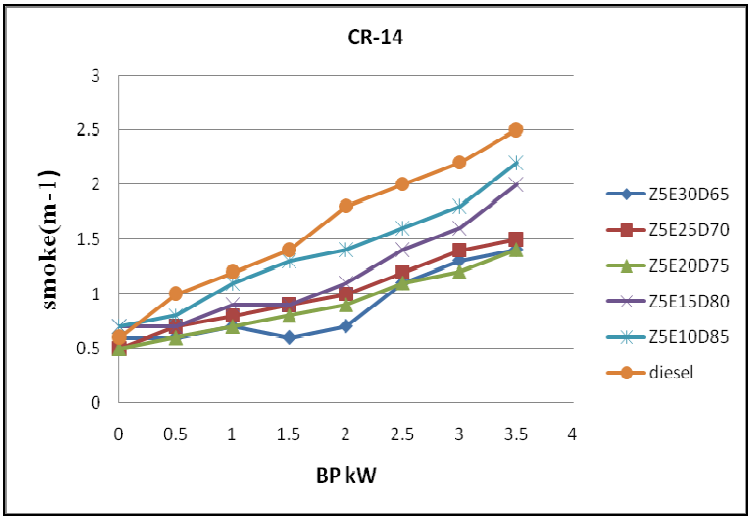

Figure 8(c): Smoke Opacity v/s Brake Power at CR-14

4. CONCLUSIONS

In this work an attempt has been made to find the suitability of various ethanol-diesel blends to reduce the exhaust emissions of CI engines. It has been established that the ethanol-diesel can be conveniently used in CI engines without any major modification and it is also validated that these are helpful in reducing the exhaust emissions and improve the overall performance of the CI engines at CR 18. The results show significant reduction in smoke ranging from 10-40%, CO emissions reduction ranging from 10-30% and HC and NOx emissions reduction ranging from 10 to 50%, with use of ethanol- diesel blends, and reduction of smoke is in the range of 10-40%. It is also concluded that a compression ratio of 16 is more appropriate for overall performance for ethanol diesel blends.

REFERENCE

1. Alan C. Hansen, Qin Zhang and Peter W. L. Lyne, "Ethanol–diesel fuel blends a review", *Bioresource Technology, Volume 96*, Issue 3, February 2005, Pages 277-285.
2. Hanbey Hazar, "Effects of biodiesel on a low heat loss diesel engine", *Renewable Energy 34* (2009) 1533–1537.
3. Neven Voca,Boris Varga,Tajana Kricka, Duska Curic, Vanja Jurisic and Ana Matin, "Progress in ethanol production from corn kernel by applying cooking pre-treatment" *Bioresource Technology Volume 100,* Issue 10, May 2009, Pages 2712-2718.
4. Avinash Kumar Agarwal, "Biofuels (alcohols and biodiesel) applications as fuels for internal combustion engines" *Renewable Energy,* 27 November 2006.
5. Hakan, Bayraktar. "Experimental and theoretical investigation of using gasoline–ethanol blends in spark-ignition engines", *Renewable Energy*, 2005; *Volume 30, Issue 11:pp1733-1747.*
6. Jason J, Daniel Marc, Rosen A, "Exergetic Environmental Assessment of Life Cycle Emissions for various Automobiles and Fuels, Exergy 2 (2002) 283-294
7. Hwanam Kima, Byungchul Choi, "Effect of ethanol–diesel blend fuels on emission and particle size distribution in a common-rail direct injection diesel engine with warm-up catalytic converter", R*enewable Energy 33* (2008) 2222–2228.
8. De-gang Li, Huang Zhen, Lu˘ Xingcai, Zhang Wu-gao and Yang Jian-guang, "Physico-chemical properties of ethanol–diesel blend fuel and its effect on performance and emissions of diesel engines", *Renewable Energy 30* (2005) 967–976.
9. Sehmus Altuna, Husamettin Bulutb and Cengiz Oner, "The comparison of engine performance and exhaust emission characteristics of sesame oil–diesel fuel mixture with diesel fuel in a direct injection diesel engine", *Renewable Energy 33* (2008) 1791–1795.

10. Amjad Shaik, ,N Shenbaga Vinayaga Moorthi, and R Rudramoorthy, “Variable compression ratio engine: a future power plant for automobiles an overview,” *Proc. IMechE Vol. 221* Part D April 2007. DOI: 10.1243/09544070JAUTO573.
11. Jincheng Huang, Yaodong Wang, Shuangding Li, Anthony P. Roskilly,Hongdong Yu, Huifen Li, “Experimental Investigation on the Performance and Emissions of a Diesel Engine Fuelled with Ethanol-diesel Blend,” *ATE 2697*, 2008.
12. T K Bhattacharya and T N Mishra, “Studies on Feasibility of using Lower Proof Ethanol-diesel Blends as Fuel for Compression Ignition Engines”,*IE (I) Journal–AG 263 145*, December 21, 2002
13. Alan C. Hansen, Peter W. L. Lyne, Qin Zhang, “Ethanol-Diesel Blends: A Step towards A Bio-Based Fuel for Diesel Engines”, *American Society of Agricultural and Biological Engineers (ASAE)* August 1, 2001.
14. Ajav, E. A. and O. A. Akingbehin, “A Study of some Fuel Properties of Local Ethanol Blended with Diesel Fuel”, *Journal of Scientific Research and Development Manuscript EE 01 003. Vol. IV*. March, 2002.
15. Eckland, E. E.; R. L Bechtold; T. J. Timbario; and P. W. McCallum, “State-of-the-Art Report on the Use of Alcohols in Diesel Engines”, *SAE Paper No. 840118*.
16. Heisey, J. B. and S. S. Lestz, “Aqueous alcohol fumigation of a single-cylinder DI CI engine,”*SAE Paper No. 811208.*
17. Likos, B.; T. J. Callahan; and C. A. Moses, “Performance and Emissions of Ethanol and Ethanol-Diesel Blends in Direct-Injected and Pre-Chamber Diesel Engines”,*SAE Paper No. 821039.*
18. Khan, N and S. R. Gouahalli, “ Performance and Emission Characteristics of a Diesel Engine Burning Unstabilized Emulsions of Diesel Fuel with Water, Methanol, and Ethanol”, *SAE Paper No. 811210.*
19. Lawson, A.; A. J. Last; A. S. Desphande; and E. W. Simmons, “Heavy-Duty Truck Diesel Engine Operation on Unstabilized Methanol -Diesel Fuel Emulsions”, *SAE Paper No. 810346.*
20. Baker, Q. A., “Use of Alcohol-in-Diesel Fuel Emulsions and Solutions in a Medium-Speed Diesel Engine”, *SAE Paper No. 810254*.
21. Irshad Ahmed Oxygenated Diesel, “Emissions and Performance Characteristics of Ethanol-Diesel Blends in CI Engines,” *Society of Automotive Engineers, Inc*. 2001-01-2475.
22. Murat Karabektas A, Murat Hosoz B, “performance and emission characteristics of a diesel engine using isobutanol–diesel fuel blends”, *Renewable Energy 34* (2009) 1554–1559.
23. GVNSR Ratnakara Rao, V. Ramachandra Raju and M. Muralidhara Rao, “Optimizing The Compression Ratio Of Diesel Fuelled C.I Engine”, *ARPN Journal of Engineering and Applied Sciences, VOL. 3*, NO. 2, APRIL 2008.

ISSN: 2319-5967
ISO 9001:2008 Certified
International Journal of Engineering Science and Innovative Technology (IJESIT)
Volume 3, Issue 3, May 2014

Performance of Low-Cost Adsorbents for the Removal of fluoride ions – An overview

Suman Mann, Dr.Anubha Mandal

Abstract: ***Fluoride is a poison that accumulates in our bones. It has been associated with cancer in young males; osteoporosis; reduced I.Q; and hip fractures in the elderly, to name a few. The permissible limit of fluoride concentration in drinking water is 1.5mg/L according to WHO guidelines. Therefore, knowledge of its removal, using best technique with maximum efficiency is needed. Among various techniques adsorption occupies a prominent place in fluoride removal. As cost is an important consideration in most developing countries, efforts have been made to explore the possibility of using various low cost adsorbents that are abundant, readily available and are derived from waste materials. In this review, lists of adsorbents are overviewed and their feasibility for the removal of fluoride is studied with various affecting parameters.***

Keywords**: adsorption, adsorbent, efficiency, low cost adsorbents.**

I. INTRODUCTION

Almost all parts of the world have reported high concentration of fluoride in drinking water. North America, Africa and Asia are the mostly affected continents of the world. Countries like India, Srilanka and China have reported high concentrations of fluoride. Rift valley countries in Africa have reported high concentrations of fluoride due to the weathering of alkaline volcanic rocks.

Contamination of drinking water by fluoride, due to its natural presence from dissolution of fluoride containing rocks, or discharge by agricultural and industrial activities, such as steel, aluminium, glass, electroplating, is one that affects human health and wellbeing.

Fluoride is an essential constituent for both humans and animals depending on the total amount ingested or its concentration in drinking water. It is purposely added to drinking water in small quantities to prevent dental caries. The presence of fluoride in drinking water, within the permissible limits of 0.5-1.0 mg L-1, is beneficial for the production and maintenance of healthy bones and teeth, while excessive intake of fluoride causes dental or skeletal fluorosis which is a chronic disease manifested by mottling of teeth in mild cases, softening of bones and neurological damage are severe cases[1]-[4]. Because of its health risks, defluoridation of drinking water is the best practicable option to overcome the problem of excessive fluoride in drinking water, where alternate source is not available. During the years following the discovery of fluoride as the cause of fluorosis, extensive research has been done on various methods for removal of fluoride from water and wastewater.

At present, there are few treatment options that are used for controlling excessive levels of fluoride in drinking water. Based on the mechanism of fluoride removal, the methods can be categorized into chemical precipitation (by alum, lime, lime and alum and calcium chloride), adsorption (activated alumina, clay and flay ash), ion exchange (by synthetic resins and bone char) and membrane technologies (reverse osmosis and electro dialysis). The methods used by industrialized countries such reverse osmosis, electro-dialysis and ion exchange require more technical support for operation and maintenance and the capital investment cost is very high. Among the various available techniques for removal of fluoride, adsorption method is relatively simple, economical and suitable for small communities.

II. OBJECTIVE OF REVIEW

The objective of this review is to contribute in the search for less expensive adsorbents and their utilization possibilities in adsorption process for the elimination of fluoride from water and wastewater.

III. ADSORPTION

Among the unit operations in water and wastewater treatment adsorption occupies an important position. Adsorption operations exploit the ability of certain solids preferentially to accumulate specific substances from

ISSN: 2319-5967
ISO 9001:2008 Certified
International Journal of Engineering Science and Innovative Technology (IJESIT)
Volume 3, Issue 3, May 2014

solution onto their surfaces [5]. Sorption, which is a general term introduced by McBain [6], includes selective transfer to the surface, and for into the bulk of liquid. In a general adsorption process, the adsorbed solutes are referred to as adsorbate and the adsorbing agent is the adsorbent.

Theoretically, the adsorption of solute on to solid particles normally takes four essential steps:
a) Solutes diffuses through the fluid to an area near the solid particle surface,
b) Solute diffuses to the external surface of the particle,
c) Solute diffuses to the pore wall,
d) Solute adsorbs to the internal surfaces of the pore wall.

Adsorption methods can be implemented for the removal of fluoride due to physical, chemical, or ion exchange interactions with the adsorbents. Two types of contacting systems of adsorption are usually encountered, namely, the batch and fixed-bed processes. Batch type processes are usually limited to the treatment of small volumes of effluents whereas the bed column systems have the advantage of continuous operation up to the point of saturation.

Adsorbent is a porous substance that has a high surface area and has the ability to absorb or adsorb other substances using intermolecular forces onto its surface. A good example of an adsorbent material is activated charcoal. B.C.Lowitz established the first use of charcoal for the removal of bad tastes and odours from water on an experimental basis in 1789-90. The credit of developing commercial activated carbon however, goes to Raphael Von Ostrejko whose inventions were patented in 1900 and 1901.

Researches were carried on different adsorbents, viz. activated carbon, processed bone char powder, activated alumina, magnesia, activated bauxite, fly ash, granular calcite, alum, lime, etc. (Choi 1979, Bhargava 1991, Killedar & Bhargava 1998a,b, and T. Wijesundara 2004)[7]-[11].

The criteria for selection of suitable adsorbent are; cost of the media and running costs, ease of operation, adsorption capacity, potential for reuse, number of useful cycles and the possibility of regeneration.

IV. ADVANTAGES OF ADSORPTION PROCESS: [12]

- **Cheap:** The cost of adsorbent is low since they are often made from locally, abundantly and easily available materials.
- **Metal Selective:** The metal adsorbing performance of different types of bio-mass can be more or less selective on different metals.
- **Regenerative:** Sorbent material can be possible to reuse after regeneration
- **No Sludge Generation:** Unlike the problems in other techniques (ex: precipitation), there is no issue of sludge generation in adsorption process.
- **Metal Recovery:** If adsorbate is a metal ion, it is possible to recover the metal ion after being desorbed from the adsorbent materials.
- **Competitive Performance:** Performance of adsorption process in terms of efficiency and cost is comparable with the other methods available

V. LITERATURE REVIEW

Pali Shahjee, B.J.Godboley, A.M.Sudame (2013) investigated or checked efficiency of low cost adsorbent (Bleaching Powder) for the removal of excess fluoride from aqueous solution. The studies were conducted under batch adsorption. The investigators concluded that the bleaching powder is a good adsorbent for fluoride removal from aqueous solution. The optimal conditions for the effective removal of fluoride by bleaching powder were found to be at pH 10, contact time 8 hours and optimum dose of adsorbent was found 7.3gm/100ml for removal of fluoride of 5ppm concentration [13].

Naba Kumar Mondal, RIA Bhaumik, Tanmoy Baur, Biswajit Das, Palas Roy and Jayanta Kumar Datta (2012) studied the removal of fluoride using Tea ash as adsorbent through batch studies. The authors reported that the adsorbent was efficient for the uptake of fluoride at pH 6 and contact time 180 minutes. Tea ash was found to me more efficient at an initial concentration of 5mg/l and temperature 303 k. The authors also reported

ISSN: 2319-5967
ISO 9001:2008 Certified
International Journal of Engineering Science and Innovative Technology (IJESIT)
Volume 3, Issue 3, May 2014

that the data nicely fitted with Langmuir adsorption isotherm indicating monolayer adsorption and adsorption of fluoride decreased with increase in temperature in the range of 303-333 K. Again the adsorption process was observed to follow a pseudo-second-order kinetic model [14].

G. Alagumuthu, V. Veeraputhiran and R. Venkataraman (2010) investigated the removal of fluoride from the water using *cynodon dactylon* as adsorbent. By conducting batch adsorption studies at constant temperature (25-32°C), the maximum removal of fluoride was 83.77 % while keeping 3.0 mg/L fluoride concentration and 1.25 g dosage of adsorbent at neutral pH., contact time 105 minutes. Various adsorption isotherm models were applied to evaluate the adsorption data. The adsorption of fluoride ions followed Redlich-Peterson isotherm as well as Langmuir isotherms. The authors concluded that the adsorbent used in this work shows superior adsorptive efficiency than previously studied defluoridation works using natural adsorbents was most effective[15].

Bhagyashree M Mamilwar, A.G.Bhole, A.M.Sudame (2012) investigated the adsorption of Fluoride using bark of babool as adsorbent. The investigators conducted batch studies and used Freundlich and Langmuir isotherms to understand the adsorption mechanism. Optimum dose of bark of babool was found 5g/L for removal of fluoride concentration of 5 mg/L. Adsorption capacity was more in the pH range of 6-8.Optimum time of contact was found 8 hrs. The removal increased with time and adsorbent dose, but with higher initial concentration decreased with time and adsorbent dose. The present study on defluoridation using bark of babool shows that the equilibrium data fits better to Langmuir isotherm as compared with Freundlich isotherm. The pseudo-second-order kinetic model fitted well as compared to pseudo first-order model [16]**.**

N. Gandhi, D. Sirisha, K.B. Chandra Shekar and Smita Asthana (2012) carried out their study on effective and cheap adsorbents for the removal of fluoride from the water. Batch adsorption studies were carried out. The experiments were carried out in laboratory on certain low cost adsorbents like concrete, ragi seed powder, Red soil, horse gram seed powder, orange peel powder, chalk powder, pineapple peel powder and multhani matti. Results indicate 86% fluoride removal for chalk powder and pineapple peal powder. Orange peel powder and horse gram seed powder showed the removal of 79% and 75%. Percentage removal for ragi seed and red mud was found to be 65% and 71%. Removal efficiency was recorded less for multani mitti and concrete which was 56 % and 53% [17].

Patil Satish, Renukdas Sameer, Patel Naseema(2012) conducted tests to investigate the efficacy of various treated natural adsorbents such as Mangrove plant leaf powder (MPLP), Almond tree bark powder (ATBP), Pineapple peel powder (PPP), Chiku leaf powder (CLP), Toor plant leaf powder (TPLP) and Coconut coir pith (CCP). Observed the effect of pH, contact time, adsorbent dose and initial metal ion concentration to remove fluoride ions from the aqueous solutions using batch studies. Uptake of fluoride ions by adsorbents at equilibrium is found to be in the order of MPLP > CCP > TPLP > CLP > PPP > ATBP. The optimum contact time for all the adsorbents was 60 minute with a adsorbent dose of 10g/l for initial fluoride concentration of 5ppm. Percentage removal at pH 2 was found to be high [18].

R. Bhaumik, N. K. Mondal, B. Das , P. Roy, K. C. Pal, C. Das, A. Banerjee, and J. K. Datta (2011) Studied the role of eggshell powder as an adsorbent for removal of fluoride from aqueous solution using batch technique. The maximum adsorption was achieved at pH 2.0-6.0. The investigators achieved around 94% removal of fluoride at initial metal ions concentration of 5 mg/l at optimum dose of 2.4 g/100ml and optimum time of 120minutes. Experimental data provided best fit with the Langmuir isotherm model, indicating monolayer sorption on a homogenous sur. The adsorption kinetics followed pseudo-second-order kinetic model indicating towards chemisorption. Intra-particle diffusion was not the sole rate controlling factor [19].

Naba Kr Mondal, Ria Bhaumik, Arnab Banerjee, Jayanta Kr Datta, Tanmoy Baur(2012) done a comparative study for removal of fluoride using activated silica gel (ASiG) and activated rice husk ash (ARHA) as adsorbents through batch studies. The authors reported that both adsorbents were efficient for the uptake of fluoride at pH2.0 and contact time 100 minutes. ASiG was found to be more efficient than ARHA with an initial fluoride concentration of 5mg/l,percentage of removal was 88.30 and 96.7 for ARHA and ASiG respectively.. The study on equilibrium sorption revealed that Langmuir isotherm model give best fit to experimental data. The nature of adsorption of fluoride on ARHA and ASiG was physical adsorption as inferred from the Dubinin-Radishkevich (D-R) isotherm model [20].

ISSN: 2319-5967
ISO 9001:2008 Certified
International Journal of Engineering Science and Innovative Technology (IJESIT)
Volume 3, Issue 3, May 2014

C.M.Vivek Vardhan and J.Karthikeyan(2011) carried out investigations for removal of Fluoride from water employing physico-chemical processes of adsorption and coagulation employing abundantly available and low-cost materials like Rice Husk, seed extracts of Moringa Oleifera (Drum stick), and chemicals like Manganese Sulphate and Manganese Chloride. Rice husk of 6g/l accomplished a removal of 83% of Fluoride from a 5mg/l of Fluoride solution requiring an equilibrium time of 3 hours. Equilibrium Isothermal data fitted well into rearranged linearised Langmuir adsorption model. Moringa oleifera seed extracts, Manganese Sulphate and Manganese Chloride accomplished removal percentages of 92, 94 and 91 of Fluoride from a 5mg/l test solution at a dosage of 1000 mg/l. A slightly acidic pH of 6.0 was found favourable for Fluoride removal by Manganese sulphate, Manganese Chloride and MOE [21].

S. T. Ramesh, R. Gandhimathi, P. V. Nidheesh and M. Taywade (2012) investigated the adsorption potential of bottom ash for defluoridation of drinking water using batch and continuous fixed bed column studies. The optimum contact time for fluoride was found to be 105 minutes with the maximum efficiency of 73.5 % at 70mg/100ml bottom ash dosage. The optimum pH was found to be pH 6 with the maximum efficiency of 83.2 %.During the column studies; increase in fluoride ion uptake with an increase in the bed height was due to an increase in the contact time. A high degree of linearity of the BDST plot indicates the validity of the BDST Model when applied to continuous column studies [22].

S. Kagne, S. Jagtap, P. Dhawade, S.P. Kamble, S. Devotta, S.S. Rayalu(2007) investigate the potential of cement hydrated at various time intervals for the removal of excess F− from aqueous solution by using batch adsorption studies. It was found that the HC shows significant F− removal over a wide range of pH (3–10). the maximum removal of fluoride was 92.37% with 10gm/l of hydrated cement, contact time 24 hours and initial fluoride concentration 5.9 mg/l.The experimental data generated from batch adsorption experiments fitted well into the linearly transformed Freundlich and Langmuir isotherms[23].

Das Kumar Malay and Attar J. Salim (2011) conducted comparative study of batch adsorption of fluoride using commercial and natural adsorbent. Different activated adsorbent samples like activated alumina, activated bauxite, Activated rice husk were taken and equilibrium studies were conducted to find a suitable adsorbent. Equilibrium adsorption study was carried out by the author and by Freundlich isotherm it was observed that activated alumina was the best as it gave minimum value of slope (0.152) and equilibrium constant (0.601), which shows that it is having maximum adsorption capacity. Activated bauxite was with slope of 0.965 and equilibrium constant 0.593 which was followed by activated rice husk with slope of 0.659 and equilibrium constant 0.155. So authors concluded activated alumina as best adsorbent and activated rice husk as inferior adsorbent.

According to Langmuir isotherm the value of RL was maximum for activated alumina (0.448) than activated bauxite (0.246) and minimum for activated rice husk is (0.152) and also the value of R^2 0.986, 0.982, 0.814 shows the same result. So activated alumina is more favourable for this adsorption with respect to activated bauxite and activated rice husk [24].

Veeraputhiran V. and Alagumuthu G (2011) studied fluoride removal from aqueous solution using Phyllanthus emblica adsorbent. The highest adsorption capacity was obtained at neutral pH with adsorbent dose 0.75g and initial metal ions concentration of 3 ppm. The percentage removal of fluoride from the solution was observed 82.1%. The adsorption of fluoride by Phyllanthus emblica was heterogeneous in nature [25].

S. A. Valencia-Leal, R. Cortés-Martinez, R. Alfaro-Cuevas-Villanueva (2012) Evaluated the Guava Seeds (Psidium Guajava) as Low-Cost Bio sorbent for the Removal of Fluoride from Aqueous Solutions. Maximum adsorption occurred between pH5.0 to 8.0.The adsorption of fluoride was found endothermic in nature Langmuir and Freundlich adsorption isotherm models were applied to evaluate the adsorption data. The pseudo-second order model describes the fluoride sorption kinetics using guava seed at different temperature. The Langmuir model best describes the isotherm's experimental data, which may indicate that the sorption mechanism of fluoride ions on guava seed is chemisorption on a homogeneous material [26].

A. V. Jamode, V. S. Sapkal and V. S. Jamode (2004) assessed the suitability of inexpensive leaf adsorbents to effectively remediate fluoride-contaminated water. The leafs of neem (*Azadirachta indica*), pipal (*Ficus*

ISSN: 2319-5967
ISO 9001:2008 Certified
International Journal of Engineering Science and Innovative Technology (IJESIT)
Volume 3, Issue 3, May 2014

religiosa) and khair (*Acacia catechu willd*) trees were used in this study. The study concludes that at the highest fluoride ion concentration (15 mg/l), the fluoride ion level in the effluent gradually decreased to 0 mg/l within 180 min at 29 ± 0.5°C when the dose of adsorbent is 10 g/l. The process adsorption by treated bio sorbents follows Langmuir isotherm, which comprises statistical and empirical data estimated from Isotherm equation [27].

Mohammad Mehdi Mehrabani Ardekani, Roshanak Rezaei Kalantary, Sahand Jorfi, Mohammad Nurisepehr (2013) compared the efficiency of Bagas, Modified Bagas and Chitosan for fluoride removal from water by adsorption. The pH value of 7, contact time of 60 min and adsorbent dose of 2 g/L were determined as optimum conditions for all three adsorbents. Chitozan and bagas did not show good capability for fluoride removal, but modified bagas showed more than 90% removal at optimized conditions, including the pH value of 7, contact time of 60 min and adsorbent dosage of 2 g/L. Both Langmuir and Freundlich isotherms show good correlation for description of results, but the Langmuir model with the correlation value of 0/99 is superior[28].

Kaushik Bandyopadhyay, Chandrima Goswami, Devaleena Chaudhuri, Arunabha Majumdar, Amal. K. Misra (2009) studied removal of fluoride from groundwater using broken concrete cubes as the adsorbing media. In batch adsorption study broken cube was found to remove about 80% fluoride at 120 minutes of contact time with adsorbent dose of 6mg/100ml at pH 7.0. In column experiment with an influent fluoride concentration of 8mg/L, pH of 7, the effluent fluoride concentration was reached 1.5mg/L at 26L cumulative flow which has been considered as cut off point of the curve [29].

Dwivedi Shubha, Mondal Prasenjit and Balomajumder Chandrajit (2014) investigated the removal of fluoride using *Citrus limetta* in batch reactor. The Freundlich isotherm gives well prediction of the equilibrium adsorption (R2 = 0.996). The specific uptake increases from 0.089 mg/g to 1.35mg/g with the increase in initial fluoride concentration from 1 mg/L to 20 mg/L.Maximum specific uptake obtained from Langmuir isotherm is found to be 1.82 mg/g. When the initial fluoride concentration is 5mg/L, the removal efficiency of mosambi peel is 82.5%. Adsorption kinetics is presented well by pseudo second order rate equation and the estimated equilibrium concentration falls within ~ 6 % error limit [30].

VI. CONCLUSION

The paper briefly highlighted the importance of adsorption process and its benefits. Also the overview of various papers publishes in various journals on removal of fluoride ions from water or wastewater by adsorption using various low cost adsorbents instead of expensive commercial adsorbents. The efficiency of different adsorbents in the removal of fluoride depends on dose of adsorbate, characteristics of adsorbent, pH, temperature, contact time, speed of agitation, etc. A review of various low cost adsorbents presented here shows a great potential for the fluoride removal. The use of commercially available adsorbents can be replaced by the inexpensive and effective low cost adsorbents. There is need for more studies to better understand the process of low-cost adsorption and to demonstrate the technology effectively.

REFERENCES

[1] Wang, Y.; Reardon, E. J. Activation and regeneration of a soil sorbent for defluoridation of drinking water. Appl. Geochem. **2001**, 16: 531-9.

[2] Lounici, H. Study of a new technique for fluoride removal from water. Desalination **1997**, 114: 241-251.

[3] Srimurali, M.; Pragathi, A.; Karthikeyan, J. A study on removal of fluorides from drinking water by adsorption onto low-cost materials. Environ. Pollut. **1998,** 99: 285-9.

[4] Hichour, M.; Persin, F.; Sandeaux, J.; Gavach, C. Fluoride removal from waters by Donnan dialysis. Sep. Purif. Technol. **2000,** 18: 1-11.

[5] Manahan, S. E. Environmental Chemistry, 6th ed., Lewis Publishers, Florida, **1994.**

[6] Amor, Z.; Malki, S.; Taky, M.; Bariou, B.; Mameri, N.; Elmidaoui, A. Optimization of fluoride removal from brackish water by electro dialysis, Desalination **1998**, 120: 263-271.

[7] D. S. Bhargava and D. J. Killedar, Batch Studies of Water Defluoridation Using Fishbone Charcoal, J. Water Pollution Control Federation, 63(6), 848-858 (1991).

[8] D. J. Killedar and D. S. Bhargava, An Overview of Defluoridation Methods (Part-I), Journal IPHE, 1, 21-29(1998a).

ISSN: 2319-5967
ISO 9001:2008 Certified
International Journal of Engineering Science and Innovative Technology (IJESIT)
Volume 3, Issue 3, May 2014

[9] D. J. Killedar and D. S. Bhargava, An Overview of Defluoridation Methods (Part-II), Journal IPHE, 2, 78-82(1998b).

[10] T. Wijesundara, Low Cost Defluoridation of Water Using Broken Bricks, 30th WEDC International Conference Vientiane, Lao PDR (2004).

[11] W. W. Choi and Y. Chen, The removal of Fluoride from Waters by Adsorption, J. AWWA, 71(10), 562- 569 (1979).

[12] Renge.V.C, Khedkar.S.V & Pande.S.V (2012) "Removal of Heavy Metals from wastewater using low cost adsorbents: A review" Scientific Reviews &Chemical Communications, Vol.2 No.4, pp.580-584.

[13] PaliShahjee, B.J.Godboley, A.M.Sudame, REMOVAL OF FLUORIDE FROM AQUEOUS SOLUTION BY USING LOW COST ADSORBENT, International Journal of Innovative Research in Science, Engineering and Technology Vol. 2, Issue 7, July 2013.

[14] NABA KUMAR MONDAL*, RIA BHAUMIK, TANMOY BAUR, BISWAJIT DAS, PALAS ROY and JAYANTA KUMAR DATTA. Defluoridation of Water by Tea Ash:An Unconventional Biosorbent, Chemical Science Transactions DOI:10.7598/cst2012.134 ISSN/E-ISSN: 2278-3458/2278-3318.

[15] G. Alagumuthu*, V. Veera puthiran and R. Venkataraman, Adsorption Isotherms on Fluoride Removal: Batch Techniques. Scholars Research Library, Archives of Applied Science Research, 2010, 2 (4): 170-185.

[16] Bhagyashree M Mamilwar, A.G.Bhole, A.M.Sudame / International Journal of Engineering Research and Applications (IJERA) ISSN: 2248-9622 www.ijera.com Vol. 2, Issue 4, July-August 2012, pp.334-338.

[17] N. Gandhi, D. Sirisha, K.B. Chandra Shekar and Smita Asthana., Removal Of Fluoride From Water And Waste Water By Using Low Cost Adsorbents.,International Journal of ChemTech Research,CODEN(USA): IJCRGG ISSN : 0974-4290 Vol.4, No.4, pp 1646-1653, Oct-Dec 2012.

[18] Patil Satish, Renukdas Sameer, Patel Naseema, Defluoridation of Water Using Biosorbents: Kinetic and Thermodynamic Study, International Journal of Research in Chemistry and Environment Vol. 3 Issue 1 January 2013(125-135) ISSN 2248-9649.

[19] R. BHAUMIK, N. K. MONDAL*, B. DAS , P. ROY, K. C. PAL, C. DAS, A. BANERJEE, and J. K. DATTA, Eggshell Powder as an Adsorbent for Removal of Fluoride from Aqueous Solution: Equilibrium, Kinetic and Thermodynamic Studies, ISSN: 0973-4945;CODEN ECJHAO E-Journal of Chemistry 2012, 9(3),1457-1480.

[20] Naba Kr Mondal, Ria Bhaumik, Arnab Banerjee, Jayanta Kr Datta, Tanmoy Baur, A comparative study on the batch performance of fluoride adsorption by activated silica gel and activated rice husk ash, INTERNATIONAL JOURNAL OF ENVIRONMENTAL SCIENCES Volume 2, No 3, 2012 , ISSN 0976 – 4402.

[21] C.M.Vivek Vardhan and J.Karthikeyan, REMOVAL OF FLUORIDE FROM WATER USING LOW-COST MATERIALS.Fifteenth International Water Technology Conference, IWTC-15 2011, Alexandria, Egypt.

[22] S. T. Ramesh, R. Gandhimathi, P. V. Nidheesh and M. Taywade. Batch and Column Operations for the Removal of Fluoride from Aqueous Solution Using Bottom Ash, Environmental Research, Engineering and Management, 2012. No. 2(60), P. 12-20 ISSN 2029-2139.

[23] S. Kagne, S. Jagtap, P. Dhawade, S.P. Kamble, S. Devotta, S.S. Rayalu, Hydrated cement: A promising adsorbent for the removal of fluoride from aqueous solution, Journal of Hazardous Materials 154 (2008) 88–95.

[24] Das Kumar Malay and Attar J. Salim, Comparative Study of Batch Adsorption of Fluoride Using Commercial and Natural Adsorbent, Research Journal of Chemical Sciences, Vol. 1(7), 68-75, Oct. (2011).

[25] Veeraputhiran V. and Alagumuthu G, Treatment of High Fluoride Drinking Water Using Bioadsorbent , Research Journal of Chemical SciencesVol. 1(4), 49-54, July (2011**).**

[26] S. A. Valencia-Leal, R. Cortés-Martínez, R. Alfaro-Cuevas-Villanueva, Evaluation of Guava Seeds (Psidium Guajava) As a Low-Cost Biosorbent for the Removal of Fluoride from Aqueous Solutions; International Journal of Engineering Research and Development e-ISSN: 2278-067X, p-ISSN : 2278-800X, www.ijerd.com Volume 5, Issue 4 (December 2012), PP. 69-76.

[27] A. V. Jamode, V. S. Sapkal and V. S. Jamode, Defluoridation of water using inexpensive adsorbents, J. Indian Inst. Sci., Sept.–Oct. 2004, 84, 163–171.

[28] Mohammad Mehdi Mehrabani Ardekani, Roshanak Rezaei Kalantary, Sahand Jorfi, Mohammad Nurisepehr, Comparison the Efficiency of Bagas, Modified Bagas and Chitosan for Fluoride Removal from Water by Adsorption, Journal of Environmental Treatment Techniques www.jett/dormaj.com (Volume 1, issue 1, pp. 1-7).

ISSN: 2319-5967
ISO 9001:2008 Certified
International Journal of Engineering Science and Innovative Technology (IJESIT)
Volume 3, Issue 3, May 2014

[29] Kaushik Bandyopadhyay , Chandrima Goswami , Devaleena Chaudhuri , Arunabha Majumdar , Amal. K. Misra, REMOVAL OF FLUORIDE FROM GROUNDWATER USING BROKEN CONCRETE CUBES AS THE ADSORBING MEDIA, IGC 2009, Guntur, INDIA.

[30] Dwivedi Shubha, Mondal Prasenjit and Balomajumder Chandrajit, Removal of Fluoride using Citrus limetta in batch Reactor: Kinetics and Equilibrium Studies, Research Journal of Chemical Sciences Vol. 4(1), 50-58, January (2014).

AUTHOR BIOGRAPHY

Suman Mann received the B.E (Civil Engg.) Degree in 2005 from NIT Hamirpur and pursuing and M.Tech. (Envt. Engg.) From Delhi Technological University (2011 to 2014). During 2005 to 2008, worked as lecturer CRRIT, Delhi. Presently working as lecturer in DTTE, Govt of NCT of Delhi (2008 to till date).

Dr Anubha Mandal is a scientist 'C' UGC. Currently working as Assistant professor in Delhi Technological University, Delhi

Accepted Manuscript

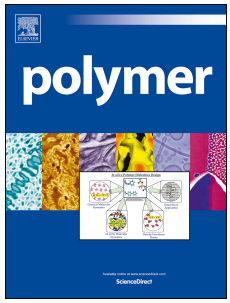

Protein functionalized Pt nanoparticles-conducting polymer nanocomposite film: Characterization and immunosensor application

Sujeet K. Mishra , Avanish K. Srivastava , Devendra Kumar , Ashok Mulchandani , Rajesh

PII: S0032-3861(14)00463-7

DOI: 10.1016/j.polymer.2014.05.061

Reference: JPOL 17014

To appear in: *Polymer*

Received Date: 22 January 2014

Revised Date: 16 May 2014

Accepted Date: 27 May 2014

Please cite this article as: Mishra SK, Srivastava AK, Kumar D, Mulchandani A, Rajesh , Protein functionalized Pt nanoparticles-conducting polymer nanocomposite film: Characterization and immunosensor application, *Polymer* (2014), doi: 10.1016/j.polymer.2014.05.061.

This is a PDF file of an unedited manuscript that has been accepted for publication. As a service to our customers we are providing this early version of the manuscript. The manuscript will undergo copyediting, typesetting, and review of the resulting proof before it is published in its final form. Please note that during the production process errors may be discovered which could affect the content, and all legal disclaimers that apply to the journal pertain.

Graphical abstract

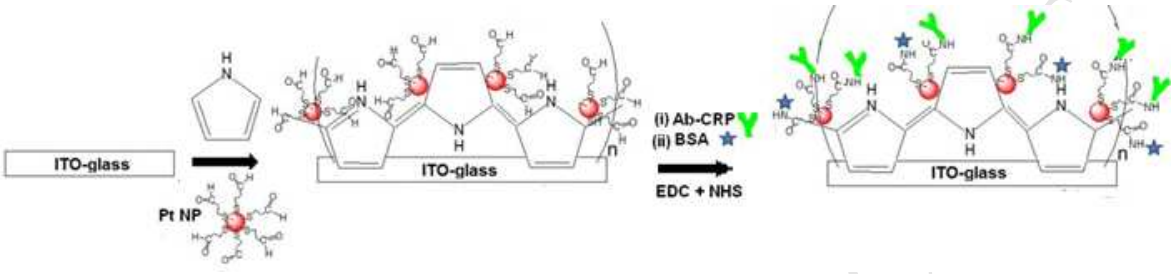

ACCEPTED MANUSCRIPT

ACCEPTED MANUSCRIPT

Protein functionalized Pt nanoparticles-conducting polymer nanocomposite film: Characterization and immunosensor application

Sujeet K Mishra[a,b], Avanish K Srivastava[a], Devendra Kumar[b] ,Ashok Mulchandani[c] and Rajesh[a*]

[a] *CSIR-National Physical Laboratory Dr. K.S. Krishnan Road, New Delhi-110012, India*

[b] *Department of Applied Chemistry, Delhi Technological University, Bawana Road, Delhi-110042, India*

[c] *Department of Chemical and Environmental Engineering, University of California, Riverside, California 92521, USA*

ACCEPTED MANUSCRIPT

Keywords: conducting polymer, nanoparticles, protein, covalent immobilization.

*Corresponding author. E-mail: rajesh_csir@yahoo.com; adani@engr.ucr.edu

Abstract

We report an electrochemically prepared 3-mercaptopropionic acid (MPA) capped Pt nanoparticles-Polypyrrole (PPy) nanocomposite film based bioelectrode for the detection of human C-reactive protein (αCRP). The electrochemical deposition provides homogeneous distribution of ultrafine Pt(MPA)-NPs within the uniform and adherent PPy film with high degree of geometrical conformity and controllable film thickness. Protein antibody, Ab-αCRP, was covalently immobilized through the site specific carboxyl groups of Pt(MPA)-NPs within the polymer nanocomposite film by carbodiimide coupling reaction. The bioelectrode interfacial surface electron transport study towards protein antigen, Ag-αCRP, was carried out by electrochemical impedance spectroscopy (EIS). The value of 'n', a Constant Phase Element exponent used as a gauge of the heterogeneity, for Pt(MPA)-PPy nanocomposite film was found to be 0.88~1 which is indicative of a rather homogenous morphology of the composite film with minimal defects. The EIS of the bioelectrode exhibited significant changes in charge transfer resistance (R_{et}) component at a low ac frequency of < 20 Hz towards Ag-αCRP detection over a linear range of 10 ng mL^{-1} to 10 µg mL^{-1} in PBS with a sensitivity of 109.74 Ωcm^2 per decade.

ACCEPTED MANUSCRIPT

1. Introduction

With the rapid development of nanotechnology over the past decade, various nanomaterials, including nanowires, nanotubes and nanoparticles have found a variety of potential applications especially in the field of protein detection and catalysts modification [1-3]. The nanomaterials are preferred as suitable matrices for antibodies immobilization with proper orientation, due to their unique optical, electrical and molecular properties and in particular their extremely large surface areas, high reactivity and beneficial chemically tailored physicochemical properties, that help to obtain a sensitive, compact and stable immunosensor [4,5]. Nanocomposites of electrically conducting polymers and metal nanoparticles have found great attention not only because of the scientific curiosity, but also for their potential applications in molecular electronic devices, gas sensors, biosensors, capacitors and catalysts [6-10]. Among conducting polymers (CPs), polypyrrole (PPy) is one of the most widely studied CPs due to its easy synthesis, reasonably high conductivity, controllability of surface properties and fairly good environmental stability [11, 12]. Electron transport properties of conducting polymer are unique because they are composed of 1-dimensional chains that have both polydispersity and packing arrangement of degree of disorder in addition to doping level. Thus, the charge carriers are transported intrachain or inter-chain by a hopping mechanism. In PPy the electrical conduction arises due to the electron movement within the delocalized conjugated π-molecular orbital backbone and positive charge defects known as polarons (radical ions coupled to a spatially extended distortion of the bond lengths). At higher charging levels, pairs of polarons combine to form bipolarons which are able to migrate along the conjugated polymer chain and provide the main charge transport mechanism within the conducting polymer [13, 14]. Moreover, PPy is biocompatible and shields the electrodes from fouling and interfering with electrochemically active materials, making it an

attractive candidate for biomedical applications [15]. The nanocomposites of PPy and noble metal particles (such as Pt, Au, Ag, and Pd) exhibit interesting and excellent physical or chemical properties (optical, electrochemical and conductive properties) due to the hybridization of metal nanoparticles and π-conjugated polymers and are currently of great research interest, essentially motivated by their high analytical sensitivity in sensing applications [16-18]. Also, the polymer coating improves the stability of the metal nanoparticles which are otherwise stable as a suspension solution only and tend to undergo irreversible aggregation over time. Among the noble metals, Pt nanoparticles are typical inorganic nanomaterials with excellent chemical and physical properties [19]. The distinctive properties of Pt at nanoscale dimensions have attracted widespread attention in their utilization for the bioassay, especially for electrochemical detection, where they can be used as conductive pathway for electron transfer, improving the electrochemical reactions at a low potential. The Pt nanoparticles are considered very effective as a matrix for the immobilization and study of various kinds of biomolecules and macromolecules, such as DNA, enzymes, other proteins and antibodies by taking advantage of their biocompatibility and high surface area [20, 21].

C-reactive protein (αCRP) is an acute phase homo-pentameric plasma protein belonging to the 'pentraxin' family, consisting of five identical ~23 kDa homologous subunits which are non-covalently associated around a central pore [22]. It is produced by the liver and has traditionally been used as a reliable biomarker for tissue injury, infection, and inflammation in human blood serum. However, studies have shown that an elevated αCRP level is also a significant indicator for possible cardiovascular diseases (CVD), such as atherosclerosis, angina, coronary heart disease, peripheral artery disease, myocardial infarction and stroke [23-26]. According to the American Heart Association and the Center for Disease Control and

Prevention, the risks for cardiovascular diseases are low for a αCRP concentration <1.0 mg L^{-1}, moderate for a αCRP level from 1.0 to 3.0 mg L^{-1}, and high for concentrations > 3.0 mg L^{-1} [27]. As a result, αCRP can serve as an important risk assessment factor for the development of cardiovascular diseases. Over the years, various assay methods for αCRP detection have been developed and improved, such as latex agglutination, nephelometry, turbidimetry, fluorescent polarization and the latest one which is the most widely used technique in the clinic is enzyme-linked immunosorbent assay (ELISA) [28-30]. Nevertheless, all these methods have common drawbacks i.e., they require long reaction times (several hours), labor-intensive processing and large and expensive equipments for measurement of the αCRP that requires expertise. Due to the risk of severe consequences for patients with high αCRP concentrations, bio-analytical devices of high sensitivity are required that allow a fast and precise diagnosis of disease at an early stage. Hu et al. has developed a CRP sensor based on Surface Plasmon Resonance (SPR) biosensing methodology, where CRP antibodies were bound to a gold (Au) surface through Protein G, having a detection limit of 8 nM (1 µg mL^{-1}) of purified CRP [31]. Meyer et al. has also established an SPR immunosensor for CRP detection based on two different anti-CRP antibodies, one for CRP entrapment and one for labeling, with a linear detection range of 16–40 nM (2–5 µg mL^{-1}) CRP in PBS buffer [32]. Recently, some other methods for CRP quantification including those based on piezoelectric microcantilevers [33], quartz crystal microbalance technology [34], microfluidics [35] and electrochemistry [36] have been developed during the past few years. Among these, the focus on Electrochemical Impedance Spectroscopy (EIS) based immunosensing method has increased significantly. EIS, a sensitive and non-destructive technique, based on the specific antigen–antibody interactions and electrochemical

transduction for analytical purposes, have gained wide interest due to their conceivable utility such as low cost, short response time, small size and sensitive platform [37].

In this work, we report a single step electrochemical polymerization of p-toluene sulphonic acid doped polypyrrole (PPy) in conjunction with 3-mercaptopropionic acid (MPA) capped Pt nanoparticles for the preparation of an electroactive Pt(MPA)-PPy nanocomposite film on an indium-tin-oxide (ITO) coated glass plate. The free carboxyl groups of the MPA capped Pt-NPs intercalated within the polymer film were utilized for the site specific immobilization of protein antibody, Ab-αCRP, using carbodiimide coupling reaction, for the construction of a bioelectrode. These 3-dimensional MPA capped Pt-NPs not only provided the high protein loading with efficient covalent binding due to their large surface area to volume ratio and availability of free pendant carboxyl groups for better probe orientation, but also facilitated the improved charge shuttling throughout the material. This site-specific and efficient bio-molecular immobilization of Pt-NPs together with the conducting polymer matrix helped in enhancing the impedance response sensitivity of the bioelectrode towards the detection of target protein antigen, Ag-αCRP, in phosphate buffer solution (PBS; pH 7.4).

2. Experimental Section

2.1 Reagents

Ab-αCRP (Cat 4C28 mAbC2) and Ag-αCRP (Cat 8C72) were obtained from Hytest (Turku, Finland). Mouse immunoglobulin-G (Ag-IgG) (Cat IGP3) was obtained from GENEI, Bangalore, India. Hydrogen hexachloroplatinate hexahydrate ($H_2PtCl_6 \cdot 6H_2O$) and sodium borohydride ($NaBH_4$) were purchased from Aldrich. Pyrrole, *p*- toluene sulphonic acid (pTSA), 3-Mercaptopropionic acid 99% (MPA), N-(3-Dimethylaminopropyl)-N'-ethyl carbodiimide hydrochloride (EDC) and N-Hydroxy Succinimide 98% (NHS) were obtained from Sigma-

Aldrich chemicals. All other chemicals were of analytical grade and used without further purification.

2.2 Apparatus

Electropolymerization, cyclic voltammetry (CV) and EIS measurements were done on a PGSTAT302N, AUTOLAB instrument from Eco Chemie, The Netherlands. CVs and EIS measurements were conducted in PBS (pH 7.4, 0.1 M KCl) solution containing a mixture of 2 mM $K_3[Fe(CN)_6]$ and 2 mM $K_4[Fe(CN)_6]$. The EIS experiments were carried out at a bias voltage of 0.3 V vs. Ag/AgCl with an ac voltage of 0.05 V in the frequency range of 1 Hz to 100 kHz. The EIS experimental data were circuit fitted by GPES (General purpose electrochemical system version 4.9, Eco Chemie) software and values of EIS parameters were obtained. XRD pattern were recorded using Bruker AXS Advance D8 powder X-ray diffractometer. Microstructural characterization of Pt(MPA)-PPy nanocomposite was carried out by high resolution transmission electron microscopy (HRTEM model: Tecnai G2 F30 STWIN with field emission gun, operated at 300 kV). Atomic force microscopy (AFM) images were obtained on VEECO/DICP2, USA scanning probe microscope and images were taken using the non-contact mode. FTIR spectra of the films were taken on a Nicolet 5700 FTIR spectrometer. All electrochemical measurements were carried out in a conventional three-electrode cell configuration consisting of the proposed modified electrode as working electrode, Ag/AgCl in saturated KCl as reference electrode and a platinum wire as an auxiliary electrode.

2.3 Preparation of bioelectrode

MPA capped Pt nanoparticles were synthesized according to the literature with slight modification [38]. For the preparation of Pt(MPA)-PPy nanocomposite film, the ITO coated glass plates (10 Ω /□) were first cleaned by sequential ultrasonic cleaning in soap solution,

acetone, ethanol, isopropyl alcohol and DI for 10 min each and dried in vacuum. The Pt(MPA)-PPy nanocomposite film was electrochemically deposited on an ITO-glass plate (0.25 cm^2) using chronopotentiometric method from an aqueous solution containing 0.1 mg mL^{-1} Pt(MPA), 25 mM pyrrole and 25 mM pTSA, at a fixed current density of 1 mA cm^{-2} with a total injected charge density of 250 mC cm^{-2}. Ab-αCRP was covalently attached to pendent carboxyl groups of MPA capped Pt NPs-PPy nanocomposite film on ITO-glass using EDC-NHS chemistry where EDC and NHS worked as a coupling agent and an activator, respectively. Pt(MPA)NPs-PPy/ITO-glass plate was first incubated in a solution mixture of 30 mM NHS and 150 mM EDC for 1 h and then in 100 µg mL^{-1} Ab-αCRP in PBS (pH 7.4), for an overnight period, at a temperature of 4°C, followed by washing with PBS and drying with N_2 gas flow. Finally, the bioelectrode was incubated in 1.0% (W/V) bovine serum albumin (BSA) solution for 30 min to block the non-specific reactive sites, if available, on the Pt-NPs and/or PPy surface, and subsequently rinsed with PBS, dried under N_2 gas flow and stored at 4 °C. The stepwise construction of the prototype assembly is schematically represented in scheme 1.

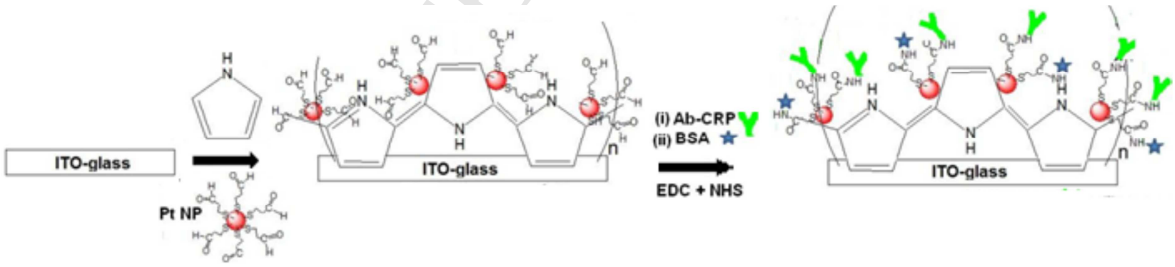

Scheme 1: Schematic representation of the stepwise fabrication of the bioelectrode

3. Results and Discussion

3.1 Micro structural characteristics

Figure 1 shows XRD spectra of both the pristine PPy and Pt(MPA)NPs-PPy nanocomposite films. A broad diffraction peak at $2\theta = 25.54^{\circ}$ (inset Fig. 1) was obtained for PPy, indicating a

low order of crystallinity due to the PPy intermolecular spacing. The XRD patterns of Pt(MPA)-PPy nanocomposite film showed a broad characteristic peak for PPy together with the faint Pt diffraction peaks indicative of the Pt NPs fully covered with PPy. These Pt(MPA)NPs characteristic peaks obtained at 2θ = 38.4°, 45.5°, and 64.70° corresponds to (111), (200), and (220) planes, respectively, of a faced center-cubic (fcc) structure.

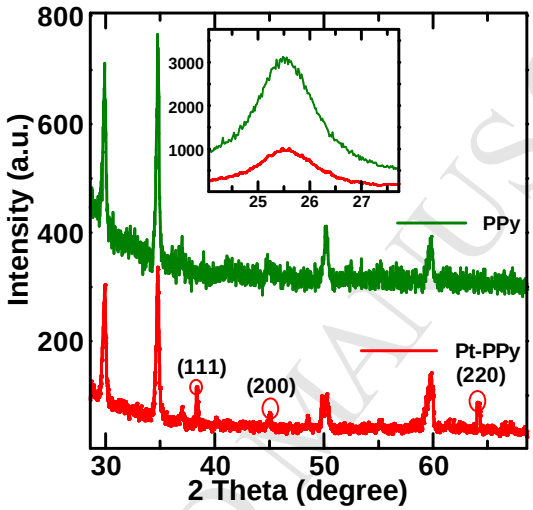

Fig.1: XRD Pattern of pristine PPy and Pt(MPA)NPs-PPy composite

Figure 2 shows the FTIR spectra of PPy and Pt(MPA)-PPy taken on an attenuated total reflection mode, which provides an additional information regarding the formation of Pt(MPA)-PPy nanocomposite. The pure PPy film (Fig. 2) shows the characteristic peaks of 893 cm^{-1} (C-H out-of-plane vibration) indicating the polymerization of pyrrole, 1036 cm^{-1} and 1176 cm^{-1} corresponding to C-H in-plane vibration and (N-C stretch bending) respectively, while the two other bands at 1405 cm^{-1} and 1515 cm^{-1} can be attributed to the symmetric and anti-symmetric ring stretching mode of PPy, indicating the extent of conjugation of the PPy structure. The FTIR spectra of Pt(MPA)-PPy composite film exhibited a sharp peak at 1677 cm^{-1} that may be attributed to C=O stretching mode of the free carboxyl groups of MPA capped Pt NPs

encapsulated in PPy matrix. Moreover, the significant changes were found both in peak's position as well as in intensity in the FTIR spectra of Pt(MPA)-PPy composite in comparison to pristine PPy, showing red shifts in the characteristic peaks at 893, 1036 and 1176 cm^{-1} to 825, 984 and 1168 cm^{-1}, respectively. This may be attributed to the doping of PPy with Pt(MPA) due to good interaction between the two moieties, as found earlier in case of PPy-Ag nanofiber composite [39].

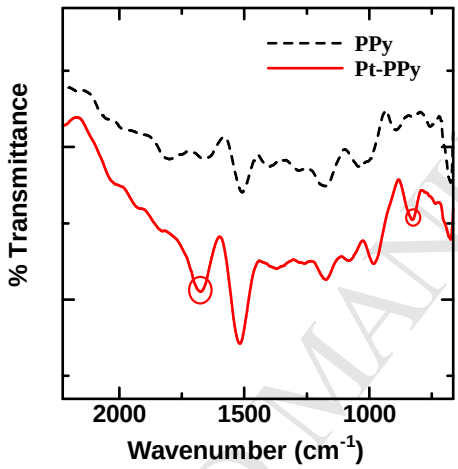

Fig.2: FTIR spectra of PPy and Pt(MPA)-PPy showing additional peaks and shift in peak positions (circle)

HRTEM characterization was carried out on the Pt (MPA)-PPy nanocomposite film, which was electrochemically deposited on a carbon-coated TEM grid by taking it as a working electrode using the same method as describe for ITO-glass support. The Pt-particles embedded in PPy exhibited a very random distribution of a homogeneous dispersion. A contour of Pt-particles revealing most of the instances very uniform formation of a nanocomposite of metal with a base-matrix of a polymer, has been marked with a white dotted line throughout the micrograph (Fig. 3a). A corresponding selected area electron diffraction pattern (SAEDP) recorded from the composite microstructure, elucidates the presence of important planes, in the form of Debye rings, of Pt-face centered cubic structure (space group: $Fm\bar{3}m$, and lattice parameter: a = 0.39

nm, ref. JCPDF card no. 040802) with the interplanar spacings of 0.23, 0.20 and 0.14 nm corresponding to hkl: 111, 200 and 220, respectively (inset in Fig. 3a). An open arrow marked on a diffuse ring shows the electron diffraction pattern of the PPy (inset in Fig. 3a), typical reciprocal space information normally obtained in case of a polymer-matrix. It is important to mention that there is also a possibility of the existence of a minor crystallinity in polymer too, nevertheless in general such materials gives rise to diffuse-ring contrast in the reciprocal space. However a coexistence of uniform rings of Pt and diffuse ring of PPy further authenticates a good quality homogeneous two phase material of a nano-composite. Atomic scale imaging performed on polymer-Pt(MPA)NPs composite clearly shows that the individual Pt-particles are immersed in the polymer matrix without any porosity leaving behind a good interface between the two dissimilar materials (Fig. 3b). In both the particles, crystallographic planes of hkl: 111 (interplanar spacing: 0.23 nm) are well oriented and constituted the entire individual crystallites. Moreover, the individual Pt-particles of about 4 to 5 nm in size are separated apart about a distance of 5 nm with a uniform linkage of PPy-matrix in between (Fig. 3b).

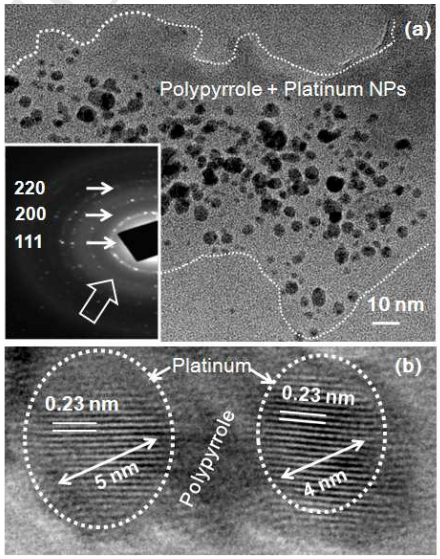

Fig.3: HRTEM image showing (a) distribution of Pt-nanoparticles in a PPy-matrix, and (b) atomic scale images of Pt-nanoparticles in the PPy matrix; Inset: SAEDP of nanocomposite

The surface morphology of the substrate was further investigated by taking the subtle AFM surface topographical images of the pristine PPy, Pt(MPA)NPs-PPy composite and biofunctionalized Ab-αCRP/Pt(MPA)NPs-PPy film, as shown in Fig. 4. AFM image of pristine PPy (Fig.4a) shows globular morphology of the polymer film with significant depressions and high points, having surface roughness parameter (R_a) value of 8.8 nm. However, this has been found to be altered to a symmetric dense grainy structure having R_a value of 2.7 nm in the Pt(MPA)NPs-PPy composite film with the formation of some large grains by nanometric subunits (Fig.4b). A significant increase in R_a value to 3.9 nm showed a comparatively high surface roughness of the composite film after protein Ab-αCRP immobilization (Fig. 4c) with a globular looking feature of the protein molecules [40]. This may be due to the non compact assembly of the protein molecules over the composite film resulting from the covalent bonding of protein to free carboxyl groups of Pt(MPA)NPs over the PPy matrix.

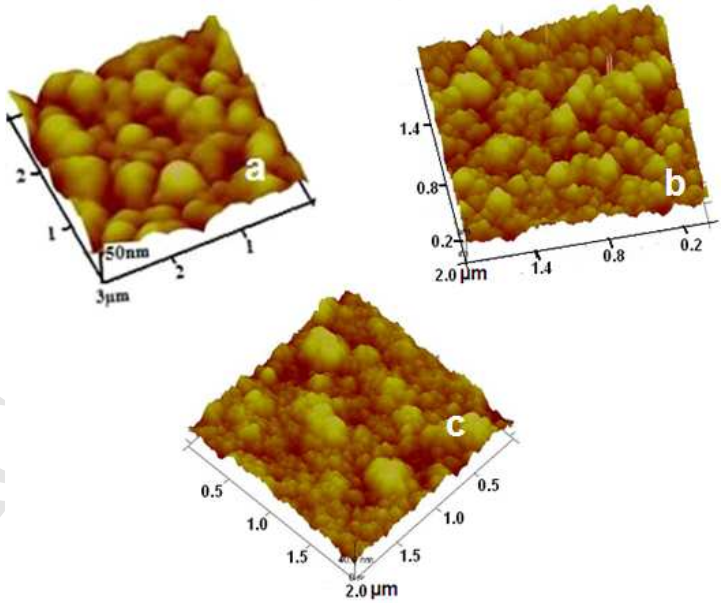

Fig.4: AFM images of (a) PPy/ITO-glass, (b) Pt(MPA)NPs-PPy/ITO-glass and (c) Ab-αCRP/Pt(MPA)NPs-PPy/ITO-glass plate

3.2 Electrochemical characterization of the bioelectrode

Alternating current (AC) impedance or EIS is known as an effective tool for the qualitative and quantitative characterization of electrochemical processes occurring in the conducting polymer films [41, 42]. EIS is a sensitive technique which can monitor the electrical response (current and its phase) of an electrochemical system after application of a periodic small amplitude AC signal in a wide range of frequencies. This has been chosen as the main characterization technique to evaluate the interfacial properties of the electrode while controlling its electrical properties [43]. An equivalent circuit was designed to fit the impedance spectra of the electrode for the complete analysis of the impedance behavior. The Randle's equivalent circuit (inset Fig. 5) is frequently used to elucidate the electrochemical properties of electrode-solution interfaces with the occurrence of Faradaic current and diffusion transport [44]. This equivalent circuit can be interpreted in terms of a simple network consisting of the bulk electrolyte resistance, R_s, in series with a R||C network made of two parallel current branches: (i) a Faradaic-current branch represented by an electron transfer resistance, R_{et}, serially connected to a Warburg impedance Z_w, and (ii) a non Faradaic-branch consisting of the double layer capacitance, C_{dl}. Two components in the circuit, C_{dl} and R_{et}, depend on the dielectric and insulating features at the electrode/electrolyte interface, and are controlled by the surface modification of the electrode while R_{et}, controls the interfacial electron-transfer rate between the redox probe in solution and the electrode support. Some factors like microscopic chemical inhomogeneity and roughness of the electrode make it difficult to describe such a system in terms of the known properties of an ideal capacitor. So, for such systems a non-intuitive circuit element called Constant Phase Element (CPE) has been used for the purpose of describing the electrochemical behavior of inhomogeneous electrode. CPE is thus related to surface inhomogeneity, roughness or fractal

geometry, electrode porosity, current and potential distribution associated with the electrode geometry and its impedance is represented by the Eqn. 1 [45]:

$$Z_{CPE}(\omega) = 1/Y_0 (j\omega)^n \quad (1)$$

where Y_0 is the frequency-independent constant relating to the surface electroactive properties, ω is the radial frequency, j is an imaginary unit, the exponent *n* arises from the slope of log Z vs. log f (and has values $-1 \leq n \leq 1$). An n value of zero corresponds to a pure resistor; a unit value of *n* corresponds to a pure capacitor, while a 0.5 value corresponds to Warburg impedance (Z_w) which is associated with the domain of mass transport control arising from the diffusion of ions to and from the electrode/solution interface. The deviation of frequency (ω) exponent n from ideal values was attributed to the homogeneities of analyzed layer, such as roughness or defects. In the present case, the value of n for the Pt(MPA)NPs-PPy composite film was found close to 1 (table 1) , which indicated a minimal defects in the fabricated nanocomposite film on the electrode surface and the CPE resembling a capacitor.

The modified Randles' equivalent circuit was used to obtain fitted Nyquist plots that match with experimental Nyquist plots through computer simulations. The Nyquist plots (real part of the impedance Z' vs. imaginary part -Z″) obtained after various steps of surface modifications of the electrode are presented in Fig. 5. The semicircle diameter of the Nyquist plot is equal to R_{et} which controls the electron transfer kinetics of the redox probe at the electrode interface. Since the Chi-squared function (χ^2) is the measure of the quality of the fitted data, a small χ^2 of the order of 10^{-4} obtained in the present case suggested an appropriate selection of the circuit model. Significant differences in the impedance spectra in terms of R_{et} values (Table 1) were observed during stepwise modification of the electrode.

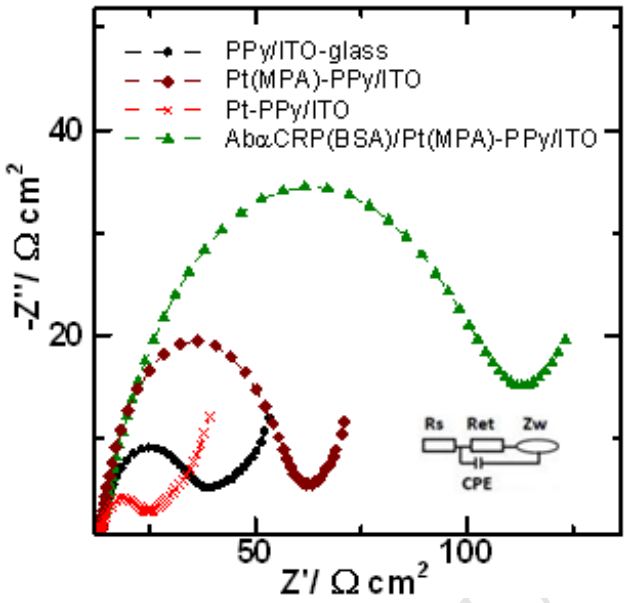

Fig.5: Nyquist plots obtained for pristine PPy-ITO glass, Pt(MPA) NPs-PPy /ITO-glass, Pt-PPy/ITO-glass and Ab-αCRP/Pt(MPA)NPs-PPy/ITO-glass in PBS (pH 7.4, 0.1 M KCl) containing 2 mM $[Fe(CN)_6]^{3-/4-}$

The bare PPy/ITO-glass electrode showed a R_{et} value of 26.8 Ω cm^2, which increases to 46.2 Ω cm^2 for Pt(MPA)NPs-PPy/ITO-glass electrode with a decrease in Y_0 value from 4.36 to 2.46 µF cm^{-2}. This increase in R_{et} value and subsequent decrease in Y_0 value for Pt(MPA)NPs-PPy/ITO-glass electrode may be attributed to the presence of negatively charged carboxyl terminal groups on the electrode surface which generates a repulsive effect towards negatively charged probe ions at the electrode/solution interface thus reducing the ability of the probing electrolyte to penetrate the layer. This assumption was further evidenced by the use of non-carboxyl functionalized Pt NPs–PPy/ITO-glass electrode which showed a drop off in R_{et} value to 14.2 Ω cm^2 with a significant increase in Y_0 value to 5.1 µF cm^{-2} due to the unhindered approach of the probe ions towards the electrode surface at the electrode/solution interface. A significant increase in the R_{et} value to 98.5 Ω cm^2 and decrease in Y_0 value to 1.88 µF cm^{-2} was obtained after the

site specific immobilization of the protein Ab-αCRP on the Pt(MPA)NPs-PPy/ITO-glass electrode. This increment in the R_{et} value and decrease in Y_0 value is due to the insulating behavior of the immobilized protein antibody layer on the bioelectrode surface, which acts as an electron communication and mass-transfer blocking layer, thereby hindering the access of redox probe towards the electrode surface and thus resulting in a sluggish electron-transfer kinetic.

Although the Nyquist plots are more commonly displayed, the data in a Nyquist plot is often poorly resolved (particularly at high frequencies), and the explicit frequency dependence is not displayed. Hence, Bode plot [Fig. 6] was used to provide a more clear description of the electrochemical system's frequency-dependent behavior. The Bode plots display both the logarithm of the total impedance |Z| as calculated by Eqn. 2 and the phase angle (φ) as a function of the logarithm of the frequency.

$$Z(\omega)=Z'(\omega)+i\,Z''(\omega) \qquad (2)$$

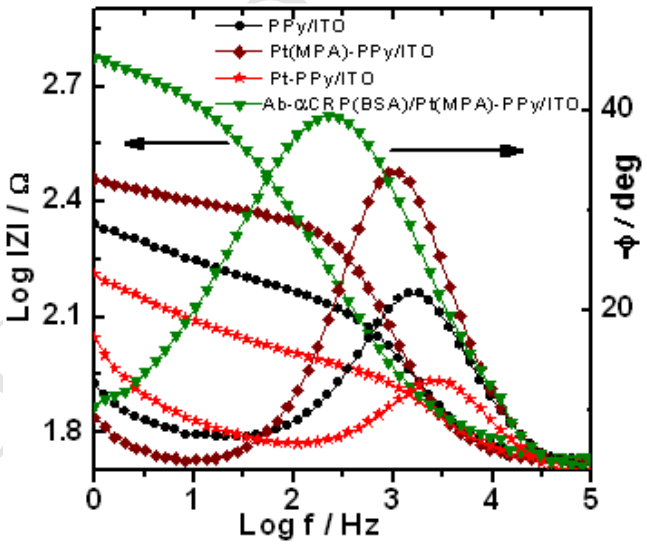

Fig.6: Bode plots of pristine PPy-ITO glass, Pt(MPA) NPs-PPy /ITO-glass, Pt-PPy/ITO-glass and Ab-αCRP/Pt(MPA)NPs-PPy/ITO-glass in PBS (pH 7.4, 0.1 M KCl) at bias voltage of 0.3 V vs Ag/AgCl with an ac voltage of 0.05 V in the frequency range of 1 Hz to 100 kHz.

In the Bode plot as shown in Fig. 6, φ was found to be nearly zero at a frequency > 25 KHz, which corresponds to in phase relationship between the applied voltage and the current, resembling the circuit element R_s. Negligible changes were obtained in the Log |Z| values for the modified electrodes with respect to changes in frequency values in this region indicating that the R_s is independent of frequency. At frequency < 25 KHz, particularly in the intermediate range of frequency where an increase in the value of φ was obtained for the modified electrodes with peak values of φ > 0° but < 90° showed the presence of a dielectric region where the signal was dominated by the dielectric pseudo capacitive circuit element, CPE. It is to be noted that in the case of bioelectrode the peak value of φ gets shifted towards the lower frequency region in comparison to both the Pt(MPA)NPs-PPy/ITO-glass and pristine PPy/ITO-glass electrodes indicating the presence of the charge storage properties i.e. showing a capacitive behavior even at low frequencies. At lower frequencies, the impedance corresponding to CPE becomes very high so the current flows only through R_{et} and Z_w. This phenomena was observed at frequency < 80 Hz for both the Pt(MPA)NPs-PPy/ITO-glass and PPy/ITO-glass electrodes while the same was observed at comparatively much lower frequency of <20Hz for the bioelectrode exhibiting a predominant charge transfer behaviour. This bio interfacial charge transfer phenomenon at a very low frequency region shows a biocompatible behaviour of the bioelectrode.

Table 1: EIS characteristic parameters at various stages of surface modification of the electrodes

Type of Electrodes	R_{et} (Ω cm^2)	CPE		Z_w (x10^{-3}) (Ω cm^2)	χ^2 (x10^{-4})	δ (μm)
		Y_0 (μF cm^{-2})	n			
PPy/ ITO-glass	26.8	4.36	0.84	5.42	3.08	56.5
Pt(MPA)-PPy/ ITO	46.2	2.46	0.88	5.94	3.15	59.1
Pt-PPy/ ITO	14.2	5.10	0.85	5.10	2.45	55.2
Ab-αCRP/Pt(MPA)- PPy / ITO	98.5	1.88	0.86	4.18	1.48	69.1

The thickness of the as prepared Pt(MPA)-PPy composite film was estimated from CPE using a modified Brug [46] equation as reported by Brayan et al. [47]. The impedance associated with a simple Faradaic reaction without diffusion can be related to CPE as shown in Eqn. 3:

$$Z(\omega) = R_s + \frac{R_{et}}{1 + (j\omega)^n Z_0 R_{et}} \quad (3)$$

The total admittance of the electrode can also be related to CPE by Eqn. (4) as

$$Y = \frac{1}{R_s}[1 - \frac{R_{et}}{R_s+R_{et}}(1 + \frac{R_s R_{et}}{R_s+R_{et}} Z_0(j\omega)^n)^{-1}] \quad (4)$$

where R_s is the Ohmic resistance and R_{et}, Z_0 and n represent global properties. Eq. (4) can be represented in terms of a characteristic time constant τ_0 as

$$Y = \frac{1}{R_s}[1 - \frac{R_{et}}{R_s+R_{et}}(1 + (j\omega\tau_0)^n)^{-1}] \quad (5)$$

where $\tau_0 = \frac{R_s R_{et}}{R_s+R_{et}} C_{eff}$

Comparing the Eqn. 4 and 5 resulted to Eqn. 6 and the effective capacitance (C_{eff}) associated with the CPE can therefore be represented as Eqn. 7

$$\tau_0{}^n = Z_0 \frac{R_s R_{et}}{R_s+R_{et}} = Z_0(\frac{1}{R_s} + \frac{1}{R_{et}})^{-1} \quad (6)$$

$$C_{eff} = Z_0{}^{1/n}(\frac{R_s R_{et}}{R_s+R_{et}})^{(1-n)/n} \quad (7)$$

whereas C_{eff} can be related to film thickness d_{eff} according to Eqn. 8

$$C_{eff} = \frac{\varepsilon\varepsilon_o}{d_{eff}} \quad (8)$$

where ε is the dielectric constant and ε_o = 8.8542 $\times$ 10^{-12} Fm^{-1} is the permittivity of vacuum. Considering the value of ε = 197 at a frequency of 75 Hz where the corresponding R_{et} was observed, the value of d_{eff} was found to be ~130 nm for Pt(MPA)-PPy composite film. All the data values of experimentally simulated EIS parameters were obtained by means of GPES software.

Davies and Compton employed a theoretical framework to determine the diffusion layer thickness δ, which helps in categorizing the type of diffusion occurring at the spatially heterogeneous electrodes such as those represented by porous electrodes, partially blocked electrodes, microelectrode arrays, and electrodes made of composite materials [48, 49]. The value of δ can be obtained from the modified Einstein equation for the root mean square displacement of diffusing particles as shown in Eqn. 9 and listed in table 1:

$$\delta = (2D\Delta E/\upsilon)^{1/2} \quad (9)$$

where D is diffusion coefficient of aqueous ferrocyanide (6.3 x 10^{-6} cm^2s^{-1}), ΔE is the potential width of the votammogram and υ is the scan rate (0.05 Vs^{-1}). The δ values obtained for the modified electrodes indicates that a case 3 type of behavior related to the voltammetric responses of spatially heterogeneous electrodes, was occurring at the electrode/electrolyte interface . This type of behavior is associated with an overlap of adjacent diffusion layers resulting from the small size of the inert part of the electrode [50].

Useful information regarding electrochemical mechanism occurring at the electrode/electrolyte interface of the bioelectrode can be acquired from the relationship between the peak current and the scan rate. The various CV obtained for the bioelectrode at different scan rates in the range from 25-125 mV s^{-1} in PBS (pH 7.4) containing 2 mM $[Fe(CN)_6]^{3-/4-}$ are shown in Fig. 7. It was observed that with the increase in the scan rate the anodic peak potential shifted towards the positive side while the cathodic peak potential shifted in the reverse direction. Besides this, the plot of the anodic (I_{pa}) and cathodic peak currents (I_{pc}) versus square root of the scan rates ($\nu^{1/2}$) showed a linear relationship with good correlation coefficients suggesting a diffusion controlled process (Inset of Fig. 7). The linear relationship between the anodic peak current I_{pa} and $\nu^{1/2}$ can be expressed by the Eqn. (10),

$I_{pa} = b\ \nu^{1/2} + c$ (10)

where slope b = 17.48 μA/(mV/s)$^{1/2}$, having a correlation coefficient of 0.993 and the intercept c = 19.60 μA.

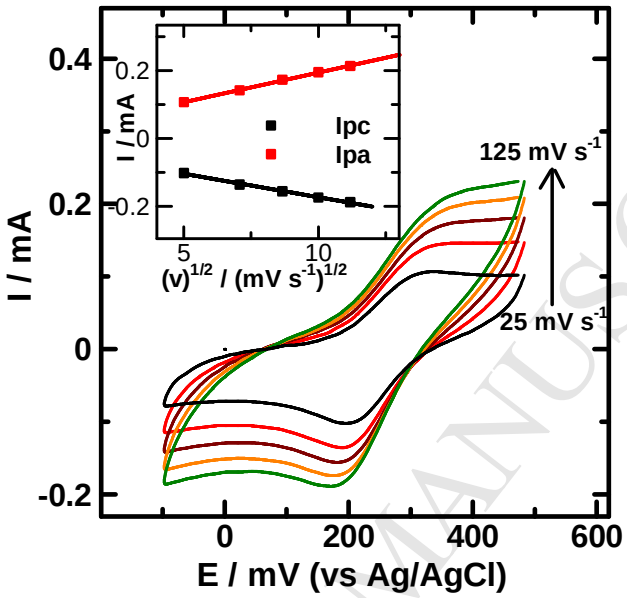

Fig.7: CV of the bioelectrode as a function of scan rate in PBS (pH 7.4, 0.1 M KCl) containing 2 mM $[Fe(CN)_6]^{3-/4-}$. Inset: plot of peak current vs $\nu^{1/2}$

3.3 Electrochemical impedance response of the bioelectrode towards protein antigen, Ag-αCRP

From a stock solution of 100 μg mL^{-1} of protein antigen, Ag-αCRP, aliquots of different concentrations were prepared in PBS. EIS response of the bioelectrode was measured after the addition of successive aliquots of different concentrations of protein antigen Ag-αCRP in PBS (pH 7.4, 0.1 M KCl) solution containing 2 mM $[Fe(CN)_6]^{3-}/[Fe(CN)_6]^{4-}$ at the scanning frequencies from 1 Hz to 10 kHz. The immunoreaction was performed in this frequency range as in the frequency region of <1 Hz bioelectrode exhibited perturbations in EIS signal which amounts to a significant variations in the circuits' elemental parameters while above 10 kHz the

EIS signal remains independent of frequency. Figure 8 shows the (a) Nyquist and (b) Bode plots of the bioelectrode obtained with different added concentrations of target Ag-αCRP. The R_{et} value of the bioelectrode corresponding to a sample solution containing no protein antigen was taken as the control sample response. Supplementary addition of successive aliquots of different concentration of protein antigen to the control sample solution leads to the formation of antibody-antigen immunocomplex at the bioelectrode surface which hinders the biointerfacial electron transfer resulting in an increase in the corresponding fitting values of R_{et} (Table 2). On comparing the changes in the values of different circuit elements after each subsequent immunoreaction with added protein antigen concentration (as shown in Table 2), the changes in R_{et} values were found to be much more prominent than those of other impedance components. Hence, it has been taken as a suitable signal response for immunosensing purpose. A small but noticeable decrease in Y_0 values (Table 2) was also observed with subsequent immunoreaction indicating a decrease in capacitive behavior of the bioelectrode with immunoreaction. The frequency spectrum as represented by the Bode plot in Fig. 8b can be approximately divided into three main regions. It was observed that both the low and high frequency region of the spectra were dominated by a resistance while the mid spectrum region by a capacitance. The high-frequency region (>7 KHz) was more related to the electrolyte ionic transfer behavior and here solution resistance R_s plays a critical role. In the intermediate range of frequency i.e. from 7 kHz to 50 Hz a phase angle greater than 40° but less than 90° was obtained, indicating a dielectric pseudo capacitive behavior at the bioelectrode/solution interface. At the low frequencies, < 20 Hz, electrode polarization and electrode kinetics becomes the principal factors contributing to the impedance and thus increases the importance of the charge transfer process, which relates to the circuit element R_{et}. In this low frequency region, we obtained significant changes in the log

modulus of |Z(f)| with the increasing antigen, Ag-αCRP concentration, which indicates that when the antigen is linked to the specific sites of the antibody on immunoreaction, the R_{et} value increases.

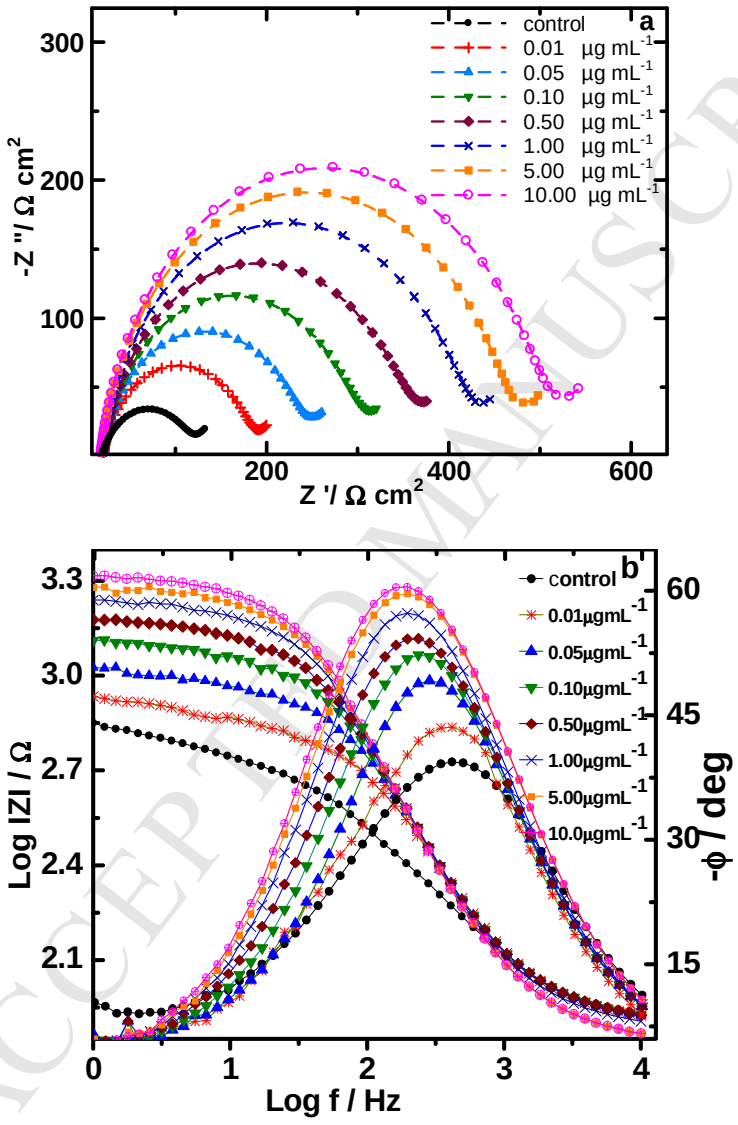

Fig.8: (a) Faradaic impedance spectra of the Ab-αCRP /Pt(MPA)-PPy/ITO-glass bioelectrode before and after incubating with different concentrations of Ag-αCRP in PBS (pH7.4) with 0.1 M KCl solution containing 2 mM $[Fe(CN)_6]^{3-/4-}$. (b) Corresponding bode plots

Table 2: EIS characteristic parameters of the bioelectrode upon immunoreaction with different concentration of Ag- αCRP

Concentration of Ag-αCRP	R_{et} (Ω cm^2)	CPE (Y_0) (μF cm^{-2})	n	Z_w (x10^{-3}) (Ω cm^2)	χ^2 (x10^{-4})
Control	98.5	1.88	0.86	4.18	1.48
0.01μg mL^{-1}	157.2	1.53	0.87	3.81	9.12
0.05μg mL^{-1}	216.7	1.33	0.87	3.72	2.29
0.10μg mL^{-1}	277.5	1.28	0.88	3.30	2.59
0.50μg mL^{-1}	331.8	1.25	0.88	3.10	3.11
1.00μg mL^{-1}	396.0	1.15	0.89	2.73	3.55
5.00μg mL^{-1}	445.2	1.11	0.90	2.70	4.48
10.00μg mL^{-1}	485.8	1.08	0.90	2.54	4.89

Figure 9 shows a linear relationship between the change in specific electron charge transfer resistance ($\Delta R_{et} = (R_{et})_{after\ immunoreaction} - (R_{et})_{control}$) and logarithmic value of Ag-αCRP concentration in the range of 10 ng mL^{-1} to 10 μg mL^{-1} and is represented by the Eqn. (11):

$$\Delta R_{et} = b \log [\text{Ag-}\alpha\text{CRP}] + c \quad (11)$$

The bioelectrode showed sensitivity (slope b of the calibration curve) of 109.74 Ω cm^2 per decade of Ag-αCRP and intercept c of 281.26 Ω cm^2 having a correlation regression coefficient of 0.990 (n = 7). The limit of detection was found out to be 4.54 ng mL^{-1} based on three times of signal-to noise ratio.The EIS detection procedure described above did not involve any pre-treatment or incubation time and requires about 12 minutes for complete assay including 3 minutes for the sample preparation. The comparison of the current bioelectrode with some recently reported CRP sensors (Table 3) shows its improved performance in terms of linear range of detection [51-53], assay time [54, 55] and sensitivity [56]. The reproducibility of the

bioelectrode for Ag-αCRP was investigated with inter-assay precision. The inter-assay precision was estimated for Ag-αCRP levels with three bioelectrodes prepared independently under similar experimental conditions. The inter-assay variation coefficient was determined to be a minimum of about 1.4% and a maximum of about 15 % over a range of 0.01 µg mL^{-1} to 10 µg mL^{-1} [Ag-αCRP], as depicted by error bar in Fig. 8, indicating an acceptable precision and fabrication reproducibility.

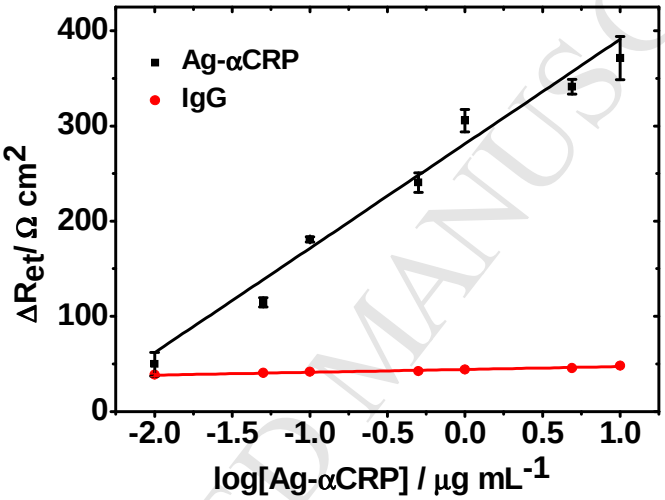

Fig.9: Concentration dependent calibration curve of bioelectrode; the error bars represent the standard deviation from three separate experiments

The stability of the bioelectrode was examined by repeatedly carrying out the impedimetric response measurements on the bioelectrode for the same sample of Ag-αCRP under identical conditions and it was found that no significant change in R_{et} was observed even after 5 repeated impedance measurements. This indicates that the bioelectrode retains its biocompatible property both in the solution and in open as well. The nonspecific adsorption is one of the major problems in immunosensing. The specificity of the bioelectrode was examined by carrying out the impedance measurement with non-specific protein antigen, mouse

immunoglobulin-G (Ag-IgG), over a concentration range of 0.01 to 10 µg mL^{-1} under identical conditions (Fig.8). Since no significant changes were found in the R_{et} values with the added aliquots of the increasing concentration of IgG with respect to the control sample without IgG, it may be concluded that non-specific interactions, if any, plays either negligible or insignificant role on the evaluation of EIS spectra using this bioelectrode.

Table 3: Comparison of analytical performance of electrochemical sensors for Ag- αCRP

Electrochemical sensor type	Transduction platform	Linear range	Limit of Detection(LOD)	Ref.
EIS	SAM/Au electrode	60 ng mL^{-1} to 6.0 µg mL^{-1}	19 ng mL^{-1}	[51]
EIS	Ab-BSA /Au-NPs/Cyst/Au electrode	5 to 25 µg mL^{-1}	-	[57]
Capacitance	interdigitated Au electrodes on nanocrystalline diamond surface	25 to 800 ng mL^{-1}	-	[53]
square-wave anodic stripping voltammetry	poly(dimethylsiloxane) -Au nanoparticle	0.5 to 200 ng mL^{-1}	307 amol in 30-µL samples	[54]
EIS	NHS/MUA/MPA/Au electrode	45 ng to 5.84 µg mL^{-1}	30 ng mL^{-1}	[56]
EIS	Pt(MPA)NPs-PPy/ITO-glass	10 to 10,000 ng mL^{-1}	4.54 ng mL^{-1}	Present work

4. Conclusion

This work demonstrates a facile in-situ electrochemical synthesis of functionalized Pt NPs intercalated conducting polypyrrole nanocomposite film deposited over an ITO-glass. The work also demonstrates the utility of combining the two types of advanced materials with complementary properties, organic conducting polymers and inorganic nanoparticles, to construct a bioelectrode for the detection of protein antigen, Ag-αCRP. The protein, Ab-αCRP, has been covalently immobilized on the biocompatible Pt(MPA)NPs-PPy nanocomposite, which provided high protein loading with site-specific protein bindings. The long chain of PPy in the polymer composite acts as a spacer between the biomolecules and the transducer, wherein the Pt nanoparticles helps in preserving the native protein conformation and reducing the steric hindrance for better probe orientation and accessibility of the biomolecules to the analyte. This high protein loading together with a fine probe orientation on the electroactive Pt leads to the construction of a highly specific and sensitive bioelectrode exhibiting a wide linear range of Ag-αCRP detection from 10 ng mL^{-1} to 10 µg mL^{-1} with a sensitivity of 109.74 Ω cm^2 per decade. Though this device protocol shows a better performance for the detection of Ag-αCRP in PBS in comparison to a few recently reported sensors under identical conditions, in terms of dynamic detection range, sensitivity and specificity, this can further be optimized with blood serum samples for clinical applications in real practice.

Acknowledgements

We are grateful to Prof. R. C. Budhani, Director, National Physical Laboratory, New Delhi, India, for providing facilities. S.K. Mishra is thankful to CSIR, India for providing a senior research fellowship (SRF). We also acknowledge Mr. V.K Tanwar and Vikash Sharma for technical assistance.

References

[1] R. V Mundra, X. Wu, J. Sauer, J. S Dordick and R. S Kane, Curr. Opin. Biotechnol. 2014; 28; 25-32.

[2] L. Hou, Z. Gao, M. Xu, X. Cao, X. Wu, G. Chen and D. Tang, Biosens. Bioelectron. 2014; 54 ; 365-371.

[3] I-T. Liu, M-H. Hon and L.G.Teoh, Ceram. Int. 2014; 40; 4019-4024.

[4] J. Wang, Anal. Chim. Acta 2003; 500; 247-257.

[5] N.L. Rosi and C.A. Mirkin, Chem. Rev. 2005; 105; 1547-1562.

[6] R.J. Tseng, J. Huang, J. Ouyang, R.B. Kaner and Y. Yang, Nano Lett. 2005; 5; 1077-1080.

[7] M. Xue, X. Ma, Z. Xie, L. Duan, Y. Jiang, M. Zhang and T. Cao, Chem. Asian J. 2010; 5; 2266-2270.

[8] R. Devi and C.S. Pundir, Sens. Actuators, B 2014; 193; 608-615.

[9] B.C. Kim, C.O. Too, J.S. Kwon, J.M. Ko, and G.G. Wallace, Synth. Met. 2011 ; 161;1130-1132.

[10] B. Domènech, K. K Ziegler, F. Carrillo, M. Muñoz, D. N Muraviev and Jorge Macanás, Nanoscale Res. Lett. 2013; 8;238-244.

[11] L.-X. Wang, X.-G. Li, and Y.-L. Yang, React. Funct. Polym. 2001; 47; 125-139.

[12] M. Ferenets and A. Harlin, Thin Solid Films 2007; 515; 5324-5328.

[13] G. Inzelt, M. Pineri, J. W. Schultze and M. A. Vorotyntsev, Electrochim. Acta 2000; 45; 2403-2421.

[14] T. Ahuja, I.A. Mir, D. Kumar and Rajesh, Biomaterials 2007;28; 791-805.

[15] K. Ramanathan, M. A. Bangar, M. Yun, W. Chen, N. V. Myung and A. Mulchandani, J. Am. Chem. Soc. 2005; 127; 496-497.

[16] J. Gong, L. Wang and L. Zhang, Biosens. Bioelectron. 2009; 24; 2285-2288.

[17] X. Yang, L. Li and F. Yan, Sens. Actuators, B 2010; 145;495-500.

[18] V. Saumya and T. P. Rao, Anal. Methods 2012; 4; 1976-1982.

[19] A. Chen and P. H-Hindle, Chem. Rev. 2010; 110; 3767–3804.

[20] Y. Yu, Q. Sun, T. Zhou, M. Zhu, L. Jin and G. Shi, Bioelectrochemistry 2011; 81; 53-57.

[21] M. Ahmad, C. Pan, L. Gan, Z. Nawaz and J. Zhu, J. Phys. Chem. C 2010; 114 ;243-250.

[22] M. H. F. Meyer, M. Hartmann, H.J. Krause, G. Blankenstein, B. M. Chorus, J. Oster, P Miethe and M. Keusgen , Biosens. Bioelectron. 2007; 22; 973-979.

[23] T. Ledue and N. Rifai, Clin. Chem. 2003; 49;1258-1271.

[24] V.M. Miller, M.M. Redfield, J.P. McConnell, Curr Vasc Pharmacol. 2007 ; 5; 15-25.

[25] N.D. Mygind, M.J. Harutyunyan, A.B. Mathiasen, , R.S. Ripa, J.J. Thune, J.P. Gotze, J.S. Johansen, J. Kastrup and C.T. Grp, Inflamm. Res. 2011; 60; 281-287.

[26] J.K. Pai, , K.J. Mukamal, , K.M. Rexrode, and E.B. Rimm, PLoS One 2008; 3; 1395-1403.

[27] B. McDonnell, S. Hearty, P. Leonard and R. O'Kennedy, Clin. Biochem. 2009; 42**;** 549-561.

[28] M.C. Peoples and H.T. Karnes, Anal. Chem. 2008; 80; 3853-3858.

[29] K. Kriz, F. Ibraimi, M. Lu, L.O. Hansson and D. Kriz, Anal. Chem. 2005; 77; 5920-5924.

[30] F. Baldini, A. Carloni, A. Giannetti, G. Porro and C. Trono , Sens. Actuators, B 2009; 139; 64-68.

[31] W.P. Hu, H.Y. Hsu, A. Chiou, K.Y. Tseng, H.Y. Lin, G.L. Chang and S.J. Chen, Biosens. Bioelectron. 2006; 21; 1631-1637.

[32] M.H. Meyer, M. Hartmann and M. Keusgen , Biosens. Bioelectron. 2006; 21;1987-1990.

[33] K.W. Wee, G.Y. Kang, J. Park, J.Y. Kang, D.S. Yoon, J.H. Park and T.S. Kim, Biosens. Bioelectron. 2005; 20; 1932-1938.

[34] N. Kim, D.K. Kim and Y.J. Cho, Sens. Actuators B, 2009; 143; 444-448.

[35] W.B. Lee, Y.H. Chen, H.I. Lin, S.C. Shiesh and G.B. Lee, Sens. Actuators, B, 2011; 157; 710-721.

[36] S. Centi, L.B. Sanmartin, S. Tombelli, I. Palchetti , M. Mascini, Electroanal. 2009; 21; 1309-1316.

[37] B. Derkus, E. Emregul, C. Yucesan and K. C. Emregul , Biosens. Bioelectron. 2013; 46; 53-60.

[38] P. R. V. Rheenen, M. J. McKelvy and W. S. Glaunsinger, J. Solid State Chem. 1987; 67; 151-169.

[39] S. Xing and G. Zhao, Mater. Lett. 2007; 61; 2040–2044.

[40] L. Yang and Y. Li, Biosens. Bioelectron. 2005; 20; 1407-1416.

[41] F. Yakuphanoglu, I.S. Yahia, B.F. Senkal, G.B. Sakr and W.A. Farooq , Synth. Met. 2011; 161; 817-822.

[42] A.D. Chowdhury, A. De, C. R. Chaudhuri, K. Bandyopadhyay and P. Sen, Sens. Actuators, B, 2012; 171; 916-923.

[43] M.I. Prodromidis, Electrochim. Acta 2010; 55; 4227-4233.

[44] J.S. Daniels and N. Pourmand, Electroanal. 2007; 19; 1239-1257.

[45] S.-J. Ding, B.-W. Chang, C.-C. Wu, M.-F. Lai and H.-C. Chang, Electrochim. Acta 2005 ; 50; 3660-3666.

[46] G.J. Brug, A.L.G. van den Eeden, M. Sluyters-Rehbach, J.H. Sluyters, J. Electroanal. Chem. 1984; 176; 275-295.

[47] B. Hirschorn, M. E. Orazem, B. Tribollet , V. Vivier, I. Frateurc and M. Musianid, Electrochim. Acta 2010; 55; 6218–6227

[48] T. J. Davies, C. E. Banks, and R. G. Compton, J. Solid State Electrochem. 2005; 9; 797-808.

[49] R. G. Compton and C. E. Banks, Understanding Voltammetry, World Scientific, London 2007.

[50] A. Solomon, Mamuru, I. Kenneth, and Ozoemena, Electroanal. 2010; 22; 985-994 .

[51] T. Bryan, X. Luo, P.R. Bueno and J.J. Davis, Biosens. Bioelectron. 2013; 39; 94-98.

[52] W. Zhan and A.J. Bard, Anal. Chem. 2007; 79; 459-463.

[53] A. Quershi, Y. Gurbuz, W. P. Kang and J. L. Davidson, Biosens. Bioelectron. 2009; 25; 877-882.

[54] F. Zhou, M. Lu, W. Wang, Z.P. Bian, J.R. Zhang and J.J. Zhu , Clin. Chem. 2010; 56; 1701-1707.

[55] N. Gan, L. Wang, H. Zhou, T. Li, W. Sang, F. Hu and Y. Cao, Int. J. Electrochem. 2012; 7; 11564-11577.

[56] N. Puri, V. K. Tanwar, V. Sharma, T. Ahuja, A.M. Biradar and Rajesh, IJIB 2010; 9; 1-5.

[57] J-Jie Zhu, J-Zhong Xu, J-Tao He, Y-Jun Wang, Q. Miao and H-Yuan Chen, Anal. Lett. 2003; 36; 1547-1556.

ACCEPTED MANUSCRIPT

ACCEPTED MANUSCRIPT

Highlights

- Pt(MPA)NPs-PPy film with high geometrical conformity and controllable thickness.
- Site-specific protein immobilization on nanocomposite film with high Ab-CRP loading
- Biocompatible film with reduced steric hindrance for better probe orientation.
- Biointerfacial impedance characterization of Pt(MPA)NP-PPy/ITO for Ag-CRP detection
- Synergistic effect of Pt(MPA) and PPy leads to selective and sensitive bioelectrode.

ACCEPTED MANUSCRIPT

QoS Provisioning in Channel Allocation Strategy in Cognitive Radio Using Fuzzy Logic

Harsh K Verma, Maninder Jeet Kaur, and Moin Uddin

***Abstract*—**In the cognitive radio scenario, the secondary users (SU) detects the vacant spectrum holes, coordinates this information among the other secondary users and selects the most suitable of the vacant spectrum band for its transmission purposes, with the condition that the functioning of the primary user is not altered. For the realization of this concept, there have been many studies, proposals for techniques, hardware and protocol suggested by the researchers. Subsequently, the focus have been on implementing smart behavior into the radio devices to enable more adequate configurations, so as to make the devices get adapted to their environment. While implementations, the main challenge is to find the most appropriate way to correctly dimension the cognitive abilities of the device according to the environment as well as the user. In this paper, we use fuzzy logic to solve spectrum management issues related to spectrum decision and allocating specific channel to the secondary user. The different solutions presented in the chapter include:(1) Estimate the probability of primary channel utilization (2) Estimate the channel availability and non-availability periods (3) Monitor the traffic and estimate the probability of channel allocation guaranteeing the required QoS.

***Keywords*—**Cognitive Radio, Fuzzy Logic, QoS (Quality of Service)

I. Introduction

INTRODUCTION of flexibility and intelligence in the wireless devices and applications have introduced the concept of Cognitive Radio. This research objective has inspired various ongoing research activities which included the decision making aspects. One of the ways is the use of "Cognitive Radio", according to this; the already licensed spectrum can be used more efficiently by introducing artificial intelligence, the decision- making to be specific, in the radio. This enables the radio to learn from its environment, considering certain parameters.

Dr. Harsh K Verma is with Dr B R Ambedkar National Institute of Technology, Jalandhar, India in Department of Computer Science Engg.(corresponding author's phone: +919463001601; e-mail: vermah@nitj.ac.in).

Dr. Maninder Jeet Kaur, was with Dr B R Ambedkar National Institute of Technology, Jalandhar, India. (e-mail: mani356@gmail.com).

Prof. Moin Uddin is with the Delhi Technological University, New Delhi, India as Pro Vice Chancellor (e-mail: prof_moin@yahoo.com).

Based on this knowledge the radio can actively exploit the possible empty frequencies in the licensed band of the spectrum that can then be assigned to other processes in such a way that they don't cause any interference to the frequency band that is already in use. This makes the efficient usage of the available licensed spectrum possible. A collaborative spectrum sensing scheme was proposed in [1].

The spectrum sensing was proposed at individual SU level and these results were compiled at the access point (AP). The access point takes the decision on sensed spectrum and evaluates the secondary user credibility using fuzzy logic system. The work we have presented for opportunistic spectrum access is based on the [1] [2] for credibility evaluation of the secondary user. In [1] and [2], the authors have considered the probability of detection, false alarm and missed detection for evaluating the credibility of a SU. But the fuzzy rules which are computed to provide probabilities did not provide good approximations. Another scheme was presented in [3], which considered spectrum utilization efficiency of the SU, its degree of mobility and the distance between the primary and secondary user to evaluate the functioning of the secondary user. The following sections detail this scheme and study the impact of the fuzzy based decision making scenario on cognitive radios system. Let us first have a brief look at the technique used. Although the basics of the fuzzy systems were discussed in the previous chapter we now have a look at the problem associated with the technique and the solutions suggested to overcome it.

II. The Fuzzy Interface

The principle components are the fuzzification module, knowledge base, interference engine and a defuzzification module.

(1) *The Fuzzification Module:*
a)It measures the value of input variables
b)It performs a scale mapping that converts the range of input values into corresponding universes of discourse.
c)It converts input data into suitable linguistic variables.

(2) *The Knowledge Base:*
i. It provides necessary definitions, which are used to define linguistic control rules and fuzzy data manipulation.
ii. It characterizes the control goals and policies of the domain experts by means of a set of linguistic control rules.

(3) *The Inference Engine:*

http://dx.doi.org/10.15242/IIE.E0314185

It is capable of simulating human decision making based on fuzzy concepts and rules.

(4) *The Defuzzification Module:*

It converts range of values of output variables into corresponding universes of discourse.

It yields a non fuzzy control action from an inferred control action.

Drawback associated with Fuzzy Systems:

Fuzzy systems have been applied to many applications such as approximation, system control applications, fuzzy classification, fuzzy clustering etc. The transparency of the fuzzy system enables interpretation and analysis of many complex systems. However, when fuzzy systems are applied to more complicated and high dimensional systems "*curse of dimensionality*" becomes more apparent (detailed in next subsection). To avoid this bottleneck to wider applications, hierarchical fuzzy system was proposed.

The Hierarchical Fuzzy Systems

The complexity of a fuzzy system increases with the increase with the number of input variables. This complexity issue is termed as "*curse of dimensionality*". In context of fuzzy systems it may be summarized as [4]:

1. Rule dimensionality: The total number of rules in the fuzzy rule base increases exponentially with the number of input variables.
2. Parameter dimensionality: The total number of parameters in the mathematical formulas for the fuzzy system increases exponentially with the number of input variables.

3. Data or information dimensionality: The number of data or knowledge set required to identify fuzzy system increases exponentially with the number of input variables.

Some drawbacks associated with curse of dimensionality are:

1. Transparency and interpretation is damaged or lost as a human is incapable of understanding or justifying hundreds and thousands of fuzzy rules and parameters.
2. As there is often limited data to an application a large number of rules and parameters result in over fitting, which destroys the generality of the fuzzy system. In other words, learning from the data becomes difficult or impossible.
3. Excessive requirement for more computation and memory [5].

To overcome these problems *Hierarchical Fuzzy System (HFS)* was introduced by Raju, Zhao and Kisner [6] in 90s. HFS consists of hierarchical number of low dimensional sub fuzzy systems called fuzzy logic modules instead of using high dimensional standard fuzzy system. These smaller fuzzy logic modules contribute to the final solution. The upper fuzzy subsystem may also take input as a combination of lower level output and an original input variable. Thus an HFS may have multiple levels and multiple sub systems at each level.

In HFS, the total number of rules increases only linearly with the increase in number of input variables as against exponential growth in standard fuzzy subsystem.
The number of rules, R is given as:

$$R = (x-1)y^2 \quad \ldots (1)$$

Where, x is the number of input variables and y is the number of membership functions. HFS system has been used in the proposed opportunistic cognitive radio model for spectrum management strategy.

III. Opportunistic Channel Allocation Decision for QoS Provisioning

In this section, we propose a fuzzy based approach for channel allocation for dynamic spectrum access. As the nature of the cognitive radio scenario is dynamic, it is characterized by uncertain and in complete information, therefore fuzzy logic is used to find a better solution for the issue related. The channel allocation is done dynamically on the basis of the information of availability of channel and for how long it will be available. This information is help us avoid the channels which the primary users acquire too frequently as it degrades the system performance hence QoS is forsaken.

The hierarchical fuzzy system proposed consists of two fuzzy controllers [7-8], in order to overcome the curse of dimensionality. One of the controllers is used to estimate the spectrum utilization for the channel. The second controller receives the input along with the two other antecedents to find the probability of the channel allocation decision.

The model consists of two FLS in hierarchical form [9-10] as shown in the Figure 1. FLS1 receives three inputs, spectral efficiency, distance and mobility and gives the probability of channel utilization by the channel. FLS2 manipulates the three inputs: channel utilization information, rate of channel available and rate of channel un-available, to define the possibility of channel allocation for spectrum access to the SU.

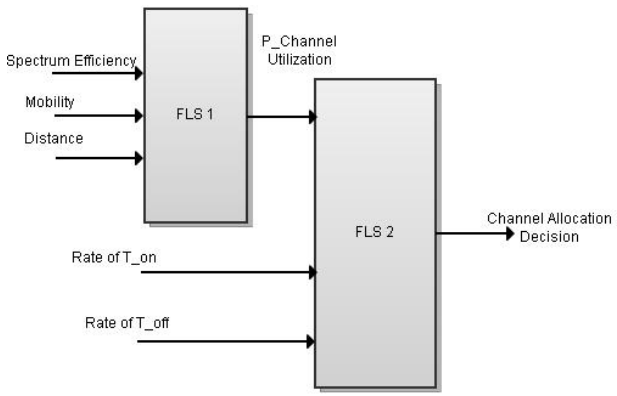

Fig. 1 Proposed Model

1. *Estimating Probability of Channel Utilization*

We use the previously stored channel information like spectral efficiency of the channel, the mobility of the SU and distance between SU and PU, to determine the probability of spectrum utilization by the channel.

The three antecedents are described for estimation of the channel utilization:

- Antecedent 1: Mobility
- Antecedent 2: Spectral Efficiency
- Antecedent 3: Distance between SU and PU

Mobility of the SU

Mobility of the secondary user is an important parameter in our design. When the SU moves at a velocity v m/s, it causes Doppler shift given by (2):

$$f_D = f_c \frac{v \cos\theta}{c} \quad \ldots (2)$$

Where, f_D is the Doppler shift, f_c is the carrier frequency and θ is the angle between the direction of arrival of received signal and direction of motion of the SU, c is the wave velocity. The mobility is important parameter because more the velocity of the secondary user more shall be the chance for SU to change position and hence QoS degradation due to non availability of the channel.

Spectrum Efficiency

Spectrum efficiency is the ratio of the required spectrum by the SU to the total available spectrum. It is an important parameter in out design because in channel utilization for dynamic spectrum access, the radio shall use the unused vacant spectrum. Spectrum efficiency refers to the information rate that can be transmitted over a given bandwidth in a specific communication system as given by (3):

$$\eta_s = \frac{BW_s}{BW_\alpha} \quad \ldots (3)$$

Where, *BWs* is the required bandwidth of the spectrum and *BWa* is the available bandwidth of the spectrum.

Distance

Distance between the PU and SU is an important parameter because SU at a closer distance should be given priority to access the spectrum. But the location of the PUs is not known. We can consider signal to noise ratio (SNR) as a proxy for distance [11] as given by (4):

$$SNR_{SU} = 10\log\left(\frac{P_t g(R)}{\sigma^2}\right) \quad \ldots (4)$$

We assume that R is the distance between the PU and SU, P_t is the power transmitted by the SU, $g(R)$ is the power gain between the PU and SU and σ^2 is the noise power measured at SU. From (4), we can derive the distance between the PU and SU.Membership functions for antecedent 1, 2 and 3 are characterized into three levels as LOW, MEDIUM and HIGH as shown in Figure 2 (a), (b) and (c) respectively. Gaussian membership functions are used for this work. The consequence (i.e. the probability of channel utilization) is divided into five levels: VERY LOW, LOW, MODERATE, HIGH and VERY HIGH as shown in Figure 2. Since we have 3 antecedents and 3 fuzzy subsets, so we need $3^3 = 27$ rules for FLS1. The rule base of [3] is referred which is based on expert opinions as shown in Table 1. The corresponding decision surfaces are shown in Figure 3.

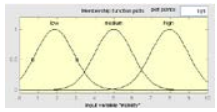

(a)

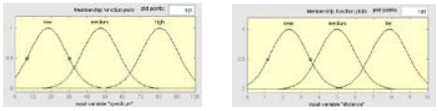

(b)(c)

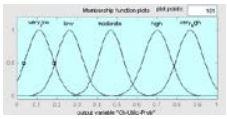

(d)

Fig. 2 Membership Function Plot for (a) Spectrum (b) Mobility and (c) Distance (d) Consequence (Probability of Spectrum Utilization)

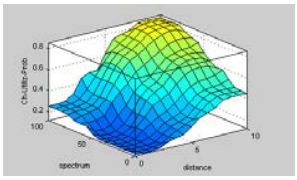

(a)

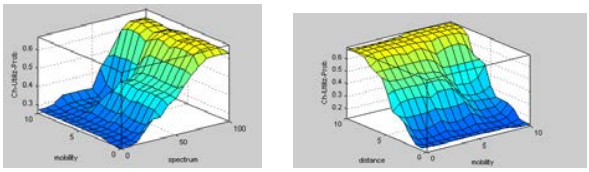

(b)(c)

Fig. 3 Decision Surface for FLS1 showing Probability of Channel Utilization variation with (a) mobility with spectrum (b) spectrum with distance (c) mobility and distance

From the above results we can see that the probability of channel utilization is affected by the distance of the SU and PU. The probability of the channel utilization by the SU is more when the distance between SU and PU is more. The probability of the channel utilization also depends on the mobility of the SU. When the mobility is high, the chance of channel utilization is also high.

TABLE I
FUZZY RULES FOR FLS1

Rule No.	Spectrum	Velocity	Distance	Prob. Channel Utilization
1	Low	Low	Near	*Very Low*
2	Low	Low	Moderate	*Low*
3	Low	Low	Far	*Low*
4	Low	Moderate	Near	*Very low*
5	Low	Moderate	Moderate	*Low*
6	Low	Moderate	Far	*Moderate*
7	Low	High	Near	*Very Low*
8	Low	High	Moderate	*Low*
9	Low	High	Far	*Moderate*
10	Medium	Low	Near	*Very Low*
11	Medium	Low	Moderate	*Moderate*
12	Medium	Low	Far	*High*
13	Medium	Moderate	Near	*Very Low*
14	Medium	Moderate	Moderate	*Moderate*
15	Medium	Moderate	Far	*High*
16	Medium	High	Near	*Very Low*
17	Medium	High	Moderate	*Low*
18	Medium	High	Far	*High*
19	High	Low	Near	*Low*
20	High	Low	Moderate	*High*
21	High	Low	Far	*very High*
22	High	Moderate	Near	*Low*
23	High	Moderate	Moderate	*High*
24	High	Moderate	Far	*Very High*
25	High	High	Near	*Very Low*
26	High	High	Moderate	*High*
27	High	High	Far	*High*

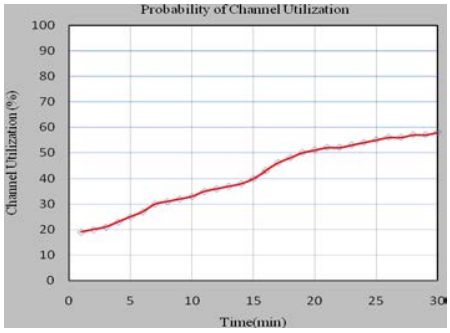

Fig. 4 Simulated Measure of Probability of Channel Utilization by within a period of time (Output of FLS1)

The output of FLS1 (probability of channel utilization) is used to compute the probability of channel allocation decision for the SU, by the use of FLS2. Depending upon the rule base of FLS1 the simulated probability of channel utilization is as shown in the Figure 4. In FLS1, we estimated the utilization of the primary channel, if it can be used by the SU for its transmission. The information obtained from FLS1 is used in FLS2 to decide whether exchanging traffic over unused primary channel is feasible and will it enhance the quality of communication. We have assumed in our work that traffic opportunistically sent over the primary channel will be preempted when the traffic generated by the primary user arrives. This will be done by switching the traffic back to the secondary channel. We also assume that the transmission takes place between either the secondary or any of the unused primary channels based on the protocol which has to be decided by the reasoning engine of the cognitive radio.

Three antecedents used for FLS2 are:

i. Probability of Channel Utilization (Output from FLS2)
ii. σ_{on} (Deviation in the duration of available periods)
iii. σ_{off} (Deviation in the duration of unavailable periods)

After the selection of the channel, the Bit Error Rate (estimated) of the channel as follows [12]:

$$BER_{estimated} = \frac{BER_S C_S + BER_p . C_p . U_{estimate}}{C_S + C_p} \quad \ldots (5)$$

BER_s is the bit error rate of secondary channel, BER_p is the bit error rate of the primary channel, C_s is the maximum channel capacity of the secondary channel and C_p is the maximum channel capacity of the primary channel and $U_{estimate}$ is given as:

$$U_{estimate} = \frac{T_{on}}{T_{off}} \quad \ldots (6)$$

Rate of T_on and Rate of T_off

The primary channel utilization is under consideration as it is to be utilized by the SU transmission. We know that the channel is not permanently carrying the information/traffic. The channel can be carrying traffic or it can be idle, over a period of time. *T_on is the period of time during which the channel is not carrying traffic* (Available) *and T_off is the period of time during which the channel is carrying traffic* (Not Available). Let us assume the deviation in the duration of available periods is σ_{on} and deviation in the duration of unavailable periods is $\sigma_{off.}$ The decision of the channel allocation is distributed over time. It depends on the number of periods during which the channel is not occupied and is available for transmission. The channel will be available when it switches between long available period and/or long unavailable period.

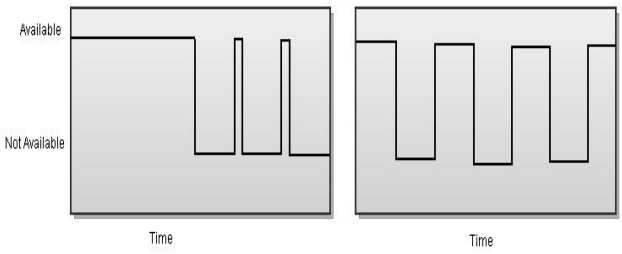

(a) (b)

Fig. 5 Two channels with same percentage of availability with (a) High σ_{on} (b) Low σ_{on}

The figure above shows two channels with same availability percentage. But the rate of *T_on* varies as we see

the deviation of the available periods. We notice that in Figure 5(a), the channel is available for one long and several short periods hence it can be utilized for allocation. But in case of Figure 5(b), the channel is available for short durations. This makes it less suitable for channel allocation as it will have more number of frequency transitions, which further will cause interference to the PU. The flowchart explaining the process is shown in the Figure 6. Gaussian membership functions are used in our work because with Gaussian function rise time is low and fluctuations are minimum. Mamdani type rule base system is used on both FLS1 and FLS2.

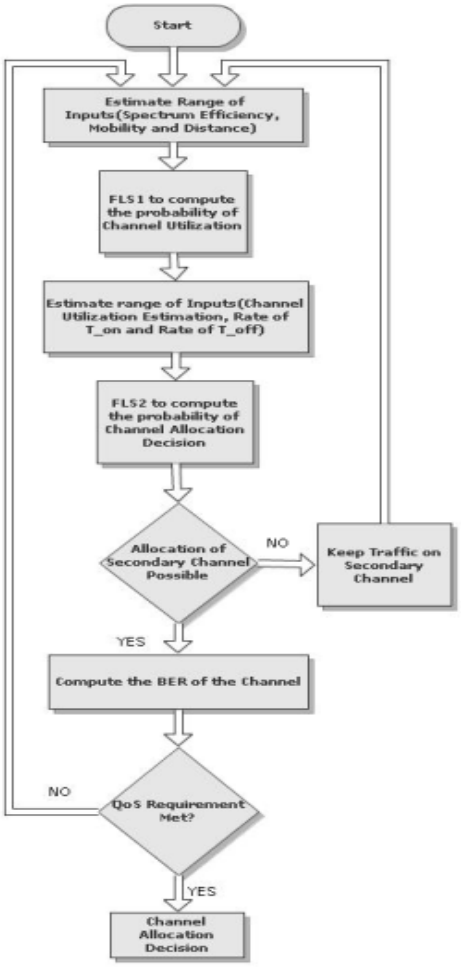

Fig. 6 Flowchart for Channel Allocation Strategy Based on Fuzzy Logic

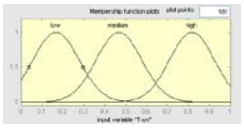

(a)

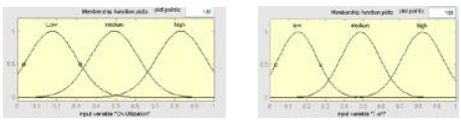

(b)(c)

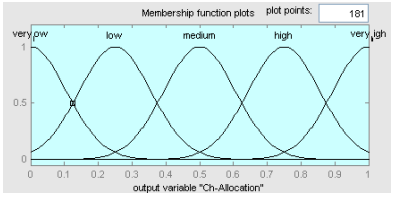

(d)

Fig. 7 Membership functions of (a) probability of channel utilization (b) rate of T_{on}(σ_{on}) (c) rate of T_{off} (σ_{off}) (d) membership function for probability of channel allocation

The membership functions for the three antecedents are shown in Figure 7 (a), (b) and (c). Figure 7(d) shows membership function for probability of channel allocation decision. The membership function is divided into LOW, MEDIUM and HIGH for the antecedents and for consequence it is divided into VERY LOW, LOW, MEDIUM, HIGH and VERY HIGH.

IV. Simulated Results

In FLS1, we consider the SU mobility in the range of 1 to 10 m/s, the distance is varied in the range 1 to 10 m and spectrum efficiency in percentage from 1 to 100. Based on the knowledge on linguistic variables 27 IF THEN ELSE rules are used for FLS2 to take decision for channel allocation for secondary users. These rules are shown in Table 5.2. If the output decision value is close to 1, that means that the decision is on favor of that variable.

In a network of PUs and SUs, the PU has higher priority of using the channel. The SU must vacate the channel so that it does not interfere with the PU functioning. However, in some situation this causes temporal connection loss of SUs. Moreover, if SU cannot vacate the channel within a period of time, it can affect the PU. So to avoid these situations, the channel allocation should be done in such a manner that the SU avoid using such channels which will be claimed by the PUs with greater possibility within a period of time. We address this issue by proposing a fuzzy based decision model which will take into account the problem by predicting the availability of the channel and also monitoring the PU traffic.

TABLE II
Fuzzy Rules for FLS2

Rule No.	Antecedent 1	Antecedent 2	Antecedent 3	Consequence
1	Low	High	High	*High*
2	Low	High	Medium	*High*
3	Low	High	Low	*High*
4	Low	Medium	High	*High*
5	Low	Medium	Medium	*Very High*
6	Low	Medium	Low	*Very High*
7	Low	Low	High	*Very High*
8	Low	Low	Medium	*Very High*
9	Low	Low	Low	*Very High*
10	Medium	High	High	*Medium*
11	Medium	High	Medium	*Medium*
12	Medium	High	Low	*Medium*

13	Medium	Medium	High	*Medium*
14	Medium	Medium	Medium	*High*
15	Medium	Medium	Low	*High*
16	Medium	Low	High	*High*
17	Medium	Low	Medium	*High*
18	Medium	Low	Low	*High*
19	High	High	High	*Low*
20	High	High	Medium	*Low*
21	High	High	Low	*Low*
22	High	Medium	High	*Low*
23	High	Medium	Medium	*Low*
24	High	Medium	Low	*Low*
25	High	Low	High	*Low*
26	High	Low	Medium	*Low*
27	High	Low	Low	*Low*

Antecedent 1 – *Prob. of Channel Utilization* Antecedent 2 – *Rate of* $T_{on}(\sigma_{on})$, Antecedent 3 – *Rate of* $T_{off}(\sigma_{off})$; Consequence – *Probability of Channel Allocation*

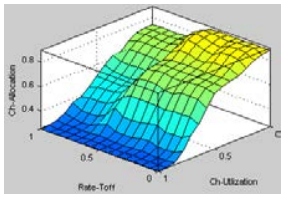

(a)

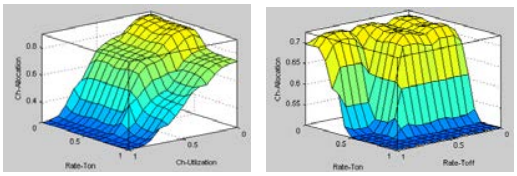

(b)(c)

Fig. 8 Decision Surface for FLS2 showing Probability of Channel Allocation Variation with (a) σ_{on} and Prob. of Channel Utilization (b) σ_{off} and Prob. of Channel Utilization (c) σ_{on} and σ_{off}

The decision surfaces for FLS2 are shown in Figure 8. We can analyze from them that the probability of channel allocation decision is high when the rate of T_{on} is high and vice versa. We will analyze the results for different situations.

The results from the FLS2 and FLS1 are analyzed for the following three scenarios:

1. Scenario 1: Channel Allocation Decision based on proposed HFS.
2. Scenario 2: Channel Allocation Decision based on FLS1 as an independent entity.
3. Scenario 3: Channel Allocation Decision based on FLS2 as an independent entity.

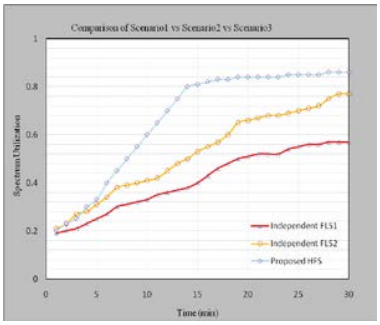

Fig. 9 Comparison of three scenarios: Propsed HFS vs Independent FLS1 vs Independent FLS2

It is difficult to represent the overall system performance with single index of performance. The proposed model overcomes this problem by modeling the system using fuzzy logic. We compare the efficiency of the proposed system by comparing it with independent FLS1 and Independent FLS2 as shown in Figure 9. The results show that the proposed scheme outperforms the two scenarios and approximately 85% of spectrum is utilized as compared to 78% in case of Independent FLS2 and 57% in case of Independent FLS1.

The proposed fuzzy model monitors the traffic by analyzing the rate of availability of the channel for SU allocation. The work presented here is a rearranged model with hierarchical fuzzy system based on [3] and proposes channel allocation decision strategy which enhances the QoS provisioning on cognitive radio such that the SU will avoid using the channel which will be claimed by PUs with greater probability. The QoS of SUs will also increase as there will be less number of temporal connection losses. Another advantage of using this model will be the PUs which utilizes the channel at frequent intervals will not be interfered by the SU transitions. Hence the required QoS will be maintained.

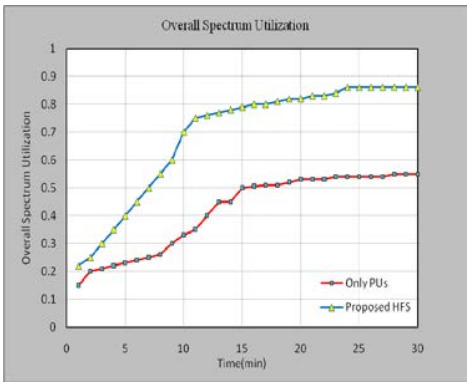

Fig. 10 Overall Spectrum Utilization for system with proposed HFS scheme and system with primary users (with σ_{on} = 0.8 and σ_{off} = 0.2)

The plots shows the overall spectrum utilization of the system for a given time period with different rates of channel availability. Figure 10 shows plot for σ_{on} = 0.8 and σ_{off} = 0.2. Figure 11 shows plot for σ_{on} = 0.2 and σ_{off} = 0.8.

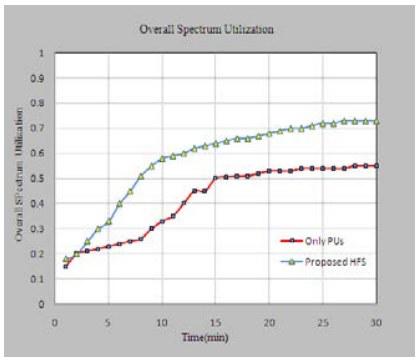

Fig. 11 Overall Spectrum Utilization for system with proposed HFS scheme and system with primary users (with σ_{on} = 0.2 and σ_{off} = 0.8)

We can see that the plot for σ_{on} = 0.8 outperforms for σ_{on} = 0.2, and clearly see the affect for channel availability information on overall spectrum utilization.

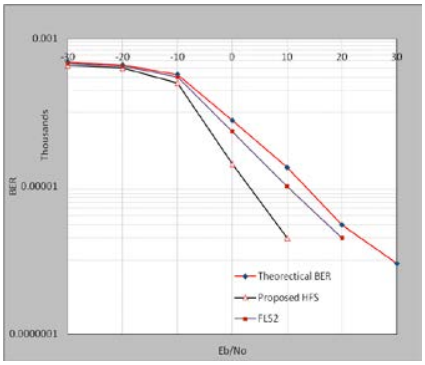

Fig. 12 BER Comparison Plot

After the selection of the channel, we study the channel allocation decision by considering the QoS in terms of BER. The inference engine compares the measures SINR with different periods of time periods of channel availability. The highest level that satisfies the required BER is chosen. This information is fed back to the transmitter and resource allocation is done at the transmitter. The proposed HFS follows the theoretical values as shown in Figure 12. It shows that the proposed HFS can be used for optimizing BER tradeoff analysis with respect to signal to noise ratio in cognitive radio scenario for better performance reliability of the system.

V. Conclusion

Looking into the prospects of soft computing techniques in the field of CR, we explore some of the spectrum access solutions using fuzzy logic technique in this chapter. In the first model, the performance of the cognitive radio is evaluated on the basis of spectrum efficiency, distance and mobility of the SU. The probability with which the channel will be utilized by the SU is calculated. But how far this model can maintain the required QoS of the system is an unexplored area so far. The SU has to vacate the channel as soon as PU is detected. If the frequency of switching of the channels between SU and PU is high, it can affect the QoS of the system because every time the SU has to terminate its communication or reduce its transmission power. In addition, it can cause temporal connection loss of the SU and also can cause interference with the PU.

So to overcome these issues, a novel channel allocation scheme is proposed which will monitor the deviation of the time periods for which the available and allocate to the SU accordingly. The channel which has low deviation of the available period (although it can have same available frequency) is avoided as these channels will be claimed by the PU with greater probability within a given period of time. The simulated results show that the proposed scheme outperforms the rest of the schemes. The overall spectrum utilization for the system is increased with the use of proposed HFS scheme. In addition the channel selected for allocation is analyzed if it meets the QoS requirements. The QoS is measured in terms of BER. The results show that the proposed scheme gives better performance in terms of BER tradeoff analysis with respect to signal to noise ratio. The inference engine compares the measures SINR with different periods of time periods of channel availability. The highest level that satisfies the required BER is chosen. This information is fed back to the transmitter and resource allocation is done at the transmitter.

References

[1] W. Yang, Y. Cai, Yo. Xu , "A fuzzy collaborative spectrum sensing scheme in cognitive radio," *International Symposium on Intelligent Signal Processing and Communication Systems, ISPACS 2007*, pp.566-569, 2007.

[2] Q. Peng, K. Zeng, J. Wang and S. Li, "A Distributed Spectrum Sensing Scheme Based on Credibility and Evidence Theory in Cognitive Radio Context," *IEEE 17th International Symposium on Personal, Indoor and Mobile Radio Communications (PIMRC'06)*, pp. 1-5, 2006.

[3] Hong-Sam T. Le and Hung D. Ly, "Opportunistic Spectrum Access Using Fuzzy Logic for Cognitive Radio Networks," *International Journal of Wireless Networks*, Springer, Vol. 18, pp. 171 – 178, 2011. http://dx.doi.org/10.1007/s10776-011-0148-y

[4] D. Wang, X. Zeng and J. A. Keane, "A Survey of Hierarchical Fuzzy Systems," *International Journal Of Computational Cognition*, Vol.4, pp. 18-29, 2006.

[5] W. Rattasiri and S. K. Halgamuge, "Computationally advantageous and stable hierarchical fuzzy systems for active suspension," in *IEEE Transactions on Industrial Electronics*, Vol.50, No.1, pp. 48-61, 2003. http://dx.doi.org/10.1109/TIE.2002.807676

[6] G. V. S. Raju and J. Zhou, "Adaptive hierarchical fuzzy controller," in *IEEE Transactions on System Man and Cybernetics*, Vol.23, No. 4, pp. 973-980, 1993. http://dx.doi.org/10.1109/21.247882

[7] G. Klir and B. Yuan, *Fuzzy sets and fuzzy logic: theory and applications*, Upper Saddle River, NJ, USA: Prentice-Hall PTR, 1995.

[8] Jan Jantzen Design of Fuzzy Controllers August, 1998. [Online] Available: http://www.iau.dtu.dk/~jj/pubs/design.pdf.

[9] Ming-Ling Lee, Hung-Yuan Chung, and Fang-Ming Yu, "Modeling of hierarchical fuzzy systems," *Elsevier Fuzzy Sets and Systems*, Vol. 138, No. 2, pp. 343-361, September 2003. http://dx.doi.org/10.1016/S0165-0114(02)00517-1

[10] Li-XinWang, "Analysis and Design of Hierarchical Fuzzy Systems," *IEEE Transactions On Fuzzy Systems*, Vol. 7, No. 5, pp. 617-624. October 1999. http://dx.doi.org/10.1109/91.797984

[11] N. Hoven and A. Sahai, "Power scaling of Cognitive Radio," International Conference on Wireless Networks, Communications and Mobile Computing, Vol.1, pp.250 – 255, 2005.

[12] A. Al-Fuqaha, B. Khan, A. Rayes, M. Guizami, O. Awwad and G. B. Brahim, "Opportunistic Channel Selection for Better QoS in Cooperative Networks with Cognitive Radio Capabilities," *IEEE Journal of Selected Areas in Communications*, Vol. 26, No. 1, 2008.
http://dx.doi.org/10.1109/JSAC.2008.080114

Author's Accepted Manuscript

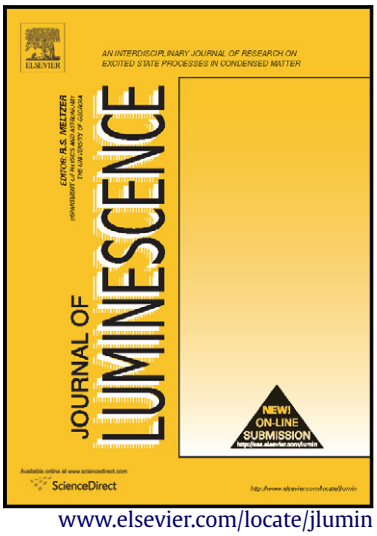

www.elsevier.com/locate/jlumin

Spectral characterization of Sm^{3+} ions doped Oxy-fluoroborate glasses for Visible Orange Luminescent Applications

Sk. Mahamuda, K. Swapna, M. Venkateswarlu, A. Srinivasa Rao, Suman Latha Shakya, G. Vijaya Prakash

PII: S0022-2313(14)00300-7
DOI: http://dx.doi.org/10.1016/j.jlumin.2014.05.017
Reference: LUMIN12702

To appear in: *Journal of Luminescence*

Received date: 18 March 2014
Revised date: 4 May 2014
Accepted date: 19 May 2014

Cite this article as: Sk. Mahamuda, K. Swapna, M. Venkateswarlu, A. Srinivasa Rao, Suman Latha Shakya, G. Vijaya Prakash, Spectral characterization of Sm^{3+} ions doped Oxy-fluoroborate glasses for Visible Orange Luminescent Applications, *Journal of Luminescence,* http://dx.doi.org/10.1016/j.jlumin.2014.05.017

This is a PDF file of an unedited manuscript that has been accepted for publication. As a service to our customers we are providing this early version of the manuscript. The manuscript will undergo copyediting, typesetting, and review of the resulting galley proof before it is published in its final citable form. Please note that during the production process errors may be discovered which could affect the content, and all legal disclaimers that apply to the journal pertain.

ACCEPTED MANUSCRIPT

Spectral Characterization of Sm^{3+} ions doped Oxy-fluoroborate Glasses for Visible Orange Luminescent Applications

Sk. Mahamuda[1], K. Swapna[1], M. Venkateswarlu[1], A. Srinivasa Rao*[1, 2], Suman Latha Shakya[3] and G. Vijaya Prakash[3]

[1]Department of Physics, K L University, Green Fields, Vaddeswaram-522 502, Guntur (Dt.), A P, India
[2]Department of Applied Physics, Delhi Technological University, Bawana Road, New Delhi-110 042, India
[3]Nanophotonics Laboratory, Department of Physics, Indian Institute of Technology-Delhi, Hauz Khas, New Delhi-110 016, India
Corresponding author, **E-mail: drsrallam@gmail.com, Tel: +91 85860 39007, Fax: +91 01127871023.*

Abstract

Oxy-fluoroborate (OFB) glasses doped with different concentrations of Sm^{3+} ions have been prepared by using conventional melt quenching technique and characterized for their lasing potentialities using the spectroscopic techniques such as FTIR, optical absorption, emission and emission decay measurements. The FTIR spectrum has been recorded to know the various functional groups present in the OFB base glass. From the absorption spectra, the bonding parameters (δ) were evaluated to find the bonding nature present between Sm^{3+} ions with its neighbouring ligands. The Judd-Ofelt intensity (J-O) parameters (Ω_λ, where λ=2, 4, and 6) measured from the experimental oscillator strengths of the absorption spectral futures, are used to evaluate the radiative parameters for the fluorescent transitions $^4G_{5/2}\rightarrow{}^6H_{5/2}$, $^4G_{5/2}\rightarrow{}^6H_{7/2}$, $^4G_{5/2}\rightarrow{}^6H_{9/2}$ and $^4G_{5/2}\rightarrow{}^6H_{11/2}$ of Sm^{3+} ions in OFB glasses. The asymmetric ratio has been evaluated to understand the local disorder of Sm^{3+} ions in the glass network. The experimental lifetimes (τ_{exp}) measured from the decay curves are coupled with radiative lifetimes (τ_{rad}) to measure quantum efficiency (η) of the prepared glasses. The experimental lifetimes (τ_{exp}) for $^4G_{5/2}$ emission state are decreasing with increase in Sm^{3+} ion concentration due to energy transfer. In order to elucidate the nature of energy transfer mechanism, the non-exponential decay curves are well fitted to Inokuti-Hirayama model for S=6, which indicates that the energy transfer mechanism is of dipole-dipole type. The branching ratio (β_R), stimulated emission cross-section (σ_{se}) and quantum efficiency (η) values measured for the most intense emission transition $^4G_{5/2}\rightarrow{}^6H_{7/2}$ (598 nm) optimises the concentration of Sm^{3+} ions as 1 mol% to produce bright visible orange lasing emission from these OFB glasses.

Keywords: *Amorphous materials, optical materials, optical properties, luminescence*

Accepted manuscript

ACCEPTED MANUSCRIPT

1. Introduction

Quite recently, glasses doped with transition metal and rare earth ions have attracted a great deal of attention because of their memory and photo conducting properties. They also find potential applications in diversified fields such as solid state lasers, luminescent solar energy concentrators, optical detectors, waveguide lasers, optical fiber amplifies, hole burning high density memories and optoelectronic devices [1-7]. It is well known that, a glassy host with phonon energies at lower end patronages radiative transitions rates very much and is much useful for the design and development of the optical devices such as up-convertors, light emitting diodes (LEDs) and memory devices [8-10]. Since the luminescence quantum efficiency and emission transitions band widths of the doped rare earth ions strongly depends on the structural changes of the host matrices, apt selection of a suitable host material is very much essential in order to obtain better luminescence efficiency needed for the design and development of an optical devices. Among various optical glasses available, borates are the most important glassy systems owing to their peculiarities such as low melting point, high optical transparency, high chemical stability and good rare earth ion solubility. They are also found to be robust and inexpensive. All the aforementioned novel characteristic features possessed by the borate glasses makes them to act as an exalting host matrices and the best choices for RE ions doping for the applications where the flexibility of size and compositions of the material are necessary. On the other hand, the high phonon energies (~1300-1500 cm^{-1}) possessed by borate glasses encourage non radiative emission process very much and cannot acts as good laser host. From this point of view, fluoride hosts are found to be superior to borates as the former hosts need not encourage non-radiative transitions. However fluoride hosts are found to be toxic, corrosive and needs to be synthesizing in absence of oxygen under controlled atmosphere. Owing to all these difficulties, fluoride hosts are not used commonly. But the addition of alkali/alkaline earth oxide/fluoride converts the boron coordination and the structural groups from one to another depending on the type and concentration of the alkali/alkaline earth oxide/fluoride. Among the oxide and mixed oxy-fluoride glass compositions, lead borate glasses doped with RE ions seems to be very attractive systems for applications in laser technology. Not only this but also the addition of fluoride compounds to borate glasses as network modifiers can reduce the redundant phonon energies of borate glasses considerably and eventually increases their mechanical strength [11-18]. Especially the fluoride compounds such as BaF_2 and CaF_2 with their less phonon energies

Accepted manuscript

ACCEPTED MANUSCRIPT

(~346 cm^{-1}) added to borate host as network modifiers, can strongly reduce the phonon energies of borates (~1300-1500 cm^{-1}) to a relatively lower values [19]. Moreover, the solubility of RE ions is also larger in the fluoride medium than in the oxide [20] and the fluoride compounds present in borates helps in reacting and removing the –OH group from the borate glass. Over and above, the fluoride compounds in a glass can reduce scattering and dispersion losses which are very much required for the construction of LEDs.

In recent years, glasses containing ZnO are playing a vital role in technology and attracting many researchers, because, ZnO being a non-toxic and non-hygroscopic in nature possesses excellent optical, electrical and magnetic properties. ZnO based glasses are very much useful in developing the optoelectronic devices, luminescent solar energy converters, gas sensors and ultraviolet emitting lasers [21]. ZnO enters in to a glass as a network modifier and breaks the B-O-B bonds (normally the oxygen's of ZnO breaks the local symmetry while Zn^{2+} ions occupies the interstitial positions) and forms co-ordinate defects known as dangling bonds. However, when ZnO forms covalent bond with four oxygen atoms in glass network, it may form ZnO_4 structural units [22, 23]. The presence of Al_2O_3 in a borate glass network will decrease the tendency of crystallization and improves the stability of the glass structure [24] besides its action as an intermediate in a glass. It is well known that intermediates have mid-position between network former and network modifier. Because of this intermediate nature aluminium may either form tetrahedral and so reinforce the network with co-ordination number 4 or loosen the network in analogy to network modifiers with co-ordination number 6. In $BaO-Al_2O_3-B_2O_3$ glass system, it was reported that [25-27], Al_2O_3 co-ordinated with the oxygen atoms and forms AlO_4 or AlO_6 units in the glass structure. It was also assumed that aluminium ions enter the glass in the form of triclusters, where the triclusters consist of three tetrahedral BO_4 and/or Al_2O_3 in the form of AlO_4 having an oxygen in common [27]. For $MO-Al_2O_3-B_2O_3$; (M = Sr, Ca and Ba) glassy system Owen [28] proposed that some of the M atom associate themselves with Al_2O_3 forming AlO_4 and the rest by reacting with B_2O_3 produces BO_4 or non-bridging oxygen ions. The influence of alkaline earth oxides (Ca, Sr and Ba) as network modifiers on the structural and insulating strength of a glass matrix $RO-Na_2O-B_2O_3$ [R=Ca,Sr and Ba] was discussed in detailed by Yusub et al.[29]. Sakka et. al [30] concluded that the ratio of Al_2O_3 / CaO can affects the glassy structure where AlO_4 is dependent on B_2O_3 content. Pernice et al. [31] reported that, in BaO-

Accepted manuscript

ACCEPTED MANUSCRIPT

Al_2O_3-B_2O_3 glassy system against devitrification process the stability of the glass was increased by Al acting as a good glass former.

In the backdrop of the above discussion, contemplating on all the scientific patronages offered by B_2O_3, BaF_2, CaF_2, ZnO and Al_2O_3, for the present investigation, we prepared a germane oxy-fluoroborate (OFB) glassy system using the aforementioned chemicals as constituent elements. As explained earlier, a good glass former like B_2O_3 added with BaF_2, CaF_2, ZnO and Al_2O_3 as network modifiers can give a better glassy system, since they combine the transparency, mechanical and chemical resistance and the feasible production with the low phonon energy of the fluoride matrices.

Among all the rare earth ions, Sm^{3+} ions are having their applications in diversified fields such as high density optical memory storage devices, under sea communication, colour display systems, solid state lasers in visible region, lasers needed for next generation nuclear fusion and gain media in the microchip laser at higher doping levels [32-34]. Sm^{3+} doped glasses give high power lasers in reddish-orange visible region, having applications in pre-clinical radiation treatment for cancer known as micro beam radiation therapy (MRT) [35]. In Sm^{3+} doped materials an efficiency gap existing around 560 nm known as "yellow gap" [36, 37] is falling in the wavelength range called amber range (590-600 nm) produced by efficient diodes made up of either III-nitrides or III phosphides. These amber LEDs are best suited for automotive applications such as day-time-running lights used in vehicles for tuning and also traffic signals. Moreover, it is impossible for the multi-phonon non-radiative decay process to exit in the host materials having high phonon energies such as borate glasses and do not affect the reddish-orange emission at ~600 nm because of the huge energy gap (~7250 cm^{-1}) existing between $^4G_{5/2}$ fluorescent level and the lower lying level $^6F_{11/2}$ of Sm^{3+} ions. Further due to the lack of lower lying excited states, Sm^{3+} doped laser materials are found to be superior to the other rare earth doped materials from the point of view of concentration quenching effect with no excited state absorption and up conversion losses.

The present paper reports the results obtained on the "spectroscopic and stimulated emission characteristics of Sm^{3+} ions in Oxy-fluoroborate (OFB) glasses" thoroughly studied by us using the spectroscopic techniques such as absorption, photoluminescence and decay measurements. The Judd-Ofelt (J-O) intensity parameters Ω_λ (λ = 2, 4, 6) determined from the measured oscillator strengths (f_{exp}) are used in evaluating the radiative properties such as

Accepted manuscript

ACCEPTED MANUSCRIPT

spontaneous transition probabilities (A_R), total transition probabilities (A_T), radiative branching ratios (β_R) and radiative lifetimes (τ_R) for the observed fluorescent levels of Sm^{3+} ions in OFB glasses. The laser characteristic parameters namely the experimental branching ratios (β_{exp}), stimulated emission cross-sections (σ_{se}), gain bandwidths (σ_{se} x $\Delta\lambda_P$), optical gain (σ_{se} x τ_R) and quantum efficiency were evaluated to optimise the doped rare earth ion concentration in OFB glasses for solid state lasers and optical fibre amplifiers in visible region.

2. Experimental

2.1. Synthesis

In the present work, the glass samples with the selected chemical composition of 15 ZnO – (5-x) Al_2O_3 –10 BaF_2 – 10 CaF_2 – 60 B_2O_3 –x Sm_2O_3 (further known as OFBSm1, OFBSm5, OFBSm10, OFBSm15, OFBSm20 and Sm25 for x = 0.1, 0.5, 1.0, 1.5, 2.0 and 2.5 mol %) were prepared by conventional melt quenching technique. The stoichiometric compositions of the batch materials about 8g were taken into an alumina crucible and heated at 1200^oC in an electrical furnace for 40-60 min until the homogeneous melt was obtained. This melt was then poured rapidly on a pre-heated brass mould and compressed rapidly with another brass mould to obtain globular shaped glass samples with uniform thickness. To eliminate thermal strains produced in glass samples, annealing was done at 400°C for 2 hrs.

2.2. Characterization

The densities of the prepared glasses were measured by using Archimedes's method with water as an immersion liquid. The XRD measurement were taken using XPERT-PRO diffractometer with CuKa radiation (k=1.54°A) in the 2θ angle range 0° - 80° with step size 0.02° s^{-1}. By using the Brewster's angle method (He-Ne laser with a wavelength 650 nm line), the refractive indices for these glasses were measured. The FTIR spectrum for an undoped OFB glass has been recorded using a Thermo scientific make Nicolet-380 spectrometer. The room temperature optical absorption spectra of these glass samples were recorded by using JASCO model V-670 UV-vis-NIR spectrometer in the spectral wavelength range 350-2000 nm with a spectral resolution of 0.1 nm. RF-5301 PC Spectrofluorophotometer was used to record the photoluminescence excitation and emission spectra for all these glasses at room temperature. Using 410 nm CW laser as an excitation source, the time-resolved photoluminescence (PL) measurements were carried out using a home-built set up. The emission from sample was coupled into a monochromator (Acton SP2300) coupled to CCD (charge coupled detector)

Accepted manuscript

ACCEPTED MANUSCRIPT

through the appropriate lenses and filters. For time-resolved PL measurements, a frequency generator (5 Hz), lock-in amplifier, digital storage oscilloscope and a monochromator (Acton SP2300) coupled to a photo multiplier tube (PMT) were employed. A laser scanning confocal microscope (Olympus, BX51) equipped with XY-piezo stage and excited with 410 CW laser was used to record PL images given by the OFB glasses.

3. Results and Discussion

3.1 XRD Spectral Analysis

Fig. 1 shows the XRD pattern of an undoped OFB glass. A broad hump at lower angles ($2\theta=28°$) authenticates the presence of Short Range Ordering (SRO) in glasses. The featureless XRD spectrum obtained confirms the non-crystalline nature of the prepared OFB glasses.

3.2 Physical properties

From the experimentally measured densities and refractive indices different physical properties of OFB glasses have been evaluated, by considering the relevant equations given in the reference [38] and are presented in Table 1. Density is an effective tool to investigate the degree of structural compactness, modifications of geometrical configurations of the glass network, change in co-ordination and the variation of dimensions of interstitial holes. Another important property for the optical materials is refractive index. Many researchers tried to bring the relation between refractive index and glass composition. In the present system of glasses the refractive index decreases with the increase of Sm^{3+} ion concentration. This is due to the dual nature of ZnO because it acts as a network modifier at very low concentrations of Sm^{3+} ion and occupies the network former positions with the increase of Sm^{3+} ion concentration. From Table 1, it can be observed that density of the glasses increasing with increase in Sm^{3+} ion concentration representing the replacement of B_2O_3 by the addition of Sm_2O_3. Molar volume also increases with increase of density and Sm_2O_3 concentration. Fig. 2 shows the variation of density and molar volume with the Sm^{3+} ion concentration. Linear relationship can be observed between Sm^{3+} ion concentration with density and molar volume. These increasing values of density and molar volume indicates that the non-bridging oxygen's (NBO's) increases in the glass network. Hence the glass network expands with the addition of Sm_2O_3 because Sm_2O_3 enters into the glass network as a network modifier, occupies the interstitial space in the network and finally generates the NBO's in the glass structure [39]. The bonding condition in the glass can be measured by using the molar refraction, which is the sum of the contributions given by cationic and oxygen ionic refractions. The high solubility of rare earth ions in the glass can be decided on the basis of low field strength values. The non-linearity response of the materials was governed by the one of the most important property like polarizability. Whenever a material is exposed for intense beam of light, the optical non-linearity will be produced by the electronic polarization. Molecular electronic polarizability of a material is an important physical property for any material as it plays a vital role in deciding the properties possessed by the material such as

Accepted manuscript

ACCEPTED MANUSCRIPT

optical absorption, chemical stability and dielectric properties. In the present work, the OFB glasses are showing low molecular electronic polarizability values indicating stability of the prepared glass. The theoretical value of optical basicity (Λ_{th}) is expressed in terms of the electron density carried by oxygen can be evaluated by using the following expression which was proposed by Duffy and Ingram [40]

$$\Lambda_{th} = \sum_i \frac{Z_i r_i}{2\gamma_i}, \gamma_i = 1.36(x_i - 0.26)$$

Here Z_i is the oxidation number of the cation i, r_i is the ionic ratio with respect to the total number of oxides γ_i is the basicity moderating parameter and is given from the Pauling electro negativity x_i. The optical basicity denotes the average electron donating power of the medium to the oxide atoms present in that medium. Increasing in optical basicity value indicates increasing covalency in the cation-oxygen bonding.

3.3 FTIR Spectral Analysis

Fig. 3 shows the FTIR spectrum of OFBSm10 glass in the region 400–4000 cm^{-1} which is used to know the functional groups involved and the local structure present in OFBSm10 glass. The bands and their assignments are given Table 2. The FTIR spectral absorption peaks can be divided into three main groups in the ranges 400–700 cm^{-1}, 800-1200 cm^{-1} and 1200–1600 cm^{-1} related to B-O-B linkages or vibrational modes produced by a network modifier or metal oxygen bonds, the asymmetric stretching relaxation of the B-O bond stretching of trigonal BO3 units and B-O stretching of the BO_4 units respectively. The bands observed in the region 1600 to 4000 cm^{-1} are due to hydrogen bonding and stretching vibrations of OH groups. The band observed at 401cm^{-1} is attributed to metal oxygen bond vibrations of Ca-O, Al-O, Ba-O [41, 42]. This band also signifies the presence of fluorine in the glass matrix. The absorption band at 451 cm^{-1} related to the "isolated" AlO_4 tetrahedral groups [43]. The band at 550 cm^{-1} attributed to Al_2O_3 that enters the glass network mainly as both AlO_6 octahedral in modifying position and also as AlO_4 tetrahedral groups [44]. The presence of stretching vibrations of B-O-B linkages can be confirms from the band at 609 cm^{-1}. The band at 673 cm^{-1} attributed to the combined B-O stretching vibrations of tetrahedral BO_4 units and AlO_4 tetrahedral groups [43, 45]. The band at 887 cm^{-1} is due to the B–O stretching vibrations in BO_4 units from di-borate groups [45]. The peak observed around 1382 cm^{-1} is attributed to the asymmetric stretching modes of BO_3, BO_2O^- borate triangles and various networks consisting six membered borate planar groups [45, 46]. The B-O bond stretching vibrations of borate units in which boron atoms are co-ordinated with

Accepted manuscript

ACCEPTED MANUSCRIPT

three oxygen atoms leads to the formation of a band around 1623 cm^{-1} [47, 48]. The bands at 2843 and 2917 cm^{-1} are attributed to hydrogen bonding in the present OFB glass. The Characteristic infrared absorption band at 3433 cm^{-1} can be assigned to the fundamental vibrations of OH group. The large amount of OH content present in a glass leads to more non-radiative losses in the glass matrix and decreases the efficiency of the materials doped with rare earth ions. From Fig. 3 it can be seen that, the intensity of OH band in OFB glasses is low. The coefficient of OH vibration (α_{OH}) at 3000 cm^{-1} is used as a measure for the OH content [49]. The content of OH in a glassy material can be estimated using the relevant expression given in our previous paper [50]. For the OFBSm10 glass, the estimated value of OH content is 16.73 ppm , which is found to be smaller than OFPrG (25ppm), OFPrGC04 (30ppm), OFPrGC24 (32 ppm) [51], ZnAlBiB (65.48ppm) [50], LBTAF (123.00 ppm) [52], LHG-8L (128ppm) [53], KBS (133 ppm) [54] and GeS2 (175.5 ppm) [55]. Comparatively, a smaller amount of OH content present in OFB glasses indicates that these materials are aptly suitable for efficient visible lasers.

3.4 Absorption Spectral Analysis

The room temperature absorption spectrum of OFB10 glass in UV-vis-NIR regions is shown in Fig. 4(a) and it consists of several in homogeneously broadened bands assigned to f-f transitions from the ground state $^6H_{5/2}$ to various excited states of Sm^{3+} ions in the host glass. Because of inhomogeneous line broadening, the crystal field fine structure is not well resolved so that only few absorption bands between limited numbers of $^{2S+1}L_J$ manifolds are clearly observed. These absorption bands are observed at 360, 374, 388, 402, 416, 435, 460, 475, 942,1079, 1226, 1405, 1471, 1523, 1585, 1882 nm and are assigned as $^6H_{5/2} \rightarrow {}^4D_{3/2}+({}^4D, {}^6P)_{5/2}$, $^6P_{7/2}$, $^4G_{11/2}$, $^6P_{3/2}+{}^4F_{7/2}$, $({}^6P, {}^4P)_{7/2}$, $^4I_{15/2}$, $^4I_{13/2}$, $^4I_{11/2}$, $^6F_{11/2}$, $^6F_{9/2}$, $^6F_{7/2}$, $^6F_{5/2}$, $^6F_{3/2}$, $^6H_{15/2}$, $^6F_{1/2}$ and $^6H_{13/2}$ transitions respectively. The absorption spectra for the remaining OFB glasses are quite similar and observed at the same wavelength with some variations in their band intensities and hence they were not shown in Fig. 4(a). All these bands are assigned as per the data given by Carnal et al. [56]. Most of the transitions observed in the spectrum were originate from electric dipole induced interactions with selection rule $\Delta J \leq 6$. Some transitions are found to be containing magnetic dipole contribution with selection rule $\Delta J = 0, \pm 1$. The visible absorption bands are appearing as weak in their intensity as they are spin forbidden. The overlap of different $^{2S+1}L_J$ levels made it difficult in assigning the absorption bands in UV-vis region. The presence of fluorides such as PbF_2 and BaF_2 in the present glasses leads to lesser intensity for the observed absorption transitions [57]. The bands observed in infrared region with energies less than 11000 cm^{-1} are found to be sharp and intense, may be because of the effective shielding provided by 5s and 5p shells on the 4f electrons. These transitions are spin allowed ($\Delta S=0$) from the $^6H_{5/2}$ ground state to ^6H and ^6F terms and are assigned to $^6H_{5/2} \rightarrow {}^6F_J$ manifolds with J=1/2, 3/2, 5/2, 7/2, 9/2 and 11/2 respectively.

Accepted manuscript

ACCEPTED MANUSCRIPT

3.4.1 Nephelauxetic effect–Bonding parameter

The nephelauxetic effect which is designated to measure the covalency of rare earth-oxygen bond in the host matrix arises because of partially filled f-shell. Whenever a rare earth ion enters into a host matrix, the electronic orbitals present in 4f configuration are deformed in the host ligand field due to the nephelauxetic effect. The overlap produced between the oxygen orbitals and the 4f orbitals, the energy level structure of the rare earth ions contracts and lead to the wavelength shift. To get an idea about the nature of Sm^{3+} ligand bond in the present work, the nephelauxetic ratios (β) and bonding parameters have been evaluated and are given in Table 3. The nephelauxetic ratio (β) is calculated by using the following relation [38].

$$\beta = \frac{\vartheta_c}{\vartheta_a} \text{ ---------- (1)}$$

Where ϑ_c is the wave number (in cm^{-1}) of a particular transition for the rare earth ion under investigation and ϑ_a is the wave number (in cm^{-1}) for the same transition of an aqua-ion. The bonding parameter δ is calculated using the formula [38, 58].

$$\delta = \frac{1-\bar{\beta}}{\bar{\beta}} \text{ ---------- (2)}$$

where $\bar{\beta}$ is the average value of β. Depending on the field of environment, the bonding parameter (δ) may be positive or negative indicating covalent or ionic bonding. In the present work, the negative values obtained for the bonding parameter (δ) indicates the bonding nature between Sm-O bond is ionic, which gradually decreases as the Sm^{3+} ion concentration increases. This result observed for the present OFB glasses are inconsistent with other Sm^{3+} doped borate, fluoroborate [59] and phosphate [32] glasses.

3.4.2 Oscillator strengths

The energies of an absorption transitions originating from the ground state of rare earth ions in a host matrix can be expressed in terms of oscillator strengths. Such experimental oscillator strengths can be measured by taking the integrated areas under the absorption peaks of the absorption spectrum by using the following expression [60, 61].

$$f_{exp} = \frac{2.303mc^2}{N\pi e^2} \int \varepsilon(\vartheta) d\vartheta \text{ ---------- (3)}$$

Here m and e are mass and charge of an electron, c is the velocity of light; N is the Avogadro's number and $\varepsilon(\vartheta)$ is the molar absorptivity of a band at a wave number ϑ (cm^{-1}).

Accepted manuscript

ACCEPTED MANUSCRIPT

By applying the J-O theory [62, 63] the calculated oscillator strengths (f_{cal}) of an electric dipole transition from an initial state (ψ_J) to an excited state ($\psi'_{J'}$) which depends on three J-O intensity parameters Ω_λ (λ=2, 4 and 6) have been determined from the least square fit between f_{exp} and f_{cal} values.

$$f_{cal} = \left[\frac{8\pi^2 mc\nu}{3h(2J+1)}\right]\left[\frac{(n^2+1)^2}{9n}\right]\sum_{\lambda=2,4,6}\Omega_\lambda(\psi_J \| U^\lambda \| \psi'_{J'})^2 \text{ ---------- (4)}$$

Where ν is the wave number (cm^{-1}) of the transition from ground state (ψ_J) to an excited state ($\psi'_{J'}$), c is the velocity of light in vacuum, m is the rest mass of an electron and $\left\|U^\lambda\right\|^2$ is square reduced matrix elements. The square reduced matrix elements needed for the present work were collected from literature as they are host invariant. The quality of the fit is usually measured by root mean square deviation (δ_{rms}) between the experimental and calculated oscillator strengths by using the following expression

$$\delta_{rms} = \left[\frac{\sum(f_{exp}-f_{cal})^2}{n}\right]^{1/2} \text{ ------ (5)}$$

Here n is the total number of energy levels included in the fitting procedure. The values of f_{exp} and f_{cal} together with the r.m.s deviation are given in Table 3. In the present system, OFBSm10 possesses highest oscillator strengths for all the transitions when compared with other glasses. From Table 3 it can be seen that, relatively small change in rare earth ion concentration in OFB glasses brings changes in the oscillator strengths and modifies the local structure around the Sm^{3+} ions.

3.4.3 Hypersensitive Transitions

According to Jorgenson and Judd [62], for some of the electric dipole transitions of rare earths called hypersensitive transitions, the position and intensity of the bands are found to be sensitive to the environment around the rare earth ions These hypersensitive transitions obey the selection rules of quadrupole transitions $|\Delta S| = 0, |\Delta L| \le 2$ and $|\Delta J| \le 2$ [64, 65]. Calculations have exposed that the intensities of these hypersensitive transitions are larger in magnitude. The polarizability also plays an important role in the hypersensitive transitions. Judd [66] noticed that the hypersensitive transitions are associated with the large values of the reduced matrix elements $\| U^2 \|$ and hence the hypersensitiveness is mainly described by the Ω_2 parameter only. In contrast to it, the $\| U^4 \|$ and $\| U^6 \|$ matrix elements for the hypersensitive transitions are small. The degree of hypersensitivity exhibited by the rare earth ion can be measured from the relative

Accepted manuscript

ACCEPTED MANUSCRIPT

variation of Ω_2 parameter for a rare earth ion in different host environments. This could also be understood from the Fig. 4(b) which shows the variation of oscillator strength of hypersensitivity transition and $\sum\Omega_\lambda$ with the concentration of Sm^{3+} ion in the OFB glasses. From the Fig. 4(b) it can be seen that, the magnitude of J-O intensity parameters depends upon the intensity of hypersensitive transition. The intensity of hypersensitive transition and $\sum\Omega_\lambda$ varies in the same manner with the variation of Sm^{3+} ion concentration. The hypersensitive transitions show differences which are the characteristic features for the co-ordination and symmetry [67]. The qualitative indication of the site symmetry can be known from the band shape and intensity of hypersensitive transitions [68]. From Table 3 it is observed that, the hypersensitive transitions $^6H_{5/2}\rightarrow{}^6P_{3/2}$, $^6H_{5/2}\rightarrow{}^6F_{7/2}$ possesses highest intensity for all the glasses.

3.4.4 J-O theory & Estimation of J-O intensity parameters

The J-O theory is the most well recognized method used to measure the three phenomenological spectroscopic parameters Ω_2, Ω_4 and Ω_6 of rare earth ions in various environments. These parameters are very helpful to know the information about efficiency and performance of the luminescent material. The Ω_2 J-O Parameter is associated with the covalency of the metal-ligand bond and can be employed to check the covalency changes in glasses [69]. The amount of covalency present in the rare earth ligand bonds can be known from the intensity and nature of the hypersensitive transitions. The magnitude of Ω_2 is also depends upon the crystal field variations of the rare earth ion from the cubic symmetry. The magnitude of intensity parameters Ω_4 and Ω_6 are interrelated to the rigidity of the host medium in which the rare earth ions are located [70]. For the present Sm^{3+} doped OFB glasses, the evaluated J-O intensity parameters are given in Table 4 along with the reported values [62, 63, 71-75]. From Table 4, it is seen that the J-O intensity parameters follow the same trend ($\Omega_6 > \Omega_4 > \Omega_2$) for all the OFB glasses and their magnitudes increases up to 1 mol% of Sm^{3+} ions and beyond decreases. The magnitudes of J-O intensity parameters are found to be high for OFBSm10 glass. The magnitude of Ω_2 is found to be lower than Ω_4 and Ω_6. Reisfeld et al [70, 76] have observed that several rare earth doped oxide glasses and chalcogenide glasses possess high magnitude of Ω_2 parameter than fluoride glasses and crystals. In fluoride glass systems, the symmetry of the sites in which the rare earth ions are situated is very large but the number such sites are very small. Additionally, they exhibit very low covalent bonding than oxide glasses. So the Ω_2 parameters obtained for fluoride glassy systems are smaller than that of oxide glassy systems. This may be due to narrow absorption and emission spectral futures observed in fluoride glasses than in oxide glasses. For chalcogenide glasses, the Ω_2 parameters were observed to be very high among all the glasses may be due to their highest covalency [76]. This implies that rare earth-oxygen covalency decreases when pure oxide glasses modified with fluorine content, which is also reflected from the bonding

Accepted manuscript

ACCEPTED MANUSCRIPT

parameters. These J-O intensity parameters are also depend upon the polarizabilities of the neighbouring ions and nature of the chemical atmosphere. From the 100% ionic model of the ligand field interaction, it is observed that the charge of fluorine and chlorine ions is -1 and their dipolar isotropic polarizabilities are 1Å^3 and 3 Å^3 respectively. This is one of the main reasons, for the existing of hypersensitive transitions which are generally dominated by the one of the J-O intensity parameter Ω_2.

3.5 Photoluminescence spectral properties

Fig. 5 shows the excitation spectrum of OFBSm glasses in the region 350-525 nm at an emission wavelength 599 nm. The inset in Fig.5 shows the excitation spectrum with wavenumber (cm^{-1}) scale. The excitation spectra have nine excitation bands at 360, 374, 388, 402, 416, 438, 461, 477, 500 nm corresponding to the transitions $^6H_{5/2}\rightarrow{}^4D_{3/2}$, $^6F_{7/2}$, $^4L_{15/2}$, $^4F_{7/2}$, $(^6P, {}^4P)_{5/2}$, $^4M_{19/2}$, $^4I_{13/2}$, $^4I_{11/2}$ and $^4G_{7/2}$ respectively. Among all these transitions, the transition $^6H_{5/2}\rightarrow{}^4F_{7/2}$ at 402 nm is very intense and hence used to record the photoluminescence spectra of Sm^{3+} doped OFB glasses. This intense excitation wavelength observed at 402 nm also indicates that the commercially available UV-blue laser diodes and blue-bluish-green light emitting diodes (LEDs) are aptly suitable to act as pumping sources for the Sm^{3+} doped oxy-fluoride glasses [77]. Though the excitation band related 402 nm is more intense than other transitions, the emission spectra in the present work were recorded at 410 nm using CW laser source because a laser source can excite the atoms to the desired level much effectively than the conventional excitation sources. As we don't have a laser source at 402 nm, we have used the nearest wavelength CW laser source (410 nm) for excitation. Fig. 6 shows the photoluminescence spectra of Sm^{3+} doped OFB glasses using 410 nm CW laser diode as an excitation source with wavenumber (cm^{-1}) scale on X-axis. The left side inset in Fig. 6 shows the photoluminescence spectra of Sm^{3+} doped OFB glasses using 410 nm CW laser diode as an excitation source with wavelength scale on X-axis. However, we have also recorded the emission spectra for Sm^{3+} doped OFB glasses by fixing the excitation wavelength at 402 nm using a commercial Spectrofluorophotometer to know the difference between the emission spectra given by 402 nm (commercial source) and 410 nm (CW laser) excitation sources. The right side inset in Fig. 6 shows the photoluminescence spectra of Sm^{3+} doped OFB glasses at an excitation wavelength 402 nm. Both the inset photoluminescence spectra shown in Fig. 6 consists of four emission bands in yellow, orange, red and NIR regions at 563, 598, 646 and 708 nm corresponding to the transitions $^4G_{5/2}\rightarrow{}^6H_{5/2}$, $^4G_{5/2}\rightarrow{}^6H_{7/2}$, $^4G_{5/2}\rightarrow{}^6H_{9/2}$ and $^4G_{5/2}\rightarrow{}^6H_{11/2}$ respectively with slight difference in their intensities. The intensity

Accepted manuscript

ACCEPTED MANUSCRIPT

of the photo luminescent bands produced by 410 nm CW laser excitation is slightly more that its counterparts produced at 402 nm using conventional excitation source. This is obvious because, the CW laser source can effectively excite the atoms to the desired level than the conventional excitation source. As shown in Fig. 6, an emission transition observed in orange region $^4G_{7/2}\rightarrow{}^6H_{7/2}$ is highly intense than the remaining transitions for all glasses. From Fig. 6 it can also be observed that, in both the photoluminescence spectra, the concentration quenching occurs at 1 mol% of Sm^{3+} ions in OFB glasses. This concentration quenching may be due to efficient energy transfer between rare earth ion sites or due to cross- relaxation mechanism produced at higher dopant concentrations.

The optical transitions $^6H_{5/2}\rightarrow{}^6F_{9/2}$ and $^6H_{5/2}\rightarrow{}^6F_{7/2}$ occurring in the absorption spectra in the NIR region are hypersensitive. In the emission spectra, the transition $^4G_{5/2}\rightarrow{}^6H_{9/2}$ at 646 nm is also recognized as hypersensitive transition. A careful observation of these absorption and emission spectra further indicate that the transition $^6H_{5/2}\rightarrow{}^6F_{7/2}$ is a threefold triplet. The reason for splitting of this transition may be due to the degeneracy produced in $^6H_{5/2}$ ground state in the crystal field [78] due to certain self-adjustment of Sm^{3+} environment in the glass network. The quenching of luminescence in the OFBSm10 glass is low due to the high intensity of the luminescence bands in Sm^{3+} ion in that glass. The high luminescence of this OFBSm10 glass is also a representation of less cross relaxation i.e. the transfer of energy in between the Sm^{3+} ions from the excited state to the ground state is low for this OFBSm10 glass when compared with other glasses due to dipole-dipole or dipole-quadrupole interactions. In the emission spectra, the transition $^4G_{5/2}\rightarrow{}^6H_{7/2}$ with the selection rule $\Delta J = \pm 1$ is a magnetic dipole (MD) allowed whereas the transition $^4G_{5/2}\rightarrow{}^6H_{9/2}$ is purely electric dipole. The intensity ratio of electric dipole to magnetic dipole transitions gives the magnitude of the asymmetry of the local environment of Sm^{3+} ions. If the intensity ratio of the electric dipole transition to the magnetic dipole transition (Asymmetry Ratio = $^4G_{5/2}\rightarrow{}^6H_{9/2}$/ $^4G_{5/2}\rightarrow{}^6H_{7/2}$) is high then the asymmetry of Sm^{3+} ions in the network is high [79]. For the present glasses the asymmetric ratios are OFBSm1=0.4464, OFBSm5=0.4786, OFBSm10=0.4313, OFBSm15=0.4899, OFBSm20=0.5019 and OFBSm25=0.5824 respectively. This asymmetric ratio is high for OFB25 glass and low for OFBSm10 glass; indicate that OFB25 glass has more local disorder and OFB10 glass have less local disorder for the Sm^{3+} ions in the present glass network. For all these glasses, asymmetric

Accepted manuscript

ACCEPTED MANUSCRIPT

ratio values are found to be less than one which is a representation of occupation of Sm^{3+} ions at inverse symmetry site.

3.6 Radiative properties

From the evaluated J-O parameters, the radiative properties such as radiative transition probability (A_R), total radiative transition probability (A_T), branching ratio (β_R), radiative lifetime (τ_R) and stimulated emission cross-section (σ_{se}) for the Sm^{3+} ions corresponding to the transitions $^4G_{5/2}\rightarrow{}^6H_{5/2}$, $^4G_{5/2}\rightarrow{}^6H_{7/2}$, $^4G_{5/2}\rightarrow{}^6H_{9/2}$ and $^4G_{5/2}\rightarrow{}^6H_{11/2}$ have been measured by using the equations in the literature [80] and these evaluated values are given in Tables 5 and 6. From Table 5, it is observed that, the radiative transition probability (A_R) values for the transition $^4G_{5/2}\rightarrow{}^6H_{7/2}$ are found to be higher than other emission transitions. The luminescence branching ratio is one of the important characteristic parameter used to describe the possibility of attaining stimulated emission from any specific transition. One can identify a potential laser transition if that transition possesses a branching ratio ≥ 0.50 [81]. The experimental branching ratio (β_{exp}) values obtained from the relative areas of the emission lines and these values are found to be in good agreement with the radiative branching ratios (β_R). From Table 5, it is observed that all the glasses have higher radiative branching ratios (β_R) (≥ 0.50) for the transition $^4G_{5/2}\rightarrow{}^6H_{7/2}$. These radiative branching ratio values [50.5% (OFBSm1), 50.6% (OFBSm5), 53.9% (OFBSm10), 52.1% (OFBSm15), 51.6% (OFBSm20) and 50.9% (OFBSm25) respectively] suggest that the glass OFBSm10 have a possibility to be used as a luminescent material for laser applications. Larger stimulated emission cross-section (σ_{se}) value is an attractive feature for low threshold, high gain laser applications, which are used to get continuous wave (CW) laser action [82]. From the observed luminescence bands, the stimulated emission cross-section σ_{se} can be evaluated by using the equation

$$\sigma_{se}\left(a_J, b_{J'}\right) = \frac{{\lambda_P}^4}{8\pi c n^2 \Delta\lambda_P} A_R\left(a_J, b_{J'}\right)$$

Here $\Delta\lambda_P$ is the emission peak wavelength and $\Delta\lambda_P$ is known as full width at half maximum which can be evaluated by integrating the intensity at the peak wavelength [82]. Out of all the radiative parameters, full width at half maximum ($\Delta\lambda_P$), stimulated emission cross-section (σ_{se}), gain bandwidths ($\sigma_{se}\times\Delta\lambda_P$), optical gain parameters ($\sigma_{se}\times\tau_R$) and quantum efficiencies (η) are the five most crucial parameters for a laser designer. These parameters calculated for the

Accepted manuscript

ACCEPTED MANUSCRIPT

transitions $^4G_{5/2} \rightarrow {}^6H_J$ (J=5/2, 7/2, 9/2, 11/2) are given in Tables 6 and 7. From Table 6, it can be seen that, Glass OFBSm10 exhibits highest values of stimulated emission cross-section (σ_{se}), gain bandwidths ($\sigma_{se} \times \Delta\lambda_P$) and optical gain parameters ($\sigma_{se} \times \tau_R$) for the transition $^4G_{5/2} \rightarrow {}^6H_{7/2}$. These radiative properties of the electric dipole transitions are liable for orange emission in Sm^{3+} doped glasses. Hence, OFBSm10 is most suitable for solid state lasers as well as fiber amplifiers in visible Orange region.

3.7 Decay measurements, cross-relaxation rates (non-radiative decay rates) and quantum efficiency

The Logarithmic decay curves recorded for $^4G_{5/2}$ level of Sm^{3+} ions in OFB glasses are shown in Fig. 7(a-f). As shown in Fig. 7(a-f), the decay curves are finely fitted to a single exponential function at lower concentrations (up to 1.0 mol % of RE) and non-exponential at higher concentrations (≥ 1.0 mol % of RE). Normally, when the concentration of the RE ion is low enough, they can act as an isolated centres and the decay from any excited level can be described by a single exponential function. When the concentration of the RE ion increases, the distance between the RE ion centres will decrease and the interaction between them increases. Such strong interactions existing between two active ions are able to transfer excitation energy from one RE ion to the other [57]. The overlap between absorption and emission bands and the existence of the trap centres around the Sm^{3+} ion are also responsible for energy transfer. The non-exponential nature of decay curves observed at higher concentration of Sm^{3+} ions in OFB glasses are due to such energy transfer process [57]. The effective decay time can be determined by the expression

$$\tau_{exp} = \frac{\int tI(t)dt}{\int I(t)dt}$$

Here I (t) is the emission intensity at time‘t’. The experimental lifetimes of the excited $^4G_{5/2}$ level have been obtained by taking first e-folding times of the decay curves and are given in Table 7 along with the radiative lifetimes. The experimental lifetimes are found to be decreasing with increase in Sm^{3+} ion concentration in these OFB glasses.

The phenomenon of photoluminescence quenching, the non-exponential nature of decay curves observed at higher concentrations and hence decrease in experimental lifetimes can be understood clearly from the possible cross-relaxation channels of emission shown in energy level

Accepted manuscript

ACCEPTED MANUSCRIPT

diagram (Fig. 8). For photoluminescence quenching the closely spaced large number of Sm^{3+} ion energy levels are also responsible. In general, the photoluminescence quenching observed can be understood through two important mechanisms. The first one is due to the energy transfer between the rare earth ions through cross-relaxation and the second one is through migration of excitation energy to the structural defects acting like energy sinks through the mechanism called multi-phonon relaxation [45]. The multi-phonon relaxation rate of an excited state depends on the energy separation of that level with the next lower lying level and phonon energy of the host material.

The exponential energy-gap law for the multi-phonon relaxation rate is given by [83].

$$W_{MPR} = \beta \exp\left(-\alpha \Delta E\right), where\, \alpha = (a\hbar\omega)^{-1}$$

Here the parameters $\beta = 6.30\times10^{-10}\, s^{-1}$, $\alpha = 420\ \ cm^{-1}$ and $\Delta E = 7211 cm^{-1}$ are host dependent and need not depends on the chosen rare earth ion. By using above equation the multi-phonon relaxation rate is evaluated and it is equal to almost zero. Hence, in the present work, for OFB glasses the multi-phonon relaxation rate is almost negligible and the non-radiative relaxation process involved in photoluminescence quenching is mainly due to the energy transfer through cross-relaxation phenomenon as shown in Fig. 8. From the energy level diagram shown in Fig. 8, the following emission and absorption channels can be identified for photoluminescence quenching through cross-relaxation mechanism at higher concentrations of the doped rare earth ion.

Emission Channels	***Absorption channels***
ET₁: $^4G_{5/2}\rightarrow{}^6F_{5/2}$ *(10551 cm^{-1})*	***AT₁:*** $^6H_{5/2}\rightarrow{}^6F_{11/2}$*(10523 cm^{-1})*
ET₂: $^4G_{5/2}\rightarrow{}^6F_{7/2}$ *(9691 cm^{-1})*	***AT₂:*** $^6H_{5/2}\rightarrow{}^6F_{9/2}$ *(9257 cm^{-1})*
ET₃: $^4G_{5/2}\rightarrow{}^6F_{9/2}$ *(8567 cm^{-1})*	***AT₃:*** $^6H_{5/2}\rightarrow{}^6F_{7/2}$ *(8133 cm^{-1})*
ET₄: $^4G_{5/2}\rightarrow{}^6F_{11/2}$ *(7301 cm^{-1})*	***AT₄:*** $^6H_{5/2}\rightarrow{}^6F_{5/2}$ *(7273 cm^{-1})*

The cross-relaxation rate (W_{CR}) can be measured from the following expression and are given in Table 6.

$$W_{CR} = \frac{1}{\tau_{exp}} - \frac{1}{\tau_R}$$

The large cross-relaxation rates at higher concentrations (≥ 1 mol %) are responsible for energy transfer process. Due to these increased cross-relaxation rates (non-radiative decay process) the quantum efficiencies also decreases at higher concentrations. Quantum efficiency is a crucial

factor that can control the performance of the material and these materials further can be used in lasers, optical fibers and planar waveguides.

The quantum efficiency for the present OFB glasses can be evaluated by using the following expression and these values are presented in Table 7.

$$\eta = \frac{\tau_{exp}}{\tau_R}$$

In the present investigation, the glass OFBSm10 has highest quantum efficiency and low cross-relaxation rates (non-radiative decay rates) than other glasses. Hence the glass OFBSm10 is most reliable lasing material to exhibit efficient visible lasing emission in the orange spectral region. The most crucial parameters like branching ratios (β_R), stimulated cross-section (σ_{se}) and quantum efficiencies (η) along with cross-relaxation rates of OFBSm10 glass are compared with other reported values in Table 8 [45, 78, 84- 89].

***3.8 Inokuti-Hirayama model analysis*.**

It is well known that, the lifetime of an excited state energy level refer to the average time for which the molecule/ion can stay in that excited state before coming down to the lower energy level by emitting a photon [90]. The excited (donor) ions can relax to lower energy state through two different methods. One method is direct energy transfer to other active ion (acceptor) and another method is energy migration among the donor ions before such energy reaches to the accepter ion [71]. If the donor and the acceptor ions are homogeneously distributed in the host matrix and the energy migration among the donor ions are negligible, then the decay curves can be fitted to the frame work of Inokuti-Hirayama (IH) model [91] to disclose the dominant mechanism of energy transfer. Therefore the IH model is explicitly applicable when the energy transfer between the donor and accepter is faster than the energy migration between the donor ions and the luminescence decay intensity in such a case is given by

$$I(t) = I_0 \exp\left\{-\frac{t}{\tau_0} - Q\left(\frac{t}{\tau_0}\right)^{\frac{3}{S}}\right\}$$

Accepted manuscript

ACCEPTED MANUSCRIPT

Here't' is the time after excitation, 'τ_0' is the intrinsic decay time of the donors in absence of acceptors. 'Q' is the energy transfer parameter defined as

$$Q = \frac{4\pi}{3}\Gamma\left(1-\frac{3}{S}\right)N_0 R_0^{\,3}$$

Depend on the value of S and the gamma function $\Gamma(X)$, which is equal to 1.77 for dipole-dipole (S=6), 1.43 for dipole-quadrupole (S=8) and 1.3 for quadrupole-quadrupole (S= 10) interactions, respectively. N_0 is the acceptor ion concentration and R_0 is the critical transfer distance which is defined as the donor-acceptor separation when the rate of energy transfer between a donor and acceptor ion is equal to the rate of intrinsic decay τ_0^{-1}.

The donor-acceptor interaction parameter C_{DA} and the energy transfer probability W_{ET} are calculated using the expressions

$C_{DA} = R_0^{(S)}\tau_0^{-1}$ and $W_{ET} = C_{DA}R_0^{(S)}$.

The energy transfer parameter (Q), critical energy transfer distance (R_0) and donor-acceptor interaction parameter (C_{DA}) are calculated by fitting the IH model are given in Table 9. The study of non-exponential behaviour of decay curves shows an increase in magnitude of energy transfer parameter (Q) and donor-acceptor interaction parameter (C_{DA}) with the increase in Sm^{3+} ion concentration which is similar to other reported Sm^{3+} doped glasses [33, 57, 71, 72, 92]. From Fig.7 (a-f), it is observed that for IH fitting model, s = 6 is well fitted with the non-exponential decay curves which authenticates that the energy transfer between the Sm^{3+} ions is due to dipole-dipole interaction. From the Table 9 it is observed that, the magnitude of Q, R_0 and C_{DA} are strongly depends on the Sm^{3+} ion concentration and these values are increasing with increase in Sm^{3+} ion concentration and found to be higher than the values reported for other glasses [33, 57, 71, 72, 92].

3.9 CIE Chromaticity Co-ordinates & Confocal Images.

Fig. 9 shows the site of colour chromaticity co-ordinates evaluated for OFB glasses doped with different concentrations of Sm^{3+} ions and are displayed in Table 7 numerically. In general, the colour purity or colour saturation can be estimated from the distance between the colour coordinates of present investigated Sm^{3+} doped OFB glasses and the colour co-ordinates of equal-energy point (0.33, 0.33), divided by the distance between the equal-energy point to the dominant wavelength point [93]. The colour co-ordinates evaluated using the above said

Accepted manuscript

ACCEPTED MANUSCRIPT

procedure for the present Sm^{3+} doped OFB glasses are situated on the border of the colour chromaticity figure which comes into view to be very closest to the bright orange colour (590–635 nm). Normally, the colour purity is 100% for the monochromatic light sources located on the border of the chromaticity diagram and 0% for white light illuminates [93]. The orange emission given by OFB glasses are also further confirmed in principle by the confocal photoluminescence images recorded under the excitation of 410 nm CW laser. Such confocal images recorded for all the OFB glasses are also shown in Fig. 9. From Fig.9 it is conspicuous that, the orange emission exhibited by OFB glasses increases with RE ion concentration up to 1 mol% and then decreases beyond. This result is inconsistent with the CIE chromaticity coordinates possessed by the glasses. Thus the CIE coordinates measured and confocal images recorded for Sm^{3+} ions in OFB glasses are complimenting to each other.

4. Conclusions

Oxy-fluoroborate (OFB) glasses doped with different concentration of Sm^{3+} ions were prepared and investigated using the spectroscopic techniques such as XRD, FTIR, absorption, emission and decay curve measurements to characterize and optimise the doped rare earth ion for visible lasing emission. Featureless XRD spectrum recorded for an undoped OFB glass confirms the amorphous nature of the prepared glasses. The FTIR spectral studies, confirms the various fundamental functional groups present in these glasses. The bonding parameters measured confirms the ionic nature of the Sm^{3+} ions with its neighbouring ligands and the degree of iconicity decreases gradually with the increase of rare-earth ion concentration. The photoluminescence spectra recorded for OFB glasses gives four emission bands in yellow, orange, red and NIR regions at 563, 598, 646 and 708nm corresponding to the transitions $^4G_{5/2} \rightarrow {}^6H_{5/2}$, $^4G_{5/2} \rightarrow {}^6H_{7/2}$, $^4G_{5/2} \rightarrow {}^6H_{9/2}$ and $^4G_{5/2} \rightarrow {}^6H_{11/2}$ respectively. In the present investigation, luminescence quenching was observed at 1 mol% of Sm^{3+} ion concentration and beyond 1 mol% the decay curves of the Sm^{3+} doped OFB glasses changes from exponential to non-exponential nature. The non-exponential decay curves are well fitted to the Inokuti-Hirayama model for S=6, indicating that the nature of interaction between Sm^{3+} ions for energy transfer through cross-relaxation is dipole-dipole type. Under 410 nm CW laser excitation, an intense orange emission has been observed at 598 nm ($^4G_{5/2} \rightarrow {}^6H_{7/2}$) in all these OFB glasses, for

Accepted manuscript

ACCEPTED MANUSCRIPT

which the branching ratio, stimulated emission cross-section and quantum efficiency values are measured and found to be maximum for OFBSm10 glass. From all these studies, it is concluded that OFB glass with 1 mol% of Sm^{3+} (OFBSm10) can act as efficient lasing material to produce intense visible orange emission at 598 nm in principle. Visible orange emission possessed by these glasses is also further confirmed by CIE chromaticity coordinates and the confocal images recorded under 410 nm CW laser excitation.

Acknowledgements

Two of the authors, Mahamuda Shaik (File No: SR/WOS-A/PS-53/2011) and Swapna Koneru (File No: SR/WOS-A/PS-35/2011) are very much thankful to Department of Science and Technology (DST), Government of India, New Delhi, for awarding them with a Women Scientist's scheme under DST-WOS (A) programme. This work is also partly supported by High-impact Research initiative of IIT-Delhi, UK-India Education Research Initiative (UKIERI) and DST, Govt. of India, New Delhi.

References

[1] M. Srinivasulu, A. S. Rao, J. Mater. Science Letter 20 (2001) 737-740.

[2] M. Venkateswarlu, M. V. V. K. S. Prasad, K. Swapna, Sk. Mahamuda, A. Srinivasa Rao, A. Mohan Babu, D. Haranath, Ceram. Int. 40 (2014) 6261-6269.

[3] R. Rama Kumar, A. S. Rao, B. C. Venkata Reddy, Opt. Mater. 4(1995) 723-728.

[4] K. Swapna, Sk. Mahamuda, A. Srinivasa Rao, T. Sasikala, L. Rama Moorthy, J. Lumin. 146 (2014) 288-294.

[5] K. Swapna, Sk. Mahamuda, A. Srinivasa Rao, S. Shakya, T. Sasikala, D. Haranath, G. Vijaya Prakash, Spectrochim. Acta. Part A 125 (2014) 53-60.

[6] Sk. Mahamuda, K. Swapna, P. Packiyaraj, A. Srinivasa Rao, G. Vijaya Prakash, J. Lumin. 153(2014) 382-392.

[7] A. Srinivasa Rao, J. L. Rao, R. Ramakrishna Reddy, T. V. Ramakrishna Rao, Opt. Mater. 4 (1995) 717-721.

[8] K. Swapna, Sk. Mahamuda, A. Srinivasa Rao, M .Jayasimhadri, T. Sasikala, L. Rama Moorthy, J .Lumin. 139 (2013) 119-12

Accepted manuscript

ACCEPTED MANUSCRIPT

[9] A. Srinivasa Rao, B. Rupa Venkateswara Rao, M.V.V.K.S. Prasad, J. V. Shanmukha Kumar, M. Jayasimhadri, J. L. Rao, R. P. S. Chakradhar, Physica B 404(2009) 3717-3721.

[10] Sk. Mahamuda, K. Swapna, A. Srinivasa Rao, T. Sasikala, L. Rama Moorthy, Physica B 428(2013)36-42.

[11] Y. Divwedi, S. B. Rai, Opt. Mater. 31 (2008) 87-93.

[12] Sd. Zulfiqar Ali Ahamed, C. Madhukar Reddy, B. Deva Prasad Raju, Opt. Mater. 35 (2013) 1385-1394.

[13] G. Dominiak-Dzik, W. Ryba-Romanowski, J. Pisarska, W.A. Pisarski, J. Lumin. 122-123 (2007) 62-65.

[14] M. V. Vijaya Kumar, K. Rama Gopal, R.R. Reddy, G.V. Lokeswara Reddy, B.C.Jamalaiah, J. Lumin. 142 (2013) 128-134.

[15] I. Arul Rayappan, K. Marimuthu, J. Phys. Chem. Solids 74 (2013) 1570-1577.

[16] W.A. Pisarski, G. Dominiak-Dzik, W. Ryba-Romanowski, J. Pisarska, J. Alloys Compd. 451 (2008) 220-222.

[17] J. Pisarska, R. Lisiecki, W. Ryba-Romanowski, G. Dominiak-Dzik, W.A. Pisarski, J. Alloys. Compd. 451 (2008) 226-228.

[18] C. Madhukar Reddy, N. Vijaya, B. Deva Prasad Raju, Spectrochim. Acta A 115 (2013) 297-304.

[19] S. A. Pollack, D. B. Chang, J. App. Phys. 64 (1988) 2885-2893.

[20] A. Lucca, M. Jacquemet, F. Druon, F. Balembois, P. Georges, P. Camy, J. L. Doulan, R. Moncorge, Opt. Lett. 29 (2004) 1879-1881.

[21] Sk. Mahamuda, K. Swapna, A. Srinivasa Rao, M. Jayasimhadri, T. Sasikala, K. Pavani, L. Rama Moorthy, J. Phys. Chem. Solids 74 (2013) 1308-1315.

[22] P. Subbalakshmi, N. Veeraiah, Ind. J. Eng. Mater. Sci. 8 (2001) 275-284.

[23] R. K. Brow, D. R. Tallent, S. T. Myers, J. Non-Cryst. Solids 191 (1995) 45-55.

[24] L. Van Wullen, W. Muller Warmth, J. Solid State NMR, 2 (1993) 279-284.

[25] H. Scholze, “Glass : Nature, Structure and Properties”, Springer, New York, (1991).

[26] J. E. Shelby, Introduction to “Glass Science and Technology”, The Royal Society of Chemistry, Cambridge, (1997).

[27] A. Naruse, Y. Abe, Takami, Yogyo- Kyokai-Shi 79 (1971) 225.

Accepted manuscript

ACCEPTED MANUSCRIPT

[28] A. E. Owen, Phys. Chem. Glasses 2 (1961) 152-162.

[29] S. Yusub, Ch. Rajyasree, A. Ramesh Babu, P.M. Vinaya Teja, D. Krishna Rao, J. Non-Cryst. Solids 364 (2013) 62-68.

[30] S. Sakka, Yogyo- Kyokai- Shi 85 (1977) 299-302.

[31] P. Perince, S. Esposito, A. Aronne and V. N. Sigaev, J. Non-Cryst. Solids 258 (1999) 1- 10.

[32] V. Venkatramu, P. Babu, C. K. Jayasankar, Th. Troester, W. Sievers, G. Wortmann, Opt. Mater, 29 (2007) 1429-1439.

[33] J. Suresh kumar, K. Pavani, T. Sasikala, A. Srinivasa Rao, Neeraj Kumar, S. B. Rai, L. Rama Moorthy, Solid. Stat. Sci. 13 (2011) 1548-1553

[34] C. K. Jayasankar, V. Venkatramu, J. Appl. Phys. 97 (2005) 093523-093527.

[35] D. N. Slatin, P. Spanne, F. A. Dilmanin, M. Sandborg, Med. Phys. 19 (1992) 1395-1400.

[36] Regina Muellar-Mach, Gerd O. Mueller Michal R. Krames, Oleg B. Shchekin, Peter J. Schmidt, Helmut Bechtel, Ching-Hui Chen, Oliver steigelmann, Phys. Status Solidi RR1. 3(7-8) (2009) 215-217.

[37] Michal R. Krames, Oleg B. Shchekin, Regina Mueller-Mach, Gerd O. Mueller, Ling Zhou, Gerard Harbers, M. George craford, J. disp. Technol. 3 (2) (2007) 160-175.

[38] A. S. Rao, Y. N. Ahammed, R. R. Reddy, T.V.R. Rao, Opt. Mater. 10 (1998) 245-252.

[39] S. Rakpinch, J. Kaewkhao, N. Sresittipokakun, K. Boonin, J. M. Park, H. J. Kim, P. Limsuwan, Physics International 4 (2013) 81-87.

[40] J. A. Duffy, M. D. Ingram, J. Inorg. Nucl. Chem. 37 (1975) 1203-1206.

[41] Y. H. Zhou, J. Lin, S. B. Wang, H. J. Zhang, Opt. Mater. 20 (2002)13-20.

[42] D. Boyr, G. Bertrand-Chadeyron, R. Mahiou, Opt. Mater. 26 (2004) 101-105.

[43] P. Tarte, Spectrochim. Acta: Part A 23 A (1967) 2127- 2143.

[44] S. Kojima, M. Kodama, Jpn. J. Appl. Phys, 33 (1994) 2886-2889.

[45] K. Maheshvaran, K. Linganna, K. Marimuthu, J. Lumin. 131 (2011) 2746-2753.

[46] Madhukar Reddy, G.R. Dillip, K. Mallikarjuna, Sd. Zulifiqar Ali Ahamed, B. Sudhakar Reddy, B. Deva Prasad Raju, J. Lumin. 131 (2011) 1368-1375.

[47] H. Scholze, Glass Ind. 47 (11) (1966) 622-628.

[48] M. Kaur1, S.P. Singh, D. S. Mudahar, G. S. Mudahar, Materials Physics and Mechanics 15 (2012) 66-73.

Accepted manuscript

ACCEPTED MANUSCRIPT

[49] H. Ebendorff-Heidepriem, W. Seeber, D. Ehrt, J. Non-Cryst. Solids 163 (1)(1993) 74-80.

[50] Sk. Mahamuda, K. Swapna, P. Packiyaraj, A. Srinivasa Rao, G. Vijaya Prakash, Opt. Mater. 36 (2013) 362-371.

[51] K. Biswas, A. D. Sontakke, J. Ghosh, K. Annapurna, J. Am. Ceramic. Society, 93 (4) (2010) 1010-1017.

[52] T. Suhasini, B. C. Jamalaiah, T. Chengaiah, J. Suresh Kumar, L. Rama Moorthy, Physica B 407 (2012) 523-527.

[53] T. I. Suratwala, R.A. Steele, G.D. Wilke, J.H. Campbell, K. Takeuchi, J. Non-Cryst. Solids 263–264 (2000) 213-227

[54] B.B. Kale, A. Jha, S.K. Apte, P.V. Adhyapak, D.P. Amalnerkar, Mater. Chem. Phys.78 (2002) 330-336.

[55] Tirtta Som, Basudeb Karmakar, Spectrochim. Acta Part A 79 (2011) 1766-1782.

[56] W. T. Carnall, P. R. Fields, K. Rajnak, J. Chem. Phys. 49 (1968) 4424-4442.

[57] S. Arun Kumar, K. Marimuthu, J. Alloys. Compd. 565 (2013) 104-114.

[58] S.P. Sinha, Complexes of the Rare Earths, Pergamon, Oxford, 1966.

[59] C. K. Jayasankar, P. Babu, J. Alloys Compd. 307 (2000) 82-95.

[60] W.T. Carnall, in: K.A. Gschneidner, L.R. Eyring (Eds.), Handbook on the Physics and Chemistry of Rare Earths, vol. 3, North-Holland, Amsterdam, 1979 (Chapter 24).

[61] R.R. Jacobs, M.J. Weber, IEEE J. Quant. Electron. QE-12 (1976) 102-111.

[62] B. R. Judd, Phys. Rev. 127 (1962) 750-761.

[63] G.S. Ofelt, J. Chem. Phys. 37 (1962) 511-520.

[64] C. K. Jorgensen, B. R. Judd, Mol. Phys. 8 (1964) 281-290.

[65] S. Tanabe, T. Ohyagi, N. Soga, T. Hanada, Phys. Rev. B 46 (1992) 3305-3310.

[66] S.N. Misra, J. Sci. Ind. Res. 44 (1985) 366-375.

[67] D. G. Karraker, Inorg. Chem. 6 (1967) 1863-1868.

[68] G. R. Choppin, D. E. Henrie, K. Buijs, Inorg. Chem. 5 (1966) 1743-1748.

[69] B. G. Wybourne, Spectroscopic Properties of Rare earths, Interscience, New York, 1975.

[70] C. K. Jorgenson, R. Reisfeld, J. Less-Common Met. 93 (1983) 107-112.

[71] B. C. Jamalaiah, M. V. Vijaya Kumar, K. Rama Gopal, Opt. Mater. 33(2011)1643-1647.

Accepted manuscript

ACCEPTED MANUSCRIPT

[72] B. C. Jamalaiah, J. Suresh Kumar, A. Mohan Babu, T. Suhasini, L. Rama Moorthy, J. Lumin. 29 (2009) 363-369.

[73] M. Jayasimhadri, L. R. Moorthy, S. A. Saleem, R. V. S. S. N. Ravi Kumar, Spectrochim. Acta Part A 64 (2006) 939-944.

[74] R. Praveena, V. Venkatramu, P. Babu, C.K. Jayasankar, Physica B 403 (2008) 3527-3534.

[75] Ch. Srinivasa Rao, C.K. Jayasankar, Optics Communications 286 (2013) 204-210.

[76] R. Reisfeld, J. Less-Common Met. 112 (1985) 9-18.

[77] B. J. Chen, L. F. Shen, E. Y. B. Pun, H. Lin, Opt. Express 20 (2012) 2802-2809.

[78] H. Ahrens, M. Wollenhaupt, P. Frobel, J. Lin, K. Barner, G. S. Sun, R. Braunstein, J. Lumin. 82 (1999) 177-186.

[79] A. Kurita, T. Kushida, T. Izumitani, M. Matsukawa, Opt. Lett. 19 (1994) 314-316.

[80] K. Swapna, Sk. Mahamuda, A. Srinivasa Rao, M. Jayasimhadri, T. Sasikala, L. Rama Moorthy, Ceram. Int. 39 (2013) 8459-8465.

[81] L. Rama Moorthy, T. S .Rao, K. Janarthanam, A. S. Rao, Y. Subramanyam, Opt. Mater. 12 (1999) 459-465

[82] S. A. Saleem, B. C. Jamalaiah, M. Jayasimhadri, A. Srinivasa Rao, Kiwan Jang, L. Rama Moorthy, JQSRT 112 (2011) 78-84.

[83] R. Reisfeld, C.K. Jorgensen, Handbook on the Physics and Chemistry of Rare Earths, in: K.A. Gschneidner, L. Eyring (Eds.), Excited state phenomena in vitreous materials, North-Holland, Amsterdam, 1987, pp. 41–44. Chapter 58.

[84] T. Suhasini, J. Suresh Kumar, T. Sasikala, Kiwan Jang, Ho Sueb Lee, M. Jayasimhadri, Jung Hyun Jeong, Soung Soo Yi, L. Rama Moorthy, Opt. mater. 31 (2009) 1167-1172.

[85] I. Arul Rayappan, K. Selvaraju, K. Marimuthu, Physica B 406 (2011) 548-555.

[86] K. Selvaraju, K. Marimuthu, J.Alloys.Compd. 553 (2013) 273-281.

[87] T. Sasikala, L. Rama Moorthy, A. Mohan Babu, Spectro. Chimica. Acta. Part A 104 (2013) 445-450.

[88] K. S. V. Sudhakar, M. Srinivasa Reddy, L. Srinivas Rao, N. Veeraiah, J. Lumin 128 (2008) 1791-1798.

[89] Y. K. Sharma, S. S. L. Surina, R. K. Singh, J. Rare earths 27 (2009) 773-780.

Accepted manuscript

ACCEPTED MANUSCRIPT

[90] A.G. Souza Filho, J. Mendes Filho, F.E.A. Melo, M.C.C. Custodio, R. Lebullenger, A.C. Hernandes, J. Phys. Chem. Solids 61 (2000) 1535-1542.

[91] M. Inokuti, F. Hirayama, J. Chem. Phys. 43 (1965) 1978-1989.

[92] C.R. Kesavulu, C.K. Jayasankar, J. Lumin. 132 (2012) 2802-2809.

[93] E. Fred Schubert, Light Emitting Diodes, 2nd ed., Cambridge University Press, New York, USA, 2006.

Accepted manuscript

ACCEPTED MANUSCRIPT

Table 1:

Various physical properties of Sm^{3+} ions in OFB glasses

Physical Property	**OFBSm01**	**OFBSm05**	**OFBSm10**	**OFBSm15**	**OFBSm20**	**OFBSm25**
Refractive index (n_d)	1.619	1.617	1.615	1.613	1.611	1.599
Density, d (gm/cm^3)	3.385	3.399	3.418	3.436	3.454	3.472
Average molecular weight, $\bar{M}$ (g)	84.66	85.65	86.88	88.12	89.35	90.58
Molar Volume (V_m) (cm^3/mol)	25.00	25.19	25.41	25.64	25.86	26.08
Sm^{3+} ion concentration, N(10^{22} ions/cm^3)	0.241	1.200	2.370	3.520	4.660	5.770
Mean atomic volume (g/cm^3/atom)	5.683	5.725	5.777	5.828	5.878	5.928
Dielectric constant (ϵ)	2.621	2.614	2.608	2.601	2.595	2.588
Optical dielectric constant ($\epsilon - 1$)	1.621	1.614	1.608	1.601	1.595	1.588
Reflection losses (R %)	5.580	5.550	5.531	5.503	5.476	5.448
Molar refraction (R_m)(cm^{-3})	8.773	8.814	8.871	8.926	8.979	9.032
Polaron radius (r_p) (Å)	3.060	1.790	1.430	1.250	1.140	1.060
Inter-atomic distance (r_i) (Å)	7.580	4.440	3.540	3.100	2.830	2.630
Molecular electronic polarizability α ($10^{-23}cm^3$)	34.80	6.960	3.520	2.360	1.780	1.430
Field strength ,F ($10^{15}cm^{-2}$)	3.210	9.360	14.70	19.20	23.10	26.60
Optical basicity ,(Λ_{th})	0.487	0.536	0.537	0.539	0.541	0.543

ACCEPTED MANUSCRIPT

Table 2:

The FTIR band positions and their assignments in an undoped OFB glass

Band Positions (cm^{-1})	**Assignments**
401	Metal oxygen bond vibrations (Ca-O, Al-O, Ba-O)
451	Stretching vibrations of AlO_4 tetrahedral groups
550	Stretching vibrations of AlO_6 octahedral groups
609	Bending vibrations of O–B–O linkages
673	Combined vibrations of BO_4 and AlO_4
887	B–O bonds stretching vibration in BO_4 tetrahedra from diborate groups
1062	B–O bonds stretching vibrations in BO_4 units
1384	B–O Stretching containing planar 6 member borate groups
1623	Stretching vibrations of BO_3 triangles
2843	Hydrogen Bonding
2917	Hydrogen Bonding
3433	Fundamental stretching of OH group

Accepted manuscript

ACCEPTED MANUSCRIPT

Table 3:

Experimental (f_{exp} x 10^{-6}), calculated (f_{cal} x 10^{-6}) oscillator strengths, their rms deviation, nephelauxetic ratios ($\bar{\beta}$) and bonding parameters (δ) of Sm^{3+} ions in OFB glasses

Transitions from	OFBSm01		OFBSm05		OFBSm10		OFBSm15		OFBSm20		OFBSm25	
$^6H_{5/2}$→	f_{exp}	f_{cal}	f_{exp}	f_{cal}	f_{exp}	f_{cal}	f_{exp}	f_{cal}	f_{exp}	f_{cal}	f_{exp}	f_{cal}
$^6H_{13/2}$	0.44	0.21	0.48	0.36	0.50	0.39	0.25	0.34	0.18	0.30	0.14	0.21
$^6F_{1/2}$	0.16	0.02	0.19	0.18	0.23	0.19	0.13	0.08	0.12	0.08	0.01	0.02
$^6H_{15/2}$	0.17	0.01	0.31	0.02	0.40	0.03	0.20	0.02	0.15	0.02	0.12	0.01
$^6F_{3/2}$	0.39	0.59	1.18	1.06	1.22	1.18	0.84	0.75	0.75	0.67	0.61	0.51
$^6F_{5/2}$	1.33	1.25	1.49	2.03	1.88	2.27	0.87	1.51	0.74	1.34	0.72	1.08
$^6F_{7/2}$	2.81	2.90	4.53	4.75	4.86	5.25	4.38	4.32	3.85	3.79	2.59	2.76
$^6F_{9/2}$	2.16	2.08	3.73	3.42	4.23	3.77	3.26	3.26	2.85	2.84	2.31	2.03
$^6F_{11/2}$	0.37	0.34	0.81	0.56	1.52	0.62	0.82	0.54	0.66	0.47	0.54	0.33
$^4I_{11/2}$	0.31	0.14	0.34	0.23	0.41	0.25	0.28	0.22	0.29	0.19	0.24	0.13
$^4I_{13/2}$	0.21	0.34	0.27	0.57	0.39	0.63	0.15	0.53	0.14	0.46	0.11	0.33
$^4I_{15/2}$	0.23	0.02	0.35	0.04	0.65	0.05	0.28	0.04	0.24	0.04	0.19	0.02
$(^6P, ^4P)_{5/2}$	0.32	0.39	0.42	0.62	0.63	0.69	0.18	0.46	0.14	0.41	0.01	0.33
$^6P_{3/2}$	3.01	2.59	7.48	4.15	7.52	4.63	6.43	3.11	5.88	2.76	4.40	2.23
$^4G_{11/2}$	0.31	0.01	0.44	0.02	0.57	0.03	0.37	0.02	0.14	0.02	0.13	0.01
$^6P_{7/2}$	0.98	1.27	1.38	2.09	1.70	2.31	1.16	2.01	0.93	1.75	0.84	1.24
$^4D_{3/2}$+ $(^4D, ^6P)_{5/2}$	0.50	0.43	1.30	0.69	2.29	0.77	1.98	0.51	1.54	0.45	1.12	0.37
δ_{rms} (x10^{-6})	±0.19		±0.90		±0.91		±0.96		±0.87		±0.60	
$\bar{\beta}$	1.0252		1.0153		1.0152		1.0146		1.0142		1.0090	
δ	–0.2461		–0.1510		–0.1500		–0.1448		–0.1407		– 0.0964	

Accepted manuscript

ACCEPTED MANUSCRIPT

Table 4:

Comparison of Judd-Ofelt Parameters ($\Omega_\lambda X10^{-20}cm^2$) and their trend for Sm^{3+}ions in OFB glasses with different hosts.

Glass System	Ω_2	Ω_4	Ω_6	Trend	References
OFBSm01	0.08±0.001	2.34±0.003	2.35±0.002	$\Omega_6 > \Omega_4 > \Omega_2$	present work
OFBSm05	0.56±0.007	3.74±0.007	3.87±0.002	$\Omega_6 > \Omega_4 > \Omega_2$	present work
OFBSm10	0.59±0.025	4.18±0.006	4.27±0.002	$\Omega_6 > \Omega_4 > \Omega_2$	present work
OFBSm15	0.27±0.008	2.81±0.021	3.74±0.001	$\Omega_6 > \Omega_4 > \Omega_2$	present work
OFBSm20	0.24±0.007	2.50±0.006	3.26±0.002	$\Omega_6 > \Omega_4 > \Omega_2$	present work
OFBSm25	0.06±0.012	2.03±0.011	2.31±0.003	$\Omega_6 > \Omega_4 > \Omega_2$	present work
0.1SmPbFB	0.39	3.66	2.44	$\Omega_4 > \Omega_6 > \Omega_2$	[62]
0.5SmPbFB	0.32	3.62	2.04	$\Omega_4 > \Omega_6 > \Omega_2$	[62]
1SmPbFB	0.31	3.28	1.92	$\Omega_4 > \Omega_6 > \Omega_2$	[62]
L5FBS	2.34	7.54	5.40	$\Omega_4 > \Omega_6 > \Omega_2$	[63]
PbF_2-TeO_2-B_2O_3	0.21	1.42	1.87	$\Omega_6 > \Omega_4 > \Omega_2$	[71]
LBTAF	0.27	2.52	2.47	$\Omega_4 > \Omega_6 > \Omega_2$	[72]
LiTFP	0.04	3.49	2.36	$\Omega_4 > \Omega_6 > \Omega_2$	[73]
(PPNSm10) P_2O_5– PbO– Nb_2O_5	3.42	2.80	1.85	$\Omega_2 > \Omega_4 > \Omega_6$	[74]
PKMASm K–Mg–Al phosphate	6.83	2.97	2.03	$\Omega_2 > \Omega_4 > \Omega_6$	[75]

Accepted manuscript

ACCEPTED MANUSCRIPT

glass

Table 5:

Transition probabilities (A_R) (s^{-1}), total transition probability (A_T) (s^{-1}), radiative and experimental branching ratios (β_R & β_{exp}) for the prominent emission transitions of Sm^{3+} ions in OFB glasses

Transition	OFBSm01		OFBSm05		OFBSm10		OFBSm15		OFBSm20		OFBSm25	
	A_R											
$^4G_{5/2}\rightarrow{}^6H_{5/2}$	20.16		22.53		23.14		20.77		20.21		19.31	
$^4G_{5/2}\rightarrow{}^6H_{7/2}$	101.27		156.53		181.52		134.94		119.89		93.21	
$^4G_{5/2}\rightarrow{}^6H_{9/2}$	36.22		66.33		73.03		49.37		43.63		31.62	
$^4G_{5/2}\rightarrow{}^6H_{11/2}$	22.13		35.60		39.50		28.76		25.31		19.57	
A_T	200.23		308.79		336.68		258.75		232.21		183.05	
	β_R	β_{exp}	β_R	β_{exp}	β_R	β_{exp}	β_R	β_{exp}	β_R	β_{exp}	β_R	β_{exp}
$^4G_{5/2}\rightarrow{}^6H_{5/2}$	0.100	0.119	0.073	0.160	0.068	0.163	0.080	0.172	0.087	0.156	0.105	0.150
$^4G_{5/2}\rightarrow{}^6H_{7/2}$	0.505	0.415	0.506	0.436	0.539	0.455	0.521	0.440	0.516	0.383	0.509	0.380
$^4G_{5/2}\rightarrow{}^6H_{9/2}$	0.180	0.251	0.214	0.255	0.216	0.322	0.190	0.272	0.187	0.240	0.172	0.232
$^4G_{5/2}\rightarrow{}^6H_{11/2}$	0.110	0.103	0.115	0.128	0.117	0.152	0.111	0.135	0.109	0.130	0.106	0.115

Accepted manuscript

ACCEPTED MANUSCRIPT

Table 6:

Emission peak wavelength (λ_P) (nm), effective band widths ($\Delta\lambda_P$) (nm), stimulated emission cross-sections (σ_{se}) ($\times 10^{-22}$) (cm^2), gain band width ($\sigma_{se} \times \Delta\lambda_P$) ($\times 10^{-28}$) ($cm^3$) and optical gain ($\sigma_{se} \times \tau_R$) ($\times 10^{-25}$) ($cm^2$ s) for the prominent emission transitions of Sm^{3+} doped OFB glasses.

Spectral parameters	OFBSm01	OFBSm05	OFBSm10	OFBSm15	OFBSm20	OFBSm25
$^4G_{5/2} \rightarrow {}^6H_{5/2}$ ($\lambda_P = 563$ *nm*)						
$\Delta\lambda_P$	8.09	8.09	7.35	9.56	10.3	11.0
σ_{se}	1.27	1.42	1.61	1.11	1.01	0.90
$\sigma_{se} \times \Delta\lambda_P$	1.03	1.15	1.18	1.06	1.04	0.99
$\sigma_{se} \times \tau_R$	6.33	4.60	4.78	4.30	4.34	4.92
$^4G_{5/2} \rightarrow {}^6H_{7/2}$ ($\lambda_P = 598$ *nm*)						
$\Delta\lambda_P$	11.o	10.3	8.09	11.8	13.2	13.2
σ_{se}	5.94	9.87	14.6	7.48	5.92	4.62
$\sigma_{se} \times \Delta\lambda_P$	6.56	10.2	11.8	8.80	7.84	6.11
$\sigma_{se} \times \tau_R$	29.7	32.0	43.4	28.9	25.5	25.2
$^4G_{5/2} \rightarrow {}^6H_{9/2}$ ($\lambda_P = 646$ *nm*)						
$\Delta\lambda_P$	13.2	10.3	10.3	14.7	16.2	17.6
σ_{se}	2.41	5.69	6.29	2.98	2.40	1.60
$\sigma_{se} \times \Delta\lambda_P$	3.19	5.86	6.47	4.39	3.88	2.82
$\sigma_{se} \times \tau_R$	12.0	18.4	18.7	11.5	10.3	8.74
$^4G_{5/2} \rightarrow {}^6H_{11/2}$ ($\lambda_P = 708$ *nm*)						
$\Delta\lambda_P$	22.1	14.7	14.0	25.0	35.3	35.3
σ_{se}	1.28	2.14	2.51	1.02	0.63	0.49
$\sigma_{se} \times \Delta\lambda_P$	2.82	3.15	3.50	2.55	2.25	1.75
$\sigma_{se} \times \tau_R$	6.37	6.93	7.44	3.95	2.75	2.70

Accepted manuscript

ACCEPTED MANUSCRIPT

Table 7:

Experimental (τ_{exp}) (μs), radiative (τ_R) (μs) lifetimes, quantum efficiencies (η), multi phonon relaxation rates (W_{NR}) (μs^{-1}) and colour co-ordinates of Sm^{3+} ions in OFB glasses.

Name of the sample	$^4G_{5/2} \rightarrow {}^6H_{7/2}$				Colour co-ordinates λ_{exc}=410 nm	
	τ_{exp}	τ_R	η (%)	W_{NR}	X-Co-ordinates	Y-Co-ordinates
OFBSm01	2802±1.9μs	4994	56.1	156.6	0.5623	0.4376
OFBSm05	2548±3.4 μs	3238	78.6	83.63	0.5813	0.4023
OFBSm10	2467±3.8 μs	2970	83.0	68.65	0.5945	0.4065
OFBSm15	2150±5.7 μs	3864	55.6	206.3	0.5831	0.3985
OFBSm20	1564±9.6 μs	4306	36.3	407.1	0.5764	0.3723
OFBSm25	1186±9.3 μs	5462	21.7	660.0	0.5623	0.3746

Accepted manuscript

ACCEPTED MANUSCRIPT

Table 8:

Comparison of branching ratio (β_R), stimulated emission cross-section (σ_{se}), quantum efficiency (η) and cross-relaxation rates (W_{CR}) of OFBSm10 glass for the prominent emission transition $^4G_{5/2} \rightarrow {}^6H_{7/2}$ ($\lambda_p = 598$ nm) with other glasses.

Name of the material	β_R	σ_{se} ($x10^{-22}$ cm^2)	η (%)	W_{CR} (μs^{-1})	Reference
OFBSm10	0.520	14.6	83	68.65	Present work
B1TS	0.500	9.24	26	747	[45]
LiTFP	0.500	6.91	-	197	[78]
NaTFP	0.501	6.23	-	195	[78]
KTFP	0.484	4.76	-	217	[78]
PKFBASm	0.080	0.99	75	76	[84]
Sm^{3+}:BNNS	0.596	9.15	85	57	[85]
Sm^{3+}:BCNS	0.402	11.8	86	56	[85]
1SLBTZ	0.624	16.0	24	1201	[86]
TZKCSm10	0.380	6.68	47	694	[87]
CaSm	0.511	5.00	-	-	[88]
PbSm	0.510	5.73	-	-	[88]
ZnSm	0.505	7.12	-	-	[88]
NCS:Sm^{3+}	0.360	3.07	-	-	[89]

Accepted manuscript

ACCEPTED MANUSCRIPT

Table 9:

Energy transfer parameter (Q), critical transfer distance (R_0) (Å), donor–acceptor interaction parameter ($C_{DA,}$ $10^{-41}cm^6 s^{-1}$) of Sm^{3+} doped OFB glasses.

Name of the Glass	Q	R_0	C_{DA}	References
OFBSm01	-	-	-	Present System
OFBSm05	-	-	-	Present System
OFBSm10	0.240	5.150	0.666	Present System
OFBSm15	0.725	6.526	2.758	Present System
OFBSm20	2.234	8.648	14.93	Present System
OFBSm25	3.320	9.191	21.52	Present System
CFB1.0	0.150	4.390	0.302	[33]
1SmPbFB	2.173	6.850	3.730	[57]
PKFBASm1.0	0.217	4.850	0.402	[71]
LBTAF1.0	0.430	5.130	13.08	[72]
PBFPSm10	0.950	7.550	0.690	[92]

Accepted manuscript

Fig. 1 : XRD spectrum of an undoped OFB glass.

Fig. 2 : Variation of density and molar volume with Sm^{3+} ion concentration in OFB glasses.

Fig. 3 : FTIR spectrum of an undoped OFB glass.

Fig. 4(a): Absorption spectrum of 1 mol% of Sm^{3+} ions doped OFB glass in UV-vis-NIR region.

Fig. 4(b): Variation of intensity of hypersensitive transition and $\sum \Omega_\lambda$ with Sm^{3+} ion concentration in OFB glasses.

Fig. 5 : Excitation spectra of Sm^{3+} ions in OFB glasses in terms of wavelength (nm). The inset figure shows the excitation spectra of Sm^{3+} ions in OFB glasses in terms of wavenumber (cm^{-1}).

Fig. 6 : Photoluminescence spectra of Sm^{3+} doped OFB glasses recorded using 410 nm CW laser in terms of wavenumber (cm^{-1}). The right inset figure shows the photoluminescence spectra of OFBSm glasses at 402 nm excitation in terms of wavelength (nm). The left inset figure shows the photoluminescence spectra of OFBSm glasses at 410 nm excitation in terms of wavelength (nm).

Fig. 7 : The decay curves for $^4G_{5/2} \rightarrow {}^6H_{7/2}$ (598 nm) emission of Sm^{3+} ions in OFB glasses when excited at 410nm.

Fig. 8 : Partial energy level diagram showing the absorption, excitation and emission mechanism and cross-relaxation channels involved in Sm^{3+} ions in OFB glasses.

Fig. 9 : CIE chromaticity co-ordinates of Sm^{3+} ions in OFB glasses having different concentrations located in the CIE 1931 chromaticity diagram along with the confocal photoluminescence images recorded at an excitation wavelength 410 nm (CW Laser).

Accepted manuscript

ACCEPTED MANUSCRIPT

ACCEPTED MANUSCRIPT

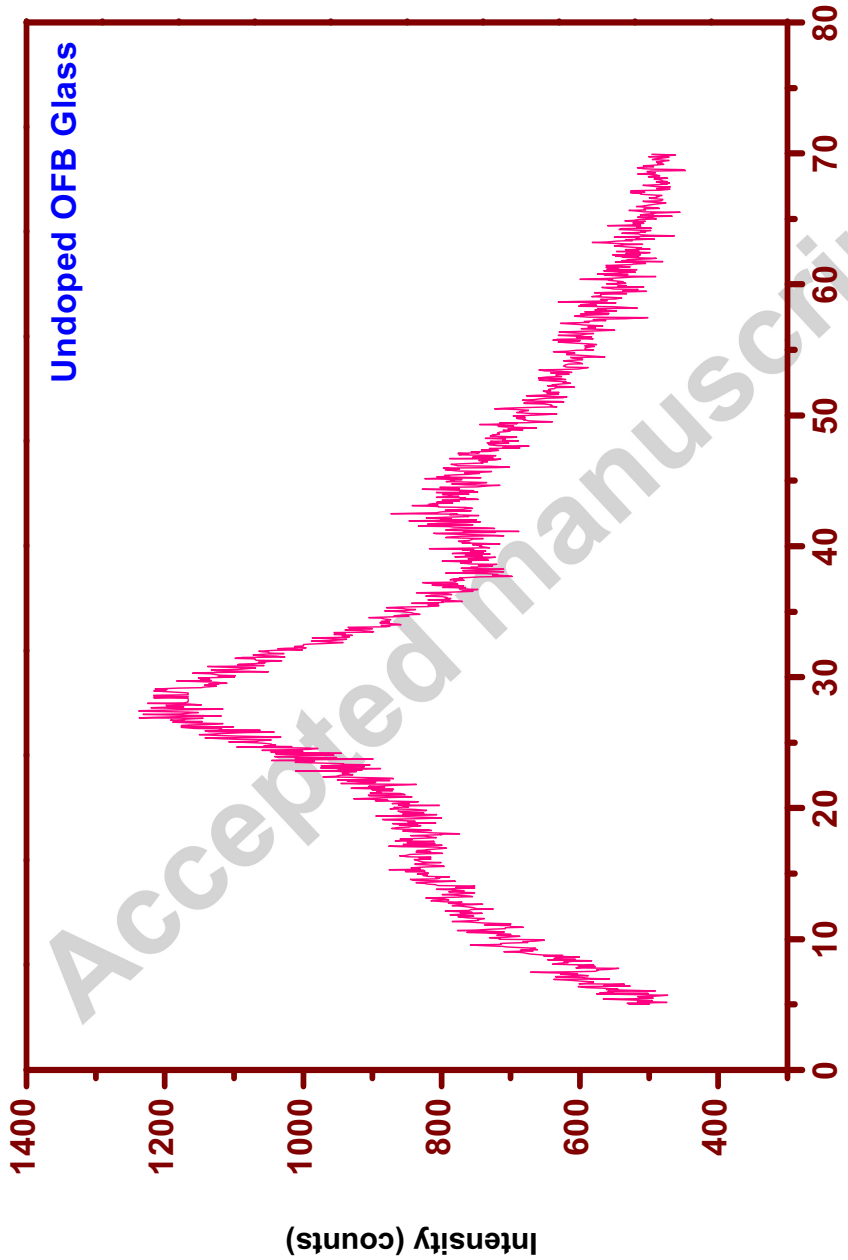

Fig. 1

Accepted manuscript

ACCEPTED MANUSCRIPT

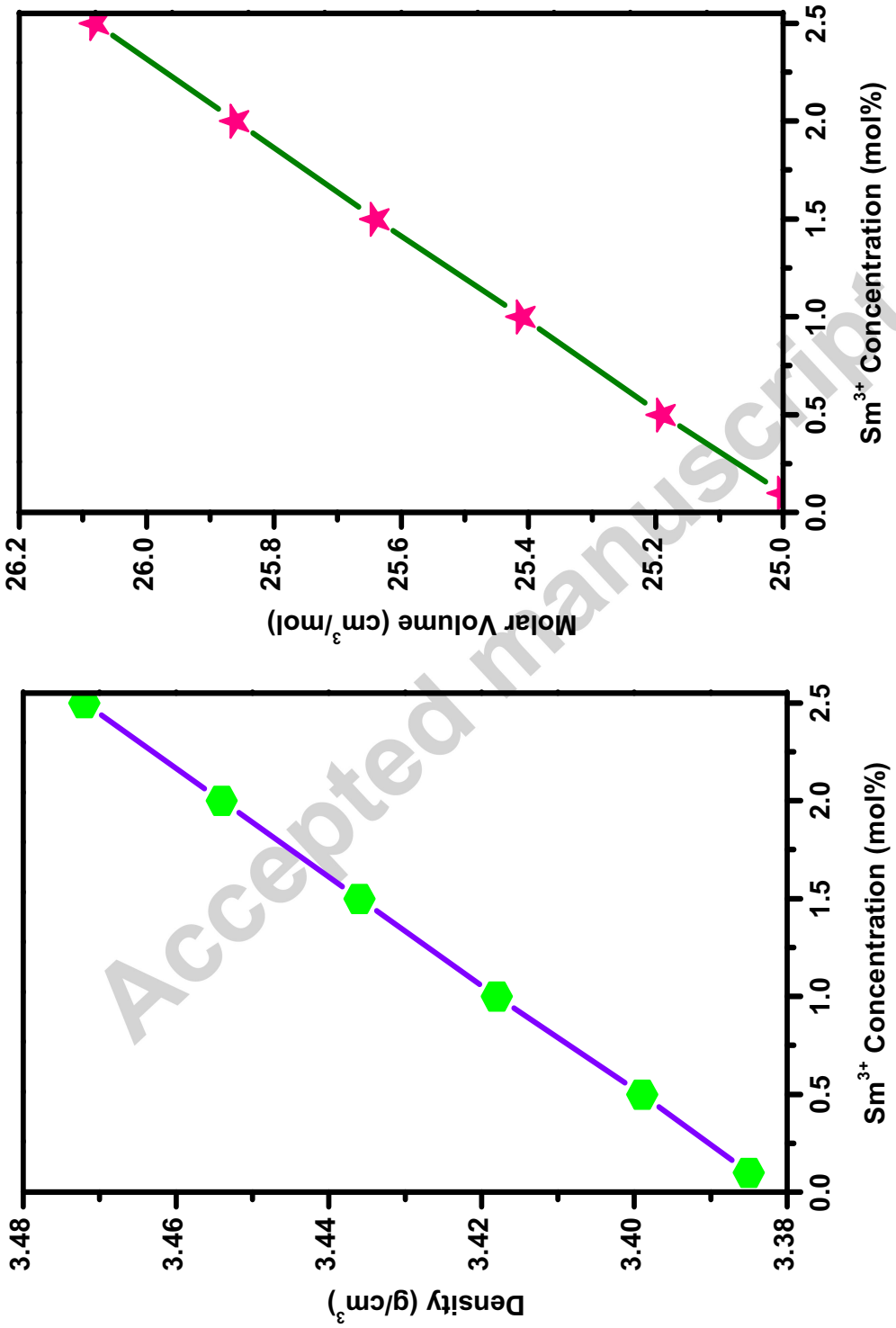

Fig. 2

Accepted manuscript

ACCEPTED MANUSCRIPT

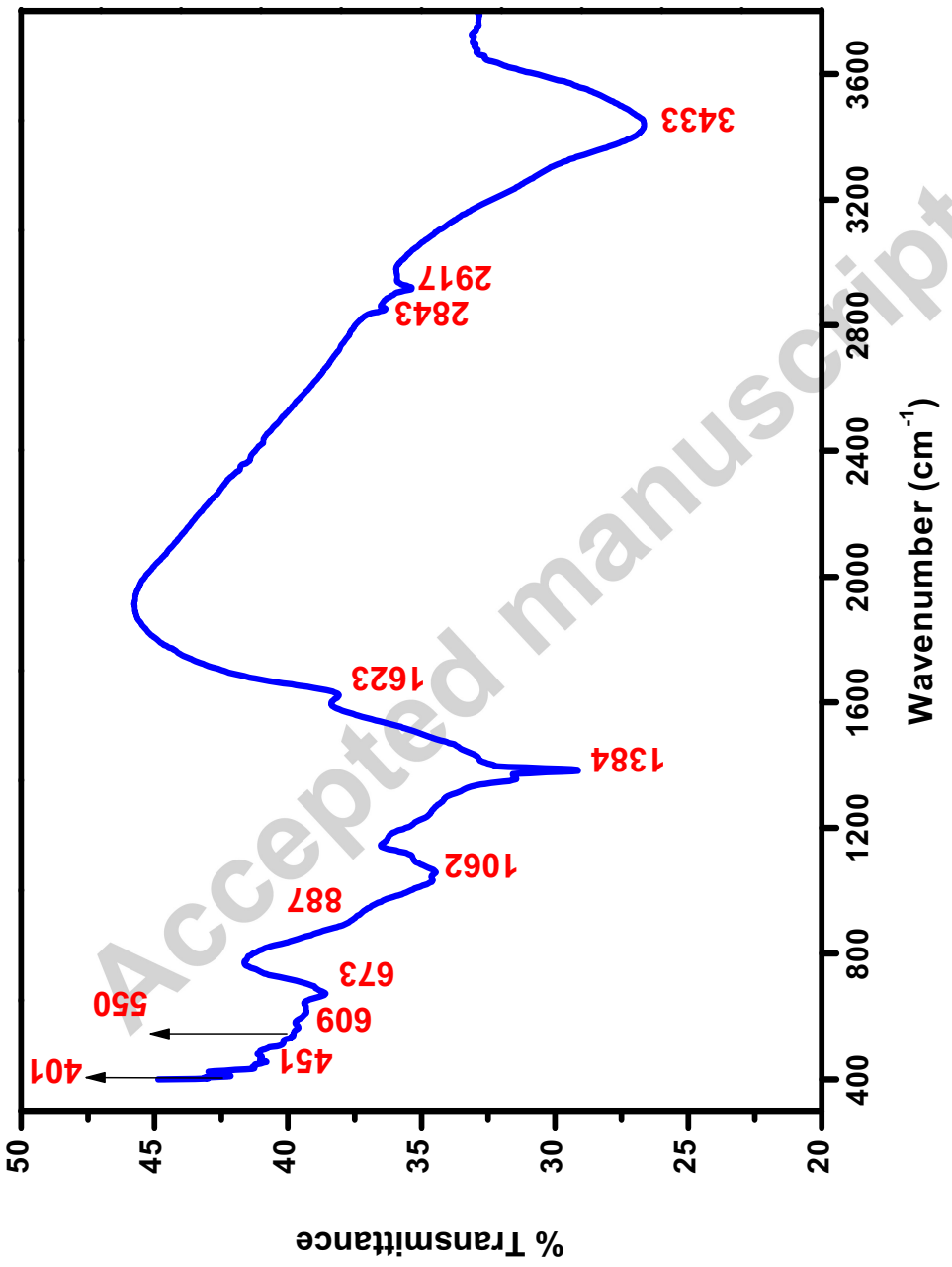

Fig. 3

Accepted manuscript

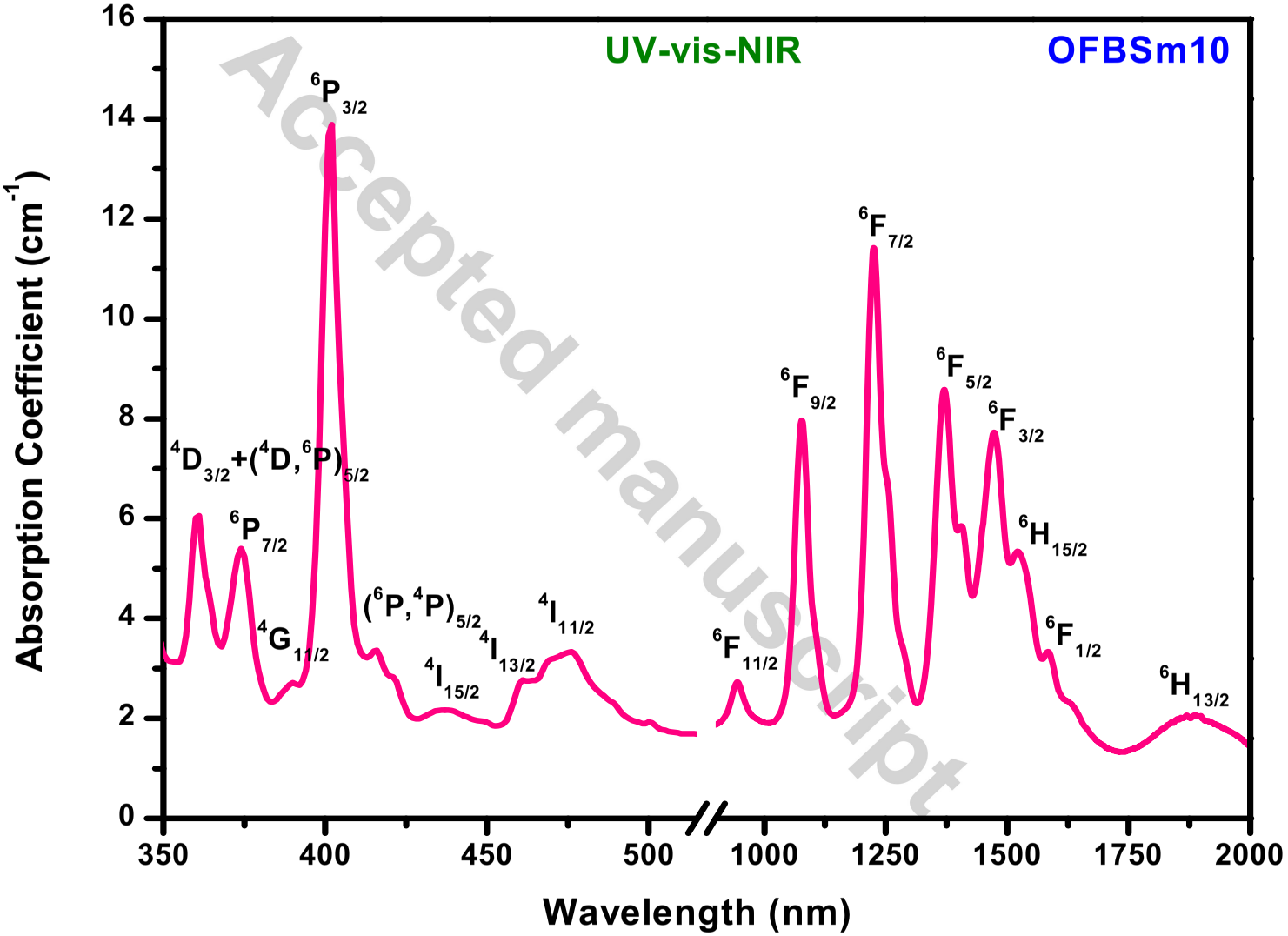

Accepted manuscript

ACCEPTED MANUSCRIPT

Fig. 4(a)

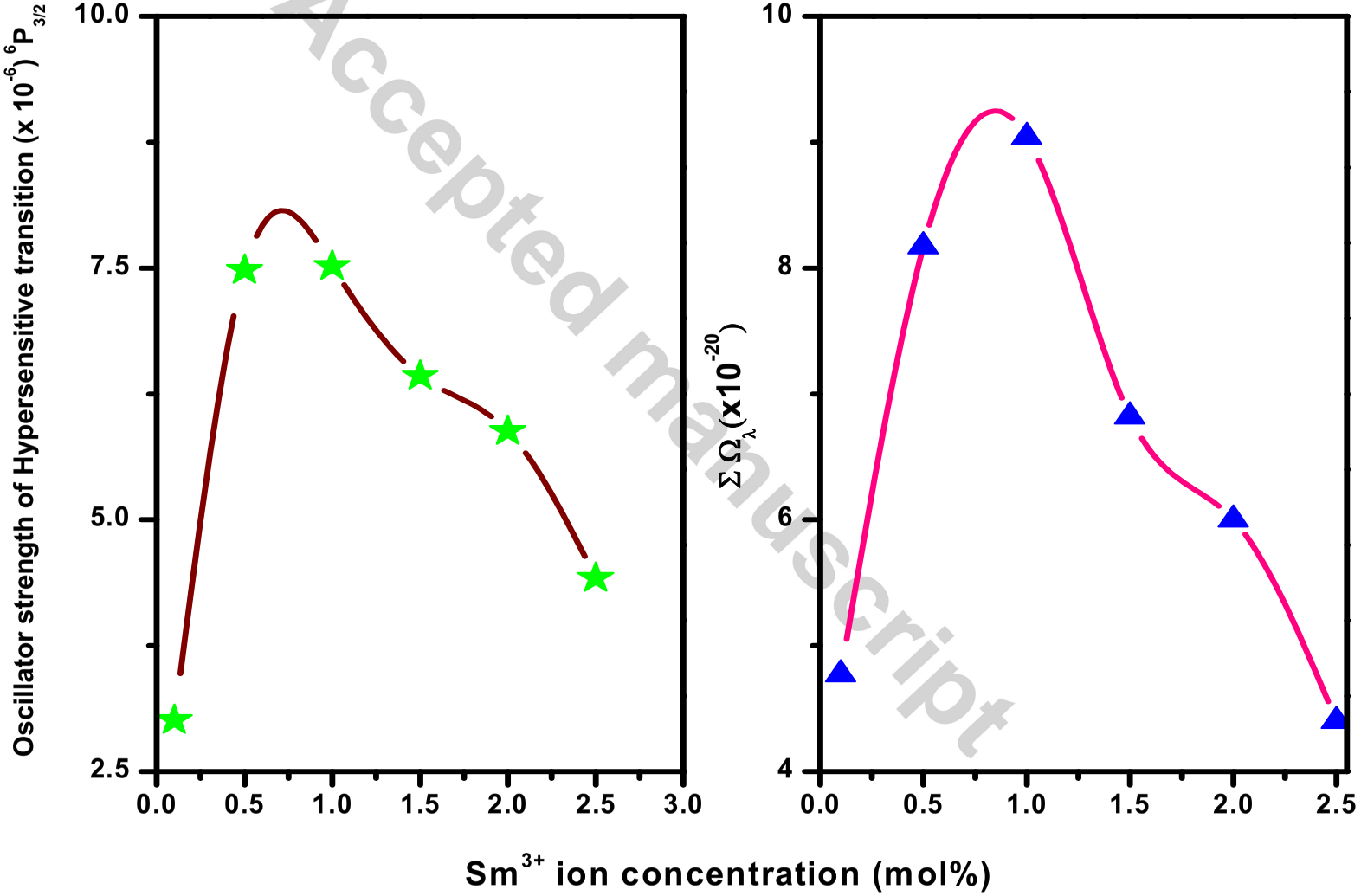

Accepted manuscript

ACCEPTED MANUSCRIPT

Fig 4. (b)

ACCEPTED MANUSCRIPT

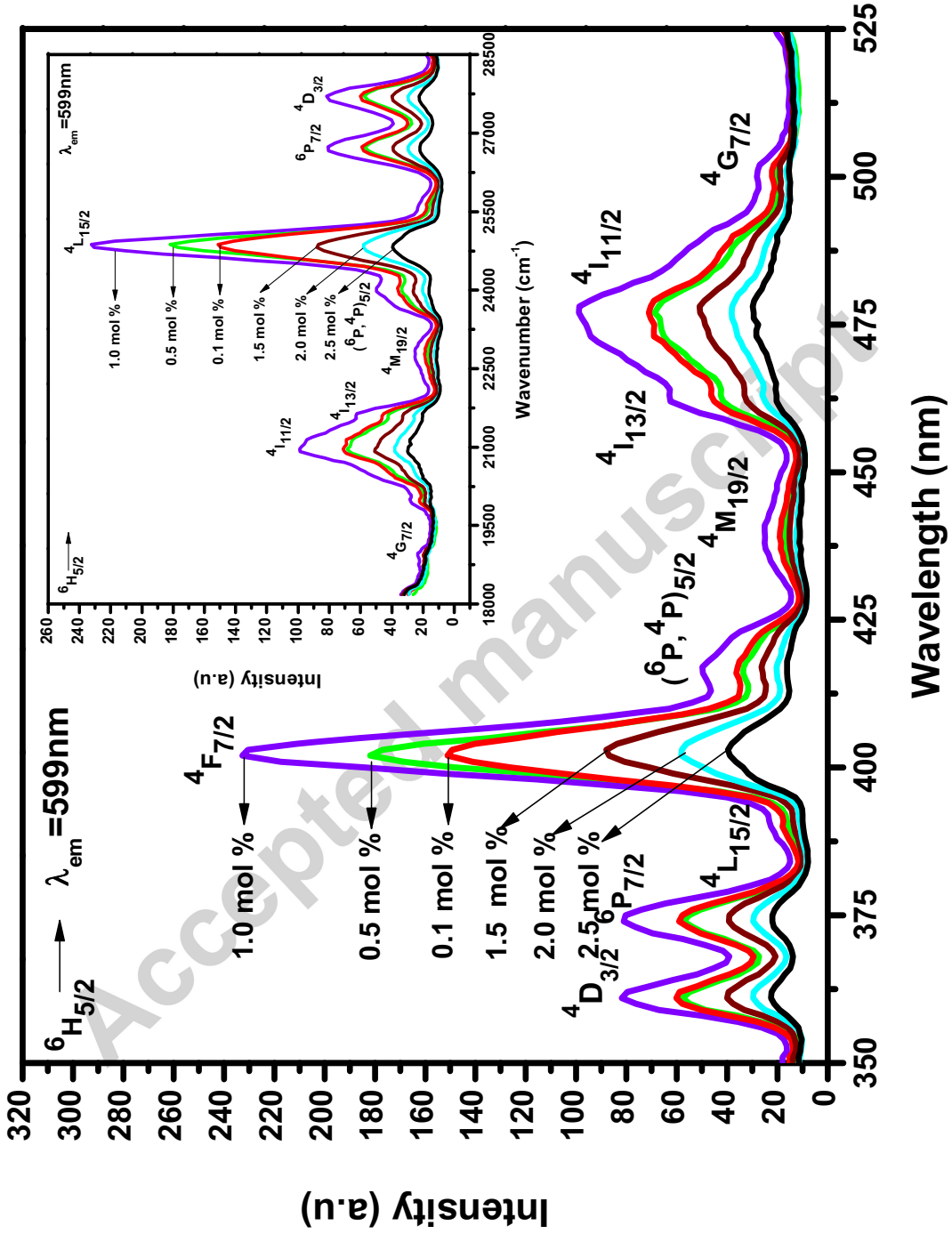

Fig. 5

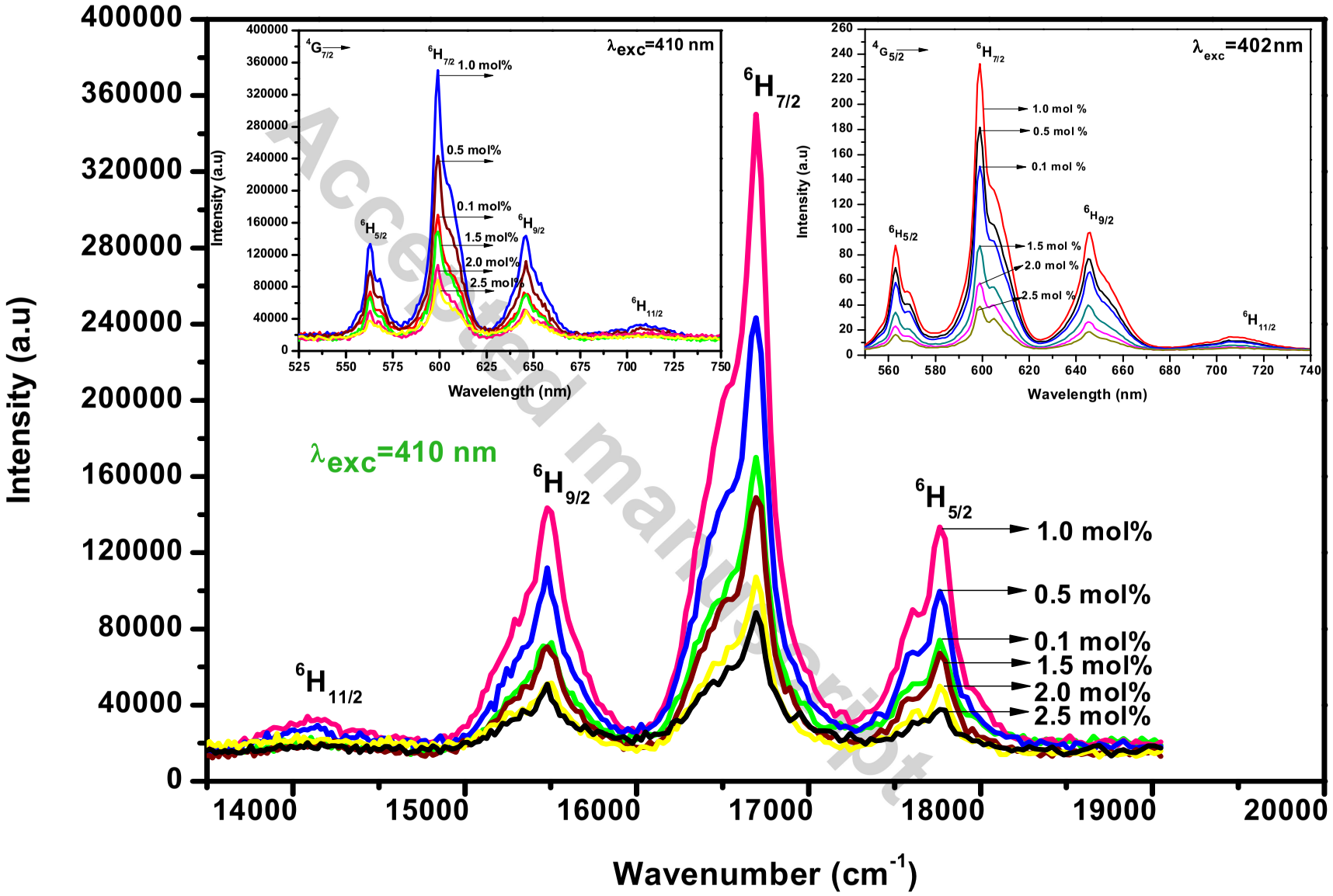

Fig. 6

Accepted manuscript

ACCEPTED MANUSCRIPT

ACCEPTED MANUSCRIPT

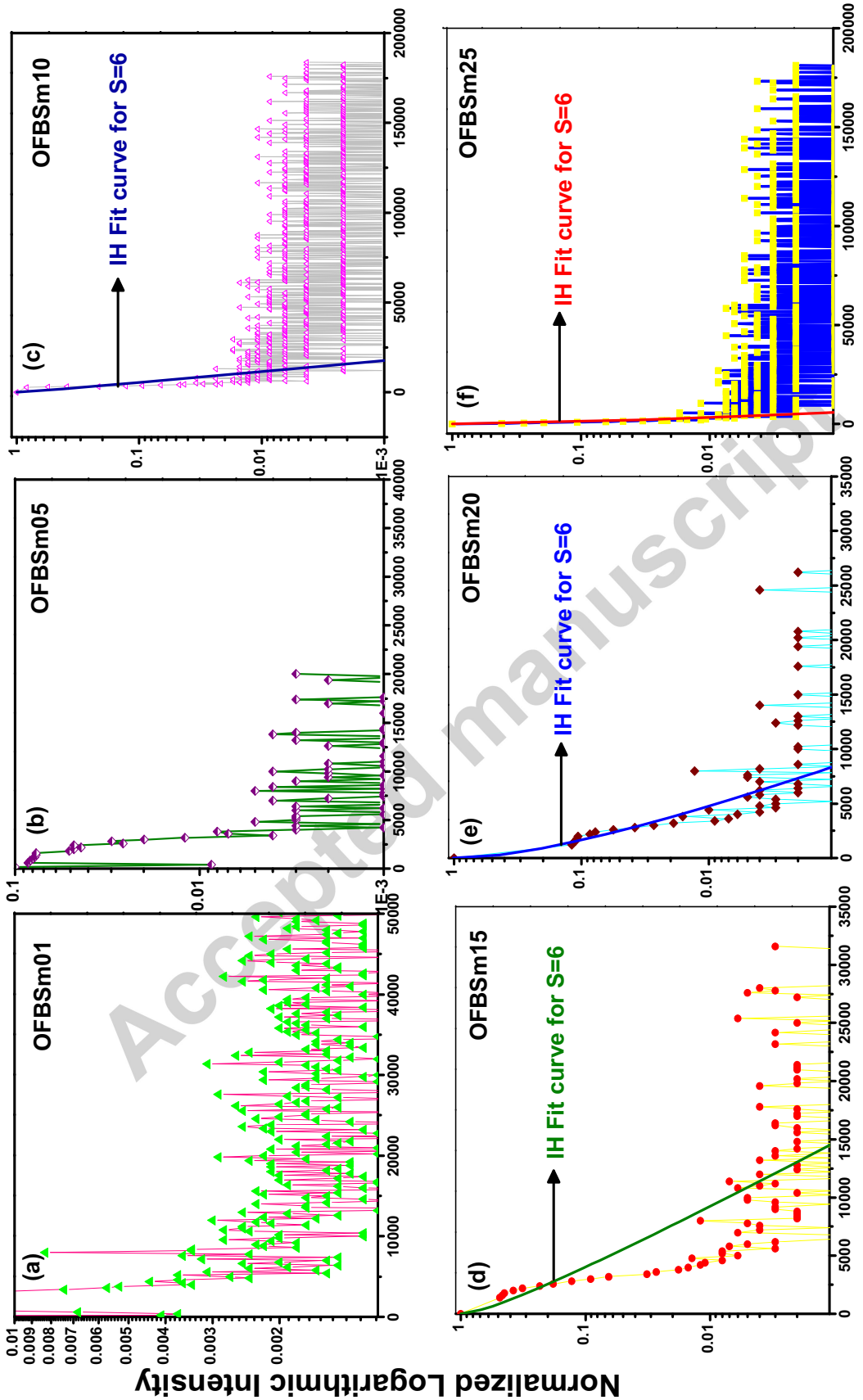

Accepted manuscript

Fig. 7

ACCEPTED MANUSCRIPT

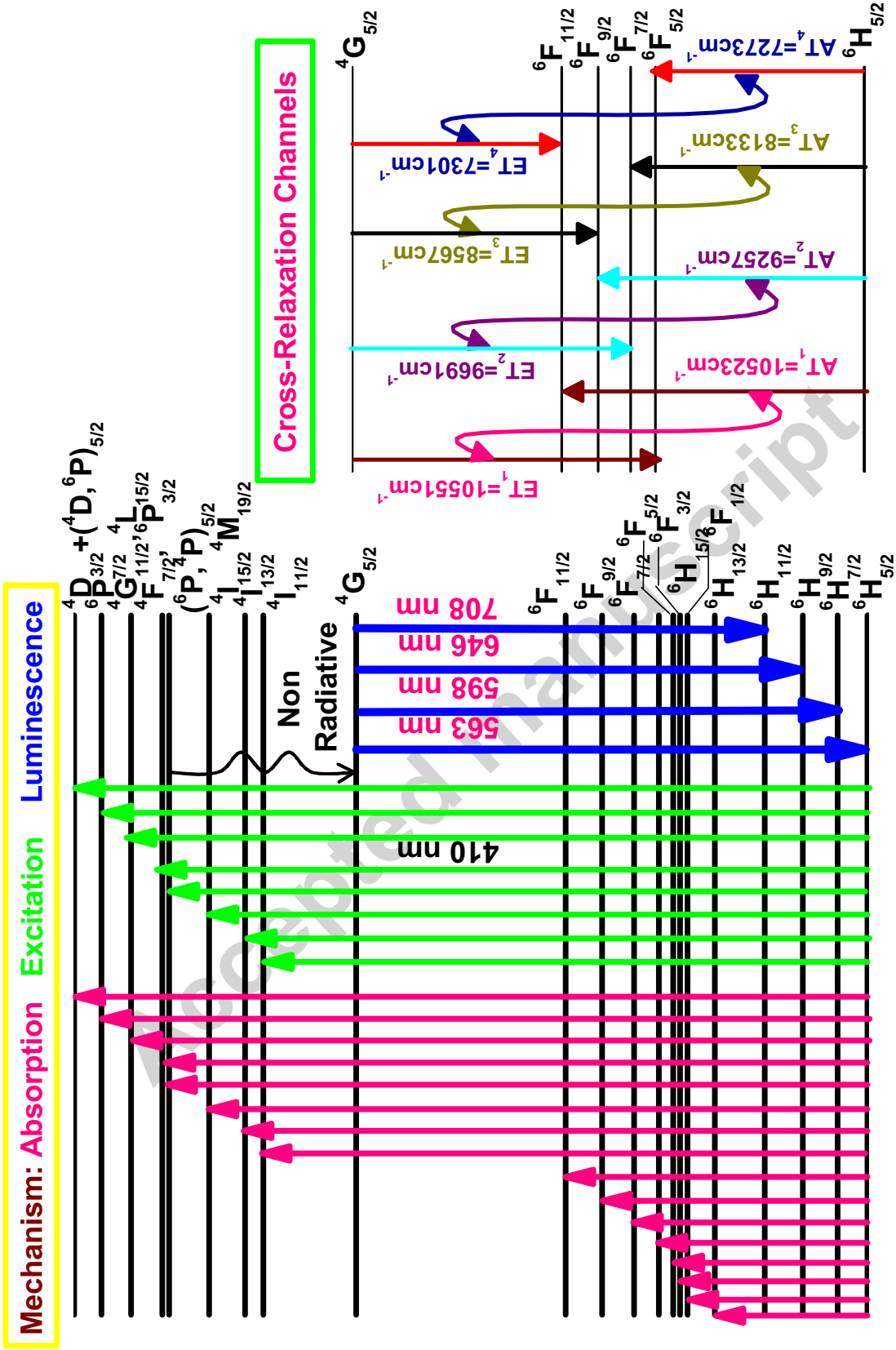

Fig. 8

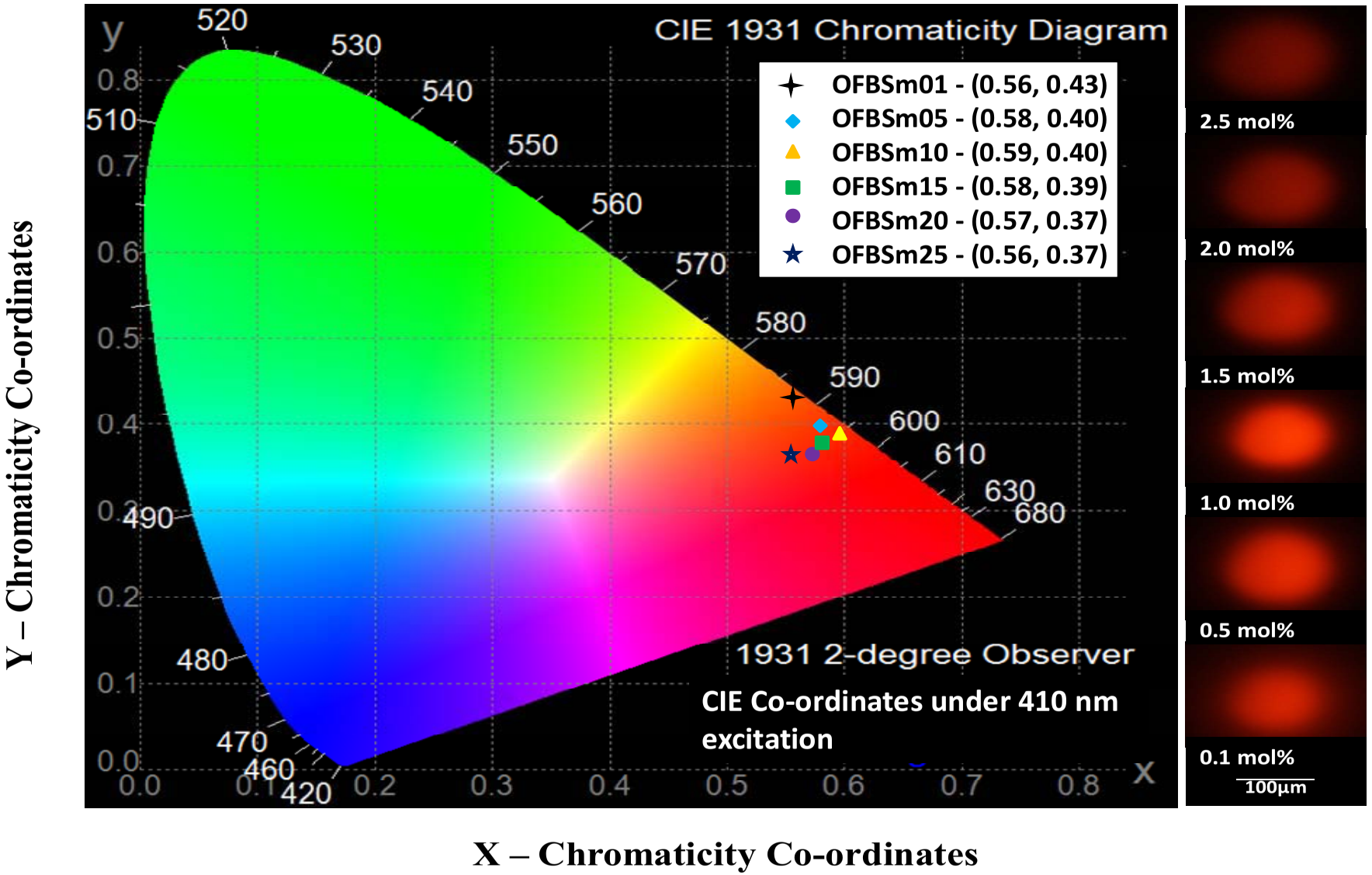

Fig. 9

ACCEPTED MANUSCRIPT

ACCEPTED MANUSCRIPT

High Lights

1. Sm^{3+} doped OFB glasses have been synthesized using melt quenching technique.
2. From the absorption spectra, J-O parameters have been calculated using J-O theory.
3. Emission cross-sections & efficiencies are calculated for laser transitions.
4. CIE colour co-ordinates were evaluated using emission spectra.
5. OFBSm1.0 glass was found to be the best for laser action in visible orange region.

Accepted manuscript

Supercooling transition in phase separated manganite thin films: An electrical transport study

Sandeep Singh, Pawan Kumar, P. K. Siwach, Pawan Kumar Tyagi, and H. K. Singh

Citation: Applied Physics Letters **104**, 212403 (2014); doi: 10.1063/1.4880725
View online: http://dx.doi.org/10.1063/1.4880725
View Table of Contents: http://scitation.aip.org/content/aip/journal/apl/104/21?ver=pdfcov
Published by the AIP Publishing

Articles you may be interested in

Anisotropic resistivities in anisotropic-strain-controlled phase-separated La0.67Ca0.33MnO3/NdGaO3(100) films
Appl. Phys. Lett. **103**, 072407 (2013); 10.1063/1.4818636

Enhanced magnetic refrigeration capacity in phase separated manganites
Appl. Phys. Lett. **95**, 092506 (2009); 10.1063/1.3204694

Magnetic separation and inelastic tunneling in self-doped manganite films
J. Appl. Phys. **106**, 043908 (2009); 10.1063/1.3197855

Studies on the cluster sizes in the mixed-phase thin films
Appl. Phys. Lett. **90**, 032508 (2007); 10.1063/1.2432945

Influence of different substrates on phase separation in La 1 x y Pr y Ca x MnO 3 thin films
J. Appl. Phys. **99**, 08S901 (2006); 10.1063/1.2162050

This article is copyrighted as indicated in the article. Reuse of AIP content is subject to the terms at: http://scitation.aip.org/termsconditions. Downloaded to IP: 14.139.251.110 On: Fri, 13 Jun 2014 06:42:17

Supercooling transition in phase separated manganite thin films: An electrical transport study

Sandeep Singh,[1,2] Pawan Kumar,[1,3] P. K. Siwach,[1] Pawan Kumar Tyagi,[2] and H. K. Singh[1,a)]

[1]*National Physical Laboratory (Council of Scientific and Industrial Research), Dr. K. S. Krishnan Marg, New Delhi 110012, India*
[2]*Department of Applied Physics, Delhi Technological University, Delhi 110042, India*
[3]*Inter-University Accelerator Centre, Aruna Asaf Ali Marg, New Delhi 110067, India*

(Received 19 March 2014; accepted 18 May 2014; published online 29 May 2014)

The impact of variation in the relative fractions of the ferromagnetic metallic and antiferromagnetic/charge ordered insulator phases on the supercooling/superheating transition in strongly phase separated system, $La_{5/8-y}Pr_yCa_{3/8}MnO_3$ ($y \approx 0.4$), has been studied employing magnetotransport measurements. Our study clearly shows that the supercooling transition temperature is non-unique and strongly depends on the magneto-thermodynamic path through which the low temperature state is accessed. In contrast, the superheating transition temperature remains constant. The thermo-magnetic hysteresis, the separation of the two transitions and the associated resistivity, all are functions of the relative fraction of the coexisting phases. © *2014 AIP Publishing LLC*. [http://dx.doi.org/10.1063/1.4880725]

Phase separation (PS) is believed to be the key ingredient of the physics of doped rare earth manganites.[1–3] It dominates the composition-temperature (x-T) diagram of intermediate and low bandwidth manganites like $Nd_{1-x}Sr_xMnO_3$,[3,4] $Sm_{1-x}Sr_xMnO_3$,[5,6] and $La_{1-x-y}Pr_yCa_xMnO_3$.[7–10] Amongst these materials, $La_{1-x-y}Pr_yCa_xMnO_3$ has emerged as the prototypical phase separated system and its different variants like bulk single crystal, polycrystals, and thin films have been investigated.[7–16] The strong nature of the phase separation has been established by the observation of (i) strong divergence of the zero filed cooled (ZFC) and field cooled warming (FCW) magnetization, (ii) pronounced hysteresis between the field cooled cool (FCC) and FCW magnetization, and (iii) prominent thermomagnetic hysteresis in the temperature and magnetic field (H) dependent resistivity (ρ) measured in cooling-warming cycles.[7–16] A study by Uehara *et al.*[7] has shown the coexistence of sub-micrometer scale ferromagnetic metallic (FMM) and antiferromagnetic/charge ordered insulator (AFM/COI) clusters and that the latter is explicit in magnetotransport measurements only at $y \geq 0.3$. Consequently, the electrical transport becomes percolative, which is evidenced by huge residual resistivity (ρ_0) for $y \approx 0.4$ in the metallic regime.[7] The study of Ghivelder and Parisi[8] on bulk $La_{5/8-y}Pr_yCa_{3/8}MnO_3$ ($y \approx 0.4$) has shown that COI phase appears at $T_{CO} \sim 230$ K and subsequently acquires AFM and FM spin order $T_N \sim 180$ and $T_C \sim 80$ K, respectively. Due to the rapid spatial and temporal variations in the relative fraction of the FMM and AFM/COI phases, large relaxation effects are also observed.[8] Further, the theoretical study by Ghivelder and Parisi[8] has predicted that interplay between temperature and separation of the system from equilibrium could create multiple blocked states. Sharma *et al.*[9] studied the same material and have established the existence of a liquid like magnetic phase in the phase separated regime, which transforms cooperatively to a randomly frozen glass like phase at low temperature. The frozen glass like phase (termed as strain glass) is believed to arise from the presence of martensitic accommodation strain.[9] Wu *et al.*[10] have demonstrated that in $La_{5/8-y}Pr_yCa_{3/8}MnO_3$ ($y \approx 0.4$) thin films the magnetic liquid like phase exhibits a supercooled glass transition. This glass transition is believed to arise due to the presence of the accommodation strain caused by distinct structural symmetries of FMM and AFM/COI phases. Their study has also provided evidence in favour of the non-ergodic nature of the magnetic liquid. Wu *et al.*[10] have shown that non-ergodicity appears when the long range cooperative strain interactions hinder the cooperative dynamic freezing of the first-order AFM/COI–FMM transition.[9,10]

The FCC-FCW and thermoresistive hysteresis are regarded as signatures of supercooling and superheating transition of the magnetic liquid formed by competing FMM and AFM phases in the presence of martensitic of accommodation strain and long range cooperative strain interactions.[8–10] Despite the exhaustive investigations on different variants of the $La_{1-x-y}Pr_yCa_xMnO_3$, the nature of the supercooling/superheating transitions, e.g., their dependence on relative fractions of FMM and AFM phases has not been probed through electrical transport measurements. The different relative fractions of the FM/AFM phases at the beginning of the magneto-thermodynamic process are expected to lead to different thermodynamic paths and yield different supercooling transition temperatures. Hence, it is important to investigate the signature of different magneto-thermodynamic paths in electrical transport. In this Letter, we report the electrical transport studies on $La_{5/8-y}Pr_yCa_{3/8}MnO_3$ ($y \approx 0.4$) epitaxial thin films. Our results demonstrate that of the two observed insulator-metal transitions (IMTs), the lower one caused by the supercooling of a magnetic liquid is non-unique, while the upper on remains constant.

The $La_{5/8-y}Pr_yCa_{3/8}MnO_3$ ($y \approx 0.4$) thin films were grown by RF magnetron sputtering of a stoichiometric (2 in.)

a)Author to whom correspondence should be addressed. Electronic mail: hks65@nplindia.org.

 © 2014 AIP Publishing LLC

This article is copyrighted as indicated in the article. Reuse of AIP content is subject to the terms at: http://scitation.aip.org/termsconditions. Downloaded to IP: 14.139.251.110 On: Fri, 13 Jun 2014 06:42:17

target in 200 mTorr of Ar + O_2 (80 + 20) mixture on single crystal (001) $SrTiO_3$ (STO) substrates maintained at ~800 °C. The lattice mismatch (ε) between the target and substrate is ≈−1.93% ($\varepsilon = (a_t - a_s)_{x100}/a_s$ where a_t and a_s are the lattice parameters of the bulk target and substrate, respectively) and hence the strain is tensile. In order to achieve optimum oxygen content, the films were annealed at ≈900 °C for 10 h in flowing oxygen.

The film thickness estimated from the X-ray reflectivity data is ~41 nm. The high resolution X-ray diffraction (HRXRD; 2θ-ω scan, ϕ-scan, and ω-2θ scan) confirmed the epitaxial nature of the films and also showed that the film is under tensile strain. The significantly reduced out-of-plane lattice constant of the film is $a_f = 3.7988$ Å ($a_{bulk} = 3.831$ Å), which confirms the presence of appreciable tensile strain. The occurrence of the step-terrace features in the surface topography further confirms the epitaxial nature of the films.

The temperature dependent magnetization (M-T) was measured using ZFC, FCC, and FCW protocols. The ZFC, FCC, and FCW data plotted in Fig. 1 show several interesting features, viz., (i) huge irreversibility in the ZFC and FCW curves, (ii) pronounced hysteresis between the FCC and FCW curves, (iii) reversible behavior of FCC and FCW curves below T ≈ 26 K, (iv) a peak in the FCW M-T around $T_P \sim 43$ K, and (v) sharp drop in ZFC M-T curve around T_P. The ZFC-FCW irreversibility, which is distinct from that of a representative spin glass state,[17] is invariably observed in phase separated manganites as a signature of cluster glass state.[18–20] The cluster glass state is prevalent in the intermediate bandwidth manganites having $x \sim 1/2$[18] or over a wide range of divalent doping (x) in low bandwidth manganites[19,20] and originates due to the coexistence of FMM and AFM/COI phases below the Neel temperature T_N. The sharp drop in the ZFC curve observed at temperature marked T_P is a signature of cluster freezing. The prominent FCC-FCW hysteresis is signature of the different magneto-thermodynamics of the system in the two protocols and arises due to the global frustration created by the AFM/COI phase that increases the energy

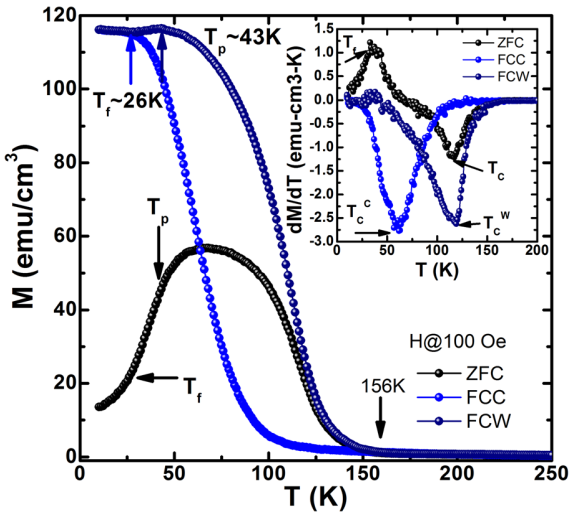

FIG. 1. The temperature dependence of ZFC, FCC, and FCW magnetization measured at H = 100 Oe. The inset shows the temperature derivative of the ZFC, FCC, and FCW curves. Various transitional features are marked in the figure.

of the system and also the degeneracy of the energy minima. Hence, the origin of the non-ergodicity is traceable to the AFM/COI phase, which alone can create frustration. The low temperature (T < 26 K) reversible behavior of the FCC and FCW has been regarded as a signature of an equilibrium state attained in the FCC protocol by Ghivelder and Parisi[9] and could be related to the blocking of system or freezing of the cluster glass. The increase in magnetization at T > 26 K is the signature of unblocking of the system states, and hence, the peak at $T_P \sim 43$ K can be regarded as the onset of cluster freezing.

The FM transition, determined from the derivative of M-T data (inset of Fig. 1), occurs at $T_C \approx 117$ K, $T_C^C \approx 63$ K, and $T_C^W \approx 120$ K in the ZFC, FCC, and FCW protocols, respectively. The protocol dependence of FM transition temperature could be regarded as evidence of non-ergodicity. A significantly lower value of FM transition temperature in FCC protocol can be considered as a consequence of supercooling,[10] whereas the FCW FM transition at $T_C^W \approx 120$ K can be taken as the equilibrium FM transition. The COI and AFM transitions are not explicit in the M-T data. This could be attributed to defect induced quenching of AFM/COI in thin film form.[12–16]

The drastic difference between the FM transition temperatures in FCC and FCW protocols can be understood in terms of the accommodation strain arising due to the distinct structural symmetry of the coexisting FM (pseudocubic) and AFM/COI (orthorhombic) phases.[11,21] The accommodation strain and the magnetic frustration induced by AFM order would create multiple minima in the energy landscape of the system and hence could hinder the nucleation of the equilibrium low temperature state. Such a scenario in turn could give rise to a liquid like magnetic phase.[9] The electrical transport characteristics of the magnetic liquid phase should depend on the relative fractions of FM and AFM/COI phases at the instant from where the low temperature state is arrived. Hence, IMT temperature (T_{IM}) corresponding to liquid like magnetic phase should be non-unique and depend on the magneto-thermodynamic path used to access the low temperature state of the system. In view of the variation in the relative fractions of FM and AFM/COI phases across T_C^W, T_{IM} must be a function of the temperature (T*) corresponding to the initial state of the magneto-thermodynamic process. This was experimentally verified by temperature dependent resistivity (ρ-T) measurement using a protocol in which the magneto-thermodynamic cycle was started from a temperature (T*), which was achieved by cooling the sample from room temperature to 6 K and subsequent warming up to T*. ρ-T was measured during cooling and warming employing the cycle T* → 6 K → T ($T > T_{IM}^W$) at H = 0 and H = 10 kOe. In view of the M-T data present above, it is obvious that each T* corresponds to a distinct ratio of FMM and AFM/COI phases. Here, we would like to mention that the impact of thermal cycling on the thermoresistive hysteresis, IMT, and peak resistivity in phase separated manganites has also been studied previously.[22,23] Mahendiran *et al.*,[22] employing a protocol of measurement different from the one used in the present case, have shown that (i) the resistivity close to and just below IMT is unstable, (ii) the resistivity increases with respect to thermal cycling, and (iii) the ρ-T

This article is copyrighted as indicated in the article. Reuse of AIP content is subject to the terms at: http://scitation.aip.org/termsconditions. Downloaded to IP: 14.139.251.110 On: Fri, 13 Jun 2014 06:42:17

behaviour is hysteretic even when the sample is warmed from just above the IMT. These studies have outlined the important role of strain and percolation in electrical transport in phase separated manganites.

The full cycle (300 K → 6 K → 300 K) ρ-T taken during cooling and warming (cooling and warming rate 1 K/min) is plotted in Fig. 2(a). In the cooling cycle IMT occurs at $T_{IM}^{C} \approx 64$ K, where ρ drops by more than four orders of magnitude within a narrow temperature window. This is generally attributed to the abrupt enhancement in the FMM fraction at the cost of the AFM/COI.[3] During the warming cycle, the ρ-T curve shows a minimum at $T_m \approx 45$ K and IMT appears at $T_{IM}^{W} \approx 123$ K. The rapid rise in resistivity just below T_{IM}^{W} corresponds to the enhanced fraction of the AFM/COI. The huge thermo-resistive hysteresis in the ρ-T curve and large $\Delta T_{IM} = T_{IM}^{W} - T_{IM}^{C} \approx 59$ K unravels the strongly phase separated nature of the system. The T_{IM}^{C} almost coincides with the FCC $T_C^{C} \approx 63$ K, while $T_{IM}^{W} \approx 123$ K is very close to $T_C^{W} \approx 120$ K. It is believed that the drastically lowered T_{IM}^{C} and T_C^{C} is caused by supercooling of the phase separated magnetic liquid consisting of FMM and AFM/COI sub-lattices.[7–13]

The zero filed cooling and warming cycle ρ-T data acquired after cooling from different T* is plotted in Figs. 2(b)–2(f). When the film is cooled down from T* ≈ 97 K, IMT not is observed in the cooling cycle. However, for all higher values of T*, IMT appears in the cooling cycles at temperature that we denote by which we denote by $T_{IM}^{C^*}$. The value of $T_{IM}^{C^*}$ for T* ≈ 105 K, 113 K, 117 K, 122 K, and 143 K are observed to be 103 K, 95 K, 88 K, 79 K, and 69 K, respectively. For values of T* ≥ 170 K, the $T_{IM}^{C^*}$ saturates to

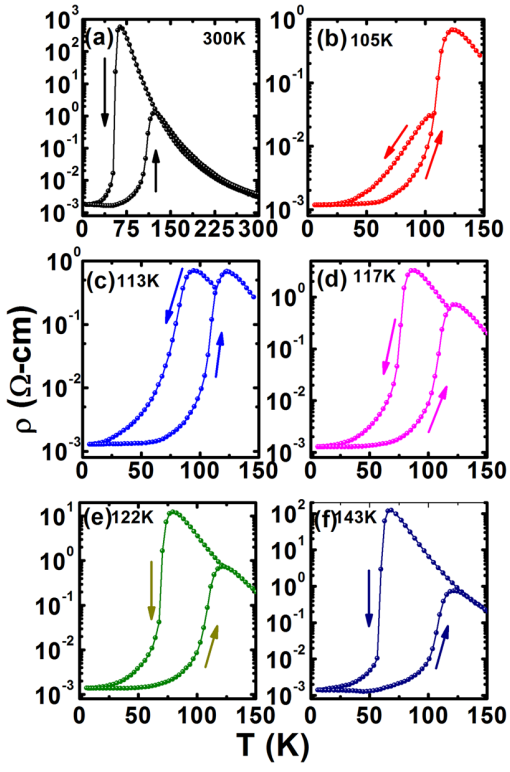

FIG. 2. Temperature dependence of resistivity measured in zero magnetic field in cooling and warming cycles after initial cooling to 6 K and subsequent warming to different T*.

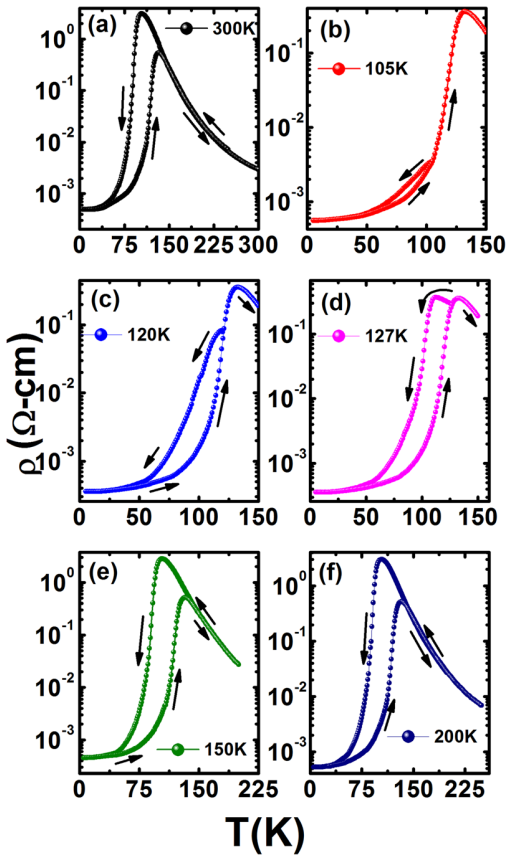

FIG. 3. Temperature dependence of resistivity measured in a magnetic field of H = 10 kOe in cooling and warming cycles after initial cooling to 6 K and subsequent warming to different T*.

$T_{IM}^{C} \approx 64$ K, the full cycle value. Interestingly, the warming cycle IMT, $T_{IM}^{W^*}$ remains independent of T*. The field (H = 10 kOe) cooling and warming cycle ρ-T data acquired after cooling from different T* are plotted in Fig. 3. The full cycle ρ-T shows $T_{IM}^{C} \approx 104$ K and $T_{IM}^{W} \approx 133$ K. At H = 10 kOe, the cooling cycle IMT shows an increase of 40 K, which, however, is only 10 K in the warming cycle. This could be attributed to the substantial suppression of AFM induced frustration in the phase separated regime. For T* = 105 K, no IMT was observed in cooling cycle, while in warming cycle IMT was observed at $T_{IM}^{W^*} \approx 133$ K. The absence of IMT for T* = 105 K shows that at this temperature the film has a dominant FMM fraction. For higher T* ($<T_{IM}^{W}$), e.g., 120 K and 127 K, IMT occurs at $T_{IM}^{C^*} \sim 119$ K and 112 K, respectively, was observed in the cooling cycle but the warming cycle IMT remained constant at $T_{IM}^{W^*} \approx 133$ K (Fig. 3). For further higher values of T* = 150 K, 200 K, and 300 K, both $T_{IM}^{C^*}$ and $T_{IM}^{W^*}$ remain constant at 104 K and 133 K, respectively. The variation of $T_{IM}^{C^*}$ and the corresponding peak resistivity measured in the cooling cycle (ρ_{IMC}) are plotted in Figs. 4(a) and 4(b), respectively. From Fig. 4, it is clear that the relative fraction of the FMM and AFM phases also controls the resistivity (ρ_{IMC}) at $T_{IM}^{C^*}$. The difference of more than two orders of magnitude in ρ_{IMC} measured at H = 0 and 10 kOe clearly reflects the colossal magnetoresistance effect. Another interesting feature seen in the zero field warming ρ-T data is the appearance (disappearance) of resistivity minimum ρ_m (T_m)

This article is copyrighted as indicated in the article. Reuse of AIP content is subject to the terms at: http://scitation.aip.org/termsconditions. Downloaded to IP: 14.139.251.110 On: Fri, 13 Jun 2014 06:42:17

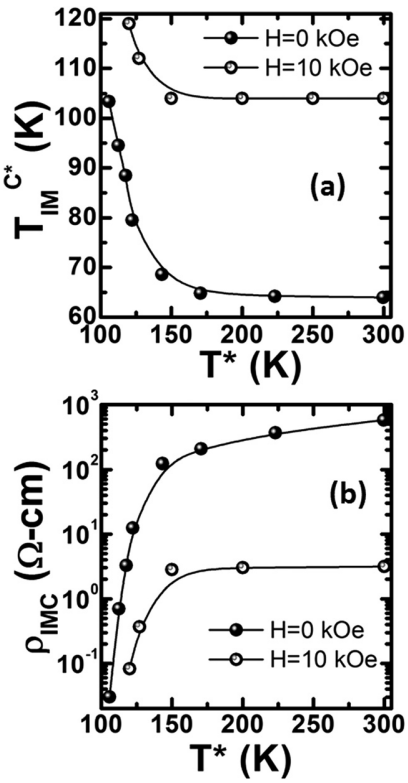

FIG. 4. (a) The variation of the T_{IM}^{C*} as a function of the characteristic temperature T^* measured at H = 0 and 10 kOe. (b) The variation of the peak resistivity measured in the cooling cycle as a function of T^*.

for all $T^* \geq 143$ K ($\leq$122 K). In the measurements carried out at H = 10 kOe, no ρ_m (T_m) is observed at all. When the sample is cooled from a T* at which the either FMM is in minority or absent, T_{IM}^{C*} saturates to the lowest value $T_C^C \approx 64$ K and the resistivity minimum reappears. This clearly shows that the AFM fraction is a key to the occurrence of resistivity minimum and is probably related to the freezing of the strain glass state.

The existence of different T_{IM}^{C*} for different $T^* < T_{IM}^W$ is an unambiguous signature of non-ergodicity, which in the present case arises due the existence of different energy configuration for each magneto-thermodynamic path. At $T^* > T_{IM}^W$, the fraction of FMM (AFM/COI) phase decreases (increases), leading to dilution of the competitive phase coexistence tendency and therefore no modulation of the IMT. The results presented above clearly show that the supercooling transition temperature is strongly dependent on T*, i.e., on the relative fraction of the two coexisting phases (FMM and AFM/COI) and hence the degree of magnetic frustration at the temperature from where the system is cooled down to access the low temperature state.

To conclude, we have shown that the electrical transport in a strongly phase separated manganite thin film is extremely sensitive to the relative fraction of the coexisting FMM and AFM/COI phases and has inherent non-ergodicity. The phase separation tendency is weakened when the fraction of AFM/COI phase is reduced. The supercooling insulator-metal transition is non-unique and depends on the relative fractions of the FMM and AFM phases at the start of the magneto-thermodynamic process. In contrast, the superheating transition has equilibrium characteristic and remains independent of the ratio of the two ordered phases.

Authors are grateful to Professor R. C. Budhani for his persistent encouragement. Dr. Anurag Gupta and Dr. V. P. S. Awana are thankfully acknowledged for magnetic (MPMS-DST facility) and magnetotransport measurement, respectively.

[1]E. Dagotto, T. Hotta, and A. Moreo, Phys. Rep. **344**, 1 (2001).
[2]E. Dagotto, New J. Phys. **7**, 67 (2005).
[3]Y. Tokura, Rep. Prog. Phys. **69**, 797 (2006).
[4]H. Kuwahara, Y. Tomioka, A. Asamitsu, Y. Moritomo, and Y. Tokura, Science **270**, 961 (1995).
[5]Y. Tomioka, H. Hiraka, Y. Endoh, and Y. Tokura, Phys. Rev. B **74**, 104420 (2006).
[6]M. K. Srivastava, A. Kaur, K. K. Maurya, V. P. S. Awana, and H. K. Singh, Appl. Phys. Lett. **102**, 032402 (2013).
[7]M. Uehara, S. Mori, C. H. Chen, and S.-W. Cheong, Nature **399**, 560 (1999).
[8]L. Ghivelder and F. Parisi, Phys. Rev. B **71**, 184425 (2005).
[9]P. A. Sharma, S. B. Kim, T. Y. Koo, S. Guha, and S.-W. Cheong, Phys. Rev. B **71**, 224416 (2005).
[10]W. Wu, C. Israel, N. Hur, S. Park, S.-W. Cheong, and A. de Lozanne, Nature Mater. **5**, 881 (2006).
[11]V. Podzorov, B. G. Kim, V. Kiryukhin, M. E. Gershenson, and S.-W. Cheong, Phys. Rev. B **64**, 140406R (2001).
[12]T. Dhakal, J. Tosado, and A. Biswas, Phys. Rev. B **75**, 092404 (2007).
[13]H. Jeen and A. Biswas, Phys. Rev. B **88**, 024415 (2013).
[14]T. Z. Ward, S. Liang, K. Fuchigami, L. F. Yin, E. Dagotto, E. W. Plummer, and J. Shen, Phys. Rev. Lett. **100**, 247204 (2008).
[15]V. G. Sathe, A. Ahlawat, R. Rawat, and P. Chaddah, J. Phys. Condens. Matter **22**, 176002 (2010).
[16]S. Singh, M. R. Fitzsimmons, H. Jeen, A. Biswas, and M. E. Hawley, Appl. Phys. Lett. **101**, 022404 (2012).
[17]J. A. Mydosh, *Spin Glasses: An Experimental Introduction*, 2nd ed. (Taylor & Francis, London, 1993).
[18]R. Prasad, M. P. Singh, P. K. Siwach, A. Kaur, P. Fournier, and H. K. Singh, Appl. Phys. A **99**, 823 (2010).
[19]V. Agarwal, R. Prasad, M. P. Singh, P. K. Siwach, A. Srivastava, P. Fournier, and H. K. Singh, Appl. Phys. Lett. **96**, 052512 (2010).
[20]M. K. Srivastava, P. K. Siwach, A. Kaur, and H. K. Singh, Appl. Phys. Lett. **97**, 182503 (2010).
[21]P. Littlewood, Nature **399**, 529–530 (1999).
[22]R. Mahendiran, A. Maignan, M. Hervieu, C. Martin, and B. Raveau, J. Appl. Phys. **90**, 2422 (2001).
[23]J. Fan, L. Pi, and Y. Zhang, J. Magn. Magn. Mater. **307**, 186 (2006).

This article is copyrighted as indicated in the article. Reuse of AIP content is subject to the terms at: http://scitation.aip.org/termsconditions. Downloaded to IP: 14.139.251.110 On: Fri, 13 Jun 2014 06:42:17

IOSR Journal of Business and Management (IOSR-JBM)
e-ISSN: 2278-487X, p-ISSN: 2319-7668. Volume 16, Issue 6. Ver. II (Jun. 2014), PP 203-209
www.iosrjournals.org

The Effect of Recession on the Buying Behavior of Consumers in New Delhi during the Economic Slowdown of 2013

Saurabh Kumar[1], Devika Singh[2]
[1](Department of Mechanical Engineering, Delhi Technological University, India)
[2](Vivekananda Law School, Vivekananda Institute of Professional Studies, India)

Abstract: *The research scouts out on the influence of recession on the purchasing deportment of consumers. The study was conducted in the West Delhi region. The purpose of this study was to examine the effect of recession on buying attitude of consumers, taking into consideration differences in spending in their goods consumption on different food, convenience and luxury items. With further expounding into the enquiry of change in shopping patterns of customers due to increase in prices or decrease in income and to analyze whether decrease in purchasing capacity of the customers have adulterated their preference for branded products. The results were checked in accordance with whether recession affects the buying behavior or not. Therefore, an attempt was put to find out the outcomes of the research that, which factors get affected in recession by a consumer.*

Keywords: *Consumer Behavior , Recession, Purchasing Power, Buying Behavior.*

I. Introduction

"The paradigm of a smoothly adjusting system of largely competitive markets that produces what consumers want, provides rewards appropriate to effort, and is assured of stable economic growth though Keynesian macroeconomic policies lost its credibility".

Rise in prices of food items and basic necessities of life due to inflation, unemployment, and low GDP creates a pre-recessionary situation which slowly and gradually affects the buying behavior of consumer of every market. Any nation going through the period of recession faces not only an internal resistance from its business sector and but also an external pressure from foreign bodies too. It becomes almost impossible for low income family to fulfill their basic requirements of daily life. Families with an average monthly income becomes hand to mouth and savings are almost none. Whereas families having earnings of more than one family member, tries to limit their budget and go for more savings for future, as it becomes very un-predictable[1]. In 2009, global real GDP fell by 0.7%, marking the first decline since the early 1930s and prompting some to compare the current crisis with the Wall Street Crash of 1929 and the Great Depression. Although global GDP rose by 5.1% the following year, fueled largely by strong growth in developing markets, the world's advanced economies continued to suffer from significant job losses, drastic cuts in consumer spending and private investment, as well as an alarming dip in global demand for consumer goods and services of all types. Growth is thought to have slowed to 4% in 2013, as consumer confidence remained low in the face of economic uncertainty Lekachman rejects the view of the economy as "an engine powered by uncovered inner motivated decisions of legions of ardently competing businessmen and hordes of their customers" and the contention that "success is ultimately related to individual merit and application" .Consumer behavior is the study of when, why, how, what and where consumers do or do not buy the products. It has elements of sociology, social, anthropology, psychology and economics, marketing wherein understanding how and why people behave in different situations with same or different circumstances[2].

The decision making procedure is subjected to various attitudes, and social influence on the purchaser. Buyer be likely to behave in certain manner including loyalty, habits, brand, and post purchase behavior.

All categories of products are not equally affected by recession. The demand for luxury goods are strongly affected while necessity goods do not experience any such large deviation in demand. However, it is many times experienced that gold, though being a luxury item, achieves a rise in its demand because of high probability of greater returns. In times of recession every rupee matters and hence the consumers use greater discretion before making the purchase decisions [3]. They refrain themselves from trying new brands and they continue to use the brands that they trust. As a result, businesses often find it difficult to position their brands in a market during a recession.

A recession is considered less harmful than depression and once it gets continued for a longer term it is than classified under depression. Many professionals and experts around the globe believe that a genuine economic recession can only be confirmed upon the negative growth of GDP for more then two following quarters. Whereas the "two quarter" definition is accepted worldwide, many economists have problem in

supporting this entire concept totally as it does not reflects on other key economic variables which might be bringing changes in economic system of a country[4].

Causes of Recession

As per Sunkel and Osvaldo, 1958, One thing that every economist firmly believes in is that recessions are somewhat that cannot be avoided. The reason for this is that in a strong economy you have stages of high growth, slow growth and no growth. In fact even fifty years after the great Depression, a really bad recession, and the answers to what causes an economic downturn or a recession is still a huge mystery. Despite of which theory you believe there is no specific answer to what causes a recession[5]. The following negative items that could cause an economic recession-

- Value of local currency going down
- Rise in Oil prices
- Inflation
- Unemployment
- Housing Bubble
- Global Economy

II. Purpose Of Study

This study aims to investigate the effect of recession on customer buying behavior during the economic slowdown of 2013 in India. The study is focused on reviewing related articles and getting the desired results through surveys of individual respondents. By doing so, the study aims at acquiring the perceptions of knowledgeable individuals about the topic. Moreover, the study aims at focusing on the following:

- To study the effect of decrease in income due to recession on different food, convenience and luxury items.
- To study the change of shopping patterns of customers due to increase in prices or decrease in income.
- To know whether decrease in purchasing capacity of the customers have adulterated their preference for branded products.

III. Research Methodology

A survey was conducted in a region of west Delhi, with the total number of respondents being 100. The sample space is divided on the basis of age and family income. All the respondents are not related to each other in any manner. The three divisions of sample space on the basis of family income(in rupees) are: (i)below 1 lakh (ii) 1 lakh to 4 lakhs (ii) above 4 lakhs. It is assumed that the opinions of one respondent cannot affect the opinions of any other respondent. The results are expressed in the form of percentages.

IV. Hypotheses

1. The taste of customer remains constant.
2. Higher amount of money is spent on shopping by those customers who shop more frequently.
3. Higher fluctuations for luxury items are experienced by those who shop more frequently than regular customers.
4. The level of knowledge about branded products among the customers is same.
5. Income has a significant effect on the consumer buying behavior.
6. Recession has significant effect on consumer buying behavior for shopping goods, convenience goods, and luxury items.

V. Objectives

1. To study the effect of change in income on consumer behavior.
2. To study the effect of change in price of luxury goods on consumer behavior.
3. To study the effect of change in income of consumer and price of commodity on brand preference.
4. To study the effect of change in income on the shopping patterns of the consumers.

VI. Problem Statement

Due to the economic slowdown during a large duration of year 2013, the consumers suffered with a decrease in their purchasing capacity. Due to this, there was a change in consumption patterns of consumers. The study aims at finding these patterns distinctively and pointing out exceptions, if any.

VII. Division Of Sample Space

Variable	Characteristic	Number Of Respondents	Total
AGE (years)	Below 22 22-30 Above 30	11 37 52	100
FAMILY INCOME (Rupees/Annum)	Below 100000 100000-400000 Above 400000	34 17 49	100

VIII. Observations and Results

- Impact of recession on income

RESPONSE	RESPONDENTS
INCREASED	**18**
DECREASED	**41**
REMAINED SAME	**36**
DON'T KNOW	**5**

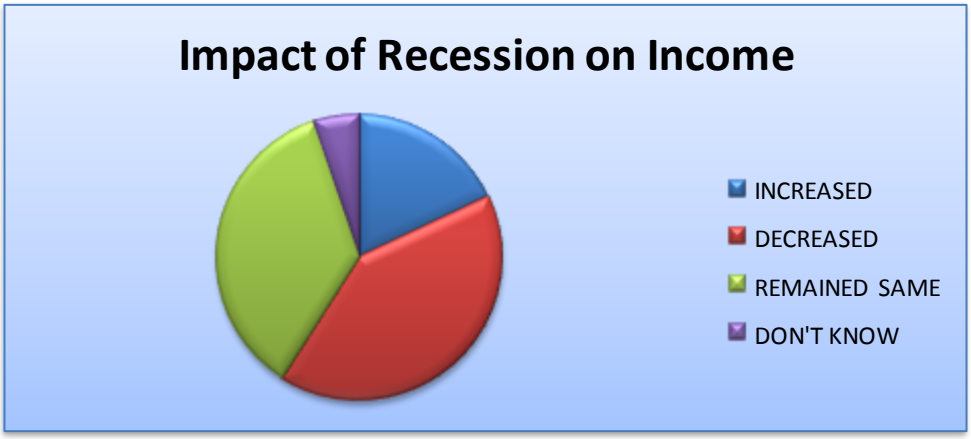

- Change in demand of gold due to increase in prices

RESPONSE	RESPONDENTS
INCREASED	30
DECREASED	42
REMAINED SAME	28

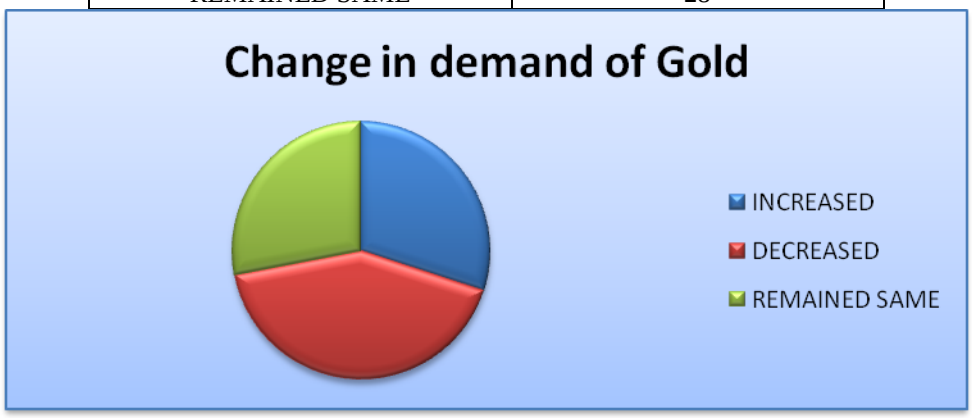

- Change in demand of inferior food products due to change in income or change in prices of normal goods:

RESPONSE	RESPONDENTS	
	INCREASE IN INCOME	DECREASE IN INCOME
INCREASED	1	29
DECREASED	12	4
REMAINED SAME	5	8
OTAL	18	41

- The distribution of expenditure(preference for products):

VARIABLE	RESPONDENTS
GROCERIES	46
PERSONAL CARE ITEMS	15
APPAREL AND ACCESSORIES	13
FURNITURE	17
OTHERS	9

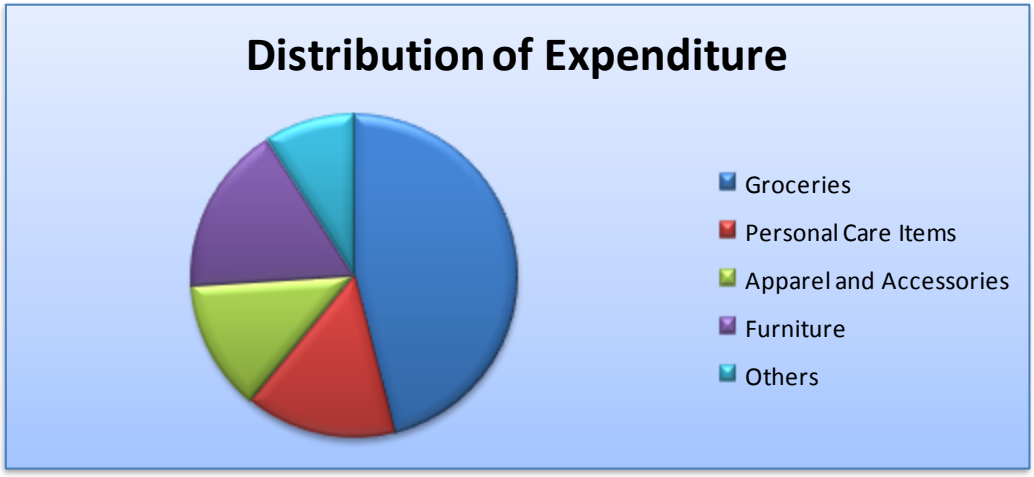

- Decrease of frequency of shopping:

RESPONSE	RESPONDENT
YES	53
NO	34
MAY BE	13

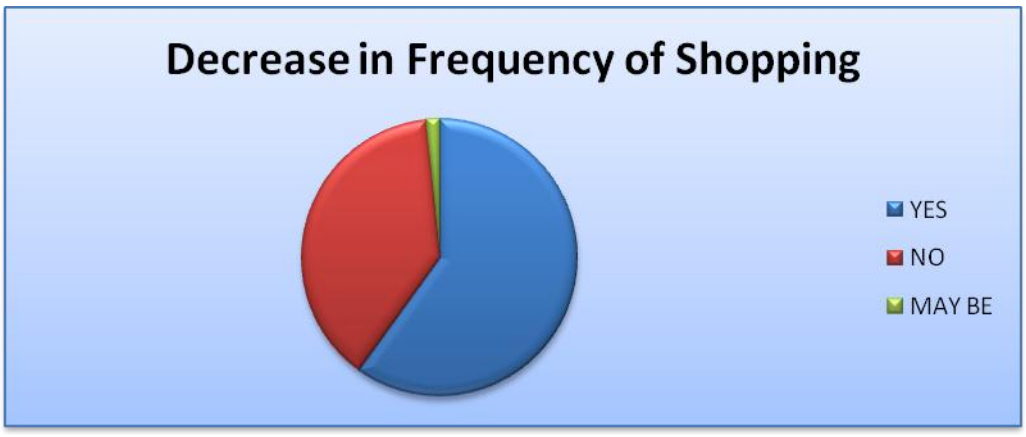

Change from Retail Store to *Kirana* Store (Grocery Store)

RESPONSE	RESPONDENT
YES	39
NO	27
NEVER VISITED RETAIL STORE	34

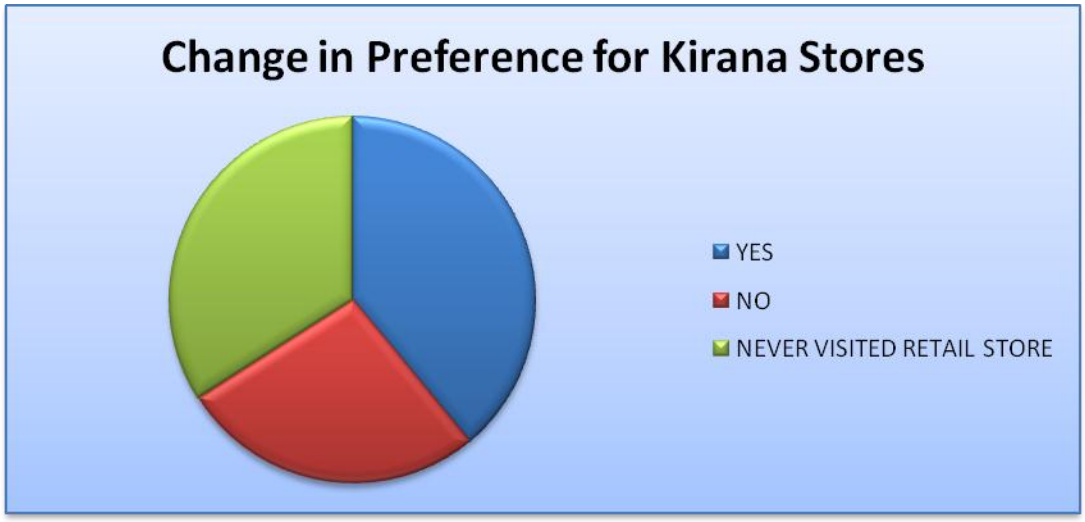

- Decrease in purchase of luxury items:

RESPONSE	RESPONDENT
YES	42
NO	21
NOT APPLICABLE	37

- In times of recession, most important factor before making a buying decision

RESPONSE	RESPONDENT
Price	31
Quality	27
Deals	11
Brand	22
Pleasure	9

- In times of recession, the preference of brand on the basis on family income:

INCOME (per annum)	RESPONSE	RESPONDENT
BELOW 100000	YES NO MAYBE	12 19 3
100000-400000	YES NO MAYBE	7 6 4
ABOVE 400000	YES NO MAYBE	27 14 8

IX. Major Findings

- A majority of 41% people expressed to have a decrement in family income in the time of recession during 2013.
- Even due to increase in prices of gold in last two quarters of 2013, there was an increase in its demand for 30% respondents. This can be attributed to the fact that gold is an article of distinction and hence treated by high class people as an item of luxury. Also, people usually invest in gold with an expectation of receiving higher returns in future.
- There was a 30% increase in the demand for inferior food products during the period. This is because, the demand for Giffen goods increase with decrease in purchasing power of consumer.
- In times of hardships, 46% respondents admitted to have a preference for basic necessities like groceries and cut down on luxuries like apparels, accessories, etc.
- 53% respondents reported a decrease in frequency of shopping.
- 42% respondents admitted to have cut down on purchasing luxury goods.
- As high as 39% respondents substituted Retail stores for *Kirana* (Grocery) Stores in search for lower prices.
- Preference for branded products took a back seat during time of recession, where 31% respondents admit to have preferred a product after considering its price.

X. Conclusion

The purpose of the study was to understand the effect of economic slowdown of 2013 on buying behavior of customers of New Delhi. The customer's buying behavior is conditioned by his/her purchasing power. This

purchasing power took a huge downturn due to increasing inflation and decreasing incomes in the year 2013. To conduct the research, a questionnaire administered survey has been conducted among 100 residents of west Delhi and the data revealed that with less money in hand, the consumer preference towards necessities increased whereas purchase of luxury items decreased, gold being an exception. In times of hardships, the branded products lost their cause to prices with people turning towards inferior quality products.

References

[1]. Kiran Sharma, Impact of recession on buying behavior of Indian Consumers, International Review of Business Research Papers Vol. 7. No. 1. January 2011. Pp. 381- 392.

[2]. Flatters, Paul, Willmott, Michael, Understanding the Post-Recession Consumers Harvard Business Review, 00178012, Jul/Aug2009, Vol. 87, Issue 7/8

[3]. Nithila Vincent, *A Study on Brand Consciousness Among Children and its Effect on Family Buying Behaviour in Bangalore City, Indian Journal of Marketing, Volume XXXVI* • Number 1 • January 2006

[4]. Stayman, D.M. and Deshpande, R. (1989), *"Situational Ethnicity and Consumer Behaviour", Journal of Consumer Research, 16*, December, pp. 361-371.

[5]. Schiffman and Kannuk, *Conumer Behaviour , Pearson 4th edition ,* (1991)

[6]. Alba, J.W. and Hutchinson, J.W. (1988), *"Dimensions of Consumer Expertise", Journal of Consumer Research, 13*, March, pp. 411-454.

[7]. Keller, K. L., *(2008) Strategic Brand Management, Second Edition, Prentice Hall of India*, New Delhi.

[8]. Alba, J.W. and Hutchinson, J.W. (1988), "Dimensions of Consumer Expertise", Journal of Consumer Research, 13, March, pp. 411-454.

[9]. Blythe, J. 2006 *Essentials of Marketing Communications. 3rd Edition Pearson Education Limited*. Essex (UK)

[10]. Bettman, J.R. and Zins, M.A. (1977), *"Constructive Processes in Consume Choice", Journal of Consumer Research, 4, September*, pp. 75-85.

[11]. Dr. A. C. Pandey and Mithilesh Kumar Pandey, IMPACT OF LIFESTYLE ON BRAND PREFERENCE OF BUYER BEHAVIOUR: A CASE STUDY OF UTTARAKHAND, International Monthly Refereed Journal of Research In Management & Technology, ISSN – 2320-0073, Volume II, August'13.

[12]. Anjali Sharma, Shruti Bhola, Shweta Malyan and Neha Patni ,Impact of Brand Loyalty on Buying Behavior of Women Consumers for Beauty Care Products- Delhi Region, Global Journal of Management and Business Studies. ISSN 2248-9878 Volume 3, Number 7 (2013), pp. 817-824

[13]. A Report by Stan Maklan, Professor Simon Knox and Kate Watson, "How is Consumer Behaviour affected

[14]. by Online Relationships?", Sponsored by The Chartered Institute of Marketing: E-Branding Forum.

[15]. R DU PREEZ, APPAREL SHOPPING BEHAVIOUR – PART 1: TOWARDS THEDEVELOPMENT OF A CONCEPTUAL THEORETICAL MODEL, SA Journal of Industrial Psychology, 2003, 29 (3), 11-14.

[16]. Hellmut Schutte, Consumer Behavior in Asia, Insead Euro-Asia Center, February 1995.

[17]. Vikram Shende, Analysis of Research in Consumer Behavior of Automobile Passenger Car Customer, International Journal of Scientific and Research Publication, Volume 4, Issue 2, February 2014.

[18]. Dr Pooja Bhatia, A Factorial Study of Consumer Buying Behaviour towards Durable Goods With Reference To Urban Working Women, International Journal on Recent and Innovation Trends in Computing and Communication ISSN: 2321-8169,Volume: 2 Issue: 3.

[19]. Sakshi Modi, Consumer Buying Behaviour: Changing Shopping Patterns, *Journal of Consumer Research, 4, Ocrober*, pp. 21-32.

[20]. Geeta Sonkusare, Impact of television advertising on buying behavior of women consumers' [With special reference to FMCG Products] Chandrapur city, International Journal of Business and Management Invention.

[21]. Verma Priyanka, An On-Field-Survey of the Impulse Buying Behaviour of Consumers in Consumer non Durable Sectors in the Retail Outlets in the City of Indore, India. *Research Journal of Management Sciences* ISSN 2319–1171. Vol. 1(4), 1-5, November (2012)

[22]. Rita Kuvykaite1, Aistė Dovaliene2, Laura Navickiene3 (2009), Impact of package elements on the consumer purchase decision economics & management.

[23]. Rundh, B. (2005). The multi-faceted dimension of packaging. British Food Journal, 107 (9), 670-684.

[24]. S Bed (2008), new consumer products branding, packaging and labeling in Nepal, the Journal of Nepalese business studies, Vol. V No. 1

[25]. S Nuntasaree and Dr. E Barry (2008), a model of male consumer behavior in buying skin care products in Thailand, ABAC Journal Vol. 29, No. 1.

[26]. L Renaud(2007), The influence of label on wine consumption : its effects on young consumers' perception of authenticity and purchasing behavior, Bologna, Italy.

[27]. Adelina Broadbridge & Henry Morgan (2007), consumer buying behavior and perception toward retail brand baby products.

Volume 2 (2014) 325-332 ISSN 2347 - 3258
International Journal of Advance Research and Innovation

Thermodynamic Performance Evaluation of Multi-Evaporators single Compressor and single Expansion Valve and Liquid Vapour Heat Exchanger in Vapour Compression Refrigeration systems using Thirteen Ecofriendly Refrigerants for Reducing Global Warming and Ozone Depletion

R. S. Mishra
Department of Mechanical & Production Engineering, Delhi Technological University, New Delhi, India

Article Info
Article history:
Received 5 January 2014
Received in revised form
20 March 2014
Accepted 28 April 2014
Available online 15 June 2014

Keywords
Vapour Compression Refrigeration Systems,
Energy and Exergy Analysis,
First and Second Law Analysis,
Irreversibility Analysis,
VCR with LVHE

Abstract
The methods for improving first law and second law efficiency have been considered in this paper by using liquid vapour heat exchanger is investigated in this paper. Detailed energy and exergy analysis of multi-evaporators at different temperatures with single compressor and single expansion valve using liquid vapour heat exchanger vapour compression refrigeration systems have been done in terms of performance parameter for R507a, R125, R134a, R290, R600, R600a, R1234ze, R1234yf, R410a, R407c, R707, R404a and R152a refrigerants. The numerical computations have been carried out for both systems. It was observed that first law and second law efficiency improved by 20% using liquid vapour heat exchanger in the vapour compression refrigeration systems. It was also observed that performance of both systems using R717 is higher but R600 and R152a nearly matching same values under the accuracy of 5% can be used in the above system .But difficulties using R152a, R600, R290 and R600a have flammable problems therefore safety measures are required using these refrigerants. Therefore R134a refrigerant is recommended for practical and commercial applications although it has slightly less thermal performance than R152a which is not widely used refrigerant for domestic and industrial applications

1. Introduction

Technology of refrigeration is absorbs heat at low temperature sink and provides temperature below the surrounding by rejecting heat to the surrounding at higher temperature. The refrigeration system of two type such as air refrigeration system and vapour refrigeration system. Vapour refrigeration systems can be classified as vapour absorption system and vapour compression system. The vapour absorption system of two types such as NH3-H20 system and LIBR systems working on single effect, half effect, double effect and Tripple effect. The simple vapour compression system which consists of four major components compressor, expansion valve, condenser and evaporator in which total cooling load is carried at one temperature by single evaporator but in many applications like large hotels, food storage and food processing plants, food items are stored in different compartment and at different temperatures. Therefore there is need of multi evaporator vapour compression refrigeration system. The use suction heat exchanger or liquid vapour regenerative heat exchanger in vapor compression system is justified because superheating in liquid suction exchanger is preferable to superheating in evaporator itself

The systems under vapour compression technology consume huge amount of electricity, this problem can be solved by improving performance of system. Performance of systems based on vapour compression refrigeration technology can be improved by following:

The performance of refrigerator is evaluated in term of first law efficiency which is known as coefficient of performance (COP) which is the ratio of refrigeration effect to the net work input given to the system. The COP of vapour compression refrigeration system can be improved either by increasing refrigeration effect or by reducing work input given to the system. It is well known that throttling process in VCR is an irreversible expansion process. Expansion process is one of the main factors responsible for exergy loss in cycle performance because of entering the portion of the refrigerant flashing to vapour in evaporator which will not only reduce the cooling capacity but also increase the size of evaporator. This problem can be eliminated by adopting multi-stage expansion with flash chamber where the flash vapours is removed after each stage of expansion as a consequence there will be increase in cooling capacity and reduce the size of the evaporator.

Work input can also be reduced by replacing multi-stage compression or compound compression with single stage compression.

Refrigeration effect can also be increased by passing the refrigerant through subcooler after condenser to evaporator.

Vapour compression refrigeration system based applications make use of refrigerants which are responsible for greenhouse gases, global warming and ozone layer depletion. Montreal protocol was signed on the issue of substances that are responsible for depleting Ozone layer and discovered how much consumption and production of

Corresponding Author,
E-mail address: professor-rsmishra@yahoo.co.in
All rights reserved: http://www.ijari.org

ozone depletion substances took place during certain time period for both developed and developing countries. Another protocol named as Kyoto aimed to control emission of green house gases in 1997[1]. The relationship between ozone depletion potential and global warming potential is the major concern in the field of GRT (green refrigeration technology) so Kyoto proposed new refrigerants having lower value of ODP and GWP. Internationally a program being pursued to phase out refrigerants having high chlorine content for the sake of global environmental problems [2].Due to presence of high chlorine content ,high global warming potential and ozone depletion potential after 90's CFC and HCFC refrigerants have been restricted. Thus, HFC refrigerants are used nowadays, showing much lower global warming potential value, but still high with respect to non-fluorine refrigerants. Lots of research work has been done for replacing "old" refrigerants with "new" refrigerants [3-8].

2. Literature Review

Reddy et al. [9] performed numerical analysis of vapour compression refrigeration system using R134a, R143a, R152a, R404A, R410A, R502 and R507A, and discussed the effect of evaporator temperature, degree of subcooling at condenser outlet, superheating of evaporator

outlet, vapour liquid heat exchanger effectiveness and degree of condenser temperature on COP and exergetic efficiency. They reported that evaporator and condenser temperature have significant effect on both COP and exergetic efficiency and also found that R134a has the better performance while R407C has poor performance in all respect.

Selladurai and Saravana kumar [10] compared the performance between R134a and R290/R600a mixture on a domestic refrigerator which is originally designed to work with R134a and found that R290/R600a hydrocarbon mixture showed higher COP and exergetic efficiency than R134a. In their analysis highest irreversibility obtained in the compressor compare to condenser, expansion valve and evaporator. **Nikolaidis and Probert [11]** studied analytically that change in evaporator and condenser temperatures of two stage vapour compression refrigeration plant using R22 add considerable effect on plant irreversibility. They suggested that there is need for optimizing the conditions imposed upon the condenser and evaporator. **Kumar et al. [12]** did energy and exergy analysis of vapour compression refrigeration system by the use of exergy-enthalpy diagram. They did first law analysis (energy analysis) for calculating the coefficient of performance and exergy analysis (second law analysis) for evaluation of various losses occurred in different components of vapour compression cycle using R11 and R12 as refrigerants. **Mastani Joybari et al.[13]** performed experimental investigation on a domestic refrigerator originally manufactured to use of 145g of R134a.They concluded that exergetic defect occurred in compressor was highest as compare to other components and through their analysis it has been found that instead of 145g of R134a if 60g of R600a is used in the considered system gave same performance which ultimately result into economical advantages and reduce the risk of flammability of hydrocarbon refrigerants. **Anand and Tyagi [14]** did detailed exergy analysis of 2 ton of refrigeration capacity window air conditioning test rig with R22 as working fluid and reached to the conclusions , that irreversibility in system components will be highest when the system is 100% charged and lowest when 25% charged and irreversibility in compressor is highest among system components. **Arora and Kaushik [7]** developed numerical model of actual vapour compression refrigeration system with liquid vapour heat exchanger and did energy and exergy analysis on the same in the specific temperature range of evaporator and condenser and concluded that R502 is the best refrigerant compared to R404A and R507A and compressor is the worst component and liquid vapour heat exchanger is best component of the system in case of exergy transfer. **Ahamed et al. [17]** had performed experimental investigation of domestic refrigerator with hydrocarbons (isobutene and butane) by energy and exergy analysis. They reached to the results that energy efficiency ratio of hydrocarbons comparable with R134a but exergy efficiency and sustainability index of hydrocarbons much higher than that of R134a at considered evaporator temperature. It was also found that compressors shows highest system defect (69%) among components of considered in the system. **Ahamed et al. [15]** emphasized on use of hydrocarbons and mixture compressor shows much higher exergy destruction as compared to rest of components in the vapour compression refrigeration system and this exergy destruction can be minimized by using of nanofluid and nanolubricants in compressor. **Bolaji et al. [18]** had done experimentally comparative analysis of R32, R152a and R134a refrigerants in vapour compression refrigerator and concluded that R32 shows lowest performance whereas R134a and R152a showing nearly same performance but best performance was obtained of system using R152a. **Yumrutas et al. [19]** carried out exergy analysis based investigation of effect of condensing and evaporating temperature on vapour compression refrigeration cycle in terms of pressure losses, COP, second law efficiency and exergy losses. Variation in temperature of condenser as well as have negligible effect on exergy losses of compressor and expansion valve, also first law efficiency and exergy efficiency increase but total exergy losses of system decrease with increase in evaporator and condenser temperature. **Padilla et**

al. [20] exergy analysis of domestic vapour compression refrigeration system with R12 and R413A was done. They concluded that performance in terms of power consumption, irreversibility and exergy efficiency of R413A is better than R12, so R12 can be replaced with R413A in domestic vapour compression refrigeration system. **Getu and Bansal [21]** had optimized the design and operating parameters of like condensing temperature, subcooling temperature, evaporating temperature, superheating temperature and temperature difference in cascade heat exchanger R744-R717 cascade refrigeration system. A regression analysis was also done to obtain optimum thermodynamic parameters of same system. **Spatz and Motta [22]** had mainly focused on replacement of R12 with R410a through experimental investigation of medium temperature vapour compression refrigeration cycles. In terms of thermodynamic analysis, comparison of heat transfer and pressure drop characteristics, R410a gives best

performance among R12, R404a and R290a. **Mohanraj et al. [23]** concluded through experimental investigation of domestic refrigerator they arrived on conclusions that under different environmental temperatures COP of system using mixture of R290 and R600a in the ratio of 45.2: 54.8 by weight showing up to 3.6% greater than same system using R134a, also discharge temperature of compressor with mixture of R290 and R600a is lower in the range of 8.5-13.4K than same compressor with R134a. **Han et al. [24]** Under different working conditions experimental results revealed that there could be replacement of R407C in vapour compression refrigeration system having rotor compressor with mixture of R32/R125/R161 showing higher COP, less pressure ratio and slightly high discharge compressor temperature without any modification in the same system. **Halimic et al. [25] had** compared performance of R401A, R290 and R134A with R12 by using in vapour compression refrigeration system, which is originally designed for R12.Due to similar performance of R134a in comparison with R12, R134A can be replaced in the same system without any medication in the system components. But in reference to green house impact R290 presented best results. **Xuan and Chen [26]** presented in this manuscript about the replacement of R502 by mixture of HFC-161 in vapour compression refrigeration system and conducted experimental study it was found that mixture of HFC-161 gives same and higher performance than R404A at lower and higher evaporative temperature respectively on the vapour compression refrigeration system designed for R404A. **Cabello et al. [27]** had studied about the effect of operating parameters on first law efficiency (COP), work input and cooling capacity of single-stage vapour compression refrigeration system. There is great influence on energetic parameters due change in suction pressure, condensing and evaporating temperatures. **Cabello et al. [28] discussed the** effect of condensing pressure, evaporating pressure and degree of superheating was experimentally investigated on single stage vapour compression refrigeration system using R22, R134a and R407C.It was observed that mass flow rate is greatly affected by change in suction conditions of compressor in results on refrigeration capacity because refrigeration capacity depended on mass flow rate through evaporator. It was also found that for higher compression ratio R22 gives lower COP than R407C. **Stanciu et al. [29]**did numerical and graphical investigation on one stage vapour compression refrigeration system for studied refrigerants (R22, R134a, R717, R507a, R404a) in terms of COP, compressor work, exergy efficiency and refrigeration effect. Effect of subcooling, superheating and compression ratio are also studied on the same system using considered refrigerants and also presented system optimization when working with specific refrigerant in the vapour compression.

Based on the literature it was observed that researchers have gone through detailed first law analysis in terms of coefficient of performance and second law analysis in term of exergetic efficiency of simple vapour compression refrigeration system with single evaporator. Researchers did not go through the irreversibility analysis.

This paper maily deal with the thermodynamic analysis of simple VCR with liquid vapour heat exchanger using thirteen eco friendly refrigerants

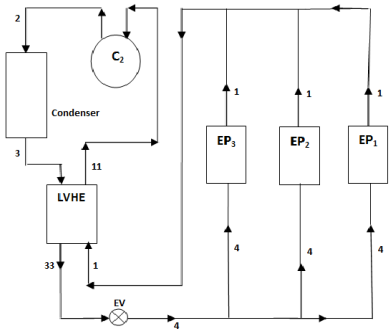

Fig: 1(a). Schematic diagram of actual multi evaporator with single compressor and single expansion valve and LVHE

To improve thermal performance of vapour compression refrigeration systems both multiple evaporator system by using liquid vapour heat exchanger for improving: First law efficiency (COP) , second law efficiency (Exergetic efficiency) and Reduction of system defect in components of system in terms of exergy destruction ratio which results into reduction of work input The multiple evaporators at the same temperature with single compressor and single expansion valve and liquid vapour heat exchanger vapour compression refrigeration system.

2.1 Mass of refrigerant flowing through each evaporator

$$m_1 = \frac{Q_1}{h_1 - h_4} \quad (1)$$

$$m_2 = \frac{Q_2}{h_1 - h_4} \quad (2)$$

$$m_3 = \frac{Q_3}{h_1 - h_4} \quad (3)$$

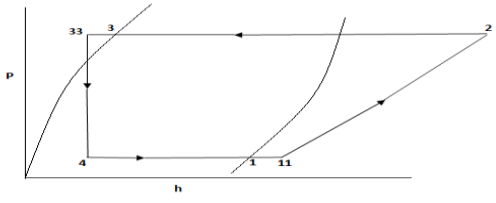

Fig: 1(b). Pressure enthalpy diagram of actual multi evaporator with single compressor, and single expansion valve and LVHE

2.2 Work required to run the compressor

$$W_{comp} = (m_1 + m_2 + m_3)(h_2 - h_1) \quad (4)$$

According to the first law of thermodynamics, coefficient of performance () defined as the ratio of the net refrigeration effect produced per unit of work input. It is given as

2.3 Coefficient of performance

$$\beta = \frac{Q_1+Q_2+Q_3}{W_{comp}} \quad (5)$$

Second law analysis (exergy analysis) According to second law thermodynamic loss of work input required to drive the system due to irreversibility occur in various states (f1 and f2) for a steady flow system is given as components of the system. Irreversibility in each component by neglecting the kinetic energy an potential energy of the system as per Eqs. (6)– (13) specified below

$$\Phi_{e1} = \chi_4 - \chi_1 + Q_1\left(1-\frac{T_0}{T_1}\right)$$
$$= m_1(h_4 - T_0 s_4) - m_1(h_1 - T_0 s_1) + Q_1\left(1-\frac{T_0}{T_1}\right)$$

(6)

$$\Phi_{e2} = \chi_4 - \chi_1 + Q_2\left(1-\frac{T_0}{T_1}\right)$$
$$= m_2(h_4 - T_0 s_4) - m_2(h_1 - T_0 s_1) + Q_2\left(1-\frac{T_0}{T_1}\right)$$

(7)

$$\Phi_{e3} = \chi_4 - \chi_1 + Q_3\left(1-\frac{T_0}{T_1}\right)$$
$$= m_3(h_4 - T_0 s_4) - m_3(h_1 - T_0 s_1) + Q_3\left(1-\frac{T_0}{T_1}\right)$$

(8)

Compressor

$\Phi_{comp} = \chi_{11} - \chi_2 + W_{comp} = m((h_{11} - h_2) - T_o(s_{11} - s_2)) + m(h_2 - h_{11}) = m T_o(s_2 - s_{11})$ (9)

Condenser

$\Phi_c = \chi_2 - \chi_3 = m((h_2 - h_3) - T_o(s_2 - s_3))$ (10)

Expansion Valve

$\Phi_{ev} = \chi_{33} - \chi_4 = m((h_{33} - h_4) - T_o(s_{33} - s_4))$
$= m(T_o(s_4 - s_{33}))$ (11)

Liquid vapour heat exchanger

$\Phi_{lvhe} = (\chi_1 - \chi_{11}) + (\chi_{x3} - \chi_{x33}) = m((h_1 - T_o s_1) - (h_{11} - T_o s_{11})) + m((h_3 - T_o s_3) - (h_{33} - T_o s_{33}))$ (12)

3.1 Total destruction

$\Phi_{total} = \Phi_e + \Phi_{comp} + \Phi_c + \Phi_{ev} + \Phi_{lvhe}$ (13)

3.2 Second law efficiency

It is defined as the ratio of exergy in product in the work required to drive the system

$$\text{Exergy output} = (Q_1 + Q_2 + Q_3)\left|\left(1-\frac{T_0}{T_1}\right)\right|$$

(14)

$$\eta_{ex} = \frac{Exergy\ Output}{Exergy\ Input} = (Q_1 + Q_2 + Q_3)\left|\left(1-\frac{T_0}{T_1}\right)\right| \Big/ W_{comp}$$

EDR is the ratio of total irreversibility in the system to the exergy product

$$EDR = \frac{\Phi_{total}}{(Q_1 + Q_2 + Q_3)\left|\left(1-\frac{T_0}{T_1}\right)\right|} \quad (16)$$

3. Results and Discussions

Using Engineering Equation Solver software [9] a numerical model is developed for tfirst law and second law analysis of the multi evaporators VCR for enhancing thermal performances. The performance parameters are calculated by assuming following specifications: Adiabatic efficiency of compressor (ζ_{comp}):75% Condenser temperature (T_c): 313K. Dead state temperature (T_0): 298K. Variation of evaporator's temperature (T_e):223K to273K. Dead state enthalpy (h_0) and entropy (s_0) of the refrigerants have been calculated corresponding to the dead state temperature (T_0) of 298K. Degree of superheating of vapour refrigerant in liquid vapour heat exchanger before compression (ΔT_{sh}): 10K. Effectiveness of the liquid vapour heat exchanger is 100%. Degree of sub cooling of liquid refrigerant in the liquid vapor heat exchanger (ΔT_{sc}): 10K. Loads on the evaporators EP1, EP2 and EP3 are 35KW, 70KW and 105KW respectively.

Fig.2 presents the variation of first law efficiency (coefficient of performance) with the evaporator temperature at 313K condenser temperature. The COP will increase with evaporator temperature this is due to the fact that COP is the ratio of the net refrigeration effect of the work required to drive the compressor, compressor work will go down due to reduction in pressure on the other hand refrigeration effect will also enhance, So COP will increase. It was observed that COP of the system using R134a and R1234ze nearly matching same values.R134a and R1234ze show better COP than R-1234yf.Although R134a having a high global warming potential (GWP) and responsible for global warming. The maximum difference observed between COPs of R134a and R1234yf is (2%-6%).

Effect of increase in evaporator temperature on second law efficiency has shown in Fig. 3. As clear from Fig.3 that exergetic efficiency increase with increase in evaporator temperature but it should be cleared that this increment up to an optimal value of evaporator temperature after that exergetic efficiency goes down with increase in evaporator temperature. R1234ze shows the lowest value of exergetic efficiency among considered refrigerants. The percentage increase in second law efficiency of R1234ze as compared with R1234yf at 243K, 248K, 253K, 258K, 263K, 268K and 273K evaporator temperature are 4.57%, 4.33%, 4.07%, 3.80%, 3.55%, 3.30% and 3.06% respectively. System defect provides the information about of amount of loss of work input (exergy) given to the system. As shown in Fig.4 that the highest system defect occurs in R1234yf.it was also observed that system defect in R1234ze only 1% higher than R134a, but with the increase in evaporator temperature this problem is eliminated. The maximum difference in system defect of R1234yf comparison with R134a is 3.7 % at 248K evaporator temperature. Fig.5 shows the effect of degree of sub cooling on COP. It is evident that sub cooling increases refrigeration capacity whereas there is no change in compressor work, hence COP increases. Both R134a and R1234ze presents maximum COP (3.18) by the 10K degree of sub cooling than R1234yf.Thus sub cooling responsible for the betterment for system performance. The effect of sub cooling on second law efficiency shown Fig.6 reveals that

both R134a and R1234ze shows better exergetic efficiency than R1234yf It is observed from Fig.7 and Fig.8 that trends of COP and exergetic efficiency are almost same for selected refrigerants, both COP and exergetic efficiency will decrease with increase in condenser temperature. Both COP and exergetic efficiency of R134a and R1234ze are 3.7 % and 3.9% at 314K condenser temperature higher than R1234yf.

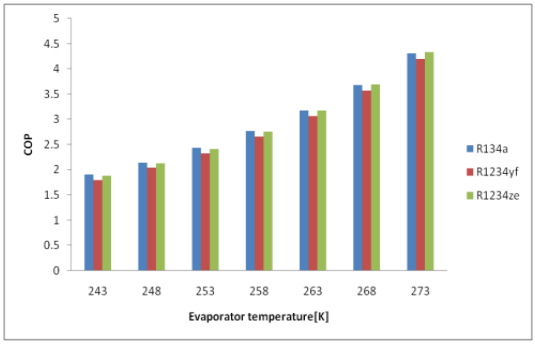

Fig: 2. Variation of COP with evaporators' temperatures

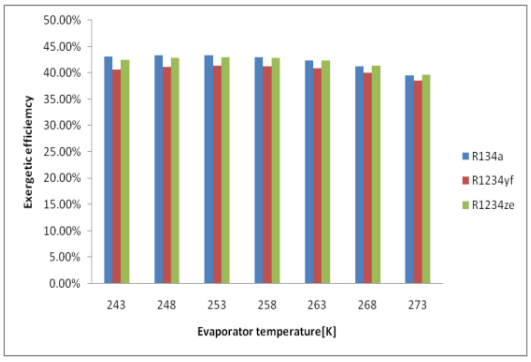

Fig: 3. Variation of exergetic efficiency with evaporators' temperatures

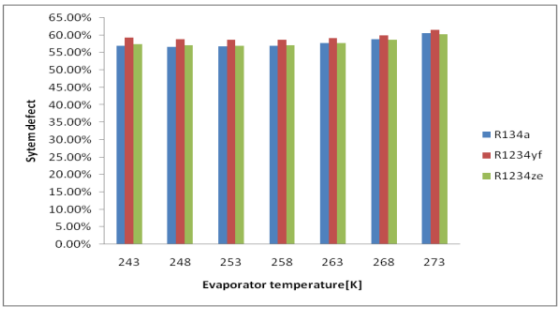

Fig: 4. Variation of system defect with evaporator temperatures

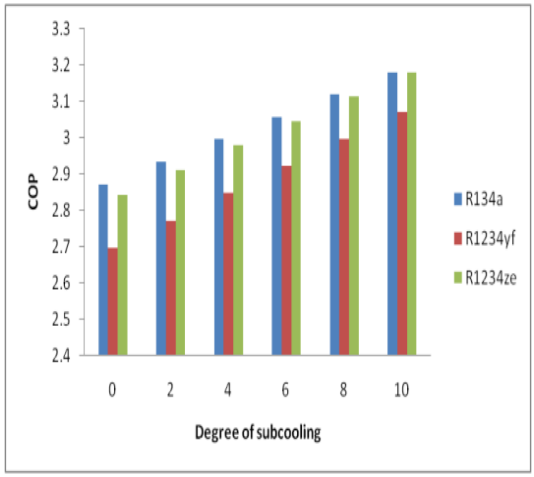

Fig: 5. Variation of COP with degree of sub cooling at condenser outlet

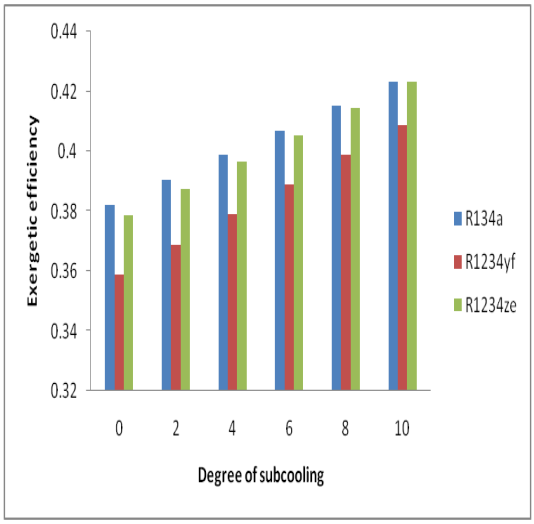

Fig: 6. Variation of exergetic efficiency with degree of sub cooling at condenser outlet

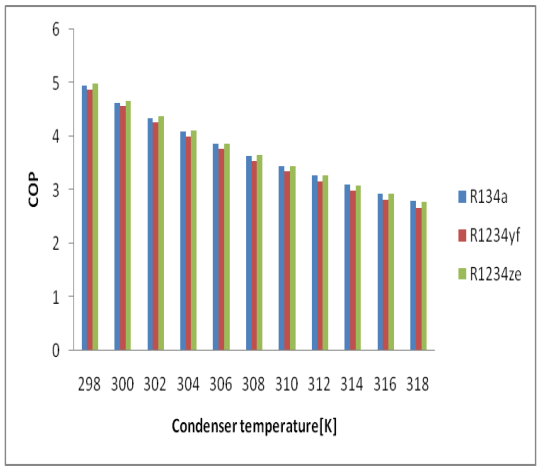

Fig: 7. Variation of COP with condenser temperature

4. Conclusions

In this paper, first law and second law analysis of an actual multi-evaporators vapour compression refrigeration system using ecofriendly refrigerants (R134a, R1234yf, and R1234ze) have been presented.

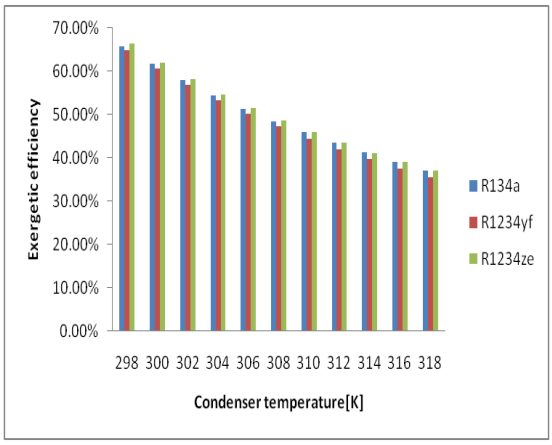

Fig: 8. Variation of exergetic efficiency with condenser temperature Conclusion

First law and second law efficiency for R134a and R1234ze are matching the same values, both are better than that for R123yf and showing 2–6% higher value of COP and second law efficiency in comparison to R123yf. Both energetic and exergetic efficiency increase with increase in degree of subcooling It was found that energetic and exergetic efficiency greatly affected by changes in evaporator and condenser temperature. R1234ze is the best among considered refrigerant since it has 238 times lower GWP values than R134a and R1234ze is ecofriendly has both ODP and GWP are lowest.

Table: 1. Multiple evaporator single compression single expansion valve vapour compression refrigeration system using eco friendly refrigerants with LVHE

Eco friendly Refrigerant	$COP_{WITH\ LVHE}$	EDR	Exergetic Efficiency
R290	3.052	1.462	0.4062
R404A	2.747	1.735	0.3656
R410A	2.931	1.564	0.390
R134A	3.104	1.421	0.4131
R152A	3.227	1.328	0.4295
R600	3.234	1.324	0.4303
R600A	3.122	1.407	0.4155
R407C	2.62	1.868	0.3487
R507A	2.80	1.683	0.3727
R1234YF	2.964	1.535	0.3945
R1234ZE	3.086	1.435	0.4107
R717	3.205	1.345	0.4265
R125	2.628	1.859	0.3497

Table: 2. Multiple evaporator single compression single expansion valve vapour compression refrigeration system using eco friendly refrigerants without LVHE

Refrigerant	$COP_{WITHOUT\ LVHE}$	EDR	Exergetic Efficiency
R290	2.97	1.53	0.3952
R404A	2.626	1.862	0.3495
R410A	2.858	1.63	0.3803
R134A	3.022	1.486	0.4022
R152A	3.177	1.365	0.4228
R600	3.161	1.377	0.4207
R600A	3.032	1.478	0.4035
R407C	2.541	1.958	0.3381
R507A	2.678	1.806	0.3564
R1234YF	2.854	1.633	0.3798
R1234ZE	2.991	1.512	0.3980
R717	3.21	1.341	0.4271
R125	2.473	2.039	0.3291

Table: 3. Multiple evaporator single compression single expansion valve vapour compression refrigeration system using eco friendly refrigerants with LVHE

Eco friendly Refrigerant	$COP_{WITH\ LVHE}$	EDR	Exergetic Efficiency
R290	3.052	1.462	0.4062
R404A	2.747	1.735	0.3656
R410A	2.931	1.564	0.390
R134A	3.104	1.421	0.4131
R152A	3.227	1.328	0.4295
R600	3.234	1.324	0.4303
R600A	3.122	1.407	0.4155
R407C	2.62	1.868	0.3487
R507A	2.80	1.683	0.3727
R1234YF	2.964	1.535	0.3945
R1234ZE	3.086	1.435	0.4107
R717	3.205	1.345	0.4265
R125	2.628	1.859	0.3497

Table: 4. Multiple evaporator single compression single expansion valve vapour compression refrigeration system using eco friendly refrigerants without LVHE

Eco friendly Refrigerant	$COP_{WITHOUT\ LVHE}$	EDR	Exergetic Efficiency
R290	2.97	1.53	0.3952
R404A	2.626	1.862	0.3495
R410A	2.858	1.63	0.3803
R134A	3.022	1.486	0.4022
R152A	3.177	1.365	0.4228
R600	3.161	1.377	0.4207
R600A	3.032	1.478	0.4035
R407C	2.541	1.958	0.3381
R507A	2.678	1.806	0.3564
R1234YF	2.854	1.633	0.3798
R1234ZE	2.991	1.512	0.3980
R717	3.21	1.341	0.4271
R125	2.473	2.039	0.3291

5. Results and Discussions and Conclusions

In this paper, first law and second law analysis of vapour compression refrigeration systems using multiple

evaporators and single compressor and single expansion valve with thirteen eco friendly refrigerants have been presented. The conclusions of the present analysis are summarized below:

1. The First law efficiency (COP) and Second law efficiency (Exergetic efficiency) of vapour compression refrigeration systems using liquid vapour heat exchanger and multiple evaporator and single compressor and single expansion valve is higher than without liquid vapour heat exchanger for above mentioned ecofriendly refrigerants.
2. The First law efficiency (COP) and Second law efficiency (Exergetic efficiency) of vapour compression refrigeration systems using R717 refrigerant is higher but is has toxic nature can be use by using safety measure for industrial applications.
3. COP and exergetic efficiency for R152a and R600 are nearly matching the same values.are better than that for R125 at 313K condenser temperature and showing higher value of COP and exergetic efficiency in comparison to R125.
4. For practical applications R-134a is recommended because it is easily available in the market has second law efficiency slightly lesser than R-152a which was not applicable for commercial applications.
5. The worst component from the viewpoint of irreversibility is expansion valve followed by condenser, compressor and evaporators, respectively. The most efficient component found to be subcooler. The R-152a has least efficiency defects for 313K condenser temperature.
6. The increase in dead state temperature has a positive effect on exergetic efficiency and EDR, i.e. EDR decreases and exergetic efficiency increases with increase in dead state temperature. Both R-152a and R-600 show the identical trends for exergetic efficiency are nearly overlapping. The exergetic efficiency for R-600 is higher than that of R-134a for the practical range of dead state temperature considered.

References

[1] E. Johnson, Global warming from HFC. Environ. Impact Asses, 1998, 18:485-492
[2] QiyuChen, R. C Prasad, Simulation of a vapour compression refrigeration cycles HFC134A and CFC12.Int Comm, Heat Mass Transfer, 1999, 26:513-521
[3] M. Padilla, R. Revellin, J. Bonjour, Exergy analysis of R413A as replacement of R12 in a domestic refrigeration system. Int J Energy Conversion and Management, 2010, 51:2195-2201
[4] H. O. Spauschus, HFC 134a as a substitute refrigerant for CFC 12, Int J of Refrigeration, 1988, 11:389-392
[5] J. U. Ahamed, R. Saidur, H. H. Masjuki, A review on exergy analysis of vapor compression refrigeration system. Int J Renewable and sustainable energy reviews, 2011, 15:1593-1600
[6] R. Llopis, E. Torrella, R. Cabello, D. Sánchez. Performance evaluation of R404A and R507A refrigerant mixtures in an experimental double-stage of vapour compression plant, Int J Applied Energy, 2010, 87:1546-1553
[7] Akhilesh Arora, S. C. Kaushik, Theoretical analysis of a vapour compression refrigeration system with R502, R404A and R507A. Int J Refrigeration, 2008, 31:998-1005
[8] V. Havelsky, Investigation of refrigerating system with R12 refrigerant replacements, Int J Applied Thermal Engineering, 2000, 20:133-140
[9] V. Siva Reddy, N. L Panwar, S. C Kaushik, Exergy analysis of a vapour compression refrigeration system with R134a, R143a, R152a, R404A, R407C, R410A, R502 and R507A, Clean Techn Environ Policy, 2012, 14:47-53
[10] R. Saravanakumar, V. Selladurai, Exergy analysis of a domestic refrigerator using eco-friendly R290/R600a refrigerant mixture as an alternative to R134a, Int J Therm Anal Calorim, 2013
[11] C. Nikolaidis, D. Probert, Exergy method analysis of a two-stage vapour-compression refrigeration-plants Performance, Int J Applied Thermal Engineering, 1998, 60:241-256
[12] S. Kumar, M. Prevost, R. Bugarel, Exergy analysis of a vapour compression refrigeration system. Heat Recovery Systems & CHP, 1989, 9:151-157
[13] Mahmood Mastani Joybari, Mohammad Sadegh Hatamipour, Amir Rahimi, Fatemeh Ghadiri Modarres, Exergy analysis and optimization of R600a as a replacement of R134a in a domestic refrigerator system. International Journal of refrigeration, 2013, 36:1233-1242,
[14] S. Anand, S. K Tyagi, Exergy analysis and experimental study of a vapour compression refrigeration cycle, Int J Therm Anal Calorim, 2012, 110:961-971
[15] J. U Ahamed, R. Saidur, H. H Masjuki, M. A Sattar, An analysis of energy, exergy and sustainable development of a vapour compression refrigeration system using hydrocarbon, International journal of Green energy, 2012, 9:707-717
[16] Camelia Stanciu, Adina Gheorghian, Dorin Stanciu, Alexandru Dobrovicescu- Exergy analysis and refrigerant effect on the operation and performance lomits of a one stage vapour compression refrigeration system, Termotehnica, 2011, 1:36-42
[17] J. U. Ahamed, R. Saidur, H. H. Masjuki, A review on exergy analysis of vapor compression refrigeration system, Int J Renewable and sustainable energy reviews, 2011, 15:1593-1600
[18] B. O. Bolaji, M. A. Akintunde, T. O. Falade, Comparative analysis of performance of three ozone-friends HFC refrigerants in a vapor compression refrigerator, Int J Sustainable Energy & Environment, 2011, 2:61-64
[19] Recep Yumrutas, Mehmet Kunduz, Mehmet Kanoglu- Exergy analysis of vapor compression refrigeration systems. Exergy, An International Journal, 2002, 2:266-272

[20] M. Padilla, R. Revellin, J. Bonjour, Exergy analysis of R413A as replacement of R12 in a domestic refrigeration system. Int J Energy Conversion and Management, 2010, 51:2195-2201
[21] H. M Getu, P. K Bansal, Thermodynamic analysis of an R744-R717 cascade refrigeration system, Int J Refrigeration, 2008, 31:45-54
[22] Mark W. Spatz, Samuel F. Yana Motta. An evaluation of options for replacing HCFC-22 in medium temperature refrigeration systems, Int J Refrigeration, 2004, 27:475-483
[23] M. Mohanraj, S. Jayaraj, C. Muraleedharan, P. Chandrasekar, Experimental investigation of R290/R600a mixture as an alternative to R134a in a domestic refrigerator, Int J Thermal Sciences, 2009, 48:1036-1042
[24] X. H. Han, Q. Wang, Z. W. Zhu, G. M. Chen, Cycle performance study on R32/R125/R161 as an alternative refrigerant to R407C, Int J Applied Thermal Engineering, 2007, 27:2559-2565
[25] E. Halimic, D. Ross, B. Agnew, A. Anderson, I. Potts, A comparison of the operating performance of alternative refrigerants, Int J Applied Thermal Engineering, 2003, 23:1441-1451
[26] Yongmei Xuan, Guangming Chen, Experimental study on HFC-161 mixture as an alternative refrigerant to R502, Int J Refrigeration, Article in Press
[27] R. Cabello, J. Navarro-Esbrı, R. Llopis, E. Torrella, Analysis of the variation mechanism in the main energetic parameters in a single-stage vapour compression plant, Int J Applied Thermal Engineering, 2007, 27:167-176
[28] R. Cabello, E. Torrella, J. Navarro-Esbr, Experimental evaluation of a vapour compression plant performance using R134a, R407C and R22 as working fluids, Int J Applied Thermal Engineering, 2004, 24:1905-1917
[29] S. A. Klein, F. Alvarado, Engineering Equation Solver, 7.441, F Chart Software, Middleton, WI.2005
[30] I. Dincer, Refrigeration Systems and Applications, Wiley, UK, 2003:26